Geomechanical reservoir modeling – workflow and case study from the North German Basin

Dissertation

Vom Fachbereich Material- und Geowissenschaften
der Technischen Universität Darmstadt
zur Erlangung des akademischen Grades
Doktor der Naturwissenschaften (Dr. rer. nat.)
genehmigte Dissertation

TECHNISCHE UNIVERSITÄT DARMSTADT

von
M.Sc. Karsten Fischer
geboren am 27. Juni 1984 in Freiburg im Breisgau, Baden-Württemberg

Referent:	Prof. Dr. Andreas Henk
Korreferent:	PD Dr. Eckardt Stein

Tag der Einreichung: 11.September 2013
Tag der Disputation: 18.Oktober 2013

Darmstadt, September 2013
D 17

Vorsitzender der Prüfungskommission:	Prof. Dr. Ingo Sass	Technische Universität Darmstadt
Referent:	Prof. Dr. Andreas Henk	Technische Universität Darmstadt
Korreferent:	PD Dr. Eckardt Stein	Albert-Ludwigs-Universität Freiburg
Prüfer:	Prof. Dr. Christoph Schüth	Technische Universität Darmstadt
Prüfer:	Prof. Dr. Michael Alber	Ruhr-Universität Bochum

Abstract

There is an increasing importance for the optimal exploitation of conventional hydrocarbon reservoirs to have detailed knowledge of the specific state of stress in a reservoir and to gain clarity on the corresponding geomechanical implications. This knowledge is even becoming mandatory for most unconventional plays. The local stress field directly affects, for instance, wellbore stability, the orientation of hydraulically induced fractures, and – especially in fractured reservoirs – permeability anisotropies. Robust information on the locally prevailing stresses is thus ideally required prior to drilling. Numerical models based on the finite element (FE) method are able to cope with the complexity of real reservoirs. Acting as predictive tools, these models not only provide quantitative information on the stress distribution, but also a process-based understanding of geomechanical reservoir behavior.

This study evaluates the potential of geomechanical FE models for the prediction of local in situ stress distribution and fracture networks in faulted reservoirs. The work of this study was conducted in cooperation with three major operators in the E&P industry and comprises two main parts. In the first methodological part, a generally applicable workflow is developed for building geomechanical FE models and calibrating them to field data. These models focus on spatial variations of in situ stress resulting from faults and contrasts in mechanical rock properties. Special techniques are elaborated regarding the transfer of the reservoir geometry from geological subsurface models to the numerical model and for the most effective application of boundary conditions. Complex fault geometries and the detailed topology of lithostratigraphic horizons can be considered on reservoir scale. In combination with reservoir-specific material parameters the incorporated horizons establish a mechanical stratigraphy inside the model. Faults are implemented as discrete planes by 2D interface elements. This allows fault-specific stresses and corresponding fault behavior to be analyzed. The resulting geomechanical models comprise high spatial resolution and several million elements. They are calculated in time spans of less than 20 hours by using high-performance computing. In addition, submodels resolving a detailed mechanical stratigraphy can be integrated into the reservoir-wide modeling for local focus.

In the second part of the study, the workflow was successfully applied to an intensively faulted gas reservoir in the North German Basin. Comprehensive datasets are provided by the field operators and project partners for building and calibrating a detailed and truly field-scale geomechanical model covering more than 400km². It incorporates a network of 86 faults and a mechanical stratigraphy of three layers comprising reservoir-specific material parameters. For the static modeling approach, the present-day regional stress field is applied as boundary condition. Static modeling results are compared to local stress measurements, e.g. orientations from borehole breakouts and magnitudes from frac data. After iterative calibration, the best-fit model reveals the recent in situ stress distribution and individual fault behavior throughout the reservoir. The results show significant local perturbations of stress magnitudes (max. ±10MPa over 1-2km distance) and only minor deviations in stress orientation from the regional trend (max. ±25°). The strong dependency on the specific fault trace, offset and interactions precludes the derivation of generally valid rules for estimating stress variations and underlines the necessity of numerical modeling. Analysis of fault-specific results indicates that critical stress states occur most likely on NW-SE trending faults in the present-day stress field.

Fracture information is inferred from a (geo-)dynamic model focusing on the major stages in the tectonic history of the reservoir and the respective past in situ stresses. Consequently, paleo-stress fields are applied as boundary condition and material parameters are adjusted. Correlation of fracture

orientations and modeled paleo-stresses in the reservoir allows the formation of fracture sets to be assigned to Triassic and Late Jurassic to Early Cretaceous times. Increased perturbation intensity in the Late Jurassic to Early Cretaceous is related to potential reactivation of NW-SE trending faults and explains the variability of the corresponding fracture set. These results elucidate how stress perturbations can explain fracture variability without the need for complex tectonic histories.

Furthermore, the dynamic model sheds light on fault zone permeability. Modeling indicates that if cataclasis is responsible for a reduced fault permeability, then it will most likely occur along E-W and NNE-SSW trending faults due to the high slip tendency values they experienced in the tectonic past. Modeling results show no such increased geomechanical exposure for NW-SE oriented faults. However, high dilation tendencies support the possibility of activity of these faults in Late Jurassic times – as proposed by fracture correlation. Low permeability of NW-SE trending faults is thus most likely the result of fluid entry and illitization, which is also observed at a wellbore close to such a fault set.

The combination of static and dynamic modeling results suggests no significant impact of critically stressed natural fractures on the recent hydraulic behavior of the entire reservoir. Additionally tests of fault block refinements and submodels demonstrate their capability to provide further increased spatial resolution in areas of particular interest. The submodel generated for the northwestern part of the case study underlines the impact of the specific connections of the fault network on the modeling results.

The outcome of this study confirms the high potential of geomechanical FE models to reveal the specific in situ stress and fault behavior, and to infer fracture characteristics from paleo-stresses. Beside the case study specific insights, the successfully applied and approved workflow can be used for future modeling of stress-sensitive reservoirs. Furthermore, the geomechanical models are not limited in application to the hydrocarbon industry. As general tools for stress prediction in undrilled rock formations, they can also be applied to deep geothermal reservoirs and underground engineering, for instance. The possibility of characterizing fault behavior makes the models additionally valuable in the fields of carbon capture and storage (CCS) and nuclear waste disposal.

Zusammenfassung

Für die optimale Nutzung konventioneller Kohlenwasserstofflagerstätten gewinnt es zunehmend an Bedeutung, genaue Kenntnis über die tektonischen Spannungen in einer Lagerstätte zu besitzen, sowie Klarheit über die mit den Spannungen verbundenen geomechanischen Auswirkungen zu bekommen. Für die meisten unkonventionellen Lagerstätten ist dies sogar zwingend erforderlich. Das lokale Spannungsfeld beinflusst beispielsweise unmittelbar die Stabilität von Bohrungen, die Orientierung hydraulisch induzierter Klüfte, und Permeabilitätsanisotropien – insbesondere in geklüfteten Lagerstätten. Verlässliche Informationen über die lokal vorherrschenden Spannungen werden daher idealerweise vor Abteufen einer Bohrung benötigt. Numerische Modelle, die auf der Finiten Elemente (FE) Methode basieren, sind in der Lage die Komplexität realer Lagerstätten abzubilden. Als Vorhersagewerkzeug liefern diese Modelle nicht nur quantitative Informationen über die Spannungsverteilung, sondern auch ein prozess-basiertes Verständnis über das geomechanische Verhalten der Lagerstätte.

Diese Arbeit untersucht das Potenzial geomechanischer FE Modelle zur Vorhersage der lokalen in situ Spannungsverteilung und Kluftnetzwerke in störungsdurchzogenen Lagerstätten. Die Arbeiten wurden in Kooperation mit drei großen Betreibern der E&P Industrie durchgeführt und sind gegliedert in zwei Teile. Im ersten methodischen Teil wurde ein allgemein anwendbarer Arbeitsablauf für den Aufbau geomechanischer FE Modelle und deren Kalibration mit Lagerstättendaten entwickelt. Diese Modelle konzentrieren sich auf räumliche Veränderungen der in situ Spannungen durch Störungen und Unterschiede in den mechanischen Gesteinseigenschaften. Es wurden Verfahren für den Übertrag der Lagerstättengeometrie von geologischen Untergrundmodellen in das numerische Modell erarbeitet, sowie Methoden für die möglichst effektive Aufbringung der Randbedingungen. Komplexe Störungsgeometrien und die detaillierte Topologie lithostratigraphischer Horizonte können auf Lagerstättenmaßstab berücksichtigt werden. In Verbindung mit lagerstättenspezifischen Materialparametern bilden die einbezogenen Horizonte eine mechanische Stratigraphie innerhalb des Modells. Mit Hilfe zweidimensionaler Grenzflächenelemente werden Störungen als diskrete Flächen abgebildet. Dies ermöglicht die Analyse störungsspezifischer Spannungen und des damit verbundenen Verhaltens der Störungen. Die resultierenden geomechanischen Modelle besitzen eine hohe räumliche Auflösung und enthalten mehrere Millionen Elemente. Mit Hilfe von Hochleistungsrechnern und entsprechender Parallelisierung können diese Modelle in weniger als 20 Stunden berechnet werden. Darüber hinaus können so genannte Teilmodelle mit einer detailliert aufgelösten mechanischen Stratigraphie in die großräumige Modellierung integriert werden und diese lokal verbessern.

Im zweiten Teil der Arbeit wurde der Arbeitsablauf erfolgreich auf eine störungskontrollierte Gaslagerstätte im Norddeutschen Becken angewendet. Die Betreiber stellten als Projektpartner umfangreiche Datensätze zur Verfügung für den Aufbau und die Kalibration eines detaillierten geomechanischen Modells im Lagerstättenmaßstab. Dieses Modell umfasst die gesamte Lagerstätte mit einer Fläche von mehr als 400km². Es beinhaltet ein Störungsnetzwerk aus 86 Störungen, sowie eine mechanische Stratigraphie aus drei Lagen mit lagerstättenspezifischen Materialparametern. In einem statischen Modellierungsansatz dient das heutige überregionale Spannungsfeld als Randbedingung. Die Ergebnisse der statischen Modellierung wurden verglichen mit lokalen Spannungsmessungen, z.B. mit Orientierungen aus Bohrlochrandausbrüchen und Magnituden aus Frac-Daten. Nach iterativer Kalibration offenbart das Modell mit der besten Übereinstimmung die heutige in situ Spannungsverteilung und das individuelle Störungsverhalten in der gesamten Lagerstätte. Die Ergebnisse zeigen deutliche lokale Veränderungen der Spannungsmagnituden (max. ±10MPa auf 1-2km) und nur geringe Abweichungen vom regionalen Trend in den

Orientierungen (max. ±25°). Die Ableitung allgemein gültiger Regeln zur Abschätzung von Spannungsperturbationen wird verhindert durch deren starke Abhängigkeit vom genauen Störungsverlauf, der Versätze und Wechselwirkungen. Dies unterstreicht die Notwendigkeit numerischer Modellierung. Die Analyse der Störungsergebnisse zeigt, dass kritische Spannungen heutzutage am wahrscheinlichsten entlang NW-SE orientierter Störungen auftreten.

Kluftinformationen wurden aus einem (geo-)dynamischen Modell abgeleitet, welches die Hauptphasen der tektonischen Vergangenheit der Lagerstätte berücksichtigt und damit die vergangenen in situ Spannungen. Als Randbedinungen wurden daher Paläo-Spannungsfelder eingesetzt und Materialparameter entsprechend angepasst. Kluftorientierungen wurden mit modellierten Paläo-Spannungen in der Lagerstätte korreliert. Dies erlaubt die Zuordnung der Kluftbildungsphasen in die Zeit der Trias und des Oberjura bis Unterkreide. Erhöhte Intensität der Spannungsperturbationen im Oberjura und der Unterkreide wird mit einer potenziellen Reaktivierung von NW-SE orientierten Störungen in Verbindung gebracht und erklärt die Variabilität des entsprechenden Kluftsystems. Diese Ergebnisse verdeutlichen, wie Spannungsperturbationen Kluftvariabilität erklären können ohne komplizierte tektonische Entwicklungen.

Das dynamische Modell gibt außerdem Aufschluss über die Permeabilität von Störungszonen. Die Modellierungen deuten darauf hin, dass wenn Kataklase für niedrige Störungspermeabilitäten verantwortlich ist, dies am wahrscheinlichsten entlang E-W und NNE-SSW verlaufender Störungen der Fall ist aufgrund der hohen „Slip Tendency“ –Werte in deren tektonischer Vergangenheit. Die Modellierungsergebnisse zeigen keine solch hohe Beanspruchung für NW-SE orientierte Störungen. Allerdings unterstützen hohe „Dilation Tendency“ –Werte die Annahme aus der Kluftkorrelation, dass diese Störungen im Oberjura aktiv waren. Die niedrige Permeabilität NW-SE orientierter Störungen ist daher am wahrscheinlichsten auf Fluideintritt und Illitisierung zurückzuführen. Letzteres wurde in einer Bohrung nahe solcher Störungen auch beobachtet.

Die Kombination der statischen und dynamischen Modellierungsergebnisse deutet auf keinen signifikanten Einfluss natürlicher, kritisch gespannter Klüfte hin auf das heutige hydraulische Verhalten der Lagerstätte. Die zusätzlich getesteten Ansätze für Störungsblockverfeinerungen und Teilmodelle zeigen deren Potenzial für weiter erhöhte räumliche Auflösung in bestimmten Bereichen. Das erstellte Teilmodell des nordwestlichen Bereichs des Fallbeispiels verdeutlicht den Einfluss der genauen Verbindungen des Störungsnetzwerks auf die Modellierungsergebnisse.

Die Ergebnisse dieser Arbeit bestätigen das hohe Potenzial geomechanischer FE Modelle zur Offenlegung der spezifischen in situ Spannungen und des Störungsverhaltens, sowie zur Möglichkeit Kluftcharakteristika aus Paläo-Spannungen abzuleiten. Neben den gewonnenen Erkenntnissen über die Lagerstätte des Fallbeispiels kann der erfolgreich angewendete Arbeitsablauf zur zukünftigen Modellierung spannungssensitiver Lagerstätten benutzt werden. Die geomechanischen Modelle sind in ihrer Anwendung jedoch nicht auf die Kohlenwasserstoffindustrie beschränkt. Als allgemeine Werkzeuge zur Vorhersage von Spannungen in nicht erbohrten Gesteinsformationen können sie beispielsweise auch in der Tiefengeothermie und Tiefbautechnik angewendet werden. Die Möglichkeit zur Charakterisierung des Störungsverhaltens macht die Modelle zudem wertvoll für die Gebiete der CO_2 Speicherung im Untergrund (CCS) und der Entwicklung atomarer Endlagerstätten.

Acknowledgment

The work of this study was accomplished in the framework of DGMK Research Project 721 funded by ExxonMobil Production Deutschland GmbH, GDF SUEZ E&P Deutschland GmbH and RWE Dea AG. Their support is gratefully acknowledged. Special thanks go to the corresponding company representatives for the great communication throughout the project, and the constructive critisism and helpful comments in the project meetings. By name, I thank especially Dr. Klaus Kronmüller, Dr. Thomas Degro, Thomas Mozer, Paul Krajewski, Dr. Antje Kellner, Dr. Christian Bücker, and Dr. Ingrid Winter.

First and foremost I thank Prof. Dr. Andreas Henk for the great opportunity to participate this research project and for the trust he had in me to accomplish the studies. I am very thankful for the countless discussions and overall outstanding supervision. He allowed me to work self-dependently and find my own ways – by always letting me know that there is an open ear. I enjoyed the great times at conferences and the local regeneration programs ranging from Heurigen in Vienna to Shrimper's Heaven in San Francisco. I also want to thank Dr. Eckardt Stein for the co-supervision of this work, his efforts in thoroughly reviewing the thesis and for the detailed feedback. I very much appreciated the close communication and honest advice.

Furthermore I am deeply grateful for the time at HTCO GmbH and the possibility to work with Dr. Axel Müller and Teodora Vatahska. Aside from university, I learned a lot from them about 3D modeling, meshing and numerical simulation in general. I always enjoyed the excellent teamwork, the friendly atmosphere and open communication. Both are shining examples for the fact that great work is based on passion for it. I am thankful for the possibility to benefit from their experience and expertise, and also for the time Dr. Axel Müller spent on reviewing the numerical part of this thesis.

Back in Freiburg, I was glad to have such great colleagues like Dr. Michael Poelchau, Gerwin Wulf and Sebastian Sturm, who were always helpful and open for serious scientific discussion – and fun. Thanks for the awesome times with hot wine in the cold, cool beer in the sun, and movies with beans. I am especially indebted to Michael for his effort in improving this thesis in linguistic issues. I hope I did not do too much harm to your mother tongue. Moreover, I thank the entire staff of the Institute of Geosciences in Freiburg for the great time and all the support – and in particular Dr. Raphael Bissen for his help during my first steps in Petrel® and Manuela Tombrink for her help in organizational matters. The support of Dr. Horst Dresmann from the University of Basel concerning tests in GOCAD® is very much appreciated as well.

I also want to thank the entire staff of the Institute of Applied Geosciences in Darmstadt and especially the group of engineering geology for the fantastic working environment and cooperation: Christoph Wagner, Chiara Aruffo, Dennis Laux, Christian Heinz, Bastian Weber, Reimund Rosmann and Stefanie Kollmann. This great atmosphere made many things so much easier. Aside from work, I thank all my friends for their countless encouragements, advice and motivation in the last years. I am so looking forward to awesome times with all of you.

Größter Dank gilt meinen Eltern für ihre Unterstützung in jeder Hinsicht, ihren Rückhalt, ihre aufbauenden Worte in anstrengenden Zeiten – und vor allem auch für den Erhalt meiner Mobilität. Meiner Schwester danke ich sehr für die vielen wunderbaren Eindrücke von über 4000 m.ü.M., die mich regelmäßig belebt haben. Nicht genug danken kann ich meiner großen Liebe Angelika für ihren Glauben und ihr Vertrauen in mich, ihr Verständnis und ihre Unterstützung. Du gibst mir meine innere Ruhe, Sicherheit und Gelassenheit. Ich freue mich sehr auf noch viel mehr gemeinsame Zeit mit dir.

Table of Contents

List of Figures

List of Tables

List of Abbreviations

APDL	Ansys® Parametric Design Language
ASR	Anelastic Strain Recovery
AVO	Amplitude Versus Offset
BC	Boundary Condition
BEM	Boundary Element Method
BHTV®	BoreHole TeleViewer
BOL	Breakout Orientation Log
CAD	Computer Aided Design
CCS	Carbon Capture and Storage/Sequestration
CFD	Computational Fluid Dynamics
CPU	Central Processing Unit
CSP	Clay Smear Potential
DEM	Distinct/Discrete Element Method
DFN	Discrete Fracture Network
DIF	Drilling Induced Fractures
DMP	Distributed Memory Parallel
DOF	Degree Of Freedom
DSI®	Dipole Shear Sonic Imagers
FBP	Formation Breakdown Pressure
FCP	Fracture Closure Pressure
FDM	Finite Difference Method
FEM	Finite Element Method
FIT	Formation Integrity Test
FMS®	Formation MicroScanner
FMI®	Formation MicroImager
FPP	Fracture Propagation Pressure
FVM	Finite Volume Method
GIS	Geographic Information System
GPGPU	General Purpose computing on Graphics Processing Units
GPU	Graphics Processing Unit
HPC	High-Performance Computing
I/O	Input/Output
ISIP	Instantaneous Shut-In Pressure
LOP	Leak-Off Pressure
LOT	Leak-Off Test
MCSS	Maximum Coulomb Shear Stress
MPC	Multi Point Constraint (contact algorithm in Ansys®)
MPI	Message Passing Interface
MPP	Massively Parallel Processing
NGB	North German Basin
NURBS	Non-Uniform Rational B-Spline
RACOS®	Rock Anisotropy Characterisation On Samples
SAS	Serial Attached SCSI (Small Computer System Interface)
RAID	Redundant Array of Independent Disks
SGR	Shale Gouge Ratio
SHmax	Maximum horizontal stress

Shmin	Minimum horizontal stress
SMP	Symmetric MultiProcessing
SSF	Shale Smear Factor
SV	Vertical stress
UBI®	Ultrasonic Borehole Imager
UCS	Uniaxial Compressive Strength
VSP	Vertical Seismic Profile
WVA	Wave Velocity Analysis
XLOT	Extended Leak-Off Test

List of Symbols

$[K]$	Stiffness matrix
μ_f	Coefficient of fault friction
μ_i	Coefficient of internal friction
A	Area
A_e	Additional elastic moduli
C	Cohesion (S_0)
$C_{0\text{-}n}$	Creep constants
C_P	Heat capacity
E	Young's modulus
F	Force
$\vec{f}$	Load vector
G	Shear modulus
g	Gravitational acceleration (9.81m/s²)
I_1, I_2, I_3	Stress invariants
J_1, J_2, J_3	Deviatoric stress invariants
K	Bulk modulus
k	Thermal conductivity
k_1, k_2	Constants in Drucker-Prager law
K_f	Pore fluid bulk modulus
K_{fr}	Framework modulus
K_s	Bulk modulus of solid grains
L	Length
p	Mean effective stress
P_P	Pore pressure
q	Generalized shear stress
R	R-value of fault-slip analysis
s_{xx}, s_{xy}, (…)	Deviatoric stresses
S_0	Cohesion (C)
S1	Largest principal stress (σ_1)
S2	Intermediate principal stress (σ_2)
S3	Least principal stress (σ_3)
T_0	Tensile strength
T_{dila}	Dilation/Dilatation Tendency
T_{slip}	Slip Tendency
u	Permeability
$\vec{u}$	Displacement vector
V	Volume
V_P	Pore fluid volume
v_p	Compressive wave velocity
v_s	Shear wave velocity
α	Biot's coefficient
α_{exp}	Thermal expansion
β	Angle between S1 and the normal direction of a shear plane
γ	Angle between S1 and fault plane
δ	Kronecker delta
ε_1, ε_2, ε_3	Principal strains

ε_e	Equivalent strain
ε_{vol}	Volumetric strain
ζ	Biot's strain parameter (Increment of fluid content)
λ	Lamé's constant
ν	Poisson's ratio
π	Number Pi (3.14159…)
ρ	Density
$\sigma_1, \sigma_2, \sigma_3$	Principal stresses (S1, S2, S3)
$\bar{\sigma}$	Mean stress
σ_e	Equivalent stress
σ_{eff}	Effective stress
σ_n	Normal stress
$\sigma_{xx}, \sigma_{yy}, \sigma_{zz}$	Normal stresses in stress tensor
τ	Shear stress
$\tau_{xy}, \tau_{xz}, \tau_{yz}, (\ldots)$	Shear stresses in stress tensor
φ	Angle of internal friction
ϕ	Porosity
ψ	Dilatancy Angle

1 Introduction

The work of this study was accomplished in the framework of the research project 721 of the German Scientific Association for Oil, Gas and Coal (DGMK[1]) entitled:

Prediction of Tectonic Stresses and Fracture Networks with Geomechanical Reservoir Models – Case Study of a Rotliegend Gas Reservoir in the North German Basin.

The project period lasted from February 2010 to June 2013. Consortium members were the three companies ExxonMobil Production Deutschland GmbH, GDF SUEZ E&P Deutschland GmbH and RWE Dea AG, in combination with the Technische Universität Darmstadt as academic partner. In addition to funding the research project, the companies provided all reservoir-specific data as the field operators of the case study reservoir in Northern Germany. All methodological development and modeling work applied to the case study was conducted independently at the Technische Universität Darmstadt – and at the Albert-Ludwigs-Universität in the first two years of the project. The use of confidential data requires figures to be anonymized and coded well names.

Subsequently, the objectives of the research project are summarized (1.1) and an outline of the accomplished work is provided (1.2). This is followed by a description of the fundamental relevance of geomechanical modeling (1.3) and an overview on the state of research (1.4).

1.1 Objectives

Research in geomechanical reservoir modeling is motivated by the fundamental and rising importance of the in situ stress field for a wide range of operations in hydrocarbon reservoirs. The specific in situ stresses that form in the complexity of oil and gas reservoirs can only be addressed by numerical models. Complex geometries of intensively faulted reservoirs in combination with non-linear material behavior are optimally handled by the finite element (FE) method. Therefore the conducted research focuses on this numerical approach.

The work of this study aims at evaluating the potential of geomechanical FE models for a reliable pre-drilling prediction of the tectonic in situ stress distribution and fracture networks on reservoir scale. Particular focus is set on the characterization of faults regarding their geomechanical exposure today and in the past, and on the inferred behavior and hydraulic properties. There are two main objectives stated for the study:

- Development of a generally applicable workflow to generate 3D geomechanical FE models of faulted reservoirs
- Application of the developed workflow to the case study reservoir

The first methodological part of the project focuses on the development of a workflow to build and calibrate geomechanical FE models, which yield reliable insights into the specific in situ stress distribution in a reservoir and reveal the stresses acting on the faults. This workflow has to be flexible and applicable to virtually any reservoir geometry, while preserving and incorporating the reservoir's complexity with as much detail as possible. Comparing the modeling outcome to field data during a step of calibration should ensure the reliability of results.

[1] Deutsche Wissenschaftliche Gesellschaft für Erdöl, Erdgas und Kohle e.V.

In the second part of the project, the developed workflow has to be applied to and tested on the intensively faulted case study gas reservoir in the North German Basin. In order to obtain results on both, recent in situ stress and fracture networks, the geomechanical models have to reflect the full complexity of the case study and provide insights into the local stress field prevailing today and at times of fracture formation and reactivation in the past. The following specific objectives of this applied part of the research project are defined:

- Buildup of a field-scale geomechanical FE model of the case study reservoir incorporating a mechanical stratigraphy and the entire fault network
- High spatial resolution of all modeling results
- Information on the specific present-day magnitudes and orientations of in situ stress in the reservoir including all local perturbations along faults and mechanical contrasts
- Disclosure of the recent stress distribution on the faults, their corresponding behavior and potentially related hydraulic properties
- Information on the temporal and spatial evolution of the fracture network by revealing the specific distribution of paleo-stress magnitudes and orientations in the tectonic history
- Disclosure of the paleo-stress distribution on the faults, their corresponding behavior and potentially related hydraulic properties in the tectonic history
- Testing the hypothesis that proposes pronounced cataclasis due to fault slip in multiple tectonic stages to be responsible for significant reduction in present-day fault permeability
- Setup of a mechanically consistent tectonic evolution of the reservoir

Besides the specific results of the case study, the tested and approved workflow represents the methodological outcome of the project and is valuable for future modeling of stress-sensitive reservoirs.

Several models have to be built in order to accomplish the development of the workflow and to provide the desired information on the case study reservoir. A comprehensive overview on all modeling conducted in this project is provided by the following study outline (1.2).

1.2 Study Outline

The objectives of the research project lead to a division of this study into a methodological and an applied part. The methodological part of the study encompasses the well-established principles of numerical simulation (2) and rock mechanics (3), as well as the newly developed workflow for geomechanical modeling (4), which is based on these principles. These three subjects are described in detail and represent the theoretical basis of this work.

In the second part of the study, the elaborated workflow and the underlying principles are applied to the case study reservoir in the North German Basin in order to test the methodology. This gas field is ideally suited for a case study due to the comprehensive datasets available for model generation and validation – and because of the intensive fault network of more than 80 faults that collectively impact the in situ stress distribution. Following a brief introduction of the case study (5), the buildup and results of multiple geomechanical models are described that increase in incorporated complexity (Tab. 1-1).

	Parameter Studies - Model	Base Model	Static Model	Submodel	Dynamic Model
Modeled Fault Geometry	Simplified, characteristic	Reservoir-specific	Reservoir-specific	Reservoir-specific	Reservoir-specific
Model Scale	Single Fault Block	Field-Scale	Field-Scale	Sub-Field-Scale	Field-Scale
Model Area	9 km²	10,000 km² (incl. load frame)	2,124 km²	254 km²	2,124 km²
Model Thickness	-	500m	1600m	1600m	1600m
Number of Faults	4	18	86	11	86
Fault Offsets / Res. Topology	not preserved	not preserved	preserved	preserved	preserved
Number of Mech. Layers	1	1	3	3	3
Number of Element Layers	1	4	16	34	16
Horizontal Element Size	10m	75m	100m	50m	100m
Total Number of Elements	20,000	1.4 million	3.81 million	3.65 million	3.81 million
Material Parameters	Literature-based	Literature-based	Reservoir-specific	Reservoir-specific	*Reservoir-specific**
Boundary Conditions	various	Present-day Stress Field	Present-day Stress Field	Present-day Stress Field	Multiple Paleo-Stress Fields
Modeled Stress Tensor	2D (plane stress)	3D	3D	3D	3D
Number of Load Steps	1	1	1	1	4
Comparison to Field Data	No	No	Yes (stress data)	Not separately (s. static model)	Yes (fracture data)

Tab. 1-1. Summary of all geomechanical models generated in this study with indication of their respective complexity. Material parameters used in the dynamic model are extrapolated from reservoir-specific data for past tectonic stages (*).

First geomechanical models are generated for preliminary studies (6) encompassing generic parameter studies (6.1) and a basic model of the case study (6.2). The parameter studies are carried out on simplified, characteristic fault block geometry in 2D (Tab. 1-1) and focus on revealing the most controlling factors for in situ stress perturbations in general. The geomechanical base model is built in 3D and includes the specific geometry of 18 major faults of the case study and one lithological layer (Tab. 1-1) in order to provide first insights into the in situ stress distribution. All reservoir-specific geometrical information is based on 3D seismic data and is provided by the project partners. These relatively simple models of the preliminary studies are also used to optimize and finalize the elaborated workflow.

Subsequently, the methodology of the workflow is applied to its full extent to the buildup of a detailed, field-scale geomechanical model of the case study reservoir (7). This model incorporates a reservoir-specific mechanical stratigraphy of three layers in combination with the described network of 86 faults, and is referred to as a static model since it applies the recent regional stress field as boundary condition (Tab. 1-1). Consequently, the static model reveals the present-day in situ stress

distribution and fault behavior, and is calibrated with local stress measurements. A submodel covering only the northwestern part of the reservoir is built additionally to test this option for locally obtaining higher spatial resolution (7.7) (Tab. 1-1).

Complementing the static approach, a (geo-)dynamic modeling approach is conducted (8) with the same geometrical model, but applying paleo-stress fields and respectively adjusted parameters (Tab. 1-1). This dynamic model reveals the in situ stress and fault behavior throughout the tectonic history and during fracture formation. Therefore the outcome of this model is compared to fracture information and also checked for correlation with recent hydraulic fault properties. In a final step of the study, the static and dynamic modeling approaches are combined for evaluation of critically stressed fractures and their potential impact on the recent hydraulic behavior of the reservoir (9).

1.3 Relevance of Geomechanical Modeling

Tectonic stresses act everywhere in the Earth's crust and emerge from the rock's lithostatic load and lithospheric plate movement (Bamford, 1976; Richardson et al., 1976; Turcotte and Oxburgh, 1974). In the upper crust, these stresses inevitably result in elastic deformation and inelastic, irreversible deformation by brittle fracturing and faulting (Zoback, 2007). In combination with the mechanical properties of the crust, the tectonic stresses control the stability and performance of all types of subsurface operations, such as underground mining, any excavations, and exploitation of hydrocarbon and deep geothermal reservoirs. Quantification of these stresses and deformations in the Earth's crust and predicting their impact on subsurface operations is the basic motivation of all geomechanical research (1.4).

The specific stress magnitudes depend on depth and the tectonic setting, as well as on the prevailing pore pressures. The orientation of stress is dictated on a large scale by the relative movement of lithospheric plates and their interaction along the plate boundaries (Zoback, 1992). These processes establish an ambient, far-field, regional stress field traditionally described by a vertical (SV) and a maximum (SHmax) and minimum horizontal stress component (Shmin) (3.1). The magnitude and orientation of this stress field vary significantly – both in time and space. Paleo-stress fields prevailing at different tectonic stages in the Earth's history differ from the recent state of stress (Kley et al., 2008), and future stress fields will be different as well due to ongoing tectonic activity and man-made impact, for instance by depleting hydrocarbon reservoirs (Herwanger and Koutsabeloulis, 2011; Morris et al., 2012). Tectonic stress thus varies temporally from geological time spans to reservoir cycles of tens of years.

In addition to this variation in time, tectonic stresses vary significantly in space. Spatial stress variations reach from the scale of lithospheric plates, to basin- and reservoir-scale, to fault block scale and even down to grain-scale. Besides large-scale changes of stress magnitudes and orientations along plate boundaries, the intra-plate stress field – which is often assumed to be homogeneous – can also vary decisively due to geological and structural elements. The local stress field in reservoirs and fault blocks is influenced particularly by faults as structural discontinuities and by different mechanical properties of lithologies and faults (Barton and Zoback, 1994; Sassi and Faure, 1997). The resulting variations of the ambient stress field in magnitude and orientation are commonly referred to as stress perturbations and give rise to a unique pattern of local stress (Tamagawa and Pollard, 2008; Yale, 2003). This local stress field can deviate up to 90° in orientation and several tens of Megapascal (MPa) in magnitude from the regional trend.

The local stress pattern of paleo-stress fields controlled the generation and re-activation of faults and fractures, and thus the fracture characteristics such as type, size and density observed today. The perturbed recent state of stress impacts the hydraulic behavior of existing faults and fractures, eventually leading to permeability anisotropies, baffles and leakage pathways. The recent local stress field further controls the generation and characteristics of newly created fractures and the stability of boreholes and excavations. Therefore the specific in situ stress is of fundamental importance especially in hydrocarbon industry for the optimal exploitation of hydrocarbon reservoirs.

The state of stress can be measured by various methods (4.8.1). However, almost all stress measurements rely on completed drillings, because stress is commonly either measured downhole under in situ conditions or in experiments on extracted drill core samples (Ljunggren et al., 2003). Drillings procedures are always kept to a minimum due to the high costs, which is reflected in the commonly small amount of available stress data. Problems arise when stress information is required before drilling and when planning reservoir operations demands area-wide stress information in undrilled parts of the reservoir. Large-scale data compilations are not capable of providing reliable local information and may lead to unfavorable decisions in reservoir development.

The lack of access and information represents the motivation for geomechanical reservoir modeling to provide more robust pre-drilling estimates of in situ stress or ideally reliable predictions. This requires the incorporation of the specific subsurface geometry and mechanical parameters, in combination with the far-field stress situation within a numerical model. The outcome of such geomechanical reservoir models provides the 3D stress and strain tensor at all subsurface locations in the reservoir and is limited only by the spatial resolution of the model.

Up to now most stress-related issues are addressed after operational failure, whose fixing is in most cases expensive and/or leads to a loss of revenue (Herwanger and Koutsabeloulis, 2011). The insights into the in situ stress distribution provided by geomechanical reservoir models can yield great benefit for various stress-related issues in reservoir development. Local stress information can help to optimize drillings, ensure the stability of wellbores and production rates. Area-wide stress distributions help to optimally position injecting and producing wells with respect to stress-related permeability anisotropies (Heffer, 2002). Wellbore stability is directly dependent on the orientation of the drill path with respect to the local principal stresses (Sperner et al., 2003). This addresses notably horizontal or strongly deviated wells. When the drilling path of a well has to cross a fault, information on the shear stress distribution helps to identify optimal locations for penetration. This can prevent direct wellbore failure and the later bending or shearing of well casing or production tubing.

Moreover, geomechanical reservoir models are able to provide the state of stress along faults in the reservoir and thus reveal their movement behavior and critical states. This information can be related to hydraulic properties (Rogers, 2003), but also to the likelihood of induced seismicity. Identifying the hydraulic properties of faults is crucial for reservoir development. While critically stress faults commonly show high permeability, intense fault slip may lead to cataclasis and clay smearing, resulting in sealing behavior of the faults and compartmentalization of the reservoir. Seismicity is most commonly induced by reservoir stimulation during hydraulic fracturing. Besides this seismic issue, hydraulic stimulations must also regard the in situ stress orientation for optimal fracturing results due to the dependency of newly generated fractures on the local stress direction.

The necessity of geomechanical reservoir models increases with rising stress-related aspects in more and more complex unconventional reservoir types, such as shale gas and tight gas reservoirs. Drilling and producing conditions are becoming increasingly difficult and subject to much higher public sensitivity. This sensitivity especially affects hydraulic stimulations, which are common practice for

enhancing production rates in conventional reservoirs and are obligatory for the exploitation of most unconventional reservoirs. Deeper geomechanical insights can improve efficiency by providing more reliable foundations for reservoir development decisions and risk management.

1.4 Geomechanical Modeling: State of Research

This is a brief overview on fundamental studies and different geomechanical modeling approaches. Apart from the subsequently cited publications, the field of reservoir geomechanics is comprehensively described and summarized by Zoback (2007). Fjaer et al. (2008) provides a more general overview on petroleum-related rock mechanics.

Since the mid 1990's, the importance of tectonic in situ stresses in subsurface operations has been increasingly recognized in science and industry – especially the impact on optimal exploitation of hydrocarbon reservoirs. This is mostly due to expensive operational failure and the demand for more efficient exploitation of conventional reservoirs. Moreover, the upcoming field of unconventional reservoirs requires a deeper understanding and consideration of tectonic stresses and mechanical properties (Cui et al., 2013; Ostadhassan et al., 2013; Suarez-Rivera et al., 2013). Numerous studies aimed for improving in situ and drill core measurement of stress, whereas other approaches focused on modeling techniques for deeper understanding of in situ stresses. This includes local stress perturbations, temporal development of in situ stress and its impact on field performance. The productivity often depends on successful hydraulic stimulation and stable horizontal wells, which are both stress-sensitive operations.

Symmetric compressional failure at the wall of a wellbore is known as borehole breakouts and represents the most well-studied method to determine in situ stress orientation. Its results has been used for many regional descriptions and compilations of tectonic stress (Barton et al., 1988; Fordjor et al., 1983; Mastin, 1984; Paillet and Kim, 1987; Peska and Zoback, 1995; Plumb and Hickman, 1985; Vernik et al., 1992; Zoback and Healy, 1984, 1992; Zoback et al., 1985; Zoback et al., 1989). Breakout measurements thus can reveal variations in stress orientation. In cases of variable wellbore breakouts in individual boreholes penetrating active faults, such perturbations are related to recent fault movement, for instance (Barton and Zoback, 1994). This phenomenon was observed in various tectonic environments and rock types. In situ and laboratory measurements of various types are indispensable for obtaining such direct information on acting stresses. However, these measurements are always spatially limited and do not provide deeper understanding of in situ stress behavior. Numerical geomechanical modeling can yield these insights and is enabled by increasingly powerful computing.

Two dimensional numerical models comprising simple fault geometries in generic parameter studies are published, amongst others, by Homberg et al. (1997), Ohlmacher and Aydin (1997) and Sassi and Faure (1997). Homberg et al. (1997) analyzed stress perturbations along major fault zones in the Jura Mountains. They interpreted pre-existing discontinuities in the crust to be responsible for major stress perturbations with directional deviations up to 50° and to play a major role in the accommodation of deformation. The studies on fault mechanics by Ohlmacher and Aydin (1997) showed that local stress trajectories around faults are primarily controlled by the frictional resistance of faults and the angle between the maximum principal stress and the fault plane. Sassi and Faure (1997) examined the effects of faults and layer interfaces in a 2D plane strain model. They found that contacting lithologies with different mechanical properties strongly affect the stress distribution. These three studies first

disclosed in detail how stress variations actually depend on the mechanical properties of rocks and faults, and on the angle between principal stress and faults.

A study published by Yale (2003) showed several examples for the stress distribution in reservoirs. He analyzed local perturbations of the regional stress field focusing on the influence of faults and horizontal stress magnitudes. Intense faulting and strong segmentation of reservoirs can result in stress decoupling in individual fault blocks and stress deviations of up to 90° from the regional trend (Yale, 2003). Further it was concluded that large differential horizontal stresses tend to suppress significant stress perturbations, while maximum and minimum horizontal stress magnitudes that are close together provide greater probabilities for rotations of in situ stresses. If minimum and maximum horizontal stresses switch due to magnitude perturbations, for instance, this directly results in orientation changes of 90°.

First geomechanical models using the Finite Element Method (FEM) (2.1) and incorporating simple reservoir geometries are published by Bourne et al. (2000), Fredrich et al. (2000), Fredrich and Fossum (2002), and van Wees et al. (2003), for instance. Bourne et al. (2000) used a combined approach of geomechanics and flow simulation to model naturally fractured reservoirs in 3D. By constraining and validating the model with seismic data, well tests and production data, uncertainties were significantly reduced and it was possible to pre-estimate physically and geologically realistic fracture networks. Fredrich et al. (2000) and Fredrich and Fossum (2002) applied 3D geomechanical simulations to model production-induced reservoir compaction. These simulations are validated by the comparison of predicted surface subsidence with field measurements, and of modeled deformation to observed casing damage.

One of the first geomechanical models, which incorporated a more sophisticated 3D reservoir structure including faults, was the work of van Wees et al. (2003). The simulation of gas depletion predicted a stabilization of the stress field and a reduced likelihood of failure for reservoirs in compressive and strike-slip regimes. In contrast, extensional regimes are suggested to lead to reservoir failure, provided that the reservoir material and/or existing faults are weak and the state of stress is close to the failure of the material (van Wees et al., 2003). Henk (2005) describes fundamental techniques for 3D finite element modeling of present-day stress orientations and magnitudes in complex fault-controlled reservoirs. The application to a case study reservoir in Northern Germany illustrates the general potential of this geomechanical modeling approach. Similar geomechanical approaches are shown to be able to predict fracture permeability and thus related sweet spots in a deeply buried carbonate reservoir (Poppelreiter et al., 2005).

Many studies have investigated the in situ state of stress in the vicinity of rock salt for two reasons: (1) stress perturbations are very intense close to salt bodies, and (2) rock salt often occurs in hydrocarbon reservoir settings, either acting directly as a regional seal or indirectly when salt tectonics resulted in the formation of structural traps, for instance. However, drilling into, through or even only close to salt bodies can be highly challenging. New important discoveries of oil reservoirs in subsalt formations in Brazil (Maugeri, 2012), for instance, increase the importance of salt-related geomechanical studies.

Ali et al. (2003) introduced the concept, construction and use of so-called mechanical earth models at a case study reservoir beneath a salt diapir. The resulting finite element model provided magnitudes and orientations of the principal stresses, and also demonstrated the practical value of geomechanical modeling in general. Fredrich et al. (2003) investigated the in situ stress field and its perturbations adjacent to different types of salt body geometries. The modeling outcome of this study can be used to plan optimized well trajectories in such geological scenarios and avoid geomechanical instable areas.

Despite additional research in this field (Fleckenstein et al., 2004; Fredrich et al., 2007; Koupriantchik et al., 2007; Mackay et al., 2008), there was a lack of clear consensus about the appropriate modeling techniques for these environments. In 2012, two partner studies were published (Luo et al., 2012; Nikolinakou et al., 2012). The first study compares different approaches for geomechanical modeling of in situ stresses close to salt bodies (Luo et al., 2012), while the second study uses a fully coupled poroelastoplastic geomechanical model to reveal stress and pore pressure evolution in adjacent sediments (Nikolinakou et al., 2012). Further modeling applied to a case study in the Gulf of Mexico and using real salt geometry was able to explain the salt-related origin of elevated horizontal stresses measured in leak-off tests (LOT) and formation integrity tests (FIT) (Nikolinakou et al., 2013). Sophisticated 3D FE models can reveal the in situ stress around salt structures, explain drilling events and thus help optimize well design and mud weight in such complex environments (Nagy et al., 2013).

The majority of the most recently published geomechanical studies are based on finite elements (e.g. (Ali et al., 2003; Nikolinakou et al., 2013; Rodriguez-Herrera et al., 2013)). Henk (2009, 2010) summarizes the increasing importance of stress and geomechanical FE models for reservoir development and shows a case study in Libya as example of applied geomechanical reservoir modeling focusing on the present day situation of in situ stress. Regarding the challenges of climate change, geomechanical FE modeling also plays an important role in the development and operation of CO_2 underground storage sites (Rutqvist, 2012a, b). Depleted gas reservoirs can be re-used for gas storage, but several aspects like fault stability have to be addressed (Orlic, 2013; Orlic et al., 2013). Geomechanical assessment of potential storage sites can evaluate the behavior of cap rock and help to estimate the risk of fault reactivation and generation of leakage pathways (Vidal-Gilbert et al., 2009; Vidal-Gilbert et al., 2010). Fault reactivation and related induced seismicity is also a major concern in mandatory hydraulic stimulation in unconventional shale gas reservoirs (Rutqvist et al., 2013).

Although the finite element method is ideally suited for geomechanical modeling (2.1), complex models are also addressed with other numerical methods, for instance by using the so-called boundary element method (BEM) (2.2). Maerten et al. (2002) applied this method to reveal stress perturbations around large faults that lead to variability in the development and orientation of secondary faults. Maerten et al. (2006) combined such a 3D boundary element model with stochastic approaches. In this way, it is possible to predict small-scale, subseismic fault distributions based on large-scale fault data. Dee et al. (2007) tested the application of an elastic dislocation forward modeling methodology based on the boundary element method to relatively simple geological structures. This study demonstrates that in principle such a model can predict fracture orientation and distributions within certain ranges of error. However, the required input quantities must be available, which includes the mapped subsurface fault network with the known distribution of displacement (Dee et al., 2007).

Besides the finite and boundary element methods, the distinct (or discrete) element method (DEM) is applied in geomechanical modeling as well using bonded-particle models (Potyondy and Cundall, 2004). Camac and Hunt (2009) describe a workflow that enables the prediction of perturbations of differential stress at any location in a rock mass. These local perturbations originate from the interaction of the far-field tectonic stress with seismically resolved faults. Areas of predicted higher differential stresses correlated directly with observed fractured rock (Camac and Hunt, 2009). Amongst many detailed studies, discrete element models can also be used to reveal constraints on the sealing capacity of faults by simulating shear in layered sequences, for instance (Terheege et al., 2013). Some studies also aimed for combining finite and distinct element techniques to benefit from the individual strengths of both methods (Guo et al., 2013; Hamdi et al., 2013; Oñate and Rojek, 2004; Seyferth and Henk, 2002).

The derivation of area-wide rock mechanical parameters from seismic data represents a promising next step for significant improvement of geomechanical models – especially those using the finite elements. Although the principles for deriving such parameters are outlined (e.g. by Gray et al. (2012)), the respective data is yet commonly scarce. Herwanger and Koutsabeloulis (2011) provided a guideline to build and calibrate geomechanical FE models with such 3D and even 4D seismic data. This data can be used to build highly sophisticated FE models on field-scale (Rodriguez-Herrera et al., 2013). The incorporation of time in 4D models helps to infer and understand the change in stresses and related deformation and fault reactivation, which occurs during hydrocarbon production (e.g. (Geertsma, 1973; Orlic and Wassing, 2013)). Such models can be correlated to the results of 4D simultaneous AVO inversion of compacting fields (Schiott et al., 2008). Alternatively, discrete fracture network (DFN) models based on a combination of deterministic and stochastic elements are able provide rock mechanical properties as a function of spatial fracture intensity (Cotrell et al., 2012).

The impact of in situ stress on the hydraulic behavior of faults and fractures was shown for instance by Heffer and Lean (1993), Barton et al. (1995), and Rogers (2003). This connection gives rise to numerical modeling, which aims at coupling geomechanical deformation and fluid flow. Heffer and Koutsabeloulis (1995) used such a coupled finite element model to simulate thermal stresses due to cold water injection. Their results correlated well with field data and show directionality trends of progressing flooding fronts towards the maximum horizontal stress axis. Heffer (2002) underlined the necessity of coupled simulations by elucidating the geomechanical changes induced by water injection in reservoirs, as for instance the decreasing temperature, increasing pore pressure and corresponding decreasing effective horizontal stresses. These changes may lead to reactivation of faults, generation of hydraulic fractures near the injection well, and anisotropic permeability changes (Heffer, 2002).

Hydrocarbon flow during production is commonly modeled by reservoir simulations using finite differences (2.2). In order to model stress-related effects impacting the fluid flow, geomechanical models can be connected to reservoir simulators. Longuemare et al. (2002) modeled the influence of production-induced geomechanical effects on fluid flow at a case study by using a partially coupled approach. The results indicate progressive strain localization on a limited number of faults when the mechanical equilibrium of the reservoir is disturbed during production. Minkoff et al. (2003) developed a loosely staggered-in-time coupling of flow and mechanical simulation codes to avoid the high demands of fully coupled models. This approach is validated in two numerical experiments against a fully coupled simulator and can be used to accurately predict reservoir production in structurally weak reservoir formations. A loosely coupled approach is also presented by Samier et al. (2008), which can couple basically any reservoir simulator with any finite element code.

Zhang et al. (2007) applied fully coupled, hydro-mechanical FE modeling to a reservoir in the North Sea and emphasized the importance of the state of stress in a reservoir prior to production. At critical initial stress states, small changes in effective stress due to production or injection are likely to trigger reservoir-wide geomechanical and hydraulic reactions, such as fault reactivations and permeability variations (Zhang et al., 2007). In contrast, non-critical initial stress states result in local reactions.

Apart from the application in applied research, geomechanical modeling has also been utilized in more fundamental research in the field of structural geology. Numerical modeling helped to quantify and understand orogenetic processes in zones of continental collisions (Seyferth, 2001). Henk (2006) showed how to study the temporal evolution and spatial distribution of stress and strain during lithospheric extension using two dimensional FE models. Furthermore, halfgraben formation and inversion can be numerically modeled by distinct and finite element methods, respectively, as demonstrated by Seyferth and Henk (2005) and Henk and Nemcok (2008).

The incorporation of thermal aspects in geomechanical FE modeling was used by Schwarz (2005) to yield quantitative insights into the evolution and structure of the Upper Rhine Graben.

The range of problems geomechanical modeling can address is extensive. It is considered in various fields of research and different numerical techniques are applied. Hence, this overview does not claim to be complete. For further information, please refer to the cited papers and references therein.

2 Numerical Simulation

A simulation in the scientific sense describes the reproduction of a system or process under conditions that are specified and controlled by the person who runs the simulation. The simulated system or process is commonly a phenomenon to which access – either in time or in space – is lacking in reality. However, the simulated construct can also be of hypothetical nature. The detailed knowledge and direct control on the setup and operation of the simulation model represent the basis for a successful simulation.

Scientific simulations can be done with real-world or computer-based models. A real-world model would be a small-scale, "artificial" version of a system built in a laboratory with appropriate material, for instance a sandbox model in geoscience as described by Harris (1974). Simulations using computer-based models most commonly take advantage of numerical methods to calculate an approximate solution of a differential equation and are thus referred to as numerical simulations. Differential equations describe the behavior of a system at a differential small part of it and represent functions of characteristic quantities (Müller and Groth, 2000). Depending on the system of interest, the respective differential equations are used, for instance Lamé's elasticity theory for considering the structural behavior of a solid exposed to a load. In such structural analyses the characteristic quantity is the displacement. Further differential equations are the Laplace equation for temperature fields, the Maxwell equations for electric and magnetic fields, and the Navier-Stokes equations for fluid dynamics. The rapid development of increasingly powerful computers allows increasingly complex models and improves the accuracy and reliability of the approximate solution significantly. Nowadays, numerical models are applied in a wide range of fields including all natural sciences, but also engineering, economics, psychology and social sciences.

The individual applications for a numerical simulation can be manifold. The most obvious reason is to improve the understanding of a complex system by disclosing unknown interdependencies or identifying the most influencing parameters on a process. Numerical simulations are also commonly used to anticipate consequences of actions in what-if scenarios. In other cases, a hidden process has to be visualized or a simulation in natural sciences is needed to corroborate a hypothesis or elucidate discrepancies with others models. To some extent, numerical simulations can be used as measurement substitutions, for instance on small scales where measurement devices would strongly affect the measurement outcome. On large scales, numerical models can complement measurements and yield spatial or temporal distributions of quantities with a resolution that cannot be measured for practical reasons.

However, it is important to keep in mind that all numerical models are idealized. They are focused on the crucial processes and their implementation in the numerical method. This idealization reduces the number of simulation-controlling parameters and a complex problem is adequately simplified (Steinhauser, 2007). Hereby it is possible to understand the acting processes and their interaction. Moreover, the input data especially in geosciences is inherently incomplete. The applicability of numerical models to literally proof or verify a hypothesis is thus at least questionable (Oreskes et al., 1994).

Beside numerical solutions to differential equations, there are also analytical mathematical procedures available, which are often described as accurate. This accuracy is referring to the mathematical aspects of the analytical solution that presumes the strict fulfillment of many requirements. These requirements commonly exclude analytical solutions for complex real-world problems and thus these procedures are limited to a very few special cases.

The following chapters provide an overview on the finite element method (2.1) and the finite element code that is used in the work of this thesis (2.1.1). Finally, the pros, cons and applications of further numerical methods are briefly described (2.2).

2.1 The Finite Element Method (FEM)

The finite element method represents the most common numerical technique for solving differential and partial differential equations. Its biggest advantages are the wide range of problems and systems that can be addressed and the possibility to resolve and simulate highly complex geometries (Müller and Groth, 2000; Schwarz, 1991; Steinhauser, 2007). The distribution of any physical quantities in a one- or multidimensional space described by respective differential equations can be obtained. The intention of this chapter is to provide an overview on the premises and the workflow of the finite element method, rather than explaining the mathematical procedures in detail. Please refer to the cited references for further and deeper introduction.

Continuum Approach

In the finite element method, the modeling domain is considered to be a continuum as described by continuum mechanics (Zienkiewicz et al., 2005). This means the mechanical behavior of solids and fluids is concerned on a macroscopic scale significantly larger than the characteristic length of the material on smaller or microscopic scale (Spencer, 2004). The discrete nature of matter is thus ignored and the material treated as uniformly distributed through space. This approach allows the definition of quantities, for instance density, velocity or displacement, as continuous functions of space and time. There are two types of equations in continuum mechanics: (1) equations that apply equally to all materials and describe fundamental laws of physics, such as the conservation of mass and energy, and (2) empirical equations, which describe the behavior of a distinct material. The latter are known as constitutive equations or constitutive laws (3.2) (Newman, 2012; Spencer, 2004). A continuum always remains a coherent medium without any fissures or cracks, no matter what loading is applied. This proposition is known as the continuum approach of the finite element method.

Fundamentals

The basic idea of this method is the breakdown of the modeling domain into a finite number of well-defined elements, such as hexahedrons and/or tetrahedrons, which are connected by common nodes. Contrasting to the entire system, the elements are easily accessible for calculation (Zienkiewicz et al., 2005). In this way, the problem is discretized, meaning problem is made discrete. In general, computers can readily solve discrete problems even if the amount is very large. The term “finite” refers to finite dimensions and number of elements contrasting to the infinite amount and infinitely small elements (infinitesimals) leading to differential equations (Zienkiewicz et al., 2005).

In the finite element method, the discretization of the model geometry into a finite number of simple and discrete sub-domains called elements is thus the crucial work step. The common connection points of these elements are called nodes. Depending on the chosen element types, nodes can either be available on the corners of elements only, or additionally as midpoints on edges or faces. Such elements are referred to as elements of higher order. Hence, the discretization process establishes also a system of a finite number of nodes (Steinbuch, 1998).

Mathematical Principles

As other numerical techniques as well, the finite element method takes advantage of the fact that any function, independent of its type, can approximately be described by a polynomial. Therefore numerical procedures use polynomials as approximate solution function for the wanted unknown function, which solves the underlying differential equation. This approximate solution function is also called ansatz function and is set up at element nodes by the product between so-called shape functions and unknown coefficients (Schwarz, 1991). The interpolation of wanted quantities for the elements is carried out via these ansatz functions at the nodes. Thus to summarize, the continuum is split into finite elements, each represented by its nodes and the respective ansatz functions, which will be used to obtain an approximate solution of the differential equation.

The solving procedure starts on element level. A polynomial as ansatz function for the interpolation is assigned to each node of an element (Zienkiewicz et al., 2005). This ansatz function describes for instance the displacement in structural analyses and comprises the coordinates of the nodes in the coordinate system of the element and unknown coefficients. The individual ansatz functions of the nodes represent an algebraic system of equations, which is then inverted for the unknown coefficients. Subsequently, these coefficients are substituted in the initial interpolation function. The approximate solution for the differential equation of one element thus results from the sum of all ansatz functions of this element. The shape functions finally allow to interpolate the nodal values to the function values continuously all over the element (Schwarz, 1991).

The coefficients of the ansatz functions have to be chosen in such a way that the deviation of the approximate solution to the accurate solution is as small as possible. However, this deviation cannot be considered due to the lack of knowledge concerning the accurate solution. In general, the coefficients are determined by the identification of an extremal value. In the Finite Element Method, the principle of minimum potential energy is most often used (Dow, 1998). This principle states that all physical quantities in a system arrange in such a way that the overall system achieves a state of minimum energy and therefore the necessity to change is also minimized. Mathematically this can be regarded as the extreme value of an integral, which includes all unknown coefficients. The first derivative of this integral with respect to the coefficients leads to an algebraic system of equations, which is often called stiffness relationship and is written in matrix notation (Eq. 2-1).

$$\vec{f} = [K] \cdot \vec{u} \qquad \text{Eq. 2-1}$$

This relationship is built first on element level. Hence, $\vec{f}$ represents the vector of the applied element load and $\vec{u}$ is the displacement vector of the element including the wanted coefficients of the ansatz function. $[K]$ is also referred to the respective element and is called stiffness matrix. This matrix comprises the boundary conditions and initial conditions, thus fixing the system of equations. All element-based local coordinates are subsequently expressed via vector transformation by global coordinates and all element matrices and column vectors are assembled to one global system of equations. The expression of the global stiffness relationship remains the same (Eq. 2-1). However, $\vec{f}$ and $\vec{u}$ become the global load and displacement vector, respectively, while $[K]$ now represents the matrix of the entire system.

After the definition of boundary and initial conditions, the unknown coefficients can be determined by solving the system of equations for $\vec{u}$ (Eq. 2-1) and the ansatz function becomes the solution function of the differential equation. The derived coefficients represent physical quantities at the nodes, the so-called degrees of freedom (DOF). In a structural analysis, these are the translational and rotational

displacements of the nodes (Müller and Groth, 2000). The application of constitutive material laws then yields further quantities like the stress and strain distribution in the modeling domain.

Time Integration

Time integration in the finite element model must be considered when dealing with unsteady, i.e. transient problems and if gravitational acceleration is included in steady problems. Time can be implicitly or explicitly integrated (Müller and Groth, 2000). In implicit time integration the degrees of freedom are determined synchronously by solving a large system of equations. The length of the time step that is considered can be chosen arbitrarily. However, each non-linear term, for instance emerging from material laws, requires a time-consuming iterative solution. Therefore the suitability of implicit time integration for very large deformations is limited (Huebner et al., 2001).

Explicit time integration provides a rapid determination of the degrees of freedom even at very large deformations. In contrast to the implicit integration, all nodes are processed one after another. Thereby no system of equations is required and in case of non-linear terms no iterative algorithm. However, the sequential working scheme precludes the interaction between nodes. This integration method is only stable, if each time step is smaller than a critical time step (Huebner et al., 2001). This makes the method hardly suitable for geological problems.

Strength and stiffness calculations in structural mechanics, as well as long-lasting transient dynamics, are usually calculated with implicit time integration. Problems arising from high-speed dynamics are prime examples for the usage of the explicit integration method.

Accuracy

In classical numerical methods, the ansatz function approximating the differential equation refers to the entire domain. The quality of the approximation can only be increased by a higher degree of the polynomial. This results in an increasing calculation effort and may also lead to oscillations, which disturb the convergence to a solution.

The finite element method enables the user to increase the quality of approximation by increasing the element density (Dow, 1998). Critical regions of the model can particularly be resolved by a higher number of smaller elements, while the polynomials of the ansatz function stay linear or quadratic. More elements also increase the calculation time, but significantly less than higher degree polynomials. Some finite element programs provide error estimators, which examine the influence of element density on the accuracy of the solution. This allows an increase in solution quality by respective mesh improvement (Dow, 1998).

In geological models, the uncertainties of many input parameters are relatively big compared for instance to engineering sciences. These uncertainties can often be more decisive to the reliability of the solution than the mesh resolution.

Frame of Reference

Applied loads change the location of the idealized material particles in a continuum. According to the principles of continuum mechanics, neighboring particles stay neighbors after any kind of motion (Spencer, 2004). There are two types of reference frames established to describe the motion of continuously distributed material that are used in finite element models: the Eulerian and the Lagrange type (Stüwe, 2007). In the Eulerian approach, which is also called spatial description, a fix reference frame is applied to describe the material motion relative to an unmoved area (de Borst et al., 2012).

Only the actual state of the moving material is recorded, which means that boundary surfaces between different materials are not clearly preserved, but are smeared.

The Lagrange approach is known as material description. It provides a reference frame that moves with the material. This means the mesh of the finite element model is connected to the material and thus moves with the material and changes its shape under deformation (de Borst et al., 2012).

While Eulerian reference frames are commonly used in fluid dynamics, the Lagrange type is the default approach in finite element codes for structural mechanics and is thus also used in finite element based geomechanical models.

Application

The finite element method is applied most of all in structural mechanics in engineering sciences as it was initially developed to solve problems in this field (Zienkiewicz et al., 2005). Besides structural mechanics, the method is also extensively used in the field of fluid dynamics, thermodynamics and electromagnetics, as well as in other branches of physics. However, finite element models have been also regularly used in geosciences and especially for geomechanical studies.

Sassi and Faure (1997) used generic finite element models to investigate local variation in the stress field resulting from faults and mechanical differences between lithologies. The method is also used to study such local stress variations commonly observed adjacent to salt bodies (Ali et al., 2003; Fredrich et al., 2003; Luo et al., 2012; Nikolinakou et al., 2012). Moreover, numerous studies demonstrated on case studies the great benefits of geomechanical reservoir modeling using finite elements as it can reveal the in situ stress in detail, its distinct impact on fluid flow, as well as production-induced deformation effects (Fredrich et al., 2000; Fredrich and Fossum, 2002; Henk, 2005; Longuemare et al., 2002; van Wees et al., 2003). Nevertheless, the finite element method is also applied to more basic research in structural geology (Henk, 2006; Ramsay and Lisle, 2000), or to numerous aspects in groundwater modeling (Kinzelbach, 1992; Wang and Anderson, 1982).

2.1.1 Ansys®

Ansys® is the finite element program chosen for the work described in this thesis. It is a commercial, large-scale multipurpose finite element software (Ansys Inc., Houston, USA). Its mechanical capabilities include static and dynamic structural analyses, as well as steady-state and transient heat transfer problems. The program allows non-linearities or secondary effects, such as plasticity, large strain, creep, contacts, temperature dependency and material anisotropy, to be included in the solution (Ansys Inc., 2012). Especially the possibility of implementing non-linear behaving frictional contacts is of importance, as this can be used to incorporate faults as discontinuities in the rock mass (2.1.2, 4.4). In addition to these capabilities, Ansys® offers flexible pre- and post-processing options and explicitly supports HPC computing of large models.

All geomechanical modeling in Ansys® was performed with the internal script language called Mechanical APDL (Ansys® Parametric Design Language). This script language provides high control of the finite element model and more precise handling than the latest graphical user interface called Ansys® Workbench™.

2.1.2 Contacts & Contact Elements

A significant enhancement of the continuum approach of the finite element method is the possibility to simulate the interaction of individually meshed continua contacting each other. Contacts are inherently non-linear problems. This can be intuitively understood assuming a scenario with two bodies that can be in contact or not (1) – and if they are in contact, they may stick (2) or slide alongside to each other (3). These are the three fundamental modes of a contact (CADFEM GmbH, 2010). Establishing of the contact itself and the change in state of established contact during the application of a load represents non-linear behavior. As all non-linearities, contacts significantly increase the calculation effort for the corresponding numerical analyses.

Contacts are realized in Ansys® by modeling one part as 'contact' and the other part as 'target'. Consequently, so-called contact and target elements are assigned to the opposing surfaces in a surface-to-surface contact of two solids (Ansys Inc., 2012). These 2D interface elements overlay the already meshed domain and share the nodes of the 3D elements of the volume mesh in place. Contact and target elements of a defined contact constitute a contact pair, which is identified by an individual variable referred to as real constant.

While target elements describe only the geometry of the respective surface, all contact-specific parameters are defined at the contact elements (Ansys Inc., 2012). Furthermore, the contact elements comprise integration points that are located either directly at the nodes or at a laterally shifted position to the nodes (Gauss integration points). During simulation, contact is searched in normal direction to the contact elements and identified at these integration points. After contact is identified and established, the contact elements are constrained at the integration points against penetration into the target surface – and eventually results are calculated at these points as well (CADFEM GmbH, 2010). Due to this contact 'communication' via integration points, no directly opposing elements and nodes are required (Fig. 2-1).

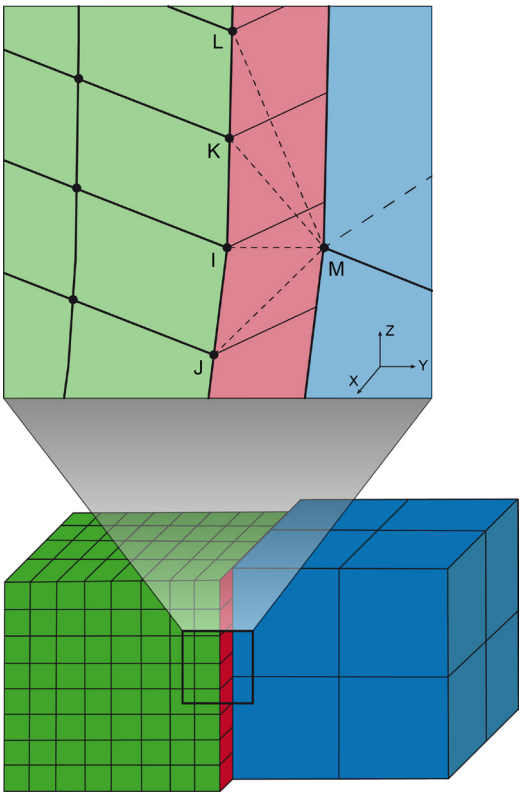

Fig. 2-1. Sketch illustrating a contact (red) between two dissimilar meshed and laterally shifted continua (green & blue). The zoomed section indicates the integration points at nodes (I, J, K, L) at the spatially higher resolved part of the contact (green).

Therefore, contacts allow interaction and large displacements between separate, individually meshed continua in a FE model without excessive distortion of elements (Fig. 2-1). In case of dissimilar meshes opposing at a contact, the contact elements should always be assigned to the spatially higher resolved side for optimal results (CADFEM GmbH, 2010).

The key feature of the contact elements is the ability to transmit physical quantities across the contact and allow mutual, physical interaction. These quantities can also be evaluated in post-processing and represent normal and shear stresses in structural mechanics, for instance, whereas in temperature field calculations the transmission of thermal energy is required. Contact-specific parameters defined at the contact elements thus also include properties describing the physical behavior of the contact (Ansys Inc., 2012). In case Coulomb friction is applied to contacts in order to simulate faults in geomechanical models, for instance, a coefficient of friction and a cohesion value can be assigned as contact-specific parameters.

Hence, faults in geomechanical models require a frictional type of contact, in which normal contact pressures, i.e. normal stresses, as well as shear stresses are transferred across the contact according to the applied friction law and material properties (Ansys Inc., 2012). However, the contact can also be defined as frictionless. This precludes any transfer of shear stress. Contrasting, a so-called 'rough' contact comprises an infinite friction coefficient in Ansys®. As soon as this type of contact is established, the nodes in contact are glued in tangential direction and no sliding can occur. In the contact type of 'no separation', the nodes in contact are glued in normal direction, but (frictional) sliding is allowed (CADFEM GmbH, 2010). Finally, 'bonded' contacts can be applied, which preclude nodal displacement in any direction. This variety of contact types and possible changes yield significant flexibility for FE modeling.

In complex models, the specific contact situations emerging during simulation often cannot be completely anticipated in beforehand. Therefore all potentially contacting continua must be prepared and all scenarios covered, which may occur during model calculation. This can be done by assigning several layers of contact and target elements to the same surfaces (CADFEM GmbH, 2010). Due to the identification of contact pairs by real constants, only the contact and target elements of the same pair interact and establish contact. This approach is applied in geomechanical modeling of complex fault patterns containing wedge-like structure, for instance. However, overconstraining the FE model by assigning duplicate pairs that describe the same contact must be avoided. This would lead to ill-conditioning of the matrix and hamper convergence.

Before any FE model including contacts can be calculated, the contact surfaces have to be checked on initial mesh penetrations and unintended gaps (Ansys Inc., 2012). These inaccuracies can result in numerical instability at onset of calculation and loading of the model. Therefore care must be taken in the geometrical buildup of the model with respect to future contact surfaces. In case some mesh penetrations and small gaps are still remaining after the geometry setup, they can also be closed directly before the calculation by manually moving the contact nodes to the target surface.

Resulting from the load applied to the model, the distance of contact and target elements increases or decreases during the simulation leading to gaps or penetration of the meshed continua (Fig. 2-2). While gaps are not problematic in principle, the fact that two solids penetrate each other, i.e. exist in the same place, is physically impossible and leads to incorrect modeling results. Once contact is establish, the applied contact algorithm thus has to limit occurring mesh penetrations and ensure the accurate solving of the contact problem. The three implemented contact algorithms of Ansys® provide different ways of counteracting mesh penetration (CADFEM GmbH, 2010).

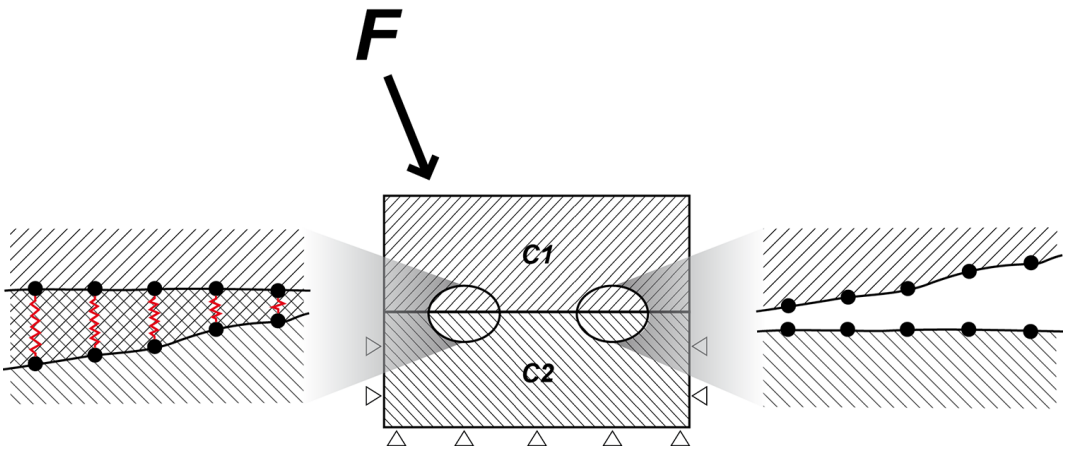

Fig. 2-2. Sketch illustrating two solid continua (C1, C2), which established contact via contact & target elements. The applied force F results in penetration (left) and gap formation (right) on element scale. Depending on the specific contact algorithm, contact stiffness is defined to limit initial mesh penetration and/or restoring forces (red) counteract and minimize the penetration.

The Penalty Method (1) considers a normal and tangential contact stiffness (Ansys Inc., 2012). The drawback of this method is that the amount of mesh penetration relies exclusively on these parameters. Higher contact stiffness results in less penetration, but leads to ill-conditioning of the global stiffness matrix and thus eventually precludes convergence of the model. Low contact stiffnesses result in high penetration and less accurate contact solutions. Hence a compromise for contact stiffness has to be found between 0 and ∞ representing no contact at all and a numerically unsolvable problem, respectively. However, this method represents the fastest way to solve contacts.

The Normal Lagrange or Pure Lagrange Multiplier Method (2) does not require contact stiffness. Instead, the approach introduces a contact force as additional degree of freedom for each contact element (Bathe, 1995). After the contact is established, these forces counteract the penetration of the mesh and can be seen as the restoring forces of 'elastic springs' (Fig. 2-2). With additional iterations, the algorithm stabilizes and satisfies theoretically exactly the contact conditions by enforcing zero penetration (CADFEM GmbH, 2010). However, the system of equations significantly increases and thus the computational effort. Chattering problems regarding the contact status (sticking – sliding) do also commonly occur and further complicate the solution.

The Augmented Lagrangian Method (3) combines the two approaches of the Penalty and Lagrange Method (Simo and Laursen, 1992). At first, a state of equilibrium is calculated by using a contact stiffness. The resulting penetrations are then minimized by applying the Lagrangian part of the algorithm (CADFEM GmbH, 2010). Although this approach is more time-consuming than the Pure Penalty Method, it commonly leads to a better conditioning of the global stiffness matrix and more accurate contact solutions. Compared to the Normal Lagrangian Method, the augmentation by the penalty term yields a smaller system of equations and thus larger models can be well handled.

This last approach is also used in the geomechanical modeling approach of this study, which incorporates contacts to implement faults as discrete discontinuities in the rock mass. The applied contact stiffness is derived by default from the mechanical properties of the adjacent elements and ranges typically between 0.1 and 10 times of the rock's Young's modulus. In geological terms, the contact stiffness can be related to a fault zone thickness, or damage zone of a fault, and can be regarded as the reciprocal value of the so-called fault zone compliance (van der Neut et al., 2008).

2.2 Further Numerical Methods

Besides the finite element method, there is also a broad range of other numerical methods available. Each method has its pros and cons, and whether it is appropriate to be applied or not depends strongly on the problem and the objectives (Steinhauser, 2007). All numerical methods use some type of discretization comparable to the finite element method. The type of discretization depends on the specific method and also whether a continuum or discontinuum approach is used. In the following, the finite volumes, finite differences and boundary elements are briefly introduced, as well as the distinct element method as numerical discontinuum approach.

Finite Volume Method (FVM)

The finite volume method represents a numerical technique that is based, as the finite element method, on the approximation of differential equations by discretization of the modeling domain. However, the differential equation approximated is almost exclusively the Navier-Stokes equation, since the origin and home of the finite volume method are computational fluid dynamics (CFD) (Hirsch, 2007). The principles of this method are the conservation of mass, momentum and energy (Patankar, 1980). Those quantities are averaged over the finite volume and this value is assigned to a point, for instance to the center points of faces of the finite volumes. Information from these points is then only transferred to direct neighbors. This is the big difference to the finite elements, where many more elements rely on each other (2.1) leading to denser matrices than it is the case in a finite volume model. Hence, the finite volume method is inherently less accurate in general terms, but due to the smaller matrices also significantly faster in solving and more memory efficient. Nevertheless, finite volume models can also consider highly complex geometries by flexibly subdividing it into numerous volumes such as hexahedrons, tetrahedrons and polyhedrons in general.

Due to these capabilities, this method is applied in the majority of CFD programs for simulating fluid flow and heat transfer problems in engineering sciences (Hirsch, 2007). The finite volumes are not the most common numerical technique used in geosciences, but some studies apply it to model transport processes or moving interface problems of salt- and freshwater (Bouzouf et al., 2001).

Finite Difference Method (FDM)

The numerical method of finite differences uses another concept than the finite element method to approximate differential equations. While the finite element method uses ansatz functions to approximate the solution of a differential equation at the element corner nodes, the finite difference method approximates the differential equation itself by using finite difference approximations replacing the derivatives and yielding a large algebraic system of equations that can be solved (LeVeque, 2007). The finite difference approximations at a given set of points can be derived with Taylor series, for instance. Finite difference models require a structured mesh, i.e. a rectangular grid of cells (Wang and Anderson, 1982). Unlike in the finite element method, the term node refers here to the center point of these grid cells, at which the described quantities represent the average of the entire grid cell. The node distances can be variable in general, but in some cases non-uniform grid sizes are difficult to use (Kinzelbach, 1992). Along with proper application and especially discretization, the finite difference method is fast and yields reliable results. However, the method cannot implement unstructured meshes, showing local refinements for instance, and is inflexible concerning the spatial resolution of boundaries (Kinzelbach, 1992). The latter fact can be seen in the grid of the case study reservoir (Fig. 4-2). Finite difference model thus cannot incorporate complex geometries.

In many cases in geosciences, the approximation of domain boundaries and interfaces with rectangular grid cells is sufficiently accurate, for instance when simulating fluid flow in hydrocarbon reservoirs or groundwater flow in aquifers (Wang and Anderson, 1982). Hence, many studies use this numerical technique to model contaminant transport, but it is also applied to seismic wave propagation models, for instance (Hirsch, 2007; LeVeque, 2007). Besides its application in geoscience, the finite difference method is applied in fluid dynamics in general, for example also in meteorological simulations.

Boundary Element Method (BEM)

In contrast to the introduced numerical methods so far, the boundary element method requires the boundary integral form of the differential equation that is to be solved (e.g. via Gauss theorem). This form can be regarded as exact or fundamental solution to the respective differential equation (Katsikiadelis, 2002). If this solution is not given, the method cannot be applied. The biggest advantage of the boundary element method over the finite element method, for example, is the lower amount of discretization. In the boundary element method only the boundary of the modeling domain must be meshed, i.e. in a 3D model only the surfaces (Crouch and Starfield, 1983). The generation, inspection and modification of this mesh is thus very feasible, while in finite element models these tasks can be of significant effort und very time-consuming at complex geometries. Due to the usage of the integral representation of the solution as continuous mathematical expression, it can be evaluated in boundary element models at any point in space and time in the modeling domain (Katsikiadelis, 2002). The solution in finite element models is only accessible at their nodes or elements.

However, the boundary element method has also some significant drawbacks. The method is not applicable to non-linear problems and lack of volume discretization allows no complex material distributions and laws to be applied. The computational advantage of the method is generally larger, the smaller the surface to volume ratio of the boundary element model is. This results from the numerical implementation of the systems of linear algebraic equations that are to be solved, whose coefficient matrices are fully populated in the boundary element method (Katsikiadelis, 2002). In the finite element method, these matrices are generally banded and symmetric, and thus the demand of storage and computation time increases linearly with the size of the problem. Both increase according to the square of the problem size in boundary element models.

In geosciences, this method is often used in geomechanical modeling of fault and fracture mechanics (Crouch and Starfield, 1983). Studies using geomechanical boundary element models revealed the potential dependency of secondary fault orientation on stress perturbations (Maerten et al., 2002). Such models are further capable of constraining the position and orientation of subseismic faults in reservoirs (Maerten et al., 2006). Besides its application in geoscience, the boundary element method is also used in fluid mechanics, acoustics and electromagnetics.

Distinct Element Method (DEM)

The continuum assumption underlying the introduced numerical methods so far ceases to be valid when the problem scale becomes similar to the characteristic length scale of the considered material structure (Zienkiewicz and Taylor, 2005). All media are discontinuous at some level of observation. At this point, surface interaction laws between particles are to be preferred over homogenized continuum constitutive laws. The discrete or distinct element method emerged from the disciplines of rock and soil mechanics and is based on spherical elements and the fundamental laws of contact physics (Cundall and Strack, 1979; Jing and Stephansson, 2007). The elements describe individual particles in a system onto which forces are applied and the resulting motion and deformation is computed.

Displacements between elements can be of unlimited extent and thus the method can be used to simulate the behavior of any granular material. The definition of bonds between the elements and the point of bond breakage further allows discrete element models to consider the fracturing mechanics of a solid. Model complexity regarding constraints and the amount of particles is only limited by the computing capacity.

This method is used in rock mechanics to model for instance the generation and distribution of joints and fissures on small scales, but also basin-scale fault system can be addressed (Potyondy and Cundall, 2004; Seyferth and Henk, 2005). Homberg et al. (1997) used distinct element models to reconstruct the local stresses around a fault, resolve the occurring stress perturbations and characterize dependencies of their behavior. Newer studies showed DEM-based techniques to predict the distribution of fractured rock that can assist the risk prediction of seal breaches in hydrocarbon reservoirs (Camac and Hunt, 2009). The usage of finite and discrete elements for different parts of a single modeling domain can be of great advantage, for instance when solids are interacting with granular media. Several attempts are thus made to combine both principles for the simulation of geomechanical problems (Munjiza et al., 1995; Oñate and Rojek, 2004; Seyferth and Henk, 2002).

Besides its applications in geoscience, the DEM is widely applied in chemistry, pharmaceutics and civil engineering for the simulation of a variety of liquids, solutions, granular materials and powders.

3 Rock Mechanics

According to Judd (1964), rock mechanics is the theoretical and applied science of the mechanical behavior of rock studying the rocks response to acting forces. Mechanical properties describe and define the rocks behavior at changing stress conditions and are commonly investigated on rock masses accessible for exploitation. The transition from rock mechanics to the related fields of soil mechanics and structural geology is smooth, but passed when the rock masses of interest are strongly weathered and fragmented or in great, non-accessible depth, respectively (Jaeger et al., 2007).

Rock mechanics deals in general with stresses and inevitably resulting strain and can be seen as the broad fundamentals, on which applied geomechanics are based. The type of strain or deformation depends on the size of the external forces and the behavior of the rock defined by its mechanical properties. Stress at an arbitrary point is described as a second rank tensor, the so-called stress tensor (3.1). Transformation of this tensor yields the principal stresses, which play an important role in geomechanics (3.1.1). Some stress terms or combinations are independent of the coordinate system are referred to as stress invariants (3.1.2).

Equations describing the stress – strain relationships of rocks are called constitutive laws (3.2). These laws are empirically established by experiments and analyses, and cannot be calculated from first principles of physics. Nevertheless, they have to obey the fundamental laws of thermodynamics, for instance. Different constitutive laws exist describing basic or more complex stress-strain relationships. Elasticity as the ability of materials to resist and recover deformations produced by external forces represents the foundation of rock mechanics (Fjaer et al., 2008). This linear relation is called linear elasticity and is present in all deformation processes to some extent, especially and sometimes exclusively at small stress changes (3.2.1). The fact that rocks are porous and permeable media requires the consideration of the fluid-filled pore space in the rock mechanical behavior. The respective extension of linear elasticity is referred to as poroelasticity and is based on the theory of Biot (1955) (3.2.2).

Sufficiently large changes in stress produce non-linear behavior of rocks, i.e. the rock fails to withstand the stresses in an elastic way. This failure leads to irreversible deformation also called plastic deformation (3.2.3). In the upper Earth's crust, rocks show brittle behavior leading to the generation of joints and faults. Various constitutive laws define respective failure criteria for this brittle deformation (3.2.3.1). Another type of permanent deformation is called creep and describes the slowly deformation or moving of material due to an acting strain rate and/or as a function of temperature (3.2.3.2).

Faults and fractures are the result of brittle deformation and play an important role in rock mechanics. Fractures are the most common type of geological structures and represent cracks or joints in rocks, along which no or very little displacement occurred (Jaeger et al., 2007). Faults are fracture surfaces that experienced significant relative displacement and are in general approximately planar features (3.3). The prevailing type of faulting in a specific stress regime depends on the principal stress configuration (3.3.1). The importance of these features in rock mechanics emerges from the fact that they separate intact rock into blocks and provide planes of weakness along which sliding may occur and stress is released (3.3.2).

In applied geomechanics, faults are one major source for stress perturbations that change the ambient stress field. Geomechanical models consider faults in various ways (4.4) and can calculate the changes in stress, which must be considered in stress-sensitive reservoir operations. Moreover, the hydraulic

behavior of faults is of high interest (3.3.3). Faults may enhance or reduce the permeability of rock formations acting as conduits or baffles to fluid flow, respectively. They can act as seals representing hydrocarbon traps or leading to so-called compartmentalization of reservoirs.

3.1 Stress Principles

Stress is defined as force acting on an area or through a theoretical cross-section and is therefore given in N/m² expressed in the SI unit Pascal (Pa) (Eq. 3-1). An alternative unit called 'psi' (pounds per square inch) is also commonly used in hydrocarbon industry and can be re-calculated to Pascal and vice versa (Eq. 3-2). The sign of stress is not universally defined. In rock mechanics and geosciences, compressive stress is defined by convention to be positive, whereas in engineering sciences it is negative. The geological convention is based on the fact that stresses in the Earth are almost exclusively compressive (Fjaer et al., 2008; Zoback, 2007).

$$\sigma = \frac{F}{A} \qquad \text{Eq. 3-1}$$

σ = stress in [Pa] or [psi]; F = force in [N]; A = area in [m²]

$$1\ Pa = 1.450377\ \cdot 10^{-4}\ psi$$
$$1\ psi = 6.894757 \cdot 10^{3}\ Pa \qquad \text{Eq. 3-2}$$

The smaller the area is, on which the force is acting perpendicularly, the larger becomes the ratio and the resulting stress (Eq. 3-1). In case the orientation of the plane is not perpendicular to the acting force, this force can be decomposed to into two components acting normal and parallel to the target plane. The decomposition of forces is based on the laws of mechanics, which state that two arbitrary forces acting on a point can be reduced by a single force. The inversion of this law is called decomposition. Mathematically speaking this represents the summation or decomposition of the force vectors. Forces acting normal and parallel to the plane yield two types of stress: the normal and shear stress, respectively. Their magnitudes depend on the specific orientation of the target plane.

The full description of the state of stress at single point requires the identification of stresses acting on three orthogonal surfaces at this location (e.g. (Fjaer et al., 2008)). Three stresses are acting perpendicular to the three surfaces and six stresses – two on each surface – are parallel to the respective surface and directed orthogonal to the other surfaces (Fig. 3-1). Regarding a Cartesian coordinate system, the normal stress on the surface perpendicular to the x-axis is called σ_{xx}, while the shear stress in y-direction on this face is τ_{xy} and in z-direction τ_{xz}. Hence, the first index refers to the face itself the force is acting on, which is identified by the normal direction of the face, while the second index states the direction of the force. This yields nine stress components in total that are commonly expressed in a second rank tensor, the so-called stress tensor (Eq. 3-3).

$$\begin{bmatrix} \sigma_{xx} & \tau_{xy} & \tau_{xz} \\ \tau_{yx} & \sigma_{yy} & \tau_{yz} \\ \tau_{zx} & \tau_{zy} & \sigma_{zz} \end{bmatrix} \qquad \text{Eq. 3-3}$$

This stress tensor is composed of nine components, but not all of them are independent. When no translational or rotational forces are applied or considered, the conjugate terms in the stress tensor are equal (Eq. 3-4) (Fjaer et al., 2008). This is also referred to as the symmetry of the stress tensor and results in only six independent components.

$$\tau_{xy} = \tau_{yx}$$
$$\tau_{xz} = \tau_{zx} \qquad \text{Eq. 3-4}$$
$$\tau_{yz} = \tau_{zy}$$

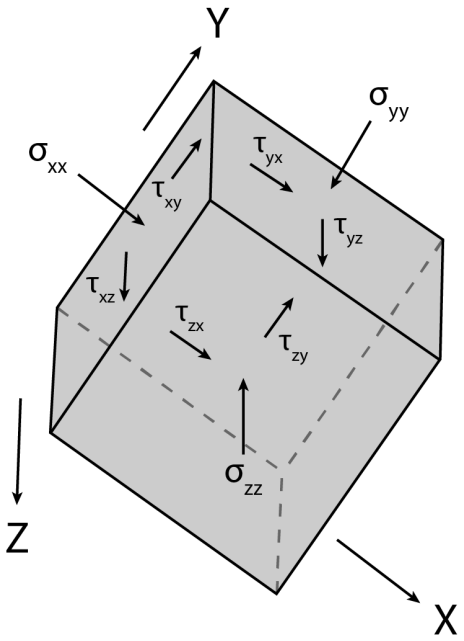

Fig. 3-1. Illustration of the components of the 3D stress tensor in an arbitrary Cartesian coordinate system. The indices of σ_{ij} and τ_{ij} refer to the normal direction of the plane the respective stress is acting on (i) and the direction of the force (j) (modified after Fjaer et al. (2008); Zoback (2007)).

3.1.1 Principal Stresses

If the full stress tensor is known in a distinct coordinate system, the stresses can be transferred and analyzed in any other coordinate system as well by using so-called tensor transformation (Zoback, 2007). In a special orientation of the coordinate system, the shear stresses mutually vanish and the stress tensor comprises a particularly simple form (Eq. 3-5). In this orientation, the x-, y-, and z-axis of the coordinate system are aligned with the so-called first, second and third principal axis (Fig. 3-2). The state of stress is then described by three normal stresses, i.e. the principal stresses σ_1, σ_2 and σ_3 (Eq. 3-5) (Fig. 3-2) (Fjaer et al., 2008). By convention, the principal stresses are defined as $\sigma_1 > \sigma_2 > \sigma_3$.

$$\begin{bmatrix} \sigma_1 & 0 & 0 \\ 0 & \sigma_2 & 0 \\ 0 & 0 & \sigma_3 \end{bmatrix} \qquad \text{Eq. 3-5}$$

The stress tensor transformation requires the definition of direction cosines (n_x, n_y, n_z) (Eq. 3-6). These are cosines of the angles between a unit vector in a chosen direction and the coordinate axes. The special orientation of the coordinate system and thus the three principal stresses are found by solving the following eigenvalue problem for σ (Eq. 3-6) (Jaeger et al., 2007).

$$\begin{bmatrix} \sigma_{xx} - \sigma & \tau_{xy} & \tau_{xz} \\ \tau_{yx} & \sigma_{yy} - \sigma & \tau_{yz} \\ \tau_{zx} & \tau_{zy} & \sigma_{zz} - \sigma \end{bmatrix} \begin{bmatrix} n_x \\ n_y \\ n_z \end{bmatrix} = \begin{bmatrix} 0 \\ 0 \\ 0 \end{bmatrix} \qquad \text{Eq. 3-6}$$

The determinant of this matrix is given by the following equation (Eq. 3-7) (Jaeger et al., 2007).

$$\sigma^3 - I_1\sigma^2 - I_2\sigma - I_3 = 0 \qquad \text{Eq. 3-7}$$

The three solutions for σ represent the principal stresses σ_1, σ_2 and σ_3, whereas I_1, I_2, I_3 represent so-called stress invariants (3.1.2). The existence of the principal stresses representing "real" roots of the stress tensor is ensured by its symmetry (3.1) (Jaeger et al., 2007).

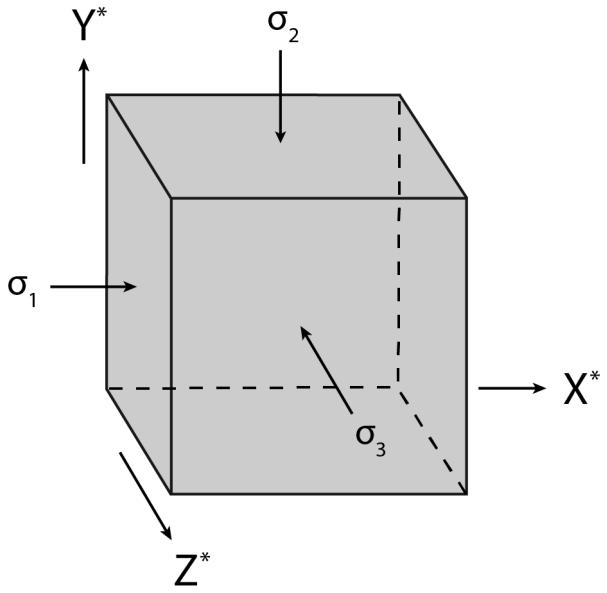

Fig. 3-2. Illustration of the stress tensor after transformation into the coordinate system comprising the principal axes (*). All shear stresses mutually vanish in this orientation and the stress tensor only comprises the three principal stresses σ_1, σ_2, σ_3 defined as $\sigma_1 > \sigma_2, > \sigma_3$ (modified after Fjaer et al. (2008); Zoback (2007)).

The concept of principal stresses is important in geosciences, because the Earth's surface inherently represents a principal stress plane due to its contact with a fluid, either air or water (Zoback, 2007). This contact precludes the support of any shear stresses and results in one principal stress being vertical to the Earth's surface and two orthogonal stresses in the horizontal plane. The state of stress in the Earth's crust is therefore defined by the magnitude of the vertical stress (SV) and the magnitude and orientation of the maximum (SHmax) and minimum horizontal stress (Shmin).

3.1.2 Invariants

During the change of the coordinate axes to a rotated set in order to derive the principal stresses, for instance, the components of the tensor change. Stress expressions or properties of the stress tensor that do not change are referred to as stress invariants. These invariants of stress are independent of the coordinate axes and have the same value in all coordinate systems. The most common stress invariants are I_1, I_2, I_3 (Eq. 3-8, Eq. 3-9, Eq. 3-10) (Fjaer et al., 2008; Jaeger et al., 2007).

$$I_1 = \sigma_x + \sigma_y + \sigma_z \qquad \text{Eq. 3-8}$$

$$I_2 = -\left(\sigma_x\sigma_y + \sigma_y\sigma_z + \sigma_z\sigma_x\right) + \tau_{xy}^2 + \tau_{yz}^2 + \tau_{xz}^2 \qquad \text{Eq. 3-9}$$

$$I_3 = \sigma_x\sigma_y\sigma_z + 2\tau_{xy}\tau_{yz}\tau_{xz} - \sigma_x\tau_{yz}^2 - \sigma_y\tau_{xz}^2 - \sigma_z\tau_{xy}^2 \qquad \text{Eq. 3-10}$$

The three principal stresses are functions of these three invariants (Eq. 3-7) and any further combination based on them will be an invariant as well (Jaeger et al., 2007). Another important stress invariant is the mean normal stress $\bar{\sigma}$, which represents the mean value of the three principal stresses (Eq. 3-11).

$$\bar{\sigma} = \frac{1}{3}(\sigma_x + \sigma_y + \sigma_z) \quad \text{Eq. 3-11}$$

This mean normal stress causes uniform compression or extension, i.e. a volumetric change of rock (Jaeger et al., 2007). In contrast, distortion of rocks results from so-called deviatoric stresses. These deviatoric stresses are derived by subtracting the mean normal stress from the stress tensor (Eq. 3-12) (Fjaer et al., 2008; Jaeger et al., 2007).

$$\begin{bmatrix} s_{xx} & s_{xy} & s_{xz} \\ s_{yx} & s_{yy} & s_{yz} \\ s_{zx} & s_{zy} & s_{zz} \end{bmatrix} = \begin{bmatrix} \sigma_{xx} - \bar{\sigma} & \tau_{xy} & \tau_{xz} \\ \tau_{yx} & \sigma_{yy} - \bar{\sigma} & \tau_{yz} \\ \tau_{zx} & \tau_{zy} & \sigma_{zz} - \bar{\sigma} \end{bmatrix} \quad \text{Eq. 3-12}$$

Equivalent to the stress invariants listed above (Eq. 3-8, Eq. 3-9, Eq. 3-10), deviatoric stress invariants are derived called J_1, J_2, and J_3 shown below (Eq. 3-13, Eq. 3-14, Eq. 3-15) (Fjaer et al., 2008; Jaeger et al., 2007).

$$J_1 = s_x + s_y + s_z = 0 \quad \text{Eq. 3-13}$$

$$J_2 = -(s_x s_y + s_y s_z + s_z s_x) + s_{xy}^2 + s_{yz}^2 + s_{xz}^2 \quad \text{Eq. 3-14}$$

$$J_3 = s_x s_y s_z + 2 s_{xy} s_{yz} s_{xz} - s_x s_{yz}^2 - s_y s_{xz}^2 - s_z s_{xy}^2 \quad \text{Eq. 3-15}$$

The first deviatoric stress invariant J_1 is always zero. The other two invariants are often used in the description of failure criteria that are primarily concerned with distortion and require the independency of coordinate axes, for instance the Drucker-Prager criterion frequently used in numerical modeling (3.2.3.1, Eq. 3-41) (Zoback, 2007).

3.2 Constitutive Laws

Equations describing the relationship between two physical quantities based on empirical studies and analyses are called constitutive laws. Constitutive laws in rock mechanics define the deformation behavior of a rock due to applied stresses (Zoback, 2007). These equations are established by experiments and rational analysis, and their respective constants have to be measured in the laboratory or in the field (Middleton and Wilcock, 1994). They cannot be calculated or derived from first principles of physics. However, constitutive laws have to obey principle laws of physics such as those of thermodynamics, for instance. The complexity of constitutive laws depends on the behavior they are describing and the phenomena incorporated.

3.2.1 Linear Elasticity

The most basic deformation behavior of rock is represented by a linear relationship between applied stress and resulting strain, in which the strain is reversible and vanishes when the load is removed. This behavior is known as linear elasticity. In this deformation type, the strain tensor is a linear function of the stress tensor (Jaeger et al., 2007).

The constitutive law describing linear elasticity is deduced from the linear behavior of a sample with the width D and the length L, which is aligned along the x-axis in a Cartesian coordinate system. This sample is uniaxially stressed in x-direction by σ_X ($\sigma_X > 0$, $\sigma_Y = \sigma_Z = 0$) reducing the length of the sample to L'. The corresponding elongation is described as the ratio of the length change to the initial length (Eq. 3-16).

$$\varepsilon_x = \frac{(L - L')}{L} \qquad \text{Eq. 3-16}$$

In case of linear elastic behavior, the relationship between the applied stress σ_X and resulting strain ε_X is linear and thus expressed by a factor relating the two quantities (Eq. 3-17).

$$\sigma_x = E \cdot \varepsilon_x \qquad \text{Eq. 3-17}$$

This linear relation in elasticity is generally known as Hooke's law (Pollard and Fletcher, 2005; Robinson and Clark, 1988). The constant E in this law is called Young's modulus or E-modulus and represents the stiffness of the sample. Following this equation, the Young's modulus is defined by the ratio of axial stress to the respective strain (Eq. 3-17). It is commonly obtained from the loading curve in unconfined uniaxial compression tests using cylindrical rock samples (Fig. 3-3).

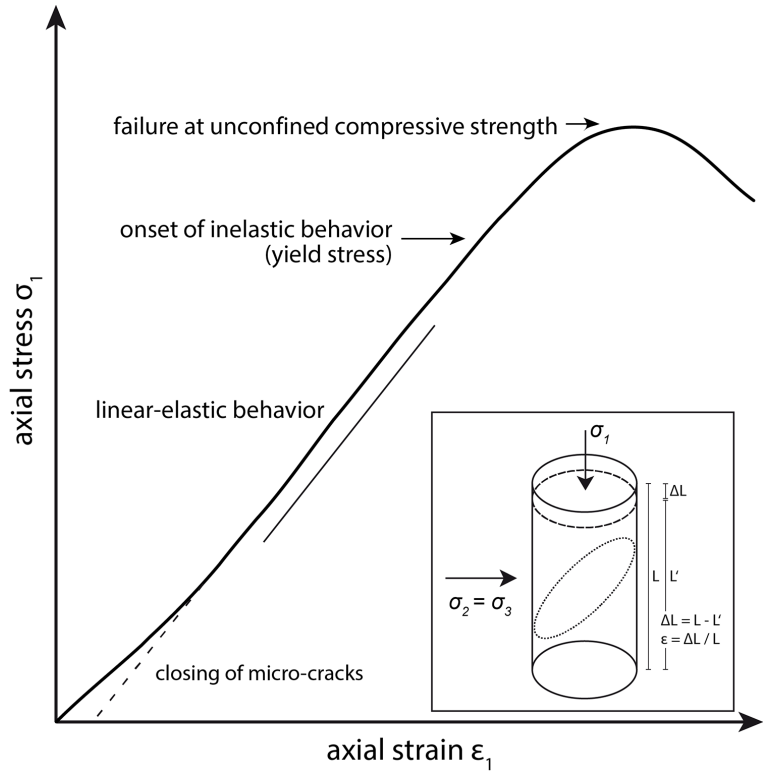

Fig. 3-3. Loading curve of an unconfined uniaxial compression test. A cylindrical rock sample is uniaxially loaded with σ_1 resulting in axial strain ε_1, which are plotted against each other. The first section of the loading curve reveals small amounts of inelastic deformation related to the closure of micro-cracks in the sample. Subsequently, the loading curve follows a linear trend representing a phase of linear elastic deformation, from which the Young's modulus is derived. After the yield stress is reached, the sample starts to deform inelastically and eventually fails at the uniaxial compressive strength as peak stress. The experiment setup is illustrated in the box (right) indicating additionally an inclined plane inside the sample along which shear failure is likely to occur (modified after Zoback (2007)).

In these tests, a cylindrical sample is uniaxially loaded with zero confining pressure. The applied axial stress and resulting axial strain is plotted against each other revealing the loading curve (Fig. 3-3). After the initial closing of micro-cracks in the sample, it commonly deforms linear elastically over a distinct range (van der Pluijm and Marshak, 2003). This type of deformation results in a linear section of the loading curve, from whose slope the Young's modulus is calculated (Fig. 3-3). The length of this

linear part depends, amongst others, on the rock type, fabric and quality of the sample. Following the linear elastic deformation of the sample, it starts to show inelastic behavior when the so-called yield stress is reached and eventually fails (Fig. 3-3). The peak stress the sample could resist is referred to as unconfined compressive strength (UCS).

The Young's modulus is also seen as the resistance against uniaxial compression. The greater the modulus is, the higher are the stresses the material can suffer. While ε_X is dimensionless, the Young's modulus is given in the same unit as stress [Pa]. Reported values in geology range from 1-150GPa (Pollard and Fletcher, 2005; Twiss and Moores, 2007), which elucidates the strong dependence on the rock type and characteristics.

Besides the reduction in length of the sample, uniaxial compression also results in lateral elongation, i.e. expansion showing an increased width D' in y-direction. The lateral elongation ε_Y is derived in the same way as ε_X (Eq. 3-18).

$$\varepsilon_y = \frac{(D - D')}{D} \qquad \text{Eq. 3-18}$$

This lateral expansion is also known as Poisson expansion (Twiss and Moores, 2007). The ratio of lateral expansion ε_Y to axial strain ε_X – representing longitudinal contraction – is known as Poisson ratio ν (Eq. 3-19).

$$\nu = -\frac{\varepsilon_y}{\varepsilon_x} \qquad \text{Eq. 3-19}$$

Both strains and thus the Poisson ratio are determined in uniaxial compression tests at a cylindrical sample in combination with the Young's modulus (Fig. 3-3). The Poisson's ratio is dimensionless and describes the material's potential to change shape and volume during deformation (Ramsay and Lisle, 2000). Due to the lateral increase in width (D' > D), lateral elongation is commonly negative ($\varepsilon_Y = \varepsilon_Z < 0$) and thus the sign of the ratio yields positive values for the Poisson ratio, which range between 0 and 0.5. The minimum and maximum value of this ratio represent perfectly compressible ($\nu = 0$) and incompressible behavior ($\nu = 0.5$). Any material that has a Poisson ratio of less than 0.5 decreases in volume under compression. Rocks commonly take values between 0.1 and 0.3 (Gercek, 2007; Pollard and Fletcher, 2005).

The Young's modulus and the Poisson ratio represent the first and second so-called elastic modulus. Elastic moduli are parameters describing the linear elastic behavior of rocks. If these two parameters are derived from unconfined uniaxial compression tests, they are referred to as static moduli due to the slow loading rates. Static moduli represent the appropriate quantities to be used in numerical simulations.

Besides the determination of the Young's modulus and the Poisson ratio by unconfined uniaxial compression tests, they are also derived from acoustic wave propagation through the rock. The elastic moduli are then calculated from the compressive and shear wave velocity in the sample and its density (Eq. 3-20, Eq. 3-21) (Fjaer et al., 2008).

$$E = \rho v_s^2 \frac{3v_p^2 - 4v_s^2}{v_p^2 - v_s^2} \qquad \text{Eq. 3-20}$$

$$\nu = \frac{v_p^2 - 2v_s^2}{2\left(v_p^2 - v_s^2\right)} \qquad \text{Eq. 3-21}$$

E = Young's modulus, ν = Poisson's ration, ρ = density, v_p = compressive wave velocity, v_s = shear wave velocity

These moduli are then referred to as dynamic elastic moduli. In these measurements, the poroelastic behavior of the rocks becomes important yielding a rate-dependency, i.e. the loading speed in a test affects the resulting moduli values (3.2.2). Therefore the resulting dynamic moduli cannot be used directly for numerical modeling.

In addition to the Young's modulus and the Poisson ratio, there are further elastic moduli available. A sample that is loaded by hydrostatic confining pressure σ_P ($\sigma_X = \sigma_Y = \sigma_Z > 0$) will experience uniform strain of volume reduction ε_{vol} ($\varepsilon_{vol} = \varepsilon_X + \varepsilon_Y + \varepsilon_Z = \Delta V/V$). The ratio of hydrostatic pressure and volume strain yields the so-called bulk modulus K (Fjaer et al., 2008). It represents the stiffness in hydrostatic compression and its inverse value is known as compressibility β of a material or rock.

A material's resistance against shear deformation is given by the shear modulus G derived from the ratio of shear stress to resulting shear strain (Zoback, 2007). This elastic modulus is naturally zero for fluids due to the fact that they cannot support shear stresses. A fifth commonly used parameter is the Lamé's constant λ, which has no physical description. This parameter relates bulk and shear modulus ($K = \lambda + 0.\overline{6}G$). Moreover, all elastic moduli are re-calculable into each other. If two moduli are known, all others can be derived by respective equations stated in literature (Fjaer et al., 2008; Jaeger et al., 2007; Pollard and Fletcher, 2005; Zoback, 2007).

3.2.1.1 Stress-Strain Relationship

Two elastic moduli are sufficient to describe the linear elastic behavior of a rock assuming that the rock is an isotropic, homogeneous material. In such a material, its response to applied stresses is independent of their orientation, i.e. the relationship between vertical stress and vertical strain, and horizontal stress and horizontal strain is the same. The principal stress axes equal the principal strain axes (Fjaer et al., 2008). A general description of stress and strain is formulated for such materials using the respective tensors and elastic moduli (Eq. 3-22) (Wang, 2000).

$$\sigma_{ij} = 2\left(\frac{E}{2+2\nu}\right)\varepsilon_{ij} + \left(\frac{E\nu}{(1+\nu)(1-2\nu)}\right)\delta_{ij}\varepsilon_{vol} \qquad \text{Eq. 3-22}$$

i, j = x, y, z; σ_{ij} = stress tensor; ε_{ij} = strain tensor; E = Young's modulus; ν = Poisson's ratio; ε_{vol} = volumetric strain

δ = Kronecker delta defined as $\delta_{ij} = 1$ when i = j and $\delta_{ij} = 0$ when $i \neq j$

In isotropic and homogeneous materials, this equation correlates the applied stresses as tensor σ_{ij} to the resulting strain tensor ε_{ij} by using the Young's modulus E, the Poisson ratio ν and the volumetric strain ε_{vol} (Eq. 3-22). However, the stress-strain relationships in isotropic elasticity can be also expressed by principal stresses and principal strains, and by any other two elastic moduli (Eq. 3-23, Eq. 3-24, Eq. 3-25) (Jaeger et al., 2007).

$$\sigma_1 = (\lambda + 2G)\varepsilon_1 + \lambda\varepsilon_2 + \lambda\varepsilon_3 \qquad \text{Eq. 3-23}$$

$$\sigma_2 = \lambda\varepsilon_1 + (\lambda + 2G)\varepsilon_2 + \lambda\varepsilon_3 \qquad \text{Eq. 3-24}$$

$$\sigma_3 = \lambda\varepsilon_1 + \lambda\varepsilon_2 + (\lambda + 2G)\varepsilon_3 \qquad \text{Eq. 3-25}$$

$\sigma_1, \sigma_2, \sigma_3$ = principal stresses; $\varepsilon_1, \varepsilon_2, \varepsilon_3$ = principal strains; G = shear modulus; λ = Lamé's constant

In summary, elasticity is the ability of a material to resist and recover deformation produced by stress and represents the foundation of rock mechanics. Elastic deformation is present to some extent in all types of deformation. If applied loads are sufficiently small, rocks respond almost always linearly. With increasing stresses, however, the elastic domain is left and permanent deformation occurs.

3.2.2 Poroelasticity

All rocks comprise pore space and fractures of varying amounts and are thus to be regarded as porous media. The space is inherently filled with fluids such as air, water, gas or oil, which flow through the medium according to pressure gradients, fluid viscosity and permeability. These fluids influence the mechanical behavior of rocks significantly. The concept of poroelasticity describes the coupled hydro-mechanical behavior of a porous-elastic solid saturated with a fluid and is based on the theory of Biot (1941) (Wang, 2000). This concept is based on three principal assumptions (Zoback, 2007): (1) the pore space system is of the material is interconnected and uniformly saturated with a fluid; (2) the total volume of pore space is small compared to the total rock volume; (3) pore pressure, externally acting stress and internally acting stress on grains are considered as statistically averaged uniform values.

An isotropic, porous and permeable medium consists of a solid and a fluid part. Externally applied stress is thus balanced partly by stresses in the solid framework and partly by a hydrostatic pressure in the fluid, the so-called pore pressure. The presence of a pore fluid thus demands a modification of the stress-strain relationship introduced above (Eq. 3-22 – Eq. 3-26) (Fjaer et al., 2008).

$$\sigma_{ij} = 2\left(\frac{E}{2+2\nu}\right)\varepsilon_{ij} + \left(\frac{E\nu}{(1+\nu)(1-2\nu)}\right)\delta_{ij}\varepsilon_{vol} - A_e\zeta\delta_{ij} \qquad \text{Eq. 3-26}$$

A_e = additional elastic moduli; ζ = strain parameter; other parameters as stated in Eq. 3-22

This formulation describes the 3D stress-strain relationship of an isotropic poroelastic solid. The equation is extended by the subtraction of a third term comprising an additional elastic modulus A_e and the strain parameter ζ. This strain parameter ζ is also known as increment of fluid content (Wang, 2000). It describes the volumetric deformation of the fluid relative to the deformation of the solid and can be derived from the change in pore volume and the compression of the fluid (Eq. 3-27) (Fjaer et al., 2008).

$$\zeta = -\phi\left(\frac{\Delta V_p}{V_p} + \frac{P_p}{K_f}\right) \qquad \text{Eq. 3-27}$$

ζ = strain parameter; ϕ = porosity; V_p & ΔV_p = pore fluid volume & its change; K_f = pore fluid bulk modulus

The change in pore volume may be the result from changes in external stresses or the pore pressure, while compression or decompression of the fluid is related to pore pressure changes. The additional elastic modulus of A_e is derived from the elastic moduli of the rock constituents, i.e. from the bulk moduli of pore fluid and solid grains in addition with porosity and the so-called framework modulus (Eq. 3-28) (Fjaer et al., 2008).

$$A_e = \frac{K_f}{\phi}\frac{\left(1-\frac{K_{fr}}{K_s}\right)}{1+\frac{K_f}{\phi K_s}\left(1-\phi-\frac{K_{fr}}{K_s}\right)} \qquad \text{Eq. 3-28}$$

K_f = pore fluid bulk modulus; K_s = bulk modulus of solid grains; K_{fr} = framework modulus; ϕ = porosity

The framework modulus is also referred to as drained bulk modulus, i.e. the bulk modulus of the material in a drained state. In such a state, the fluids are able and have time to dissipate local pressure increases. This expression of A_e is based on the so-called Gassmann or Biot-Gassmann equation.

3.2.2.1 Effective Stress

In many applications and studies, including this study, the concept of effective stress is considered. This concept is based on the work of Terzaghi (1923) in soil mechanics and based on the idea that the behavior of rock is governed by the difference of applied stress and internal pore pressure, i.e. the so-called effective stresses (Wang, 2000). Accordingly the stress tensor σ_{ij} of applied external stresses is modified to the effective stress tensor $\sigma_{eff\,ij}$ (Eq. 3-29).

$$\sigma_{eff_{ij}} = \sigma_{ij} - \delta_{ij}\alpha P_p \qquad \text{Eq. 3-29}$$

$\sigma_{eff\,ij}$ = effective stress tensor; σ_{ij} = stress tensor; P_p = internal pore pressure; α = Biot's coefficient

δ = Kronecker delta defined as $\delta_{ij} = 1$ when $i = j$ and $\delta_{ij} = 0$ when $i \neq j$

The Kronecker Delta δ_{ij} implies that the pore pressure P_P influences only the normal components of the stress tensor and not the shear components. The parameter α is known as Biot or Biot-Willis coefficient of pore pressure in the effective stress for bulk volume (Wang, 2000). It defines the pore pressure efficiency in counteracting confining pressure leading to volumetric strain (Nur and Byerlee, 1971). The Biot coefficient is derived from the bulk modulus of the drained rock and the individual grains (Eq. 3-30).

$$\alpha = 1 - \frac{K_{fr}}{K_s} \qquad \text{Eq. 3-30}$$

α = Biot coefficient; K_{fr} = drained bulk modulus; K_S = bulk modulus of solid grains; $K_{fr} < K_S$

Due to the fact that the drained bulk modulus is always lower than the bulk modulus of the solid grains, the value of the Biot coefficient ranges between 0 and 1 ($0 < \alpha < 1$). The less porosity is available in a rock, the lower is the Biot coefficient and thus the influence of the pore pressure. In turn, the pore pressure has greatest influence in highly porous formations or saturated soils or sands resulting in the original assumption of Terzaghi of $\alpha = 1$ (Terzaghi, 1923). Reported α - values of various sandstones range between 0.64 – 0.85 (Wang, 2000).

3.2.2.2 Impact on Elastic Moduli

The poroelastic behavior of rocks inherently affects the measurements of elastic moduli (Wang, 2000; Zoback, 2007). The faster a load is applied on a fluid-saturated poroelastic rock, the higher is the appearing stiffness, for instance. This is because the pore fluid has no time to drain away and is thus carrying some of the applied stress, which results in the higher stiffness measured. The described condition or behavior is referred to as undrained. Relatively slow loading rates allow the drainage of fluids and the dissipation of local pressure increases. The measured stiffness is thus lower under these so-called drained conditions. The transition from drained to undrained behavior strongly depends on the permeability of the rock and the viscosity of the fluid with which der rock is saturated (Wang, 2000).

The dependency of the measurement of elastic moduli on the strain rate is particularly important in measurements using acoustic wave propagation (Fjaer et al., 2013). These measurements reflect always undrained conditions. The strain rate dependency leads to a frequency dependency characteristic for the rock and its fluid saturation. In general, lower frequencies yield lower velocities of the acoustic waves resulting in lower elastic stiffness – and vice versa (Zoback, 2007). Measurements of elastic moduli using compressive and shear waves therefore provide so-called dynamic moduli, which are commonly higher than static moduli obtained from uniaxial compression

tests (Holt et al., 2013). Dynamic moduli are derived by various methods using different frequency bands. Reflection seismics comprise frequencies of about 10-100Hz, whereas sonic logs in wellbores use approximately 10kHz (Zoback, 2007). The highest frequencies are used in ultrasonic laboratory measurements of drill cores applying about 1MHz.

All dynamic moduli must be converted to static equivalents in order to be used in numerical modeling (Herwanger and Koutsabeloulis, 2011; Holt et al., 2013). This is done by correlation of dynamic moduli with reservoir-specific measurements of static moduli. The more measurements are available, the more reliable is this conversion process and the higher the quality of the input data for the numerical model. The application of published correlations (e.g. (Eissa and Kazi, 1989; Morales and Marcinew, 1993)) is unfavorable, but inevitable if no reservoir-specific data is available. In case such general correlations are used, care must be taken concerning the specific frequency of the measurement, from which the dynamic moduli are obtained.

3.2.3 Plastic Deformation

At sufficiently large stresses rocks fail to withstand them elastically and react inelastically. Inelastic deformation is irreversible and thus the rock deforms permanently. This permanent deformation is referred to as plastic deformation or plasticity (Jaeger et al., 2007). Commonly a finite yield stress of a material must be exceeded that it starts to deform plastically. The so-called failure of a material or rock is characterized by a singularity representing a sudden change in deformation behavior. Such non-linear behavior is characteristic for the various types of plastic deformation described.

Subsequently the most applied failure criteria in brittle deformation of the Earth's crust are discussed, as well as the failure types of shear, tensile and compaction failure (3.2.3.1). In addition, creep behavior is briefly addressed representing continuous plastic deformation (3.2.3.2). This slow material movement results from constant loads and/or temperatures. The mathematical theory of creep behavior is also referred to as viscoelasticity (Jaeger et al., 2007).

3.2.3.1 Brittle Behavior

Reservoirs of any type accessible for exploitation and thus relevant for geomechanics are located in the upper Earth's crust. This domain is characterized by brittle deformation behavior, i.e. the rocks fail under sufficiently high stresses by brittle shear, tensile or compaction failure. Failure is a sudden, complex process that is still not fully understood (Zoback, 2007). Therefore all models or criteria for failure represent simplified descriptions of realistic rock behavior (Fjaer et al., 2008). The level of stress at which brittle failure occurs is referred to as the strength of the rock against the respective type of failure, for instance tensile strength defining the stress level that limits tensile failure. Rock strengths must be related to the tests by which they are measured.

The most common test scenario for rocks is the unconfined uniaxial compression test leading to shear failure (Fig. 3-3). A cylindrical sample is loaded axially ($\sigma_1 > 0$) with zero confining pressure ($\sigma_2 = \sigma_3 = 0$). After experiencing a phase of elastic deformation, brittle shear failure eventually occurs along an inclined plane through the sample at a peak stress referred to as unconfined compressive strength (UCS) (Zoback, 2007). If loading proceeds after this point, the subsequent behavior is described as strain hardening or softening depending whether the material is able to resist more or less load with ongoing plastic deformation.

Shear Failure

Brittle shear failure occurs instantaneously at a distinct stress level. Microscopic failures inside the rock coalesce into a through-going plane, along which the rock is sheared and fails (Lockner et al., 1991). In other words, if the shear stress along any plane in the rock is sufficiently high, shear failure occurs along this plane. The stress level required for shear failure is known as critical shear stress τ_{max}. The assumption that this critical shear stress depends on the stress acting normal on the potential fault plane is called Mohr's hypothesis (Eq. 3-31) (Fjaer et al., 2008).

$$|\tau_{max}| = f(\sigma) \qquad \text{Eq. 3-31}$$

The fact that the critical shear stress is a function of the normal stress implies that in a plot of shear stress against normal stress a line will separate a safe region from a region of failure (Fig. 3-4). States of stress are generally plotted in such diagrams as Mohr circles mounted by the largest and least principal stress, i.e. σ_1 and σ_3 (Fig. 3-4). The smaller the difference between those two principal stresses is, the smaller is the resulting Mohr circle. Small circles below the failure line represent safe states of stresses. An increasing difference between σ_1 and σ_3 results in larger circles until they ultimately touch the failure line. At this state of stress, i.e. at these conditions, the rock experiences shear failure. Therefore no circle can exceed the failure line in size, since this would represent a state of stress the rock cannot sustain. Shear failure criteria describe this function of normal stress $f(\sigma)$ in Mohr's hypothesis (Eq. 3-31) (Fjaer et al., 2008). The simplest solution for $f(\sigma)$ represents a constant value, implying that shear failure occurs at a material-specific level of shear stress. This is known as the Tresca criterion (Eq. 3-32) (Fjaer et al., 2008).

$$\tau_{max} = \frac{1}{2}(\sigma_1 - \sigma_3) = C \qquad \text{Eq. 3-32}$$

The constant C in this equation represents the so-called inherent shear strength of the rock, also known as cohesion. In the plot of shear stress versus normal stress, this criterion represents a straight horizontal line. However, studies showed that rock strength against shear failure increases monotonically with increasing confining pressure (Zoback, 2007). This fact is regarded in the most frequently used Mohr-Coulomb criterion for shear failure (Eq. 3-33).

$$\tau_{max} = \mu_i \sigma_n + C \qquad \text{Eq. 3-33}$$

The Mohr-Coulomb criterion describes the critical shear stress by a linear function, in which μ_i is known as the coefficient of internal friction of the rock and C as cohesion. This criterion represents an inclined failure line in the $\tau - \sigma$ plot, whose slope is defined by μ_i and that intercepts the τ – axis at C (Fig. 3-4). The coefficient of internal friction μ_i is the tangent of the angle of internal friction φ. The equation further implies that the Tresca criterion can be seen as a special case of the Mohr-Coulomb criterion for cases when $\mu_i = 0$ (Eq. 3-33) (Fjaer et al., 2008).

The result of an unconfined compression test of a rock sample yields a Mohr circle ranging from the origin ($\sigma_3 = 0$) to the magnitude of σ_1, which equals in this case the unconfined compressive strength UCS (Fig. 3-4). The application of a confined pressure in a compression tests shifts the resulting Mohr circle to the right and increases the resistance against shear failure. The latter is elucidated by the slope of the failure line allowing larger Mohr circles at higher confining pressures (Fig. 3-4). Internal pore pressure P_P of the rock yields lower effective stresses, thus shifting the circle to the left and closer to the failure line (Fig. 3-4) (Fjaer et al., 2008).

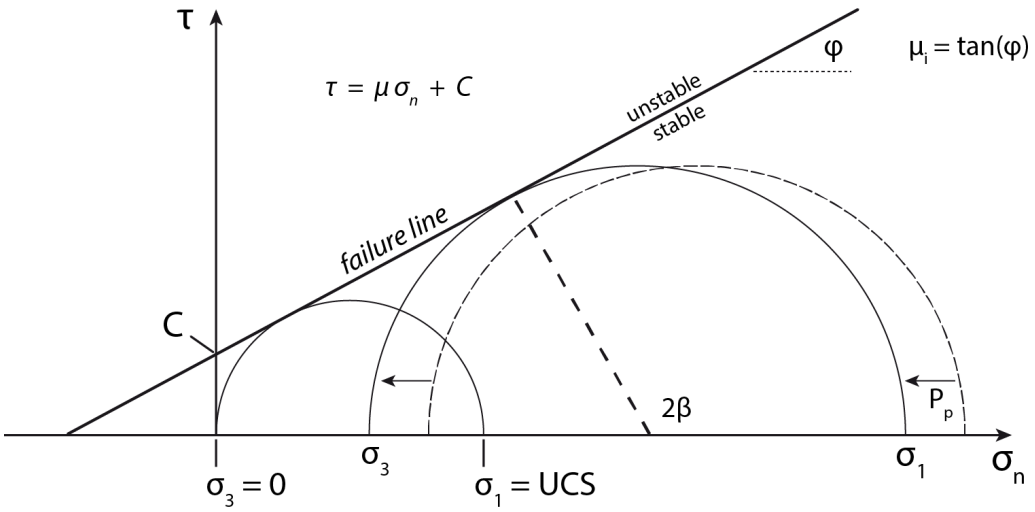

Fig. 3-4. Diagram plotting shear stress τ against normal stress σ_n. The Mohr-Coulomb criterion represents an inclined failure line with the slope of μ_i and intercept C representing the coefficient of internal friction and the cohesion of the rock, respectively. This failure line separates stable and unstable states of stress described by Mohr circles. When a circle touches this failure line the rock fails, which is the intention in rock mechanical tests establishing the criterion for a specific rock. All variables are explained in the text (modified after Fjaer et al. (2008); Zoback (2007)).

Mohr circles of multiple compression tests under different confining pressures yield a so-called Mohr envelope instead of a straight failure line (Fig. 3-5). This envelope shows parabolic shape and thus strongest change in stable stress states at low confining pressures and approximates the linearized failure line with higher confining pressures. Finally, the envelope would turn into a horizontal line at the transition from brittle to plastic behavior (van der Pluijm and Marshak, 2003). The plotting of the intermediate principal stress σ_2 inside the Mohr circles demonstrates that it has no impact on the size of the biggest circle (Fig. 3-5). Therefore this stress magnitude does not influence the point of failure described by the Mohr-Coulomb criterion.

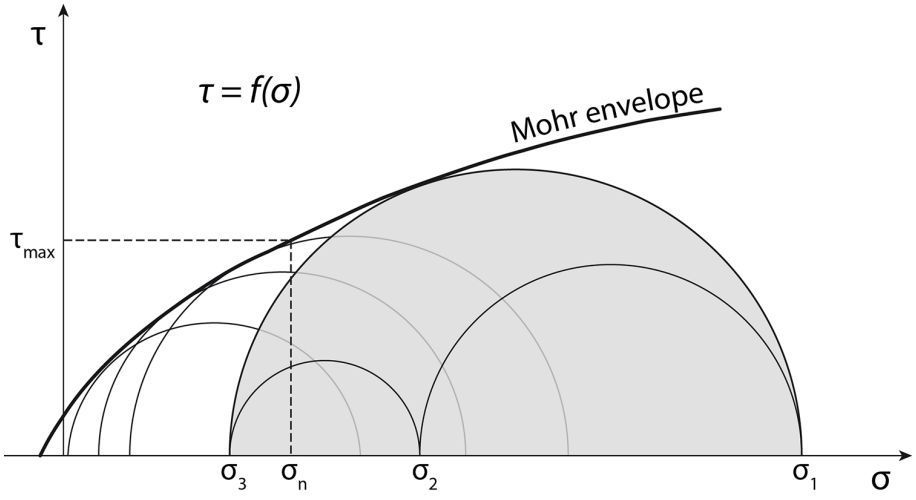

Fig. 3-5. Mohr circles of four compression tests with different confining pressures plotted in the τ-σ space. A Mohr envelope is built based on these circles describing the Mohr-Coulomb criterion. The circles including the intermediate principal stress σ_2 demonstrate that σ_2 does not affect the definition of the Mohr-Coulomb failure criterion.

The state of stress at which shear failure occurs is reached when the respective Mohr circle contacts the failure line. This is the intention in rock mechanical tests with different confining pressures establishing the criterion for a specific rock. The shear and normal stresses at this point of failure can be described by the largest and least principal stress and the angle β (Eq. 3-34, Eq. 3-35, Fig. 3-5).

$$\tau_{max} = \frac{1}{2}(\sigma_1 - \sigma_3)\sin 2\beta \qquad \text{Eq. 3-34}$$

$$\sigma_n = \frac{1}{2}(\sigma_1 + \sigma_3) + \frac{1}{2}(\sigma_1 - \sigma_3)\cos 2\beta \qquad \text{Eq. 3-35}$$

The angle β represents the angle between the largest principal stress σ_1 and the normal direction of the shear plane and therefore describes its orientation. This angle β is controlled by the angle of internal friction φ and thus also by the related coefficient μ_i of the Mohr-Coulomb criterion (Eq. 3-36, Fig. 3-4).

$$\varphi = 2\beta - \frac{\pi}{2} \qquad \text{Eq. 3-36}$$

This dependency implies that the orientation of the failure plane is independent of confining pressure due to the fact that μ_i is a constant in the Mohr-Coulomb criterion (Fjaer et al., 2008). The equations describing shear and normal stress at the point failure further elucidate the independency of the intermediate principal stress σ_2 in the Mohr-Coulomb criterion (Eq. 3-34, Eq. 3-35).

While the unconfined compressive strength (UCS) equals the magnitude of the largest principal stress σ_1 in unconfined compressive tests, it can also be calculated based on the cohesion and coefficient of internal friction of the rock (Eq. 3-37) (Zoback, 2007).

$$UCS = 2C\left[\sqrt{(\mu_i{}^2 + 1)} + \mu_i\right] \qquad \text{Eq. 3-37}$$

Example values for the coefficient of internal friction, cohesion and unconfined compressive strength of rocks are given in Tab. 3-1. These values may vary significantly depending on the rock type and sample quality, for instance.

	general range	common values
Unconfined Compressive Strength (UCS)	30 – 300 MPa	100 – 150 MPa
Coefficient of internal friction (μ_i)	0.5 - 2	± 1.2
Cohesion (C)	1 – 40 MPa	10 – 20 MPa

Tab. 3-1. Overview on value ranges and common values for unconfined compressive strength UCS, coefficient of internal friction μ_i and cohesion C summarized after Pollard and Fletcher (2005); Zoback (2007).

Beside the expression of failure by τ_{max} and σ_n (Eq. 3-34, Eq. 3-35), the Mohr-Coulomb criterion can also be expressed directly by principal stresses, the angle of internal friction and the cohesion (Eq. 3-38) (Fjaer et al., 2008).

$$\sigma_1 = \frac{1 + \sin\varphi}{1 - \sin\varphi}\sigma_3 + 2C\frac{\cos\varphi}{1 - \sin\varphi} \qquad \text{Eq. 3-38}$$

In a plot of the largest principal stress σ_1 against the least principal stress σ_3, this equation describes a straight line in this two-dimensional principal stress space with a positive intercept at the σ_1 axis. For a more general description of the Mohr-Coulomb criterion, the convention of $\sigma_1 > \sigma_2 > \sigma_3$ is abandoned, which results in two lines ($\sigma_1 > \sigma_3$ & $\sigma_1 < \sigma_3$) (Fjaer et al., 2008). These lines are symmetric around a bisecting line representing the hydrostatic condition ($\sigma_1 = \sigma_3$), while the intermediate stress is σ_2 and neglected due to the nature of the Mohr-Coulomb criterion. The same projection in the σ_1-σ_2 and σ_2-σ_3 – space considers σ_3 and σ_1 as neglected intermediate stress, respectively, and yields two characteristic lines as well.

These projections can be assembled in three dimensional principal stress space, in which they build up a hexagonal, pyramid-shaped surface (Fig. 3-6). This surface is known as the failure surface of the

Mohr-Coulomb criterion. The origin in two dimensions elucidates the fact, that the shape of this failure surface reflects the independency of the intermediate principal stress (Fjaer et al., 2008). However, the resulting sharp corners of this failure surface cause problems in numerical modeling. These problems are avoided using other failure criteria including the intermediate principal stress.

The von Mises failure criterion takes all three principal stresses into account in a relatively simple solution (Eq. 3-39). Despite its lacking physical foundation, it is mathematically attractive and used as basis for other, more sophisticated criteria (Fjaer et al., 2008).

$$k_1 = \sqrt{(\sigma_1 - \sigma_2)^2 + (\sigma_1 - \sigma_3)^2 + (\sigma_2 - \sigma_3)^2} \qquad \text{Eq. 3-39}$$

Besides the principal stresses σ_1, σ_2, and σ_3, the constant k_1 in this equation is related to the materials cohesion. Therefore the von Mises criterion can be seen as equivalent to the Tresca criterion (Eq. 3-32). In both criteria, shear failure occurrence is independent of the stress level. In three dimensional principal stress space, the von Mises criterion shows a rotational symmetry around the hydrostatic axis (Fig. 3-6). This failure criterion is often used to describe the yield in metals, but cannot be directly used for rocks.

Comparable to the Mohr-Coulomb criterion representing the generalization of the Tresca criterion, the von Mises criterion is extended to the so-called Drucker-Prager criterion, thus also referred to as Extended von Mises criterion (Eq. 3-40) (Fjaer et al., 2008).

$$k_2(\sigma_1 + \sigma_2 + \sigma_3 + k_1)^2 = (\sigma_1 - \sigma_2)^2 + (\sigma_1 - \sigma_3)^2 + (\sigma_2 - \sigma_3)^2 \qquad \text{Eq. 3-40}$$

The constants k_1 and k_2 in the equation are related to the cohesion and internal friction of the material, respectively (Eq. 3-40).

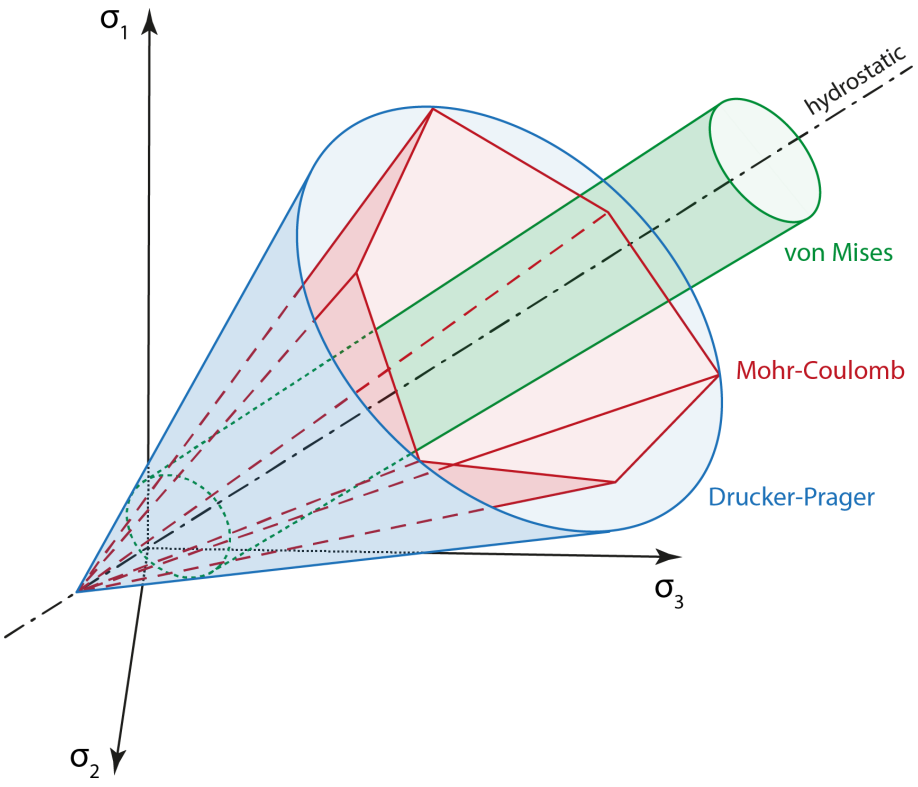

Fig. 3-6. Illustration of the failure surfaces of the von Mises (green), Mohr-Coulomb (red) and Drucker-Prager criterion (blue) in three dimensional principal stress space. The central axis represents hydrostatic conditions ($\sigma_1 = \sigma_2 = \sigma_3$). The characteristic hexagonal shape of the Mohr-Coulomb failure surface results from the independency of the intermediate principal stress (modified after Fjaer et al. (2008)).

In addition, the Drucker-Prager criterion is commonly expressed by using the stress invariants I_1 and J_2, which are introduced above (3.1.2) (Eq. 3-41) (Jaeger et al., 2007; Zoback, 2007).

$$\sqrt{J_2} = k_1 + k_2 I_1 \qquad \text{Eq. 3-41}$$

This equation shows that the Drucker-Prager criterion is reduced to the von Mises criterion when k_2 equals zero (Eq. 3-41). The failure surface in three dimensional principal stress space is represented by a cone around the hydrostatic axis (Fig. 3-6).

The Drucker-Prager criterion was initially developed to describe the plastic deformation of soils (Drucker and Prager, 1952), but is nowadays one of the most used criteria for plastic deformation in numerical calculations in general. The commercial FE code Ansys® that is used in this study can also apply the Drucker-Prager criterion to simulate plastic deformation of solids in three dimensions.

While the incorporation of the intermediate principal stress is mandatory for numerical calculation of plastic deformation in solids, it is not the case for modeling frictional fault behavior by interface or contact elements. Therefore, the Drucker-Prager criterion is commonly applied in finite element analyses to model the plastic deformation of solid volumes, whereas the Mohr-Coulomb criterion is taken to describe the frictional behavior of distinct fault faces (3.3).

Tensile Failure

Tensile failure – corresponding to shear failure – occurs when the effective tensile stress exceeds a critical limit, i.e. the tensile strength T_0 expressed in [Pa]. This tensile strength represents the rock resistance against tensile failure and is relatively low ranging between 1-40MPa in general and does rarely exceed 10MPa (Zoback, 2007). Hence rocks cannot sustain tensile stresses very well, which is one of the reasons why tensile stresses are extremely rare in the subsurface of the Earth. Tensile failure is a highly localized and inhomogeneous process that creates only one or very few fracture planes normal to the tensile stress. New fractures originate mostly at preexisting cracks and favorable fabric characteristics. Moreover large fractures grow increasingly faster than smaller fractures (Fjaer et al., 2008).

A tensile failure criterion specifies the stress required to yield tensile failure. Regarding rocks as isotropic media, the stress responsible for tensile failure will be the least principal stress σ_3 (Eq. 3-42).

$$\sigma_3 = -T_0 \qquad \text{Eq. 3-42}$$

Due to the fact that tensile failure occurs predominantly at the tip of cracks, the so-called Griffith criterion describes the failure at those locations by shear and normal stress (Eq. 3-43) (Fjaer et al., 2008). Failure occurs when the tensile strength is exceeded.

$$\tau^2 = 4T_0(\sigma_n + T_0) \qquad \text{Eq. 3-43}$$

The Griffith criterion yields steeper slopes of the failure line at low confining pressures, which matches the experimental observations resulting in the Mohr envelope (Fig. 3-5). While this criterion thus provides a reasonable failure description at low confining pressures, the Mohr-Coulomb criterion is significantly more accurate at higher confining pressures. A modified version of the Griffith criterion thus regards the Griffith criterion for tensile conditions ($\sigma_n < 0$) and the Mohr-Coulomb criterion for compressive conditions ($\sigma_n > 0$) (Fjaer et al., 2008). In this approach, the critical shear stress at $\sigma_n = 0$ is determined by the Griffith criterion to be $2T_0$ (Eq. 3-43) and is used as cohesion value.

Tensile failure plays an important role in the stimulation of hydraulic fractures also known as hydraulic fracturing. This reservoir operation is commercially applied in the petroleum industry since the early 1950s and is based on increasing fluid pressures in an isolated section of the borehole until the least principal stress becomes tensile and exceeds the commonly low tensile strength of the rock (Fjaer et al., 2008). This leads to tensile failure and fractures in the target horizon. At some distance from the borehole, the fractures propagate normal to the direction of the local least principal stress following favorable trends in the rock fabric. In normal and strike-slip regimes this stress is oriented horizontally yielding vertical hydraulic fractures.

The pumped fluids are mixed with solids in order to ensure a permanent aperture of the created fractures. Without this solid part, the fractures would close when pumping ceases and fluid pressure is reduced. The created fractures improve hydrocarbon flow to the wellbore and thus this procedure is applied especially in low permeability reservoirs, but also in conventional reservoirs to further increase production rates. In geomechanical modeling, hydraulic fracturing can provide important magnitude measurements of the least principal stress during so-called extended leak-off tests (4.8.1).

Compaction Failure

Compaction failure represents the third type of failure besides shear and tensile modes (Fig. 3-7). Failure by compaction describes a decrease in pore space known as pore collapse and occurs predominantly in high porosity rocks (Fjaer et al., 2008).

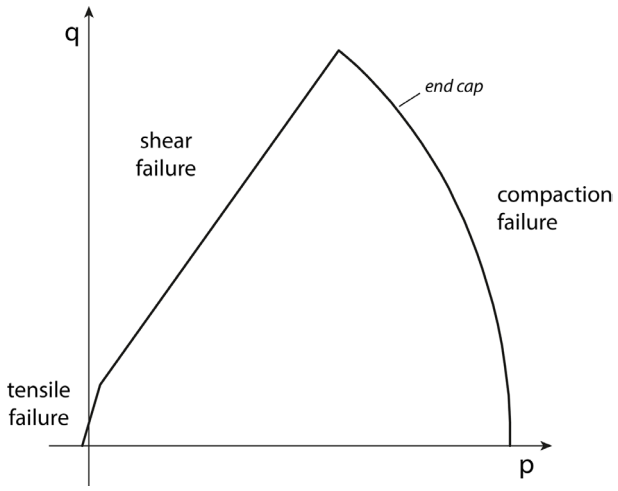

Fig. 3-7. Illustration of a q-p diagram plotting the generalized shear stress q against the mean effective stress p. The failure line depends on the material properties of the rock and separates regions of tensile, shear and compaction failure. Compaction failure requires high confining pressures to occur and is often assumed to be shear-enhanced compaction (modified after Fjaer et al. (2008)).

Pore collapse results from grain rotation and re-orientation yielding a closer packing and thus compacting the material. Alternatively or additionally grain crushing may occur, in which the material grains break and fill the pore space. Both mechanisms represent permanent deformation of the rock and require high confining pressures to occur.

In 3D principal stress space, this type of failure describes an upper so-called end cap, which closes the failure surface at high stresses. This end cap can be also shown in so-called q-p plots (Fig. 3-7). Such plots are commonly used to display stress states and failure conditions instead of using shear and normal stresses (τ-σ plots) (Fig. 3-4, Fig. 3-5) or the principal stress space (σ_1-σ_2-σ_3 plots) (Fig. 3-6). These diagrams plot the generalized shear stress q (Eq. 3-44) against the mean effective stress p (Eq. 3-45), which both are invariants of stress.

$$q = \frac{1}{\sqrt{2}}\sqrt{(\sigma_1 - \sigma_2)^2 + (\sigma_2 - \sigma_3)^2 + (\sigma_1 - \sigma_3)^2} \quad \text{Eq. 3-44}$$

$$p = \frac{1}{3}(\sigma_1 + \sigma_2 + \sigma_3) \quad \text{Eq. 3-45}$$

In this type of representation a failure line defined by the material properties of the rock separates regions of tensile, shear and compaction failure. Experiment or modeling results can be plotted in such diagrams to evaluate the closeness of the state of stress to failure.

3.2.3.2 Creep Behavior

Shear, tensile and compaction failure represent types of plastic deformation that occur instantaneously and do not explicitly depend on time. Another type of permanent deformation is known as creep behavior and is based on inelastic strain accumulation. Creep describes the slow movement and deformation of a material under a long-term and constant stress load. The mathematical theory of creep behavior is referred to as viscoelasticity (Jaeger et al., 2007)

In contrast to shear failure for instance, creep deformation represents a time-dependent deformation. In addition to the time of exposure, the specific creep-rate depends on the applied load, the material properties and the temperature (Fjaer et al., 2008). Creep deformation is generally subdivided into three stages (Fig. 3-8).

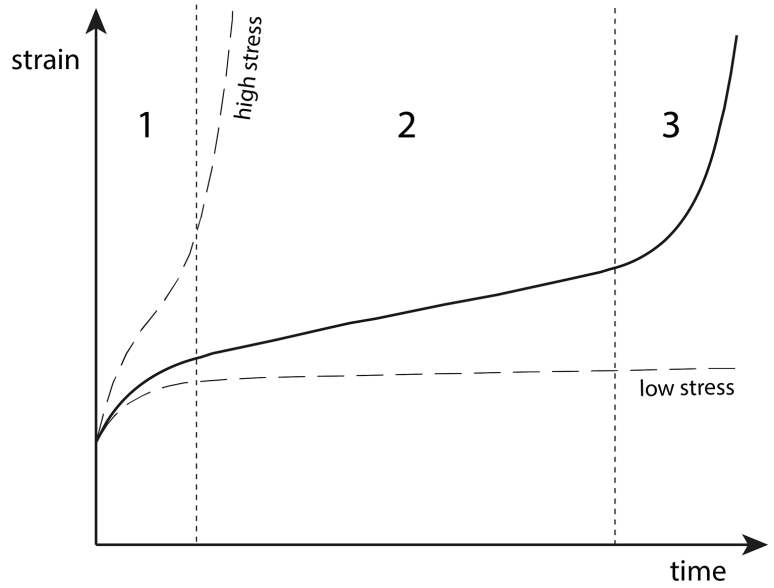

Fig. 3-8. Strain vs. time diagram showing the three characteristic stages of creep: (1) primary or transient creep, (2) secondary or steady state creep, and (3) tertiary or accelerating creep (solid line). The dashed lines indicate creep behavior at low and high stress leading to different developments of the stages (modified after Jaeger et al. (2007)).

The first stage is called primary or transient creep and is characterized by a decrease in strain rate over time (Fig. 3-8). If the applied stress load is reduced during this stage, deformation will decrease as well. The second stage is known as secondary or steady state creep (Fig. 3-8). The deformation rate in this stage stays constant over time. However, even if the applied stress load ceases, the deformation will not vanish. The third and last stage of creep is called tertiary or accelerating creep (Fig. 3-8). The deformation rate in this stage increases significantly with time, which leads rapidly to the ultimate failure of the material. The length and specific course of the stages strongly depends on the material and the loading conditions. In practice almost no material will run through all these stages equally (Fjaer et al., 2008).

The parameter most controlling the creep behavior and the development of the three stages is the magnitude of applied stress (Fjaer et al., 2008). Low and moderate stresses probably result in stabilization after a distinct period of creep (Fig. 3-8). High stresses lead to a fast run through all stages and end in ultimate failure. The time scales of the creep stages comprise an extensive range from several minutes to years. Higher temperatures accelerate creeping in general, but the specific impact of temperature depends on the material.

It is important to note that even steady state creep can lead to ultimate failure. This means creep deformation can yield the failure of a rock that is loaded below its maximum strength in case the load is maintained long enough. This fact reduces the long-term uniaxial strength of rocks (Farmer, 1983).

Various mathematical models describe the creeping behavior of rock and vary in their degree of sophistication. Creep tests providing the required constants determining the creep behavior of specific rocks are complicated and time-consuming, and thus only rarely available in practice. The most common example in geomechanics for which creep behavior must be regarded in all numerical simulations is rock salt (Henk, 2010). Creep in rock salt increases with deviatoric stress and confining pressure, and strongly with increasing temperatures. The intense plastic behavior of salt is explained microscopically by so-called dislocation gliding (Fjaer et al., 2008). Newer studies also underlined the impact of creep behavior in shale gas reservoirs (Sone and Zoback, 2013).

3.3 Faults & Faulting

The results of brittle deformation are faults and fractures. These phenomena occur on laboratory and geological scale, and play an important role in rock mechanics. Fractures represent cracks or joints in rocks, which experienced no or only very little displacement, and are the most frequent type of geological structure (Jaeger et al., 2007).

However, the most important result of brittle deformation in the crust is faulting. Faults are approximately planar discontinuities in the rock resulting from shear deformation and comprise significant displacement. The surface of these shear fractures is called fault plane and is described by strike and dip. The strike of a fault is defined by the direction of any horizontal line on the fault plane and is commonly measured in degrees relative to North (0°N). The dip angle describes the angle between a horizontal plane and the fault plane. This dip angle can also decrease with depth at so-called listric faults occurring in half graben formation, for instance. Therefore, faults are not necessarily always planar features.

Motion occurs along a fault either in the direction of strike or in the direction of dip, and thus faults are divided into strike-slip and dip-slip faults, respectively. Strike-slip faults often comprise nearly vertical fault planes and are characterized by right- or left-handed movements distinguishing dextral from sinistral faults. This fault type is also known as wrench or transcurrent faults (Jaeger et al., 2007). Dip-slip faults are separated into normal and reverse faults. Normal faults show a downward moving hanging wall, while reverse faults describe an upward movement (Fig. 3-9). Shallow dipping normal faults are called detachment faults and a dip angle of 45° separates reverse faults (> 45°) from thrust faults (< 45°) (Jaeger et al., 2007).

3.3.1 Tectonic Faulting Regimes

The three different fault types are discussed by Anderson (1951) using the Mohr-Coulomb theory of shear failure (3.2.3.1). This theory generally states that shear failure results in one or a pair of

conjugate shear planes passing through the direction of the intermediate principal stress and are inclined at an angle (γ) of less than 45° to the largest principal stress. The Anderson classification scheme projects this relationship to the faulting process and describes prevailing tectonic faulting regimes based on the orientation configuration and the relative magnitudes of the three principal stresses (Anderson, 1951; Twiss and Moores, 2007). The assumption of one principal stress being vertical (S_V) and the two others horizontal (SHmax & Shmin), yields three possible regimes (Tab. 3-2, Fig. 3-9).

Tectonic Regime	σ_1	σ_2	σ_3
Normal Faulting	S_V	S_{Hmax}	S_{hmin}
Reverse Faulting	S_{Hmax}	S_{hmin}	S_V
Strike-Slip Faulting	S_{Hmax}	S_V	S_{hmin}

Tab. 3-2. Overview on the Anderson classification of tectonic faulting regimes. In normal, reverse and strike-slip faulting regimes, the vertical stress (SV), the maximum (SHmax) and minimum horizontal stress (Shmin) represent different principal stresses (σ_1, σ_2, σ_3) (Anderson, 1951).

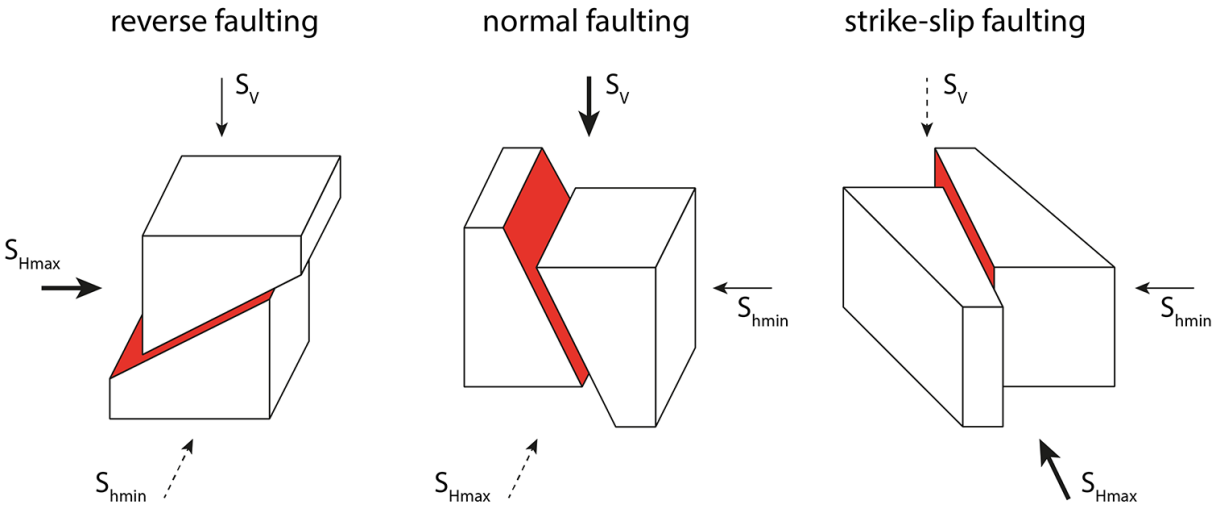

Fig. 3-9. Illustration of the three tectonic regimes in the classification after Anderson (1951). In the reverse, normal and strike-slip faulting regime, the first (bold arrow), second (dashed arrow) and third principal stress (thin arrow) represent the vertical (SV), maximum (SHmax) and minimum horizontal stress (Shmin) in different ways. The angle (γ) between the fault plane (red) and the first principal stress is always less than 45° (modified after Fjaer et al. (2008); Jaeger et al. (2007); Zoback (2007)).

In reverse faulting regimes, the vertical stress represents the least principal stress, while the maximum and minimum horizontal stress are the first and second principal stress (Tab. 3-2). This results in upward movement of the hanging wall of fault blocks (Fig. 3-9). Normal faulting regimes are characterized by the vertical stress exceeding both horizontal stresses leading to a downward movement of the hanging wall (Tab. 3-2). Strike-slip regimes comprise the vertical stress as intermediate principal stress and thus being smaller than the maximum and larger than the minimum horizontal stress. Fault blocks in strike-slip regimes move laterally alongside each other (Tab. 3-2).

The angle γ between the fault plane and the first principal stress is in all tectonic regimes less than 45° and depends on the angle of internal friction φ of the material (Eq. 3-46) (Jaeger et al., 2007).

$$\gamma = \left(\frac{\pi}{4}\right) - \left(\frac{\varphi}{2}\right) \qquad \text{Eq. 3-46}$$

The angle γ commonly takes values of around 30° establishing a 60° angle between two conjugated shear planes. This angle is not to be confused with the angle β mentioned before, which represents the angle between the first principal stress and the normal of the fault plane (Eq. 3-36).

Due to the fact that the classification after Anderson (1951) is based on the Mohr-Coulomb criterion, the resulting tectonic faulting regimes can be plotted as characteristic Mohr circles in τ-σ space (Fig. 3-10).

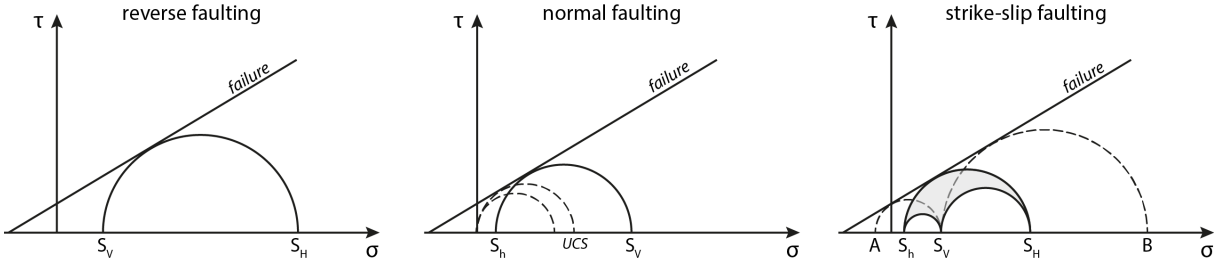

Fig. 3-10. Diagrams of shear (τ) vs. normal stress (σ_n) showing characteristic Mohr circles for the three tectonic faulting regimes of the Anderson classification. The right bound of a Mohr circle always represents the first principal stress σ_1, whereas the left bound is fixed by the least principal stress σ_3. The inclined line represents the Mohr-Coulomb failure criterion separating safe stress states below it from unstable states above (modified after Jaeger et al. (2007)).

In reverse faulting regimes, the vertical stress established by rock density (ρ), gravity (g) and depth (z), represents the least principal stress σ_3 (Jaeger et al., 2007). Failure in a distinct depth level thus requires a sufficiently high maximum horizontal stress (SHmax = σ_1) resulting in a Mohr circle large enough to touch the failure line (Fig. 3-10). In tectonic normal faulting regimes the vertical stress represents the first principal stress demanding a sufficiently low minimum horizontal stress (= σ_3) for failure to occur. This implies that in case the vertical stress is lower than the unconfined compressive strength (UCS) of the rock, the rock fails at tensile least principal stresses (Fig. 3-10).

Strike-slip regimes are characterized by a vertical intermediate principal stress and thus the Mohr circle is mounted by the maximum and minimum horizontal stress (Jaeger et al., 2007). This implies that if the maximum horizontal stress is only slightly larger than the vertical stress, the magnitude of the minimum horizontal stress must be close to the magnitude at a point A for faulting to occur (Fig. 3-10). In turn, the maximum horizontal stress has to reach the magnitude at a point B, if the minimum horizontal stress is only slightly lower than the vertical stress.

3.3.2 Geomechanical Impact of Faults

The geomechanical importance of faults emerges from the fact that faults represent planes or zones of weakness, which separate intact rock masses into fault blocks and may slip depending on the applied stress. Faults are generated by brittle shear failure and significant along-strike or down-slip displacement, and are typically regarded as cohesionless (van Wees et al., 2003; Vidal-Gilbert et al., 2009; Zoback, 2007). It can be argued that faults are inherently cohesionless discontinuities or the remaining cohesion after fault generation is sufficiently small compared to prevailing stress on the fault to be neglected. This assumption is justifiable in most cases of fault consideration.

While brittle failure generates faults and is commonly described by the Mohr-Coulomb criterion, the frictional behavior of faults is expressed by the so-called Coulomb criterion also known as Amontons' law (Fjaer et al., 2008). In this modification of the Mohr-Coulomb criterion, the cohesion is defined to be zero along fault and the coefficient of internal friction μ_i of the rock is replaced by the friction coefficient of the fault μ_f. (Eq. 3-47) (Zoback, 2007).

$$\tau = \mu_f(\sigma_n - P_P) \qquad \text{Eq. 3-47}$$

This criterion states that sliding along a fault occurs when the applied stress reaches a critical shear stress τ at the fault plane, which is a function of the respective effective normal stress $(\sigma_n - P_P)$. Increasing pore pressure on a fault thus brings a fault closer to slip by lowering the effective normal stress (Eq. 3-47) (Zoback, 2007).

In contrast to the coefficient of internal friction of rocks μ_i, the friction coefficient of faults μ_f is hard to determine. Experiments showed that this friction coefficient ranges for most rocks between 0.6-0.8 (Byerlee, 1978). These values in combination with the Coulomb frictional failure theory provide predictions that are generally consistent with stress states measured in the Earth's crust (Townend and Zoback, 2000). Pronounced movement along faults and resulting cataclasis can lower the friction coefficient significantly and especially the presence of specific minerals in the fault, such as clays, talc or serpentinite, are shown to have this effect (Carpenter et al., 2009, 2011; Stankowich and Ewy, 2003; Zoback et al., 1987). Recent studies have demonstrated that also small amounts of graphite are able to dramatically lower fault friction (Rutter et al., 2013).

When accumulated stress overcomes the frictional strength of faults according to the Coulomb criterion, the stress is released by sliding. Depending on the friction and orientation of faults, this mechanism occurs prior to brittle shear failure of intact rock. In other words, whenever a fault or fracture is favorably oriented to the largest principal stress and comprises a lower overall strength than the intact rock, stress is released by fault slip instead of generating new faults and fractures (Zoback, 2007). Due to the fact that discontinuities like faults and fractures comprise almost always lower strengths than intact rock masses and are highly abundant in the subsurface of the Earth in many different sizes and orientations, fault slip is assumed to be the governing mechanism for stress release in the Earth's upper crust (Zoback, 2007). This implies that the frictional strength of pre-existing faults and fractures limits the possible range of stress magnitudes established in this part of the crust.

Stress release by fault slip inevitably results in seismicity of different magnitudes depending on the amount of stress released. This process may be based on tectonic activity leading to earthquakes or is induced by reservoir operations such as hydraulic fracturing (3.2.3.1) (Fjaer et al., 2008). Due to the limited applied stress in such operations, induced seismicity in reservoirs is characterized by low magnitudes (Richter magnitude < 2-3) and is often referred to as microseismicity being significantly smaller than those of average and large earthquakes. However, the potential of reservoir operations to trigger significant seismicity (Richter magnitude > 4-5) is currently still unclear.

Reservoir depletion can lead to a significant change in the state of stress and the re-activation of faults in the reservoir and in the overburden. Especially thick reservoirs with high porosities are prone to this problem as those yield highest relative compaction and extension of overburden. Fault re-activation may lead to seismicity and the generation of leakage pathways (Rutqvist et al., 2013). Further results may be significant surface subsidence and severe damages of nearby facilities. Real-time monitoring and 4D reservoir modeling are thus upcoming fields of interest inside reservoir geomechanics (Herwanger and Koutsabeloulis, 2011).

Besides their movement potential, many geomechanical studies focus on faults, because they represent a major source of stress perturbations (Barton and Zoback, 1994; Henk, 2010; Maerten et al., 2002; Tamagawa and Pollard, 2008; Yale, 2003). This means they alter the regional, ambient stress field in magnitude and orientation. While small faults may affect the stress pattern only in an area of a few hundred meters around a fault, large-scale faulting and especially active faults can rotate the in situ stresses of up to 90° to the regional trend throughout entire fault blocks (Tamagawa and Pollard, 2008;

Yale, 2003). Stress perturbations resulting from active faults are detected by changing wellbore breakouts, for instance (Barton and Zoback, 1994). These variations of in situ stress are highly important during the planning and application of any stress-sensitive reservoir operations. This is why geomechanical reservoir models require the incorporation of all existing faults for the prediction of the in situ stress field in the inter-fault space and undrilled parts of the reservoir.

The hydraulic behavior of faults is additionally of high interest in rock mechanics. Permeability measurements of the Earth's crust in general yield a significant discrepancy of 3-4 orders of magnitude between the small- and the large-scale analyses (Townend and Zoback, 2000). While laboratory measurements provide permeabilities of 10^{-18}–10^{-19} m², corresponding in situ measurements reveal values range between 10^{-16}–10^{-17} m² on the scale of 1-10km (Huenges et al., 1997). This is explained by active or critically stressed faults behaving hydraulically conductive and increasing the crust's permeability (Townend and Zoback, 2000; Zoback and Townend, 2001). The critical stress state of crustal faults is based on the fact that the lithosphere as a whole must support plate driving forces (Townend, 2003). While the lower crust and the upper mantle show ductile behavior, the upper crust is subject to brittle deformation and as mentioned above, the faults are most susceptible for stress release by slip and therefore generally in a critical state (Zoback et al., 2002). Critically stressed faults are characterized by ratios of resolved shear to normal stress of 0.6-0.8 corresponding to the typical friction coefficient of faults (Byerlee, 1978). The conductive behavior is assumed to result from slip and related brecciation on these faults counteracting sealing mechanisms (Townend and Zoback, 2000). By increasing the permeability of the crust, the faults help to maintain approximately hydrostatic fluid pressures and prevent overpressures. This in turn allows the intraplate crust to sustain higher differential stresses.

3.3.3 Faults in Reservoirs: Baffles or Conduits?

The hydraulic behavior of faults does not only affect the strength of the crust, but is also of utmost importance on reservoir-scale in hydrocarbon exploitation. Faults are structural heterogeneities affecting the entrapment, migration and flow of hydrocarbons. Therefore they impact the production significantly and must be incorporated in all reservoir simulation models (Aydin, 2000).

Faults can act as conduits enhancing fluid flow and hydrocarbon migration, but also as baffles or seals impeding it. Especially in reservoirs comprising complex migration and accumulation patterns, faults may directly control migration pathways by allowing or inhibiting cross- and along-fault fluid flow depending on their properties and characteristics (Lampe et al., 2012). There are two fundamental aspects determining the hydraulic behavior of a fault: (1) juxtaposition of horizons due to displacement along faults and (2) fault rocks representing fault zone products created by deformation during fault slip (Aydin, 2000; Yielding et al., 2010). Both lead to structural variations in permeability.

The first aspect is a geometric criterion that evaluates the displacement along the fault and the resulting juxtaposition of horizons. Reservoir lithologies juxtaposed to impermeable lithologies like shale yield sealing faults inhibiting fluid flow (Allan, 1989). Such faults can act as side-seals to reservoir compartments. Fault geometry and slip distribution must be mapped accurately to determine this condition and also the recorded stratigraphy must be sufficiently detailed. Then the juxtaposition relationships are assessable by fault-plane maps and so-called Allan diagrams (Allan, 1989; Yielding et al., 2010). In addition to these 2D tools, true 3D approaches are increasingly applied. However, especially the distribution of slip is difficult to map along complex fault zones and below seismic resolution (Aydin, 2000).

The second aspect addresses the fault rock being the deformation product of fault slip and constitutes the core of a fault (Aydin, 2000). This material is composed of fine grained material and commonly provides lower porosity and permeability, and a higher capillary threshold pressure than the reservoir rock (Fisher and Knipe, 2001; Knipe et al., 1997). The specific type of fault rock depends on the composition and rheology of the faulted sequence, as well as on the burial and temperature history during and after faulting (Yielding et al., 2010).

In siliciclastic sequences, particularly the clay content of the wall rocks is decisive. Clays smeared into the fault zone provide high sealing capacities (Yielding et al., 1997). However, smearing of clays and shale can be disrupted by sufficiently large displacement along the fault. Three quantities are commonly determined to assess the sealing potential by clay and shale smearing (Yielding et al., 2010): (1) the clay smear potential (CSP) describes the general probability of clay smear occurrence, (2) the shale smear factor (SSF) predicts the likelihood of intact smearing, and (3) the shale gouge ratio (SGR) distinguishes between fault rocks dominated by clay smear or disaggregation zones and cataclasites.

Besides the clay content, the stress conditions during faulting affect the fault rock and thus the hydraulic behavior of the fault. Disaggregation zones form by fault slip under low confining pressures, i.e. at shallow burial depths, and are characterized by grain reorientation without grain crushing. These zones comprise similar hydraulic properties as their host rock (Yielding et al., 2010). High effective stresses yield cataclasis and grain fracturing, which result in collapsing porosity and lower permeability.

The maximum temperature at the fault after the faulting process also influences the fault rock. This temperature depends on the burial depth and the prevailing geothermal gradient, and controls post-deformation quartz cementation of disaggregation zones and cataclasites (> 90°C) (Fisher and Knipe, 2001). In extreme cases, shear heating and the formation of pseudotachylyte occurs indicating seismic activity (van der Pluijm and Marshak, 2003). The outlined factors controlling fault rock constitution imply that the related hydraulic behavior is never constant or homogeneous, but may vary irregularly over individual fault surfaces. Sealing capacity can be established by juxtaposition or appropriate fault rock occurrence only and does not require both mechanisms to be present (Jones and Hillis, 2003). Counteracting any sealing potential, a damage zone surrounding the fault is commonly created during fault shearing and commonly enhances the permeability normal and parallel to the fault by joints (Aydin, 2000). Joint density and width of the damage zone are suggested to rely on the slip magnitude at the specific fault.

In general, two types of fault seals must be distinguished based on their impact in time (Yielding et al., 2010). Seals inhibiting hydrocarbon flow on geological time-scale affected their migration and entrapment. This type of seals and their integrity is important in exploration and appraisal to ensure commercial accumulation is still available when the reservoir is exploited. On production time-scale, sealing faults act as baffles to hydrocarbon flow and complicate exploitation. These faults are the most significant cause of compartmentalization of hydrocarbon reservoirs (van Hulten, 2010). Compartmentalization limits the production of hydrocarbons due to such permeability barriers and represents one fundamental risk in field development and production (Fox and Bowman, 2010). Especially mature clastic-dominated fields commonly become increasingly difficult to produce yielding lower economic returns (Morris et al., 2012).

Compartmentalization and the responsible seals cannot be directly imaged with reflection seismics, for instance. This fact is referred to as the fault seal “problem” (Yielding et al., 2010). Instead compartmentalization is detected by indirect observations of fluid behavior in adjacent wells. Such

observations include different hydrocarbon contacts or reservoir pressures across faults, as well as poor overall flow performance in the reservoir. The mandatory process of predicting sealing faults is known as fault seal calibration and is done either as laboratory or subsurface calibration (Yielding et al., 2010). While hydraulic properties of fault zone samples are measured and then mapped on faults in the lab calibration, the subsurface calibration utilizes designed algorithms (CSP, SSF, SGR) to capture the sealing behavior of faults. Insights are then inferred from the comparison of these quantities with those of known faults.

The state of stress represents a third and major parameter of increasing importance that influences the hydraulic behavior of faults besides juxtaposition and fault rock conditions. Numerous studies showed that faults are permeable and represent conduits for fluid flow when they are active or critically stressed, i.e. close to failure (Barton et al., 1995; Chanchani et al., 2003; Heffer and Koutsabeloulis, 1995; Hennings et al., 2012; Morris et al., 2012; Rogers, 2003; Tamagawa and Pollard, 2008; Zhang et al., 2007). However, the critical stress state of a fault is a leakage and not a sealing criterion (Yielding et al., 2010). If a fault is not critically stressed, it does not necessarily represent a baffle or seal. In summary according to Yielding et al. (2010), a fault is sealing if the reservoir horizon is juxtaposed against a non-permeable lithology like shale, or generated fault rock is hydraulically sealing and the fault is not in a critical state of stress.

The state of stress of faults and thus the capability of supporting fluid flow strongly depends on their orientation with respect to the in situ stress field (Barton et al., 1995; Heffer and Koutsabeloulis, 1995). Faults in favorable orientation and active in the prevailing stress state are shown to correlate with intervals of higher productivity in hydrocarbon reservoirs (Chanchani et al., 2003). Effective stresses along and around faults vary in time. Due to the corresponding evolution of hydraulic properties, individual faults may behave as a seal and as a conduit at different times as well (Evans et al., 1997; Zhang et al., 2007). This also implies that changes in the in situ stress field during depletion of hydrocarbon reservoirs affect related fracture permeability and may lead to increasing heterogeneity of reservoir permeability in general (Fox and Bowman, 2010; Heffer, 2002; Heffer and Koutsabeloulis, 1995; Zhang et al., 2007). These changes furthermore impact fault seal integrity and the conductivity of fault zones leading to improved or impaired well communication. Decreasing fluid pressures due to reservoir depletion can reduce the critical state of stress along faults to stable conditions. The corresponding decline in permeability can eventually result in sealing behavior and lead to so-called production-induced compartmentalization (Morris et al., 2012).

The large amount of factors influencing the hydraulic behavior of faults including lithological juxtaposition, fault rock type and cementation, and varying stress states, for instance, makes it almost impossible to generalize the hydraulic function of faults (Czauner and Madl-Szonyi, 2011). Furthermore, an active fault may act as a conduit, but successive movement resulting in cataclasis leads to a sealing behavior and thus the opposite hydraulic properties. In some cases they even act simultaneously as both and control fluid flow direction-dependently acting vertically as conduit and transversely as barrier (Czauner and Madl-Szonyi, 2011).

4 Geomechanical Modeling Workflow

The workflow for building 3D geomechanical reservoir models applied in this study is subsequently presented in detail. It is based on the work of Henk (2009, 2010) and enhanced for large-scale geomechanical models of reservoirs covering several hundreds of square kilometers. In contrast to other geomechanical approaches, this workflow focuses on the specific stress distribution prior to production and not on production-related impact on the stress field. In addition to building the field-scale model (4.1), techniques for internal resolution increase on fault block-scale are developed (4.2.1). The geomechanical models of the case study reservoir are generated using this workflow (7, 8), as well as the preliminary studies carried out before (6).

This workflow requires two separate datasets for the setup of the geomechanical reservoir model (Fig. 4-1). The first dataset of input data is used to build the geomechanical model, while comparing modeling results to the second dataset of calibration validates the model. Input data must comprise information on the specific reservoir geometry, material parameters and the regional stress field.

The reservoir geometry includes faults and lithostratigraphic boundaries that are both initially derived from seismic data and can be provided by maps or 3D geological models, e.g. Petrel® projects. This surface information is transferred to the finite element program and used to build up fault block volumes. The lack of direct export and import mechanisms for surface information between proprietary software packages for geological and finite element modeling demands alternative ways of geometry transfer (4.1). Three approaches are developed and described below (4.1.1, 4.1.2, 4.1.3). They consider point data that is exported from the geological model and used to re-generate surfaces in the pre-processor of the finite element program. The generated fault block volumes are then discretized into a large number of preferably hexahedral elements in order to apply the finite element method (4.2). The smaller the element size is, the higher the accuracy of the results will be and the longer the model will take to be solved. Hence, a compromise has to be found between a sufficiently high mesh resolution and feasible computing times.

Reservoir-specific material parameters of all participating lithologies and faults are mandatory as input data as they describe their mechanical behavior (4.3). These parameters can be obtained from in situ measurements, as well as from laboratory tests on drill cores. The more sophisticated the applied material laws in a geomechanical model, the more parameters are generally required. At least the elastic properties such as the Young's modulus and the Poisson's ratio have to be provided. The material data is then assigned to the respective elements in the model. Faults can be regarded in the geomechanical model in two different ways (4.4). Either they are implemented as zones of weaker mechanical properties or as distinct planes of weakness modeled as a contact of two individually meshed continua. Both approaches have pros and cons (4.4.1, 4.4.2).

The third part of input data addresses the regional, ambient stress field, which represents the boundary conditions of the geomechanical model (4.5). This includes the lithostatic load acting as vertical stress on top of the model, as well as the magnitude and orientation of the maximum and minimum horizontal stress. Regional stress gradients are provided by published large-scale data compilations (Röckel and Lempp, 2003; Zoback, 1992). A homogenous stress field showing distinct magnitudes is established in the finite element model by calibrated displacements of the model boundaries (4.5.1). However, for large-scale geomechanical reservoir models, a highly effective way of applying these boundary conditions had to be found, which uses the so-called cut-boundary displacement method (4.5.3).

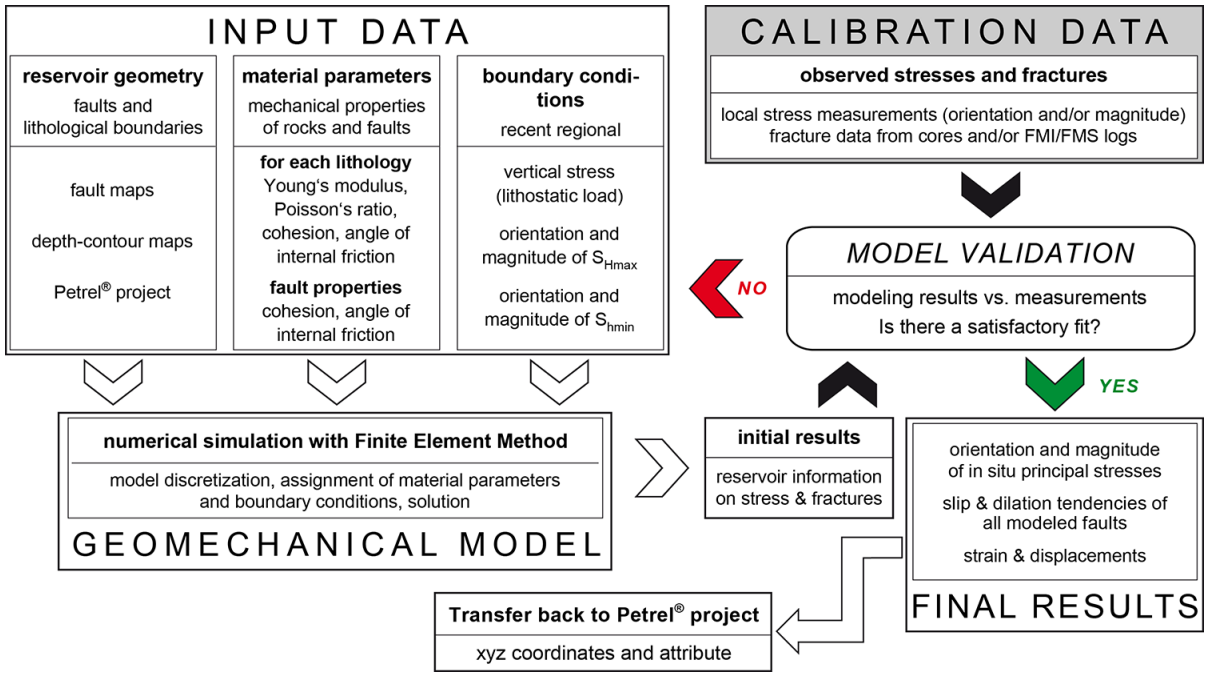

Fig. 4-1. Overview on the workflow for building 3D geomechanical reservoir models based on the finite element method (modified after Henk (2009, 2010)). Data that is taken as input must not be used for calibration purposes to avoid circular reasoning.

Based on this input data the geomechanical finite element model is build and calculated (Fig. 4-1). The solution time depends on the total amount of elements, the number of faults and the way of implementing them, as well as on the computing capacity available for calculation (4.6.1). Results comprise the principal stresses and strains at any subsurface location in the modeling domain. Further quantities can be calculated as needed, such as the differential or mean stress distribution (4.7).

Following the initial calculation, the results are compared to the second dataset of field measurements in the step of model calibration (4.8). The calibration dataset includes local stress measurements and fracture data from various sources. Hydraulic fracturing and leak-off tests can provide information on the least principal stress magnitude, whereas breakout orientation logs and drilling induced fractures reveal the stress orientation, for instance. In addition to stress data, image logs and/or core descriptions yield insights into the fracture patterns.

Commonly the first comparison of modeling results with this field data shows only a partial fit that has to be improved. This is done by adjusting poorly constrained parameters in the input section. The friction coefficient of the faults and the magnitude of the maximum horizontal stress are prime examples of such parameters. The adjustments are performed iteratively and always within geologically reasonable limits. It is of utmost importance that input and calibration data are separated in the beginning and no input data is used for calibration. This would lead to circular reasoning and a meaningless fit.

At some point the fit between modeling results and calibration data is satisfactory and the reliable results can be taken for further interpretations. In case needed, stress data can be transferred back to the initial geological modeling for input in flow simulations (Fig. 4-1).

4.1 Geometry Transfer

The most labor-intensive step in the buildup of a geomechanical finite element model addresses the reservoir geometry. Lithostratigraphic horizon and fault surfaces are commonly derived from interpretation of 2D/3D seismic and are ideally available as a geological subsurface model that is geometrically consistent with all available data, e.g. a Petrel® project.

One of the main objectives of 3D geological reservoir modeling in hydrocarbon industry is the evaluation of property distribution throughout the reservoir and simulation of fluid flow during production. The fluid flow simulation is commonly done with the numerical method of finite differences (2.2) and therefore a respective grid is generated in the geological model by default (Fig. 4-2). Due to the fact that this grid is already available, it would be straightforward to use it for geomechanical modeling as well. However, the finite element mesh of the geomechanical model has to fulfill distinct requirements. The FE mesh has strictly to regard boundaries and faults, and has to have dual grid nodes along the fault faces for implementing 2D interface elements (2.1.2, 4.4.2). The finite difference (FD) method is based on different principles and thus the grid does not regard these requirements (Fig. 4-2).

Moreover, faults in the FD mesh are represented by stepped staircases of the hexahedral grid cells. The hydraulic properties of those cells corresponding to the fault zone are adjusted by so-called fault zone multipliers. Faults are thus not described as discrete surfaces, which is necessary in this geomechanical modeling approach. Therefore, reservoir geometry has to be rebuilt and discretized properly in the finite element software to maintain the geometrical complexities of the subsurface reservoir structure.

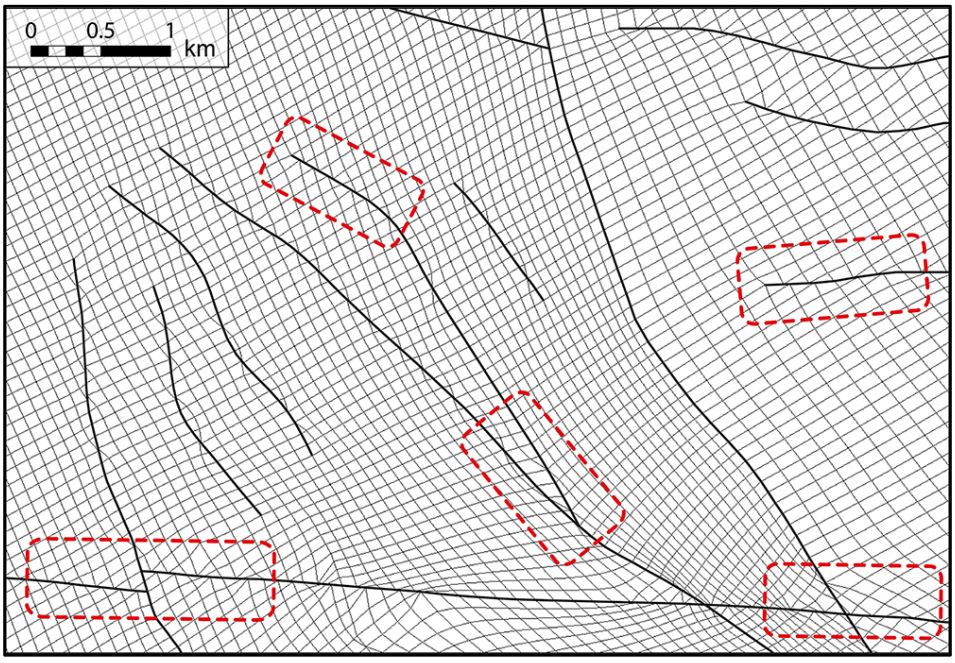

Fig. 4-2. Orthogonal top view on the finite difference grid of the case study reservoir model. Faults are marked as bold black lines. The grid is irregular aligned to the faults (e.g. red frames), which is suitable for the finite difference method, but not for the geomechanical modeling using finite elements. Thus a separate FE mesh has to be newly generated.

Up to now there is no possibility to export and import horizons and faults directly as surfaces in an appropriate CAD file format from the geological modeling software to the finite element program. Due to this lack of direct interfaces, other ways for transferring the reservoir geometry are developed as described below (4.1.1, 4.1.2, 4.1.3). All of them take advantage of definite coordinate information of point data that is exported from the geological model and used to re-build the geometry in the numerical software.

4.1.1 Basic Geometry Transfer

The basic geometry transfer option uses the extraction of points along horizon lines (Fig. 4-3). Horizon lines represent the intersection lines between lithological horizons and faults. These lines are generated in the geological modeling process during structural modeling and cutting of the horizon by the faults. Based on the extracted points of horizon lines, these are re-generated in the finite element software by 3D splines. Subsequently, multiple of these splines enclosing the horizon surface of a fault block are taken to create a so-called Coon's patch of the interior surface. A Coon's patch is a surface whose topology is interpolated by the slope of the bounding lines (Barnhill, 1982; Goodman and O'Rourke, 2004) (Fig. 4-3). In the same way fault surfaces can be created by using horizon line splines of different depth level enclosing fault surfaces.

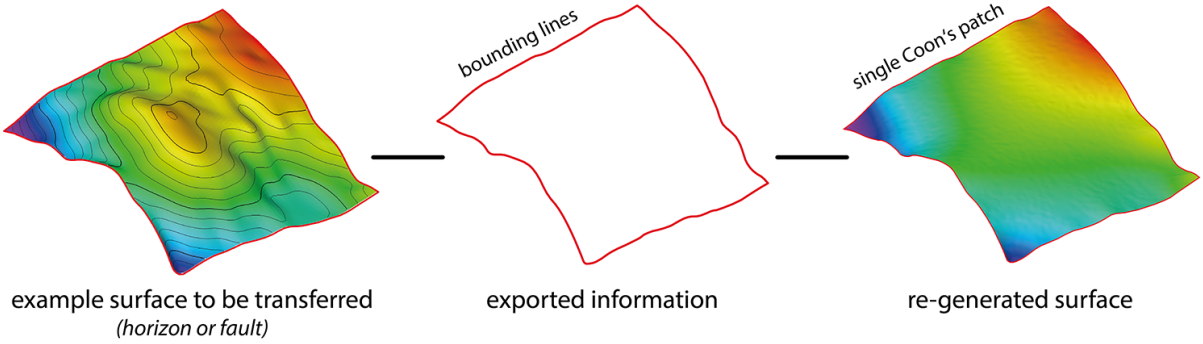

Fig. 4-3. Illustration of the basic transfer for geometry takeover from the geological model to the finite element software. In this approach, a surface (left) is transferred by using only the information on the bounding lines representing the horizon lines in the geological model (center). The surface is re-generated by creating a so-called Coon's patch based on the transferred lines (right). Pronounced interior topology of the surface cannot be preserved by this method.

The conversion of the horizon lines into points inside Petrel® commonly yields an extensive amount. This large number of points results from the conversion process itself and does not necessarily reflect seismic interpretation. In 3D seismic data, on which all geometry information is ideally based, not every seismic inline and crossline are interpreted, but commonly only every 10^{th} or 5^{th}. At those interpreted seismic slices, fault pillars are set indicating the faults trace. Multiple pillars are combined and describe and build up the respective fault surface with which the horizons are cut.

The final course of the fault faces is interpolated between those pillars covering the seismic slices with missing interpretation. This procedure directly affects the accuracy of horizon lines due to their origin in cutting horizons with faults. Consequently only those points along the horizon lines that are coincident with fault pillars are to be taken for the re-generation of horizon lines in the finite element software. The usage of all points resulting from the conversion process would multiply the effort without increasing the actual geometrical accuracy of the model.

The re-generated surfaces of horizons and faults are stitched and used to create solid fault block volumes with different lithological layers. The volumes are subsequently discretized with 3D elements while the faults are modeled as contacts (4.2). This basic approach represents the fastest way to transfer the subsurface geometry to the finite element software and build the geomechanical model. However, the larger the created Coon's patch is, the more information on the internal topology of the surface is lost. Therefore this option is best suited for field-scale models with no pronounced horizon topology.

4.1.2 Advanced Geometry Transfer

The advanced geometry transfer option represents a modification of the basic transfer that results in a significant increase in geometrical accuracy. Points along horizon lines are generated and chosen in the same way as in the basic transfer (4.1.1). In addition to the horizon lines, a network of auxiliary lines is created inside the geological model (Fig. 4-4). These auxiliary lines subdivide the inter-fault space in numerous segments and are following exactly the horizon or fault topology derived from seismic interpretation. The additional line information is transferred to the finite element software in the same way as for the horizon lines, i.e. via point data. All lines are subsequently re-generated by 3D splines (Fig. 4-4). The amount and distribution of auxiliary lines depends on the topology of the horizon or fault surface.

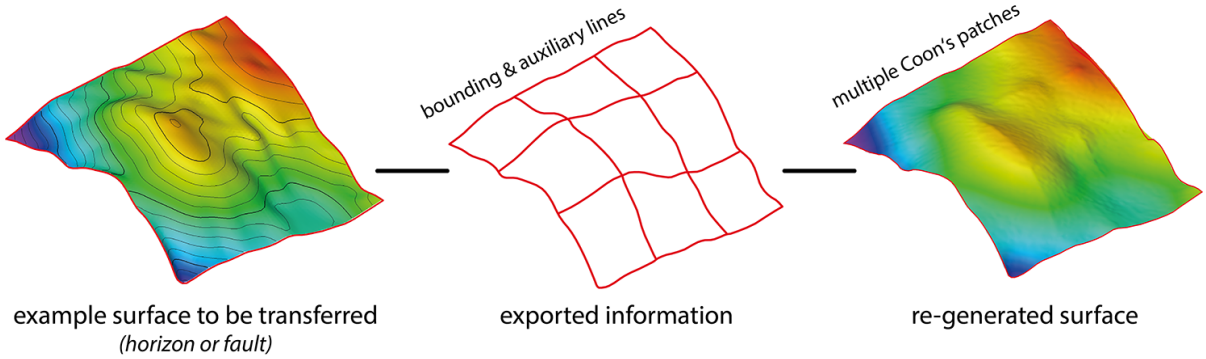

Fig. 4-4. Illustration of the advanced transfer for geometry takeover from the geological model to the finite element software. In order to more accurately preserve the topology of a surface (left), a network of auxiliary lines describing the topology is transferred in the same way as the bounding horizon lines (center). The surface is re-generated by creating multiple Coon's patches based on the transferred lines (right). This method preserves surface topologies to a great extent.

Significantly more Coon's patches are then created in the finite element software based on the splines of horizon lines and the auxiliary network. The individual Coon's patches are thus considerably smaller and the internal topology of any face – horizon or fault – is preserved more accurately than in the basic approach (Fig. 4-4). Solid fault block volumes are generated based on these surfaces and discretized for application of the numerical method.

This advanced transfer generally offers the best compromise between effort and geometrical accuracy, especially regarding field-scale geomechanical reservoir models whose geometry is to be considered in detail. Therefore this approach was used in the buildup of the case study models (7, 8).

4.1.3 High-Resolution Geometry Transfer

The high-resolution geometry transfer represents the third elaborated option for geometry takeover from the geological model to the finite element software. This approach maintains full geometrical complexity of the reservoir as described in a Petrel® project, for instance. The transfer is based on the extraction of high resolution point clouds from the grid of the geological reservoir model. These point clouds can likewise describe lithological boundaries and fault surfaces in highest detail. All surfaces are re-generated from the point cloud as mathematically precise freeform surfaces, so-called NURBS surfaces (Non-Uniform Rational B-Spline) (Piegl and Tiller, 2010). Only in this way, the surfaces can be used for further volume modeling and discretization.

The crucial step of NURBS surface re-generation from the point cloud can be done by reverse engineering software (e.g. Geomagic Studio®), which is originally meant to transform 3D scan data into highly accurate, native CAD models.

Reverse engineering programs are able to deal with large point clouds. Commonly a polygon mesh of the point cloud is built first, which is subsequently converted to the NURBS surface. This surface is a mathematically described freeform surface and often comprises several patches resulting from the conversion process (Fig. 4-5). The amount and shape of these patches depends on the complexity of the surface. (Fig. 4-5).

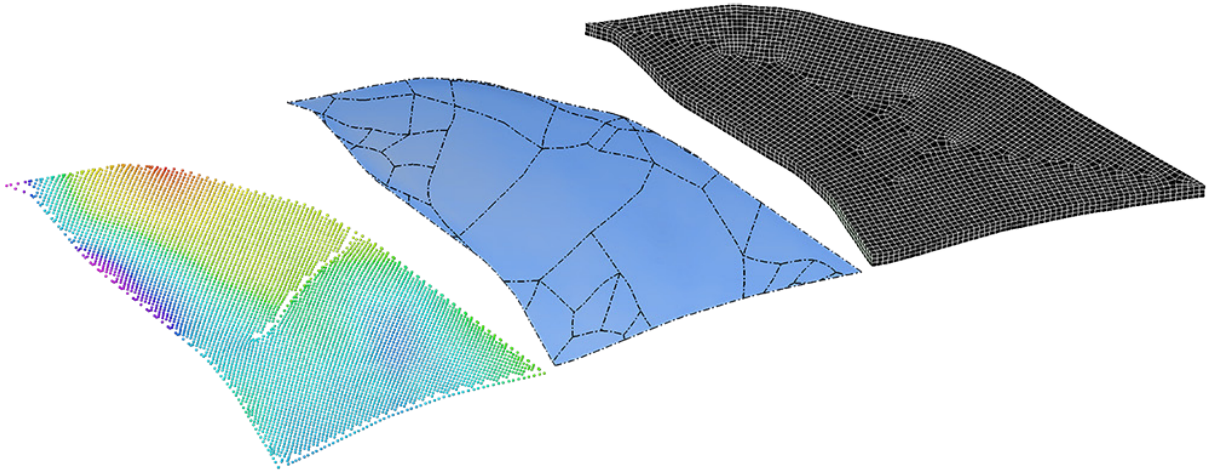

Fig. 4-5. Intermediate steps in the high-resolution transfer applied to a fault block of the case study reservoir. The point cloud of the fault block that is to be transferred is isolated first (left, depth-contoured). This point cloud is processed in reverse engineering software to a NURBS surface, which shows characteristic patches (center). These patches are neglected in the meshing process using a so-called virtual topology (right). If needed, this approach allows to disregard minor or conceptual faults that are visible in the point cloud data (left), but shall not be considered in the geomechanical model.

In the same way as in the basic and advanced transfer, the surface information on horizons and faults is used to build solid fault block volumes that are discretized to apply the finite element method. A so-called virtual topology representing an overlay on the patches of the NURBS surface prevents the generated mesh from regarding the patch boundaries (Fig. 4-5). As mentioned in the description of the basic transfer option (4.1.1), the way 3D seismic data is interpreted must be considered in the geometry transfer. This addresses the high-resolution approach in particular, because the high resolution is referring only to the high accuracy in preserving what is available in the geological model. The loss-free takeover thus also considers any inaccuracies. This fact must be regarded in all following interpretation of the geomechanical modeling results.

This third approach can be applied to virtually any reservoir geometry and yields highest accuracy as no geometrical information is lost (Fig. 4-6). However, it is also the most labor-intensive way and is suitable only for detailed, fault-block size submodels of a reservoir, but not for field-scale geomechanical models comprising numerous faults.

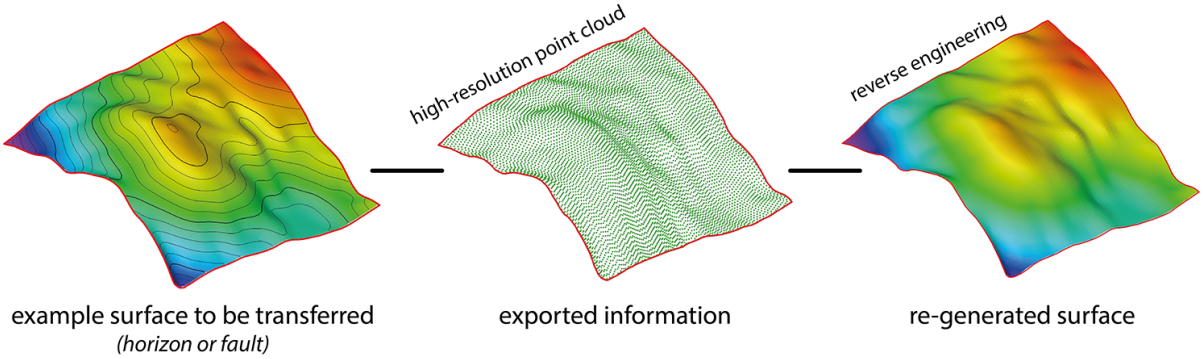

Fig. 4-6. Illustration of the high-resolution transfer for geometry takeover from the geological model to the finite element software. This approach maintains the full geometrical complexity of the reservoir by transferring a point cloud describing the surfaces. Reverse engineering software is then used to recover so-called NURBS surfaces for volume generation. This method can be applied to arbitrarily complex reservoir geometries.

4.1.4 Summary of Geometry Transfer

Three approaches for transferring the reservoir geometries from the geological model to the finite element software are elaborated and described (Fig. 4-7). All of them re-generate surfaces of lithostratigraphic horizons and faults based on definite, exportable point data. The resulting surfaces are used to build up volumes of fault blocks comprising several lithological layers. While the internal horizons maintain their topology, the top and bottom of the final geomechanical model are commonly defined to be planar representing distinct depth levels. All volumes are discretized to apply the finite element method. Each of the described approaches has its pros and cons, and is suitable to certain scenarios.

The basic transfer is the fastest approach and can be applied to geomechanical models of large reservoirs with no pronounced horizon topology or in preliminary models, for instance. The advanced transfer considers the surface topologies with high accuracy by still being feasible to field-scale models of large reservoirs. Due to the compromise between accuracy and effort, this approach represents the most applicable method for most geomechanical reservoir models. The high-resolution transfer requires significant effort, but preserves full complexity of the reservoir geometry available in the geological model. Moreover, it can be applied to arbitrarily complex reservoirs. However, the uncertainties concerning the geometry in the geological model are not diminished and must be kept in mind in later interpretations.

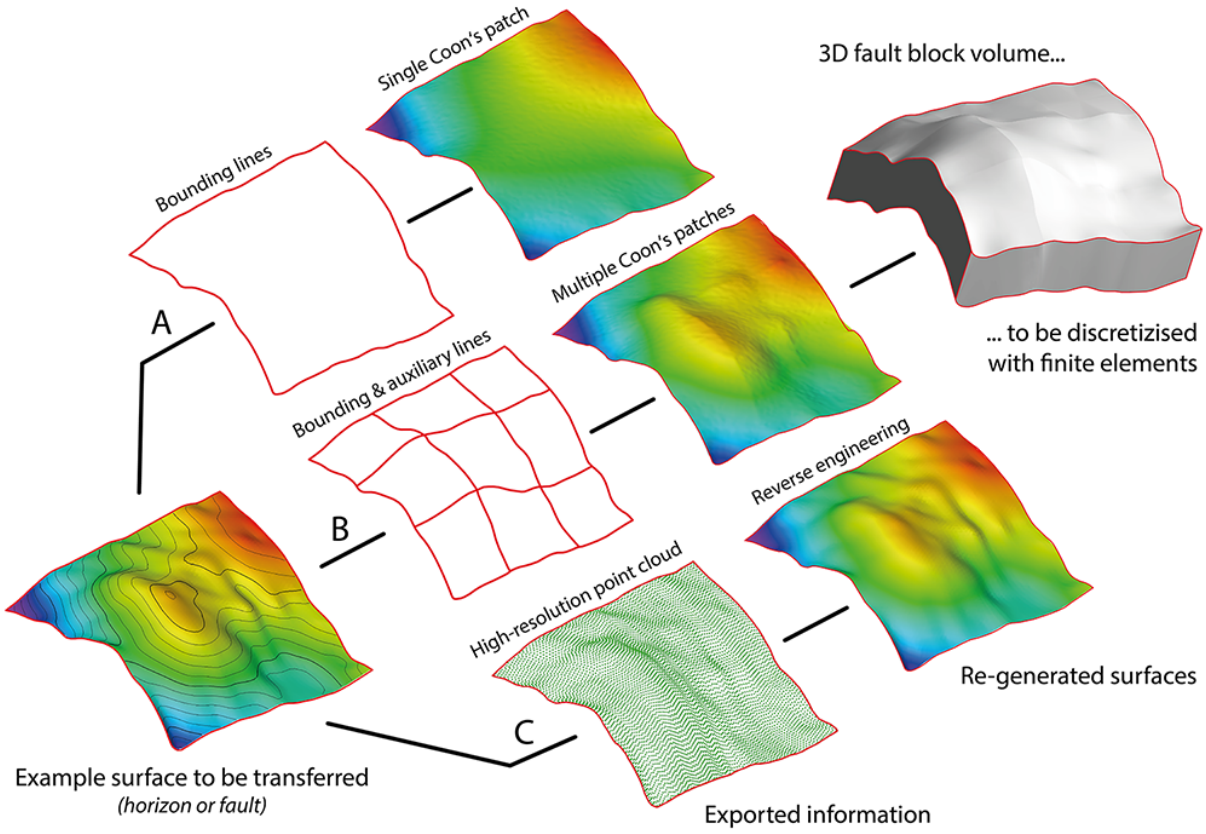

Fig. 4-7. Illustration of the three options for the reservoir geometry transfer from a geological subsurface model to the numerical simulation using an arbitrary surface for demonstration. In case the bounding lines of the example surface are used exclusively to create a Coon's patch, only little topological information is preserved in the re-generated surface (A). By adding a network of auxiliary lines, the resulting Coon's patches are significantly smaller and the internal topology is preserved much more accurately (B). The most accurate option uses a high-resolution point cloud and reverse engineering techniques for surface reproduction (C). However, this is also by far the most labor-intensive approach and not suitable for field-scale models.

4.2 Model Discretization

The key step in the finite element method is the discretization of the modeling domain. In geomechanical reservoir models, this domain are the fault block volumes generated from the surfaces of lithostratigraphic horizons and faults. The process of discretization is most commonly referred to as meshing. In order to mesh a 3D structure with a finite number of 3D elements, the structure has to consist of true volumes and must not be a surface representation.

Higher spatial resolutions of the mesh, i.e. smaller elements, yield in general more accurate results of the finite element model (2.1). However, smaller element sizes result in larger amounts of elements and limitations of computing capacities are reached rapidly. Solution times of one week, for instance, are not feasible, because a model has to be solved multiple times for troubleshooting and during the calibration stage. Hence, a compromise between resolution and calculation times has to be found depending on the provided computing power. Geomechanical finite element models with several lithologically and mechanically different layers have to address a minimum of 3-4 element layers to each of those units (Fig. 4-8). This is because the results of elements, which share nodes with elements connecting different mechanical layers, are affected by the transition in mechanical properties.

Adding element layers without decreasing the horizontal element size yields increasingly platy elements that eventually reach untolerable aspect ratios. The strong influence of the number of element layers on the increase in absolute element numbers during decreasing horizontal element size, demands a compromise between vertical and horizontal resolution and element shape.

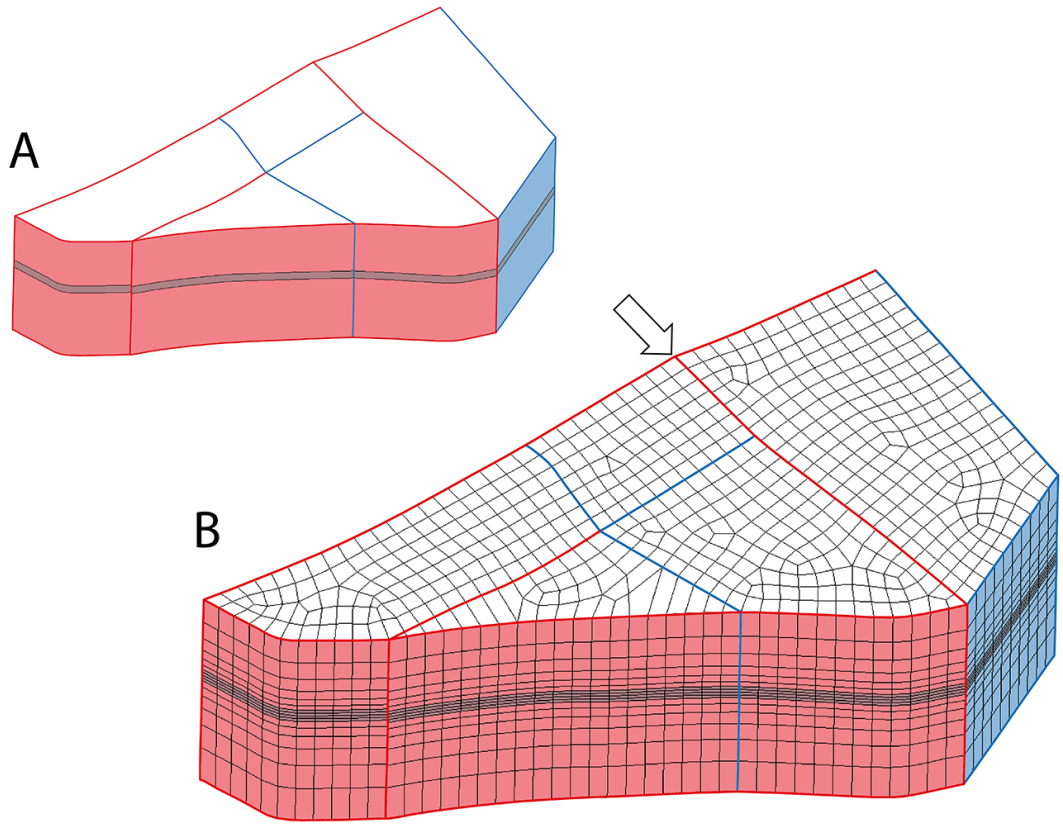

Fig. 4-8. Illustration of five neighboring fault block volumes of the case study reservoir in unmeshed (A) and meshed state (B). Red color indicates the fault faces and their outlines. Shifts in the element distribution across these surfaces, as marked by the arrow, are handled by the contact elements. Blue color indicates surfaces resulting from the generated auxiliary lines (4.1.2). Along those faces, the element distribution must be coincident on both sides to ensure proper merging of nodes and a seamlessly continuous mesh. The grey central layer represents the reservoir horizon as region of interest towards which the mesh is refined vertically. The top surface of the prismatic volume at the bottom center shows the example of a 2D mesh that should be locally refined.

The meshing process commonly starts with the definition of an area element size in the horizontal dimension, or alternatively by defining distinct element subdivisions along the horizontal edges of the volumes. Based on this information, the surfaces on top of the model are meshed with 2D elements representing the basis for the 3D mesh. Vertical edges are divided into the desired amount of vertical element layers and then the 2D mesh is swept (sweeping algorithm) through the model creating the 3D element mesh.

Non-uniform vertical subdivisions allow focusing on the specific area of interest, such as the reservoir horizon (Fig. 4-8). In case the general horizontal element size yields coarse meshes in certain areas (Fig. 4-8), those can be improved by so-called scaling factors lowering the element size locally. These factors are applied to a keypoint or node and modify the meshing it the nearby area. If these factors are applied to the 2D mesh in the beginning, the scaling to smaller elements is also preserved in the 3D mesh during the sweeping process.

The 3D meshing approach using the sweeping - algorithm is only suitable for volumes comprising opposing start and end faces with the same amount of corner points and a regular distribution of lateral faces (Ansys Inc., 2012). However, the participating faces do not need to be planar. More complex volumes must be meshed by individually assigning element subdivisions along the edges. Such structures often require the use of tetrahedrons instead of hexahedral elements.

In case contact elements are used to model faults as distinct planes of weakness, these 2D elements are assigned to opposing faces of fault blocks overlying the 3D elements (2.1.2). Due to the fact that a fault may separate a large fault block from two smaller blocks, the 3D elements may not be directly opposing each other but are slightly shifted (Fig. 4-8). This shift results from the element division along edges of different lengths. The contact elements are able to deal with this shift and can even consider entirely different mesh sizes on neighboring blocks (4.2.1, Fig. 4-9). In contrast, the mesh at the faces of fault blocks where no fault is considered must be merged (Fig. 4-8). These faces result from the auxiliary lines used for better topology preservation of the horizons (4.1.2). The merging of the mesh at these boundaries provides a continuous mesh and thus they are not recognized in the later calculation. In order to merge the mesh at those locations the nodes have to coincide exactly, which requires the same edge lengths and subdivisions.

The type of elements used for discretization depends on the degrees of freedom that are to be addressed (2.1). Higher-order versions of elements can tolerate more irregular shapes, but in practice an increase in mesh resolution is to be preferred.

4.2.1 Fault Block Refinements

Field-scale geomechanical models hardly meet the expectation of providing highly resolved local stress information, which is demanded for optimizing actual reservoir operations. The field-scale geomechanical model in this study, for instance, comprises almost 4 million elements and an element size inside the reservoir layer of 100m x 100m in the horizontal and 25m in vertical dimension (7.3). This is a high spatial resolution regarding the size of the reservoir covering more than 400km² and typically of the same order as corresponding geomodels containing poro-perm information, for instance. Nevertheless, the application of modeling results for practical purposes demands local results and higher spatial resolutions, which also allow considering more details such as a finer mechanical stratigraphy.

Further increasing of the horizontal element size of the entire geomechanical model would result in excessive, unreasonable calculation times. On the other hand, highly resolved geomechanical models

of individual fault blocks would be able to provide the demanded resolution within acceptable calculation times, but cannot account for the complex in situ stress condition emerging from the surrounding fault network. Their accuracy and value thus would be limited. The best option suggested in this study to provide local results without neglecting the environment and still maintaining feasible calculation times are so-called fault block refinements (Fig. 4-9).

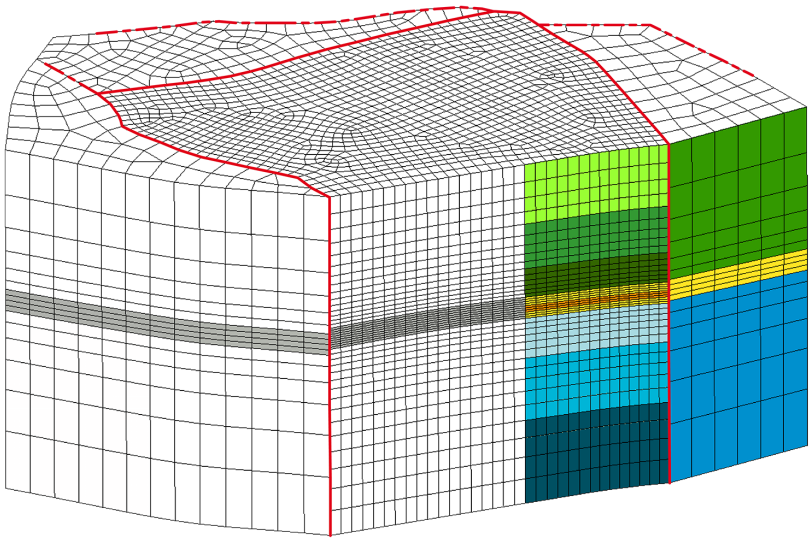

Fig. 4-9. Illustration of four meshed fault blocks elucidating the concept of fault block refinement. Contact elements along the faults (red) allow differently sized meshed on both sides. In this way, the spatial resolution in single or multiple fault blocks can be significantly increased. This yields not only higher accuracy in general, but also provides the possibility of a refined mechanical stratigraphy (shades of green, yellow, and blue colors).

This approach is enabled by the use of contact elements representing the faults. These elements can deal with dissimilar meshes on both sides of the contact/fault (Fig. 4-9). In this way, the resolution within single or multiple fault blocks can be significantly increased, while these blocks are still embedded in the fault network of the reservoir. The element size inside the reservoir layer can be lowered from 100m x 100m x 25m down to 50m x 50m x 10m, for instance (Fig. 4-9).

In order to avoid numerical artifacts the transition in element size should be smooth. This can be ensured by lowering it stepwise in the surrounding as well. In addition to the increased numerical accuracy, the increased number of element layers allows to consider a finer mechanical stratigraphy (Fig. 4-9). Instead of using an average value for similar sandstone units, they may be considered individually, for example. This provides higher geological accuracy in the target area of the model. However, the realization of these possibilities also requires an appropriate dataset for input and calibration.

Fault block refinements can be incorporated in any field-scale geomechanical model that implements faults by 2D interface elements. Any fault block fully enclosed by faults can be refined in this way. In order to increase resolution further and more area-wide, submodels of reservoir parts have to be built (7.7).

4.3 Material Parameters

The material parameters describe the rheological behavior of the lithologies included in the geomechanical model. Type and amount of parameters depend on the applied material law(s). Independent of the specific mechanical behavior, density (ρ) must be defined in any case when gravitational acceleration is applied.

Modeling elastic deformation by Hooke's law requires the Young's modulus (E) and Poisson's ratio (ν) to be described representing the elastic moduli (3.2.1) (Fjaer et al., 2008). These two mechanical parameters represent the minimum that must be assigned in order to run a structural finite element model. Alternatively other elastic moduli can be regarded, such as bulk (K) and shear modulus (G). In case poroelastic behavior is to be regarded, the pore pressure (P_p), permeability (u), porosity (Φ) and Biot coefficient (α) are required (3.2.2). Structural-thermal analyses necessitate parameters describing the thermal conductivity (k), heat capacity (Cp), and thermal expansion (α_{exp}).

Incorporation of plastic deformation in the model demands failure criteria to be considered. Commonly the Mohr-Coulomb criterion or the Drucker-Prager criterion is used (3.2.3) (Fjaer et al., 2008). They require the cohesion (C or S_0) and angle of internal friction (φ) of the material (3.2.3.1). The dilatancy angle (ψ) is optionally defined as third parameter describing volume gain during plastic deformation (Alejano and Alonso, 2005). In addition, creep can be considered as inelastic behavior (3.2.3.2). This requires the definition of various constants ($C_{0\text{-}n}$) describing the type and behavior of the creep or viscoplastic deformation. Creep type then relates to the strain rate being a function of stress, strain, and/or temperature. The corresponding behavior can be a hardening or softening, for instance.

The required material parameters must be as reservoir-specific as possible, because most of them show significant deviations even within the same rock type. While some parameter measurements can be done fast and with relatively little effort, others require laboratory experiments on drill cores (4.3.1). This takes significantly more time and effort, and is commonly done for individual wells only. Hence, in most reservoirs material measurements are distributed heterogeneously, which complicates parameter correlation. If reservoir-specific data is sparse, published values from similar reservoirs have to be used to fill gaps, but this increases uncertainties.

After all parameters that are required for the applied material laws are compiled, they are assigned to the respective elements in the geomechanical model. This can be done is several ways (Herwanger and Koutsabeloulis, 2011). The most common approach is the assignment of uniform material parameter to each layer. If material data is limited, this is inevitable and justifiable. Other approaches use geostatistical techniques to populate the model with mechanical properties (Mohamed et al., 2008). The optimal way would be to use information on the distribution of mechanical properties derived from seismic data (4.3.1). However, in most cases such information is not available.

The assignment of material properties establishes a mechanical stratigraphy (Ali et al., 2003). This mechanical stratigraphy does not necessarily coincide with the geological equivalent, because units are defined by their mechanical properties instead of fabrics or mineralogy, for example. On the one hand, this material subdivision should be as detailed as possible, but on the other hand one mechanical layer must comprise multiple element layers (4.2). This limits the resolution according to the available computing capacities. The usage of fault block refinements can locally provide more detailed mechanical subdivisions in individual fault blocks, but requires a complete geomechanical model (4.2.1).

4.3.1 Data Sources

The material parameters required for geomechanical models can be derived from a range of measurements. Multiple measurements at the same location using different methods are desirable to correlate the resulting parameters.

Density values are derived from respective density logs covering large intervals. They are commonly available for all layers, because they are used to integrate the density of the overburden to obtain the vertical stress gradient. Geomechanical logging tools, such as Dipole Shear Sonic Imagers (DSI), use piezoelectric transmitters to excite compressional and shear wave propagation in the formation around the wellbore (Arroyo Franco et al., 2006). Wide-band piezoelectric hydrophones act as receivers for the excited waves in about 3m distance in the same logging tool. These logs provide reliable acoustic measurements of compressional and shear wave velocities (v_P & v_S) in situ over a distinct interval. The resulting velocities and can be recalculated to dynamic Young's moduli and Poisson's ratios (3.2.1) (Fjaer et al., 2008). Both values provide the basis of the mechanical stratigraphy as they are measured also above and below the reservoir horizon.

Information on the 3D distribution of elastic properties throughout the reservoir can be obtained from wide-angle, wide-azimuth seismic data (Gray et al., 2012). This requires the preservation of amplitude information at the offset ranges used in AVO inversion (Herwanger and Koutsabeloulis, 2011). Such data allows to resolve lateral heterogeneity in the material parameters that could be not addressed otherwise. Besides information on elastic properties, this method can also provide further information on the in situ stress distribution (Gray et al., 2012), which could be used in model validation (4.8).

All dynamic elastic properties are dependent on the frequency of the acoustic wave and must be converted to static moduli that can be used in numerical modeling. This is done by published correlations (Eissa and Kazi, 1989; Morales and Marcinew, 1993) or ideally by using reservoir-specific measurements of static moduli.

Measurements of static elastic moduli use rock mechanical tests on drill cores and are highly desirable for geomechanical modeling (Fig. 3-3, 3.2.1). The provided static moduli can be directly used for modeling and also to convert the usually more abundant dynamic moduli. The experimental setup for determining Young's modulus and Poisson's ratio in uniaxial compression tests is described in literature (e.g. (Fjaer et al., 2008; Jaeger et al., 2007)). Application of poroelastic behavior requires further quantities. While pore pressure and porosity are provided by in situ measurements and logs, respectively, the Biot coefficient and permeability need to be obtained from standard laboratory measurements (Bär, 2012; Qiao et al., 2012). Such experiments on drilled samples are also necessary to derive thermal properties for structural-thermal models (Popov, 2008; Popov et al., 2012; Popov et al., 2003).

Parameters required for including plastic deformation in the geomechanical model are measured in triaxial compression tests on drill cores. Drill cores taken from the same depth interval are tested at different confining pressures in order to derive the cohesion of the tested rock and its angle of internal friction (3.2.3.1)(Jaeger et al., 2007). The more samples are tested, the more accurate is the determination of these values. The application of further inelastic deformation behavior in the geomechanical model described by creep laws requires several constants. They describe the behavior of the rock beyond the point of yielding and vary depending on the specific creep law applied. In order to determine these constants, long-term creep tests using very slow strain rates have to be applied (Berest et al., 2005). Due to the high effort, creep laws are mostly applied in geomechanical models to simulate rock salt, for which the constants are relatively well-known (Henk, 2010).

4.4 Fault Incorporation

The incorporation of faults is one of the most crucial aspects in geomechanical modeling due to their weakening role in the rock mass. In the approach of this study, they are particularly important due to

their potential to generate stress field perturbations. Geological faults represent shear fractures in the rock showing relative displacement along the plane of the fracture, i.e. the fault plane (3.3) (Fjaer et al., 2008). Depending on the mechanical properties on the faulted rock and on the faulting conditions, the fault can exhibit a relatively precise plane of displacement or a zone of damage comprising considerable thickness. Similar to these geological descriptions, faults can be incorporated into a numerical model in two general ways.

The first option considers faults as zones of weakness in the geomechanical modeling domain. 3D elements that are cut by interpreted faults receive modified material parameters accounting for the faults' mechanical weakness (4.4.1). The mesh does not have to be aligned to the faults to do so. The second option considers faults as distinct planes of weakness, which are modeled with 2D interface elements as contacts between two fault blocks (4.4.2). Both approaches have pros and cons that are subsequently described, and affect many aspects in the modeling process from meshing until post-processing. Both approaches do not describe fault propagation itself. This can only be simulated by distinct element models or combined FEM/DEM approaches (2.2).

4.4.1 Faults as Zones of Weakness

Faults can be incorporated into geomechanical models by modifying the elastic and failure properties of those 3D elements that are cut by interpreted faults (Herwanger and Koutsabeloulis, 2011). In this way, the fault is considered to be a zone of weakness with a considerable thickness. This refers to the damage zone resulting from displacement along the fault plane. In order to apply this approach, the finite element mesh is continuous throughout the model. The mechanical parameters that are assigned to the fault zone elements are modified in elastic and failure properties. Those modifications may refer to the amount of displacement the faults experienced in the past and to the expected damage.

The advantage of this approach is the continuous mesh. No non-linearly behaving contacts are considered in such models. This means the only non-linearities that have to be regarded during calculation concern the material laws when failure criteria are considered for plastic deformation. Less computing-intensive non-linear problems lead to faster solution times. In addition, coupling of fluid flow and changing stress fields in and around faults is facilitated significantly, because the stress changes can be directly linked to the hydraulic properties (Herwanger and Koutsabeloulis, 2011). Hence the approach is applied, for example, in a study addressing the critically stress state of a faulted reservoir prior to production modeled by coupled geomechanical and flow simulation (Zhang et al., 2007).

This approach has also some drawbacks. The fact that faults are modeled within the continuous mesh of the geomechanical model yields problems, since faults are by definition zones of high deformation. However, the approach does not allow actual displacements and in case of large deformation, element distortion results in numerical instabilities and can prevent convergence. In addition, the post-processing of such models provide, amongst others, the principal stresses for all elements, but no fault-related quantities like shear and normal stresses acting on them. The evaluation of fault behavior is thus more complicated and limited.

4.4.2 Faults as Planes of Weakness

Instead of modifying the material properties of elements, the second approach implements existing faults as distinct planes of weakness cutting the finite element model. This approach is used in the case study model (7) and uses specific 2D interface elements simulating the fault plane. These interface

elements are also referred to as contact elements (2.1.2). They are defined at opposing sides of interpreted faults and thus dual grid nodes are required along the faces of the contacting parts. This must be regarded during the build-up of the model and the discretization process. The big advantage of this approach is that the contact elements allow for actual displacements between the different parts of the model. In this way, large deformations yield no distortion of elements and no numerical problems emerge (2.1.2).

The contact elements are capable of simulating Coulomb friction, which requires a friction coefficient and a value for cohesion. With some exceptions, faults are commonly assumed to have no cohesion and only a friction coefficient has to be assigned. Similar to the modification of the material parameters in the first approach, constraining this friction coefficient can be difficult as there are no measurements available. For this reason, a default value is typically assumed and adjusted in the later stage of model calibration (4.8). During calculation, the state of contact of the faults can change from sticking to sliding in case stresses overcome the cohesive and frictional strength of the fault. This reflects the non-linear behavior. However, non-linearities are computing-intensive in solving, which means the computing effort is increasing the more faults are included. Non-linear material laws regarding plastic deformation further increase the computing demand.

The benefit of the larger effort in calculation and meshing are fault-specific shear and normal stresses, which the contact elements are able to transmit. These quantities can be received as contact results and used for evaluation of the faults behavior by calculating slip & dilation tendencies (Morris et al., 1996). This approach is applied to the geomechanical model of the case study and is used in various other published studies (Angus et al., 2010; Henk, 2010; van Wees et al., 2003; Vidal-Gilbert et al., 2009).

A further enhancement of this approach to address fault zones with a considerable thickness could be realized in two ways. A combination of both described approaches can be used, in which contact elements are applied and in addition the mechanical properties in the elements adjacent to the faults are modified. The element distance to the fault may influence the applied modification, relating to the increased damage dealt by fault displacement to areas close to the fault plane. Alternatively, the value of contact stiffness described in chapter 2.1.2 can be used. This value controls the mesh penetration along contacts and is by default derived from the mechanical properties of the nearby elements. Manual modification of this stiffness may be used to simulate broader fault zones along implemented contacts.

4.5 Boundary Conditions

The definition of boundary conditions represents a fundamental part in finite element modeling. Boundary conditions are the conditions the numerical model has to fulfill, in other words they are constraints for the models behavior. These constraints are also referred to as loads. Loads can be applied to the solid model, i.e. to the vertices (keypoints), lines, areas, and volumes of the geometrical model, or to the finite element representation, i.e. to the nodes and elements. Independent of the type of assignment, the solver requires all loads to refer to the finite element model. All loads applied to the solid model are thus automatically transferred to the nodes and elements at the beginning of the solution process. Both types of load application have pros and cons.

Solid model loads are independent of the mesh. If the mesh is regularly modified to test its impact on the solution, for instance, the loads can remain. This type of loading is also faster applied in a graphical way, because the solid model inherently has fewer entities than the finite element

representation. However, elements generated in the meshing process are in the currently active element coordinate system. This can lead to different coordinate systems of the solid and the finite element model leading to different loading directions.

Finite element loads are not prone to such problems, because the loads are applied to the nodes and elements. This allows a much more direct control over the boundary conditions of the model, but in case of mesh modifications, the loads have to be applied again. The usage of scripting for modeling (e.g. Ansys® Mechanical APDL®) reduces this effort. Care must be taken when both types of loading are mixed. This can lead to replacement of finite element loads by newly assigned solid loads, for example. Hence, the usage of direct finite element loads represents the optimal way to apply boundary conditions and is used in this study.

The type of loads depends on the discipline of the numerical model, i.e. whether it addresses a structural, thermal or magnetic problem, for instance. The units of applied boundary conditions must be regarded at all times. False units do not necessarily produce a solution error, but lead to erroneous results. Constraints of the degrees of freedoms that are calculated represent the first type of loads. They are applied at selected nodes and address displacements [m] in X, Y, and Z direction in structural models, for instance. The second type of loads is called concentrated loads or forces. In structural models these can be physical forces [N] in distinct directions. Surface loads as third type refer to surfaces such as pressures [N/m² = Pa] or heat fluxes [W/m²]. These three types of loads are commonly applied to nodes or element faces. The fourth type of loads always refers to entire elements or regions and is called body load. A frequency [Hz] in structural models is a classic example. Inertia loads can be seen as a subtype of body loads that required the model to have a mass. The most common load of this type is gravitational acceleration [m/s²].

The load of a geomechanical finite element model has to reflect the full stress configuration encompassing the modeling domain. This includes the vertical stress (SV), the maximum (SHmax) and minimum horizontal stress (Shmin). Geomechanical reservoir models are commonly built with a planar top and bottom reflecting distinct depth levels, while the horizon topology of the layers inside the model is accurately preserved (4.1). The nodes at the bottom of the model have to be fixed in vertical direction for numerical reasons. This is represented by zero displacement constraints. Consequently the nodes are still able to move in horizontal direction. The vertical fixation cannot be compared to natural phenomena and thus an underburden layer beneath the areas of interest is mandatory to provide rebound and avoid any impact of this boundary condition on the results.

The top boundary condition of the model is reflecting the vertical stress (SV) by a pressure surface load equal to the lithostatic load of the overburden at this depth. This is based on the integration of the overburden density derived from density logs (Eq. 4-1).

$$S_V = \int_0^z \rho(z)\, g\, dz \qquad \text{Eq. 4-1}$$

S_V = vertical stress; z = depth; ρ(z) = rock density at depth z; g = Earth's gravity (9.81m/s²)

The vertical stress gradient inside the geomechanical model is established by defining densities to all layers and applying gravitational acceleration as an inertia/body load. A part of the vertical stress is directly conveyed into horizontal stress due to the rock's mechanical response (3.2.1). However, this part alone neither provides the full horizontal stress magnitudes actually prevailing, nor direction-dependent differences of maximum and minimum horizontal stress (unless anisotropic Poisson ratios are applied). Therefore, the horizontal stresses and ratios originating from lithospheric plate movement must be considered by respective horizontal boundary conditions.

Information on the direction and magnitude of the horizontal stresses is provided by large-scale data compilation of stress measurements such as the World Stress Map project, for instance (Sperner et al., 2003; Zang et al., 2012; Zoback, 1992). Lateral boundary conditions have to establish the regional maximum and minimum horizontal stress magnitudes. This can be done by inward directed displacements of nodes along the outermost boundaries of the model. Those boundaries have to address the 90° orientation of the horizontal stresses relative to each other and the regional direction of the stress field (Fig. 4-10). More and less pronounced displacements regard the maximum and minimum horizontal stress magnitude, respectively. In order to obtain the accurate magnitudes, those displacements have to be calibrated at an 'empty' version of the geomechanical model lacking the fault network, but honoring the specific mechanical stratigraphy (4.5.1, Fig. 4-10).

One set of boundary conditions is called a load step and reflects in geomechanical models a distinct stress field configuration. In case multiple stress field configurations are to be considered, for instance various paleo-stress fields, multiple load steps are defined. The solution of the model is then obtained for each load step individually. This is done in the build-up of the dynamic model of the case study (8). Alternatively to including several load steps into a single model, one model could address one load step, i.e. one paleo-stress field. However, this precludes any integrated evaluation of the results regarding the total strain resulting from all past tectonic stages, for instance.

4.5.1 Calibrated Displacements

In contrast to the relatively straightforward application of gravity as body force and the vertical boundary conditions as surface pressure and fixation, respectively, the lateral boundary conditions reflecting the horizontal stresses are more challenging to apply. Displacements of the nodes along the lateral outer boundaries of a finite element model are able establish a horizontal stress field inside.

In order to address the orientation of the maximum and minimum horizontal stress, the outer boundaries have to be rectangular and perpendicular to respective direction of the horizontal stress generated (Fig. 4-10). Inward directed node displacements along these boundaries then generate in the absence of faults a homogeneous stress field throughout the model.

Larger displacements lead to higher stress magnitudes and vice versa. The displacement values yielding the desired horizontal stress magnitudes are determined iteratively in a geomechanical model lacking the fault network, but with consideration of the general mechanical stratigraphy and the other boundary conditions (Fig. 4-10). The determination of the accurate displacement values is an iterative process due to the interaction between the generated horizontal stresses, the vertical stress and gravity effects. Initial displacements to start the iterative determination are estimated. Following the calculation, the generated homogeneous horizontal stress magnitudes are compared at the chosen calibration depth to the desired magnitudes representing the regional stress field undisturbed by faults. The deviation yields correction factors that modify the displacements accordingly. Information on the regional stress magnitudes is derived from published gradients of the reservoir area. Local reservoir-specific measurements are not utilized at this point, but are used for calibration (4.8).

This iterative determination process of the lateral displacements commonly takes 10-20 iterations and finally yields displacements producing the accurate magnitudes of maximum and minimum horizontal stress. These displacements are then applied as lateral boundary condition to the outer boundaries of the geomechanical model comprising the reservoir area with the fault network (Fig. 4-11).

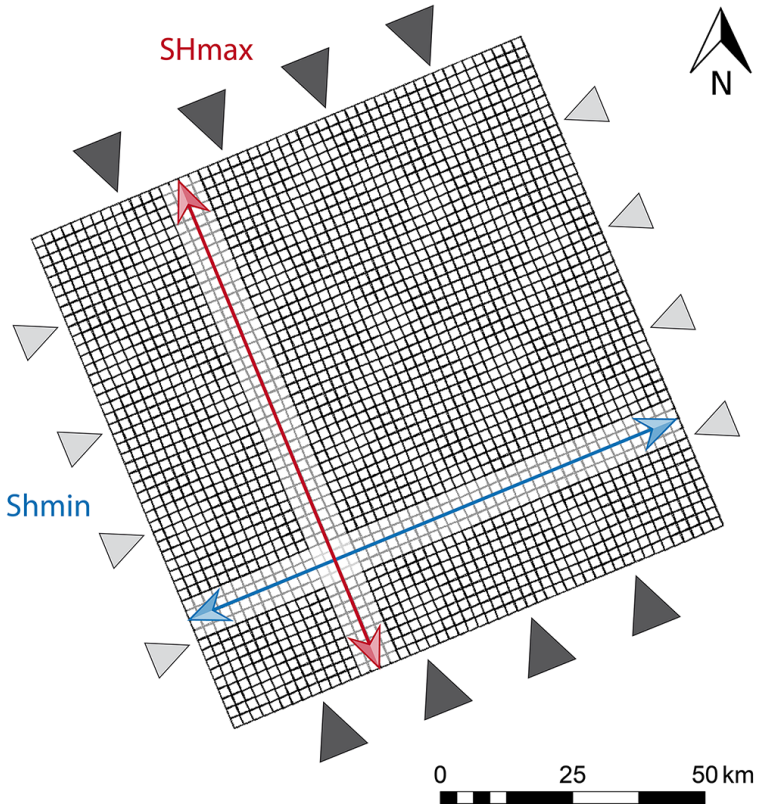

Fig. 4-10. Top view on the geomechanical load frame model used for calibration of displacements (triangles) along the outer boundaries. Those displacements yield the required maximum (red) and minimum (blue) horizontal stress magnitude inside the model. The rectangular boundaries address the orientation of the horizontal stresses in the regional stress field.

4.5.2 Permanent Load Frame

Geomechanical finite element models comprise the reservoir area with the modeled fault network in their center surrounded by a load frame. Lateral displacement boundary conditions generating the horizontal stresses are applied to the load frame (4.5.1). This load frame is rectangular to address the relative orientation of maximum and minimum horizontal stress and is significantly larger than the reservoir area to ensure a homogeneous ambient stress field is established around the reservoir area (4.5.1).

The load frame can be a permanent part of the geomechanical model. In this way, it represents the natural outer boundaries of the geomechanical reservoir model and is calculated each time the model is solved. The results of the load frame area are of no interest and thus the mesh is coarsened towards the outer boundaries to save elements and computing time (Fig. 4-11).

At the circular inner boundary of the reservoir area, the element size of the reservoir area and the load frame has to be equal in order to provide a continuous mesh (Fig. 4-11). Alternatively, the mesh can be refined towards the reservoir area, without reaching exactly the element size of the reservoir. So-called internal multipoint constraint algorithms (MPC) can then be used in Ansys® to simulate a bonded contact as connection along the inner frame of the reservoir. This MPC contact technology is able to establish a bonded contact between dissimilar meshes without introducing additional contact elements (Ansys Inc., 2012). It works the better the smaller the difference between the respective element sizes is. The resulting larger element size in the load frame yields less elements and saves computing time. However, permanent load frames directly connected to the reservoir area always increase the calculation effort significantly. This affects especially large field-scale geomechanical reservoir models and is the reason for the elaboration of a more effective approach (4.5.3).

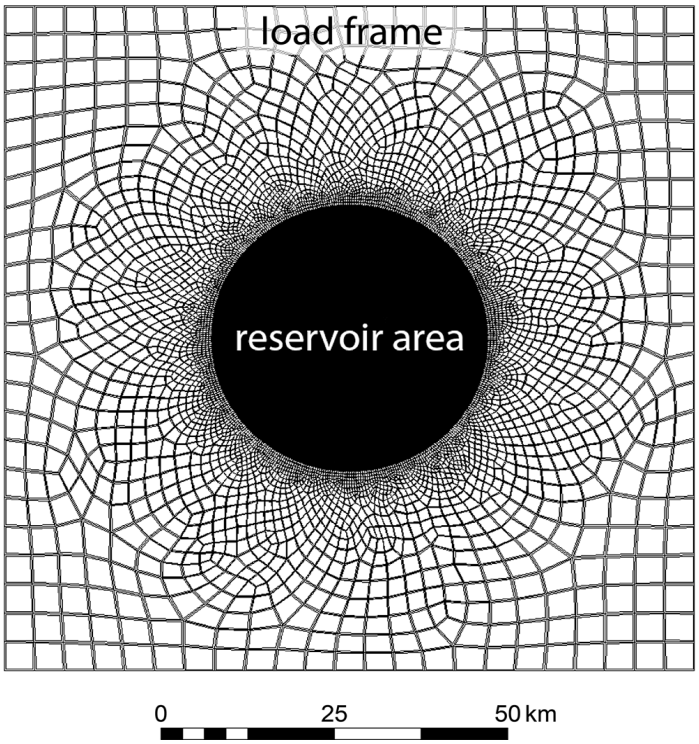

Fig. 4-11. Top view on a geomechanical model comprising a permanent rectangular load frame encompassing the reservoir area. The element size is coarsened to the outer boundaries of the load frame and is refined towards the reservoir. Permanent load frames have to be calculated each time the model is solved, which significantly increases the computing time. The inner part of the model is black, because of the large number of comparatively small elements.

4.5.3 Separate Load Frame Model

Despite the coarsening of the mesh in the rectangular load frame of geomechanical models, the amount of elements in this frame is still very large. These elements require computing capacities, but are outside the area of interest. A more effective approach is elaborated based on the so-called cut-boundary displacement method and aims at decoupling the rectangular load frame from the reservoir model.

Volumes are generated around the fault block volumes of the reservoir area building up a circular inner frame, at whose boundary the geomechanical model ends (Fig. 4-11). This geomechanical reservoir model is thus significantly smaller and represents a cylinder with a planar top and bottom at distinct depth levels (4.1.4). Besides this cylindrical reservoir model, a separate rectangular load frame mode is build comparable to the empty geomechanical model mentioned before (Fig. 4-10). This large load frame model is coarsely meshed and comprises the same thickness and mechanical stratigraphy as the reservoir model. The load frame is also located by its coordinates at the same position as the reservoir model, but is significantly larger. The calibrated displacements are applied to this separate load frame model and due to the coarse mesh this model is solved rapidly providing the homogeneous stress field as result.

The circular outer boundary of the cylindrical reservoir model, i.e. the cut-boundary in this case, is selected and the coordinates of all corresponding nodes are exported. This coordinate information is imported into the solved load frame model. Specific displacements are then interpolated for all nodes based on the results of the load frame model, i.e. the homogeneous stress field (Fig. 4-12). The resulting node specific displacements are used as lateral boundary conditions for the cylindrical reservoir model (Fig. 4-12).

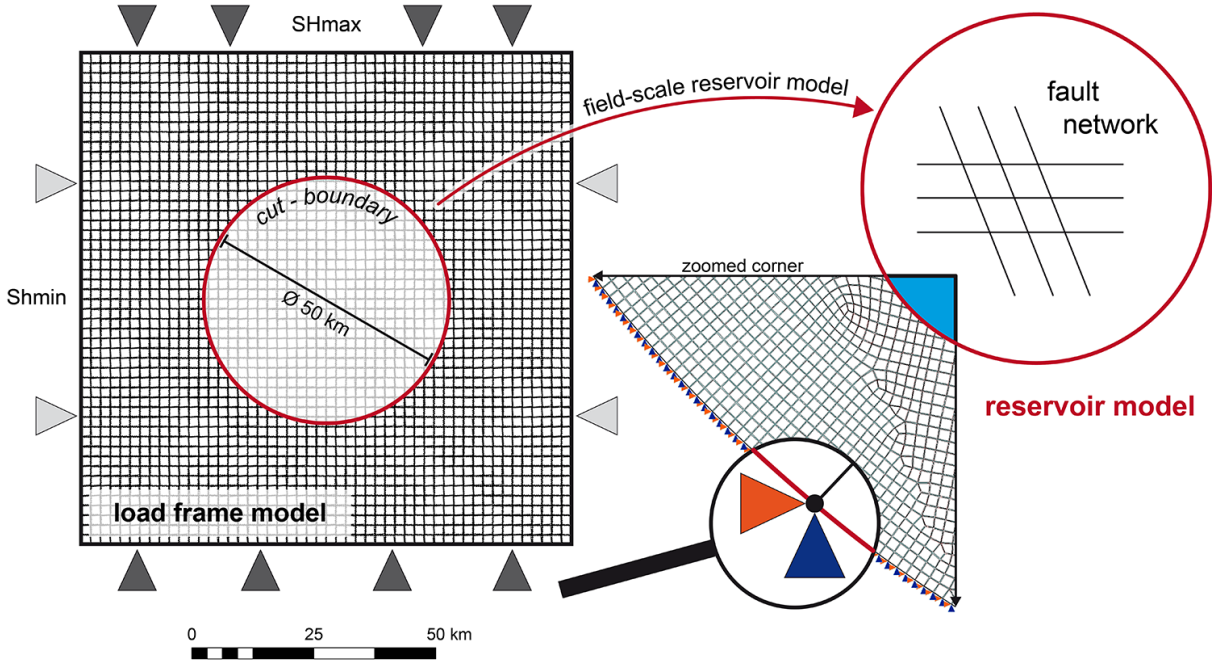

Fig. 4-12. Overview on the workflow using the cut-boundary displacement technique for decoupling the rectangular load frame from the reservoir model. The load frame is calculated separately with calibrated displacements (left). Node coordinates of the cut-boundary (red), i.e. the circular outer face of the reservoir model, are taken to interpolate node specific displacements for those nodes based on the results of the rapidly solved load frame model. These node specific displacements (center) transfer the homogeneous stress field accurately from the load frame model to the cylindrical reservoir model (right).

In this way, the calibrated stress field is transferred to the reservoir model and no directly connected load frame is necessary. Testing this approach with an empty cylindrical reservoir model demonstrates the accurate transfer.

The cut-boundary displacement method is based on the St. Venant's principle, which implies that stress and strain concentration effects are a relatively local phenomena and if the boundaries of the secondary models using the interpolated boundary condition are sufficiently far away from the stress concentration, reasonably accurate results can be achieved. This latter assumption represents the most important restriction of the technique and it must be verified at all times that this assumption is adequately satisfied. With respect to this geomechanical application, it has to be ensured that a sufficient distance between the faults and the cut-boundary is maintained. Different radii of the cylindrical model can be tested to ensure the required distance.

This approach offers the most efficient way of applying lateral boundary conditions to the geomechanical reservoir model. The saving of elements resulting from the lack of an outer load frame allows higher mesh resolutions in the reservoir area at constant calculation times. Different remote stress magnitudes and orientations can be easily addressed by rotation and calibration of the separate load frame model, from which the specific displacements are then transferred.

However, this technique cannot be applied along or crossing faults simulated by contact elements as these faults perturb the stress field and are therefore prone to comprise stress concentrations. The required sufficiently large distance between nodal displacement constraints and stress concentrations thus cannot be maintained. In addition, contact pressures across contact elements representing the faults are neglected. This missing information inevitably leads to erroneous results.

4.6 Model Solving

Following the geometrical build-up of the model and its discretization, the compilation and assignment of reservoir-specific material parameters and the application of boundary conditions, the geomechanical model is calculated by solution algorithms, so-called solvers. A finite element analysis can be of static or transient type, i.e. a steady state or a time-dependent development is calculated, respectively (Müller and Groth, 2000). The geomechanical model of this study is of static type, however, other approaches apply transient geomechanical models to study depletion effects during hydrocarbon production, for instance.

The selection of the solver is the first step in solving the model. There are typically two types of solvers: direct and iterative solvers. Direct solvers are based on the direct elimination of equations. This requires a factorization of the initial sparse linear system of equations into a lower triangular matrix, which demands a lot of disk space or main memory (Ansys Inc., 2012). Iterative solvers do not require matrix factorization. They iterate towards the solution using series of very sparse matrix – vector multiplications together with a preconditioning step. This requires less time and memory per iteration than direct factorization. Nevertheless, direct solvers can be faster in case large numbers of iterations are required in order to reach an acceptable solution with iterative solvers.

Direct solvers are robust, but also computing and I/O-intensive, and can be applied to solve almost all types of finite element analyses. They are best suited for non-linear problems and are thus optimal for geomechanical modeling. Direct solvers are also taken for linear analyses comprising ill-conditioned matrices or very poorly shaped elements. The direct solver in Ansys® (2.1.1) used in the case study comprises different memory modes, which have significant impact on the computing time. They are referred to as in-core and out-of-core memory mode (Ansys Inc., 2012). The in-core memory mode uses in-core factorization of the matrix and requires the factored matrix to be fully accommodated by the main memory. Hence, the physical main memory has to be sufficiently large. This mode commonly yields the best performance, but is only the default for small jobs due to the memory requirements.

The out-of-core mode respectively uses out-of-core factorization, i.e. the factored matrix is sourced out to the hard disk. Parts of the matrix, so-called fronts, are loaded into the main memory and are solved in succession resulting in significant I/O between hard disk and memory. The optimal version of this out-of-core mode can be applied, when the largest of all fronts fits completely into the main memory. Otherwise a non-preferable minimum version of this mode is used, which is considerably slower. The optimal out-of-core memory mode yields an optimal balance between memory usage and I/O from disk and thus is taken for large models, such as field-scale geomechanical reservoir models.

Besides the selection of the solver, further solution settings must be specified. Large deformations are explicitly allowed in geomechanical models, for instance. In addition, convergence values for forces and displacements are defined, as well as the number of numerical substeps the solver can take for the calculation of a load step. In case multiple load steps are addressed, care must be taken regarding the deletion and re-application of boundary conditions. Any leftover from previous load steps may lead to ill-conditioning of the model. Following the solver selection and definition of solution settings, the geomechanical finite element model is solved. Increasing model size and complexity demands the usage of high-performance computing techniques (4.6.1).

4.6.1 High-Performance Computing

Small geomechanical models, for instance of generic parameter studies (6.1), can be calculated on local workstations. In order to yield reasonable computing times for large geomechanical finite element models, significantly more powerful computing devices and special techniques are required, which are referred to as high-performance computing (HPC). High-performance computing does not only describe powerful hardware, but represents an integrated computing environment including hardware, software, algorithms and programming tools (Dongarra et al., 1995).

In order to calculate models in a HPC run, the type of parallelization must be specified. Parallelization describes the way the computing task is split to multiple cores and/or computing nodes to be calculated simultaneously. Two basic types of parallelization are commonly used: symmetric multiprocessing (SMP) and massively parallel processing (MPP). In symmetric multiprocessing, the task is calculated by multiple cores of a single computing node, i.e. a single server. All cores are sharing and using the same memory address space of this node and thus the method is also called shared-memory parallel processing. In contrast, massively parallel processing splits the task to multiple computing nodes, which comprise individual physical memory and commonly multiple cores. This approach is also known as distributed memory parallel (DMP) computing. The calculating cores of different nodes communicate via a so-called message passing interfaces (MPI). Several MPI types are available, for instance Intel MPI or Open MPI.

Both types of parallelization require the definition of the nodes and cores addressed. In addition to the usage of central processing units (CPU), also graphics processing units (GPU) can be included in the calculation process. This technique is called general purpose computation on graphics processing units (GPGPU). Effective usage of GPUs for computing requires the outsourcing of appropriate parts of the code. In proprietary finite element codes such as Ansys®, the respective option for GPU acceleration is available in a general way only.

The optimal type of parallelization and hardware configuration depends on the specification of the numerical model. It was found that the field-scale geomechanical models of this study comprising large amounts of non-linear contacts are best solved with SMP parallelization due to the communication demand arising from the contacts. Although more cores generally speed up the calculation, an excessive amount of cores yield at some point the opposite effect due to the increasing communication.

The output information that solvers commonly provide can be used to determine the optimal HPC environment and resources required. The solver output commonly states:

- number of equations to be solved in model calculation
- solver type
- type of memory mode
- allocated memory
- equation solver computational rate [GFlops]
- equation solver effective I/O rate [MB/s]
- times used for pre-processing, solution pre-processing, computing solution

The evaluation and comparison of this information is called benchmarking and reveals potential problems in the selection of memory mode, memory allocation, and also computing performance depending on CPU type, architecture and speed.

4.7 Post-Processing

Post-processing comprises the reviewing and visualization of the calculated solution of the geomechanical model. In general, finite element analyses provide two types of results: primary data and derived data (Ansys Inc., 2012). Primary data includes the degree of freedom solution at all nodes of the model, i.e. displacements in structural model and temperatures in thermal models, for instance. This information is also referred to as nodal solution data. Derived data represents results calculated from the primary data, i.e. stress and strain in structural analysis and thermal gradients and fluxes in thermal analysis. These results are calculated for each element and are thus also known as element solution data. If this information is averaged at the nodes, it is also referred to as nodal solution data.

The most common visualization of results are contour plots showing the distribution of a scalar quantity on selected elements or defined planes cutting the finite element model. They are able to visualize distributions of both primary and derived data in a continuous and comprehensive way. Due to the fact that derived data is calculated per element and is thus discontinuous, these results are typically averaged at the nodes to provide continuous contours. Another type of visualization are vector plots showing the variation of both magnitude and direction of a vector quantity as arrows. While the direction of the vector quantity is expressed by the arrow orientation, the respective magnitude is considered by its color or size. Vector quantities from primary and derived data can be visualized in this way.

A third general type of reviewing results uses paths. Paths are arbitrary lines through the model defined by coordinates of points following well paths in reservoirs, for instance. Output quantities are mapped onto this path, i.e. the quantity is interpolated along the path based on the results of the model. The variation of the mapped quantity along the path is then plotted as diagram. Alternatively, all elements cut by the path are selected and any quantity can be displayed as contours or vectors on them. In this way, paths can reveal stress gradients through the model or help to precisely select the elements describing a wellbore. Information from these elements at a distinct depth level can be taken for the comparison of modeling results with field data (4.8).

4.7.1 Provided Result Quantities

Finite element programs derive by default various stress and strain quantities. Due to the origin of the finite element analysis in engineering, the respective convention is commonly used describing tensile stress positive and compressive stress negative. However, in rock mechanics, tectonophysics and structural geology, the convention describes compressive stress being positive (3.1). Compressive stresses are thus recalculated to positive values and are typically given in Megapascal [MPa].

The provided and most important stress quantities in geomechanical modeling are the three principal stresses σ_1, σ_2, and σ_3 ($\sigma_1 > \sigma_2 > \sigma_3$) (3.1.1). These stresses represent the vertical, maximum and minimum horizontal stress. The specific correlation then depends on the tectonic regime. Beside the principal stresses, the axial stresses SX, SY, and SZ are also of interest in geomechanical modeling, when the vertical stress changes its correlating principal stress due to changes in the mechanical properties, for instance.

Another stress quantity provided by finite element programs by default is the widely used von Mises stress, also known as equivalent stress (Eq. 4-2). This quantity describes a 3D state of stress by a single positive value and is part of the von Mises failure criterion that is used to describe yield in metals (Fjaer et al., 2008; Jaeger et al., 2007).

$$\sigma_e = \sqrt{\frac{(\sigma_1 - \sigma_2)^2 + (\sigma_2 - \sigma_3)^2 + (\sigma_3 - \sigma_1)^2}{2}} \quad \text{Eq. 4-2}$$

This quantity is used to comprehensively present the 3D stress information with consideration of all three principal stresses. Corresponding to the stress value, the von Mises strain is commonly provided as well, which is based on the respective principal strains ε_1, ε_2, and ε_3, and the Poisson's ratio ν (Eq. 4-3).

$$\varepsilon_e = \frac{1}{1+\nu}\sqrt{\frac{(\varepsilon_1 - \varepsilon_2)^2 + (\varepsilon_2 - \varepsilon_3)^2 + (\varepsilon_3 - \varepsilon_1)^2}{2}} \quad \text{Eq. 4-3}$$

These stress and strain quantities represent the basis for post-processing and result analysis. While these quantities are derived and available for all 3D elements throughout the model, the usage of contact elements for fault implementation provides fault-specific shear and normal stresses. These stresses are directly plotted as contours onto the respective elements.

4.7.2 Further Result Quantities

The principal stresses, as well as the shear and normal stresses acting on the faults, are taken for calculating further quantities of interest. The usage of script languages for modeling and post-processing allows array parameters to be applied for additional calculations. In general, an array is a data structure representing a collection of variables, or fictional elements, in a regular spacing (Godse and Godse, 2009). Each element in an array is accessed by a specific index. Arrays comprise as many dimensions and variables as are defined in the setup of the array.

After the size and dimensionality of an array is defined, values are assigned to the variables of the array representing the stress and strain quantities of the geomechanical model. Following the filling of the array, it is used for calculating arbitrarily complex operations. Vector operations refer to mathematical operations on distinct columns, while matrix operations affect entire matrices. Typical stress quantities to be derived in geomechanical modeling are the mean stress and differential stress magnitudes (Eq. 4-4, Eq. 4-5).

$$\sigma_m = \frac{1}{3}(\sigma_1 + \sigma_2 + \sigma_3) \quad \text{Eq. 4-4}$$

$$\sigma_d = \sigma_1 - \sigma_3 \quad \text{Eq. 4-5}$$

The mean stress represents the arithmetic mean of the three principal stresses σ_1, σ_2, and σ_3 (Eq. 4-4), and thus provides information on total stress distribution. The distribution of mean stress may yield insights to potential hydrocarbon migration directions throughout the reservoir (Henk and Nemcok, 2008). Differential stress is calculated by the difference of the largest (σ_1) and least principal stress (σ_3) (Eq. 4-5). Regarding Mohr diagrams, the differential stress determines the size of the Mohr circle at a specific state of stress (3.2.3.1). Increasing differential stress results in larger Mohr circles and the rock approximates to shear failure. According to Sibson (1996), the relationship between prevailing differential stress and tensile strength of the rock also controls the type of brittle failure when pressurized fluids infiltrate.

Another stress quantity used in geomechanical studies is the so-called critical Coulomb stress (σ_{CC}) (Pollard and Fletcher, 2005; Tamagawa and Pollard, 2008). It is calculated using the largest (σ_1) and least principal compressive stress (σ_3), and the coefficient of internal friction (μ_i) (Eq. 4-6). Positive

critical Coulomb stresses indicate an increasing probability of existing conjugate fractures to shear (Tamagawa and Pollard, 2008).

$$\sigma_{CC} = \frac{(\sigma_1 - \sigma_3)\sqrt{1 + \mu_i{}^2}}{2} - \frac{\mu_i(\sigma_1 + \sigma_3)}{2} \quad \text{Eq. 4-6}$$

The described stress quantities address the stress distribution throughout the reservoir. In order to evaluate and characterize the fault behavior, the shear (τ) and normal stress (σ_n) derived from the contact elements are used. The ratio of both represents the slip tendency (T_{slip}), which describes the fault's tendency to move (Eq. 4-7) (Morris et al., 1996). This slip tendency is normalized additionally to the friction coefficient of the fault (μ_f) resulting in a range of values between zero and one. The probability for movement along the fault increases as the normalized slip tendency increases.

$$T_{slip} = \frac{1}{\mu_f}\left(\frac{\tau}{\sigma_n}\right) \quad \text{Eq. 4-7}$$

The second fault-specific quantity is referred to as dilation tendency. It is derived from the normal stress (σ_n) on the faults and the largest (σ_1) and least principal stress (σ_3) (Eq. 4-8). This ratio describes the tendency of the fault to open or dilate. The resulting values also range from zero to one. Higher values represent a higher likelihood of fault opening.

$$T_{dila} = \frac{(\sigma_1 - \sigma_n)}{(\sigma_1 - \sigma_3)} \quad \text{Eq. 4-8}$$

4.8 Model Calibration

The setup of a geomechanical model always requires some assumptions to be made, for instance regarding poorly constrained parameters. These assumptions are mandatory to setup the model, but inherently bear uncertainty. In order to counteract and reduce this uncertainty, the model must be compared to field data. It has to be ensured that the modeling outcome reflects real-world observations, which are not comprised in the model input. For this reason the modeling results are compared to local measurements in a process referred to as calibration or validation of the model. This iterative process utilizes a dataset of measurements strictly separate from input data.

Appropriate data for the calibration process includes all types of stress and fracture measurements in the reservoir. Stress data comprises especially the magnitude and orientation of the horizontal stresses (4.8.1), since the vertical stress is relatively well-defined by integrating the overburden density. Fracture data encompasses the strike, dip direction and dip angle of faults and fractures, and spatial information on fracture patterns and relative densities (4.8.2).

Within the calibration process all stress magnitudes and orientations measured in the field, as well as fracture characteristics are compared to the respective modeling results. Detailed information on the specific drilling trajectories of all wells is mandatory in order to compare the results at the accurate subsurface location. Therefore all well paths are transferred from the geological subsurface model to the geomechanical finite element model (4.7).

The initial comparison between modeling results and measurements yields most commonly no satisfactory fit. This requires an iterative procedure to start, in which poorly constrained parameters of the input data and boundary conditions are adjusted to improve this fit and make the model to better reflect reality. Prime examples of such poorly constrained parameters are commonly the friction

coefficient of the incorporated faults and the magnitude of the intermediate principal stress. The specific parameter to be changed, the extent and type of change, strongly depends on the specific reservoir and corresponding background knowledge. Preliminary parameter studies on small models help by providing insights into the most important parameters in beforehand.

All adjustments in the calibration process have to be always applied on a larger scale and within geologically reasonable limits. Small-scale adjustments to reproduce individual measured values do not improve the model and may lead to wrong final conclusions.

The iterative calibration process finally provides optimal values for initially poorly constrained parameters and a satisfactory fit between the results of the geomechanical model and field measurements. Correlation diagrams help to evaluate the quality of this fit. This evaluation always has to regard the uncertainties of calibration data. After the iterative calibration, the geomechanical model is validated and its results can be used for further interpretations.

Following initial calibration, this process is to be proceeded with new and improved data. The range and quality of data that is available for calibration determines the quality of the model and its results. However, it is proposed that at some point the improvement by additional calibration data ceases. Besides the calibration data, the quality of input data is also decisive for meaningful model calibration and eventually limits calibration improvements.

4.8.1 Stress Data

Stress data for calibration purposes can be derived by a variety of measurements – in situ and in laboratory. One of the most frequently available stress information is the magnitude of the least principal stress measured in normal and extended leak-off tests (LOT/XLOT) during hydraulic fracturing (Fjaer et al., 2008; Lin et al., 2008; Ljunggren et al., 2003; Reynolds et al., 2006). The principles of this method are outlined in more detail due to the high abundance of this type of measurement and its relevance for the case study.

Leak-off tests are based on fluid injection into the rock formation and its mechanical response due to the resulting pressure conditions. Injecting fluid at constant rates into an isolated section of the wellbore linearly increases the bottom hole pressure over time and tensile stress is generated in the borehole wall. At some point, a hydraulic tensile fracture forms perpendicular to the least principal stress and the fluid starts to leak off. This is indicated by a departure from the linear trend. The pressure at this singularity is referred to as leak-off pressure (LOP), which roughly estimates the least principal stress magnitude. However, tortuosity due to casing perforations, amongst others, commonly increases the obtained pressure above the least principal stress. In other cases no clear leak-off pressure can be detected.

Continuing pumping leads to the formation breakdown at a peak pressure, at which unstable fracture propagation away from the wellbore occurs. This peak pressure is called formation breakdown pressure (FBP) (Fig. 4-13). The pressure drops, because the fluid flow into the fractures is larger than the pumping supply. During extended leak-off tests and hydraulic fracturing pumping is proceeded at this point and the sudden pressure drop following the formation breakdown stabilizes and reaches a constant level. During this phase, the created fractures are propagating and thus this pressure level is called fracture propagation pressure (FPP) (Fig. 4-13). After pumping is stopped and the test interval is shut-in, the pressure rapidly declines and eventually slows down (Fig. 4-13). During this decline the created fractures close gradually (Fjaer et al., 2008).

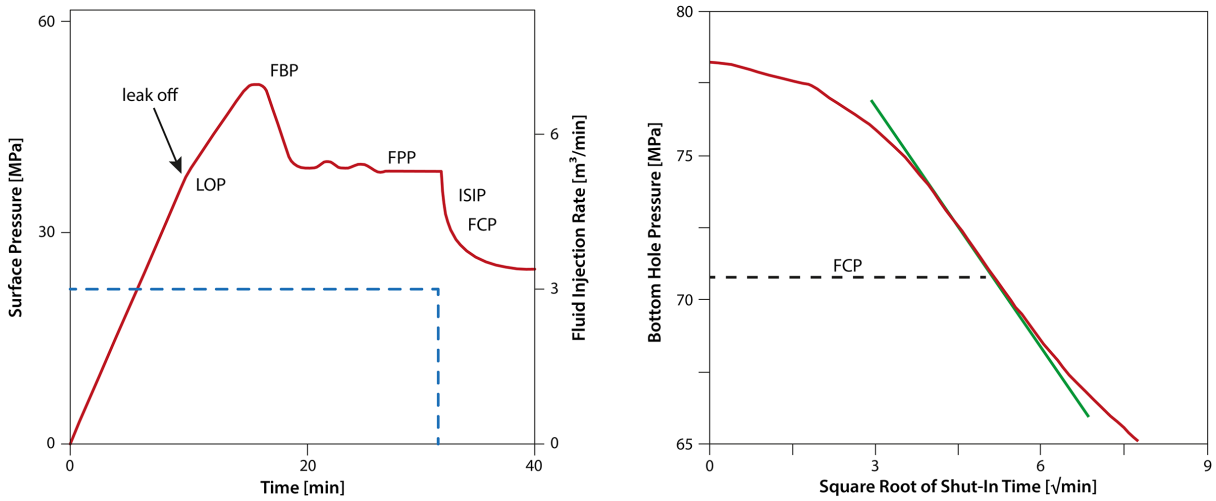

Fig. 4-13. Diagram showing the idealized overall pressure trend and injection rate during an extended leak-off test (left) and an example of the detailed determination of the fracture closure pressure (FCP) in a square root of time plot (right). Along the pressure trend (red) induced by fluid injection (blue), the leak-off (LOP) and formation breakdown pressure (FBP) is indicated, as well as the fracture propagation pressure (FPP), the instantaneous shut-in pressure (ISIP) and the fracture closure pressure (FCP) (left / modified after Gaarenstroom et al. (1993)). Diagrams displaying pressure against the square root of time after shut-in allow a more precise determination of the fracture closure pressure (FCP) representing the magnitude of the least principal stress (right).

The pressure measured directly after the shut-in is called instantaneous shut-in pressure (ISIP). Due to the additional pressure left in the fracture during closing, the instantaneous shut-in pressure is often larger than the least principal stress magnitude and is regarded as its maximum estimate (Fjaer et al., 2008). The fracture closure pressure (FCP) is reached in the instant when the fracture walls initially touch and thus equals magnitude of the least principal stress (Reynolds et al., 2006).

This moment is represented by a sudden decrease in the rate of pressure decline. In special diagrams plotting for instance pressure against the square root of time after the shut-in, the curve follows a linear trend as long as the fracture remains open (Fjaer et al., 2008). The fracture closure pressure is reached when the pressure decline leaves this linear trend. An estimate for the lower limit of the closure pressure is obtained from so-called Horner plots, for example. Several successive pumping tests analyzing the re-opening of created fracture and yielding multiple measurements of the fracture closure pressure provide increasingly precise information on the least principal stress magnitude.

The determination of the maximum horizontal stress magnitude requires techniques utilizing observations of compressive and tensile wellbore failure (Zoback et al., 2003). Rather than exactly determining this magnitude, it is commonly only constrained by the knowledge of the vertical and minimum horizontal stress in combination with the frictional stress limits beyond which faulting occurs (Reynolds et al., 2006; Sibson, 1974; Zoback and Healy, 1984). The maximum horizontal stress magnitude thus more often represents a poorly constrained parameter to be varied in the iterative calibration procedure.

Stress orientations inside the reservoir are most commonly derived from borehole breakouts and drilling induced tensile fractures around the wellbore (Grote, 1998; Zoback et al., 1985) (Fig. 4-14). Borehole breakouts represent zones of compressional failure along the wellbore wall on opposing sides of the borehole, where the stress concentration exceeds the rock strength. The horizontal axis across these failure zones represents the direction of the minimum horizontal stress (Fig. 4-14). The

probability of breakouts increases the larger the stress difference becomes between the two stresses perpendicular to the wellbore.

Ultrasonic image logs and caliper logs are the most reliable tools to detect breakouts, which appear as dark bands and zones of larger diameter, respectively. While the larger diameter intuitively reflects the broke out rock, the dark bands in ultrasonic image logging results from low-amplitude reflections of the breakout. Complementing the breakouts, drilling induced fractures (DIF) form in the wellbore wall due to tensile stresses. These are located in a 90° shift to the breakouts and are located thus in direction of the maximum horizontal stress (Fig. 4-14) (Brudy and Zoback, 1999; Sperner et al., 2003).

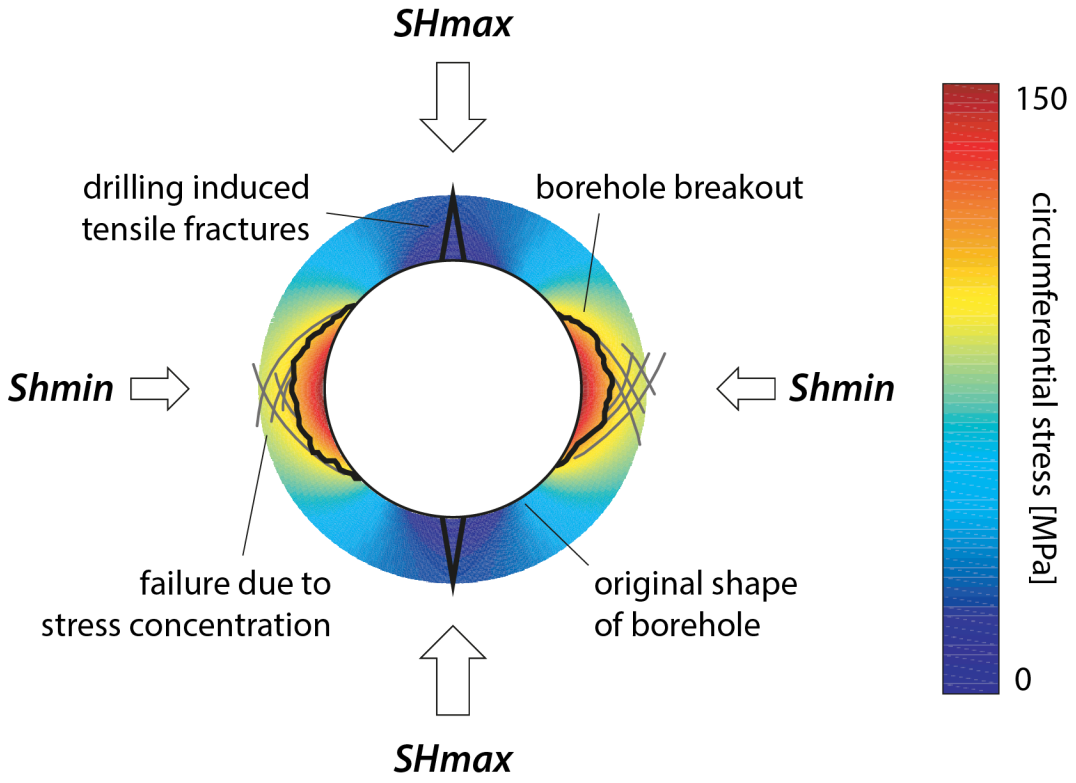

Fig. 4-14. Sketch of a borehole showing the occurrence of borehole breakouts perpendicular to the maximum horizontal stress (SHmax) and drilling induced tensile wall fractures (DIF) parallel to SHmax. Colors represent the effective circumferential stress, also called hoop stress, acting in tangential direction around the wellbore. This stress varies significantly with the position around the wellbore and the distance to the wellbore wall. The size of the breakouts and drilling induced fractures do not correspond to the magnitude of hoop stress and are only indicated for illustration purposes (modified after Sperner et al. (2003); Zoback (2007)).

Drilling induced fractures are detected in electrical image logs as opposing dark stripes, for instance. These stripes display the fracture planes as zones of high electrical conductivity resulting from their filling with drilling mud or pore fluid.

Regionally prevailing stress direction is commonly derived from large-scale data compilations like the World Stress Map (Zang et al., 2012; Zoback, 1992) and is used as input data for the definition of boundary conditions. However, local measurements of stress orientation throughout the modeled reservoir represent crucial calibration data. Particularly those measurements showing significant deviations from the regional trend are useful for determining scenarios that model these orientations by stress perturbations.

Beside these in situ measurements, stress magnitudes and orientations are also derived from laboratory measurements on drill cores. Two widely used methods are based on anisotropies detected by ultrasonic wave velocities analysis (WVA) and on anelastic strain recovery (ASR) (Matsuki, 2008;

Ren and Hudson, 1985). Both methods ideally require an oriented extraction of the drill core, but are then able to provide stress magnitudes and orientations of all three principal stresses. Another laboratory measurement that yields the full stress tensor is called RACOS® analysis (Rock Anisotropy Characterisation On Samples) (Braun et al., 1999). It is based on loading-dependent compensation of deformation and fracturing, and uses oriented extracted drill cores. This method further allows applying sedimentary structures for later orientation of the drill core in case this information is not available.

Such laboratory analyses complementing in situ measurements are highly desirable. However, their availability suffers under the fact that drill cores are normally very rare and must be used for numerous other tests as well. An ideal stress dataset for model calibration comprises stress results of different types of measurement at the same wellbores. This allows optimal correlation of results and evaluation of uncertainties. While the uncertainty of stress orientation measurements is reported to be 10-15° for laboratory and in situ techniques, no corresponding values are stated for magnitude measurements in extended leak-off tests, for instance. Missing uncertainties must be estimated in all conscience. Consideration of uncertainties in model calibration is important due to the fact that improvements of the fit between modeling results and measurements below the range of uncertainty do not yield any increase in reliability.

4.8.2 Fracture Data

Information on the distribution and type of fractures in the modeled reservoir represents important calibration data as well, since fracture characteristics are directly controlled by the prevailing in situ stress field. Therefore natural fracture sets typically reflect the paleo-stress field under which they were created. Followingly acting paleo-stress fields and the recent stresses may have re-activated these fractures or lead to critical states of stress enhancing their hydraulic properties (Ameen, 2003). The recent hydraulic behavior depends on the timing of these effects and their potential consequences in the past. While fractures critically stressed today may enhance the hydraulic behavior of the reservoir, such critical states of stress in the past could have resulted in fluid flow and mineralization, leading to poor hydraulic properties.

Fractures and faults cross-cutting wellbores are commonly detected by image logs (Johnston and Wachi, 1994; Lee, 1994). These logs yield the strike, dip direction and dip angle (Gaillot et al., 2007). Besides direct video imaging of the borehole wall, two geophysical methods are predominantly used, which are based on ultrasonic wave propagation and electrical resistivity. The most commonly used ultrasonic tools are the so-called Ultrasonic Borehole Imager (UBI) and BoreHole TeleViewer (BHTV). Amongst resistivity image logging, the Formation MicroScanner (FMS) and Formation MicroImager (FMI) are typically applied. Image logs using electrical resistivity provide best resolutions in water-based drilling fluids.

Fracture planes diagonally cutting the logged wellbore appear as sinuous lines in the resulting image (Fig. 4-15). The steeper the fracture or fault planes dips, the more pronounced is the curve. Consequently, it is difficult to identify vertical fractures, since the curve evolves to a vertical line that is hardly visible or completely missing. The position of the sinusoid minimum yields the dip direction and thus the strike of the fracture plane (Fig. 4-15). The arc tangent of twice the amplitude – or height of the sinusoid – divided by the borehole diameter describes the dip angle (Gaillot et al., 2007).

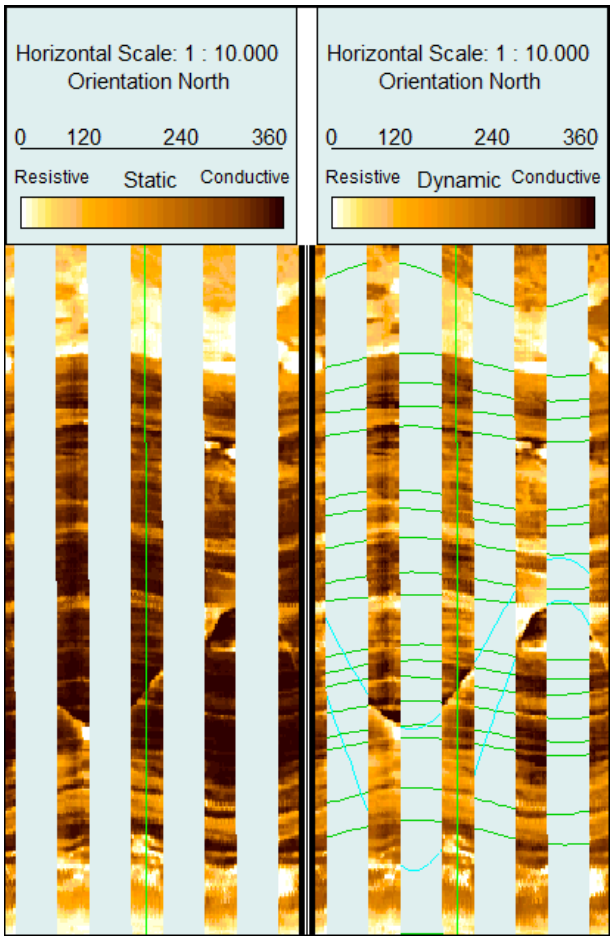

Fig. 4-15. Example of an image log section (FMS) showing the typical sinuous curve of a resistive shear fracture cutting the wellbore (turquoise line). According to the position of the curve with respect to the 360° scale, this fracture plane is dipping in to the southeast. The image log section is extracted from FMS logs provided for the case study.

FMS/FMI logs further allow distinguishing conductive from resistive fractures (Fig. 4-15). This characteristic may be used to separate younger fractures being conductive due to fluid flow from older fractures already filled with resistive precipitations (Henk, 2010). In some cases, this information can then be related to specific tectonic stages of the reservoir area.

Even if this conductivity differentiation cannot be made, the strike and dip of the fractures visualized in stereoplots allow a comparison to possible fracture geometries inferred from recent and paleo-stress distributions revealed by the geomechanical model – including all perturbations. Especially in the dynamic modeling of various past tectonic stages, the observed fracture patterns can be used for comparison with the model predictions, since these patterns can be seen as the 'frozen' representation of paleo-stress states . In order to compare the fracture characteristics to the in situ stress orientation, the latter can be displayed in vector plots. In addition, strain localizations under paleo-stress fields may correlate with varying fracture intensities observed today.

During the comparison of fracture patterns to in situ stress orientations, it is important to regard the impact of the tectonic regime. It controls the way the principal stresses and thus the respectively aligned shear and extensional fractures are orientated in space (Fig. 4-16). Tensile fractures form parallel to the first principal stress and normal to the least principal stress, while conjugated shear fractures mount the characteristic 60° angle around the first principal stress axis.

Varying correlation of vertical stress (S_V), maximum (S_H), and minimum horizontal stress (S_h) being σ_1, σ_2, and σ_3, leads to different fracture patterns (Fig. 4-16) (3.3). In vertical wellbores, for instance,

shear fractures are significantly easier to determine in image logs in extensional and compressive regimes than in strike-slip regimes.

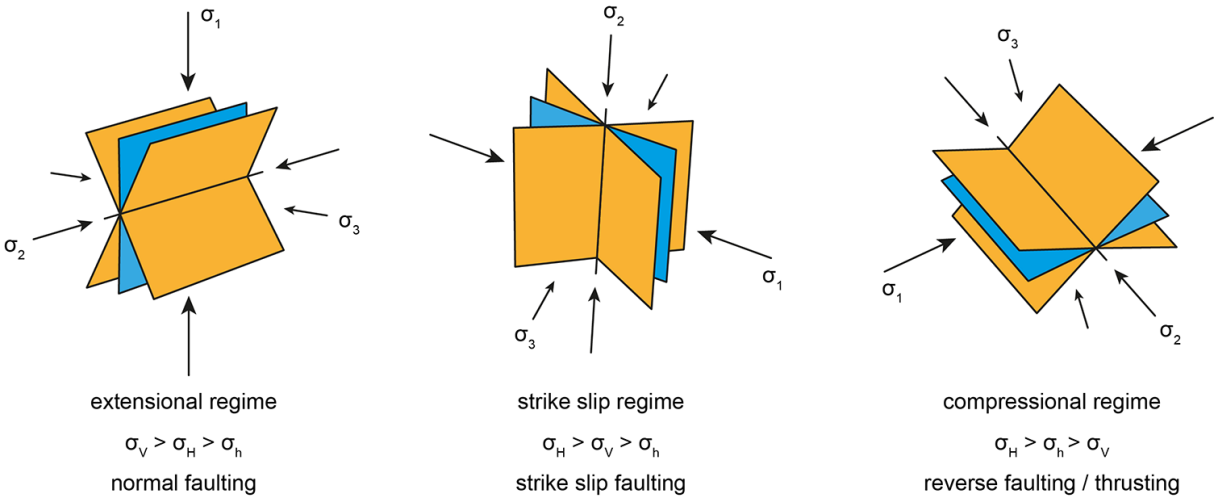

Fig. 4-16. Illustration of the characteristic development of shear (yellow) and tensile fractures (blue) under different tectonic regimes. Tensile fractures tend to form parallel to the first principal stress and normal to the least principal stress. Conjugated shear fractures mounting the characteristic 60° are also oriented at the first principal stress axis. The varying correlation of the vertical stress (S_V), maximum (S_H) and minimum horizontal stress (S_h) being σ_1, σ_2, and σ_3, leads to different fracture patterns in the three tectonic regimes (modified after Ramsay and Huber (1997)).

5 Introduction of Case Study

The elaborated methodological approach of this research project is applied to a large case study gas reservoir in Northern Germany. The field is located in the Rotliegend of the North German Basin in more than 4km depth and covers an area of more than 400km². The reservoir horizon is an about 15-20m thick, aeolian sandstone of the Wustrow member in the Upper Rotliegend II. The reservoir is intensively faulted and comprises more than 80 faults, which are mostly traceable from the overlying basal Zechstein down to the Carboniferous (pers. comm. K. Kronmüller). These faults impact the local stress field significantly and show different hydraulic behavior. The large amount of available data and the intense faulting makes the mature gas reservoir ideally suited as case study for geomechanical modeling of in situ stresses.

In the following, the geological characteristics of the case study reservoir area are discussed. This includes a brief overview on the North German Basin (5.1), information on the Rotliegend of this basin representing the reservoir strata (5.2), and a summary of the tectonic history of the area (5.3).

5.1 North German Basin

The case study reservoir is located in the North German Basin (Fig. 5-1), which covers the northern part of Germany and represents the central part of the Southern Permian Basin (Ziegler, 1990). Both basins belong to the large Central European Basin System ranging from the North Sea to Poland and from Norway to the German midlands (Littke et al., 2005; Littke et al., 2008). Rifting and thermal subsidence of the lithosphere initiated the development of this basin system in the Late Carboniferous and Early Permian (Bachmann and Grosse, 1989; Scheck and Bayer, 1997, 1999; Ziegler, 1990).

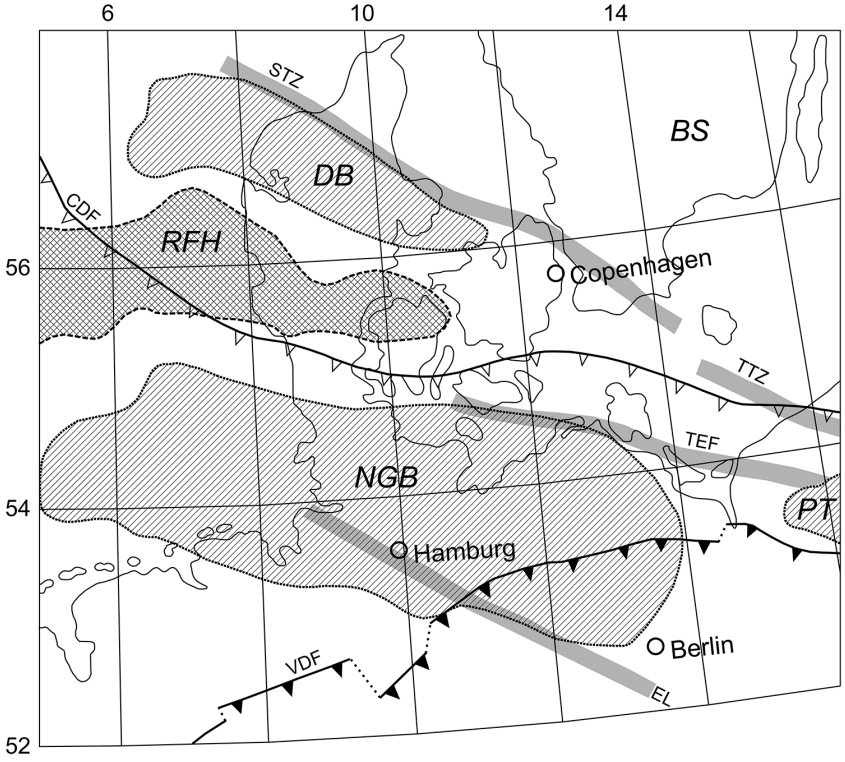

Fig. 5-1. Position of the North German Basin (NGB) in Northern Europe. The Variscan Deformation Front (VDF) and Caledonian Deformation Front (CDF) are marked with lines showing filled and empty triangles, respectively. The Sorgenfrei-Tornquist Zone (STZ), the Teisseyre-Tornquist Zone (TTZ), the Trans-European Fault System (TEF) and the Elbe-Line (EL) are indicated as grey shadings. The Danish Basin (DB), the Polish Trough (PT), the Ringkobing-Fyn High (RFH) and the adjacent Baltic Shield (BS) are pointed out by different patterns (modified after Scheck and Bayer (1999)).

The Northern and Southern Permian Basin were the two main areas of subsidence at those times, separated by the Ringkobing-Fyn chain of structural highs (Glennie, 1990) (Fig. 5-1). The Southern Permian Basin is bound by this chain of highs in the north and the Harz mountains and the Elbe Fault System in the south, comprising the WNW-ESE elongated North German Basin in its center (Ziegler, 1990). The basin developed on crust, which was affected by the Caledonian and Variscan Orogeny (DEKORP-BASIN Research Group, 1999). Nowadays the Caledonian Deformation Front only tangentially contacts the basin in the north, whereas the Variscan Deformation Front crosses the southeastern part of the North German Basin considerably (Fig. 5-1).

Further in the north beyond the Ringkobing-Fyn High, the Danish Basin and the Sorgenfrei-Tornquist Zone are located (Fig. 5-1) (Scheck and Bayer, 1999). The Sorgenfrei-Tornquist Zone and the following Teisseyre-Tornquist Zone define the boundary to the Precambrian terranes of the Baltic Shield and the East European Craton. South of the North German Basin, the Variscan chain is located. The Precambrian terranes can be distinguished from the Paleozoic European basement by their magnetic fields. Precambrian crust shows chaotic, short-wave anomalies, whereas the Paleozoic crust displays long-wave anomalies (Krawczyk et al., 2008). According to Scheibe et al. (2005), all gravity and magnetic anomalies in the North German Basin can be explained by the physical parameters of the basin lithologies and do not necessarily imply a relief change of the crystalline basement. The Mohorovicic discontinuity is mostly traced as flat and continuous boundary throughout the North German Basin (DEKORP-BASIN Research Group, 1999) and consequently also the crustal thickness distribution shows only minor variations in this area (Ziegler and Dezes, 2006).

The stratigraphic record of the basin begins in the late Early Permian (van Wees et al., 2000). Bachmann et al. (2008) describes nine important depositional cycles of sedimentation in the Central European Basin System. These cycles range from a few million years to 75 million years and are bound by major erosional unconformities. Sedimentation of the stated cycles ranges from the Altmark Subgroup in the Early Permian to deposition in the southeastern North Sea in Miocene times (Bachmann et al., 2008). The sedimentary basin fill of the North German Basin from Permian to Quaternary reaches up to 8km in total thickness and comprises a smoothly on-lapping northern margin and a fault-controlled southern margin (Doornenbal and Stevenson, 2010; Krawczyk et al., 2008; Scheck and Bayer, 1999; Schwarzer and Littke, 2007). Beneath this basin sequence, carbonate and clastic sediments from Carboniferous and Devonian times rest on deformed Caledonian basement (Brink et al., 1992; Franke, 1995).

The area of the North German Basin on land is characterized by lowlands with a topographical average of 25m above sea level (Maystrenko et al., 2008). Adjacent areas of the basin in the North Sea and Baltic Sea show a shallow bathymetry as well.

5.2 Rotliegend of the North German Basin

The reservoir horizon of the case study was deposited in the North German Basin area in Rotliegend times approximately 260 million years ago. The sandstones deposited in those times comprise the most important gas reservoirs in northwestern Europe and were the target of more than 10,000 drilled wells (Doornenbal and Stevenson, 2010).

In the Permian, the basin area was located in the northern hemisphere desert belt between 10°-30°N (Glennie, 2007). All Rotliegend sediments were deposited in an arid environment and when the basin was entirely land-locked. The aridity increased during the Permian. Terminal playa and saline lake environments developed in the central and deepest parts of the basin leading also to the deposition of

halite (Gast, 1991). Rotliegend sediments can be subdivided into three parts: Lower Rotliegend sediments and volcanics, and two parts of Upper Rotliegend sedimentary rocks (Schroeder et al., 1995). The Lower Rotliegend units comprise mostly volcanic depositions and build up the Altmark subgroup, while sedimentary rocks of the Upper Rotliegend I are summarized in the Müritz subgroup.

The second part of the Upper Rotliegend sedimentary units comprise a combined thickness of up to 2000m and represent the Havel and Elbe subgroup (Fig. 5-2) (McCann, 1998; Plein, 1995; Stollhofen et al., 2008). Continental siliciclastics and minor evaporites were deposited in arid to semi-arid climates and characterize this Upper Rotliegend II strata (Glennie, 1972, 1983). The economically most important Rotliegend reservoir sandstones of the Southern Permian Basin are found in these units. Their evolution and facies types are therefore investigated in detail (Gast, 1991).

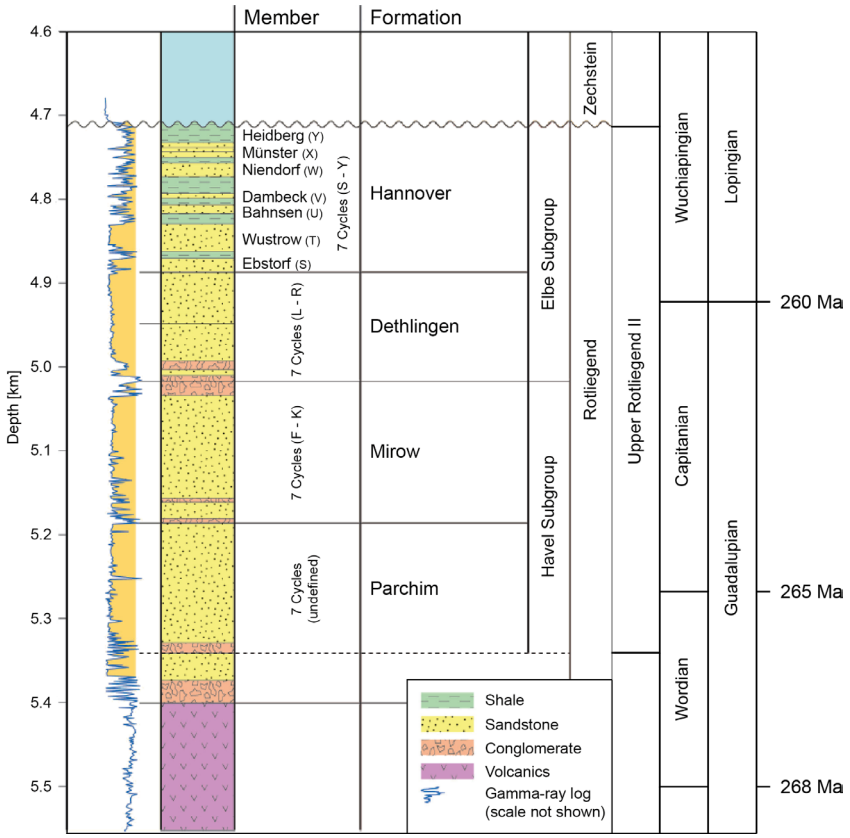

Fig. 5-2. Stratigraphic sequence and gamma ray log of the well Söhlingen Ost Z1 in the Schneverdingen Graben in Germany, which is closely to the east of the case study reservoir. The sequence shows the stratigraphy of the Upper Rotliegend II in context of the global stratigraphy - with the Wustrow member being the second cycle in the Hannover formation of the Elbe subgroup (Gast, 1991; Gast, 2006) (modified after Doornenbal and Stevenson (2010); Menning et al. (2012)).

The Upper Rotliegend II is divided into four fining-upward successions, which are the Parchim, Mirow, Dethlingen and Hannover Formation (Fig. 5-2) (Gast, 1995; Gebhardt et al., 1991; Hoffmann, 1990). Each formation covers a time span of approximately 2 million years (Vackiner, 2013). The Parchim and Mirow formation compose the Havel subgroup and are dominated by aeolian and – to a lesser extent – by fluvial sandstone sequences (Fig. 5-2) (Gast et al., 1998). The overlying Elbe subgroup encompasses the Dethlingen and Hannover formation and comprises a thickness of about 1500m at the center of the North German Basin. The sediments of the Elbe subgroup covered an area of up to 1500km in E-W direction and 400km in N-S (Glennie, 2007). Sandstones of both, the Dethlingen and Hannover Formation, are characterized by cyclic aeolian and fluvial depositions (Fig. 5-2). While these sands are deposited during regressive stages of extensive saline lakes, salts and shales are deposited during highstands (Gast, 1991). Aeolian and fluvial (wadi) sandstones and conglomerates represent the two main reservoir facies (Fig. 5-3) (Glennie and Provan, 1990).

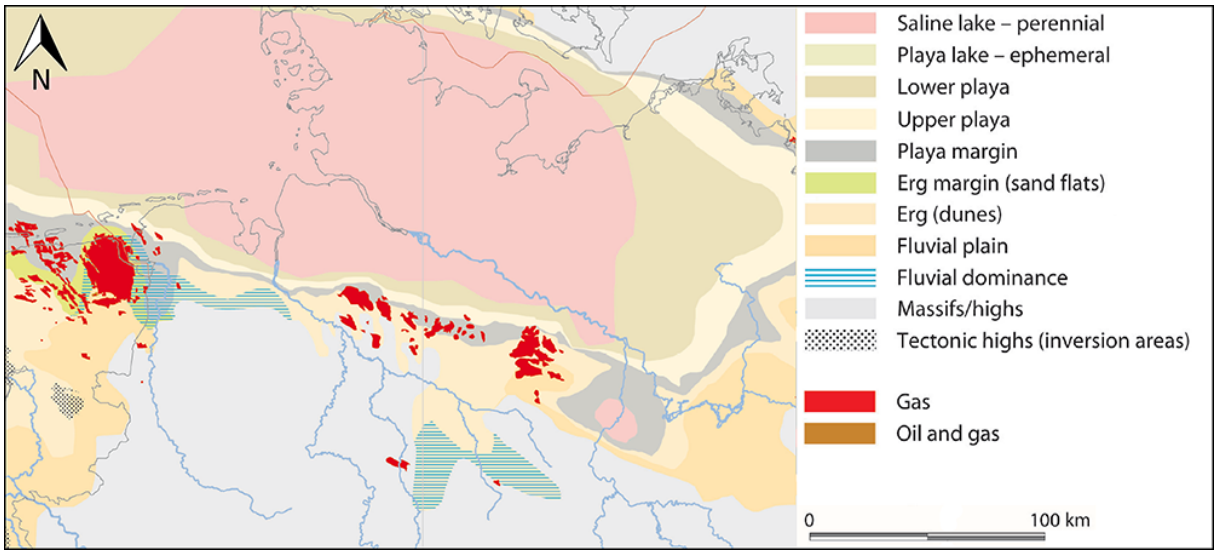

Fig. 5-3. Facies distribution in Northern Germany at deposition times of the Elbe subgroup. Rotliegend gas reservoirs (red) are all located south of the Elbe river along the southern margin of the North German Basin. Particularly the large Groningen gas field in the Netherlands can be identified in the west of this map (modified after Doornenbal and Stevenson (2010)).

Easterly paleowinds are assumed to be responsible for the accumulation of aeolian dunes at the belt of the ephemeral lake (Fig. 5-3) (Gast, 1988, 1991; Rieke et al., 2001). These aeolian sandstones of the Elbe subgroup are the major target of gas exploration in the Rotliegend and provide the most economic gas reservoirs in the Southern Permian Basin area (Doornenbal and Stevenson, 2010; Stollhofen et al., 2008). However, the quality of reservoir sandstones can vary significantly across fields. This can be related to changes in depositional and diagenetic environment. Independent of the level of diagenesis, the aeolian sandstones generally show the best porosities and permeabilities and thus form the best reservoirs (Glennie, 1998; Turner et al., 1993). Porosity and permeability normally increases with better sorting and coarser grain sizes (Gaupp et al., 2005).

In global stratigraphic context, the Hannover Formation of the Elbe subgroup is located in the Wuchiapingian and was deposited between 260-258Ma (Vackiner, 2013). It includes seven deposition cycles forming the respective members: Ebstorf, Wustrow, Bahnsen, Dambeck, Niendorf, Munster, and Heidberg (Fig. 5-2). The Wustrow member of the Hannover formation is the second of the seven cycles and can reach thicknesses of 35-40m (Gast et al., 1999). This member represents the most economic reservoir sandstone in Germany and also the reservoir horizon of the case study (Gast et al., 1998; Plein, 1995; Schroeder et al., 1991; Schwarzer and Littke, 2007). In the United Kingdom and the Netherlands, the equivalent members are referred to as Upper Leman and Upper Slochteren sandstone, respectively. Preserved porosities and permeabilities in the aeolian Rotliegend sandstones can vary between 2 – 20% and from less than 0.1mD to more than 100mD, respectively (Gaupp et al., 2005; Schöner et al., 2008). Even in the same depositional facies, the permeability shows a wide spread for a specific porosity. Porosity and Permeability are both significantly influenced by diagenetic alteration.

The gas of Rotliegend reservoirs in the basin area is assumed to be related predominantly to Westphalian coal of the Upper Carboniferous, but also pre- and post-Westphalian source rocks may have contributed (Gerling et al., 1999; Hoffmann et al., 2001; Vackiner, 2013). Gas reservoirs in the German basin area commonly comprise combined structural and fault traps, while carbonates, anhydrites and salt characterize the Zechstein and represent a regional top seal (Doornenbal and Stevenson, 2010; Kiersnowski et al., 1995). Only few fields are known showing shale layers acting as seals within the Rotliegend units.

Nowadays the Rotliegend sandstones in the North German Basin are located in depths between approximately 3500m to 5500m (Fig. 5-2), which is also valid for the case study reservoir. Gas reservoirs in the Rotliegend have been only found along the southern margin of the North German Basin (Fig. 5-3).

5.3 Tectonic Evolution

The North German Basin and in particular the enclosing Central European Basin System are located on a variety of crustal domains, which represent the result of long-term processes of terrane amalgamation. The North German Basin developed on crust, which was affected by the Caledonian and Variscan Orogeny (DEKORP-BASIN Research Group, 1999).

The Caledonian Orogeny describes the assembling of the Old Red Continent by Baltica, Laurentia and Avalonia in the Late Ordovician and Silurian (Drozdzewski et al., 2009). The Tornquist Zone, as a recent major fault zone, emerged in these times from the closure of the Tornquist Sea between Avalonia and Baltica (Krawczyk et al., 2002). The Variscan Orogeny took place in the Devonian and Carboniferous and describes the collision of Laurussia and Gondwana forming the Variscan orogen (Ziegler, 1990). This orogeny culminated during the Early to Middle Carboniferous and resulted in the formation of the super-continent Pangea. North of the Variscan Deformation Front, the Variscan foreland basin was formed by extensional crustal processes (Drozdzewski et al., 2009).

The North German Basin is superimposed on this Variscan Foreland Basin (Bachmann and Grosse, 1989; Brink, 2005a; Brink et al., 1990; Ziegler, 1990). This fact is important for two reasons. First, the post-Variscan structural evolution of the North German Basin may have been significantly affected by the complex crustal accretion history. Stress and strain are most often linked to major structural and compositional discontinuities in the crust. Faulting in Permian and younger lithologies is thus likely to have been governed by pre-Permian crustal weaknesses.

Second, the Variscan Foreland Basin developed along the NE-SW striking front of the Variscides (Maystrenko et al., 2008). However, the North German Basin is NW-SE oriented. This implies an essential change in the stress regime. Although the main Variscan shortening direction was NW-SE and the related compressional structures within the fold belt thus strike NE-SW, most of the structural elements in the Variscan foreland, such as wrench faults, strike WNW-ESE (Drozdzewski et al., 2009). This fact has to be considered in the dynamic modeling approach (8), when it comes to the age of faults and the potential geomechanical exposure they could have experienced.

The structural basin evolution of the North German Basin can be divided in four major tectonic stages, which correspond to the changing dynamic and kinematic regimes (Kley et al., 2008) (Fig. 5-4). Except for Cenozoic developments, the varying strain patterns of these stages are well constrained.

In Late Carboniferous / Early Permian times, the North German Basin was formed simultaneously to the Danish Basin and the Polish Trough. This first stage was coined by extensive and widespread volcanism occurring contemporaneous all over Europe (Scheck and Bayer, 1999). Brink (2005b) referred the magmatic activity to a heat anomaly in the Earth's mantle, which is nowadays represented by the Tibesti – Hotspot in Northern Africa. During this magmatic stage, approximately 48'000 km³ volcanic material accumulated in the NE German Basin (McCann, 1998).

The thermal destabilization of the crust resulting from the intense magmatism is suggested to be the controlling factor for initiation of basin evolution (Scheck-Wenderoth and Lamarche, 2005). Subsequent thermal relaxation further explains a significant amount of subsidence during Permian and

Triassic times (van Wees et al., 2000). In this first tectonic stage, the basin area was part of an E-W trending belt of dextral motion between the Ural and Appalachian thrust belts (Arthaud and Matte, 1977). Normal and transtensional faults developed in this stage during and following the magmatic activity (Kley et al., 2008) (Fig. 5-4-A).

The second tectonic stage describes extension in the Early Triassic to Middle Jurassic, which corresponds to the beginning break-up of Pangea (Fig. 5-4-B). Pronounced E-W directed extension along N-S trending normal faults resulted in the formation of the North Sea Central Graben, Horn Graben and Glückstadt Graben (Brink et al., 1992; Kley et al., 2008; Yegorova et al., 2008). After the beginning of normal faulting during the Buntsandstein, the extensional regime culminated in Keuper times. Further, in this time the Zechstein salt began to evolve its characteristic structures. Ongoing subsidence of the first and second tectonic stage is well documented in burial history diagrams of specific wells in the case study reservoir (Fig. 5-5). These diagrams are elaborated in a confidential basin modeling study carried out by the project partners.

The third stage covers rifting processes from Late Jurassic to early Late Cretaceous, which correspond to the break-up of Pangea. During this stage, the Lower Saxony Basin was formed with a 7km vertical offset at its southern border. The NW-SE striking of this basin contrasts the dominant N-S trend of the Triassic graben structures and suggests an anti-clockwise rotation of the extensional direction (Fig. 5-4-C). Following the Triassic E-W extension, also regional uplift occurs in this third stage creating the Pompeckj Block south of the Ringkobing-Fyn highs (Kley et al., 2008). These generally vertical displacements are most pronounced in the northern part of the Northwest German Basin (Baldschuhn et al., 1991) and caused the removal of Jurassic and Triassic sediments (Fig. 5-5) (Schwarzer and Littke, 2007).

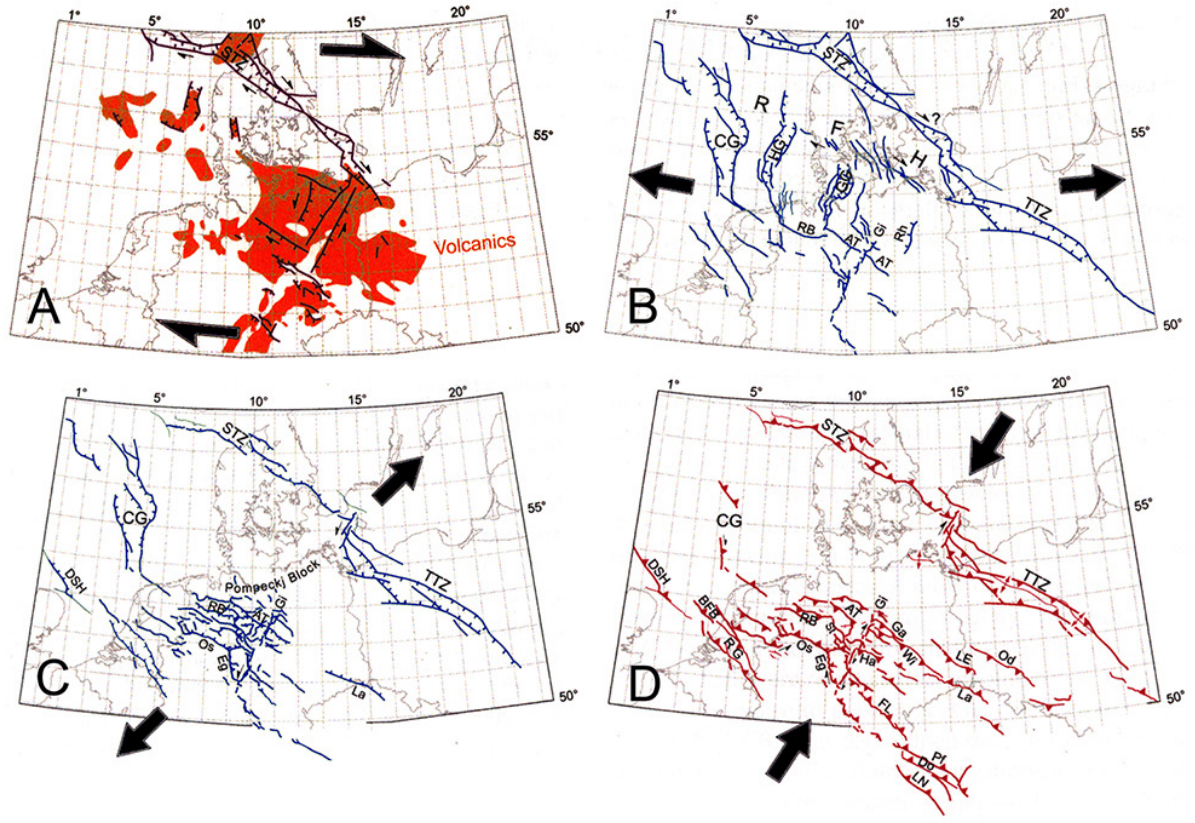

Fig. 5-4. Overview on the four major tectonic stages of structural basin evolution according to Kley et al. (2008). A) E-W directed transtension in Late Carboniferous to Permian time. B) E-W directed extension from Early Triassic to Middle Jurassic. C) NE-SW directed extension from Late Jurassic to early Late Cretaceous. D) NE-SW directed contraction and inversion in Latest Cretaceous to Late Oligocene (modified after Kley et al. (2008)).

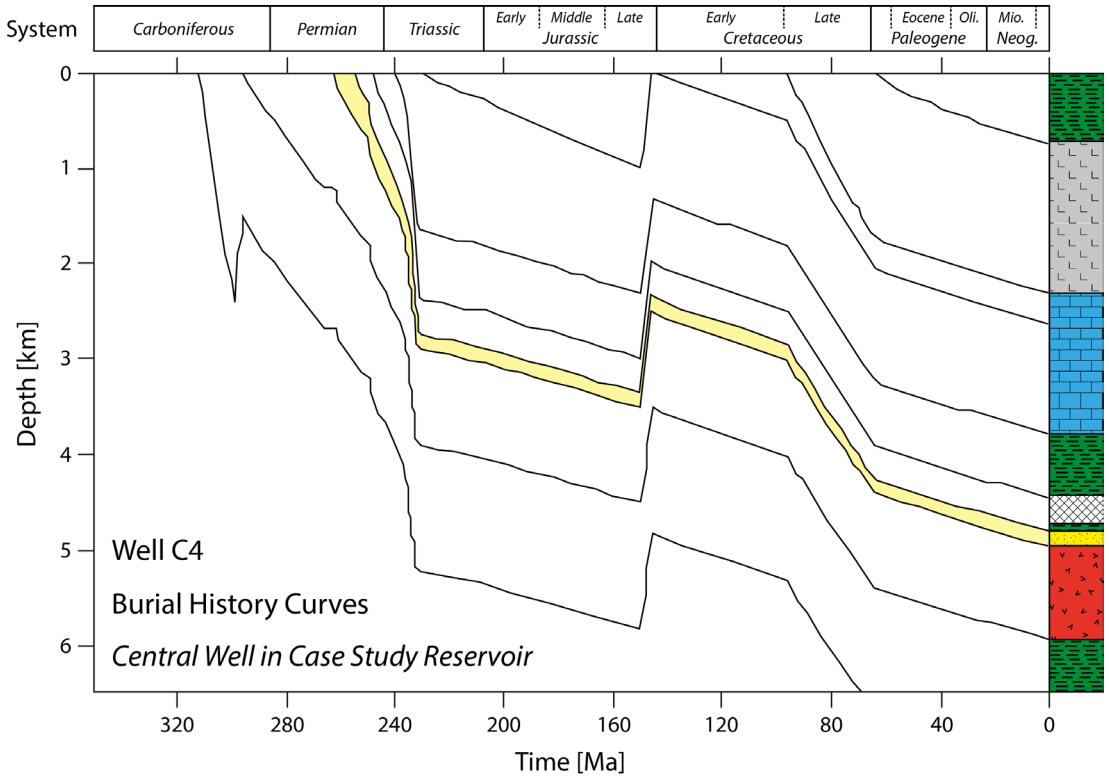

Fig. 5-5. Burial history curves of well C4 in the center of the case study reservoir indicating the depth of Rotliegend sandstones (yellow) since the Permian. Burial history diagrams of multiple wells in the reservoir area were elaborated in a confidential basin modeling study of the field operators. The recent stratigraphy and related thicknesses (right) varies between the individual wells. However, the general trend of burial and uplift is the same throughout the reservoir.

The regionally occurring uplift during this extensional, third tectonic stage is important, because it directly affected the reservoir area. This is confirmed by the burial history of a central well in the case study reservoir showing uplift in late Jurassic times (Fig. 5-5).

The fourth stage of basin evolution covers the time span between Late Cretaceous and Late Oligocene. After the closure of the Tethyan Ocean, the continent collision of Eurasia and Africa-Arabia results in the Alpine Orogeny (Ziegler, 1990). At the beginning of this fourth tectonic stage, the general direction of contraction was NNE-SSW (Fig. 5-4-D), but strong local deviations are observed (Kley et al., 2008). The whole of Europe was affected by the collision-induced compressional stresses, which resulted in the inversion of several basins along reactivated normal faults generated in the previous extensional stages. Especially zones of strong crustal heterogeneity caused strain localization, as for instance the Elbe Fault System. The reservoir area experienced a decelerating in subsidence, but no uplift in this compressive phase (Fig. 5-5).

In addition, the Late Cretaceous inversion caused further mobilization of the Zechstein salt. This led to a decoupling of pre-Zechstein lithologies from Mesozoic successions, which played an important role in the development of the recent stress field (Bayer et al., 1999; Röckel and Lempp, 2003). Latest inversion phases were contemporaneous with NW-SE to E-W direction extension creating the Upper Rhine and Eger rifts (Dèzes et al., 2004).

The following Neogene times are characterized by complex kinematics (Kley et al., 2008). In general, the situation in the Cenozoic cannot be explained by one single consistent, far-field plate tectonic regime. However, the recent stress field in the North German Basin implies further rotations in the times of Late Eocene to Middle Miocene.

The present-day state of stress in the North German Basin is documented by data from various sources that is compiled by Röckel and Lempp (2003). This data compilation shows that the orientation of the maximum horizontal stress in the subsalinar exhibits a fan-like pattern across the North German Basin. Moving from east to west, the maximum horizontal stress changes its orientation from NNE-SSW to NW-SE. According to the data from Grote (1998), which is included in this data compilation, the maximum horizontal stress is NNW-SSE directed in the case study reservoir area (Fig. 5-6).

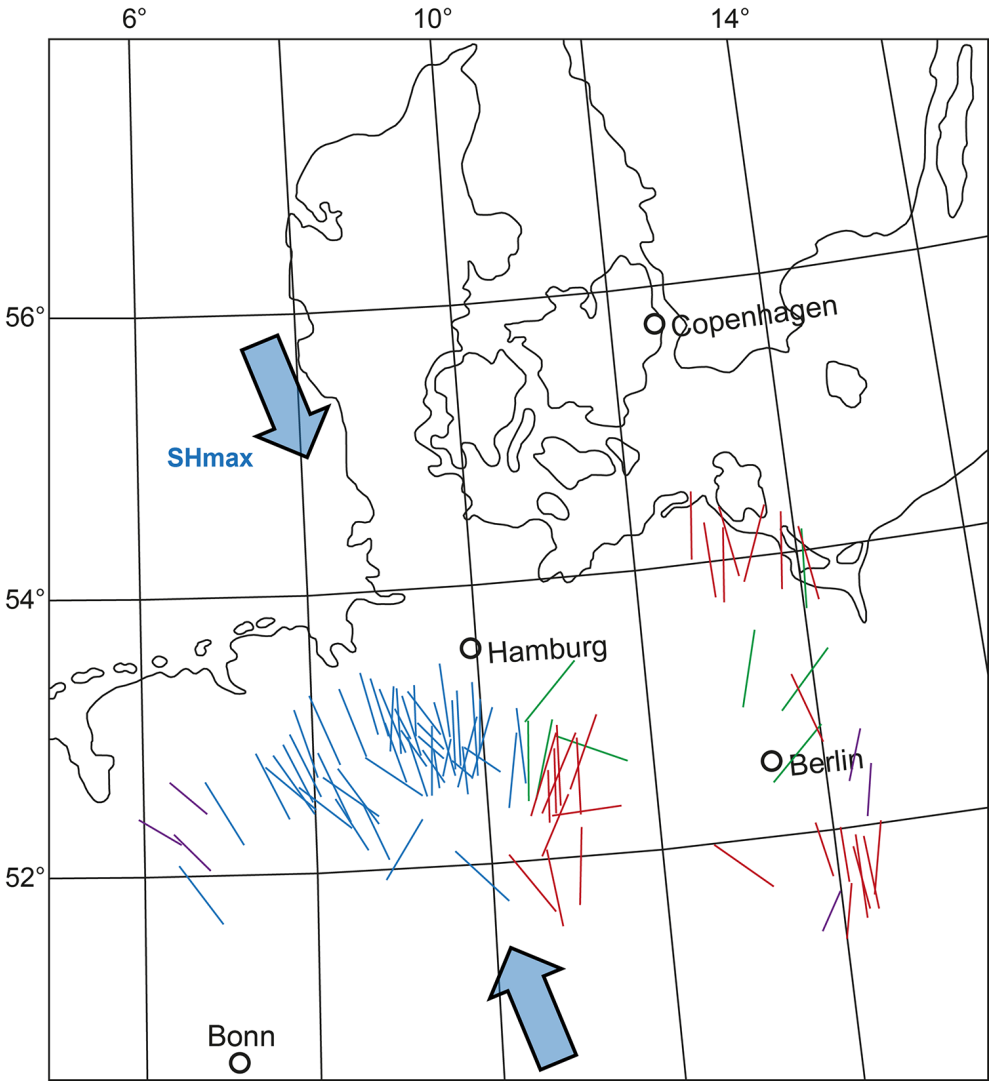

Fig. 5-6. Overview on the orientation of the maximum horizontal stress in the North German Basin. The shown data is colored to indicate the different sources. The majority of data is taken from Grote (1998) (blue) and Röckel and Lempp (2003) (red), while additional data is published by Roth et al. (1998) and Roth and Fleckenstein (2001) (green), and within the World Stress Map Project (purple). The large blue arrows indicate the assumed regional stress orientation in the case study reservoir area of NNW-SSE.

This introduction of the case study intends to provide only a geological overview and does not claim to cover all aspects of the North German Basin in detail, since this would go beyond the scope of this work. Please refer to the cited papers and references therein for further information on specific topics.

6 Preliminary Studies

The first working steps in the research project are represented by preliminary studies preceding the buildup of the field-scale model of the case study reservoir. Parameter studies provide first insights in parameter sensitivity, the type of prevailing deformation and the distribution and characteristics of stress perturbations in the reservoir area (6.1). Following the parameter studies, a basic geomechanical reservoir model is built incorporating the major faults and one mechanical layer only (6.2). This base model shows first in situ stress distributions and perturbations at the reservoir-specific fault geometries.

6.1 Parameter Studies

The parameter studies were carried out within a separate master thesis in a first stage of the research project prior to building and calibrating the geomechanical field-scale model of the case study (Fischer, 2010). These generic parameter studies are based on typical fault block geometry of the reservoir area. The mechanical properties of Rotliegend sandstones are assigned to the fault block and the recent remote stress in the North German Basin is implemented as boundary condition in the default scenario. Subsequent systematic parameter variation yields first insights into the characteristics of in situ stress distribution and perturbations. All studies are performed with the commercial FE code Ansys®, which is also used for the static and dynamic field-scale model (7, 8).

In the following, the objectives stated for these preliminary studies (6.1.1), the modeling approach (6.1.2), and the most important results are summarized (6.1.3). For further details and results, please refer to the corresponding master thesis focused on these studies (Fischer, 2010).

6.1.1 Objectives

The main objective of these generic parameter studies is to attain crucial background information in beforehand of building and calibrating the field-scale geomechanical model. Systematic variation of input parameters shall provide insights into the individual parameter sensitivity. This information is valuable in the calibration process of the reservoir model. Furthermore, the most controlling factors for the in situ stress perturbations are to be identified. The application of simple geometries facilitates the observation of general trends and correlations. These findings help to interpret results of more complex models significantly.

Another objective is to attain information about the overall potential for recent stress perturbations in the reservoir. This contributes to the definition of realistic expectations for the outcome of the static reservoir model (7). The parameter studies can also help to develop ideas of those factors, which could have been the most controlling ones in the past. This becomes relevant in the dynamic modeling approach of the research project (8).

6.1.2 Modeling Approach

The fault block geometry applied in these parameter studies is deduced from provided fault maps of the case study reservoir and from published illumination of Base-Zechstein reflectors (Doornenbal and Stevenson, 2010). Both sources show E-W and approximately NNW-SSE trending faults building up rhombus-like fault block shapes in different spatial dimensions. This shape is taken as characteristic

fault block geometry in the 2D models of the parameter studies. The edge length of the idealized rhombus-like block is initially set to 1000m and the block is uniformly enclosed by a rectangular load frame (Fig. 6-1-A). This frame surrounds the fault block with considerable distance. Boundary conditions are applied to the outer edges of the frame and different material properties can be assigned to fault block and load frame area.

In addition to this geometrical default setup, two series of the parameter studies consider geometrical changes. One series considers size scaling of the central block, whereas another series addresses the incorporation of an extended fault system by implementing eight additional identical blocks surrounding the central one.

The application of idealized geometry data copes with the objectives of the parameter studies. Exact reproduction of the reservoir geometry will be considered in the base model (6.2) and static reservoir model (4.1). This approach also facilitates the discretization of the geometry. The model is meshed with 2D quadrilateral planar elements, which are decreased in size along and inside the fault block to an element edge length of 10m (Fig. 6-1-B). The faults defining the fault block are meshed with contact elements simulating Coulomb friction (2.1.2, 4.4.2).

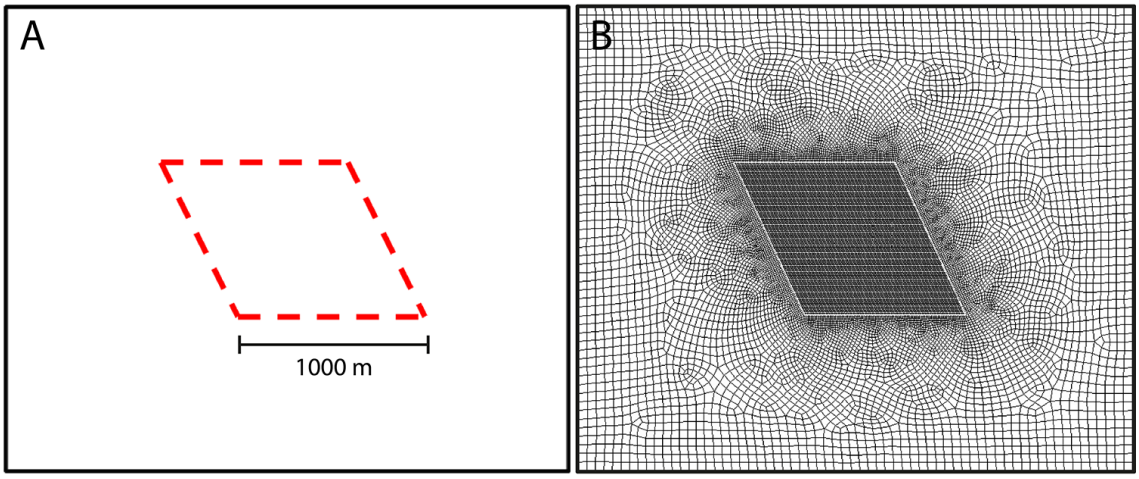

Fig. 6-1. A) Sketch of the rectangular load frame of 2700m x 3200m (black) enclosing the central fault block (red). B) The mesh of the model comprises element edge lengths of 50m at the outer load frame areas and 10m along and inside the fault block. This results in a total of about 20,000 elements per model.

Following the discretization of the model, material properties are assigned to the surface and contact elements defining the mechanical behavior. The description and simulation of elastic deformation requires the definition of elastic moduli (3.2.1). In this study, averaged values of Young's modulus (E) and Poisson's ratio (ν) for Rotliegend sandstone are taken from Trautwein (2005) (Tab. 6-1). In order to determine the onset of plastic deformation, the coefficient of internal friction (μ_i) and cohesion (C) must be specified. These values are taken from Moeck and Backers (2006) (Tab. 6-1). Plastic deformation is considered in a separate series of the studies only and is not part of the default model.

The usage of published values in these preliminary parameter studies is based on the fact that reservoir-specific material parameters were not yet available at this point in time. However, these studies focus on the relative contribution of various parameters and not on absolute values. The subordinate difference in values does thus not affect the outcome. Reservoir-specific values are finally used in the setup of the field-scale geomechanical model (7.2.1). The faults behavior is modeled by Coulomb friction. A default value of 0.4 is initially assumed for the friction coefficient and subsequently in- and decreased in a separate variation series.

Young's modulus*	36.43 GPa
Poisson's ratio*	0.23
Coefficient of internal friction**	0.5
Cohesion**	22.5 MPa
Fault friction coefficient	0.4

Tab. 6-1. Overview on the mechanical parameters considered in the parameter studies. Due to the lack of reservoir-specific data at that time, values published by Trautwein (2005)* and Moeck and Backers (2006)** are used. Plastic deformation, and thus the coefficient of internal friction and the cohesion, are not part of the default model. The friction coefficient of the faults is initially assumed and subsequently varied in both directions.

Following the identification of typical fault block geometry, the model build-up, discretization and the assignment of material parameters, the boundary conditions are specified. The recent regional stress field in the reservoir area is considered in the default scenario of the parameter studies. This requires the magnitude of the vertical, maximum and minimum horizontal stress, as well as the orientation of the horizontal stresses.

The current state of stress in the North German Basin is documented by data from various sources and is compiled by Röckel and Lempp (2003). This data compilation shows that the orientation of the maximum horizontal stress in the subsalinar exhibits a fan-like pattern across the North German Basin. Moving from east to west, the maximum horizontal stress changes its orientation from NNE-SSW to NW-SE. According to the data from Grote (1998), which is included in this data compilation, the maximum horizontal stress is NNW-SSE directed in the case study reservoir area (Tab. 6-2). This direction is taken as the default orientation of the maximum horizontal stress in the parameter studies, but is varied in a separate variation series to consider paleo-stress orientations.

Regarding the stress magnitudes, Röckel and Lempp (2003) determined a gradient for the vertical stress of about 24.3MPa/km in the North German Basin (Fig. 7-4). Assuming an average depth of the reservoir horizon of about 4700m, this yields an overburden pressure of 114.24MPa (Tab. 6-2). Due to the lack of data, such a gradient is not available for the maximum horizontal stress. However, there are no indications that the maximum horizontal stress component in the subsalinar layer exceeds the vertical stress (S_V). Only very local changes to strike-slip regime are reported (Bücker and Strobel, 2003) Therefore the tectonic regime in the subsalinar of the North German Basin is characterized as a normal faulting regime and a value of $0.9 \cdot S_V = 102.8$MPa is considered as an approximate recent magnitude of the maximum horizontal stress on reservoir level (Tab. 6-2). This assumption agrees with the results and propositions of Moeck et al. (2009). The gradient for the minimum horizontal stress was shown to be 14.6MPa/km (Röckel and Lempp, 2003). This results in a minimum horizontal stress magnitude of 69.53MPa.

Vertical stress magnitude*	114.24 MPa
Maximum horizontal stress magnitude*	102.81 MPa
Minimum horizontal stress magnitude*	68.54 MPa
Maximum horizontal stress orientation	NNW-SSE

*Magnitudes refer to a reservoir depth of 4700m.

Tab. 6-2. Summary of the assumed recent state of stress at the reservoir location in the North German Basin and on reservoir depth. These values are applied as boundary conditions in the parameter studies. Stress gradients and orientation are taken from Röckel and Lempp (2003).

At hydrostatic pore pressures, the theoretical minimum in a normal faulting regime is assumed to be $0.6 \cdot S_V$ (Zoback, 2007). Lower least principal stress magnitudes would lead to fracturing and faulting. Due to the proximity of the gradient to this limit, it is likely that this in fact controls the minimum horizontal stress magnitude in the reservoir area and thus the minimum horizontal stress magnitude is set to $0.6 \cdot S_V = 68.54$MPa in the parameter studies (Tab. 6-2).

Most models of the parameter studies are two dimensional. This is justifiable with respect to the reservoir horizon, because its lateral size significantly exceeds its thickness. Hence, the shape of the horizon is essentially that of a plate. The appropriate state of plane stress assumes that normal stress and shear stresses directed perpendicularly to a chosen plane are zero (Ramsay and Lisle, 2000). This inherently results in a simplification of the stress tensor and only two principal stresses are left with σ_1 representing the maximum horizontal stress and σ_2 the minimum horizontal stress. The overburden load of 114.24 MPa (S_V) is only incorporated in the series of 3D models of the parameter studies.

The described remote recent stress field represents the boundary condition of the default model in the parameter studies. All stress fields are applied by inward-directed displacements of the nodes along the load frame's outer edges (4.5.1). These displacements generate a distinct and completely homogeneous stress field inside the load frame. The stress magnitudes depend directly on the specific amount of displacement. The required displacements of the desired state of stress have to be determined in beforehand in an iterative process using an empty version of the load frame (4.5.1). In the series of the parameter studies considering different (paleo-) stress magnitudes, this load frame calibration has to be done individually for all magnitude configurations. This is also the case when the size of the load frame is changed. However, different orientations of the horizontal stresses can be obtained by rotation of the load frame and re-applied mesh generation.

The type of modeling results of the parameter studies are the basically the same as for a field-scale geomechanical models – except for the lack of the third dimension (in most cases) (4.7.1). Based on the information of the stress tensor throughout the model, the magnitudes and orientation of the principal stresses can be visualized in contour and vector plots. Stresses are also used to calculate further stress quantities (4.7.2). The fault-specific shear and normal stresses revealed by the contact elements yield slip and dilation tendencies indicating the faults movement behavior.

The default model considers all input parameters that represent the recent state of the reservoir as outlined above (Tab. 6-1, Tab. 6-2). Besides this default scenario, five basic modeling series are performed (Fig. 6-2) and three more exceptional series. Each series varies only one parameter, while the others are set to the values of the default model. Combining all parameter variations with each other would have multiplied the effort and complexity, and would have been unfeasible to interpret.

The first variation series deals with the effect of different maximum horizontal stress magnitudes (Fig. 6-2). Due to the lack of a specific maximum horizontal stress gradient for the case study reservoir, the value of $0.9 \cdot S_V$ is assumed for the recent state. The variation of maximum horizontal stress magnitude elucidates the quality of this basic assumption and shall simulate possible paleo-stress fields in combination with the varying orientations of the maximum horizontal stress in the second variation series (Fig. 6-2). By varying the friction coefficient in the third series, the sensitivity and impact of this commonly unknown parameter is examined (Fig. 6-2). The second and third variation series consider additionally a maximum horizontal stress magnitude of $0.65 \cdot S_V$ besides the default magnitude of 0.9. In the fourth series, the load frame lithology is changed to simulate probable juxtaposing of Rotliegend sandstone to shale (Fig. 6-2). However, the shale values used are rough estimates and need to be replaced by reservoir-specific data on the long term.

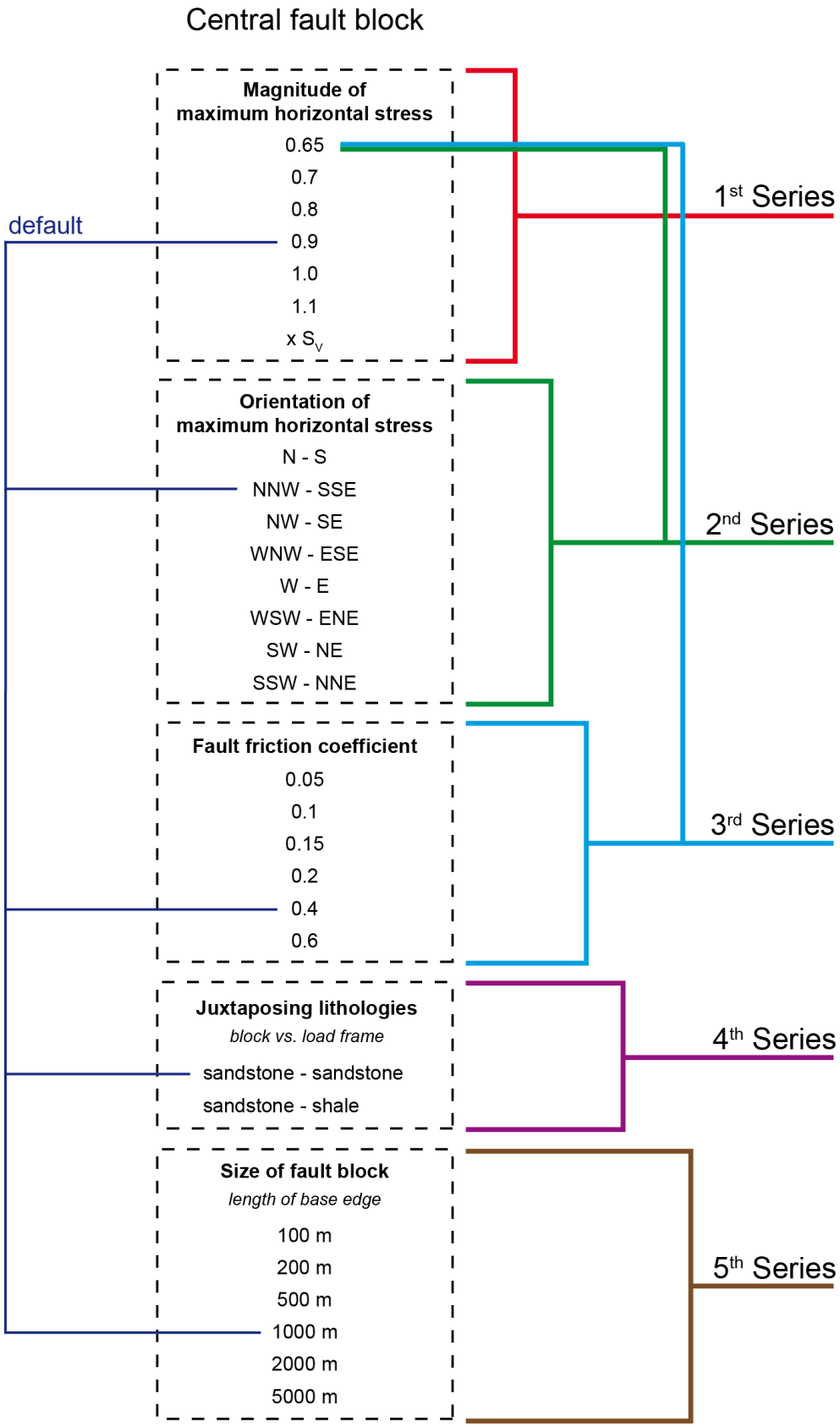

Fig. 6-2. Overview on the five basic variation series. Beside the varied parameter of a variation series, all other parameters stay on the default values (left). The only exceptions are the second and third variation series. These series are additionally calculated with a SHmax magnitude of $0.65 \cdot S_V$.

The fifth series considers several fault block sizes defined by the block's edge lengths (Fig. 6-2). This shall reveal the dependency of stress perturbations on the size of the model.

The sixth series concerns the simulation of a more realistic extended fault system. This is done by encompassing the central fault block by eight copies. All additional contacts are modeled as faults building up a fault system. The seventh series considers the examination of the onset and development of plastic deformation in the model. This series shall indicate the state of deformation (elastic/plastic) for the default model and for the other variation series. A 3D model is set up representing the final series. The 3D model is built to gain insight in the truly three dimensional state of stress and deformation. In this way, the 2D approach assuming plane stress is evaluated.

6.1.3 Results of Parameter Studies

The results of the parameter studies, including those of the default model, are visualized by contour and vector representations. Contour plots show a characteristic distribution of lower first principal stress magnitudes crossing the fault block in this stress' direction, whereas the magnitudes in the rest of the load frame are slightly elevated. This is attributed to the pure presence of the fault block and its surrounding faults. This phenomenon is not observed in contour representations of the second principal stress, i.e. the minimum horizontal stress, mean or differential stress.

Stress plots of the default model further reveal limited perturbations in stress magnitude at the corners of the fault block. These perturbations comprise characteristic shapes for individual stress quantities, such as the magnitude of the maximum and minimum horizontal stress, the mean stress and differential stress (Fig. 6-3). The focusing of load at the corners is proposed to be responsible for the development of these stress minima and maxima, while their specific orientation depends on the direction of stress relative to the faults.

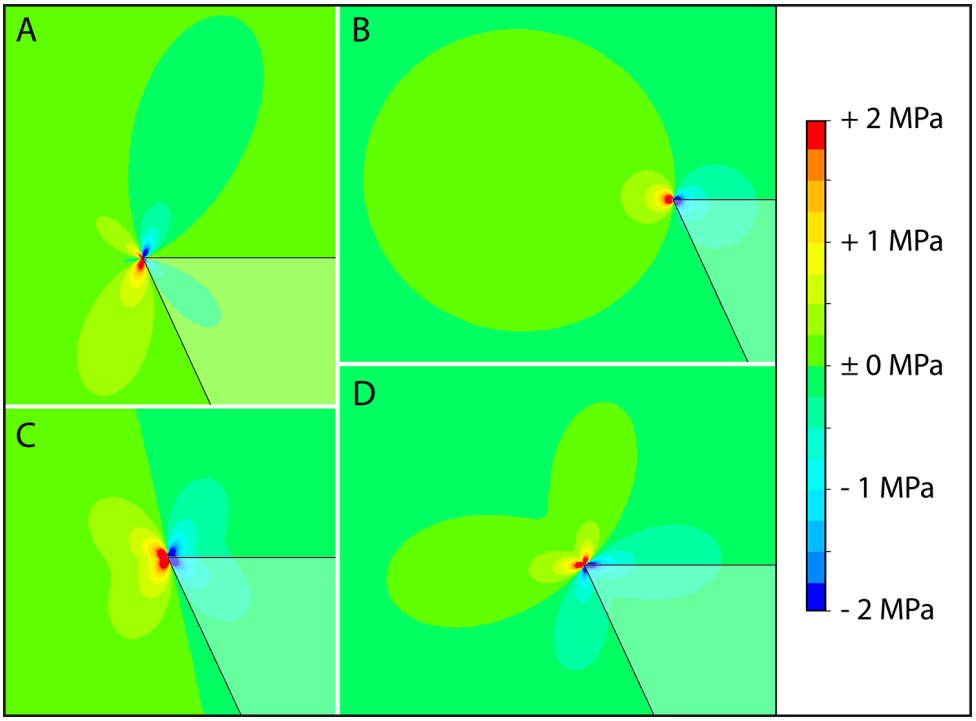

Fig. 6-3. Overview on the characteristic perturbations of stress magnitude at the NW-corner of the fault block in the default model showing (A) differential stress, (B) mean stress, (C) maximum horizontal stress, and (D) minimum horizontal stress. The first principal stress, i.e. the maximum horizontal stress, is oriented NNW-SSE. The scale indicates the deviation from the regional background stress level.

The distribution of all calculated stress quantities comprise magnitude perturbations, which deviate 2-3 MPa from the background at most and spatially extend no more than about 50-60 m from the corners of the fault block. In addition, area-wide magnitude perturbations of in situ stress deviate always less than 0.5 MPa from the background. Vector plots of the default model show no perturbation of stress orientation around the fault block. This infers that the occurrence of magnitude perturbation is not necessarily linked to perturbations in orientation.

The lack of orientation perturbation can be attributed to the particular combination of input parameters in the default model. In combination with the limited perturbations of stress magnitude, this leads to the assumption that the overall potential for stress perturbations is low and the recent state represents a more or less stable state. This hypothesis is corroborated by the distribution of equivalent elastic strain and Maximum Coulomb Shear Stress (MCSS), which both lack clear local concentrations.

Fault-specific shear and normal stresses are used to calculate slip and dilation tendencies describing the faults movement behavior in the default model. While the E-W trending faults comprise slip tendencies of about 0.3, the NW-SE oriented fault pair shows virtually no tendency to slip. This difference is based on the almost parallel orientation of this western and eastern fault to the maximum horizontal stress, whereas the E-W trending faults are inclined in an acute angle. However, this geometrical relation leads in turn to a high dilation tendency of the NW-SE directed faults, being significantly higher than those of the E-W trending pair. The fault behavior overall supports the hypothesis of a stable recent stress state.

The results of the variation series provide insights into parameter sensitivity and general dependencies. Increasing and decreasing the magnitude of the maximum horizontal stress does not significantly change the overall stress distribution, and occurrence and size of perturbations. The changes in stress distribution are relatively small compared to the large variation range of the maximum horizontal stress (>50 MPa). Higher magnitudes lead to a proportional increase in slip tendency at all faults, which is more pronounced at the E-W trending faults showing higher slip tendencies in general. However, even at maximum horizontal stress magnitudes exceeding the vertical stress, the highest slip tendencies do not reach a value of 0.5 and therefore movement is unlikely. The consequences of a potentially inaccurate assumption of the maximum horizontal stress magnitude being $0.9 \cdot S_V$ are thus considered to be low.

The rotation of the stress field around 360° in steps of 22.5° simulates the impact of paleo-stress fields. First, the respective results reveal that the characteristic distribution of low magnitudes crossing the fault block in direction of the maximum horizontal stress is not only adjusting its orientation, but is also significantly influenced in shape at distinct configurations. Second, the specific orientation of maximum horizontal stress with respect to the direction of faults directly controls the shape, size and overall occurrence of stress perturbations at the fault blocks corners. These results demonstrate the important role of stress orientation on the development of in situ stress distribution and perturbations.

The friction coefficient of the faults is a poorly constrained parameter, which can be considered 0.4 as default values. The variation of this parameter in a dedicated modeling series reveals its fundamental impact on the in situ stress distribution. Higher friction coefficients increasingly restrict perturbations. Lowering fault friction results in minor changes until a distinct tipping point is reached, from which on the stress perturbations become significantly intensified and affect large areas (Fig. 6-4). This intensification corresponds to partial and increasing slip along the faults indicated also by maximum slip tendencies. Fault slip also results in a change in shape and orientation of stress perturbations. Lower magnitudes of the maximum horizontal stress hamper the intensification.

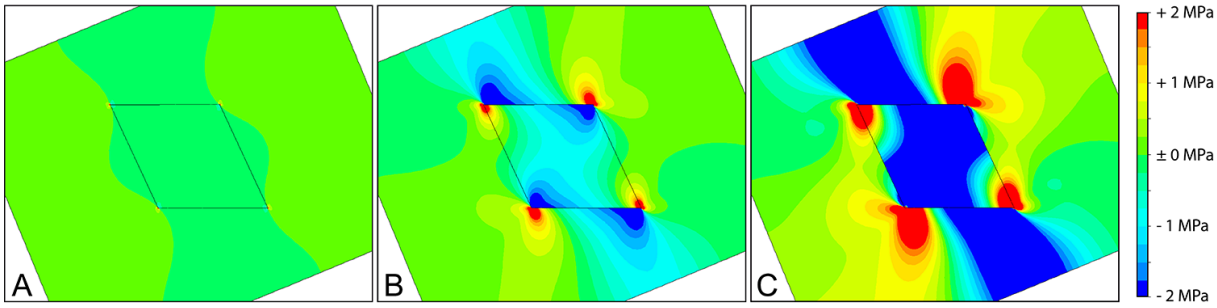

Fig. 6-4. Distribution of equivalent stress (von Mises stress) changing with decreasing coefficients of fault friction from 0.4 (A), to 0.1 (B) and 0.05 (C). The scale indicates the deviation from the regional background stress level. The maximum horizontal stress is oriented NNW-SSE.

Fault friction is thus a very crucial parameter for the distribution of in situ stress and its perturbations. It is shown that this coefficient predominantly determines the onset of movement along the faults, which in turn controls the perturbation intensity. The occurrence of fault movement is found to be also dependent on the remote stress magnitudes.

The fourth series assessed the impact of mechanical parameters on the in situ stresses by assuming a juxtaposition of different lithologies. While the Poisson's ratios of the assumed sandstone and shale are similar (0.23 vs. 0.25), the Young's modulus is distinctly lower for the shale (36.43GPa vs. 12GPa). This results in considerably lower mean stress magnitudes in shale load frame than in the sandstone fault block. The lower Young's modulus of the shale prevents the high stresses established in the sandstone part.

Besides the different distribution of stress magnitudes, these models show significant orientation perturbations (Fig. 6-5). Vectors of maximum horizontal stress in the load frame close to the faults are re-directed perpendicular to the faults. This can be seen best at the NNW-SSE trending faults, where re-orientations of up to 90° from the remote stress direction occur. These orientation perturbations can be attributed to the lower stiffness and stronger deformed shale in contrast to the sandstone. A closer look reveals additionally a small counterclockwise rotation of the vectors inside the fault block (Fig. 6-5). This rotation results most probably from the fact that the shale is not able to consistently transmit the remote stresses to the sandstone fault block.

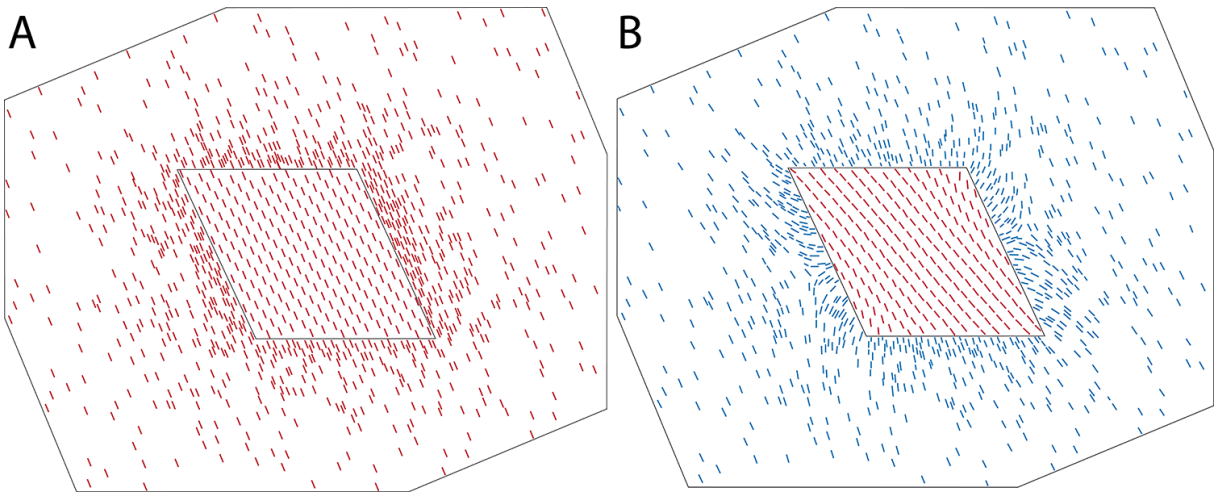

Fig. 6-5. Stress trajectories of the maximum horizontal stress in the load frame and fault block. In the default model, frame and fault block both represent sandstone (red) showing no stress re-orientations (A). The change of load frame lithology to shale (blue) results in significant perturbations in stress orientation (B).

The implemented mechanical difference resulted in major changes of the overall in-situ stress distribution and the occurring perturbations in magnitude and orientation. This series demonstrates the fundamental influence of the mechanical parameters and underlines the importance of reservoir-specific values for any geomechanical modeling.

Changing the absolute size of the fault block in the fifth series shows a proportional relationship between block size and the size of the stress perturbation at the corners. The overall shape and distribution of occurring perturbations remains constant in this series. Therefore the absolute size of structural elements is considered not to be a controlling element on in situ stress perturbations. However, relative sizing between different fault blocks is not investigated in this series, but the sixth series evaluates the impact of an extended fault system. The latter reveals that stress perturbations become smaller and less intense, the more inward their sources are located in a dense fault system. This appears to be a gradual effect. In addition, fault systems seem to lower the area-wide stress magnitudes.

A special series considered the onset of plastic deformation in the model. It is shown that the maximum horizontal stress has to exceed the vertical stress considerably ($>1.2 \cdot S_V$) in order to produce plastic deformation. Hence, it can generally be stated that the parameter studies are located in the field of elastic deformation. Although the mechanical parameters of cohesion and internal friction are not reservoir-specific, this underlines the assumption of an overall stable recent state of stress in the reservoir.

Following some scenarios with extreme parameter combinations, the final series addresses 3D representations of the default model with vertical and partially inclined fault surfaces. The results reveal significantly stronger magnitudes for the perturbations in the 3D models compared to the 2D model (Fig. 6-6). However, the overall distribution and characteristic shapes of stress perturbations remain. Fault orientation show only minor impact on the distribution of in situ stress, but leads to significant differences in the movement behavior of the faults. Especially the faults that are aligned almost parallel to the maximum horizontal stress are affected. The inclination of those faults results in high slip tendency and lower dilation tendency – both due to the vertical stress component.

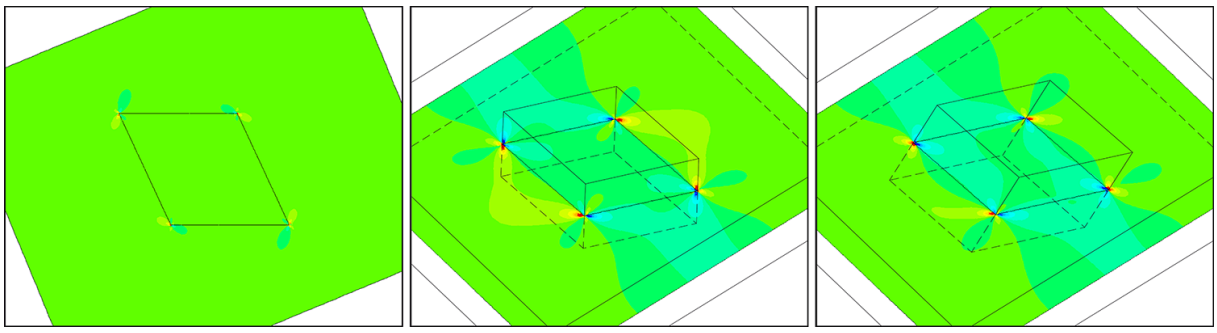

Fig. 6-6. Distribution of differential stress between maximum and minimum horizontal stress in the 2D default model (left), the first 3D model with entirely vertical faults (center) and the second 3D model with partially inclined faults. In the 3D models, the evaluation plane intersects the model horizontally at medium depth.

It was found that the 2D and 3D models are very similar to some extent. The overall stress distribution and the characteristics of the perturbations match very well, for instance, but the magnitudes comprise some differences. Eventually geometrical changes in the third dimension result in considerable differences, especially in fault behavior. Hence, as soon as a geomechanical model incorporates gravity and overburden pressure, and the results are supposed to comprise the highest possible accuracy and reliability, a 3D modeling approach is recommended. This higher accuracy in 3D is based on the use of the full stress and strain tensor.

6.1.4 Summary of Parameter Studies

The recent remote stress field in the case study reservoir area is set as boundary condition in a default scenario, in combination with material parameters describing a fault block of Rotliegend sandstone juxtaposed to the same lithology in the simulated surrounding. The faults separating the rock volumes comprise an assumed friction coefficient of 0.4.

This default model shows no perturbations in orientation of maximum horizontal stress for the assumed recent state of the reservoir. However, the magnitudes of the in situ stress are perturbed at the corners of the fault block. These perturbations exhibit magnitudes deviating about 2-3MPa from the background depending on the specific stress quantity, and reach at most 50-60m into the rock body. Area-wide perturbations of in situ stress magnitudes comprise deviations of less than 0.5MPa from the respective background. Hence, it can be concluded that the overall recent potential for stress perturbations in the reservoir is relatively low and the recent state of the reservoir is stable. This is underlined by the fact that the combination of reasonable assumptions for maximum horizontal stress on the one hand and the implemented parameters defining the failure criteria on the other hand, revealed no occurrence of plastic deformation.

The parameter studies showed that the fault friction, the mechanical rock properties, the specific fault geometry and the orientation of the maximum horizontal stress with respect to the faults can be seen as the most controlling parameters for the in situ stress. These parameters have a strong direct impact on the modeling outcome and revealed stress perturbations.

In contrast, other parameters can be regarded as minor factors and less sensitive. The absolute size of the fault block plays a subordinate role, for instance. Its variation resulted in a proportional change of the stress distribution and perturbations. The pore pressure is also considered to be of minor importance for the relative distribution of in situ stress orientation and its local perturbations. This assumption is based on the concept of effective stress. Changes in pore pressure will change the effective stress magnitudes, but not their orientation. Pore pressures play a more important role in time-dependent models simulating reservoir depletion and corresponding stress changes due to compaction.

The exact magnitude of the maximum horizontal stress seems to play a secondary role as well. The consequences of magnitude variation are very small, unless the maximum horizontal stress does not exceed the vertical stress or approaches the minimum horizontal stress.

It should be kept in mind that these subordinate factors gain significantly in importance by the interaction with other parameters. The correlation between the friction coefficient and the maximum horizontal stress magnitude represents a prime example.

The accuracy of the 2D results is generally lower compared to 3D modeling using the full stress and strain tensor. Detailed geomechanical reservoir models thus have to consider all three dimensions. Nevertheless, the most controlling factors in 3D stay most controlling in 2D and could be identified in these parameter studies.

6.2 Geomechanical Base Model

This first geomechanical model of the case study reservoir is of basic type and a first-order representation of reservoir geometry. Contrasting to the majority of models in the parameter studies, this model considers the full 3D stress and strain tensor, and represents the foundation of the following more sophisticated static geomechanical reservoir model. All major faults are based on seismic data and are incorporated accurately in combination with one lithological layer. This layer comprises a planar top and bottom, and does not preserve the horizon topology.

The base model helps to improve the modeling workflow and provides early insights into fault behavior and the in situ stress distribution in the reservoir. Especially the impact of reservoir-specific fault geometry on stress perturbations is evaluated. In the following, the objectives of this base model (6.2.1), the modeling approach (6.2.2), and the most important results are described (6.2.3).

6.2.1 Objectives

This base model of the case study reservoir shall represent the foundation of future models and test the principles of the modeling workflow. Furthermore it helps to improve the workflow prior to applying it to the buildup of the detailed field-scale geomechanical model.

The model aims for first descriptions of the in situ stress distribution and related perturbations by incorporating the fault geometry actually interpreted from 3D seismic and provided by the project partners. These perturbations directly result from the specific fault network of the reservoir. In addition to the in situ stress distribution, the movement behavior of the major faults is examined in the recent state of stress.

6.2.2 Modeling Approach

In a first step, all faults in the provided geological model of the case study reservoir are separated into primary and secondary faults depending on their vertical offset, total length and position in the fault network. The trace of 18 major faults is then extracted by coordinates of points. All faults are already verticalized in the geological model due to the extensive lateral dimensions of the reservoir horizon in contrast to its small thickness. In combination with the fact that no horizon topology is to be regarded in this base model, only the horizontal coordinates (x, y) are considered.

The point coordinates describing the faults are used to re-generate the individual fault traces by so-called splines. This is done in two dimensions. The number of points required to accurately reproduce the faults trace strongly depends on the curvature of the fault (Fig. 6-7). In a second step, auxiliary lines subdivide the inter-fault space of the reservoir into several segments and additional lines are created to establish a rectangular load frame around the reservoir area. The applied load frame in this base model comprises a size of 100km x 100km (Fig. 6-7). Subsequently, all splines and lines are used to generate planar surfaces, which are then meshed with 2D mechanical elements and extruded to 3D.

The element size is set to 75m for the reservoir and coarsens in the outer load frame (Fig. 6-7). By extruding the two dimensional mesh parallel to the depth axis, a 3D mesh is generated. The fault splines become vertical fault faces identical to the fault in the geological model. All faults are meshed with 2D contact elements. Element nodes along the auxiliary faces are merged to ensure a continuous mesh. The length of vertical extrusion defines the thickness of the modeled lithological layer. The base model is extruded 500m from 4700m to 5200m depth and is subdivided into 4 element layers of 125m thickness.

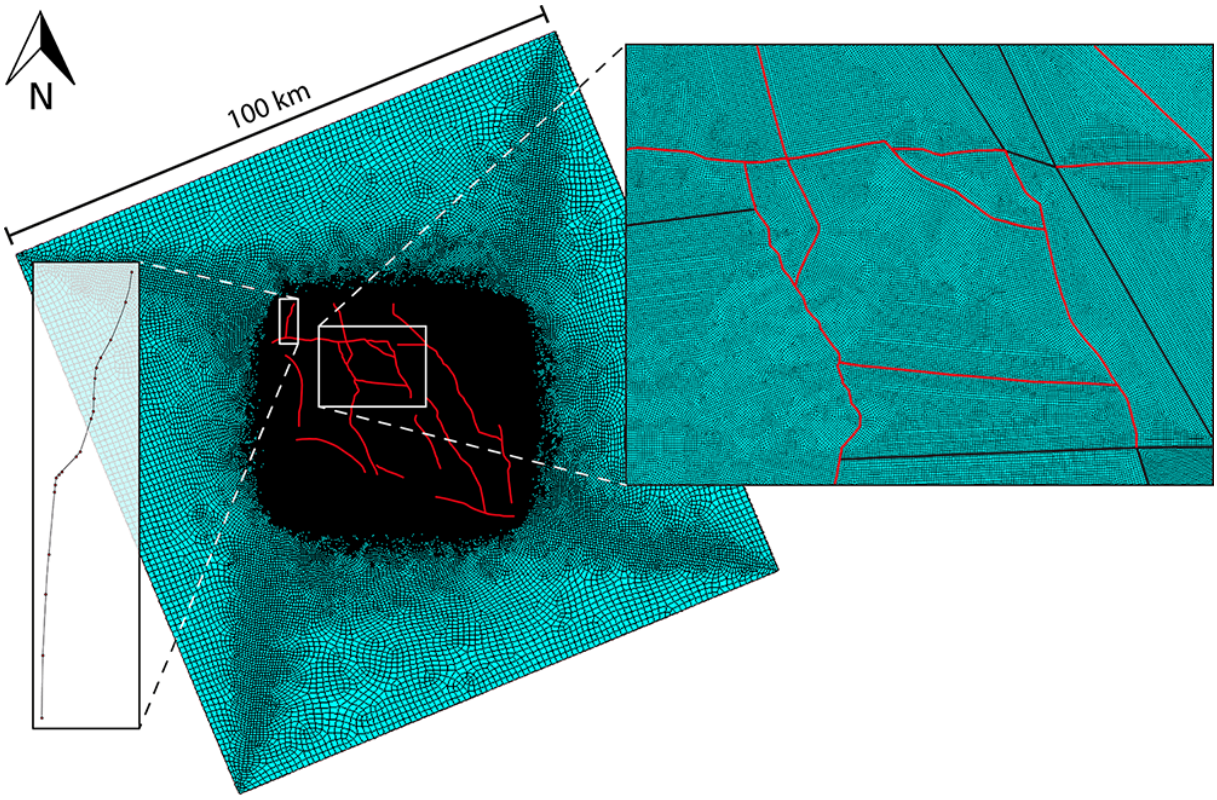

Fig. 6-7. Top view on the meshed base model comprising more than 1.4 million elements (center). The faults (red) are re-generated from point coordinates by using so-called spline functions (left). The amount of points used at specific parts of the fault depends on the respective curvature. Beside the faults also auxiliary lines are generated subdividing the inter-fault space to distinct segments (right).

The approach outlined above is – in a geometrical sense – the simplest one, as it is based on a 2D fault representation in map view and considers neither horizon lines, nor any topology of the lithological surfaces between the faults. This is justified for the intention of this base model and the due to the dimensions of the case study reservoir.

Mechanical properties and boundary conditions used for the base model are adopted from the default model of the parameter studies. This default model combines the 'most likely' parameters to describe the present state and the ambient stress conditions in the case study reservoir area. Hence, all faults are modeled assuming a friction coefficient of 0.4, while for the Rotliegend sandstone a Young's modulus of 36.4GPa and a Poisson's ratio of 0.23 are used. Plastic deformation is not considered at this stage, because the parameter studies showed that elastic deformation is prevailing. While the base of the model is fixed with respect to vertical displacements, a pressure boundary condition of 114.24MPa acts on the top of the model. This value results from the vertical stress gradient of Röckel and Lempp (2003) and an assumed depth of 4700m. For the magnitudes of maximum and minimum horizontal stress, $0.9 \cdot S_V$ and $0.6 \cdot S_V$ are used, respectively. The maximum horizontal stress is oriented NNW-SSE, which is implemented by a counter-clockwise rotation of the load frame (Fig. 6-7). In order to generate a vertical stress gradient inside the model, it is subject to gravitational acceleration.

6.2.3 Results of the Base Model

Post-processing of the base model includes the common visualizations in contour and vector plots, displaying maximum and minimum horizontal stress magnitudes and also re-calculated stress quantities such as mean and differential stress (4.7.2) (Fig. 6-8). The results of the base model reveal magnitude perturbations, which are generated especially around the fault tips and at strong curvatures

of the faults. These perturbations show deviations of more than 1.5MPa from the regional value and considerable lateral extent of up to 400-500m distance to the faults (Fig. 6-8). The specific perturbation shapes differ between individual stress quantities, but the locations of the perturbations remain generally constant. Stress maxima and minima are most pronounced very close to the faults and lose intensity rapidly in greater distance (Fig. 6-8).

The results further indicate that perturbations can be intensified by neighboring faults. This effect is rare in the base model due to the incorporation of only the major faults (Fig. 6-8). However, it is assumed that denser fault networks will show this phenomenon more frequently. This interaction results increasing complexity of in situ stress distribution and underlines the need for geomechanical modeling, and especially of models incorporating full geometrical complexity.

The small size of some magnitude perturbations in the base model let them appear as numerical instabilities (Fig. 6-8). However, all stress concentrations presented in the contour plots result in fact from the distinct geometry of the faults, which is resolved by the small element size applied.

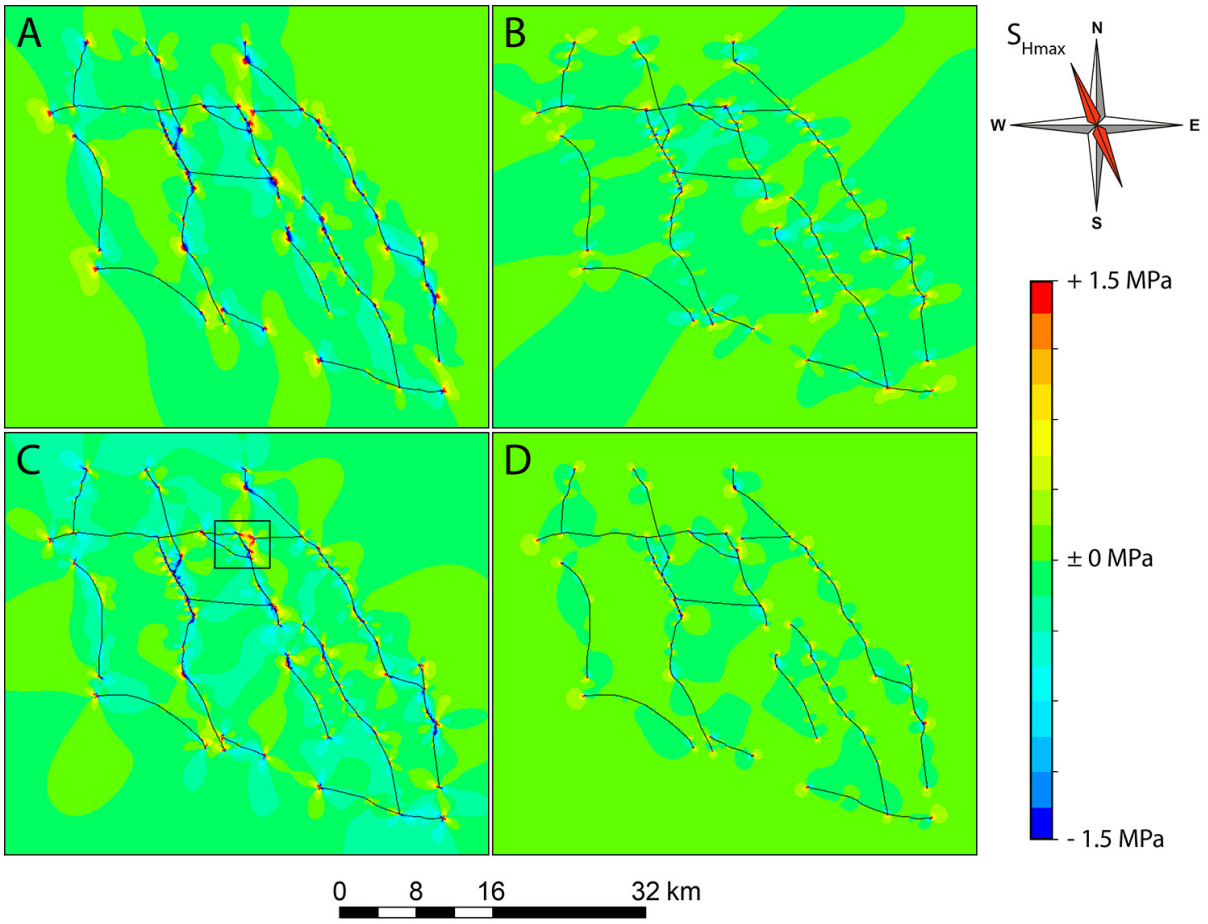

Fig. 6-8. Top view on the distribution of the maximum (A) and minimum (B) horizontal stress magnitude, and the differential (C) and mean stress (D) in the base model of the case study reservoir. The maximum horizontal stress is directed NNW-SSE and all faults comprise a friction coefficient of 0.4. Due to the different magnitude ranges, the legend indicates the deviation from the background stress level (right). The small rectangle illustrates the part of the model enlarged in Fig. 6-9 (C).

As indicated by the parameter studies, stress orientation is not significantly disturbed in case a friction coefficient of 0.4 is used for the faults. In combination with the rather local perturbations of stress magnitude, this emphasizes the assumption of a relatively stable state of stress in the case study reservoir area.

Lowered fault friction yields considerable intensification of perturbations and also re-orientation of the principal stresses in the vicinity of faults. This matches the observations of the parameter studies. Intense perturbations at very low fault friction can eventually lead to changes in the tectonic regime, i.e. the maximum horizontal stress exceeds the vertical stress magnitude and becomes the first principal stress (Fig. 6-9). This phenomenon can occur very locally and seems to be facilitated by interaction of neighboring faults. Observed changes in the tectonic regime in the North German Basin could be attributed to such behavior (Bücker and Strobel, 2003).

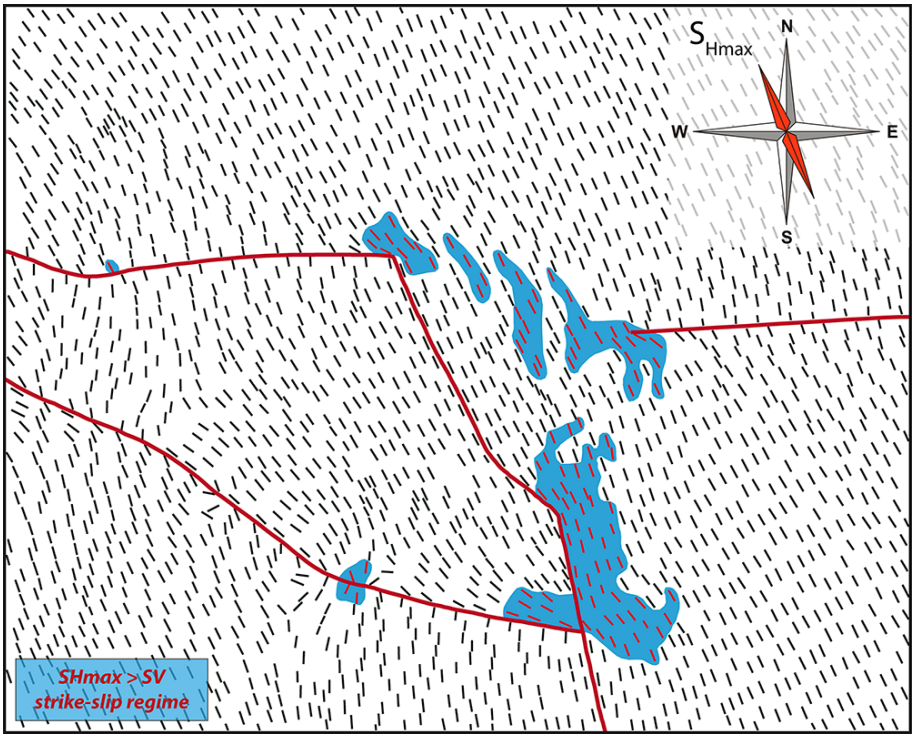

Fig. 6-9. Top view on stress trajectories of the maximum horizontal stress at very low friction (< 0.1) in the enlarged part of the base model indicated in Fig. 6-8-C. In greater distance to the faults, the trajectories follow the regional NNW-SSE trend. In the vicinity of the faults, significant re-orientations occur of up to 90° from the ambient stress direction. At some locations (blue), the maximum horizontal stress magnitude exceeds the vertical stress and becomes the first principal stress. Hence, the tectonic regime switches from normal faulting to strike-slip. Such a change directly impacts related fracture patterns (4.8.2).

Due to the fact that the orientation of shear and tensile fractures depends on the first and least principal stress orientation, the tectonic regime in turn directly controls all fracture patterns as it describes the relative order of the three principal stresses (3.3.1). Such local changes in paleo-tectonic regimes thus imply changes in fracture patterns that could be also observed in outcrop analogues of reservoir rocks, for instance. However, such local switches in the tectonic regime could only be observed at very low fault friction ($\mu_f < 0.1$).

Besides the distribution of in situ stress and its perturbations, the fault behavior is analyzed using the specific shear and normal stresses acting on the fault surfaces. These stresses are taken to calculate slip and dilation tendencies (4.7.2). Both tendencies range in values from 0 to 1 and indicate the faults proximity to slip or dilate. The slip tendency distribution in the base model suggests that none of the faults tends to slip under the considered boundary conditions and material properties (Fig. 6-10). However, some faults are more prone to slip than others as they show a significantly higher slip tendency. Fault segments oriented NNW-SSE, i.e. in direction of the maximum horizontal stress, exhibit the lowest slip tendencies (blue). A certain acute angle between the maximum horizontal stress and the fault orientation leads to the highest slip tendency values (green). If the angle becomes too large, the slip tendency decreases again.

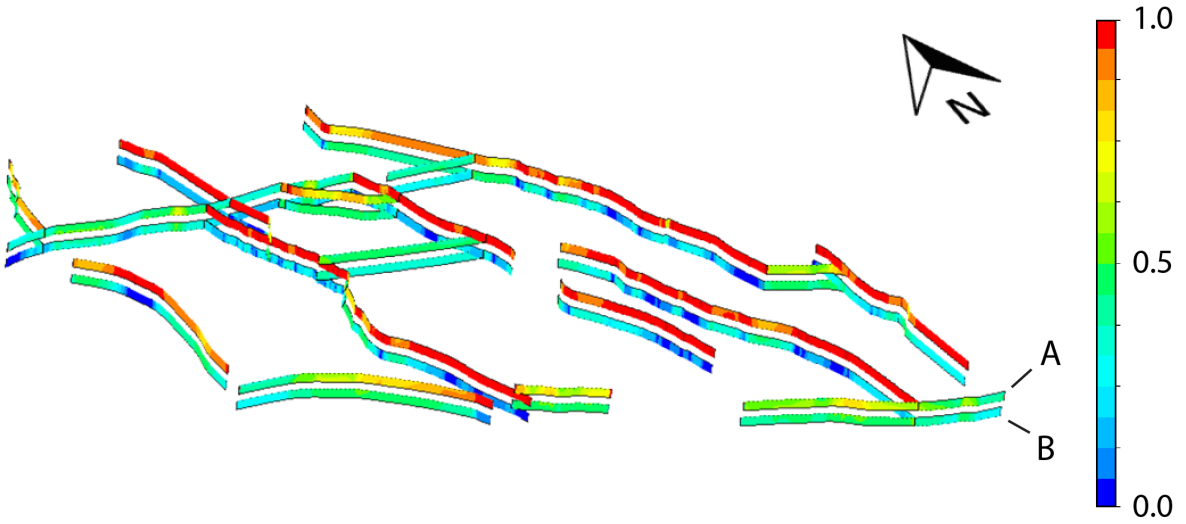

Fig. 6-10. Distribution of the dilation (A) and slip tendency (B) on the fault surfaces in the base model. This plot represents two perspective views from the southwest onto the fault network that are overlain for better comparison. Slip and dilation tendency values range from 0 to 1 indicating the likelihood of fault slip or opening, respectively. The distribution of both tendencies reveals a strong dependency on the orientation of the maximum horizontal stress. Please refer to Fig. 6-7 and Fig. 6-8 for spatial scaling.

The distribution of the dilation tendency reveals an orientation dependency as well (Fig. 6-10). The more parallel the fault segments are to the maximum horizontal stress, the higher is their tendency to dilate and vice versa. This strong dependency of the slip and dilation tendency on the orientation of the maximum horizontal stress can be attributed to its pronounced magnitude significantly exceeding the minimum horizontal stress. Moreover, no anisotropies or differences in the material parameters and juxtapositions are implemented in the model. Those are suggested to lead to further variations in the fault-specific stress distribution and are regarded in the static geomechanical model of the case study.

6.2.4 Summary of Base Model

The base model of the case study reservoir accurately incorporates 18 major faults in one lithological layer. This 3D model provides first insights into the in situ stress field of the reservoir. The results suggest a rather uniform and stable state of stress in large parts of the case study reservoir. However, local perturbations in stress magnitudes are observed in the vicinity of faults in general, especially near the fault tips and due to the interaction of faults. Local stress re-orientations are subordinate, but are enhanced if lower fault friction coefficients are assumed. Depending on fault orientation relative to the local stress field substantial variations in slip and dilation tendency are observed.

The base model represents a valuable starting point for further modeling and the buildup of the static geomechanical reservoir model. Testing the workflow at this base model helped to eliminate potential sources of errors in all parts of the workflow. The handling of the FE program's internal script language that is used could be improved and optimized for large models. Furthermore the experience made with the base model helps to estimate more reliably the computing demand for models exceeding 1 million elements and comprising a large number of faults.

7 Static Model of Case Study Reservoir

Following the preliminary parameter studies (6.1) and the base model of the case study reservoir (6.2), the detailed static geomechanical model is built. This field-scale model incorporates a mechanical stratigraphy of three layers, the topology of the reservoir horizon, and a network of more than 80 faults. The model is referred to as static due to the fact that it regards the recent state of stress as boundary condition and thus reveals insights into the in situ stress distribution prevailing today. The size and complexity of the model demands high-performance computing (HPC) techniques to achieve reasonable solution times. Reliable modeling results are obtained by calibrating the model with various field data such as in situ stress measurements. In this way, the model is validated and its results can be used for further interpretations and applications.

The next chapters describe the objectives of the static geomechanical model (7.1), the data provided for input and calibration (7.2), the setup of the model (7.3), its calibration and final results (7.5, 7.6). In addition to the field-scale model a submodel covering the northwestern part of the case study reservoir is presented with its setup and results (7.7). All modeling results are finally compared and discussed (7.8, 7.9).

7.1 Objectives

The static geomechanical model of the case study reservoir represents the backbone of the research project. The model has to cover the entire reservoir and be geometrically as detailed as possible. Accomplishing the buildup and solution of this field-scale model can be regarded as a major objective, since the included complexity with respect to the number of faults is exceptionally high. The modeling outcome is to be validated by a comparison of modeling results to field measurements. Successful validation of the model represents another important objective and ensures reliable results for further interpretations. This static model is thus used to demonstrate that the elaborated geomechanical workflow is generally applicable to complex geometries and reservoirs with a large number of faults.

The primary final objective of this static geomechanical model is to provide highly resolved, detailed insights into the recent in situ stress distribution of the intensely faulted reservoir. Focus is set particularly on stress perturbations induced by faults and mechanical differences. This shall extend our knowledge on the characteristics of these perturbations and their potential interactions. Including this information on perturbations, the modeling outcome can provide a thorough description of the local state of stress at all subsurface locations in the reservoir.

The secondary objective concerns the description of the faults movement behavior under the recent in situ stress field. The application of 2D interface elements (4.4.2), allows the analysis of fault-specific shear and normal stresses on existing implemented faults mapped in seismics. Based on these stresses, the likelihood of fault slip and opening can be deduced by calculating slip and dilation tendencies. This description of fault behavior can reveal critically stressed faults and fault segments, and potentially related trends. These faults and stress states are to be examined for potential correlations to the reported hydraulic fault behavior.

Moreover, this detailed geomechanical model will represent the basis for the following dynamic modeling approach, considering paleo-stress fields of the major past tectonic stages of the reservoir area as boundary conditions (8).

7.2 Data Compilation

Before the static geomechanical model of the case study reservoir is built, the data basis is compiled and prepared. The model buildup requires input data, which regards the reservoir geometry, material properties and information on the regional stress field (7.2.1). Besides this input data, additional datasets are mandatory for calibrating the geomechanical model to local stress measurements in the reservoir (7.2.2). Information on the regional stress field required as boundary conditions is taken from published compilations rather than reservoir-specific in situ stress measurements to avoid circular reasoning.

After the screening of all available data, calibration data is separated from input data. These datasets are kept separate during the entire modeling process. The usage of data likewise for input and calibration purposes would lead to circular argumentation and a meaningless fit. Interpretations based on such models can be seriously misleading.

In this research project, most data is provided by the project partners, i.e. the field operators, in form of a geological model inferred from 3D seismic and well data (Petrel® project), log files, and internal reports. Information on the regional stress field in the case study area is taken from published large-scale data compilations of Northern Germany (Grote, 1998; Röckel and Lempp, 2003).

The following two chapters describe in detail the data provided for input (7.2.1) and calibration (7.2.2) of the static geomechanical model of the case study. The application of this data in the model setup is described separately (7.3).

7.2.1 Input Data

Reservoir Geometry

The most important part of input data is the geometry of the case study reservoir. It is based on 3D reflection seismic and comprises information on all lithostratigraphic horizons and faults (Fig. 7-1). The geometry is provided as consistent Petrel® project. Seismic interpretation and the full 3D modeling process were performed by the project partners. The Petrel® project represents the currently agreed structural model of the field operators. The 3D reservoir geometry is transferred to the finite element code in the model setup (7.3). The model provided at the start of the research project is taken as state of the art and is used for the buildup of the geomechanical model. While minor changes in fault position or the removal of faults is possible after the buildup, addition of new faults and major changes in geometry can be potentially labor-intensive.

All faults in the provided Petrel® project are verticalized due to the large lateral dimensions of the reservoir and its relatively small thickness of 15-20m (Fig. 7-1). The fault verticalization represents a given fact in the available data and is not decided or done within the modeling process of this research project. Inclination of faults could have been incorporated in geomechanical model as well. According to the project partners, most faults are traceable from base Zechstein down to the Upper Carboniferous (pers. comm. K. Kronmüller). Small faults comprising very minor vertical displacements and those located below salt bodies are commonly not detected in seismics. Instead they are inferred from the production behavior of nearby wells. These faults are thus conceptual and the accurate determination of their location is challenging. Changes in the agreed model concern most often the trace of these minor faults. All following overviews on the fault network are made in ArcGIS® with original coordinate data taken from the Petrel® project (e.g. Fig. 7-3, Fig. 7-5, et seq.).

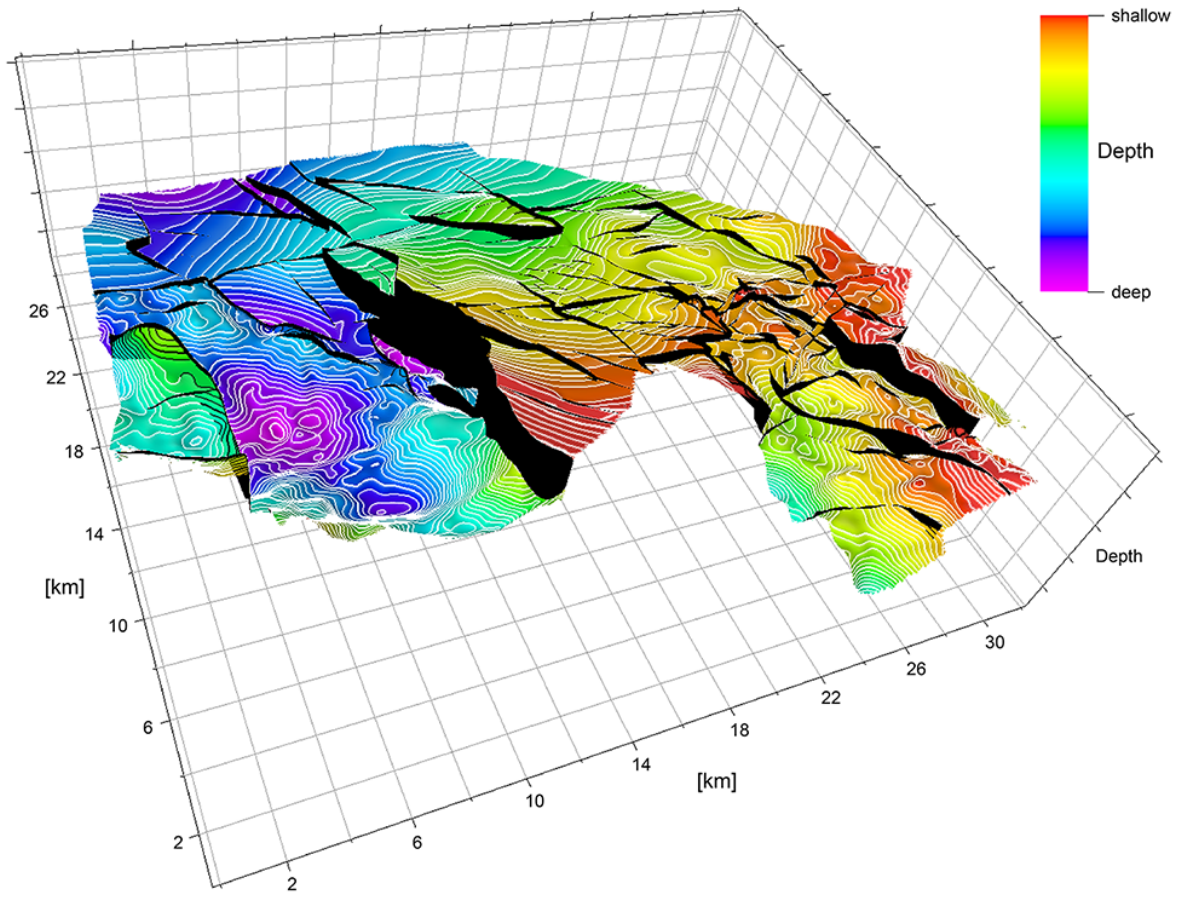

Fig. 7-1. Overview on the depth-contoured reservoir top (Top Wustrow) of the case study in a perspective side view. The color scale encompasses 500 m in depth. Visualization is 10x vertically exaggerated to elucidate the different vertical displacements along faults.

Besides the information on lithostratigraphic horizons and faults, the provided Petrel® project further comprises the trajectory of the drilling paths of all wells in the reservoir. This information is crucial during the calibration of the model, when results of in situ stress measurements are to be compared to the modeling outcome. The well paths then provide the accurate subsurface location for this comparison.

Material Parameters

Reservoir-specific material parameters are the second important part of input data and are derived from the internal report #1 and sonic logs. The internal report #1 describes the results of rock mechanical testing on multiple drill cores of the reservoir sandstone at four wells. Triaxial tests were carried out using confining pressures of 10MPa, 30MPa, and 60MPa. In some cases, the maximum confining pressure was limited to 50MPa. The results of these tests yielded the pre- and post-failure static Young's modulus, the angle of internal friction and the cohesion of the sandstone samples. Dynamic measurements using ultrasonic wave propagation were performed additionally on the same drill cores. Post-failure results and the dynamic moduli show great variation and are not considered in the geomechanical model.

The most important results taken from this internal report #1 are the static Young's moduli of the reservoir sandstone (Tab. 7-1). These values show low variability except for samples of one well (L1), which yields a significantly lower Young's modulus (Tab. 7-1). This phenomenon may correlate with the use of larger samples sizes in comparison to the other wells. Larger samples may comprise

discontinuities and weakening heterogeneity that is not included and regarded in smaller samples. This problem could be scaled up to the cell size of the geomechanical models of tens of thousands cubic meters. On this large scale, the actual elastic moduli are suggested to be significantly lower than those of drill core samples measured. This upscaling problem is a field of ongoing research (Pouya and Chalhoub, 2008).

Despite the fact that the parameter studies indicated elastic deformation only, the cohesion and angle of internal friction are included in the general data compilation and summarized for a potential future use (Tab. 7-2). These values describe the linear Mohr-Coulomb criterion and are determined using varying confining pressures.

Well	Formation	Number of tested cores at confining pressures (low-medium-high)	Sample size for triaxial tests (length / diameter)	Static Young's Modulus
A1	Wustrow	3 (1-1-1)	60 mm / 30 mm	27.96 GPa
D5	Slochteren	14 (2-6-6)	60 mm / 30 mm	27.74 GPa
J1	Wustrow	21 (7-7-7)	60 mm / 30 mm	29.32 GPa
L1	Wustrow	9 (3-3-3)	100 mm / 50 mm	19.59 GPa
			Total average:	26.15 GPa

Tab. 7-1. Overview on the (pre-failure) static Young's moduli measured by triaxial testing (internal report #1). The results consider the sandstone of the Wustrow and Slochteren formation. While samples of well A1, D5 and J1 show low variability in the Young's modulus, the samples of well L1 are larger and yield significantly lower values.

Well	Cohesion	Angle of Internal Friction
A1	6.92 MPa	49.09°
D5	8.11 MPa	45.86°
J1	12.03 MPa	51.84°
L1	7.20 MPa	47.20°

Tab. 7-2. Overview on the material parameters of cohesion and angle of internal friction, which describe the linear Mohr-Coulomb criterion and plastic deformation. Values are taken from results of the internal report #1.

In addition to the rock mechanical test results, geomechanical sonic logs of five wells are provided. These sonic logs are so-called DSI logs (Dipole Shear Sonic Imagers) that provide the velocities of compressional and shear waves in the formation around the wellbore (4.3.1). These velocities can be recalculated to dynamic Young's moduli and Poisson's ratios in combination with density information obtained from respective density logs, (3.2.1, Eq. 3-20, Eq. 3-21). While the rock mechanical tests provide only insights into the mechanical properties on reservoir level, this log data yields additional material parameters for over- and underburden layers.

The recalculated log data, i.e. the dynamic elastic moduli, and the information from density logs is plotted against depth (Fig. 7-2). These plots are used to determine trends in the parameter variation for the transitions between overburden, reservoir, and underburden. Such trends are analyzed for the Poisson ratio, dynamic Young's modulus and density. The Poisson ratio is observed to constantly decrease in all logs at the transition from overburden to reservoir horizon and rises again at the transition to the underburden layer (Fig. 7-2).

The dynamic Young's modulus behaves ambiguously. It exhibits in two thirds of the logs lower values within the reservoir horizon than in the over- and underburden, and develops vice versa in the rest. However, the large amplitude of the data significantly complicates the determination. Such ambiguous behavior is also observed for the density. It decreases in all logs at the transition from overburden to reservoir, but following increase in the underburden occurs only in the minority of logs (Fig. 7-2).

In order to set up the general trend for the mechanical stratigraphy of the three modeled layers, the following trends are proposed as most prominent and are applied: (1) the Poisson ratio decreases from overburden to reservoir and increases again in the underburden without reaching the overburden value (Eq. 7-1); (2) the Young's modulus is equal in over- and underburden and slightly lower in the reservoir (Eq. 7-2); (3) the density decreases from overburden to reservoir and stays constant at the transition to the underburden (Eq. 7-3).

$$\boldsymbol{\nu}_{Overburden} > \boldsymbol{\nu}_{Underburden} > \boldsymbol{\nu}_{Reservoir} \quad \text{Eq. 7-1}$$

$$\boldsymbol{E}_{Overburden} = \boldsymbol{E}_{Underburden} > \boldsymbol{E}_{Reservoir} \quad \text{Eq. 7-2}$$

$$\boldsymbol{\rho}_{Overburden} > \boldsymbol{\rho}_{Underburden} = \boldsymbol{\rho}_{Reservoir} \quad \text{Eq. 7-3}$$

ν = Poisson ratio; E = Young's modulus; ρ = Density

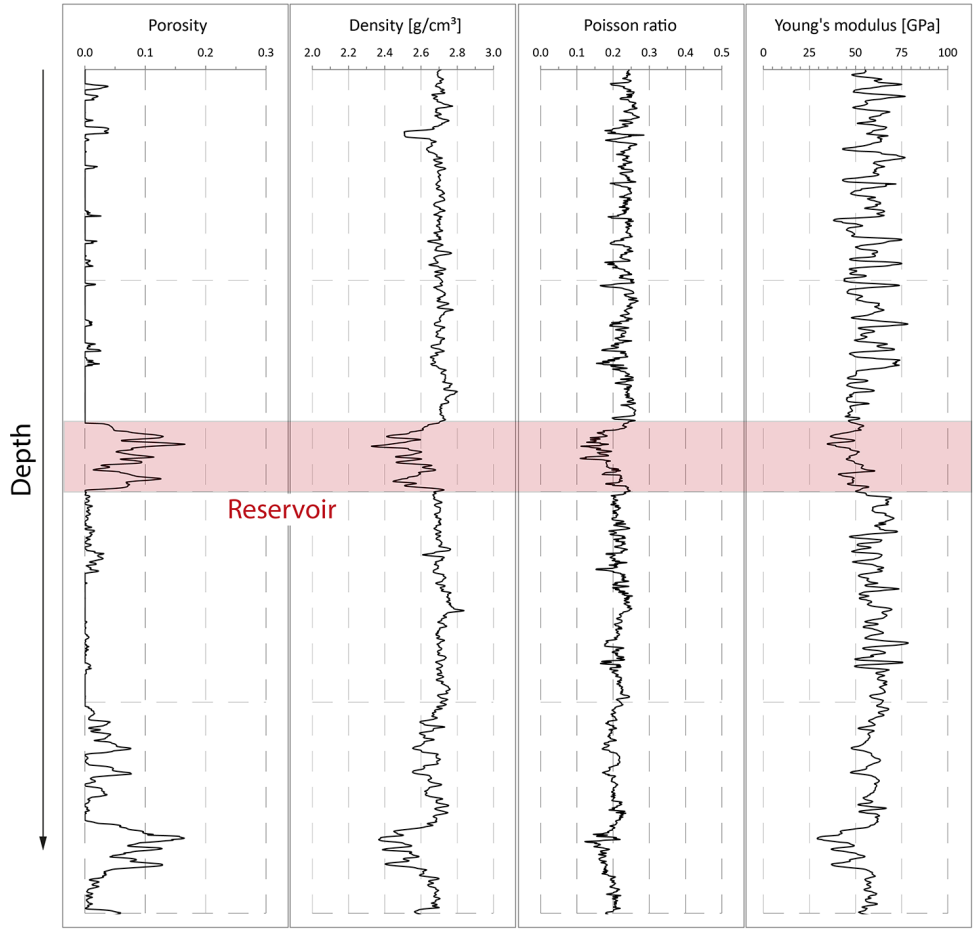

Fig. 7-2. Representative evaluation plot of the recalculated dynamic elastic moduli and density at well N1. Porosity log information is shown to indicate the depth interval of the reservoir horizon (red). In these plots, the trends described in the text are inferred and values graphically estimated.

After the trends are described, absolute dynamic values are estimated graphically from the plots. This rough approach of determination is justifiable due to the amplitude of the calculated parameters (Fig. 7-2). The derived values build up sets of uniform parameters for density, Poisson ratio and Young's modulus (Tab. 7-3). Uniform parameters are applied, because the data basis of five 'punctual' sets of information does not allow making robust interpolation of lateral material variations on the scale of square kilometers.

The frequency dependence of the dynamic Young's modulus precludes its direct use for numerical geomechanical modeling. It has to be recalculated to a usually lower static equivalent (3.2.2.2) (Holt et al., 2013). There are several published empirical equations available that correlate the dynamic and static Young's modulus (Eissa and Kazi, 1989; Morales and Marcinew, 1993). However, these equations always work with empirical constants, which were derived under conditions and for rocks that may differ significantly from the case study sandstone.

Instead of using such equations, the average value of the dynamic Young's modulus of the reservoir horizon is thus directly correlated with an average value of the experimentally determined static Young's modulus (Tab. 7-1). The respective values for over- and underburden are then linearly extrapolated from this reservoir value. Based on the assumed average moduli of 50GPa and 55GPa for the reservoir and over-/underburden, respectively, this equals an extrapolation factor of 1.1. The average static Young's modulus of the reservoir horizon of 26.15GPa thus yields 28.77GPa for over- and underburden (Tab. 7-3). This rather simple conversion is justifiable due to the available data, and variation and uncertainties of the underlying measurements.

	Bulk density [kg/m³]	Poisson's ratio	Dynamic Young's modulus [GPa]	Static Young's modulus [GPa]
Overburden	2700	0.24	55	28.77
Reservoir	2600	0.17	50	26.15
Underburden	2600	0.21	55	28.77

Tab. 7-3. Summary of the uniform material parameters defined as individual sets for the reservoir horizon, over- and underburden. The dynamic Young's modulus of over- and underburden is extrapolated from the reservoir horizon, for which static and dynamic values are available.

In summary, the available information on material parameters is used to define one set of uniform parameters for each of the three modeled layers (Tab. 7-3). These material descriptions are based on results of rock mechanical tests on drill cores and in situ measurements by DSI® logs. Dynamic Young's moduli derived from sonic logs are converted to static equivalents by using reservoir-specific experimental data instead of published correlations.

An overview shows the wells, at which DSI® logging was carried out, and those providing core samples for rock mechanical testing (Fig. 7-3). In situ measurements are predominantly applied in the eastern parts of the reservoir, whereas rock mechanical tests are applied on samples of wells in the central and western areas. At no well both types of measurements are available. Overlapping of measurements at one or multiple wells in future approaches could help to improve the correlation of measurements and the conversion of dynamic to static elastic moduli.

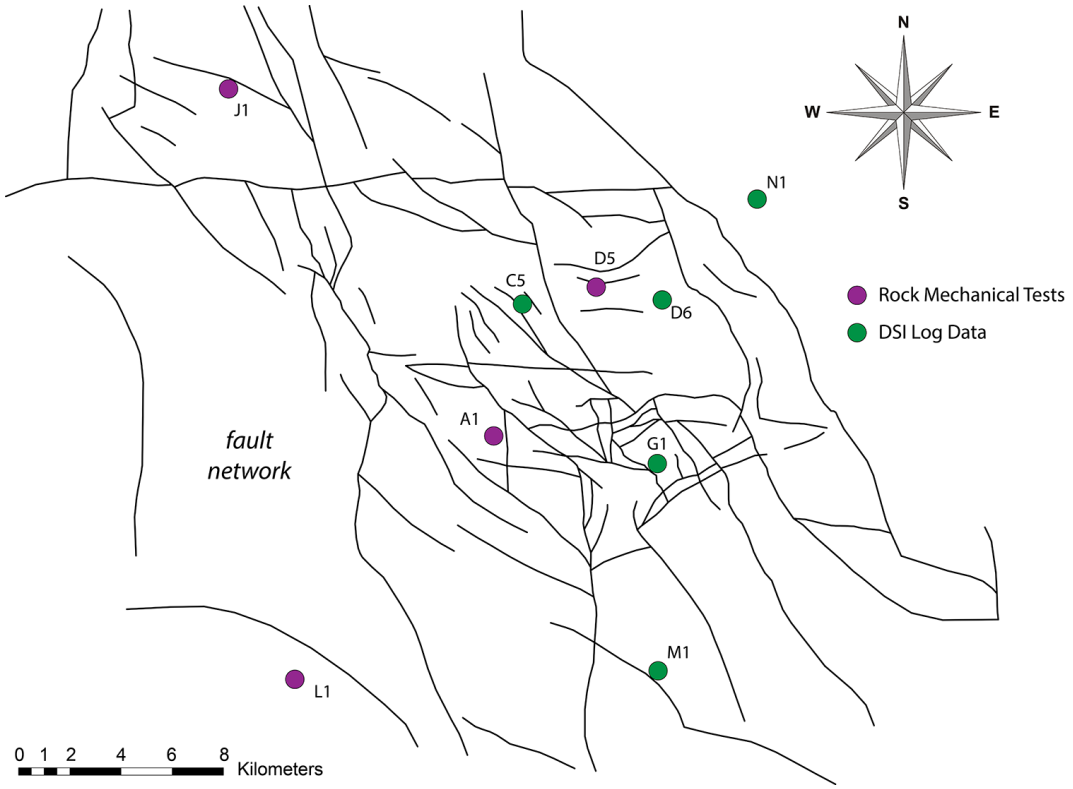

Fig. 7-3. Top view on the fault network of the case study reservoir showing an overview on wells, at which information on material parameters is derived.

Regional Stress Field

The third part of input data has to describe the boundary conditions of the numerical model, i.e. the regional ambient stress field in the case study area. This description of the stress field is highly similar to the one assumed in the parameter studies (6.1.2). It includes the vertical stress gradient and the magnitude and orientation of the maximum and minimum horizontal stress. An additional internal report #2 provides the reservoir-specific vertical stress gradients at three wells in the reservoir, which are calculated by the integration of the respective overburden density (Tab. 7-4).

Well	Vertical Stress Gradient
A1	23.260 MPa/km
D5	23.583 MPa/km
J1	23.534 MPa/km
Total average:	23.459 MPa/km

Tab. 7-4. Overview on the vertical stress gradients provided by the internal report #2 at the wells A1, D5 and J1. These gradients show small variability and are used to define an average gradient used for the boundary conditions.

Based on these three vertical stress gradients, an average gradient of 23.459MPa/km is derived representing the entire reservoir area. This gradient is very similar to the gradient published by Röckel and Lempp (2003), i.e. 24.3MPa (Fig. 7-4), and is used to define the lithostatic pressure load applied to the top surface of the model depending on its depth level (4.5). Besides the vertical stress gradient, further information on the horizontal stress orientation and magnitude in the North German Basin is directly derived from published data (Grote, 1998; Röckel and Lempp, 2003; Roth et al., 1998; Roth

and Fleckenstein, 2001). This data is based on different methods such as borehole breakouts, drilling induced fractures, core disking and hydraulic fracturing.

Data compilations show that the maximum horizontal stress in the subsalinar exhibits a fan-like pattern across the North German Basin (Fig. 5-6) (5.3). Moving from east to west, the maximum horizontal stress changes its orientation from NNE-SSW to NW-SE. Especially according to the data from Grote (1998), the maximum horizontal stress orientation is assumed to be NNW-SSE in the case study reservoir area (Fig. 5-6). The minimum horizontal stress is 90° rotated to this orientation, i.e. it is directed ENE-WSW.

In addition to the vertical stress gradient and the orientation of the horizontal stresses, the horizontal stress magnitudes are required. Röckel and Lempp (2003) published a gradient of the minimum horizontal stress magnitude for the North German Basin being 14.6MPa/km (0.62 · SV) (Fig. 7-4). As mentioned before, however, the theoretical minimum in a normal faulting regime at hydrostatic pore pressures is proposed to be 0.6 · SV (Zoback, 2007) (6.1). Any lower least principal stress magnitudes would lead to fracturing and faulting. Due to the proximity of the published gradient to this limit, it is likely that this limit in fact controls the minimum horizontal stress magnitude, and thus the minimum horizontal stress is assumed directly to be 0.6 · SV.

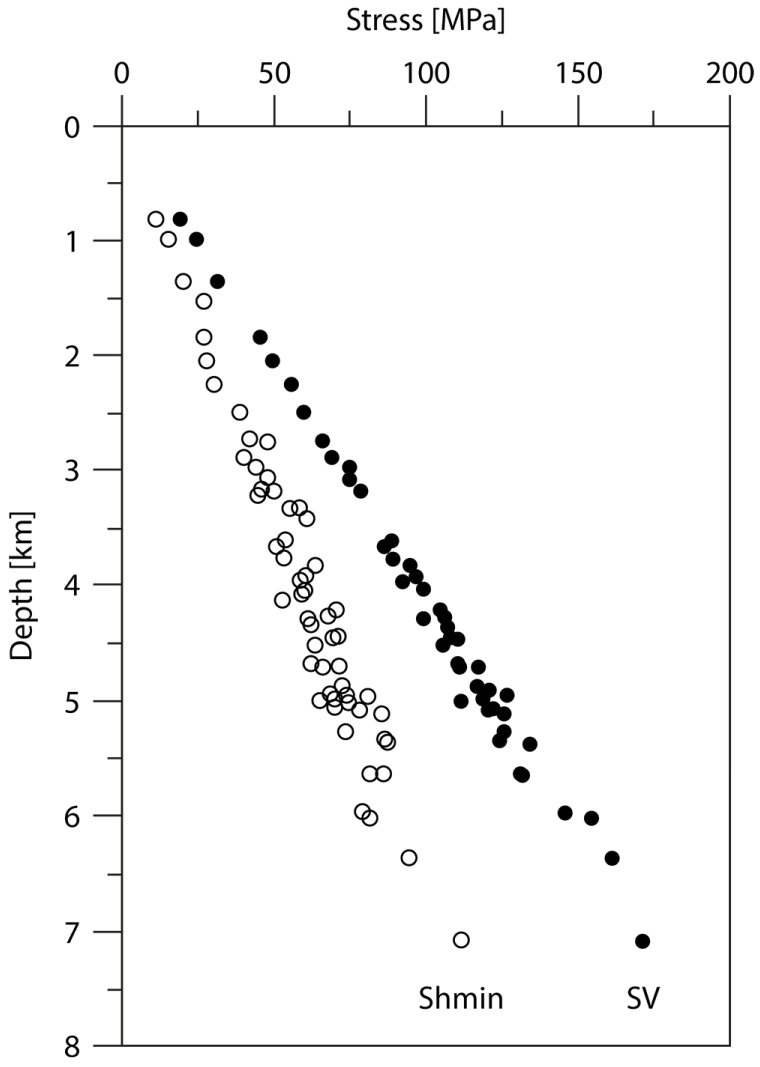

Fig. 7-4. Overview on the magnitudes of vertical stress (SV, points) and minimum horizontal stress (Shmin, circles) at various depths in the subsalinar of the North German Basin representing the largest and least principal stress, respectively. According to this data compiled by Röckel and Lempp (2003), the gradient of vertical stress is 24.3MPa/km, while the minimum horizontal stress gradient equals 14.6MPa/km (modified after Röckel and Lempp (2003)).

Due to the lack of data, such a gradient is not available for the maximum horizontal stress. However, there are only very local indications that the maximum horizontal stress component in the subsalinar layer exceeds the vertical stress (Bücker and Strobel, 2003; Moeck et al., 2009). Therefore the effective tectonic regime in the subsalinar of the North German Basin is characterized as a normal faulting regime (3.3.1) and a value of $0.9 \cdot S_V$ is considered as an approximate recent description of the maximum horizontal stress magnitude. The description of the vertical stress gradient and the magnitude and orientation of the horizontal stresses completes the boundary conditions and thus also the input data section (Tab. 7-5).

Vertical Stress Gradient (SV)	23.459 MPa/km
Maximum Horizontal Stress ($SHmax_)$	$0.9 \cdot S_V$
Minimum Horizontal Stress (Shmin)	$0.6 \cdot S_V$
Orientation of SHmax	NNW-SSE

Tab. 7-5. Overview on the description of the regional ambient stress field in the case study reservoir area derived from data of the internal report #2 and published data compilations. This part of input data is used to define the boundary conditions.

7.2.2 Calibration Data

The calibration data provided by the consortium partners comprises stress measurements performed in situ and on drill cores in laboratory experiments. This data is separated from the input data and includes information from internal reports on hydraulic fracturing and ultrasonic wave velocity analyses on drill cores (WVA), as well as published stress orientation data based on borehole breakouts (Grote, 1998).

The project partners provided internal post-job reports of hydraulic fracturing procedures from 18 wellbores, which are screened for values of the fracture closure stress (FCP) (4.8.1). This closure stress can be seen as equivalent to the magnitude of the least principal stress, which represents the minimum horizontal stress in a normal faulting regime. All values are consistently recalculated to [MPa]. In total, 14 measurements of the minimum horizontal stress magnitude could be derived that are reliable and suitable for calibration (Tab. 7-6).

Well	Minimum Horizontal Stress
B1	61.60 MPa
C1	63.70 MPa
C3	70.88 MPa
C4	66.00 MPa
C6	72.00 MPa
C7	66.60 MPa
C9	76.30 MPa
D1	66.21 MPa
F1	59.60 MPa
F2	74.90 MPa
F3	60.49 MPa
F5	67.40 MPa
F6	67.55 MPa
G1	71.70 MPa

Tab. 7-6. Summary of fracture closure pressures at 14 wells in the case study reservoir representing the local minimum horizontal stress magnitude on reservoir level. All values are derived from internal post-job reports of hydraulic fracturing.

In some reports, multiple suggestions of the fracture closure pressure are made based on different methods. The summarized values represent the conclusion of the contractors for the most reliable value and in case this is not indicated in the report, an average value or the overall most realistic one is taken. The reports cover hydraulic fracturing carried out from 1994 to 2006. The quality of the provided reports differs and not all 18 reports offer reliable information. Moreover, no report states a measurement error. According to the project partners, the measurements are assumed have a maximum error of ± 5MPa, but this uncertainty is not confirmed and can be occasionally also higher.

Nevertheless, these frac reports are highly valuable due to the fact that they provide local stress magnitude information throughout the reservoir. This information represents a key dataset in the calibration data. Stress magnitudes in the reservoir are additionally determined by ultrasonic experiments on drill cores. The corresponding results are described in two internal reports.

Internal report #2 comprises the results of ultrasonic wave velocity analyses on drill cores at three wells. These experiments yield the magnitude of the minimum and maximum horizontal stress and their orientation (Tab. 7-7). Some measurements refer to drill cores of the underburden and are not considered. Internal report #3 provides further ultrasonic magnitude measurements on drill cores from reservoir level and provides additionally the orientation of the maximum horizontal stress from breakout orientation logs (Tab. 7-7). Both internal reports on ultrasonic experiments state measurement errors of ±2MPa for magnitudes and ±15° for orientations. These magnitudes of maximum and minimum horizontal stress in combination with their orientation represent valuable calibration data.

Well	*Minimum Horizontal Stress Magnitude*	Maximum Horizontal Stress Magnitude	Maximum Horizontal Stress Orientation
A1	*92.97 MPa*	95.30 MPa	158°N
D5	*93.73 MPa*	97.05 MPa	163°N*
J1	*92.05 MPa*	97.90 MPa	187°N

Tab. 7-7. Result summary of ultrasonic wave propagation analyses on drill cores of the case study reservoir. The presented values partly represent averages and are taken from the internal report #2 and #3. The stress orientation at well D5 is derived from breakout orientation logs instead of ultrasonic experiments (*). Measurement errors are ±2MPa for magnitudes and ±15° for orientations.

The summary shows that the magnitudes of minimum horizontal stress measured by this method are all considerably higher than those reported from hydraulic fracturing (Tab. 7-6) and stated in publications (Röckel and Lempp, 2003). According to the project partners, this represents a common phenomenon and is assumed to be a methodological problem of the ultrasonic measurements. The high values are strongly doubted due to the significantly more reliable measurements during hydraulic fracturing.

Within the work for the internal report #2 and #3, the magnitudes of the horizontal stresses were calculated in relation to the vertical stress, which was deduced from the well-specific integrated density of the overburden. These integrated densities are also used in the application of boundary conditions to determine the pressure load of the vertical stress on top of the geomechanical model (7.2.1). However, these densities and the resulting vertical stress gradients are used as one averaged value and in combination with the horizontal stress gradients suggested by Röckel and Lempp (2003). Hence, the specific magnitudes of the maximum and minimum horizontal stress, which are derived at single wellbores in relation to the well-specific vertical stress, can be considered for calibration without violating the premise of separation between input and calibration data.

Besides this internal information provided by the project partners, published data on the orientation of the maximum horizontal stress is compiled (Fig. 7-5). Grote (1998) described the stress orientations in the subsalinar of the North German Basin at more than 60 wellbores. These orientations were obtained by breakout orientation logs and ultrasonic analyses on drill cores. In total, 14 of the wellbores listed are located inside the case study reservoir area and can be used for calibration (Tab. 7-8).

Well	Orientation of the Maximum Horizontal Stress
A1	163°N
C6	164°N
C9	146°N
D4	164°N
D5	180°N
E1	164°N
F2	204°N
F5	179°N
H1	165°N
I1	143°N
J1	186°N
K1	159°N
L1	162°N
O1	145°N

Tab. 7-8. Summary of the maximum horizontal stress orientation published by Grote (1998) for those wells in the case study reservoir area. The measurement error is stated to be ±15°.

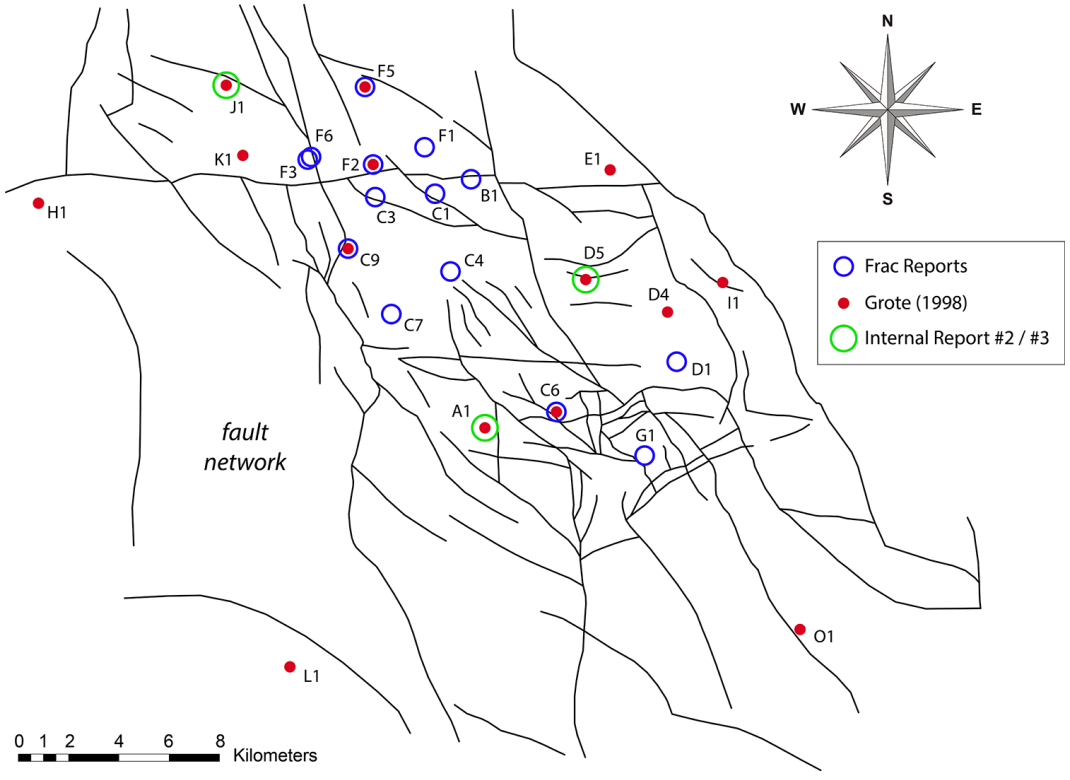

Fig. 7-5. Overview on the distribution of calibration data derived from internal reports on hydraulic fracturing (blue) and ultrasonic experiments (green), as well as from published data compilations (red).

The orientations published by Grote (1998) are also part of the large scale data compilation, on which the description of the regional stress field is based that represents input data (Fig. 5-6). However, only the general published orientation pattern, to which this data contributes, is regarded as input data and not individual measurements or values. Therefore this does not conflict with the separation of input and calibration data.

The graphical overview on all available calibration data also reveals an unfavorable situation (Fig. 7-5). Stress magnitude measurements of hydraulic fracturing and ultrasonic experiments show no overlap, which would help to estimate uncertainties.

7.3 Model Setup

7.3.1 Geometry

The setup of the static geomechanical model of the case study reservoir starts with the geometrical buildup. The geometry transfer from the Petrel® project to the finite element software Ansys® is achieved using the advanced geometry transfer option (4.1.2). In this way, the topology of the reservoir horizon and its distinct depth distribution throughout the reservoir is accurately preserved, and thus also the vertical displacements along faults and resulting juxtaposition of lithological layers.

The advanced transfer is performed for the top surface of the reservoir horizon only (7.2.1) due to the fact that the topology of the underlying horizon is highly similar. Therefore it is justifiable to duplicate this top reservoir surface and apply it additionally as bottom representation of the reservoir layer. This approach yields a constant thickness of the reservoir layer, which is decided to be 100m to honor the cumulative effect of various sandstone units within this part of the Hannover formation (Fig. 7-6). The assumption of equal top and bottom topology and the corresponding constant thickness is supported by the relatively uniform thickness of the sandstone layers in the case study reservoir (Fig. 7-6).

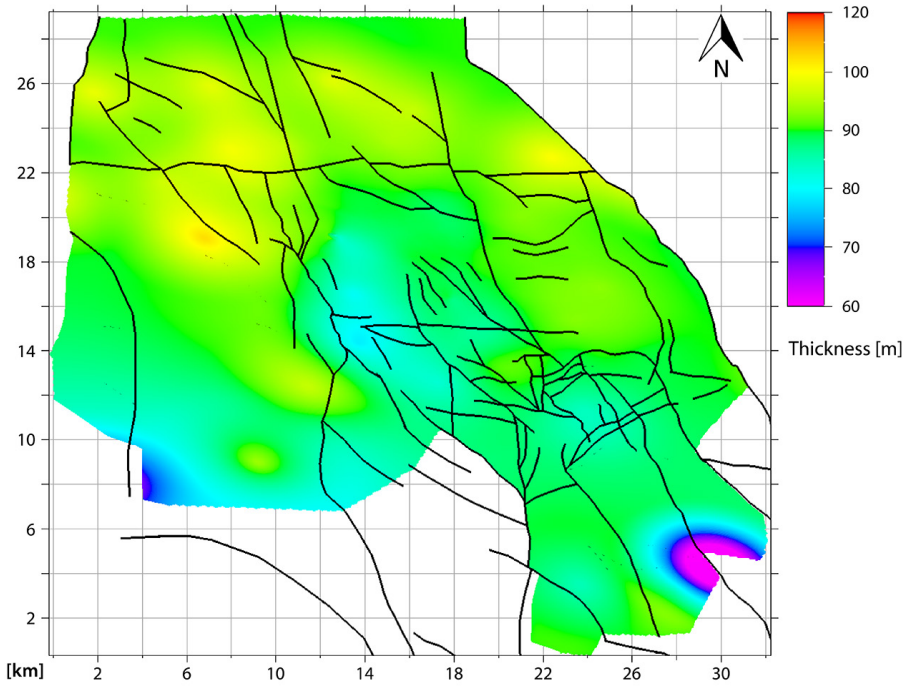

Fig. 7-6. Overview on the thickness of multiple sandstone units in the case study reservoir including the reservoir member. The uniform distribution supports the assumption of a constant thickness and equal topology of reservoir top and bottom.

A smaller thickness of about 15-20m representing the Wustrow member only in combination with the lateral scale of this geomechanical model is not practicable for numerical reasons (7.3.2).

Following the transfer of reservoir geometry, the depth distribution reflecting the reservoir topology can be compared between the geomechanical model and the geological subsurface model (Fig. 7-7). This comparison reveals the high accuracy of the applied approach for geometry transfer. Within those areas of the case study, for which the reservoir horizon is interpreted in 3D seismic, both models show equal depth distributions (Fig. 7-7). Outside these interpreted areas, the depth of the reservoir horizon had to be extrapolated during the geometrical buildup of the geomechanical model.

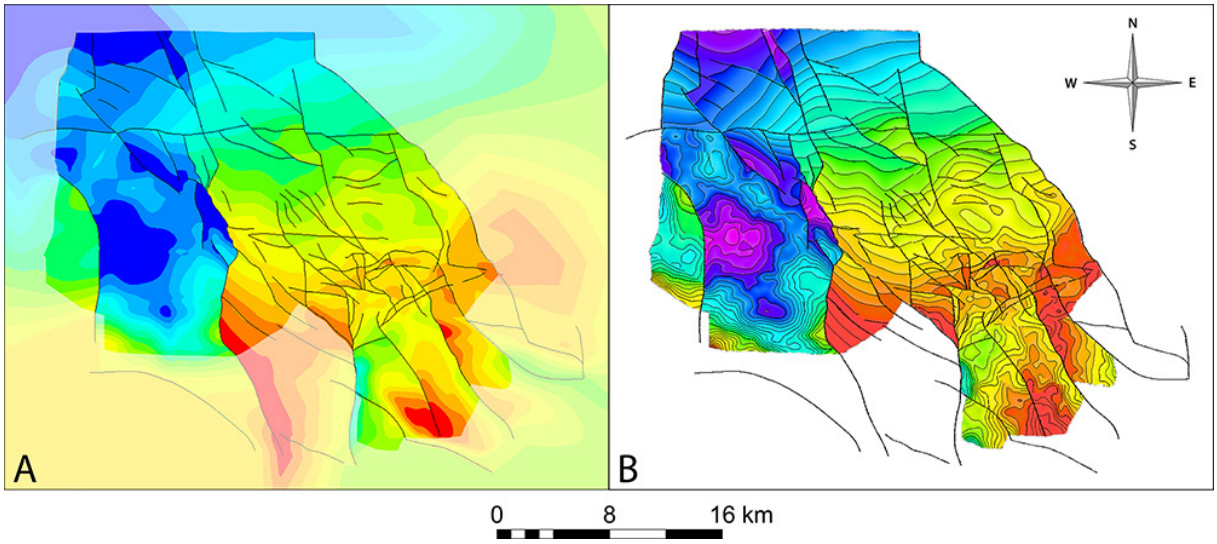

Fig. 7-7. Comparison of the equally scaled depth distribution of the reservoir horizon (red=shallow, blue/purple=deep) in the geomechanical FE model (A) and the original geological subsurface model (B). Seismic interpretation of the reservoir horizon is limited to the central part of the reservoir. In these areas, the comparison elucidates the high accuracy of geometry transfer. Aside these interpreted areas, the reservoir depth must be projected and extrapolated for the FE model (white areas).

Both surfaces bounding the reservoir horizon are crossed by the faults and auxiliary subdivisions of the inter-fault space (Fig. 7-8). The latter are created to preserve the topology in the geometry transfer more accurately. The emerging pattern of faces is also used to create an uppermost top of the model and a respective bottom, both in significant distance to the horizon surfaces of the reservoir (Fig. 7-8). Top and bottom of the model are set to constant depths of 4000m and 5600m, respectively, i.e. these faces are planar and show no topology. This allows optimal application of boundary conditions. The planar top surface of the model and the top surface of the reservoir describe an overburden layer above the reservoir and in the same way an underburden layer is regarded beneath the reservoir (Fig. 7-8).

Volumes describing the three layers geometrically are generated based on the respective horizon surfaces, the faults and auxiliary faces (4.1.2) (Fig. 7-9). The auxiliary faces are used for volume generation, but are not regarded as subdivisions in the model calculation. This disregarding is ensured by merging the respective element nodes later on providing a continuous mesh (4.2).

The additional two layers of overburden and underburden are important to embed the reservoir – as the region of interest – and preclude any negative impact of boundary conditions (Fig. 7-9). The assignment of individual material parameters to the three layers establishes a mechanical stratigraphy in the geomechanical model.

While the central reservoir layer comprises a constant thickness of 100m and maintains the depth level of top reservoir and all faults displacements, the over- and underburden have a fixed upper and lower depth level, respectively, and thus vary in thickness.

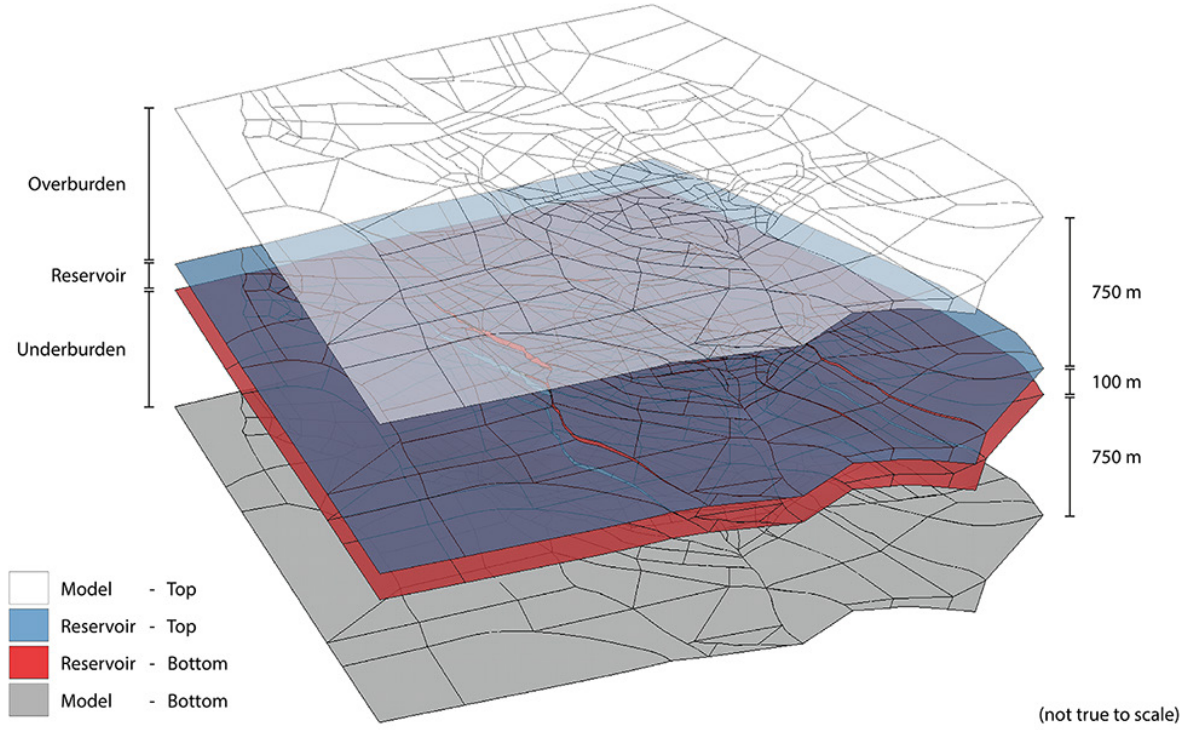

Fig. 7-8. Overview on the layering of the static geomechanical reservoir model. Black lines represent faults and auxiliary subdivisions creating the characteristic face pattern. The top reservoir surface (blue) is accurately transferred from the Petrel® project maintaining its depth and topology. Due to the high similarity in topology (Fig. 7-7), these faces are also used as bottom of the reservoir layer (red). This duplication yields a constant thickness of the reservoir layer, which is assumed to be 100 m. Top (white) and bottom (grey) of the model are planar and limit the about 750 m thick over- and underburden layer.

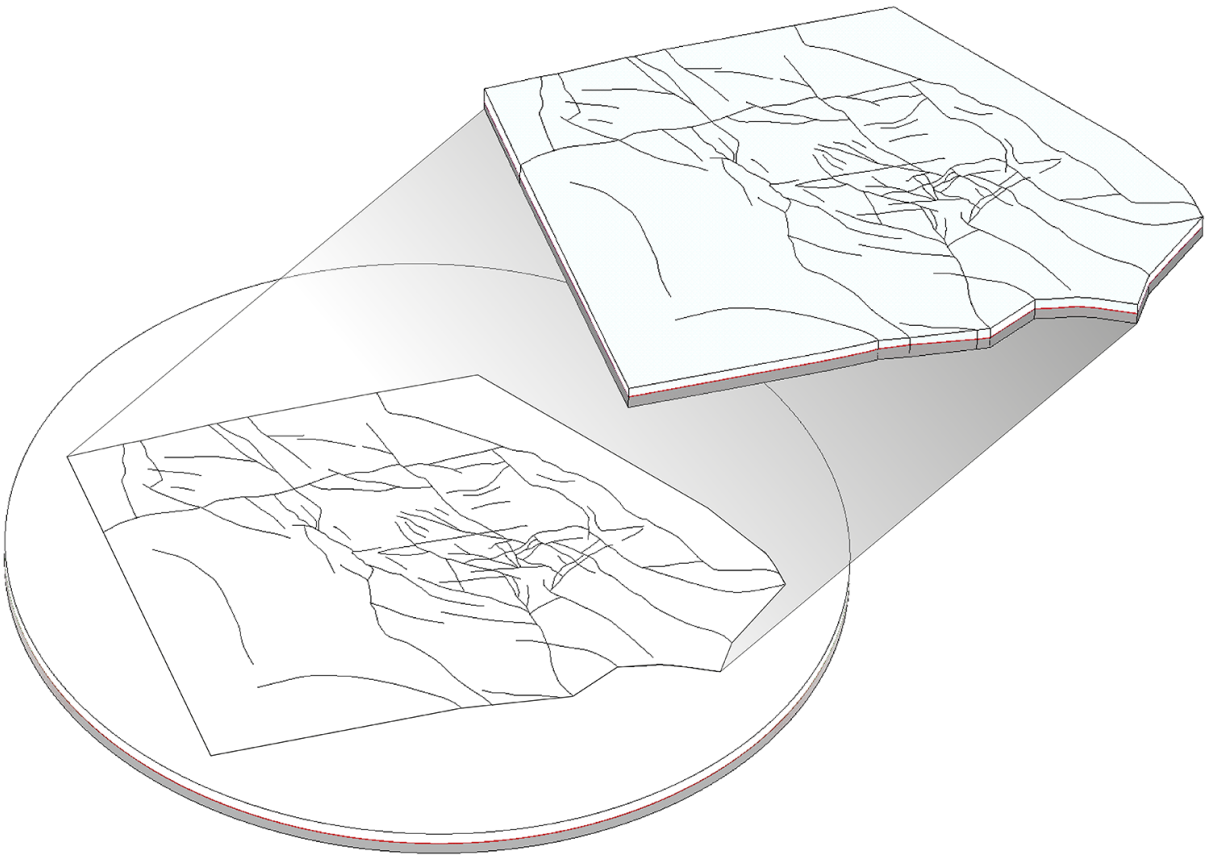

Fig. 7-9. Perspective view on the geomechanical model after the volumes of overburden (white), reservoir (red), and underburden (grey) are generated. Surrounding the fault network (black lines), additional faces and volumes are built and yield the final cylindrical shape of the geomechanical model, which offers greatest flexibility regarding boundary conditions.

Over- and underburden exhibit an average thickness of 750m assuming a vertically centered reservoir layer (Fig. 7-8). In areas of missing seismic interpretation additional faces and volumes of the horizon have to be created. This affects especially the NE- and SW-part of the reservoir (Fig. 7-7). The additional geometry is generated by interpolating and estimating the trend of the horizon from the interpreted areas (Fig. 7-8).

Furthermore, faces and volumes are created around the reservoir area building up the circular outer boundary of the model (Fig. 7-9). The depth of the reservoir horizon inside the surrounding volumes and along this vertical outer face is extrapolated from available depth information nearby. This geometrical buildup finally yields a cylindrically shaped geomechanical reservoir model, which is highly flexible in addressing varying boundary conditions (Fig. 7-9).

7.3.2 Discretization

The volumes of the geomechanical model are discretized with 3D mechanical elements (4.2). A final horizontal element size of 100m is set for all elements after an initial coarser calculation using 120m. Over- and underburden are vertically divided into 6 element layers, which symmetrically decrease in thickness towards the central reservoir layer (Fig. 7-10). This vertical mesh refinement focuses high resolution on the region of interest (4.2). The reservoir layer is vertically divided into 4 element layers of constant thickness (Fig. 7-10). Based on the reservoir thickness of 100m, this yields elements in the reservoir of 100m x 100m x 25m (length x width x depth) representing the highest calculated resolution of the geomechanical model.

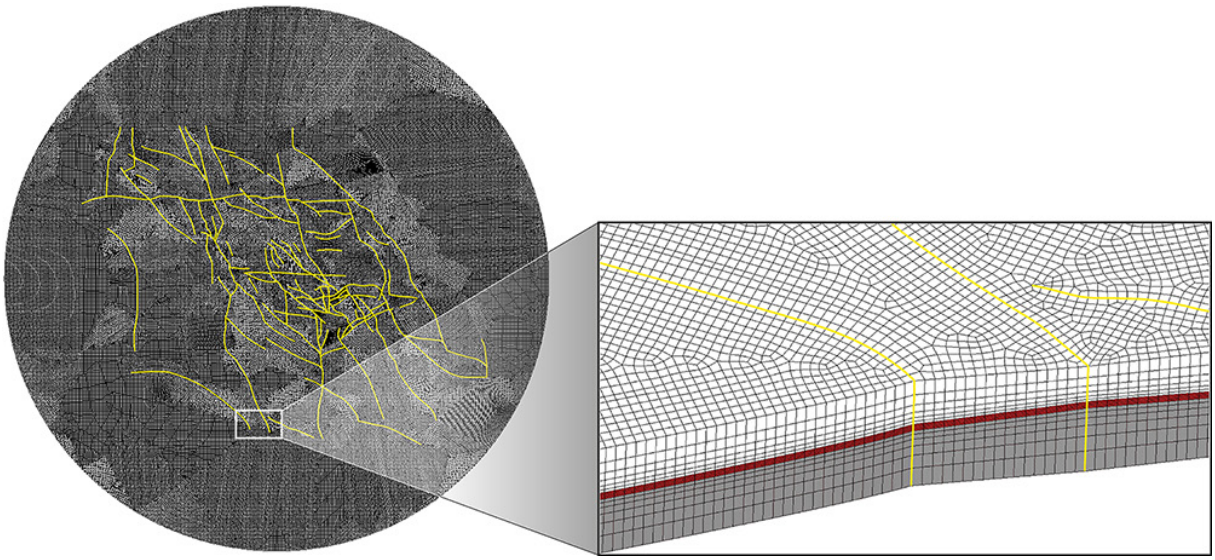

Fig. 7-10. Top view on the meshed static geomechanical model of the case study reservoir (left) showing the implemented fault network (yellow). The total diameter of the cylindrical reservoir model is 52km. The horizontal element size is set to 100m. Overburden, reservoir and underburden are vertically subdivided into 6, 4, and 6 element layers, respectively (right). The elements in the over- and underburden (white/grey) are vertically refining towards the reservoir layer (red), which comprises an element size of 100m x 100m x 25m (length x width x depth). This model comprises 3.81 million elements.

At least 3-4 vertical element layers for individual mechanical units are necessary to provide reliable stress results of a mechanically uniform layer. A reservoir thickness of less than 100m would lead to smaller thicknesses of the reservoir elements and thus extremely plate-like shapes, which are numerically unfavorable and at some ratios problematic. Counteracting this development by further decreasing the horizontal element size is precluded by the inevitably corresponding intense increase in absolute element numbers. Besides this numerical limitation, the constant reservoir thickness of 100m is justified by assuming the cumulative effect of multiple sandstone units in the Hannover formation.

Similar material parameters legitimate the representation of multiple stratigraphic sequences by one unit in the mechanical stratigraphy.

Following the volume meshing of the fault blocks, 2D contact elements are assigned to the opposing sides of fault blocks representing the faults (Fig. 7-10) (4.4.2). These elements simulate Coulomb friction and require a friction coefficient. At those boundaries of the fault block volumes that do not represent faults but auxiliary subdivisions, the element nodes are merged resulting in a continuous mesh. In this way, the auxiliary subdivisions are not regarded in the calculation. 3D elements and contact elements combined result in a total number of 3.81 million elements for the static geomechanical reservoir model of the case study (Fig. 7-10).

7.3.3 Material Parameter

After discretization of the model, material parameters are assigned to the three layers and the contact elements simulating the faults. These parameters set up the mechanical stratigraphy and define the mechanical behavior of the lithological layers and faults during the simulation (4.3). Reservoir-specific mechanical parameters for overburden, reservoir and underburden are derived from trends in geomechanical DSI logs and from the results of rock mechanical tests on drill cores (7.2.1). The latter are especially used for the mandatory conversion from dynamic to static elastic moduli. Density information is derived from respective density logs.

The reservoir-specific material parameters finally assigned to the geomechanical model include density, Poisson ratio and Young's modulus. Individual sets of these three parameters are prepared for each layer based on the available input datasets (Tab. 7-9) (7.2.1, Tab. 7-3). Due to the fact that the preliminary parameter studies propose only elastic deformation in the prevailing state of stress in the case study area, plastic deformation is not regarded and thus the parameters of cohesion and angle of internal friction are not required.

	Bulk density [kg/m³]	Poisson's ratio	Young's modulus [GPa]	Friction coefficient of faults
Overburden	2700	0.24	28.77	0.4
Reservoir	2600	0.17	26.15	0.4
Underburden	2600	0.21	28.77	0.4

Tab. 7-9. Summary of the three sets of uniform material parameters that are assigned to the overburden, reservoir, and underburden layer of the static geomechanical model. These values are derived from sonic logs and rock mechanical tests on drill cores (7.2.1).

As in the parameter studies (6.1) and the base model (6.2), the friction coefficient of the faults is assumed to be 0.4, since there is no reservoir-specific superior description. This parameter is defined to be constant in all three layers and uniform for all fault orientations (Tab. 7-9). Due to its uncertainty, the fault friction is adjusted as one key variable in the later calibration of the model to obtain a best fit between modeling outcome and calibration data.

7.3.4 Boundary Conditions

In order to complete the description of the static geomechanical model, the boundary conditions for the numerical simulation have to be defined and applied. The constraints at three boundaries have to be specified: (1) the planar top face of the model, (2) the planar bottom face, and (3) the circular

vertical face representing the lateral boundary of the model (4.5). The bottom of the model has to be fixed for numerical reasons, i.e. the nodes of the elements along this face are selected and zero vertical displacement constraints are applied. These nodes can move in the horizontal dimension, but are fixed in vertical direction.

This vertical fixation is inherently wrong, because no such fixation exists in the Earth's subsurface. However, it is numerically necessary and justified as long as this boundary is in considerable distance to the region of interest, i.e. the reservoir horizon. The underburden layer below the reservoir diminishes the negative impact and provides realistic mechanical rebound.

The planar top of the model is loaded with a pressure constraint equal to the vertical stress at this depth. Based on the derived average vertical stress gradient of 23.459MPa/km (7.2.1), this yields 93.836MPa at 4000m depth, i.e. the depth level of the model's top surface. The vertical stress inside the model is generated by the defined density of the materials and applied gravity. If the model would be clamped by rigid lateral boundaries allowing no horizontal extension, the vertical stress in combination with the mechanical behavior of the rock (Poisson's ratio) would generate distinct horizontal stresses. However, the maximum and minimum horizontal stress would be equal and considerably smaller than in reality due to the missing tectonic stress component. The ambient tectonic stress field thus has to be reflected by separate boundary conditions (4.5.1).

These lateral boundary conditions for the cylindrical geomechanical reservoir model are generated and applied by using a separate load frame model and the cut-boundary displacement method (4.5.3). First, the separate load frame model is built. This model represents a large rectangular block. The model is oriented with its lateral faces normal to the direction of the maximum horizontal stress, which is assumed to be NNW-SSE (7.2.1). The model is located by its coordinates at the position of the reservoir model, but significantly exceeding it in size with edge lengths of 130km. This load frame comprises the same total thickness as the reservoir model and the same layering of overburden, reservoir and underburden with their respective thicknesses and material properties (Tab. 7-9). The reservoir layer in the load frame model is planar and vertically in the center of the model, i.e. at the average depth of the reservoir. To this very depth level, the reservoir layer is extrapolated at the circular outer boundary of reservoir model. Therefore the stratigraphic order, layer thicknesses and respective depth levels are equal at this virtual transition between geomechanical reservoir model and load frame. This is required for the appropriate transmission of the layer-specific stresses.

The top and bottom boundary conditions applied to the load frame model are the same as for the reservoir model. Due to the lack of faults, additional inward-directed displacements of the nodes along the lateral outer boundaries of the load frame model generate a homogeneous stress field inside (4.5.1, 4.5.3). While the direction of the horizontal stresses is set by the orientation of the rectangular model, their magnitudes depend to the amount of lateral displacement. These displacements are then iteratively calibrated until the magnitudes of $0.9 \cdot SV$ and $0.6 \cdot SV$ for maximum and minimum horizontal stress are obtained as defined in the input data compilation (Tab. 7-10) (7.2.1, Tab. 7-5).

The depth at which the magnitudes are requested and calibrated is referred to as calibration depth and is defined to be 4800m, representing the approximate center of the reservoir. Target stresses of maximum and minimum horizontal stress at this calibration depth are calculated manually in beforehand (Tab. 7-10). This calculation has to consider the 750m thick overburden layer and the upper 50m of the reservoir layer with their respective densities. The iterative calibration finally yields the specific displacements that generate these target stresses (Tab. 7-10).

	Vertical Stress (SV)	Maximum Horizontal Stress	Minimum Horizontal Stress
Agreed Definition	$\nabla S_V = 23.459$ MPa/km	$0.9 \cdot S_V$	$0.6 \cdot S_V$
Target Stress Magnitudes (at 4800 m depth)	114.98 MPa*	103.48 MPa	68.98 MPa
Lateral Displacements	-	179.1724 m**	79.0808 m**

*The vertical stress at 4800m calculates from the average vertical stress gradient of 23.459MPa/km for 4km of overburden above the model, 750m of model internal overburden (ρ = 2700kg/m³), and 50m of reservoir rock (ρ = 2600 kg/m³) with considering gravitational acceleration of 9.81m/s².
**The listed displacements are applied inward-directed to both opposing lateral boundaries of the load frame normal to the horizontal stress that is to be generated.

Tab. 7-10. Overview on the target magnitudes of vertical stress, maximum and minimum horizontal stress at the calibration depth of 4800m representing the average depth of the reservoir. The stated displacements precisely generate the horizontal stress magnitudes, whose regional values are defined in the input data compilation (7.2.1, Tab. 7-5).

The determined lateral displacements complete the boundary conditions that describe together the ambient regional state of stress described in the input data (7.2.1, Tab. 7-5). The results of this load frame model are used to interpolate node-specific displacements for the circular outer boundary of the cylindrical reservoir model (4.5.3). In this way, the horizontal stresses are conveyed from the load frame model to the static geomechanical model representing the lateral boundary conditions. This step completes the boundary conditions and thus the setup of the static geomechanical model allowing for initial calculation.

7.4 Computing

Prior to calculation, the solution configuration has to be defined, such as the type of analysis and the solver used for calculation (4.6). The geomechanical reservoir model represents in general terms a finite element model, on which a static structural analysis is performed. A ‘static’ structural analysis does not incorporate time, but calculates the steady state of a model – contrasting to ‘transient’ analyses directly implementing time as dimension. This relation is not to be confused with the ‘static’ in the description of the model, which is meant in a geodynamical context and describes model’s focus on the recent ambient stress field as boundary condition.

Like all other numerical models in this study, the static geomechanical reservoir model is calculated using a direct solver (4.6), which represents the most robust solver for complex structural models comprising non-linear features. The build-up and discretization of the faults inevitably result in minor gaps and mesh penetrations. This nonconformance must be reduced by adjusting opposing pairs of contact elements to each other. Otherwise severe problems in contact solution and convergence of the numerical model emerge.

One set of boundary conditions describes the recent ambient stress field and represents the load of the geomechanical model. This load is applied in a single so-called load step, but the actual loading of the boundary conditions in the calculation is subdivided into several substeps.

The implemented faults as non-linearities require the full Newton-Raphson method for solving the systems of equations (Zienkiewicz and Taylor, 2005). The memory mode used for calculation strongly depends on the available hardware and especially on the provided amount of main memory (4.6). If all solver data can be accommodated in the main memory, the incore memory mode is preferably used. Otherwise the optimal out-of-core mode is applied.

The solution of the numerical model is obtained when forces and displacements inside the model are in equilibrium, i.e. as soon as their convergence values are below the convergence criterion. The converged model comprises the steady state solution of the structural analysis, and stresses and strains are then inferred from the displacements (2.1).

The objective of incorporating the case study geometry in high detail on field-scale yields large amounts of elements due to the need of resolving the geometrical details. The implementation of faults as non-linear contacts further increases numerical complexity. The static geomechanical model of the case study reservoir described in detail above comprises 3.81 million elements and 86 faults representing non-linear contacts. This amount of elements and the computing-intensive nonlinearities demand computing capacities for solving, which significantly exceed those of a local workstation. Reasonable calculation times can only be achieved with high-performance computing on dedicated compute servers. Two systems are used for calculation of the static model: the compute cluster of the bwGRiD[2] at the Albert-Ludwigs-Universität Freiburg and an in-house server of the group of engineering geology at the Technische Universität Darmstadt. In the following, the computing details and solution speed of the static geomechanical model on both systems are provided.

7.4.1 bwGRiD

The static geomechanical model is first calculated on compute servers of the bwGRiD at the Albert-Ludwigs-Universität Freiburg. Since 2010, the bwGRiD aggregates local computing cluster at eight Baden-Württemberg state universities into one single grid. A uniform working environment is provided at all bwGRiD facilities allowing easy location changes and the flexible usage of large amounts of computing resources. The cluster in Freiburg is accessed via a web portal, in which Ansys® Mechanical APDL® was implemented during and due to these studies.

In order to submit the model as batch job to the computing cluster, a special script file of the geomechanical model has to be generated. The default script file comprises large parts of coordinate information resulting from the geometry transfer. Script commands create splines, faces and volumes based on this data and discretize those. Eventually material parameters and boundary conditions are assigned. This pre-processing takes about 45 minutes for the static model using the default script. This is because pre-processing is not parallelized and must be performed sequentially on a single core.

The large time span for pre-processing leads to problems on the cluster. As soon as the job passed the queuing system and it is his turn to be calculated, the job is scheduled for using tens of cores, but it addresses only one. The job is thus aborted after some minutes, because of blocking resources without using them. In addition, the different operating systems on workstation and compute server seem to lead to small differences in the execution of geometry commands. Due to the geometrical complexity and these small (incomprehensible) differences, the geometry buildup commonly fails and the job is aborted before the model is solved.

Therefore a separate, robust computing script file is created from the final default script. This second script comprises a direct description of the finite element mesh. The individual definition of large amount of elements and nodes results in large ASCII file sizes of more than 1GB, but also in much faster pre-processing times of less than a minute. The material parameters, boundary conditions and

[2] bwGRiD (http://www.bw-grid.de), member of the German D-Grid initiative, funded by the Ministry for Education and Research (Bundesministerium für Bildung und Forschung) and the Ministry for Science, Research and Arts Baden-Württemberg (Ministerium für Wissenschaft, Forschung und Kunst Baden-Württemberg).

solution settings are implemented in this separate script. This approach is successfully applied for all model calculations on the cluster of the bwGRiD.

In first calculations, the static geomechanical model comprises a slightly coarser resolution with 120m of horizontal element size. In combination with all faults representing 86 non-linear contacts, this model yields more than 8 million equations to be solved (Tab. 7-11). The calculation is done using SMP parallelization (4.6.1) on a high-memory compute server (HP® ProLiant® DL785 G5) of the computing cluster in Freiburg. The chosen server provides 32 cores (AMD® Opteron® 8360, 2.44GHz) and 512GB of main memory. Due to the large amount of main memory, the model is calculated using the in-core memory mode (4.6). This job allocated 354GB of main memory during calculation and used effective I/O rates of 1874MB/s (Tab. 7-11). The latter elucidates the performance increase due to incore factorization of the matrix (4.6). Despite the large amount of 32 cores, the computational rate did not exceed 20.7GFlops – probably due to the bottleneck of the bus. This relatively low computational rate is regarded as the main reason for the model to require about 29 hours of solution time (Tab. 7-11).

The same model is also calculated on a second server of the bwGRiD cluster in Freiburg (Dell® PowerEdge® M610x), which comprises 12 cores of another type (Intel® Xeon® X5650, 2.66GHz) (Tab. 7-11). This server only provides 24GB of main memory. Hence the solver has to work in the optimal out-of-core memory mode resulting in only 19GB allocated memory and an effective I/O rate of 362 MB/s (Tab. 7-11). However, the solver reaches computational rates of 49GFlops and the model is solved in less than 15 hours. The significantly higher computational rate is assumed to be the crucial factor for this speed up and is referred to the different type of CPU, which seems to be more suitable to the calculation demands of the geomechanical models of this study.

7.4.2 In-House Computing Capability

The experiences gained in the usage of the bwGRiD cluster in Freiburg are considered during the purchase of a dedicated compute server at the engineering geology group at the Technische Universität Darmstadt. The increase in resolution from 120m to 100m horizontal element size rises the amount of elements from 2.6 to 3.8 million, and the equations to be solved from 8 to 11.6 million (Tab. 7-11). This high resolution model demands more than 520GB of main memory to be calculated in-core. Due to the fact that compute servers comprising more than 512GB of main memory are hardly affordable, the configuration of the server was focused on fast hard drives to swap solver data.

The high resolution version of the static model is finally calculated on an in-house compute server (Dell® PowerEdge® T710) that comprises two powerful hexacore processors (Intel® Xeon® X5690, 3.46GHz, 12M cache, 6.4GT/s) providing 12 cores in total, 192GB of main memory (12x16GB), together with a redundant array of independent disks (RAID) of six hard drives (SAS, 15k, 6GBit/s).

The use of a specialized in-house server drops the need for a separate optimized compute script saving a significant amount of time. Best performance results of the calculation of the static geomechanical model on this in-house server state computational rates of 51.18GFlops and effective I/O rates of 796MB/s (Tab. 7-11). This yields a solution time of about 19 hours.

The relatively high I/O rate can be referred to the array of high-performance hard disks, which plays an important role when using the out-of-core memory mode. Experience gained at the bwGRiD cluster thus successfully helped to configure an appropriate in-house server.

	Server #1 bwGRiD / Univ. Freiburg	Server #2 bwGRiD / Univ. Freiburg	In-house server TU Darmstadt
Model Resolution	Medium	Medium	High
Horizontal Element Size	120 m	120 m	100 m
Amount of Elements	2,657,632	2,657,632	3,810,784
Number of Equations	8,044,515	8,044,515	11,599,571
CPU Type	AMD® Opteron® 8384 2.64 GHz	Intel® Xeon® X5650 2.66 GHz	Intel® Xeon® X5690 3.46 GHz
Number of Cores	32	12	12
Parallelization	SMP	SMP	SMP
Main Memory	512 GB	24 GB	192 GB
Memory Mode	in-core	optimal out-of-core	optimal out-of-core
Allocated Memory	353.68 GB	19.16 GB	29.75 GB
Equation Solver Computational Rate	20.73 GFlops	49.30 GFlops	51.18 GFlops
Equation Solver Effective I/O Rate	1873.7 MB/s	361.6 MB/s	796.0 MB/s
Pre-Processing Time	78.3 s	43.1 s	45.1 min
Solution Time	1d 05h 42min	14h 30min	19h 04min

Tab. 7-11. Overview on representative computing details of the static geomechanical model with medium and high resolution calculated on two servers of the bwGRiD cluster in Freiburg and the in-house server at the Technische Universität Darmstadt.

7.5 Model Calibration

The fundamental purpose of calibrating the static geomechanical reservoir model is to correlate the model to reality. It is to determine whether the model reproduces measured stress magnitudes and orientations that are not regarded as input data. Therefore the modeling outcome is compared to separately compiled, reservoir-specific measurements representing the calibration data (7.2.2). This comparison evaluates the results of the geomechanical model and improves the model in a next step by adjusting poorly constrained parameters.

The following chapters describe the calibration workflow and the variations of uncertain parameters to find the best fit between modeling results and calibration measurements (7.5.1). Furthermore the incorporation of lateral variations in lithostatic load in the boundary conditions is discussed due to the presence of salt in the overburden (7.5.3). The calibration outcome is finally summarized and discussed (7.5.4, 7.5.5).

7.5.1 Workflow & Variations

The calibration workflow starts with preparatory work concerning the handling of stress results of the geomechanical model. Contour and vector plots of various quantities provide good overviews on the area-wide distributions. In order to compare the modeling outcome with field measurements at distinct subsurface locations, however, these results of the model have to be extracted more precisely. Therefore, the coordinates of all well paths are determined in the Petrel® project and used to generate the same paths inside the finite element program. This allows the selection of all elements in the geomechanical model cut by the drilling paths of specific wells (Fig. 7-11).

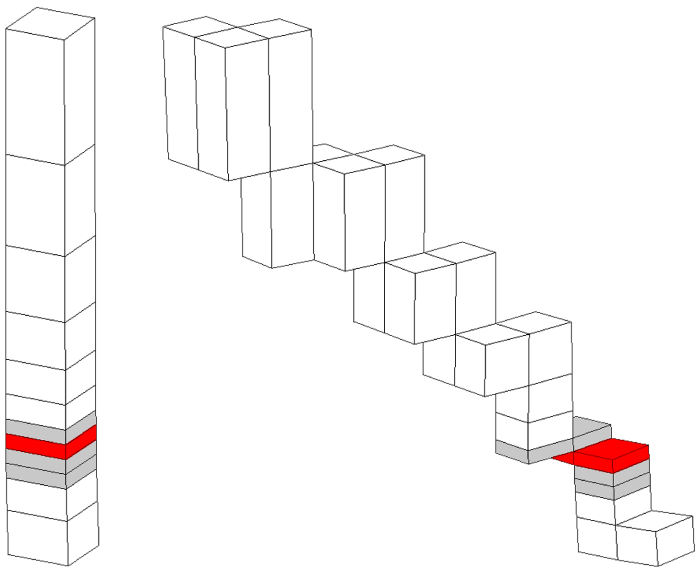

Fig. 7-11. Elements cut by the almost vertical drilling path of well A1 (left) and the deviated path of well C9 (right). Modeling results for calibration purposes are taken from the second element layer (red) of the reservoir horizon (grey).

Magnitudes and direction cosines of the principal stresses at the nodes of those elements are extracted from the model (Fig. 7-11). This is done for all wellbores by a self-written macro in the internal script language of the finite element program (Ansys® Mechanical APDL®). The macro generates ASCII files with node-specific magnitude and orientation information for the elements of each wellbore. This information is directly subdivided by the macro into three blocks corresponding to the overburden, reservoir and underburden layer (Fig. 7-11).

Stress orientations and magnitudes for the calibration process are taken from the specific depth the respective calibration data belongs to. Due to the vertical mesh resolution, most results are taken from the second of the four layers of the reservoir horizon (Fig. 7-11). The results from the uppermost layer of reservoir nodes are affected by the transition of material properties from the overburden to the reservoir layer and have to be neglected. By using the drilling paths taken from the Petrel® project and the respective depth of calibration data, a comparison at the correct subsurface location is ensured. This process is only limited by mesh resolution.

Principal stress magnitudes are re-calculated to [MPa]. This identifies the vertical, maximum and minimum horizontal stress in the proposed normal faulting regime. Principal stress orientations are derived from the direction cosines. The direction of maximum horizontal stress is calculated to an azimuth value relative to geographic north for a direct comparison with published data. After the optimal handling of modeling results is elaborated, it is first performed on the results of the default version of the static geomechanical model to start the calibration process.

In the default version of the static geomechanical model, some parameters are less well constrained than others. Within the calibration process, these uncertain parameters are varied within their geological limits yielding multiple variations of the static geomechanical model (Tab. 7-12). The results of these individual model configurations are compared to calibration data searching for the best fit. The most prominent of the poorly constrained parameters are the friction coefficient of the faults and the magnitude of the maximum horizontal stress.

The vertical and the minimum horizontal stress are constrained by integrating the density of the overburden and measuring the fracture closure pressure during extended leak-off tests, respectively (7.2). Information on the magnitude of the maximum horizontal stress is usually not available but could be determined by empirical relationships using the shape of borehole breakouts, for instance (Zoback et al., 2003). However, no suitable borehole breakouts are found in the image logs provided for the case study reservoir.

Model Version	SHmax / SV	Shmin / SV	Friction coefficient of faults	Alternative friction for E-W trending faults
Default	0.9	0.6	0.40	-
1	0.9	0.6	0.30	-
2	0.9	0.6	0.20	-
3	0.9	0.6	0.15	-
4	0.9	0.6	0.10	-
5	0.9	0.6	0.05	-
6	0.9	0.6	0.6	0.1
7	0.9	0.6	0.1	0.6
8	0.7	0.6	0.1	-
9	0.7	0.65	0.1	-
10	0.85	0.8	0.1	-

Tab. 7-12. Overview on the 10 major model variations that are calculated during the calibration of the static geomechanical reservoir model. In this calibration process, model version #4 yielded the best match between modeling results and measurements. Direction-dependent fault friction coefficients are a promising approach, but yielded no superior match so far.

Hence, this magnitude is varied and tested in the calibration process. The maximum horizontal stress is lowered to 0.85 & 0.7 · SV, while the minimum horizontal stress was partly increased at the same time (Tab. 7-12).

The most promising parameter for model calibration is the friction coefficient of the faults due to its high impact on in situ stress distribution (6.1). Starting with a default value of 0.4, it was successively lowered in multiple steps to observe if increasingly pronounced stress perturbations yield a better match with the measured stress values (Tab. 7-12). The impact of direction-dependent friction coefficients is additionally tested. Besides some minor, preliminary calculations of the static model and in addition to the default version, ten modeling scenarios are solved during the calibration process in total (Tab. 7-12).

The calculation of the individual models is time-consuming. Solution times vary between 19 to 50 hours depending on the applied hardware. Post-processing of each model, i.e. the result analysis, calculations and comparison, is also labor-intensive due to the size of the result files.

7.5.2 Preliminary Calibration Results

The initially assumed default configuration of the static geomechanical model already yields promising results. During calculation of the stated calibration scenarios (Tab. 7-12), an improved and relatively best fit between modeling results and measurements of stress magnitudes and orientations is achieved with a friction coefficient of 0.1 and a horizontal stress configuration of SHmax / Shmin = 0.9/0.6 · SV (Tab. 7-12).

Higher friction coefficients yield less pronounced stress perturbations providing a worse match with the measured values, whereas lower values produce a wrong trend compared to field observations. Lowering of the maximum horizontal stress magnitude yields a worse match with magnitudes derived from the ultrasonic measurement results of the internal report #2 and #3. Increased minimum horizontal stress magnitudes result in a general misfit with the outcome of the hydraulic fracturing data. Stress perturbations in those models with changed horizontal magnitudes do not provide local stress distributions that compensate the general deviation.

The application of direction-dependent friction coefficients represents a promising approach due to its more fault-specific characterization. However, a general assumption of separating E-W trending faults to a group of higher or lower friction coefficients compared to the rest of the faults yielded no better match. This suggests that the grouping of faults to sets of constant friction must be more specific and maybe based on their tectonic history. Such information could be deduced from the following dynamic modeling approach (8).

The satisfactory match resulting from calibration is best revealed by an overview map showing all deviations between measured and modeled stress magnitudes and orientations indicated at the specific wellbore locations (Fig. 7-12, Fig. 7-13). Both, the modeled stress magnitudes and the orientations, match well with the measured calibration data – especially regarding the potential errors of measurements (7.2.2).

The results show a significant discrepancy only for the minimum horizontal stress magnitudes modeled and measured by ultrasonic wave velocity analysis (WVA) on drill cores (Fig. 7-12). While the maximum horizontal stress magnitudes achieve a very good fit and match the overall magnitude assumptions, the respective minimum horizontal stress magnitudes are considerably higher than the modeled values and those measured by hydraulic fracturing (7.2.2).

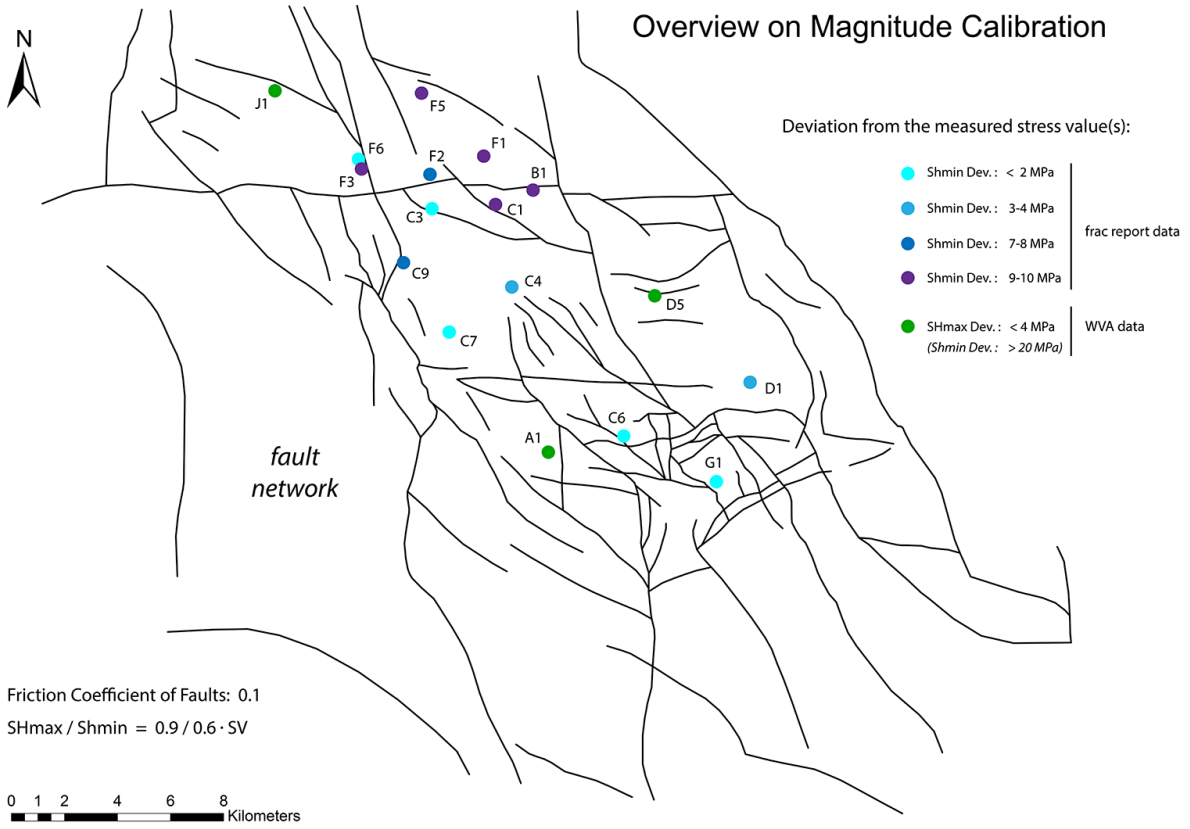

Fig. 7-12. Top view on the fault network of the case study reservoir with all deviations between measured and modeled horizontal stress magnitudes indicated at the specific wellbore locations. Measurement results are taken from reports on hydraulic fracturing and ultrasonic wave velocity analysis (WVA) on drill cores.

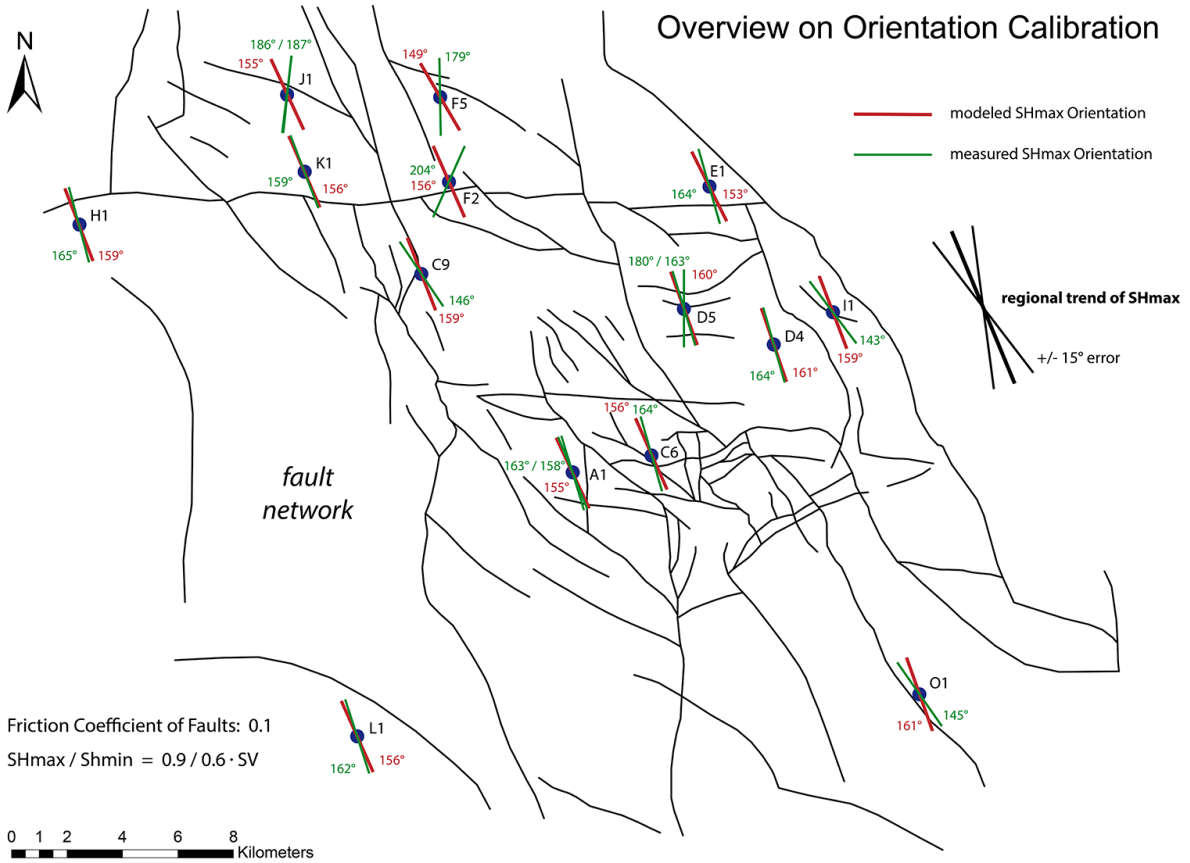

Fig. 7-13. Top view on the case study fault network with all measured and modeled orientations of the maximum horizontal stress indicated at the specific wellbore locations. Measurement results are taken from internal report #2 / #3 and from Grote (1998). Both used ultrasonic wave velocity analysis (WVA) on drill cores and breakout orientation logs (BOL).

Despite significant stress perturbations, the model cannot reproduce these high minimum horizontal stress magnitudes. This underlines the assumption that there is a methodological problem in the ultrasonic determination of minimum horizontal stress magnitudes as proposed by the project partners. Therefore these values are neglected in the evaluation of calibration results (7.2.2).

Except for these measurements, the horizontal stress magnitudes match very well. Measured magnitudes of the maximum horizontal stress available at three wellbores differ less than 4 MPa from modeling results (Fig. 7-12). At 7 out of 14 wellbores, the modeling results of minimum horizontal stress magnitude deviate also less than 4MPa from reliable measurements – and at no wellbore more than 10MPa (Fig. 7-12). This represents a satisfactory magnitude match regarding the unknown error of minimum horizontal stress measurements in hydraulic fracturing (7.2.2).

Field measurements and the geomechanical model show relatively homogeneous orientations of the horizontal stresses throughout the reservoir. Only 3 of 14 wells show deviations in orientation between measurement and modeling result larger than the stated error of 15° (Fig. 7-13). This wide-range concordance in homogeneous direction also indicates the good calibration result, since significant orientation perturbations are predicted by the model, but not at the specific wellbore locations.

The overviews on calibration results also reveal a striking spatial distribution of deviations. In the comparing overviews on magnitudes and orientations (Fig. 7-12, Fig. 7-13), the most pronounced deviations between modeling results and measurements focus on the northern part of the case study reservoir. In this area, a large salt wall crosses the reservoir in the overburden (Fig. 7-14).

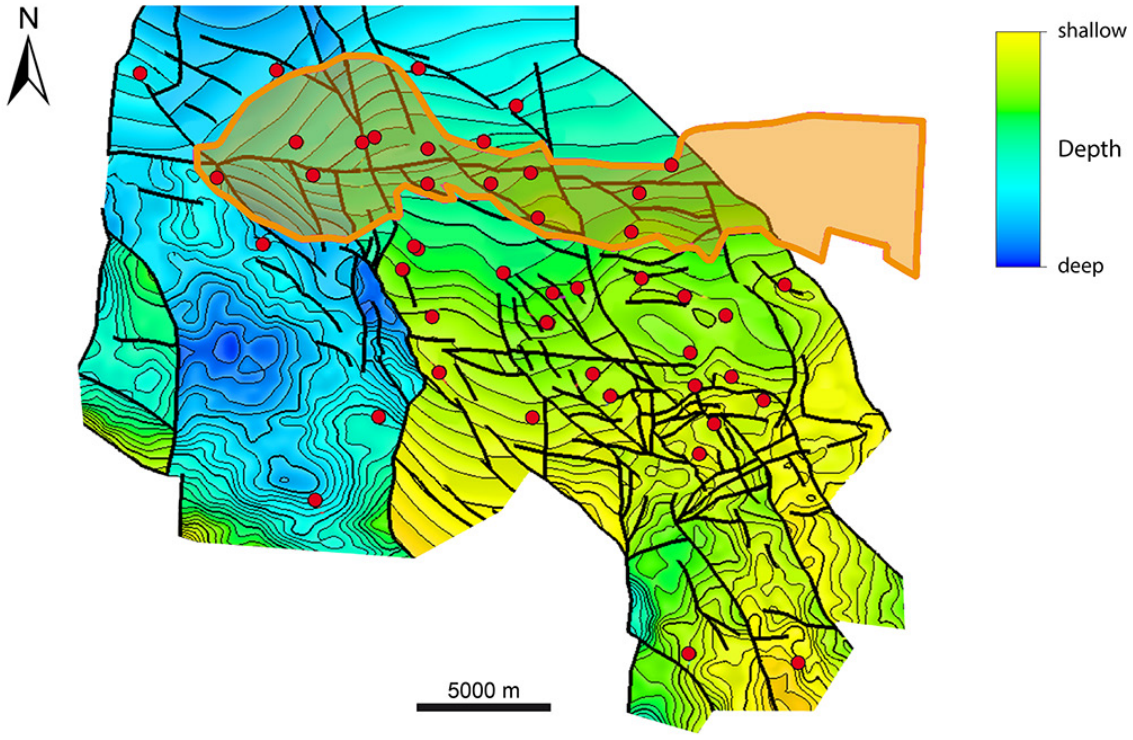

Fig. 7-14. Top view on the depth-contoured map of the case study reservoir. Faults (black) and wells (red) are indicated together with the outline of the overburden salt wall (orange) in the northern part of the reservoir.

A connection between measurement-modeling deviations and salt occurrence is suggested by the spatial overlap, but also by the nature of misfits. All deviations in minimum horizontal stress magnitude exceeding 4MPa are caused by relatively low measured magnitudes and higher modeled magnitudes. This fact supports the hypothesis of a potential salt impact. Lower magnitudes measured can be attributed to the presence of less dense salt in the overburden lowering the vertical stress and

thereby also the horizontal stress magnitudes. In order to test this hypothesis, the salt body influence is regarded in the static geomechanical model in a following final step of calibration.

7.5.3 Salt Incorporation

The large salt wall outlined in the depth-contoured map of the reservoir (Fig. 7-14) is located in the Zechstein sequence above the Rotliegend reservoir sandstone. The incorporation of the salt body in the geomechanical model thus can be achieved by locally adjusting the top boundary condition, while the internal setup of the model is not affected. In order to assess the dimensions of the salt wall, the project partners provided a schematic overview (Fig. 7-15). This overview describes the outlines of the overhang and the stem of the salt body in top view and in cross-section.

The schematic top view on the northern part of the reservoir shows the lateral dimensions of the salt overhang and the position of the salt stem (Fig. 7-15). The salt wall is E-W elongated. It extends several tens of kilometers in this direction and comprises a width in N-S direction of about 4km. The WSW-ENE oriented schematic cross section through the salt stem is indicated by a grey line (Fig. 7-15). This cross section reveals the vertical position of the Rotliegend reservoir sandstone, the overlying stratigraphic successions and the Zechstein salt wall (Fig. 7-15).

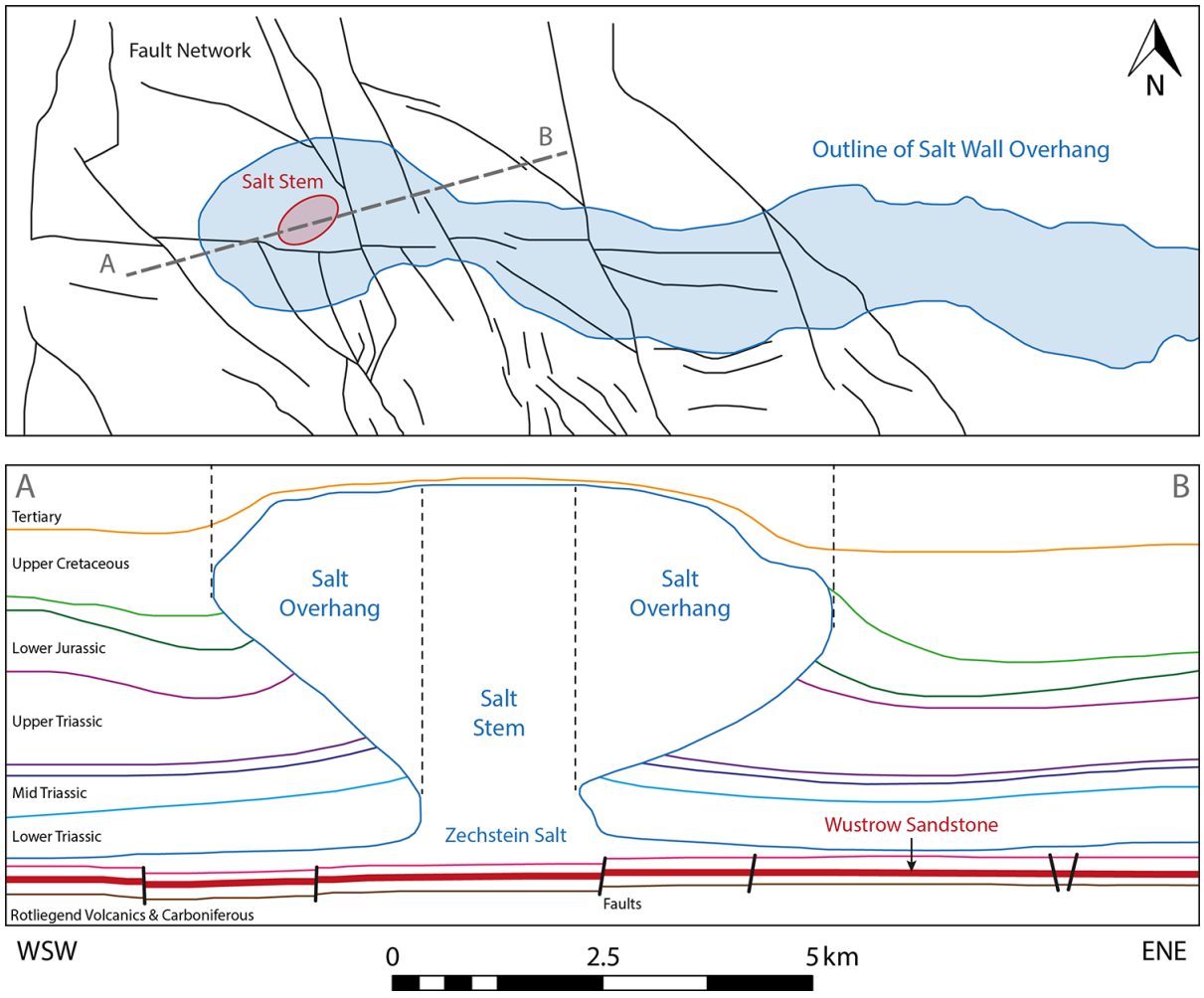

Fig. 7-15. Schematic overview on the northern salt wall in the reservoir overburden. The top view (top) shows the lateral dimensions and the position of the salt wall, salt stem and the cross section (bottom). Regarding an average reservoir depth of 4800 m, the cross section reveals a maximum salt thickness at the stem of about 4 km, which is gradually decreasing in the overhang areas. The reservoir horizon (red) and overlying stratigraphic sequences are outlined in the cross section as well.

The salt body exhibits the typical shape and comprises a thickness of about 4km at its stem, which is gradually decreasing towards the outer areas of the overhang (Fig. 7-15).

In addition to these schematic overviews, highly detailed point clouds representing the top and bottom surfaces of autochthonous and allochthonous salt are provided for the case study area. This data includes the description of the northern salt wall as allochthonous salt body (Fig. 7-16). The point clouds reveal the specific 3D shape of the salt wall, its lateral dimensions and thickness at all subsurface locations in high detail (Fig. 7-16). The distribution and characteristics of smaller allochthonous salt bodies and the layer of autochthonous Zechstein salt is additionally covered by this dataset.

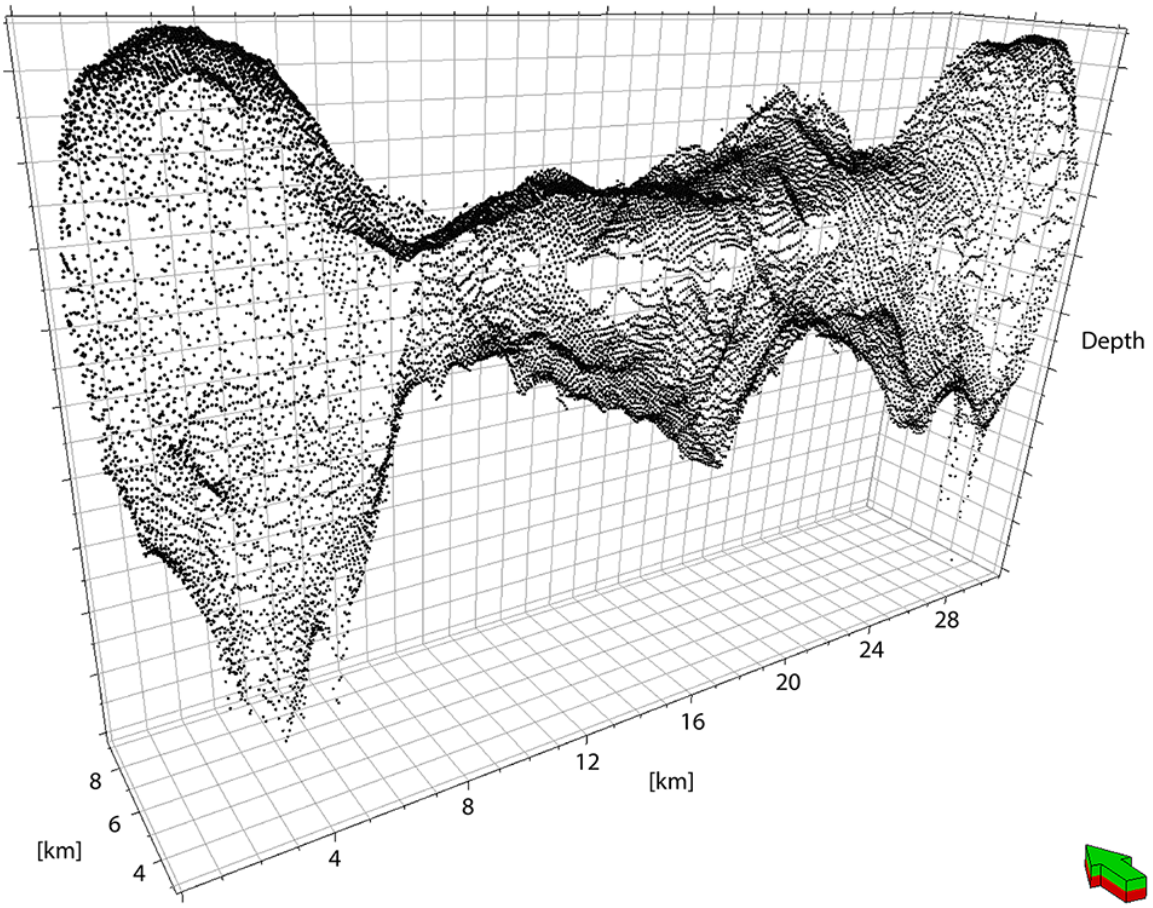

Fig. 7-16. Perspective side view on the point cloud describing the geometry of the northern salt wall in the overburden of the reservoir. The green arrow is N-S directed. This detailed description elucidates the western position of the main salt stem and scaling indicates the large lateral extent. This graphical representation is vertically exaggerated.

This highly detailed information on the thickness distribution and lateral dimension of the Zechstein salt can be used to calculate and apply respectively highly accurate modifications of the top boundary condition. However, the resolution of this data exceeds the spatial resolution of the geomechanical model. Information on the spatial extent of overburden salt thus has to be adjusted to model resolution.

Therefore, the overburden pressure representing the top boundary condition of the geomechanical model is modified at distinct pre-existing areas. These areas are selected from the face pattern of the model, which results from faults and auxiliary lines (Fig. 7-17). The lateral dimensions of the salt wall are regarded in the selection of faces in the best way possible.

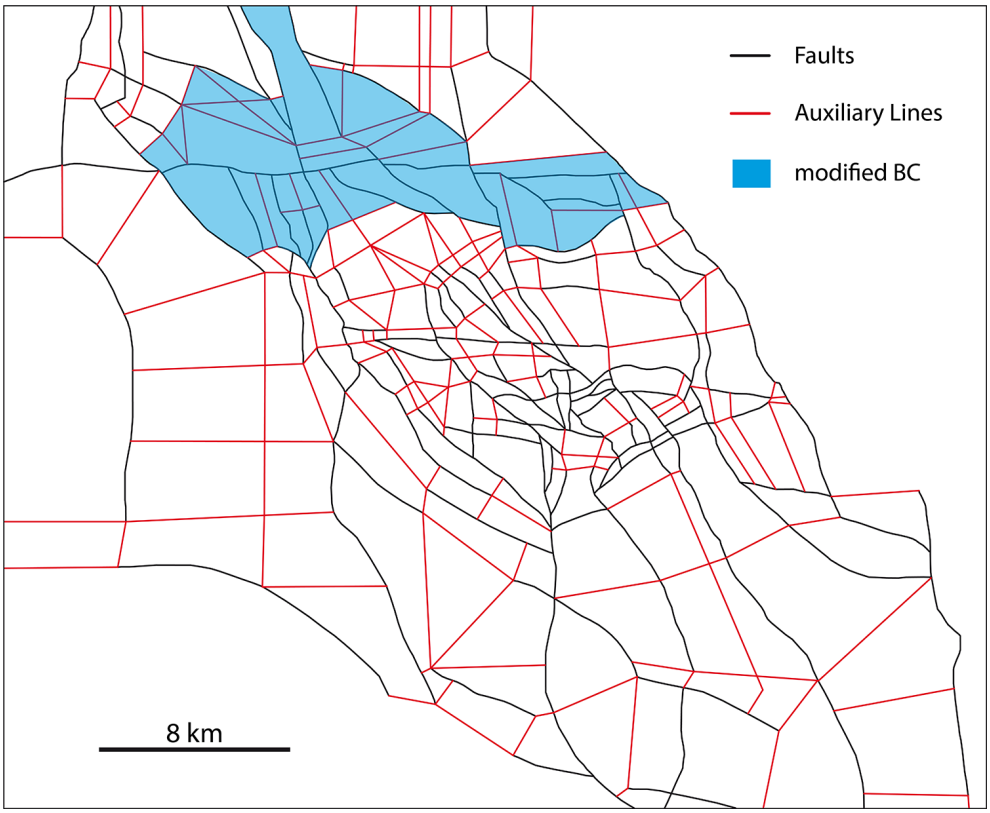

Fig. 7-17. Top view on the face pattern of the static geomechanical reservoir model. This pattern arises from the trace of faults (black) and the auxiliary subdivisions (red), which are incorporated to accurately reproduce the horizon topology. The area affected by the northern salt wall is defined by selecting the respective faces (blue). At these faces, the lithostatic pressure load is modified representing the top boundary condition (BC).

In the static geomechanical model calculated so far, the applied lithostatic load is derived from the density of the overburden integrated at three wells and is averaged to a representative value for the entire top of the model (7.2.1). Rock salt has a relatively low density and the spatial variation in salt thickness had not yet been taken into account in the integration of the overburden density. The amount of modification of the lithostatic pressure at the selected areas thus depends on the proposed density reduction by the salt wall. In addition to the spatial distribution of the Zechstein salt, average salt densities are provided by gravity modeling studies of the project partners.

The average densities are used in combination with an averaged assumed thickness of the salt wall (Tab. 7-13). The average salt thickness is assumed to be 2km for the entire area covered by the salt wall. This approach is justifiable due to the accuracy in applying the top boundary condition to the pre-existing faces and due to the uncertainty of provided values (Fig. 7-17). These densities are averages and do not consider locally occurring anhydrite accumulations, for instance, which counteract the pressure reduction due to their high densities. It is thus reasonable to assume an average salt thickness between the maximum thickness of 4km at the stem and the thinner areas in the overhang (Fig. 7-15). By locally reducing the lithostatic pressure load on the top of the model, the vertical stress is expected to decrease in these areas, but also the maximum and minimum horizontal stress magnitudes due to the mechanical effect of the Poisson's ratio.

The modeling results after incorporation of salt effects show that the magnitude of vertical stress at reservoir level and the elastic equivalent strain are significantly affected by the locally reduced pressure load (Fig. 7-18). The maximum and minimum horizontal stress magnitudes are also reduced as expected, but only to a minor amount. The modeled horizontal stress orientations do not change significantly as well.

Despite the relatively low impact of the salt implementation on the horizontal stresses, the salt is part of the final calibrated static geomechanical reservoir model of the case study as it definitely improves the model setup.

Area	Material	Density	Thickness	Pressure Load at 4 km depth
Salt Wall Area	Salt	2170 kg/m³	2 km	89.493 MPa
	Host Rock	2391 kg/m³	2 km	
Rest of Reservoir	Host Rock	2391 kg/m³	4 km	93.836 MPa

Tab. 7-13. Summary of the boundary conditions at the top of the static geomechanical model at 4km depth. In the area of the salt wall, 2km out of 4km of overburden are assumed to be salt leading to a reduced pressure load. The integrated density of the overburden host rock is an average taken from the internal reports #2 and #3, whereas the salt density is derived from gravimetric modeling provided separately by the project partners.

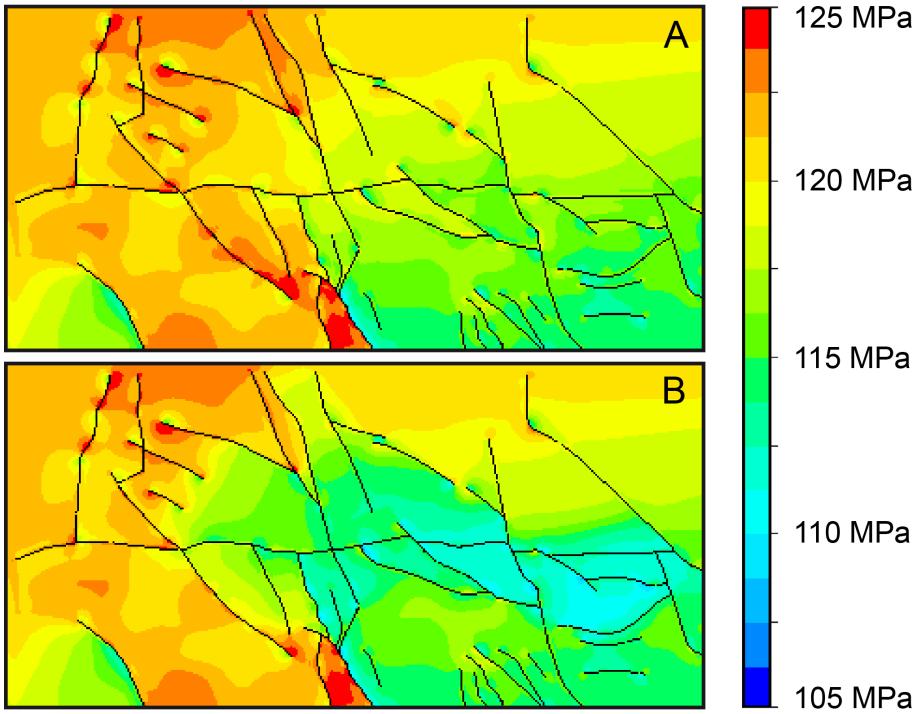

Fig. 7-18. Top view on the vertical stress magnitudes at reservoir level regarding exclusively host rock in the overburden (A) and considering 2km of rock salt (B). The local reduction of lithostatic load leads to significant differences in vertical stress. The scaling is constant at both contour plots.

7.5.4 Final Calibration Results

The final calibration results of the static geomechanical model show an overall satisfactory match between modeling outcome and stress measurements. Incorporating the overburden salt yields some minor changes in the magnitudes of maximum and minimum horizontal stress and further improvement. Due to the small modifications, the overview plots on general deviations shown above are still valid for the best fit model (Fig. 7-12, Fig. 7-13). In summary, all 14 minimum horizontal stress magnitudes measured during hydraulic fracturing deviate by less than 10MPa from the modeling results, half of them deviate by no more than 4MPa (Tab. 7-14, Fig. 7-19).

Well	**Measured** Minimum horizontal stress	**Modeled** Minimum horizontal stress	Deviation
B1	61.60 MPa	72.35 MPa	10.75 MPa
C1	63.70 MPa	73.36 MPa	9.66 MPa
C3	70.88 MPa	71.81 MPa	0.93 MPa
C4	66.00 MPa	69.17 MPa	3.17 MPa
C6	72.00 MPa	70.06 MPa	1.94 MPa
C7	66.60 MPa	67.06 MPa	0.46 MPa
C9	76.30 MPa	69.87 MPa	6.43 MPa
D1	66.21 MPa	70.24 MPa	4.03 MPa
F1	59.60 MPa	68.98 MPa	9.38 MPa
F2	74.90 MPa	67.64 MPa	7.26 MPa
F3	60.49 MPa	70.10 MPa	9.61 MPa
F5	67.40 MPa	75.13 MPa	7.73 MPa
F6	67.55 MPa	68.46 MPa	0.91 MPa
G1	71.70 MPa	71.45 MPa	0.25 MPa

Tab. 7-14. Overview on the measured magnitudes of minimum horizontal stress and the modeled values of the calibrated geomechanical model. The respective deviation is stated as absolute value.

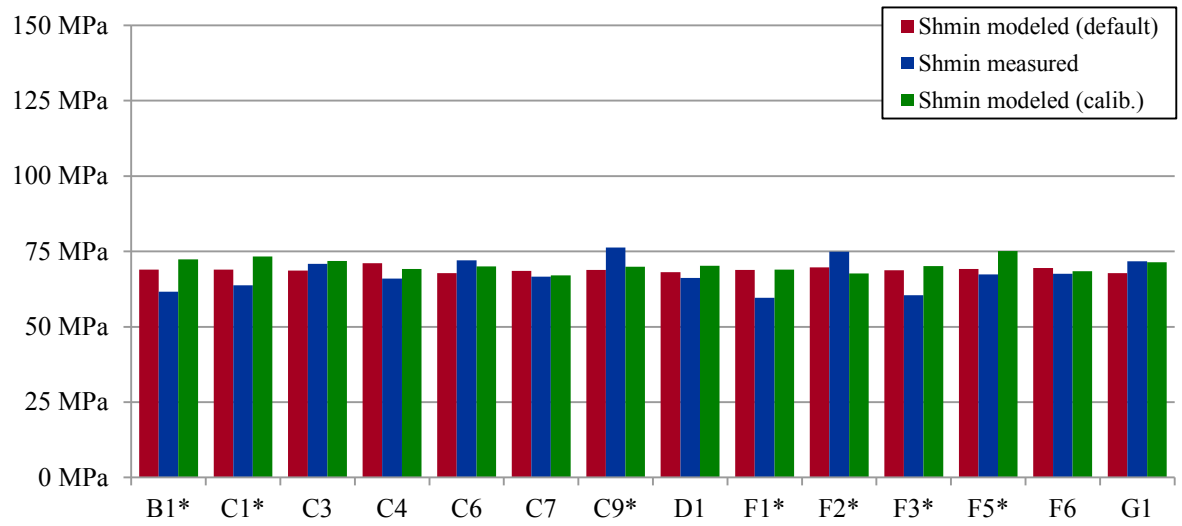

Fig. 7-19. Diagram comparing the measured magnitudes of the minimum horizontal stress (Shmin) with the values of the default and calibrated geomechanical model. Only 7 wellbores (*) show a deviation larger than 4MPa and all of them are located in the northern part of the reservoir.

Those wells, at which the deviation of minimum horizontal stress magnitude is larger than 4MPa are all located in the northern part of the reservoir under or close to the salt wall (Fig. 7-12, Fig. 7-19, 7.5.5). Measurements of the maximum horizontal stress magnitude do all match the modeled values very well (Tab. 7-15, Fig. 7-20). The respective deviations are always less than 4MPa. The diagrams comparing measured and modeled magnitudes of both horizontal stresses further indicate the improvement due to calibration by additionally plotting the results of the default model (Fig. 7-19, Fig. 7-20).

In 11 of 17 horizontal stress magnitude comparisons, the calibration yields improved trends of the modeled values approaching the measurements. This includes all three maximum horizontal stress comparisons, for which the calibration yields smaller deviations. Only in six of the seven most deviating cases in the minimum horizontal stress comparison, the calibration resulted in a wrong trend. The deviations at those northern wells are suggested to be affected by the salt.

Well	**Measured** Maximum horizontal stress	**Modeled** Maximum horizontal stress	Deviation
A1	95.30 MPa	96.54 MPa	1.24 MPa
D5	97.05 MPa	93.96 MPa	3.09 MPa
J1	97.90 MPa	98.53 MPa	0.63 MPa

Tab. 7-15. Overview and comparison of the measured and finally modeled magnitudes of maximum horizontal stress. The respective deviation is stated as absolute value.

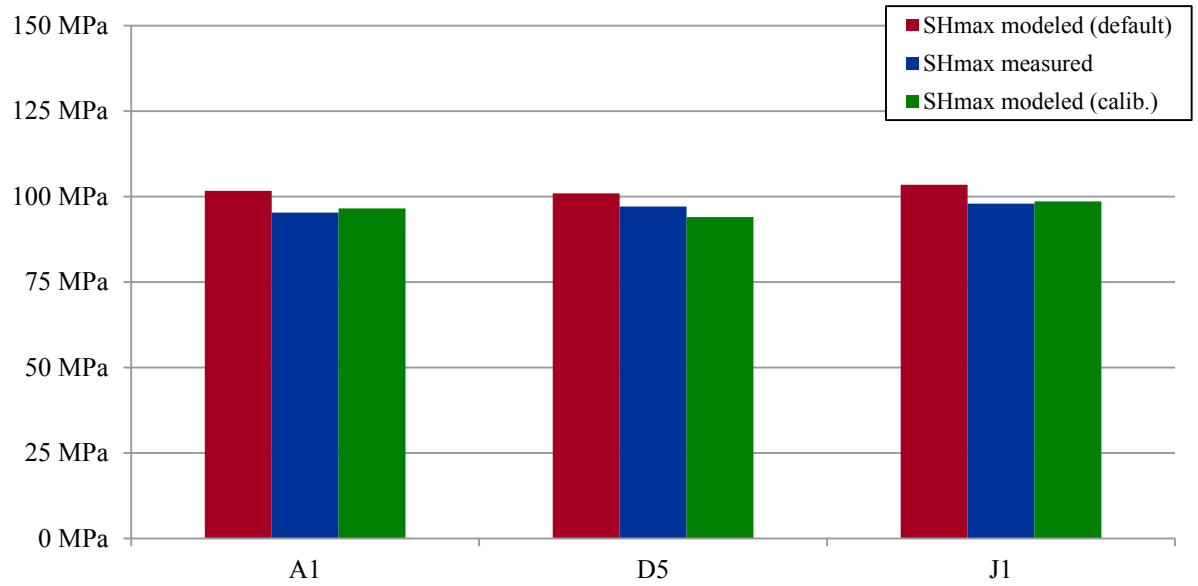

Fig. 7-20. Diagram comparing the measured magnitudes of the maximum horizontal stress (SHmax) with the values of the default and calibrated geomechanical model. At all wellbores, the calibration yields improved values.

A final correlation diagram elucidates the improvement in the match of horizontal stress magnitudes due to calibration (Fig. 7-21). This diagram includes minimum and maximum horizontal stress magnitudes before and after calibration and indicates the proximity to the theoretical perfect fit. Those wellbores showing large deviations in minimum horizontal stress magnitude, which potentially result from the impact of the northern salt wall, are left out in this plot.

In addition to the minimum and maximum horizontal stress magnitudes, the measured and modeled orientations of the maximum horizontal stress are summarized (Tab. 7-16, Fig. 7-22). Except for 3 out of 14 wells, all measured orientations deviate no more than the stated error of 15° from the modeling results.

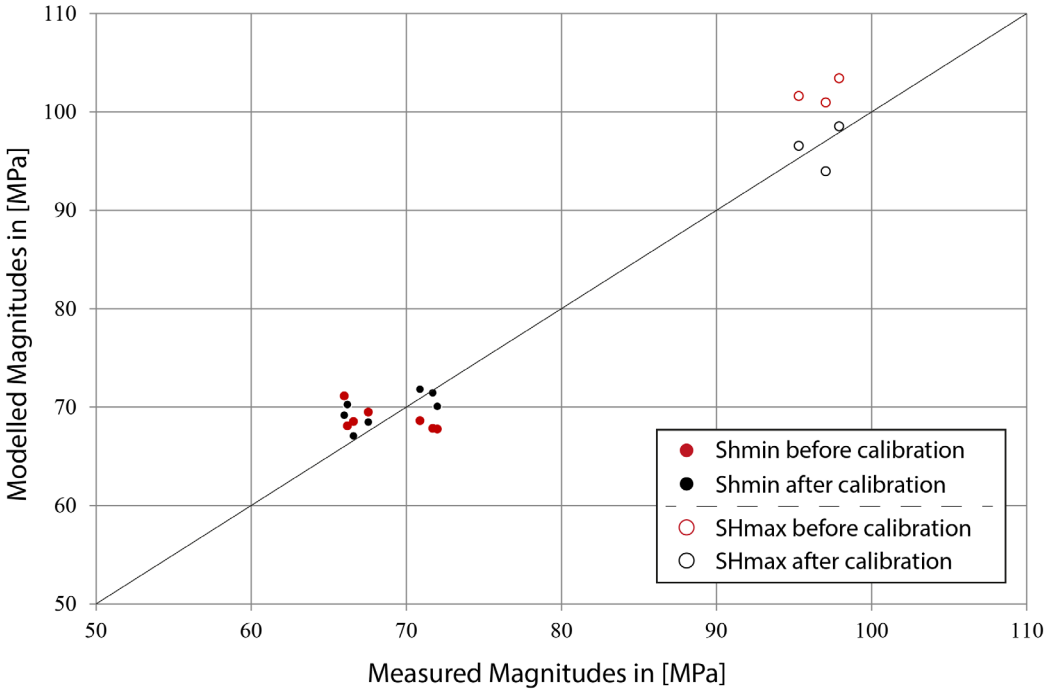

Fig. 7-21. Correlation between measured and modeled magnitudes of the minimum and maximum horizontal stress before (red) and after calibration (black). Each point represents the data at a single wellbore. Calibration leads to a vertical shift, since only the modeled magnitude is affected. For a perfect fit, all points would lie on the bisecting line of the diagram. Northern wellbores that are potentially affected by the salt and showing deviations in minimum horizontal stress of more than 5MPa are neglected in this plot.

The adequacy of the stated measurement error of 15° is underlined by the two available orientation measurements at well D5 deviating from each other by 17° (Fig. 7-22). Both modeled and measured orientations of the maximum horizontal stress follow the regional NNW-SSE trend. Calibration leads only to minor changes in orientation of maximum horizontal stress within the range of error (Fig. 7-22). However, the increase in orientation perturbations in the calibrated model in relation to this constant orientation distribution at the wellbore locations indicates good quality of the model from the beginning. Significant changes in modeled orientation would result in misfits at the majority of wellbores.

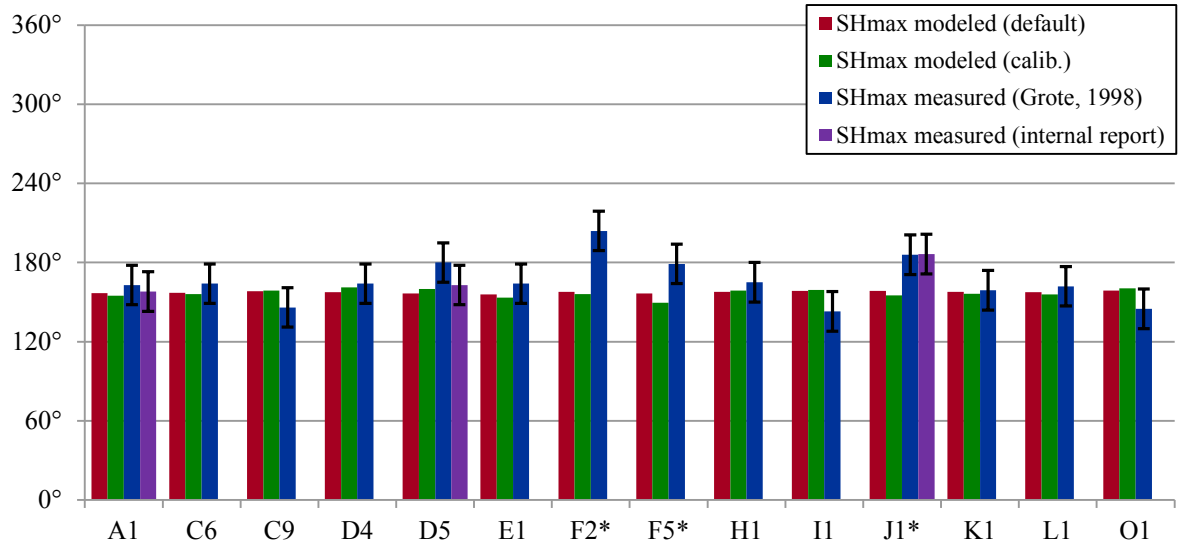

Fig. 7-22. Diagram comparing the measured orientations of the maximum horizontal stress (SHmax) with the orientations of the default and calibrated geomechanical model. Error bars indicate the stated measurement error of 15°. Independent orientation measurements at well D5 elucidate that this error is appropriate. Only 3 wells show deviations between measured and modeled orientations larger than this range of error, all of them located in the northern part of the reservoir.

Well	Modeled SHmax orientation	Measured SHmax orientation (internal report)	Measured SHmax orientation (Grote, 1998)	Deviation from intern report	Deviation from Grote (1998)
A1	154.9 °N	158 °N	163 °N	3.1 °	8.1 °
C6	156.1 °N		164 °N		7.9 °
C9	158.7 °N		146 °N		12.7 °
D4	161.1 °N		164 °N		2.9 °
D5	160.0 °N	163 °N	180 °N	3.0 °	20.0 °
E1	153.3 °N		164 °N		10.7 °
F2*	156.2 °N		204 °N		47.8 °
F5*	149.6 °N		179 °N		29.4 °
H1	158.8 °N		165 °N		6.2 °
I1	159.2 °N		143 °N		16.2 °
J1*	155.1 °N	187 °N	186 °N	31.4 °	30.9 °
K1	156.4 °N		159 °N		2.6 °
L1	155.9 °N		162 °N		6.1 °
O1	160.5 °N		145 °N		15.5 °

Tab. 7-16. Measured and modeled maximum horizontal stress orientations as azimuth in [°N] listed together with the respective deviations. Both measurement sources state an error of ±15°. The difference in measurements at well D5 elucidates this uncertainty. Three wells (*) show deviations between modeling results and measurements larger than the range of error.

The three deviating wells show the respective deviations before and after calibration, and are also located in the northern part of the reservoir under or close to the salt wall. Since orientation perturbations are most controlled by the faults, this suggests missing or imprecise information on fault geometry, for instance (7.5.5).

In general, the final results of calibration yield a satisfactory match between measured and modeled horizontal stress magnitudes and orientations. In about 80% of all comparisons between modeled and measured maximum horizontal stress orientation, the modeling outcome matches the respective measurement within the stated range of error (Tab. 7-16). The evaluation of the match of minimum horizontal stress magnitudes is complicated due to a missing measurement error of the magnitudes obtained during extended leak-off tests. However, it is assumed that a deviation of up to 10MPa is beyond the range of measurement error (Tab. 7-14) and suggests some missing information – probably influenced by the salt occurrence in these areas.

Deviations of up to 4MPa are assumed to be within the range of measurement error and thus the match especially of maximum horizontal stress magnitudes is very satisfactory (Tab. 7-15). Moreover the respective comparison diagram elucidates the positive impact of the calibration (Fig. 7-20, Fig. 7-21). It is important to note that a decrease in deviation between modeling and measurements of any type, below the stated measurement error are not providing further reliability of the results.

This satisfactory match in calibration could be further improved by additional more specific adjustments of salt incorporation and fault friction, for instance. In the following, the calibration outcome is discussed in detail (7.5.5).

7.5.5 Discussion of Calibration

The final stage of calibration provides the best fit between modeling results and field measurements. It is based on the application of a uniform friction coefficient of 0.1 to all faults. This friction coefficient is low, but not unrealistically low. As other studies show, such a value can be reached by intensive cataclasis or mineral smearing in a fault (Carpenter et al., 2009; Stankowich and Ewy, 2003). Although this friction coefficient is assumed in model calibration, it solely represents the best obtained fit and does not necessarily reflect reality for the entire fault network. This value might be true for some faults or fault segments, whereas individual other faults could exhibit significantly higher values. Consequently, the application and assumption of this coefficient comprises space for fault-specific improvement.

One of the striking observations in the calibration results is the relatively low range of modeled and measured orientations of the maximum horizontal stress around the regional trend of NNW-SSE (157.5°N). Modeled orientations at the wellbore locations of the respective measurements furthermore show no significant increase in re-orientations due to calibration. This generally low amount of orientation perturbations in the reservoir can be explained by the dominant maximum horizontal stress in the recent state of stress. Such a dominant maximum horizontal stress magnitude, considerably exceeding the minimum horizontal stress, prevents strong re-orientations of in situ stress (Yale, 2003). In this way, the assumption of the maximum horizontal stress magnitude being $0.9 \cdot SV$ is also indirectly proven to be correct, since the measurements confirm the low occurrence of orientation perturbations.

The calibrated model does show significant re-orientation of the horizontal stresses (7.6), but these perturbations occur along faults and are most intense very close to those. The wells in the case study reservoir commonly maintain a distinct distance to nearby faults and thus also keep this distance to the variation in stress orientation. The measurements at three wellbores in the case study reservoir, i.e. F2, F5 and J1, do show considerable deviations from the regional stress orientation, which are not reproduced by the geomechanical model.

All of these three wells are located in the northern part of the reservoir, but only well F2 is located directly under the salt wall. According to the project partners, the faults around this well F2 are conceptual since they are not detectable in seismic data under the salt. However, the faults trace is of importance to stress perturbations and especially to the intensity of re-orientations. The fact that the geomechanical model comprises stress re-orientations close to faults and the existence of multiple faults in the vicinity of this well, suggests that slightly different fault geometries at this location would lead directly to the observed stress orientation. Besides this potential geometrical inaccuracy of the model, the author of the respective data compilation questions the quality of this measurement, because only one pronounced breakout was measured (Grote, 1998). The questionable quality of the measurement and of the fault network precludes any reasonable solution to this problem at this point.

The measured stress orientation also deviates significantly from the regional trend and the modeling results at well F5. This area is not located under the salt wall and the orientation measurement quality is not doubted (Grote, 1998). Nevertheless, the project partners describe the faults northerly adjacent to the wellbore as stepped and shifted, and only partly traceable in the seismic data. The modeled stress orientation reveals perturbations around and in between the overlapping area of the faults (Fig. 7-23). While the orientation of maximum horizontal stress is rotated counter-clockwise south of the overlapping faults – where the wellbore was drilled – the stress orientation inside the fault overlap is rotated clockwise to a direction of about N-S (Fig. 7-23). This latter orientation of maximum horizontal stress represents the measured orientation of 179°N (Grote, 1998).

The fact that the stepped faults are only partly traceable in seismics and modeling results show the measured orientation in the step-over of the faults, strongly suggests that the well (at least at the measurement location in the reservoir sandstone) is positioned in such a fault setting. Possible scenarios for this positioning could involve multiple step-overs of faults instead of the single one described, or also a slightly different position of the mapped faults with respect to the deviated wellbore (Fig. 7-23). A significant damage zone around these faults could be a further explanation. However, the wellbore is not reported to cross the faults and the schematic cross section shown above also describes the southern of the two faults in this area as ENE dipping (Fig. 7-15).

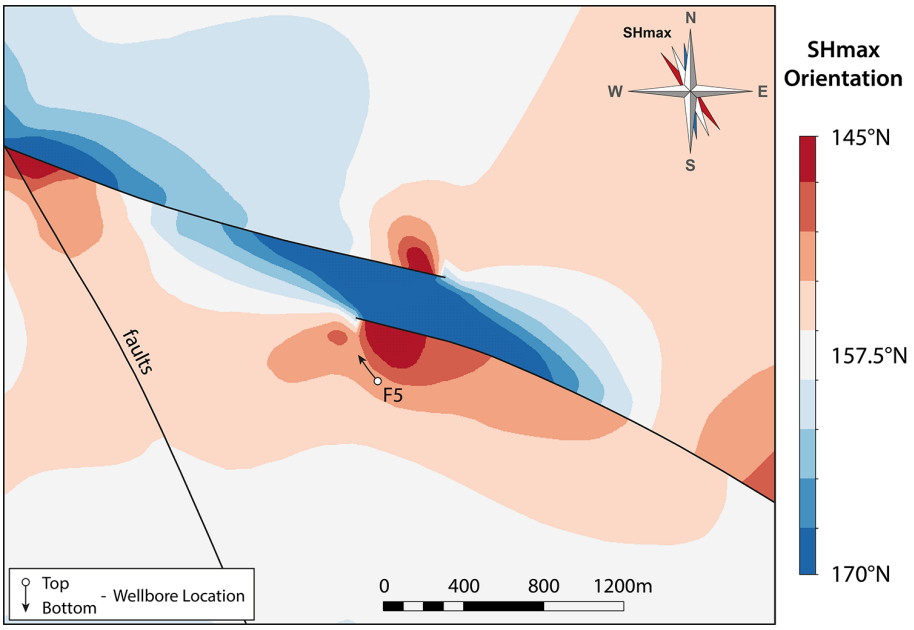

Fig. 7-23. Top view on the area of well F5 in the calibrated static geomechanical model of the case study. According to the project partners, the ESE-WNW trending faults (black) are stepped and only partly traceable in seismics. The well F5 (arrow) is deviated towards NW and according to the given information located south of the fault step-over. While this area is dominated by counter-clockwise rotation of maximum horizontal stress (SHmax) (red), the area inside the fault overlap shows the measured orientation of about N-S. White colors represent the regional NNW-SSE trend of the maximum horizontal stress.

This example illustrates how the lack of precise fault geometry yields significant deviation in the calibration of the geomechanical model. The uncertainty of faults mapped in seismic data can result from complicating materials in the overburden like rock salt, but faults can also simply be on border of seismic resolution. Such subseismic faults may still influence the in situ stress field and its perturbations considerably.

Significant deviations between modeled and reliably measured orientation of the maximum horizontal stress are also observed at well J1. Independent on the friction coefficient applied to the nearby ENE-WSW trending fault, the re-orientation of the maximum horizontal stress cannot by reproduced by the geomechanical model. At this location the adjacent fault is clearly visible in seismics and does not cross the wellbore. Geometrical inaccuracy of the mapped fault is thus excluded to be responsible for the misfit. According to the provided data, this well is very close to the mapped fault. It is therefore possible that some smaller subseismic faults in a damage zone around this fault yield the measured re-orientations at the wellbore. Such a damage zone should be observable in image logging of the well, but this information is not available.

Besides faults as one major producer of stress perturbations, the parameter studies showed that also the mechanical parameters have a large impact on in situ stress magnitudes and orientations (6.1). The material parameters are not modified in the variation series of model calibration (7.5.1), because the

applied properties are relatively well-constrained by using DSI® logs in combination with rock mechanical tests on drill cores. Nevertheless, local variations in the mechanical parameters may be responsible for the re-orientations observed. Juxtaposition of mechanically different lithologies along the fault close to well J1 can lead to the changes in stress direction. According to the project partners, the nearby fault shows an offset of 10-20ms, which equals about 25-50m. This would be sufficient to produce stress perturbations by juxtaposition of mechanically different sandstone units, for instance.

The deviations in minimum horizontal stress magnitudes of up to 10MPa in model calibration are most probably outside the range of measurement error (7.5.4). The fact that these wellbores are located in the area of the salt diapir suggests inaccurate fault geometries to be most likely responsible for the resulting misfits, since the salt complicates precise seismic interpretation.

Material variations are assumed to contribute to deviations in stress magnitude. Lateral variations in mechanical parameters could not be implemented into the model due to the limited amount of available information. Despite the lack of better data, generic model variations are carried out to determine the impact of changing material parameters in the static model (Tab. 7-17).

In two modeling series, the Young's modulus of all three layers is uniformly increased and decreased by 20% of its assumed average value. The Young's modulus of the reservoir is thus changed from 26.15GPa to 20.92GPa and 31.28GPa. This change is not unrealistic since the individual maximum and minimum value of the Young's modulus determined by rock mechanical tests is 19.59GPa and 29.32GPa, respectively. The fault friction is set to the default value of 0.4 and all other parameters and boundary conditions are those of the calibrated geomechanical model.

Well	Modeled minimum horizontal stress: **default material**	Modeled minimum horizontal stress: **-20% Young's modulus**	Modeled minimum horizontal stress: **+20% Young's modulus**
B1	69 MPa	59 MPa	77 MPa
C1	69 MPa	59 MPa	77 MPa
C3	69 MPa	59 MPa	77 MPa
C4	71 MPa	61 MPa	80 MPa
C6	68 MPa	58 MPa	76 MPa
C7	69 MPa	60 MPa	78 MPa
C9	69 MPa	59 MPa	78 MPa
D1	68 MPa	59 MPa	77 MPa
F1	69 MPa	59 MPa	77 MPa
F2	70 MPa	60 MPa	78 MPa
F3	69 MPa	59 MPa	77 MPa
F5	69 MPa	60 MPa	78 MPa
F6	69 MPa	59 MPa	78 MPa
G1	68 MPa	58 MPa	77 MPa

Tab. 7-17. Overview on the additional variation series investigating the impact on changes in mechanical parameters. The Young's modulus is decreased and increased by 20% of its average value, while faults comprise a friction coefficient of 0.4 and all other parameter settings equal those of the calibrated static model. This table elucidates the major impact of the Young's modulus on the resulting stress magnitudes at the wells for which minimum horizontal stress magnitudes are measured during hydraulic fracturing.

The results of these studies show that changes in the mechanical properties yield significant changes in the magnitude distribution (Tab. 7-17). The applied variation in Young's modulus resulted in up to 10MPa increased and decreased magnitudes of the minimum horizontal stress. Smaller changes than 20% in the elastic moduli are assumed to be more common and thus magnitude variations of less than 10MPa are likely to be caused by lateral material variations. However, the fact that no well deviates more than 10MPa supports in turn the assumption of the averaged material parameters being representative for the case study reservoir.

Lateral variations in material parameters can be referred to differences in diagenesis and facies, for instance. In addition, large salt bodies may also influence the development of mechanical parameters of the stratigraphic units above and below the diaper. This influence potentially results from the different thermal conditions due to the higher heat capacity of rock salt compared to the host rock. Such an impact cannot be excluded for the case study. Therefore the extensive salt wall in the northern part of the case study reservoir give rise to manifold uncertainty addressing not only the fault geometry, but the mechanical parameters as well. This increased overall uncertainty is assumed to be responsible for the increasing misfits in model calibration in the northern part of the case study reservoir.

Nevertheless, the magnitudes and orientations at some wells in the area of the salt wall do match: well C3 and F6 with respect to the magnitudes of minimum horizontal stress and well K1 regarding the orientation of the maximum horizontal stress. This circumstance may also indicate that the misfits are also caused by high variability of material parameters.

The rather small changes in horizontal stress magnitudes due to the incorporation of salt in the top boundary condition can be attributed to the type of lateral boundary condition. The conveyed displacements represent a large tectonic component responsible for the maximum horizontal stress. This probably prevents large changes of horizontal stress magnitudes originating from the vertical stress changes.

Although the calibration was successful and yielded a satisfactory match, the process of calibration should not be regarded as completed (4.8). Additional information can further improve the fit and thus the quality of the model. Direction-dependent variation of the faults friction coefficient represents one promising approach, since the assumption of a uniform friction does not consider the different history of the faults. Interacting fault pattern with individual friction sets are assumed to yield even more specific insights than the calibrated static geomechanical model provides at the moment. The dynamic model of this study might help to deduce refined values of the fault friction from corresponding tectonic activity in the paleo-stress states.

Area-wide information on material parameters allowing the incorporation of lateral heterogeneity in mechanical behavior will also improve the model significantly. Such information could be derived from 3D seismics, for instance (Gray et al., 2012; Herwanger and Koutsabeloulis, 2011). Besides such a sophisticated approach by improving material data, additional geomechanical logging at specific wellbores would also considerably increase the model quality.

7.6 Results of the Static Model

The results of the calibrated static geomechanical model comprise the full 3D stress and strain tensor for all 3D elements, as well as shear and normal stress of all faults (4.7). This data provides unique insights into the recent in situ stress and strain distribution of the case study reservoir and into the movement behavior of the simulated faults. The modeling results are visualized by contour plots showing the in situ distribution of various calculated stress and strain quantities inside the reservoir and on the fault faces. Quantities like stress orientations can be visualized by vector plots, but due to the high spatial resolution of the model contour plots of stress azimuth are more comprehensible.

In order to visualize the geomechanical modeling results inside the reservoir layer, all generated contour plots of stress and strain quantities represent top views on the second element layer (Fig. 7-24). Visualizing the results on a horizontal cross-cutting plane passing through different layers is not practicable due to the varying depth of the reservoir. By using the chosen element layer, the plotted results always belong to the reservoir and the corresponding accurate depth level (Fig. 7-24).

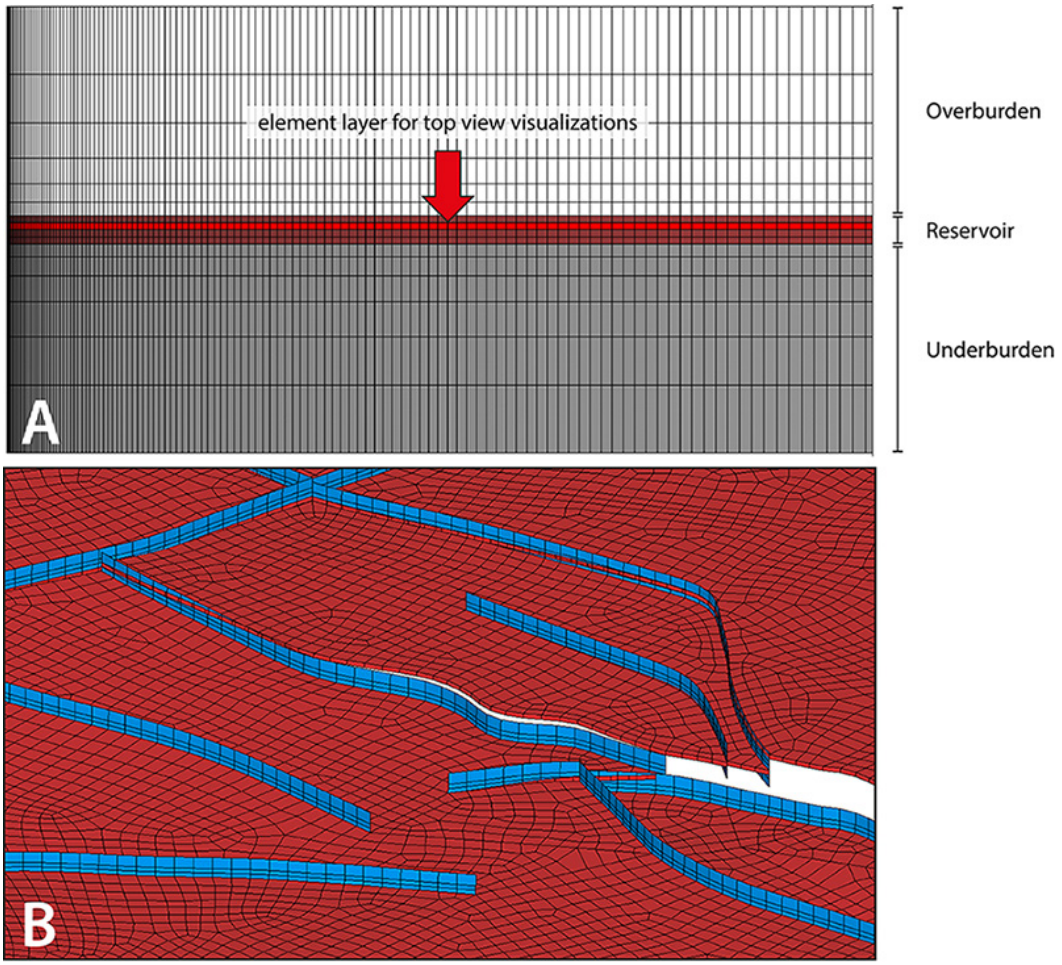

Fig. 7-24. Side view on the static geomechanical model (A) showing the three layers of overburden (white), reservoir (red) and underburden (grey). The second element layer of the reservoir is indicated (red arrow), which is utilized for all top view contour and vector plots of stress and strain quantities. The lower part of the figure emphasizes the variable depth of this element layer corresponding to vertical displacements along faults (blue) that are accurately considered in the model.

The previously shown direct comparison of the depth distribution between the element layer of the reservoir in the FE model and the horizon in the original geological subsurface model demonstrates the accuracy in geometry transfer (Fig. 7-7). All stress and strain results presented on this element layer are thus visualized at the specific depth of the reservoir.

The first results shown in the following figures reveal the in situ distribution of principal stress magnitudes. Due to the prevailing normal faulting regime, σ_1 represents the vertical stress (Fig. 7-25), and σ_2 and σ_3 the maximum and minimum horizontal stress, respectively (Fig. 7-26, Fig. 7-27). The vertical stress magnitude correlates with the varying depth of the reservoir. Deeper parts naturally show higher vertical stress, for instance at the graben structure in the eastern part of the reservoir. Perturbations along faults and at fault tips are exceptions, but can be occasionally observed. The vertical stress distribution also elucidates the impact of the lowered lithostatic load in the northern part of the reservoir due to the consideration of salt in the top boundary condition (Fig. 7-25). The outline of the salt body can be traced along the gradient in magnitude. Specific changes outside the seismically interpreted reservoir area – especially in vertical stress magnitude – must be evaluated with care since the depth and topology are only extrapolated and not described in input data.

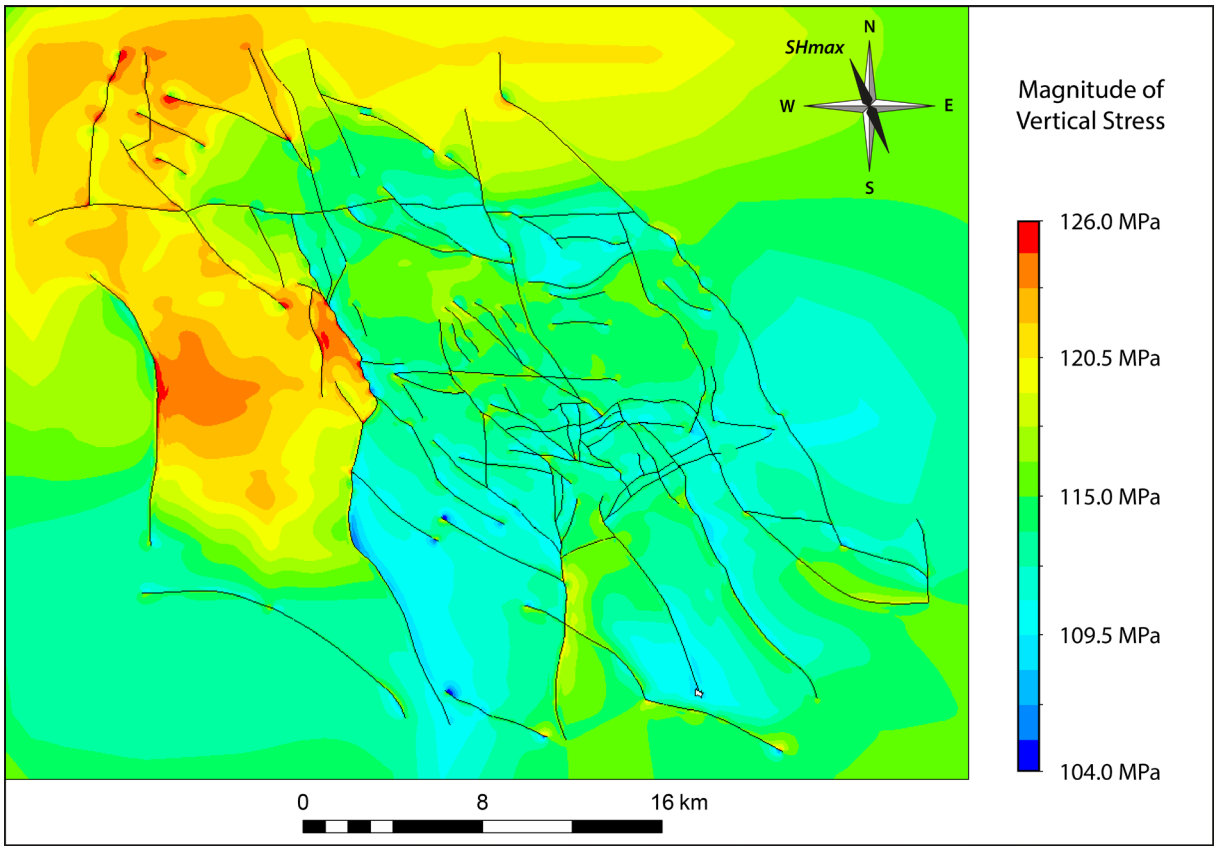

Fig. 7-25. Top view on the static geomechanical model showing the contoured distribution of the vertical stress magnitude (σ_1) in [MPa] inside the reservoir layer. The contours are scaled to an interval of 22MPa.

In contrast to the distribution of vertical stress in the reservoir, the maximum and minimum horizontal stresses show significant perturbations at fault tips, curvatures and vertical displacements (Fig. 7-26, Fig. 7-27). Perturbations in both stress quantities show butterfly-like, concentric to elongated shapes. Interaction in dense parts of the fault network is also proposed to lead to more area-wide increase or decrease in magnitudes. The intensity of magnitude perturbations is generally highest at the source and gradually decreases with increasing distance. This decrease appears to be of rapid exponential nature rather than linear. Contrasting to the figure of vertical stress inside the reservoir (Fig. 7-25), the horizontal stress plots show contours scaled to an interval of 20MPa (Fig. 7-26, Fig. 7-27).

Therefore it is hard to state the exact spatial range of perturbations in maximum and minimum horizontal stress magnitude, but depending on the specific setting severe impact in distances of 1-2 kilometers can be assumed. The legend and scaling further indicates maximum deviations from the background stress magnitudes of up to 10MPa in these perturbations.

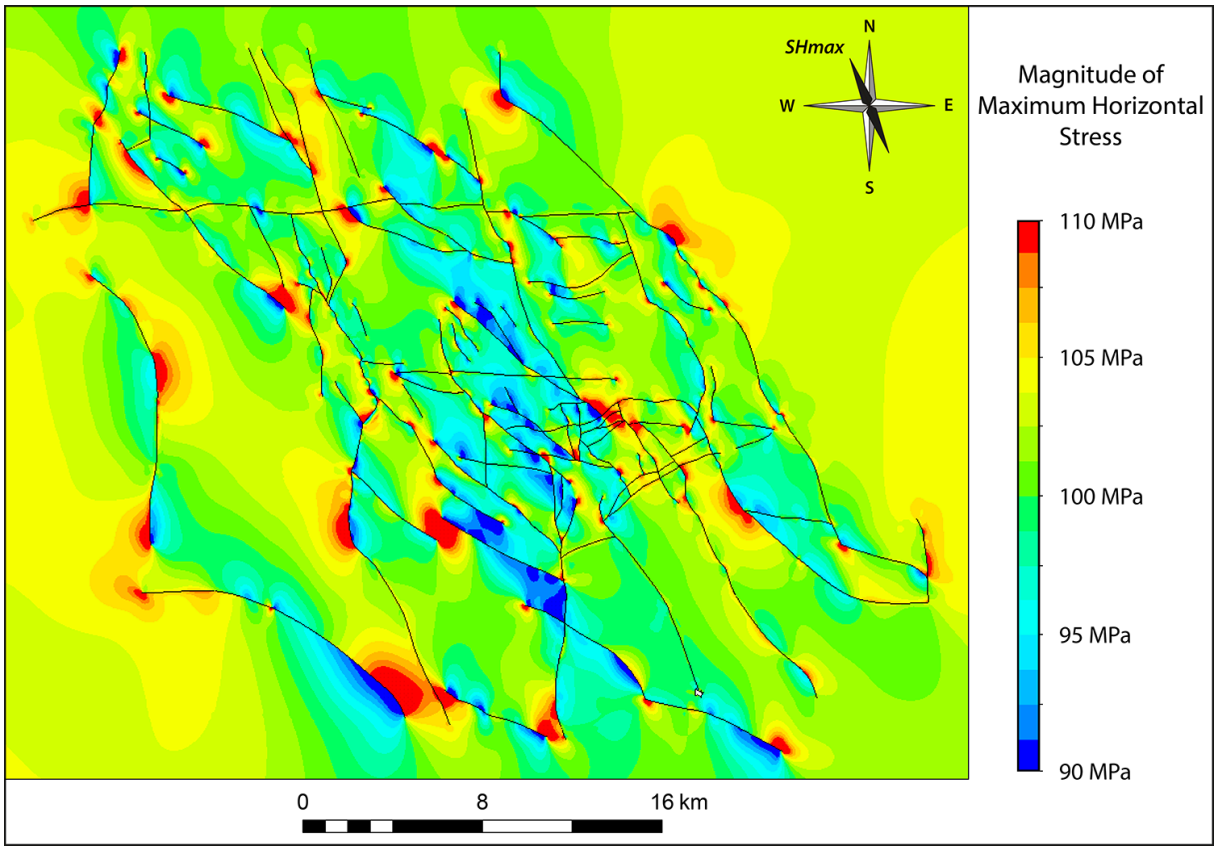

Fig. 7-26. Top view on the static geomechanical model showing the contoured distribution of the maximum horizontal stress magnitude (σ_2) in [MPa] inside the reservoir layer. The contours are scaled to an interval of 20MPa.

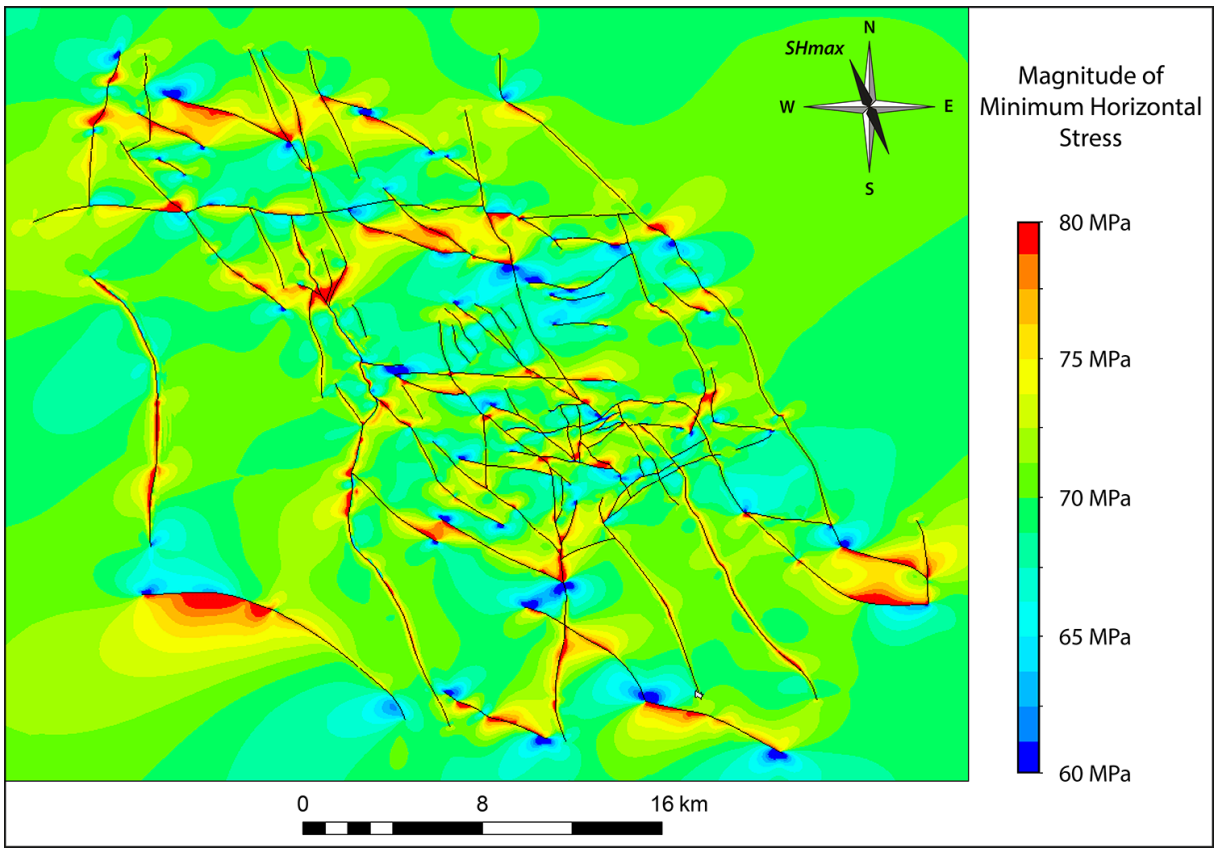

Fig. 7-27. Top view on the static geomechanical model showing the contoured distribution of the minimum horizontal stress magnitude (σ_3) in [MPa] inside the reservoir layer. The contours are scaled to an interval of 20MPa.

The comparison of the distribution of maximum and minimum horizontal stress magnitudes reveals no concurrent behavior in the development of perturbations. This missing analogy affects the specific location, shape and intensity of the magnitude perturbations. In other words, maxima and minima in both magnitudes may – but do not necessarily develop at the same locations in the reservoir and in case they do, their intensity commonly differs. Instead, the magnitude distribution plots indicate a strong dependency of the magnitude perturbations on the distinct orientation of faults and their curvatures relative to the respective stress, as well as on the interaction with perturbations of neighboring faults. No generally valid rules for the perturbation behavior of principal stresses could be established, which underlines the necessity of robust geomechanical models.

Based on the principal stresses, several further stress quantities are derived (4.7). The mean stress represents the arithmetic mean of the three principal stresses. Its visualization reveals circular perturbations at fault tips and curvatures as predicted by the preliminary studies (6). The contours are scaled to an interval of 20MPa. In addition to local perturbations, distinct areas show higher and lower mean stress magnitudes compared to the average background (Fig. 7-28). Some of these area-wide stress changes correlate with reservoir depth and corresponding vertical stresses. With respect to the constant contour scale interval of 20MPa, the perturbations of mean stress are significantly less pronounced and spatially more limited than those of the horizontal principal stresses.

The visualization of mean stress further demonstrates that perturbations do not occur regularly at fault tips. This could also be observed in the contoured distributions of maximum and minimum horizontal stress, but was less striking due to the overall higher frequency of occurring perturbations.

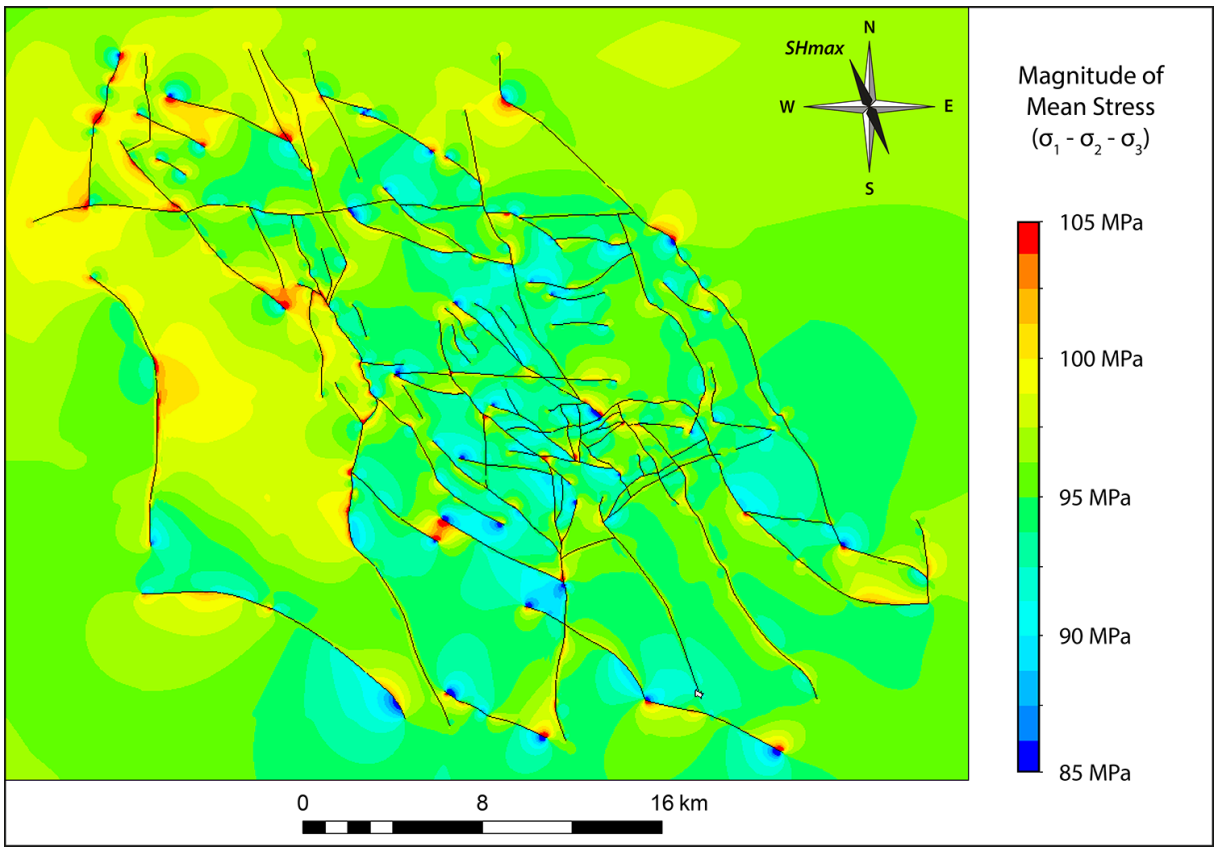

Fig. 7-28. Top view on the static geomechanical model showing the contoured distribution of the mean stress magnitude in [MPa] inside the reservoir layer. The contours are scaled to an interval of 20MPa.

The second stress quantity calculated from the principal stresses is the differential stress between largest and least principal stress (Fig. 7-29). Contrasting to the previous figures, the color contours in

this plot are scaled to an interval of 30MPa for better representation. The distribution of differential stress shows area-wide magnitude changes and local perturbations – both very similar to those of the vertical and minimum horizontal stress (Fig. 7-25, Fig. 7-27), on which the calculation of differential stress is based (4.7.2). The distribution of differential stress shows overall lower magnitudes in the area of the implemented salt wall in the northern part of the reservoir and higher magnitudes in the western graben structure (Fig. 7-29). Both directly result from lowered and increased vertical stress, i.e. the largest principal stress. In addition, only the very pronounced local perturbations at faults in the northwestern corner and in the southern areas are revealed by the contour scaling interval of 30 MPa.

Due to the calculation of differential stress, perturbations representing minima in least principal stress occur as maxima in the differential stress distribution and vice versa (Fig. 7-29, Fig. 7-27). The largest principal stress is primarily controlled by the depth level of the reservoir and therefore its distribution comprises more area-wide changes in magnitudes. These magnitude changes counteract or amplify the minima and maxima of least principal stress in the derivation of the differential stress. The lack of local perturbations in the largest principal stress distribution facilitates the recognition of least principal stress perturbations in the differential stress contours.

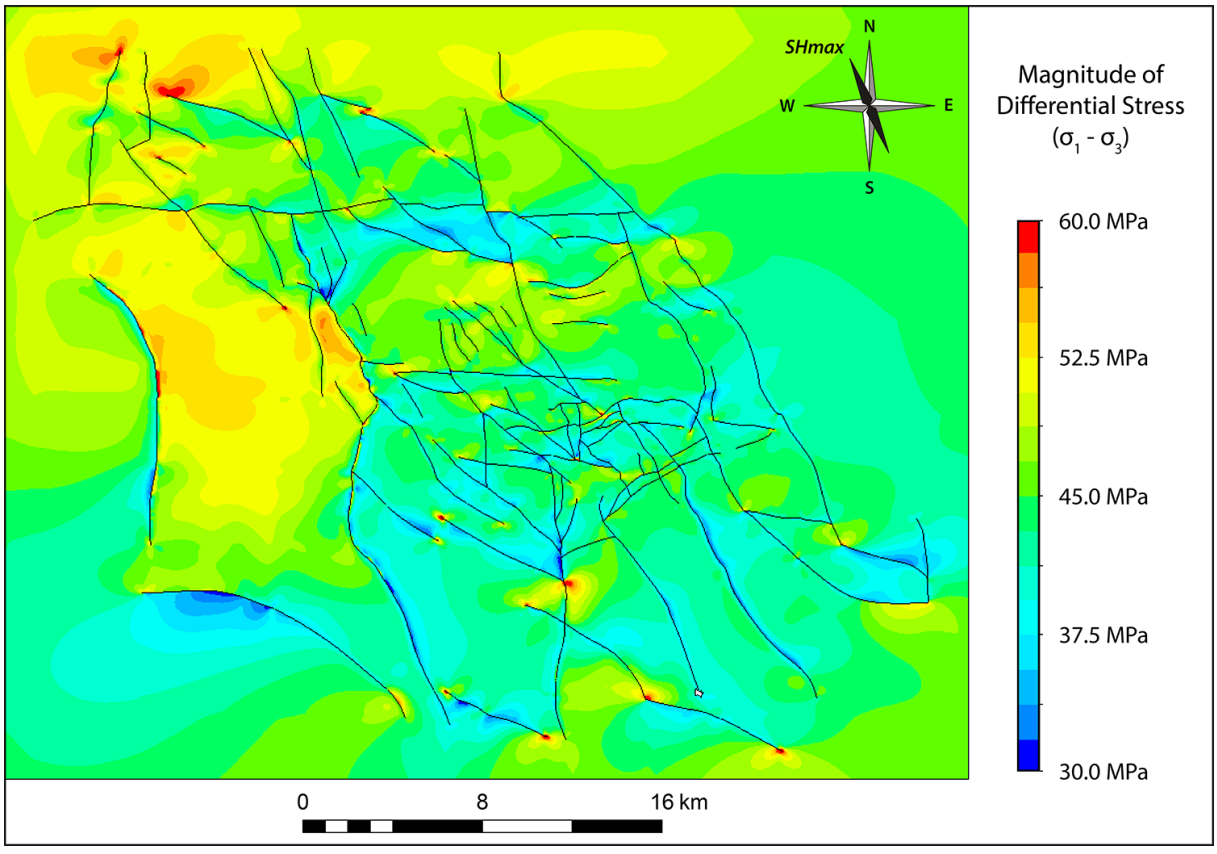

Fig. 7-29. Top view on the static geomechanical model showing the contoured distribution of the differential stress magnitude in [MPa] inside the reservoir layer. The contours are scaled to an interval of 30MPa.

Besides the magnitudes of principal stresses and additionally calculated stress quantities, the distribution of stress orientation represents another major outcome of the geomechanical modeling. The most common representation of orientation data are vector plots. Vectors for all three principal stresses can be plotted for the same element layer inside the reservoir as applied for the contour plots shown above. Each element provides one vector by default. However, this leads to an excessive amount of overlapping vectors that cannot be distinguished from each other. Decreasing vector size is insufficient to solve this visualization problem due to the high spatial resolution. The selection of every second or third element vector significantly lowers the plotted vector density, but inherently

reduces the resolution and amount of results as well. Furthermore the model shows only minor re-orientations, which are hard to identify in vector representations due to the small amount of rotation. The high resolution of the geomechanical model and the minor intensity of occurring re-orientations thus preclude comprehensive vector visualizations of the modeling results and a different post-processing approach is applied.

The 3D stress tensor includes the stress components σ_X, σ_Y, σ_Z, σ_{XY}, σ_{XZ} and σ_{YZ}. The results of these components are stored as an array parameter for all elements and are used to calculate the direction cosines of the principal stresses. The direction cosines are the cosines of the angles between the three principal stresses and the coordinate axes. Hence, each principal stress direction is fully described by three direction cosines a, b and c, which belong to the angles between the stress vector and the X-, Y- and Z-axis, respectively. Due to the fact that the angles vary between 0° and 180°, the direction cosines consequently vary between 1 and -1. Assuming the Z-axis equals the vertical depth axis, the vertical principal stress vector is described by $a \approx 0$, $b \approx 0$ and $c \approx 1$. The two horizontal principal stresses would therefore comprise $c \approx 0$, while a and b vary corresponding to the horizontal directions. Based on these revealed direction cosines, an azimuth value of the maximum horizontal stress (σ_2) is calculated using the arc tangent and is expressed in °N.

The azimuth value of the maximum horizontal stress is then plotted as contour representation on the chosen element layer of the reservoir (Fig. 7-30, Fig. 7-31, Fig. 7-32). In order to elucidate the deviation from the far-field stress direction, a diverging color scale is used. The scaling interval is chosen to be ± 12.5° (Fig. 7-30, Fig. 7-31) and ± 22.5° from the regional trend (Fig. 7-32). The smaller scaling range (± 12.5°) yields a more intense visualization of re-orientations, which is better suited to reveal all orientation trends along and across the faults (Fig. 7-30).

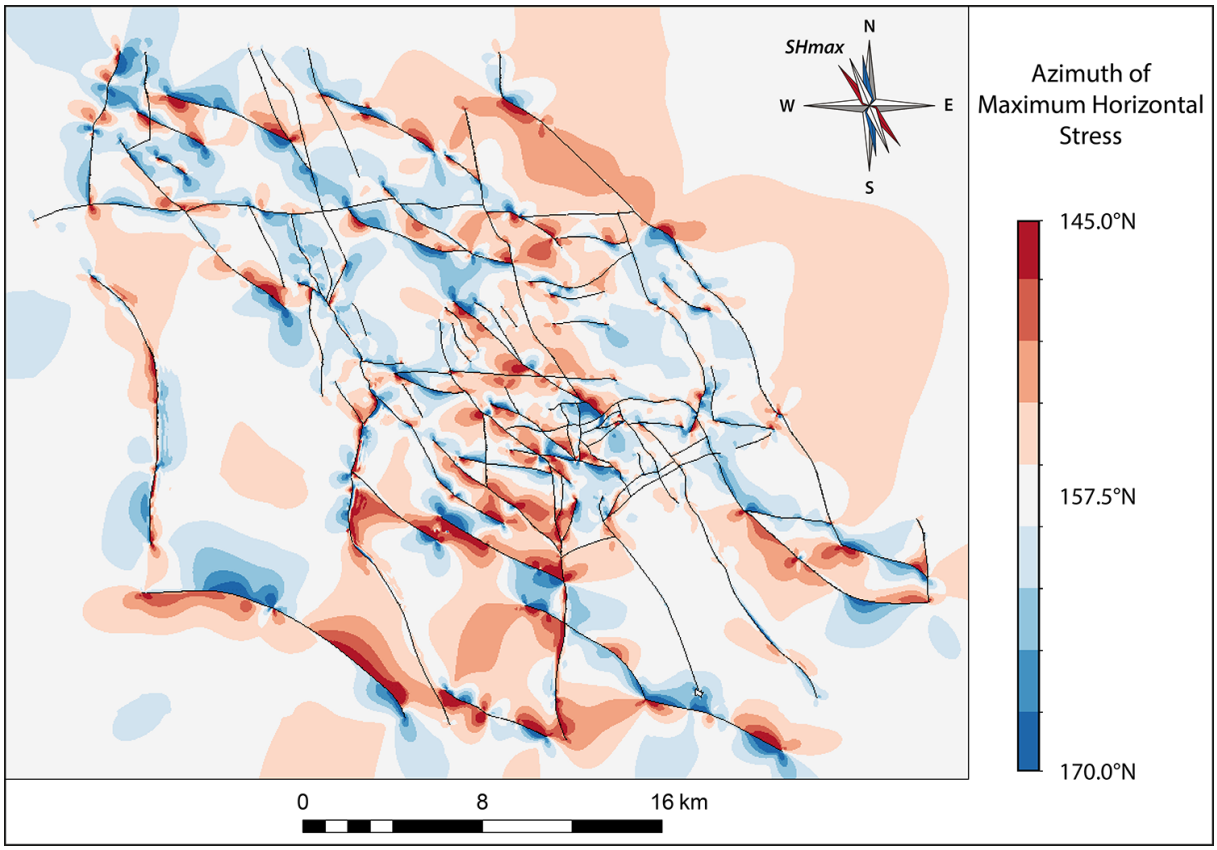

Fig. 7-30. Top view on the static geomechanical model showing the contoured distribution of the maximum horizontal stress direction in [°N] inside the reservoir layer. The contours are scaled to an interval of ± 12.5° from the regional trend.

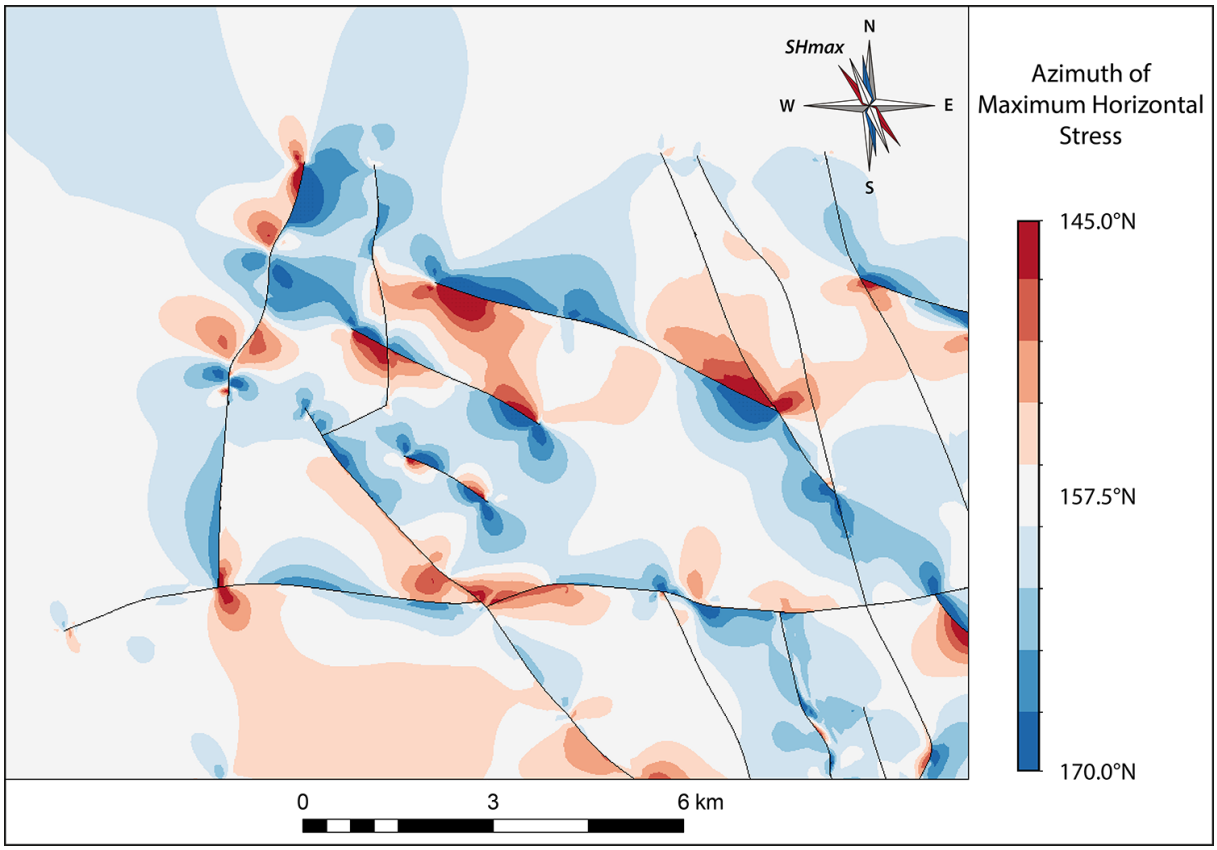

Fig. 7-31. Top view on the northwestern part of the geomechanical model showing the contoured distribution of the maximum horizontal stress direction in [°N]. The contours are scaled to an interval of ± 12.5° from the regional trend.

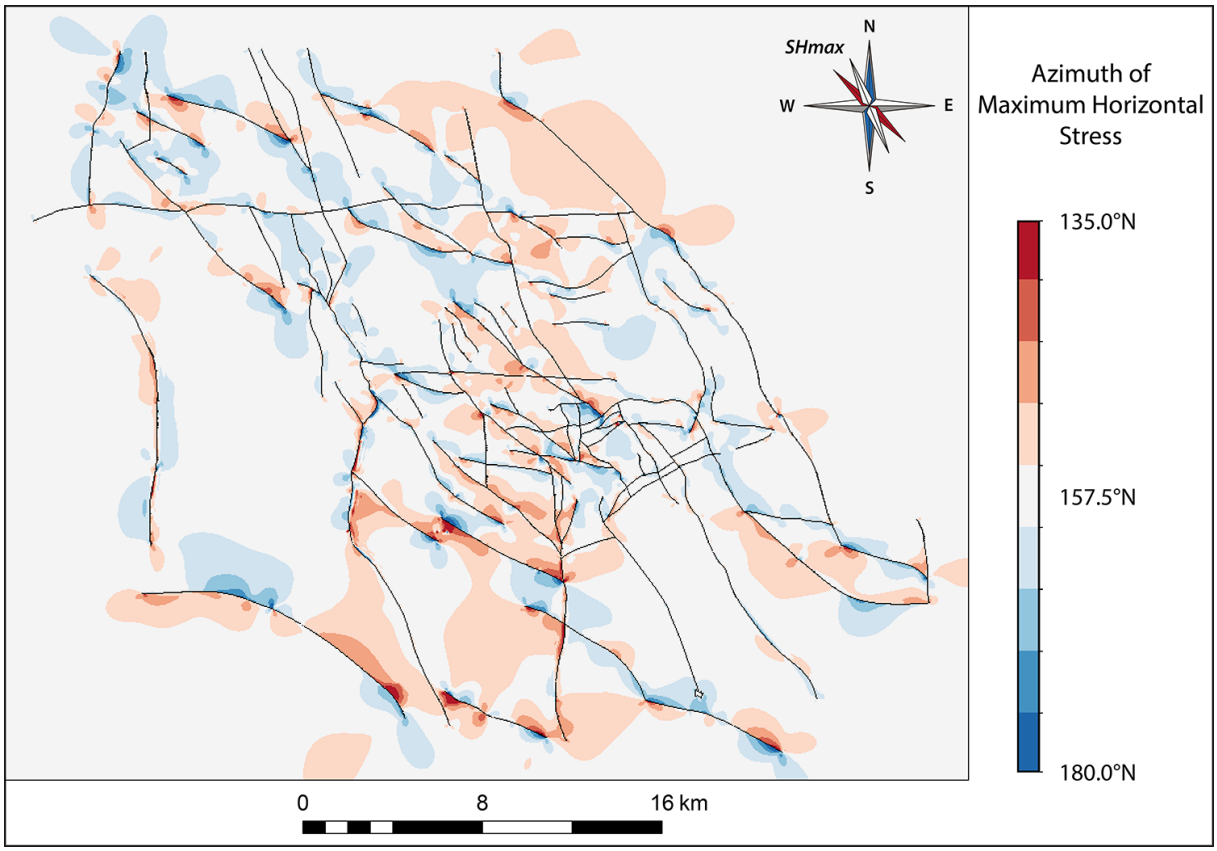

Fig. 7-32. Top view on the static geomechanical model showing the contoured distribution of the maximum horizontal stress direction in [°N] inside the reservoir layer. The contours are scaled to an interval of ± 22.5° from the regional trend.

Noisy parts in the contour plot, i.e. areas of small abrupt changes in the coloring, probably result from the calculation of the azimuth value and very small-scale changes in the tectonic regime. Very close to faults the maximum horizontal stress can exceed the vertical stress in some elements due to magnitude perturbations. This affects the calculation of the azimuth value, which refers to the maximum horizontal stress being σ_2. However, these are very local phenomena and do not affect the general distribution of stress orientation in the reservoir.

By zooming into the northwestern part of reservoir, the rotation of the maximum horizontal stress along differently oriented faults is shown in high detail (Fig. 7-31). Especially NW-SE trending faults show a characteristic distribution of clockwise and counterclockwise rotation of σ_2. The interaction of orientation perturbations and the specific transitions in re-orientation are complex and strongly depend on the specific structure and density of the fault network. The plot comprising the larger scaling range (± 22.5°) elucidates the maximum amount of re-orientation of the maximum horizontal stress from the regional trend, which is estimated to be 20°-25° (Fig. 7-32). This demonstrates the minor extent of perturbations in stress orientation in the case study reservoir – especially compared to the more pronounced perturbations in stress magnitudes. These results also demonstrate that perturbations in stress magnitude and orientation are separate phenomena and not necessarily occurring in the same intensity.

In addition to the 3D stress tensor, the geomechanical FE model provides the respective 3D strain tensor as well, which is used to calculate and plot contoured strain representations (Fig. 7-33). The equivalent elastic strain, or von Mises strain, is a well-suited quantity to visualize the overall strain in the reservoir regarding all three principal components (Fig. 7-33). This quantity represents the strain equivalent to the von Mises stress (4.7). Instead of absolute values, only a relative scale is provided.

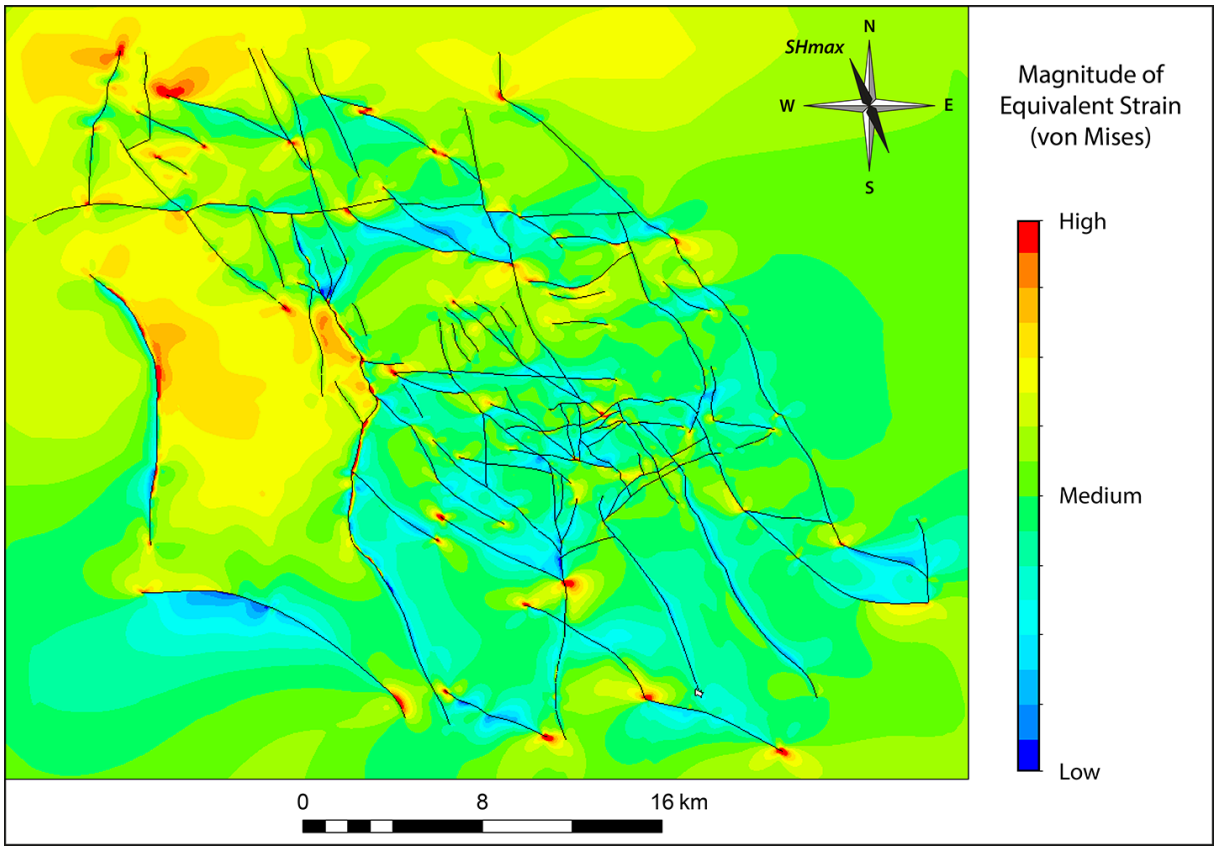

Fig. 7-33. Top view on the static geomechanical model showing the contoured distribution of the equivalent elastic strain, also referred to as von Mises strain, inside the reservoir layer.

Instead of focusing on the absolute numbers, which are relatively low, these strain results should be seen as an indication of strain localization in the reservoir resulting from the specific in situ stress. Therefore the relative scaling is more appropriate. Areas of high strain are closer to rock failure in general and prone to accommodate higher fracture densities. Due to the fact that only the elastic domain is regarded in the geomechanical model, only elastic strains are comprised in the results.

The comparison of the equivalent elastic strain distribution to the differential stress in the reservoir reveals a striking similarity (Fig. 7-29, Fig. 7-33). This results from the linear relationship between stress and strain in the model and the apparent dominance of ε_1 and ε_3 in the calculation of the equivalent strain (4.7). Since the static geomechanical model of the case study reservoir focuses on the recent in situ stress and fault behavior, strain results are of minor importance at this point and more important in the following dynamic modeling regarding paleo-stress states (8).

One of the most significant advantages of this geomechanical modeling approach is the use of 2D interface elements to simulate faults (2.1.2, 4.4.2). These elements allow direct evaluation of stresses acting on the fault faces. Shear and normal stresses are provided by default and can be used for further calculations (Fig. 7-34, Fig. 7-35). All fault-specific stresses and additionally derived quantities, such as the slip and dilation tendency, are contoured on the fault faces and plotted as oblique views from an elevated viewpoint southwest of the reservoir.

The shear stress distribution on faults shows a strong dependency on the orientation of faults and the maximum horizontal stress (Fig. 7-34). Acute angles between this second principal stress and the faults result in higher shear stresses, whereas parallel or normal orientations yield lower values or even zones of zero shear stress. In addition to this expected relationship, the shear stress distribution also reveals a significant dependency on the mechanical properties (Fig. 7-34).

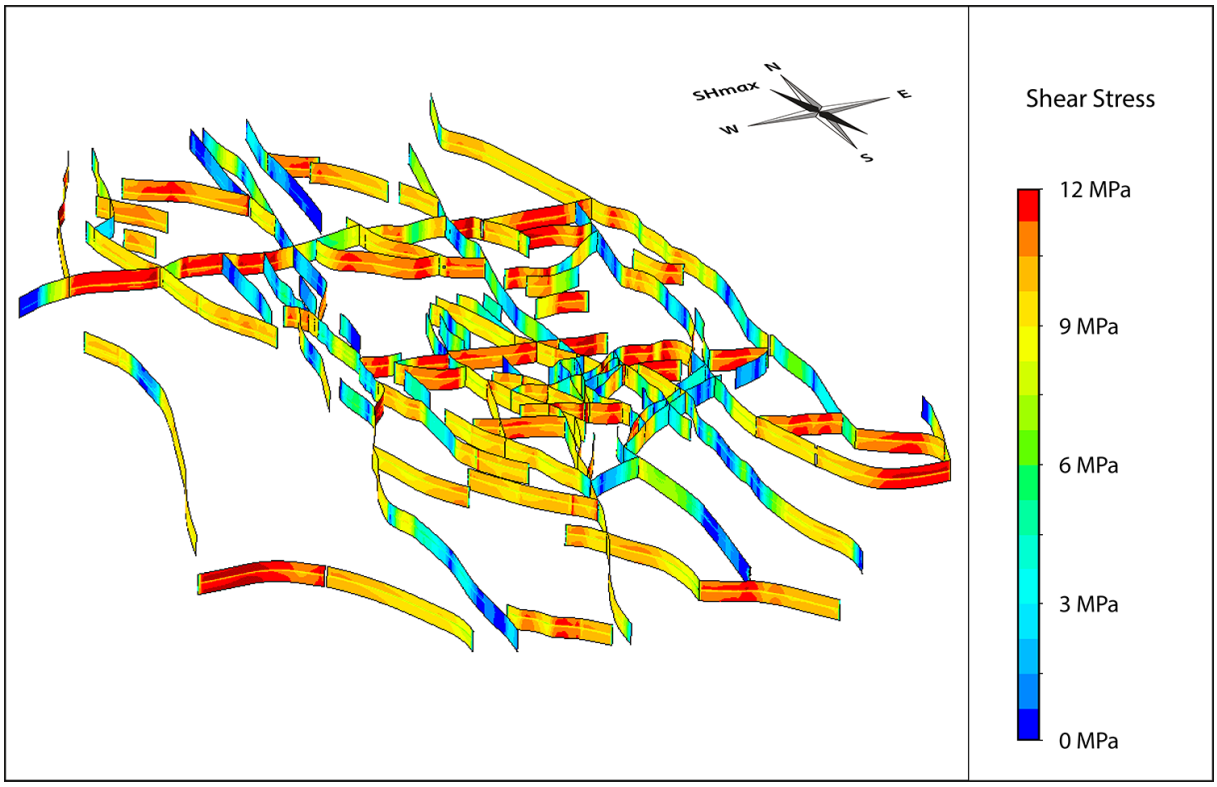

Fig. 7-34. Oblique overview from the southwest on the faults of static geomechanical model showing the contoured distribution of the shear stress in [MPa]. The friction coefficient of all faults is 0.1 for this plot.

Almost all faults show a segmentation of shear stress magnitude according to the mechanical stratigraphy of the three implemented layers. Along fault segments showing high shear stress in the over- and underburden (orange/red), the reservoir layer constantly comprises slightly lower values indicated by a thin brighter line (yellow). However, at fault segments of zero shear stress (blue), the reservoir layer often maintains higher values of shear stress (turquoise) (Fig. 7-34). Therefore the shear stress is not always lowest inside the reservoir layer.

Local differences in shear stress cause stress perturbations that lead to laterally irregular stress distributions in the lithological layers along the faults (Fig. 7-34). These lateral perturbations are then strongest close to their sources, which are the faults itself – as well as juxtaposition of mechanically different layers across vertical displacements.

The distribution of normal stress on the fault faces also reveals an orientation dependency on the direction of faults and the maximum horizontal stress (Fig. 7-35). Faults oriented perpendicular to the maximum horizontal stress exhibit generally the highest normal stresses. However, the normal stress is also significantly affected by the changing mechanical properties (Fig. 7-35). All faults throughout the reservoir show lower normal stresses for the reservoir layer compared to the over- and underburden. This directly results from the mechanical stratigraphy and represents a different behavior of fault stress distribution compared to the shear stress. Stress perturbations along the faults do also affect the normal stress distribution.

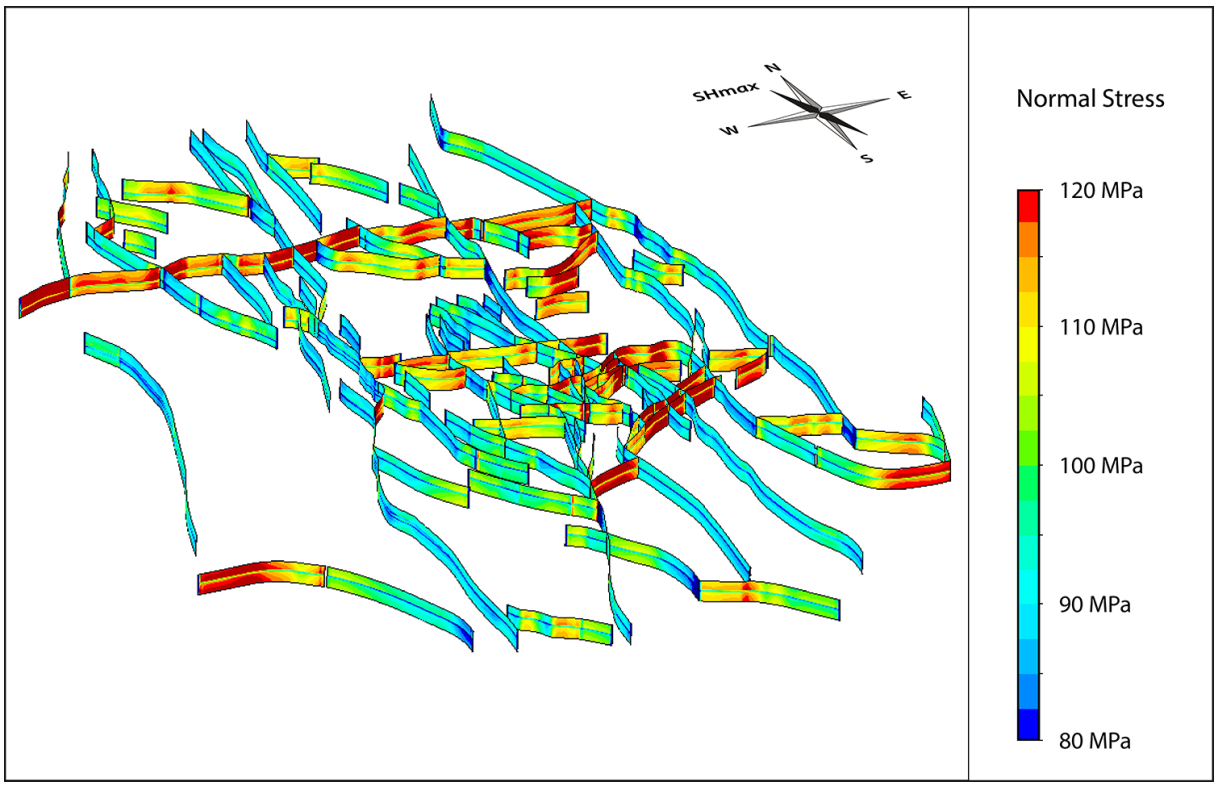

Fig. 7-35. Oblique overview from the southwest on the faults of static geomechanical model showing the contoured distribution of the normal stress in [MPa]. The friction coefficient of all faults is 0.1 for this plot.

Shear and normal stresses provided for the fault faces are used to calculate the slip and dilation tendency (4.7), which indicate the faults proximity to move and open, respectively. The slip tendency strongly depends on the friction coefficient of the faults. During the model calibration, the best fit between modeling results and field measurements is obtained at a friction coefficient of 0.1.

The low friction coefficient results in high slip tendency values for all approximately NW-SE trending faults (Fig. 7-36). As this low coefficient may not necessarily be valid for all faults and in order to provide a better identification of the most critically stressed fault segments, a second distribution of the slip tendency is shown with a fault friction coefficient of 0.2 (Fig. 7-37).

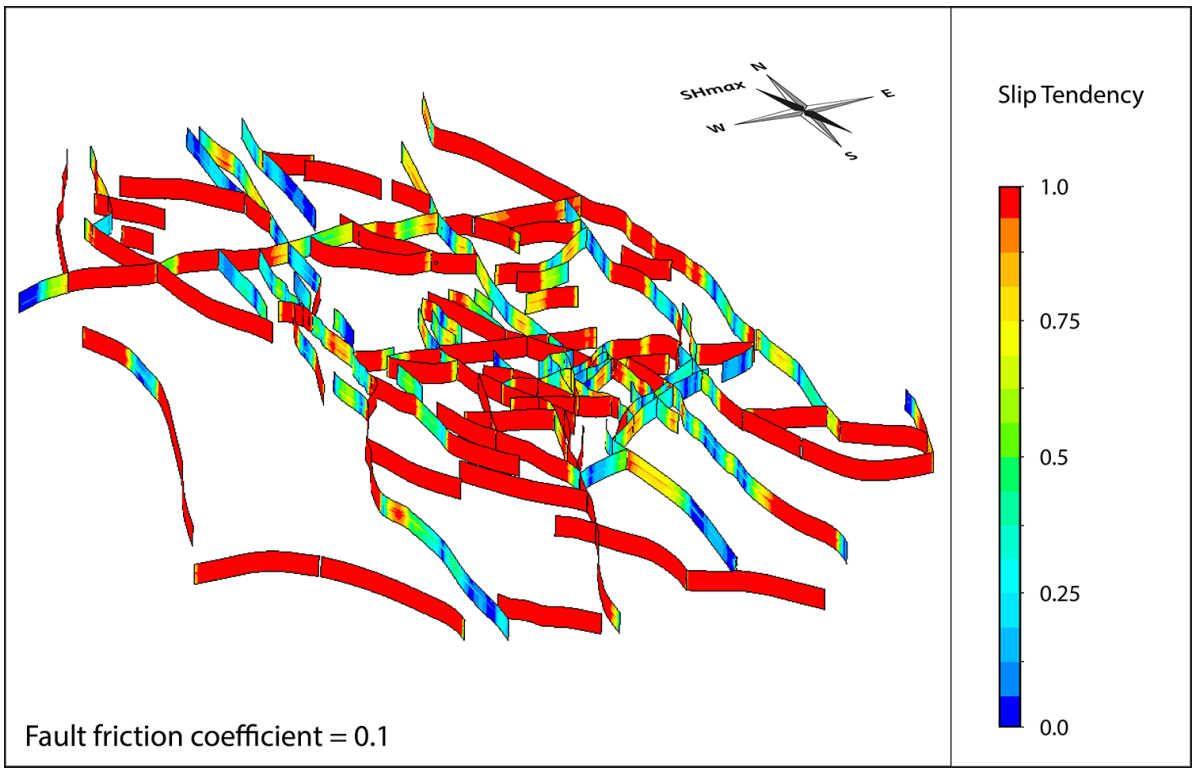

Fig. 7-36. Oblique overview from the southwest on the faults of static geomechanical model showing the contoured distribution of the slip tendency. The friction coefficient of all faults is 0.1 for this plot.

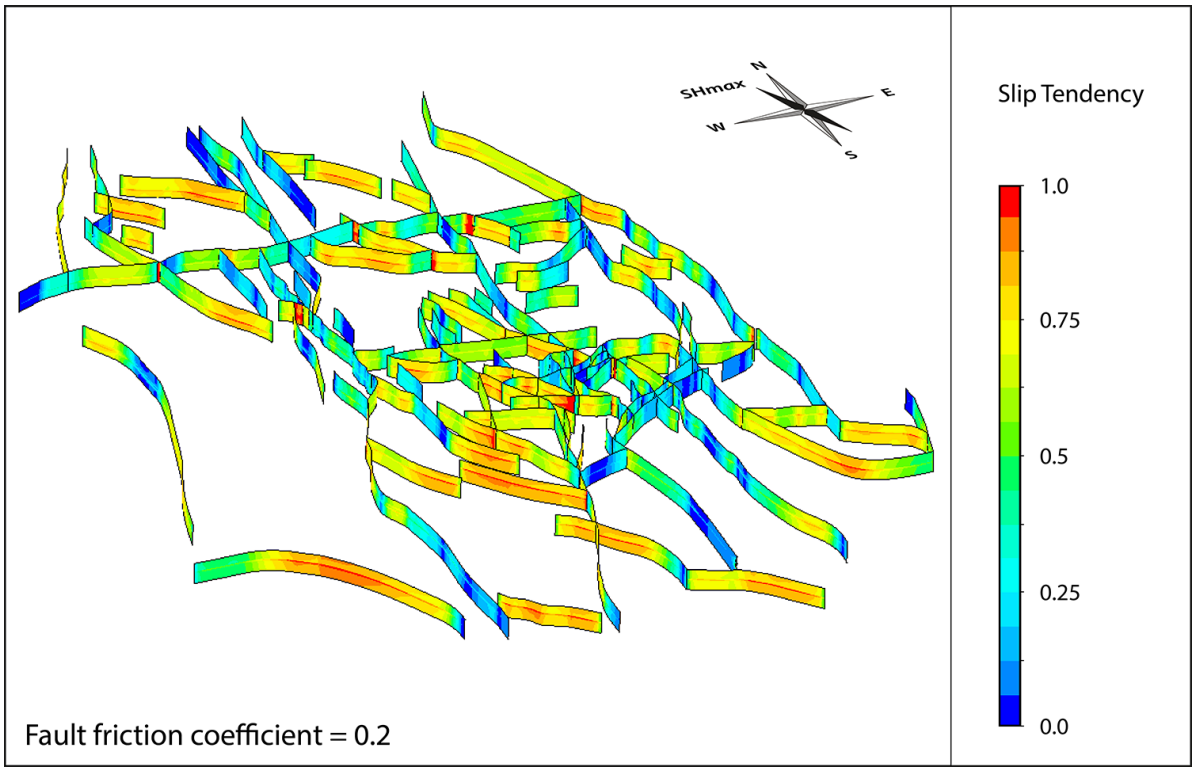

Fig. 7-37. Oblique overview from the southwest on the faults of static geomechanical model showing the contoured distribution of the slip tendency. The friction coefficient of all faults is 0.2 for this plot.

The slip tendency distribution of the fault network reveals the same dependency on fault orientation and direction of the maximum horizontal stress as shown in the preliminary studies (6). While acute angles between the maximum horizontal stress and the fault faces produce the highest proximity to move, parallel and perpendicular settings yield low slip tendencies (Fig. 7-36, Fig. 7-37).

The results of static geomechanical model further elucidate the impact of the mechanical stratigraphy of the fault behavior. Highest slip tendencies are first reached in the reservoir, while the values of those fault segments in the over- and underburden are lower (Fig. 7-37). This is shown by a thin red line following the reservoir layer. High slip tendencies are also reached first at crossovers of multiple, properly oriented faults. However, at these crossovers the high values span over the entire model and are not limited to the reservoir layer. The lateral variations in shear and normal stress resulting from stress perturbations inherently affect the slip tendency distribution as well.

Besides the slip tendency, the normal stress is used together with the largest and least principal stress to calculate the dilation tendency (4.7). This quantity represents the likelihood of the faults to open under the acting state of stress. The distribution of the dilation tendency on the fault network also shows a strong dependency on the orientation of faults and the maximum horizontal stress, but different from the slip tendency. Faults aligned parallel to the direction of the maximum horizontal stress are most prone to open, while faults oriented perpendicular to this stress show lowest values (Fig. 7-38). The gradual transition between maximum and minimum values is significantly affected by the occurrence of stress perturbations and the mechanical properties. However, the impact of the mechanical stratigraphy is lower than for the slip tendency and most prominent in areas of low dilation tendencies. Along those fault segments, the reservoir horizon shows higher values than the over- and underburden (Fig. 7-38).

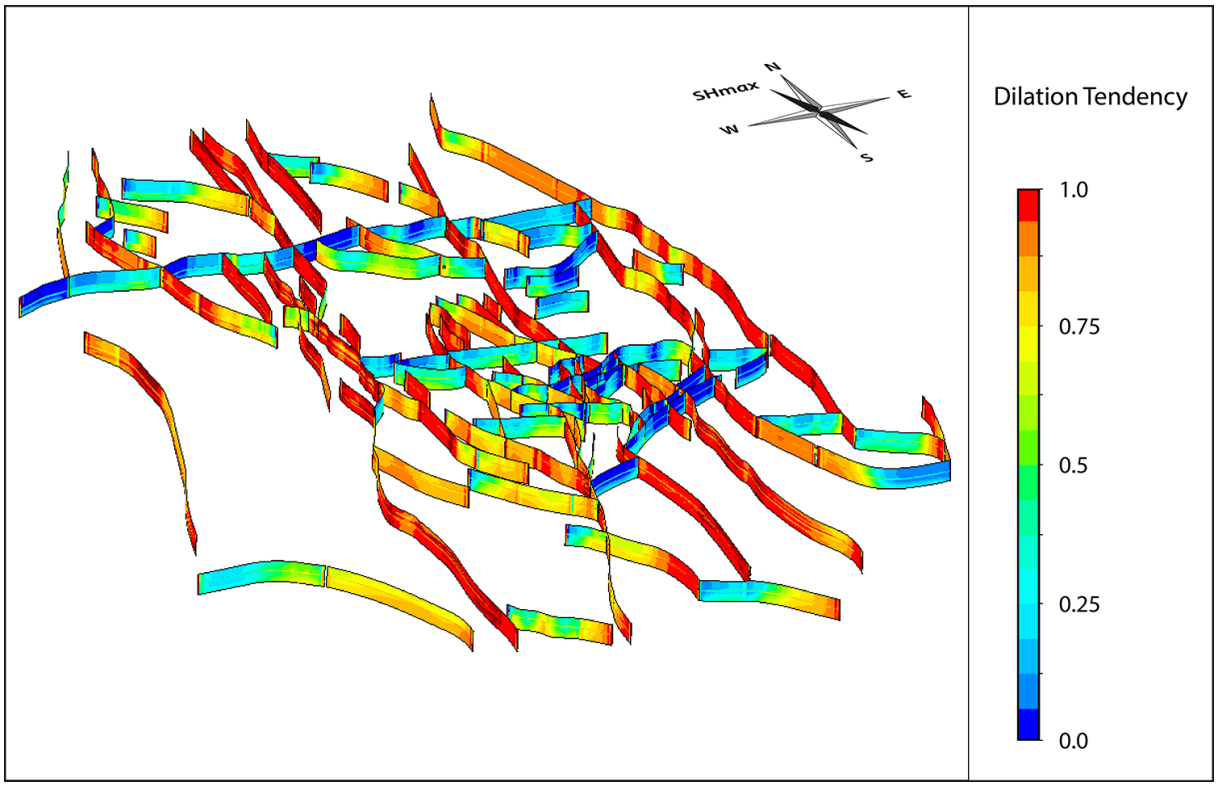

Fig. 7-38. Oblique overview from the southwest on the faults of static geomechanical model showing the contoured distribution of the dilation tendency. The friction coefficient of all faults is 0.1 for this plot.

Changes in the friction coefficient of the faults do not significantly affect the distribution of the dilation tendency. The differences in distribution observed during the lowering of the friction coefficient in the calibration process are subordinate. A characteristic feature occurring at low fault friction is a difference in dilation tendency between over- and underburden. At some fault segments showing intermediate dilation tendency, the underburden exhibits slightly larger values than the overburden (Fig. 7-38). This difference is less abundant at higher fault friction.

During the result evaluation of the fault network, one has to keep in mind that the nodes at the bottom of the model are only fixed in vertical direction and are free to move horizontally. Hence, the boundary conditions do not affect the fault behavior and the plotted results.

In addition to the contour representation of stress and strain on elements at reservoir level and on the fault faces, the outcome of the static geomechanical model can be evaluated by using the drilling paths of wells. These well paths were used in the model calibration. After transferring the path information to the FE model, the elements cut by the path can be selected and contoured with any result quantity. In this way, the least principal stress magnitude can be visualized along an existing or planned drilling path in the reservoir (Fig. 7-39). This reveals the differences in σ_3 magnitude throughout the mechanical stratigraphy. The variations in magnitudes between the lithological layers result from the different mechanical properties, but the magnitudes are also affected by stress perturbations close to the wells. Therefore, the specific stress magnitudes are differing between the wellbores (Fig. 7-39). Instead of selecting and contouring the elements cut by the well path, any quantity can also be mapped virtually onto the path and plotted as a diagram.

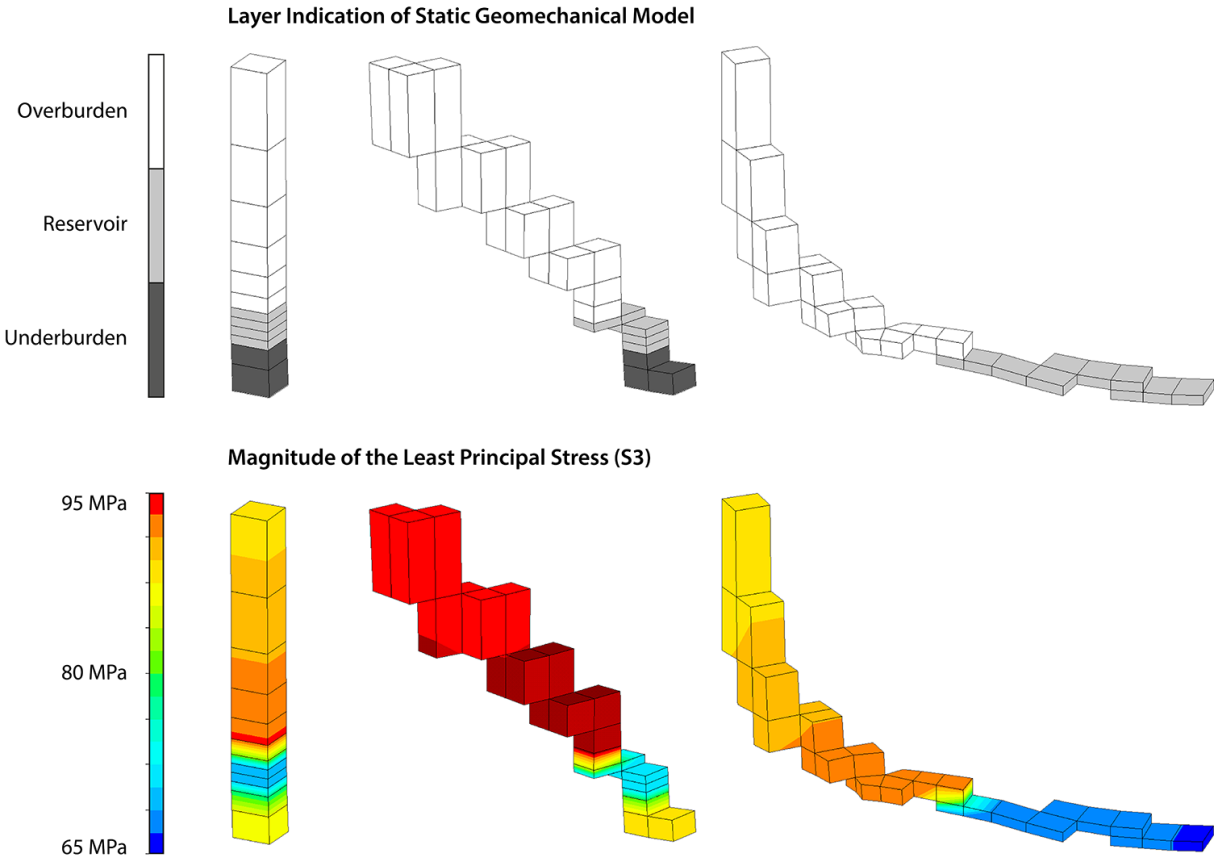

Fig. 7-39. Overview on the elements selected by three well paths in the case study reservoir. In the top row, the elements of the drilling path belonging to well A1 (left), C9 (center) and C7 (right) are colored in shades of grey indicating the lithological layers. In the bottom row, the selected elements of the well paths are contoured with the magnitude of least principal stress in [MPa]. The scaling is constant for all three wellbores.

7.7 Submodel of the Case Study Reservoir

The objective of the research project to build a field-scale geomechanical model has to be reconciled with the expectation of very local stress information demanded for optimizing actual reservoir operations. The static geomechanical model comprises element sizes in the reservoir layer of 100m x 100m in the horizontal dimension and 25m vertically, which represents a very high resolution regarding the scale of the reservoir that covers more than 400km² (7.3). However, on the scale of a potential drilling operation within a fault block, a significantly higher resolution of the resulting stress information is required.

Higher mesh resolutions also naturally increase the results quality of any finite element analysis and further allow to incorporate more details, for instance regarding the mechanical stratigraphy (4.2.1). Due to limitations in computing capacity, however, the element size cannot be arbitrarily lowered for the entire field-scale model. The increase in mesh resolution must be achieved on a more local scale. Two approaches are developed and suggested in this study. The first approach is a so-called fault block refinement, in which the spatial resolution is increased in individual fault blocks fully enclosed by faults (4.2.1). Any additional or more area-wide resolution increase requires the build-up of a so-called submodel, i.e. a separate model of a part of the reservoir.

The following chapters describe the objectives of the submodel built within this study (7.7.1), its setup (7.7.2) and results (7.7.3). The outcome of the submodel is then compared to the results of the field-scale model in order to evaluate the pros and cons of this approach (7.8).

7.7.1 Objectives

A submodel basically represents a smaller geomechanical model covering only a part of the reservoir. By focusing on a more limited region, the model can be richer in details and comprise higher spatial resolution at lower or constant solution times. The primary objective of the submodel in this study is to test the feasibility and value of this approach, and its outcome regarding the inevitable loss of details and interaction due to the missing encompassing fault network. The size of impact of the surrounding fault network on the in situ stress distribution and fault behavior is evaluated.

In addition, the increase in quality of the results, i.e. the dependency of the results on the mesh resolution, is determined. This allows in turn conclusions on whether the mesh resolution of the field-scale model is high enough to adequately reveal the true size of stress perturbations.

7.7.2 Model Setup

The submodel of the case study covers the northwestern corner of the reservoir (Fig. 7-40). This model incorporates exactly the same horizon geometry as the field-scale model (7.3) and a network of 11 faults in total. Fault block volumes are built based on the faces of lithostratigraphic horizons and faults, as well as auxiliary subdivisions (4.1.2). All geometry input required for the build-up is the same as for the field-scale model. This ensures an identical geometry representing the basis for an accurate comparison between both models.

The reservoir part of the submodel is embedded in a circular frame in the same way as the field-scale model (Fig. 7-41). However, the diameter of the completed submodel comprises 18km and is thus significantly smaller. Especially in the geometrical build-up of the model, the reduction in effort is most significant.

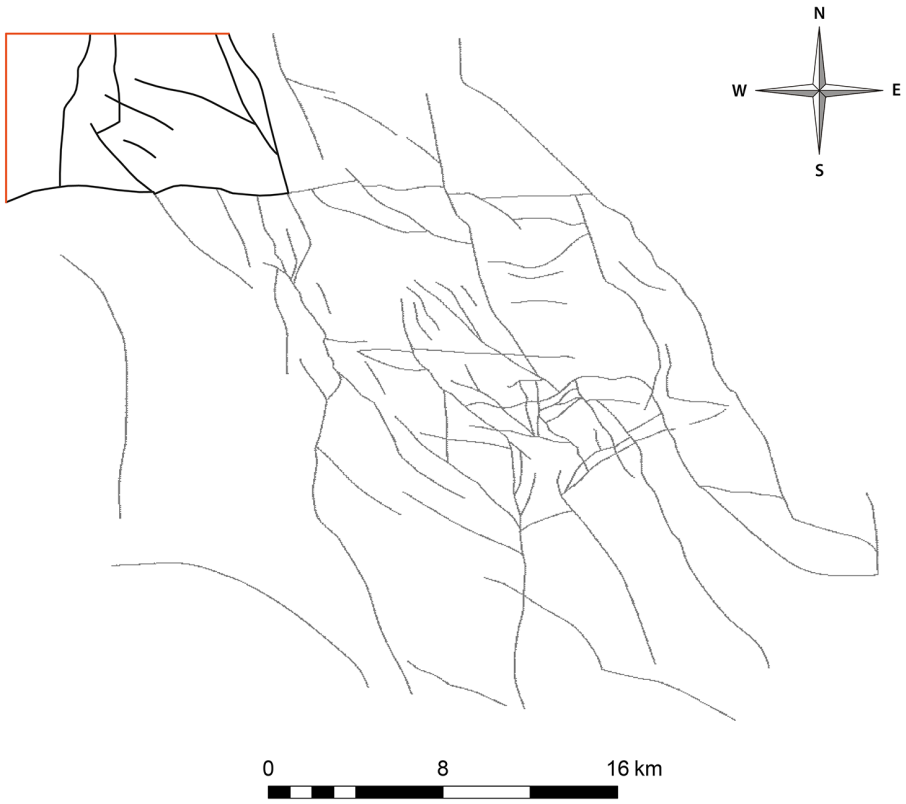

Fig. 7-40. Overview on the fault network of the case study indicating the northwestern part of the reservoir, which is incorporated in the submodel (bold). In total, 11 faults (bold black lines) are considered in the submodel. The model is limited to the north and west by planar faces (orange).

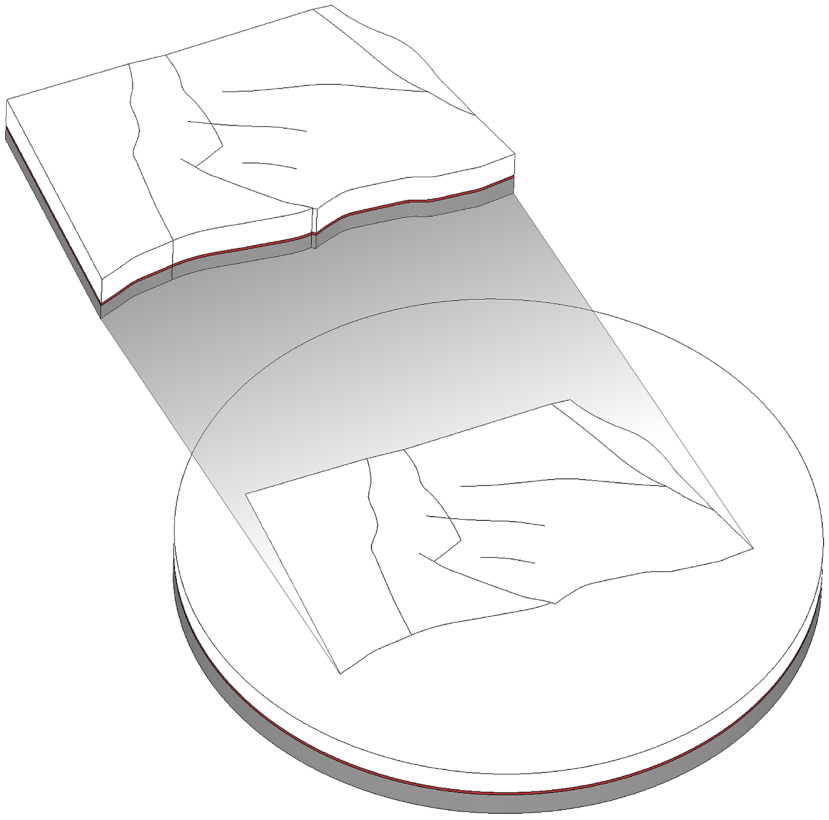

Fig. 7-41. Perspective view on the submodel after the volumes of overburden (white), reservoir (red), and underburden (grey) are generated. The fault network of the reservoir area is embedded into a circular frame as the field-scale geomechanical model. The cylindrical model comprises a diameter of 18km.

Following the geometrical build-up, the submodel is discretized with a horizontal mesh size of 50m, which is half the size of the field-scale model (Fig. 7-42). The over- and underburden comprise 14 element layers and 6 element layers represent the reservoir horizon. This yields an element size of 50m x 50m x 16m for the reservoir. In contrast to the field-scale model, the submodel incorporates 11 faults only, which are also simulated as non-linear contacts by 2D interface elements. In total, the submodel contains 3.65 million elements and thus almost the same amount as the field-scale model.

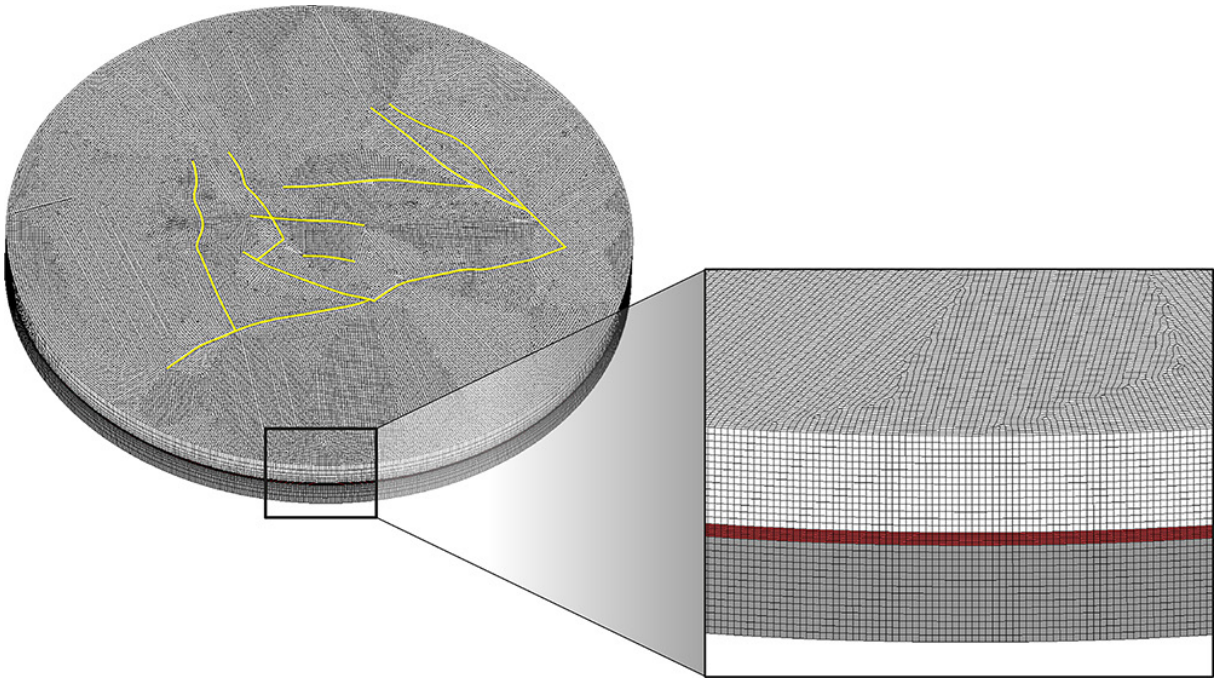

Fig. 7-42. Diagonal view on the meshed submodel. The submodel comprises a horizontal element size of 50m and 34 vertical subdivisions yielding 3.65 million elements in total. It requires approximately the same solution time as the field-scale model. The cylindrical submodel has a diameter of 18km.

Since the submodel shall reflect the calibrated field-scale model as accurately as possible, the same material parameters of the three implemented layers are considered (7.3.3). This also applies to the definition and application of boundary conditions (7.3.4). In addition to the bottom fixation and identical pressure load on top of the model, the lateral displacements are interpolated from the same load frame model. In summary, this submodel reflects the calibrated field-scale model in all details, except for the spatial resolution, the extent of the incorporated fault network and the salt implementation. Due to almost the same number of elements, the submodel requires approximately the same time for calculation than the field-scale model.

7.7.3 Results of the Submodel

Post-processing of the submodel, i.e. calculations of additional result quantities and visualizations, is done using the same routines as in the field-scale model (7.6). Therefore, the top views on in situ stress distributions also show the second element layer of the reservoir. The viewpoint for all visualizations, especially of the fault quantities, had to be changed to focus on the submodel area.

The following figures represent an overview on the high resolution results of the submodel showing the distribution of minimum horizontal stress magnitude, the orientation of the maximum horizontal stress and the fault-specific shear and normal stress, as well as the related slip and dilation tendency (Fig. 7-43, Fig. 7-44, Fig. 7-45). Regarding the overall values and distribution of magnitudes and orientations, the submodel results match the outcome of the spatially lower resolved field-scale model.

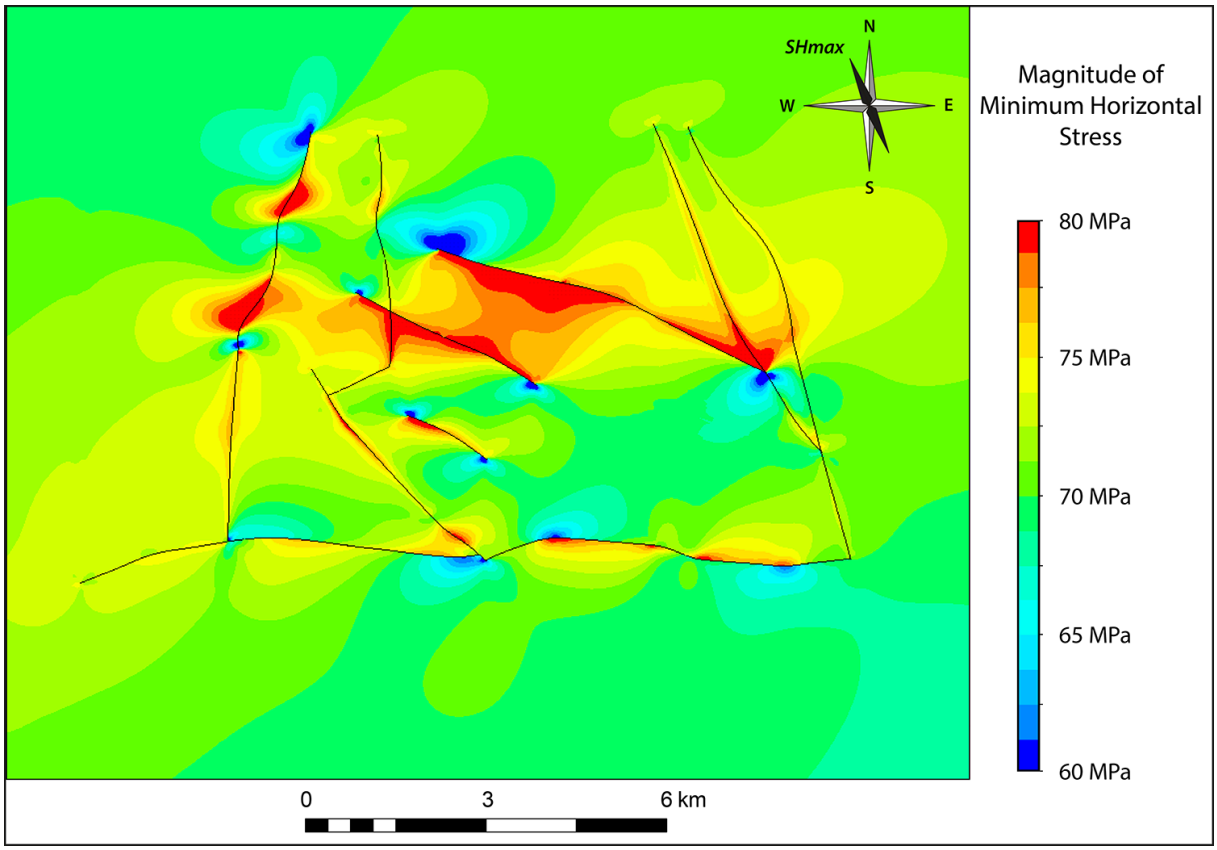

Fig. 7-43. Top view on the geomechanical submodel showing the contoured distribution of the minimum horizontal stress magnitude (σ3) in [MPa] inside the reservoir layer. The contours are scaled to an interval of 20MPa.

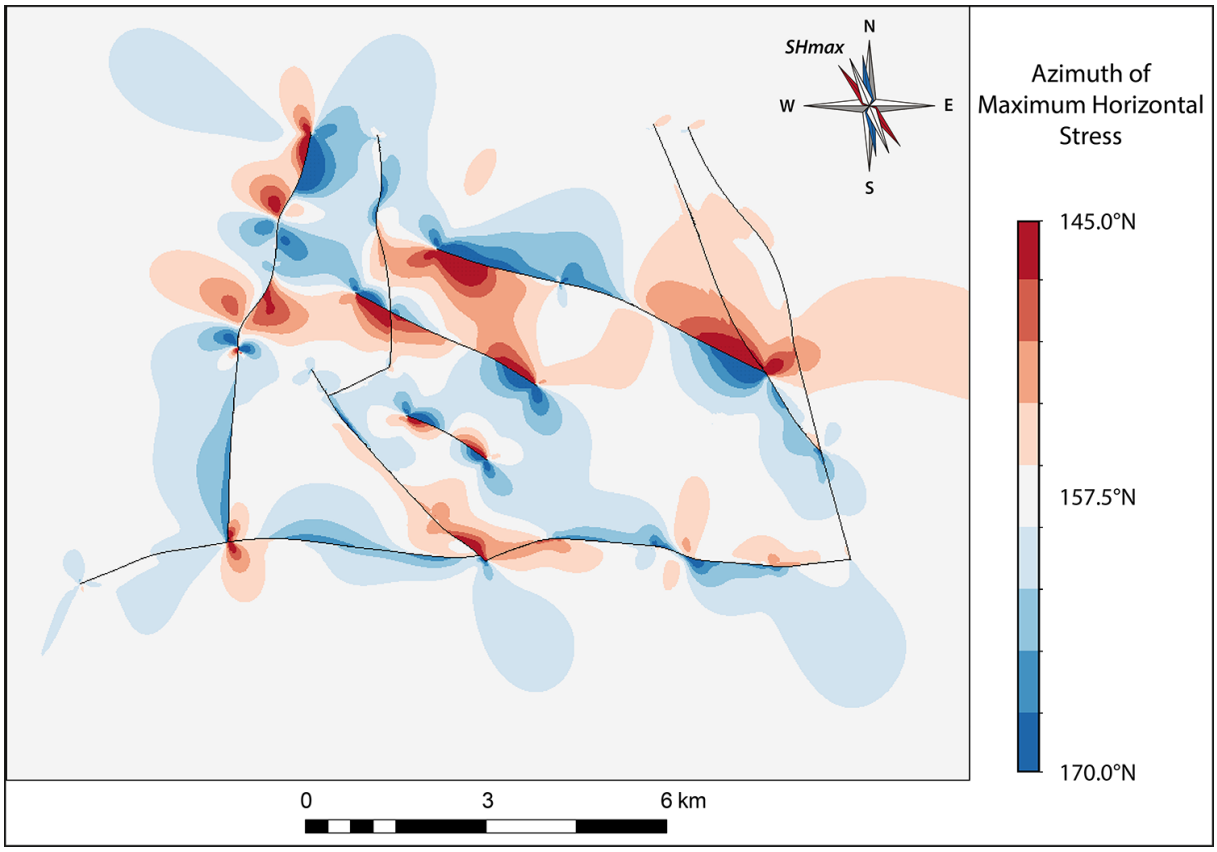

Fig. 7-44. Top view on the geomechanical submodel showing the contoured distribution of the maximum horizontal stress direction in [°N] inside the reservoir layer. The contours are scaled to an interval of ± 12.5° from the regional trend.

The distribution of the minimum horizontal stress magnitude in the reservoir part of the submodel shows distinct perturbations (Fig. 7-43). As shown by the field-scale model, these spatial variations in magnitude are generated at fault tips, curvatures and due to interaction of neighboring or crossing faults. However, the magnitude distribution clarifies that not all fault tips, curvatures or crossings directly result in perturbations. The most intense parts of single perturbations do not extend more than approximately 1km from the source, but neighboring faults can impact the entire area between or close to them. This is indicated by the two WNW-ESE trending faults in the center of the submodel, which significantly elevate the minimum horizontal stress magnitude between them (Fig. 7-43).

The distribution of maximum horizontal stress orientation shows equal occurrence of clockwise and counterclockwise rotations along faults (Fig. 7-44). While the locations of orientation perturbations mostly coincide with those of magnitude perturbations, the respective intensity and shapes are unique. Moreover, significant re-orientations seem to be spatially more restricted than variations in magnitude. The small, isolated WNW-ESE trending fault in the center of the submodel shows a characteristic pattern of re-orientation, which can also be observed on the two larger faults north of it directed in the same way (Fig. 7-44). Close to the WNW corner of the fault, the maximum horizontal stress is rotated clockwise on the NNE side and counterclockwise in the SSW. The other fault tip shows exactly the opposite behavior.

The shear and normal stress distribution on the faults reveals the same orientation dependency as described for the field-scale model (Fig. 7-45). The same holds true for the distribution of slip and dilation tendency. In addition to this intuitive relationship, the closer and rotated view on the contoured fault quantities emphasizes the impact of the mechanical stratigraphy. All distributions comprise deviating values for the thin reservoir horizon leading to a vertical segmentation. This phenomenon is hidden by the high slip tendency values resulting from the low friction coefficient. The lateral impact of stress perturbations is observed as well (Fig. 7-45).

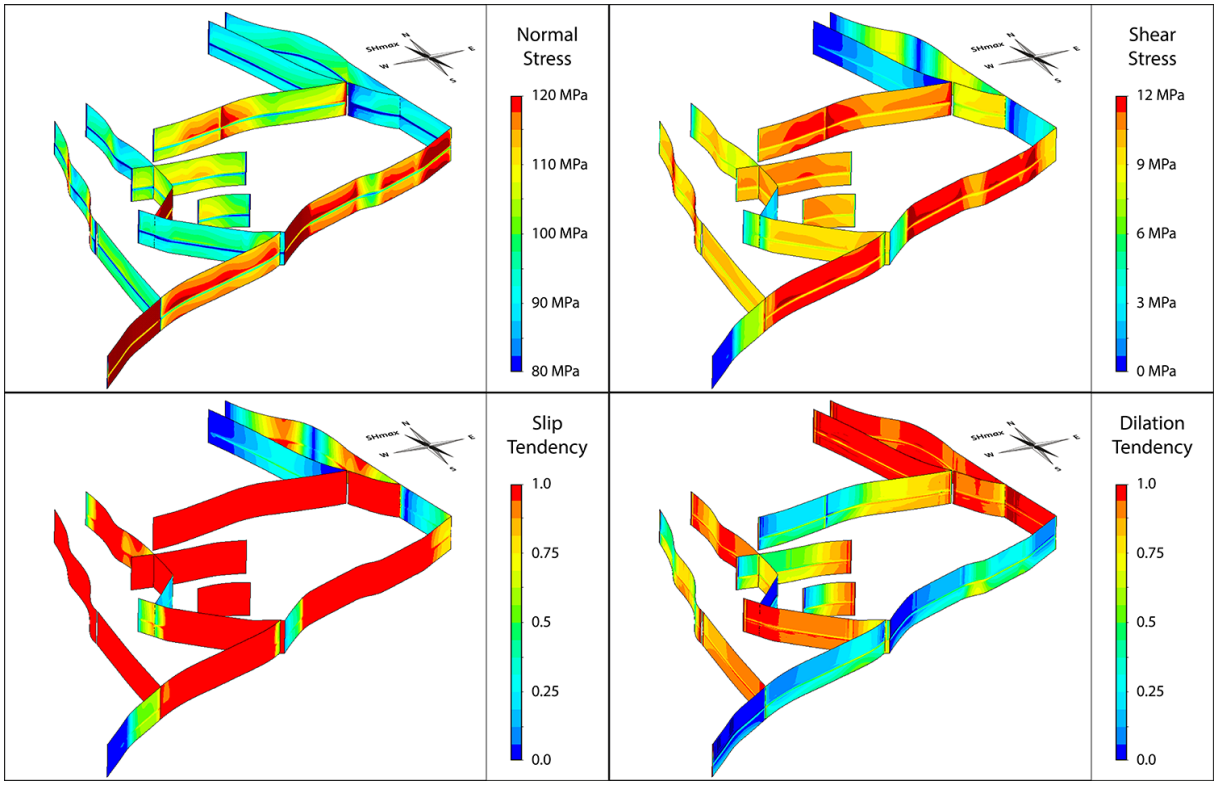

Fig. 7-45. Summary of the fault-specific normal and shear stresses (top) in [MPa] and the calculated slip and dilation tendency (bottom) indicating the faults movement behavior. All four contoured quantities show an impact of the mechanical stratigraphy and lateral perturbations in their distribution, but to different amounts.

7.8 Comparison of Field-Scale Model to Submodel

The field-scale geomechanical model of the case study reservoir considers the entire fault network and thus all interaction and large-scale variations of the in situ stress. Its spatial resolution is high regarding the size of the model, but limited due to computing capacities and related solution times. The submodel comprises only the northwestern part of the case study reservoir. This focus allows significantly higher spatial resolutions. However, the loss of the encompassing fault network around the reservoir part of the submodel inherently affects its outcome. The direct comparison of the field-scale model to the submodel evaluates the validity of the submodeling approach and shows the pros and cons of both models.

The direct comparison of the mesh illustrates the difference in sizing (Fig. 7-46). The significant decrease in horizontal element size by 50% from 100m to 50m, as well as the increase in total vertical subdivisions from 16 to 34, is not feasible for the field-scale model – but for the submodel. Higher degrees of discretization naturally improve the numerical approximation and thus the outcome quality of finite element analyses (Zienkiewicz et al., 2005). This effect diminishes at some point, at which further decrease in element size leads to very minor improvements only. At this point, the results are independent from mesh resolution and therefore any finite element analysis should ideally consider such a degree of discretization.

Besides illustrating the increase in resolution in the submodel, the mesh comparison underlines the high spatial resolution considered in the field-scale model. In order to compare the outcome of both models properly, the results of the field-scale model are visualized exactly in the same view and scale as those of the submodel. The result quantities compared include the distribution of minimum horizontal stress magnitude (Fig. 7-47), mean stress magnitude (Fig. 7-48), orientation of maximum horizontal stress (Fig. 7-49) and the shear and normal stress on the faults (Fig. 7-50).

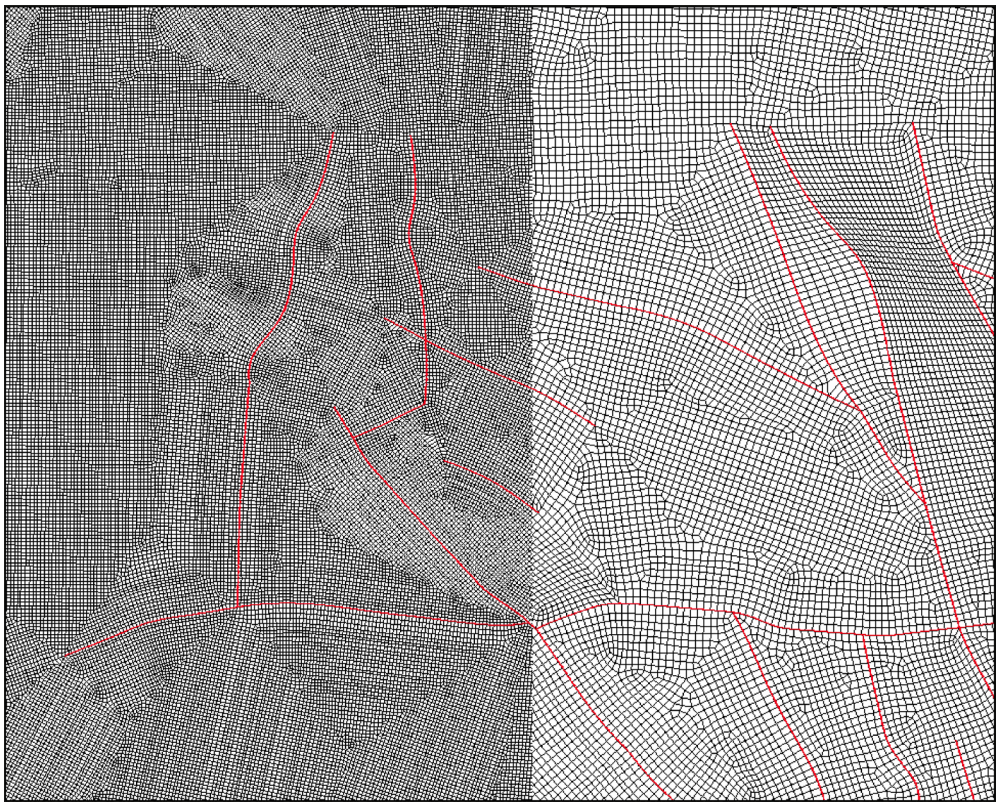

Fig. 7-46. Comparison of the mesh between the submodel (left) and the field-scale geomechanical reservoir model (right). The submodel comprises a horizontal element size of 50m, whereas the field-scale model shows 100m. For scaling, please refer to Fig. 7-43 and Fig. 7-44.

The comparison of the minimum horizontal stress magnitude shows highly similar results and no significant overall decrease in perturbations (Fig. 7-47). This clarifies the fact that the mesh resolution is sufficiently high in the field-scale model to yield numerically accurate results. Nevertheless, the comparison also reveals some differences. The southeastern part of the fault network shows slightly decreased magnitudes in the field-scale model, which can be attributed to the incorporation of salt in the top boundary condition (Fig. 7-47). This lowered overburden load was not considered in the submodel.

Along the most eastern N-S trending fault of the submodel and at the central junction of the southern E-W trending fault, the field-scale model exhibits elevated magnitudes contrasting to the submodel (Fig. 7-47). The relatively less elevated magnitudes observed between the central WNW-ESE trending faults in the field-scale model cannot be directly referred to the salt, because it does not spatially extent that far. In addition, the northerly adjacent minimum of magnitudes is slightly smaller in the submodel. This may be a far-field impact of either the nearby salt or connected encompassing fault network in the field-scale model.

The comparison of mean stress distribution in the submodel area shows similar behavior (Fig. 7-48). The salt impact yields lowered magnitudes in the southeastern parts, but lower magnitudes are also observed in the northeast outside the area of adjusted overburden pressure (Fig. 7-48).

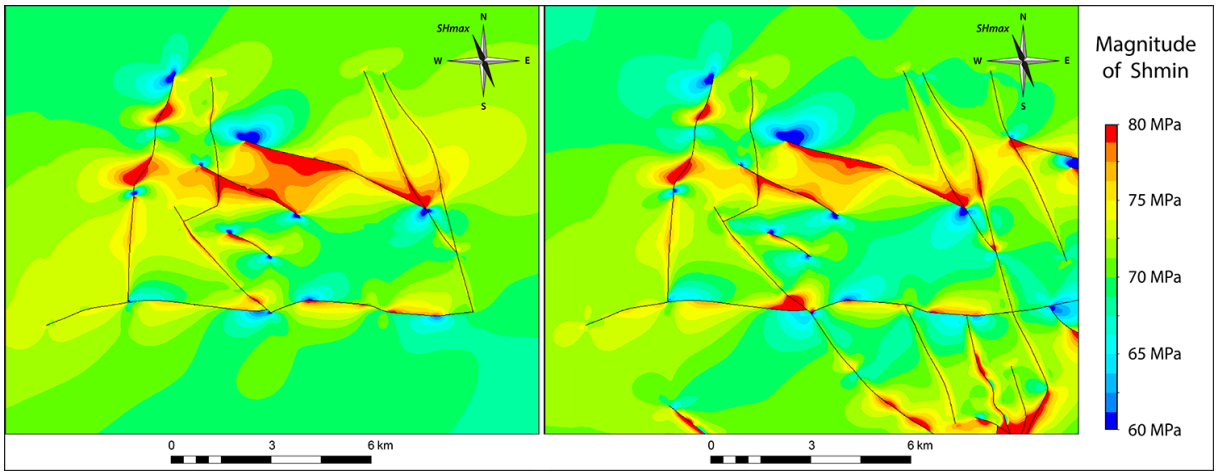

Fig. 7-47. Comparison of the distribution of minimum horizontal stress magnitude in [MPa] between the submodel (left) and the field-scale model (right).

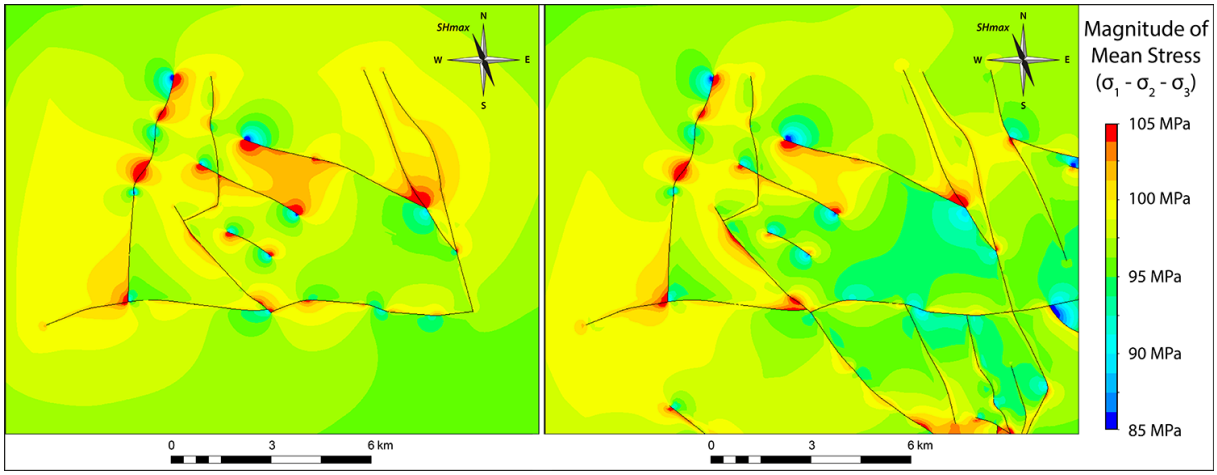

Fig. 7-48. Comparison of the distribution of mean stress magnitude in [MPa] between the submodel (left) and the field-scale model (right).

Moreover, the magnitudes and related perturbations along the southern E-W trending fault are differing between the submodel and the field-scale model (Fig. 7-48). In the eastern part of the fault, these differences can be attributed to the salt, but differences occurring at the same fault junction recognized in the previous plot are suggested to result from the missing encompassing fault network. The mean stress distribution at WNW-ESE trending faults in the center of the submodel is affected in the same way as the minimum horizontal stress (Fig. 7-48). Additionally, the small isolated fault shows significantly less pronounced perturbations in the field-scale model.

Besides the distribution of magnitudes, the orientation of maximum horizontal stress is compared. This comparison shows high similarity and thus underlines the satisfactory resolution of the field-scale model as well (Fig. 7-49). Some minor differences in the northern part can be related to the coarser contouring scale of the orientation distribution, which is more sensitive to a finer mesh. The most striking differences can be observed along the most eastern NNW-SSE trending fault of the submodel and at the northern end of the NW-SE trending fault in the southern center. In the submodel, both of these faults end in the south at the E-W trending fault, whereas they proceed in the fault network of the field-scale model (Fig. 7-49). This gives rise to the conclusion that the impact of the missing encompassing faults in submodel is most significant for directly connected faults.

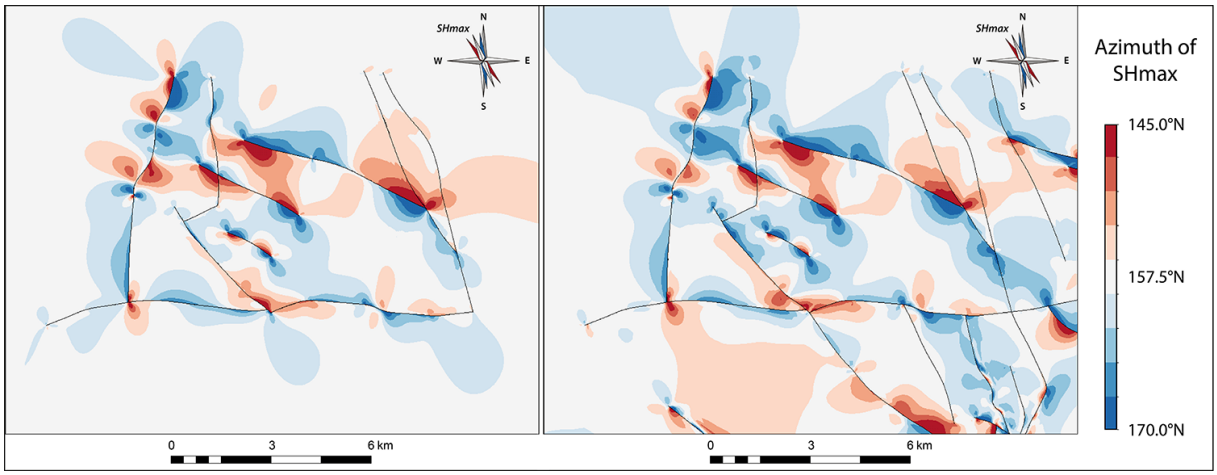

Fig. 7-49. Comparison of the distribution of maximum horizontal stress orientation in [°N] between the submodel (left) and the field-scale model (right).

The fault-specific shear and normal stresses are also compared between the field-scale model and the submodel. This comparison shows similar distributions as well (Fig. 7-50). However, the increase in vertical resolution in over- and underburden is significant. Therefore the lateral and vertical size of contact elements is raised. Despite the similarity, the distributions reveal slightly lower stress magnitudes in the field-scale model in general. This effect is most prominent on faults that extend in the field-scale model further to the south (Fig. 7-50). The higher vertical resolution in over- and underburden reveals more precise and less noisy stress distributions along faults in the submodel. This can be observed best at the shear stress along the eastern N-S trending faults and at the normal stress along the E-W trending faults. The generally minor differences in the distribution of fault-specific stresses can be referred to the fact that the distribution of magnitude perturbations is not severely changing as well (Fig. 7-47 / Fig. 7-48).

In summary, the build-up of the submodel required less effort than the field-scale model. However, the effort for generating, solving and post-processing of a geomechanical model does not decrease linearly with model size. If a submodel is worth the effort thus strongly depends on the new or improved outcome it may provide. A submodel definitely includes higher resolved insights into the local stress field by the price of neglecting the surrounding fault network.

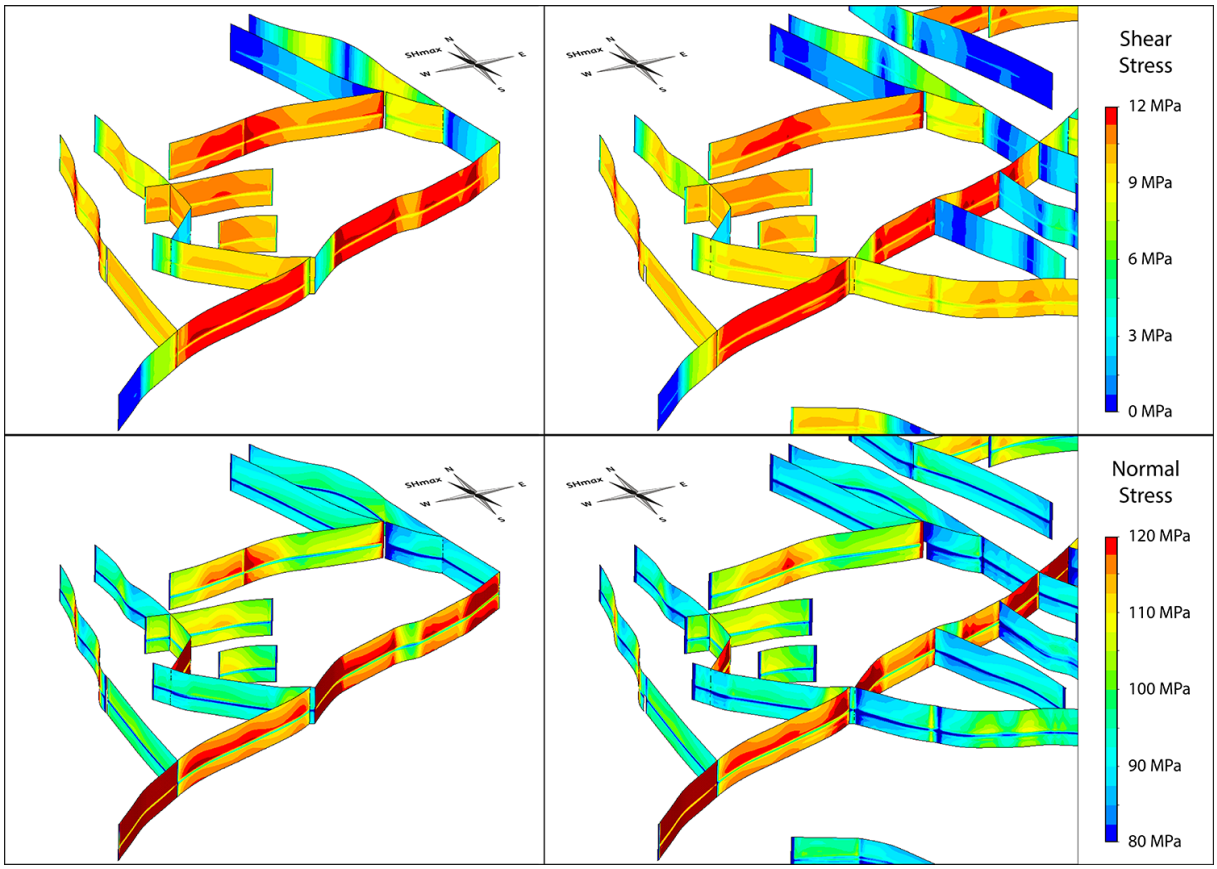

Fig. 7-50. Comparison of the distribution of shear stress (top) and normal stress (bottom) in [MPa] between the submodel (left) and the field-scale model (right). (The magnitude variation at the WNW-ESE trending fault in the center of the submodel may result from subordinate meshing or merging errors.)

The comparison of results elucidated the relatively minor impact of the missing encompassing fault network. This impact is naturally largest at the boundary of the submodel towards the excluded part of the fault network. In the interior of the submodel, the impact on the results depends considerably on the specific connection of the faults. Faults fully included in the submodel are less prone to show different behavior or change in stress magnitude and orientation distribution than those faults that are "cut" from the fault network due to the spatial limits of the submodel. Due to the small amounts of cropped faults in the northeastern submodel of the case study, this phenomenon is maybe more limited than it would be the case for submodels of other parts of the reservoir.

The comparison of the results between the field-scale model and the submodel clarifies that the mesh resolution of the field-scale model is sufficiently high to yield numerically accurate results. No general decrease in the size or other change of stress perturbations is observed, which would indicate a mesh dependency. Higher spatial resolution only smooths the result visualization.

7.9 Discussion of Static Model

The static geomechanical model of the case study reservoir is successfully built and truly field-scale as it covers an area of more than 400km². It comprises a mechanical stratigraphy of three layers and 86 faults in total representing an extensive fault network (7.3). The model is calibrated against field data and provides novel and unique insights into the in situ stress and strain distribution of an intensely faulted gas reservoir (7.6). These results cover the entire reservoir including all undrilled parts of the reservoir. The revealed complexity of local stress variations underlines the necessity of numerical geomechanical modeling approaches.

The applied geomechanical modeling workflow focuses on revealing the specific present-day in situ stress distribution throughout the intensely faulted case study reservoir prior to production start. The temporal evolution of this in situ stress field during the subsequent production stage is not the scope of this approach. However, the impact of timing cannot be neglected in general, but potential impact is mostly limited to the geomechanical sonic logs. Their timing relative to production and decreasing pore pressure in the corresponding fault blocks may affect the inferred mechanical properties. However, this impact is assumed to be negligible regarding the general uncertainty of these parameters.

Temporal changes are unlikely to have significant impact on the applied reservoir geometry, the results of rock mechanical tests on drill cores, on stress measurements during hydraulic fracturing and the regional stress field. Severe changes in reservoir geometry during production, sufficiently strong to require their consideration in the model, are typically only observed in unconsolidated reservoirs of great thickness. The results of rock mechanical tests on drill cores could only be affected by timing if the corresponding wellbores are drilled after intense exploitation of the respective fault blocks by neighboring wells – which is not reported. Moreover, the local stress measurements during hydraulic fracturing increase fluid pressure by injection to overcome and determine the total magnitude of the least principal stress. Preceding production-related changes in pore pressure thus does not affect these results. Furthermore, the far-field state of stress in the case study area is likely to remain constant over the entire production cycle of the reservoir.

Pore pressure is also not explicitly regarded as degree of freedom in the calculation of the geomechanical model. Finite element models are generally able to incorporate fluid pressures, but such a coupling complicates the model significantly and increases computation times. Moreover it is assumed that the pore pressure can be regarded in terms of effective stress (3.2.2.1). In other words, the pore pressure counteracts the absolute principal stresses and lowers their magnitudes, but to equal amounts and does not change the orientation of the principal stresses. The revealed relative distribution of in situ stresses and their perturbations is thus assumed to be largely unaffected and only the scaling would change. In cases of severe overpressures in distinct reservoir compartments, this assumption cannot be made.

As in any numerical modeling approach, the uncertainties of input and calibration data are critical and affect the quality and reliability of the geomechanical modeling results. While the chosen transfer of reservoir geometry preserves provided topologies very well (4.1.2), the underlying seismic interpretation yielding the reservoir geometry in the first place inherently comprises uncertainty. This uncertainty in interpretation is hard to quantify and has to be kept in mind. Especially under salt bodies, this uncertainty can be decisive for the in situ stress distribution as it effects the exact position of the faults. Furthermore the assumption of a constant and significantly larger thickness of the reservoir layer is justified and reasonable for this modeling approach (7.3.1). Resolving the true thickness, its actual variation and multiple sandstone and shale layers would increase the geomechanical model considerably. This could be done in submodels, but is computationally not feasible for a field-scale model as it raises the demand in computing capacities significantly and also requires more detailed information on the material parameters to model the mechanical stratigraphy. As long as this more detailed information on the material properties is not available, any layer refinement would be affected in turn by the uncertainty of new assumptions. The increase in model quality would be questionable.

In general, a wider and more solid basis of material parameters is desirable, since they are important for the modeling outcome. Rock mechanical tests of the reservoir sandstone at four wells represent the

input data of static material parameters for the geomechanical model. According to the contractor conducting the rock mechanical tests, the reservoir sandstone shows variable strengths, failure and post-failure behavior depending on the well location and the contents in clay and silt (internal report #1). Besides the results of these tests, multiple sonic logs provide information on the dynamic parameters. However, only 3 out of 5 logs could be used completely. One log did not reach the reservoir level and the second log lacks density information required for calculating Young's modulus (3.2.1). The data basis for material properties was thus smaller than expected in the beginning.

Moreover, the reservoir-specific correlation and conversion of dynamic to static parameters was complicated by the fact that the datasets are not taken from the same wells and do not overlap. Such an overlap would have represented a great improvement for estimating uncertainties and for parameter conversion. More data that is sufficiently overlapping could be used to set-up a reservoir-specific conversion function, for instance. This was not feasible with the sparse and heterogeneously distributed data. The impact of only slightly varying material parameters is demonstrated in the discussion of calibration (7.5.5). This sensitivity underlines the importance of incorporating also lateral variations in material parameters. Due to the limited availability of drillings, true three dimensional information on material parameters can only be provided by 3D seismics (Gray et al., 2012). This type of dataset represents an ideal basis for geomechanical modeling, but is rarely available.

Besides the description of lithostratigraphic horizons, the project partners provided geometrical information on the fault network of the case study reservoir. All faults are provided within an agreed structural model of the project partners and are verticalized in beforehand due to the small thickness of the reservoir horizon (7.2.1). The lack of inclination affects especially the modeled fault behavior in the static geomechanical model. This impact is demonstrated in the 3D models of the preliminary parameter studies (6.1). The overall impact is assumed to be low due to the steep dipping angles of the majority of faults. Nevertheless, for detailed submodels the exact fault geometry can be incorporated. The more extensive the incorporated stratigraphy of geomechanical models gets, the larger becomes the impact of fault inclination and the more carefully it must be regarded. In such models, some faults will also truncate, which is strongly affecting the stress distribution and fault behavior.

In addition to seismically mapped faults, the provided geological model comprises faults, which could not be interpreted in seismic data due to very low offsets, for instance. Other faults are below seismic resolution and are referred to as subseismic faults. These conceptual faults are inferred from the production behavior of neighboring wells. The precise location of such faults is naturally difficult to determine. However, the origin of faults and the degree of certainty regarding their exact location is not indicated in the structural model. Thus, it was not possible to select faults depending on their uncertainty and all faults – especially in the production area of the reservoir – are taken into account for the geomechanical model. Only very small faults showing no offset and faults far outside the production area are neglected. This means that some conceptual faults are incorporated in the geomechanical model, which may follow different traces than those defined. This directly affects the modeled stress perturbations and their interaction. In addition, subseismic faults that are not detected by production behavior may disturb the in situ stress to some extent as well.

The results of the static geomechanical model show high slip tendency values across a large number of faults. These high values result from the low friction coefficient of 0.1, on which the ratio of shear and normal stress is normalized (4.7.2). This value is suggested by the model calibration. As mentioned in the discussion of calibration, this low value reflects the best fit between modeling results and field measurements, and may vary between the faults of the reservoir (7.5.5). In fact it is likely that the

coefficient of friction varies depending on the tectonic history, thickness and rheological properties of individual faults. A friction coefficient directly affects the stresses a fault is capable of withstanding. Higher friction coefficients allow higher shear stresses to be maintained, for instance. In this way the fault friction controls the movement behavior of the fault and also the stress perturbations in the surrounding. The implementation of fault-specific friction coefficients would significantly improve the geomechanical modeling results. (Geo-)Dynamic forward modeling elucidates the faults tectonic history and potentially allows an inference of recent frictional and hydraulic properties.

Calibration of the static geomechanical model is a process sensitive to measurement uncertainty. The heterogeneously distributed data used for calibration complicated uncertainty estimation. In addition to extended leak-off tests, information on the least principal stress magnitude is provided by the results of ultrasonic wave velocity analyses (WVA) on drill cores. However, the measurements are derived at different wells throughout the reservoir and thus could not be compared directly. More precise information on uncertainties and error ranges helps to improve the calibration procedure. It could also be improved by more measurements yielding the magnitudes and orientations of all three principal stresses at a single point. If reliable, such information is ideal and can be taken from methods like ultrasonic wave velocity analyses (WVA), anelastic strain recovery (ASR) and so-called RACOS® measurements (4.8.1). These methods require core material for testing, which traditionally is rare due to the related costs. However, these costs could amortize rapidly with respect to the potential application of reliable geomechanical modeling results.

Although the calibration yielded a satisfactory fit between modeling results and field measurements, especially regarding the related uncertainties, this process could have been extended. Each parameter variation demands the calculation of the geomechanical model. The solution time of approximately one day on average plus the required pre- and post-processing limited the possible parameter variations tested in this study. Additional variation cycles that focus on different friction coefficients of specific fault sets are likely to yield improved fits. More reasonable processing times would require more powerful hardware.

The correction of the top boundary condition for salt during the calibration process elucidates the importance of lateral differences in overburden load. Ideally the entire stratigraphic column up to the Earth's surface is included in the geomechanical model. This is unfeasible for geomechanical models of deep reservoirs. In those cases, the pressure load of the top boundary condition ideally regards the lateral variation in lithostatic load across the reservoir.

Stress paths, as shown in the results of the static model (7.6), can also be used in strictly vertical direction and instead selecting and contouring the respective elements, the stress can be plotted as a diagram. By interpolating the principal stresses on such a vertical path, the stress gradients are revealed at any location in the model. The representative diagram of the principal stress trends reveals two important aspects (Fig. 7-51).

First, the vertical stress equals the second principal stress in the overburden and changes to be the first principal stress in the reservoir layer and underburden. This elucidates the possibility of changes in the tectonic regime resulting from changes in mechanical properties. Such changes affect the characteristics of natural and hydraulically induced fractures, for instance.

Second, the diagram reveals relatively steep stress gradients of the maximum and minimum horizontal stress in the over- and underburden. The increase in magnitude with depth in these layers does not reflect observed and published data (Röckel and Lempp, 2003). This is probably caused by the lateral displacement boundary conditions that are vertically constant.

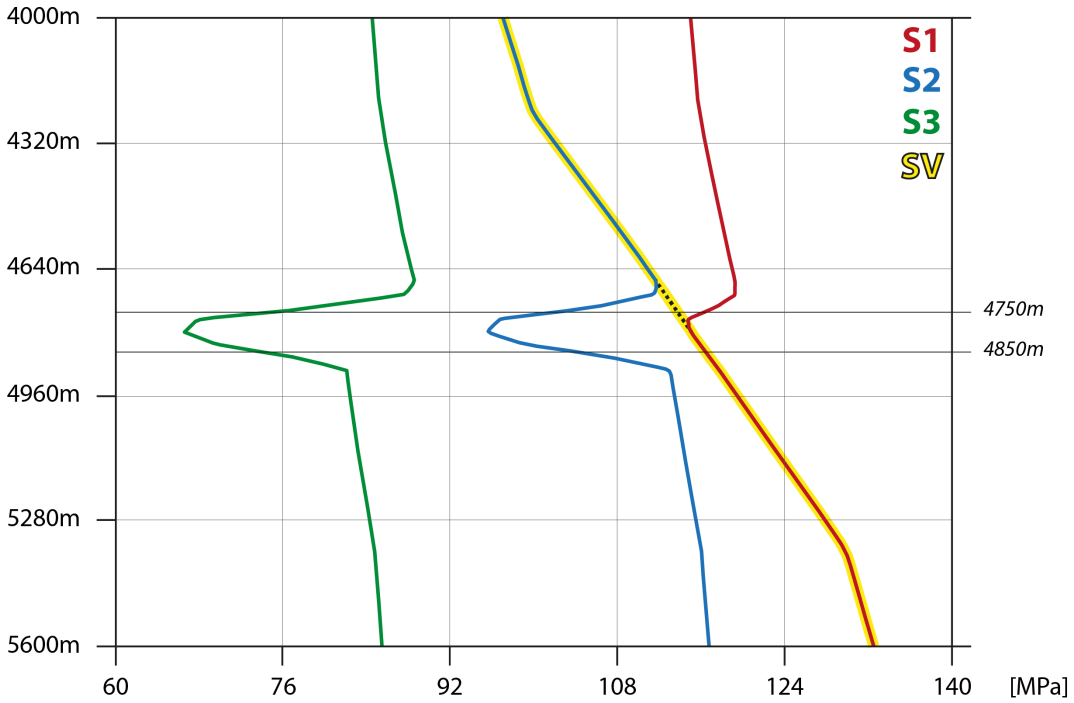

Fig. 7-51. Vertical trend of the least (green), intermediate (blue) and first principal stress (red) at well C5 in the static geomechanical model. The reservoir layer ranging on average from 4750m to 4850m depth is indicated by horizontal lines. The vertical stress (yellow) equals the second principal stress within the overburden and changes to be the first principal stress in the reservoir layer and underburden.

However, the phenomenon does not affect the stress magnitudes on reservoir level, which match measured information, and thus the outcome of the geomechanical modeling approach is not influenced. The numerically inevitable, coarse vertical resolution in the reservoir of 4 element layers precludes a finer description of the stress gradients inside the modeled reservoir layer. Geomechanical models including a larger stratigraphy and focusing on results at several layers must correct for this effect. In this case, a correction could be made by vertical gradients in lateral displacements increasing with depth and a calibration of the load frame model to distinct horizontal stress gradients.

In order to meet the demands in local resolution of geomechanical information for real-world applications and planning, two approaches are described. While the fault block refinements can be realized within field-scale models with relatively low effort, the submodeling approach is more labor-intensive, but has great potential. The results of the submodel show that the negative but minor impact of the missing encompassing fault network depends on the connection to the part included in the submodel (7.7.3). Hence, care must be taken at submodeling parts of reservoirs comprising a highly interconnected fault network.

Overcoming the problems of scale will be an ongoing challenge in geomechanical modeling, since large-scale effects must be regarded in models on lower scales. In addition, further small-scale aspects must be regarded additionally, such as subseismic faults and facies changes.

8 Dynamic Model of Case Study Reservoir

The dynamic model of the case study represents a forward-modeling approach regarding the tectonic history of the reservoir area. This approach aims for a mechanically consistent simulation of the entire tectonic evolution of the reservoir and considers various paleo-stress fields since Permian times, which differed significantly from the recent state of stress. The dynamic model allows insights into the development of the fracture network of the reservoir and reveals the kinematic history of the faults.

The simulated in situ paleo-stresses, that were responsible for fracture generation and reactivation, shall help to establish a description of the temporal and spatial evolution of the reservoir's fracture network. This description may be used for predictions in undrilled parts of the reservoir. The revealed geomechanical state of the faults in the past is tested on a potential correlation with the recent hydraulic fault behavior. The obtained insights complement the outcome of the static model and complete the geomechanical modeling of the case study reservoir.

In the following, the objectives of the dynamic model are described in detail (8.1), as well as the required preparatory work (8.2), the model setup (8.3) and the modeling results (8.4). Thereafter the entire dynamic approach is discussed (8.5).

8.1 Objectives

The overall intention of the dynamic model is to provide a mechanically consistent simulation of the tectonic evolution of the reservoir. Therefore the field-scale model has to consider the paleo-stress fields at all major past tectonic stages since basin initiation in the Permian (5.1). Major stages are those phases in time, whose prevailing stress configuration had significant impact on the development of the fracture and fault network. The significance arises from the time length of the phase or pronounced tectonic activity. A geomechanical model of the reservoir is calculated that is specifically modified for these stages and provides snapshot-like insights into the in situ stress distribution at those times. A fully transient, i.e. time-depending, model is beyond the scope of this study.

Primary objective of this forward-modeling approach is to obtain a description of the temporal and spatial development of the reservoir's fracture network and its characteristics. This description is inferred from the specific in situ stress distributions at the past tectonic stages simulated by the model and the effects of faults and mechanical stratigraphy. This stress evolution including all variations in magnitude and orientation controlled the generation and reactivation of the fractures observed today. The dynamic model is validated by comparing the fracture sets and properties proposed by the in situ stress modeling to fractures actually determined in image logs.

Besides information on the fracture network, the dynamic model shall reveal the stress distribution on the fault faces during different paleo-stress stages. The movement behavior of the faults at the respective times is then inferred from these fault-specific stresses. Especially the behavior of E-W trending faults is of interest. Those are proposed by production behavior, but not mappable in seismics and are suggested to be strike-slip faults lacking sufficient juxtaposition and contrast in impedance.

Regarding the paleo-stress distribution on faults and their behavior, the hypothesis is to be tested which proposes a predictable correlation between intense geomechanical exposure of faults throughout their tectonic history and a significantly reduced permeability due to increased cataclasis. Faults that were critically stressed and/or experienced movement under multiple and different tectonic stress

fields would act as baffles or seals in the present-day reservoir. Such a correlation could help to predict sealing faults and to deal with compartmentalization of reservoirs.

8.2 Preparation of Dynamic Modeling

Prior to the setup and calculation of the dynamic model, some preparatory work is required in beforehand. The major paleo-stress stages that are to be modeled representing the tectonic history of the reservoir area must be described. This description has to encompass all aspects that are differing from the static model of the present-day situation, on which the dynamic model is based.

First, the major tectonic stages in the history of the reservoir area must be identified. The major stages are those comprising the largest overall impact on the development of the fracture network and the faults in the reservoir. This impact can arise from a large time span the respective paleo-stress fields are prevailing and/or from intense tectonic activity during a specific phase. The identification and definition of the paleo-stress stages for dynamic modeling should be done in consideration of the general evolution of the reservoir area, such as the overall basin evolution, for instance. Determining the stages in multi-disciplinary geological approaches provides a more thorough and solid description of the tectonic phases.

This first step of assessing the major tectonic stages to be incorporated in the dynamic modeling is highly decisive. Neglecting important phases in the tectonic history will inevitably result in incomplete modeling results. In the worst case, these results lead to wrong interpretations and conclusions, whereas in the best case some aspects cannot be explained. However, missing prioritization and incorporating numerous minor phases will result in unfeasible calculation and post-processing times. Hence, as less stages as possible have to be defined, but as many as necessary for covering the tectonic history. The major stages of the dynamic model of the case study are identified in the tectonic evolution of the Central European Basin System and summarized below (8.2.1).

Following the definition of the major tectonic stages to be modeled, the burial history of the reservoir horizon must be clarified. The burial history in combination with the thermal history is commonly available for hydrocarbon reservoirs prior to geomechanical modeling due to its relevance in assessing maturation ages, for instance, and evaluating the reservoir potential. The burial history describes the depth of the reservoir horizon and other units beginning with their depositional age and lasting until today. Burial curves showing the depth over time are determined by the so-called backstripping technique (Gluyas and Swarbrick, 2004). In his technique, the thickness of overlying layers is sequentially taken off in order to reconstruct the burial history of each unit.

The reconstruction of the burial history has to regard compaction of the lithological units. Compaction represents the progressive loss of porosity due to imposed overburden load resulting in a reduction of thickness. The rate of compaction is determined from typical porosity-depth or porosity-effective stress relationships (Gluyas and Swarbrick, 2004). Initial porosities as starting points differ significantly between shale and carbonate muds (~60-80%) and sands (~40%), for instance, and also the rate of porosity decline is different. Compaction and porosity loss results in increased density and more rigid rock behavior. This process progressively decreases with increasing burial and significantly affects material parameters and the prevailing stresses. The burial histories of various wells in the reservoir region were provided by the project partners. Based on this information, the reservoir depth of the case study at the major tectonic stages is identified (8.2.2).

The change in depth is inevitable related to the change of material parameters due to compaction. This change has also to be addressed as detailed as possible in the geomechanical modeling of paleo-stress stages. Density increases with time and depth during porosity decline and directly affects the vertical stress. Therefore the change in density is also regarded in the dynamic model of the case study (8.2.3).

Besides the rock density, ongoing burial and compaction naturally changes the mechanical properties as well. While compaction is generally assumed to increase the stiffness of the rock, the final Young's modulus is also likely to be affected by a variety of additional aspects, such as cementation type, microfractures and bedding structures, amongst others (Crawford et al., 2010). The development of Poisson's ratio during the burial history is also ambiguous and no relationship is established so far. The absence of any clear and reservoir-specific knowledge on how mechanical parameters possibly vary with increasing subsidence complicates reasonable estimations for modification of these parameters (8.2.3).

The most important aspect in the dynamic modeling addresses the specific paleo-stress fields acting on the reservoir horizon. The vertical stress depends on the respective paleo-densities. The corrected overburden density in combination with gravity and the burial depth of the reservoir defines the lithostatic load applied on top of the geomechanical model at each stage. The corrected density of the implemented layers yields the vertical stress gradient inside the model. In this way, the reconstructed reservoir depths and paleo-densities yield the vertical paleo-stress for the dynamic model of the case study (8.2.4).

In addition to the vertical stress, the horizontal stress configuration at the chosen stages must be defined and conveyed to boundary conditions. This addresses the orientation and magnitudes of the maximum and minimum horizontal stress. The orientation of the horizontal stresses and the tectonic regime are commonly given by the identification of the tectonic phase, i.e. the orientation of structural elements timed to the respective stage indicates the stress field orientation. Determining the magnitudes of maximum and minimum horizontal stress is more complicated.

The overall order of the vertical stress, maximum and minimum horizontal stress representing the principal stresses is described by the prevailing tectonic regime of the tectonic stage. Further constraint on the stress magnitudes can be provided by so-called R-values (Eq. 8-1).

$$R = \frac{(\sigma_2 - \sigma_3)}{(\sigma_1 - \sigma_3)} \qquad \text{Eq. 8-1}$$

The R-value is derived from fault-slip analyses and describes the relation of the principal stress magnitudes at the investigated paleo-stress stages (Angelier, 1979). This value offers more constraint on the relation between the stress magnitudes, but it does not yield absolute values.

In order to define the absolute horizontal stress magnitudes, it is proposed to express them in relation to the vertical stress, which is relatively well constrained from burial history and decompacted densities. While the magnitude of vertical stress is determined in beforehand and fixed, the factors describing the horizontal stress magnitude in relation to the vertical stress are varied. The objective are magnitudes, whose relationship matches the proposed R-value and that yield plausible magnitudes also in context of the tectonic history. A relatively large difference between vertical and maximum horizontal stress magnitudes may represent a more stable normal faulting regime and vice versa. These R-values are also used in the dynamic model of the case study to obtain more justifiable assumptions for horizontal stress magnitudes (8.2.4).

This preparatory work of compiling the parameters, which describe the major tectonic phases as accurate as possible, is mandatory for the proposed dynamic modeling approach. In the following, all aspects outlined above are applied to the case study reservoir.

8.2.1 Major Tectonic Stages

The case study reservoir is located in the North German Basin, which is part of the Southern Permian Basin that in turn is embedded in the Central European Basin System. The major tectonic stages the reservoir horizon encountered in its history are thus stages in the evolution of these basins.

Four decisive tectonic stages from latest Carboniferous times to the present-day stress configuration are described by Kley et al. (2008). This description of the regions structural evolution represents the most recent publication on this topic and is based on relatively well constrained deformation patterns of these intervals. The four tectonic stages are described in the overview on the tectonic evolution of the reservoir area (5.3) and are briefly summarized below in the context of defining the respective boundary conditions.

The first tectonic stage implemented in the dynamic model of the case study covers transtension prevailing from latest Carboniferous to Permian times. Normal and transtensional NE-SW trending faults – and associated basins – are proposed to be generated under this stress field in the latest phase of the Variscan orogeny (Fig. 8-1). Instead of applying simple shear boundary conditions to the load frame, the regional dextral strike-slip setting is conveyed to corresponding orientations of principal stresses. It is assumed that the horizontal stresses at those times are not sufficiently high on reservoir level to exceed the vertical stress. Therefore a normal faulting regime is proposed concerning the relative magnitudes of vertical, and maximum and minimum horizontal stress.

The orientation of many normal faults and graben structures evolved in this stage suggests an ENE-WSW direction of the minimum horizontal stress representing the least principal stress (Fig. 8-1-left). The separate load frame model of this first stage is thus rotated 22.5° counter-clockwise to address this orientation of the horizontal stresses (Fig. 8-1-right). This configuration is assumed to represent best the ambient stress field orientation prevailing.

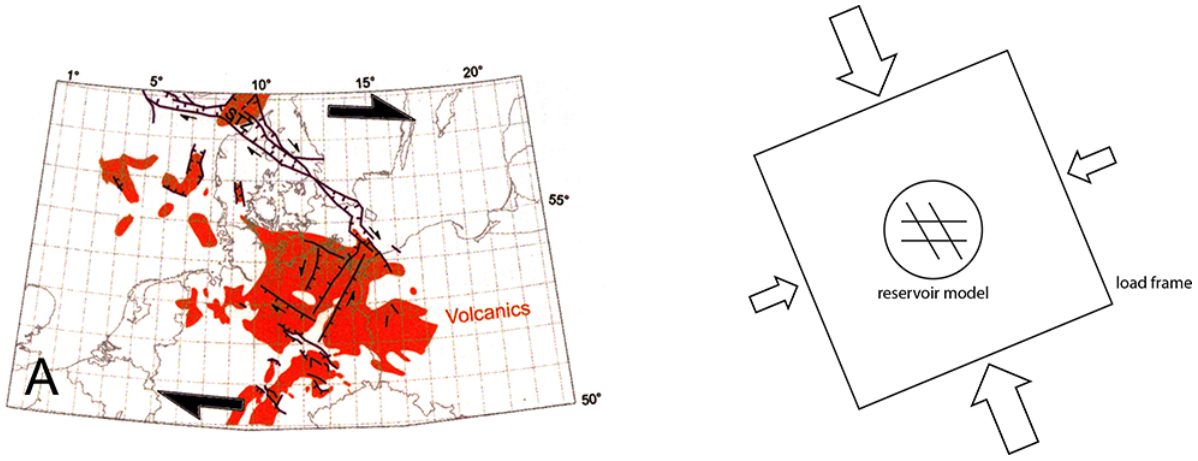

Fig. 8-1. Description of the first major tectonic stage of the reservoir area in latest Carboniferous to Permian time according to Kley et al. (2008)(left) and its takeover to boundary conditions of the dynamic geomechanical model (right). While the cylindrical reservoir model remains unchanged, the encompassing rectangular load frame is rotated to account for the defined directions of the maximum and minimum horizontal stress represented by large and small arrows, respectively. The fault pattern indicated inside the cylindrical model is purely schematic and does not reflect the reservoir-specific fault orientations.

The first tectonic stage presumably ended in Late Rotliegend to Zechstein time when faulting waned and thermal subsidence took over. The following second tectonic stage ranges from Early Triassic to Middle Jurassic (Kley et al., 2008). This stage is characterized by substantial E-W directed extension resulting in numerous graben structures along N-S trending normal faults (Fig. 8-2-left). Some graben structures are slightly rotated towards NNE-SSW and thus the extension direction might be rotated to ESE-WNW direction as well.

Conveying this mostly Triassic E-W extension of the second stage to boundary conditions of the geomechanical model yields a load frame model, whose edges are aligned N-S and E-W (Fig. 8-2-right). The least principal stress is oriented E-W in direction of the extension, whereas the maximum horizontal stress acts in N-S direction.

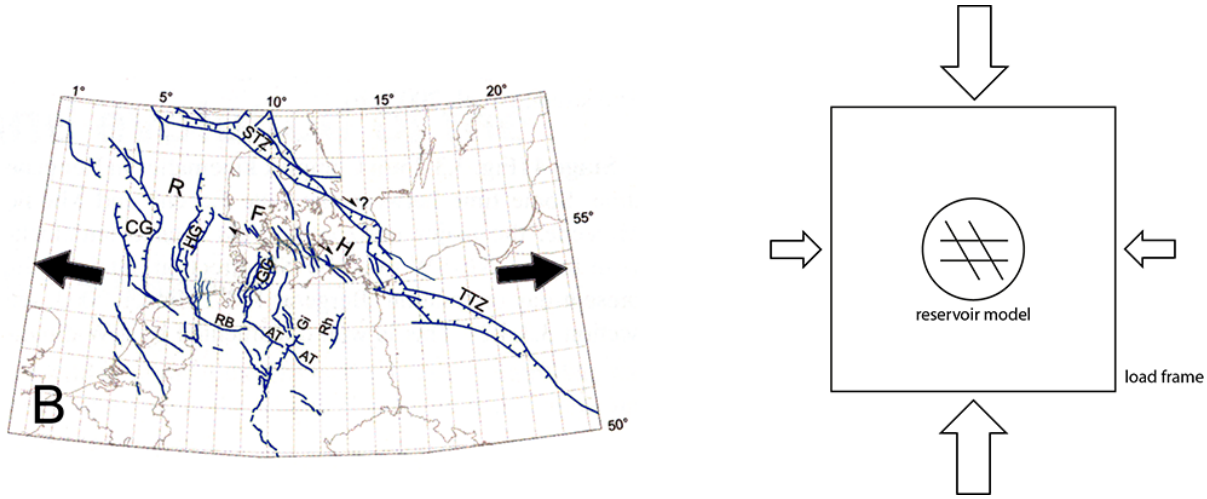

Fig. 8-2. Description of the second major tectonic stage of the reservoir area in Early Triassic to Middle Jurassic time according to Kley et al. (2008)(left) and its takeover to boundary conditions of the dynamic geomechanical model (right). While the cylindrical reservoir model remains unchanged, the encompassing rectangular load frame is rotated to account for the defined directions of the maximum and minimum horizontal stress represented by large and small arrows, respectively.

The third tectonic stage represents a phase of further extension (Fig. 8-3-left). The change of evolving graben structures from the Triassic N-S trend to NW-SE suggests a counter-clockwise rotation of the extension direction (Kley et al., 2008). Consequently the respective load frame model is rotated by 45° in order to account for a NE-SW direction of the least principal stress (Fig. 8-3-right). The maximum horizontal stress is thus aligned NW-SE in this stage.

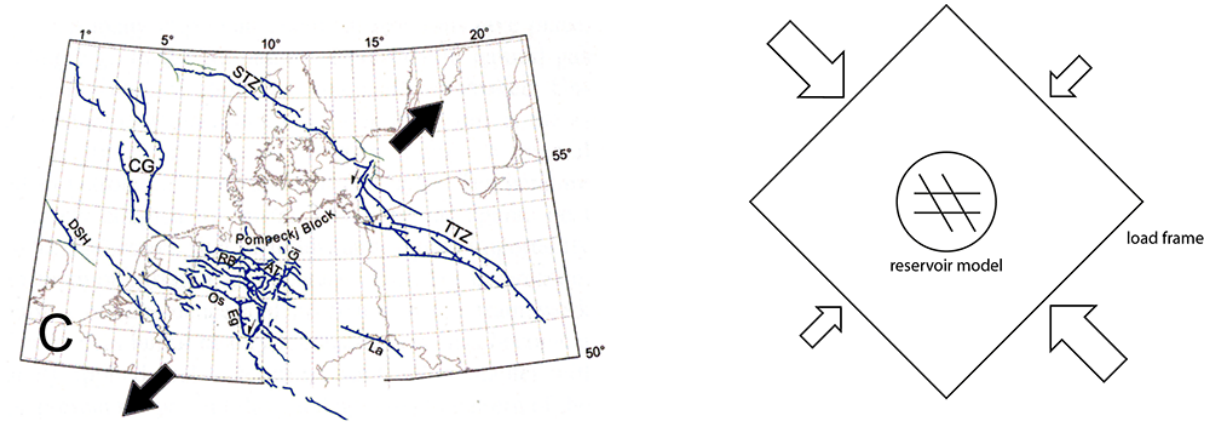

Fig. 8-3. Description of the third major tectonic stage of the reservoir area in Late Jurassic to early Late Cretaceous time according to Kley et al. (2008)(left) and its takeover to boundary conditions of the dynamic geomechanical model (right). While the cylindrical reservoir model remains unchanged, the encompassing rectangular load frame is rotated to account for the defined directions of the maximum and minimum horizontal stress represented by large and small arrows, respectively.

After these stages of extension in the reservoir area, the fourth tectonic stage represents a phase of inversion and contraction (Kley et al., 2008). This compressive reverse faulting regime is assumed to have acted from latest Cretaceous times to Late Oligocene. The general direction of contraction at the onset is NE-SW (Fig. 8-4-left). Therefore the load frame model does not need to be rotated, but the maximum and minimum horizontal stress assignment swaps (Fig. 8-4-right). In this way, the maximum horizontal stress is aligned NE-SE in direction of contraction.

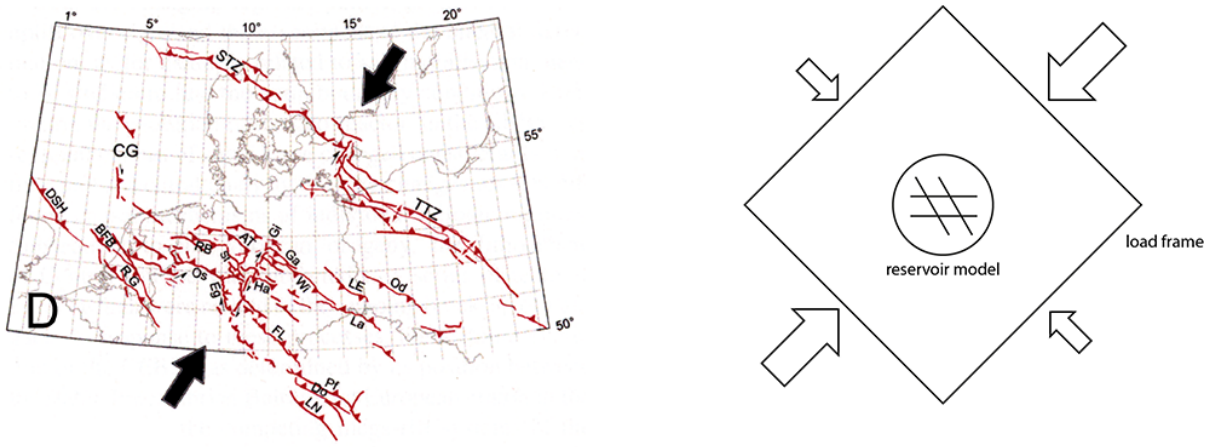

Fig. 8-4. Description of the fourth major tectonic stage of the reservoir area in Late Jurassic to early Late Cretaceous time according to Kley et al. (2008)(left) and its takeover to boundary conditions of the dynamic geomechanical model (right). While the cylindrical reservoir model remains unchanged, the encompassing rectangular load frame is rotated to account for the defined directions of the maximum and minimum horizontal stress represented by large and small arrows, respectively.

After this phase of compression, the orientation of maximum horizontal stress rotated to the present-day orientation of NNW-SSE in the time between Late Eocene and Middle Miocene. The recent situation is not considered as separate stage in the dynamic modeling since this is explicitly covered by the static geomechanical model.

These four tectonic stages are assumed to have had the largest impact on the development of the fault and fracture network in the case study reservoir area and are thus applied in the dynamic modeling. Additional intermediate stages could cover transitional intervals between these major stages, but are hard to define and are thus left out. Following this definition of major stages and the fundamental setup of boundary conditions, the specific magnitudes of paleo-stresses are elaborated after the burial history at these stages is clarified (8.2.2), and density changes (8.2.3) and the vertical stresses are determined (8.2.4).

8.2.2 Burial History

The burial history of the reservoir horizon is important due to compaction effects and density changes, and related impact on the lithostatic load of the overburden yielding the vertical stress. The burial history of the case study reservoir area was determined at numerous wells within a basin modeling study of the project partners. According to the study results, the reconstruction of the burial history included a variable heat flow history and assumed erosion of 1000m at Kimmeridgian times.

Resulting burial curves are provided for five wells located in modeled domain. The trends of the burial curves are very similar and minor differences occur only in the specific final depth of the reservoir horizon and the individual thicknesses of overlying sequences (Fig. 8-5). The data on which the burial curves are based is not provided. Hence, approximate depths of the reservoir horizon at the defined major tectonic stages are defined graphically in the available diagrams (Fig. 8-5). The dynamic modeling approach aims at snapshot-like insights into the in situ stress distribution at the major

tectonic stages. Therefore the reservoir depth within these stages is determined at points that are assumed to be characteristic.

Due to the strong subsidence in Permian times, the depth of the reservoir in the first stage is not clearly detectable in the burial curve diagrams. Moreover, the uncertainty especially in this oldest stage is highest. Thus the internal overburden of the geomechanical model of about ±750m is assumed to be superimposed on the reservoir horizon in this first tectonic stage.

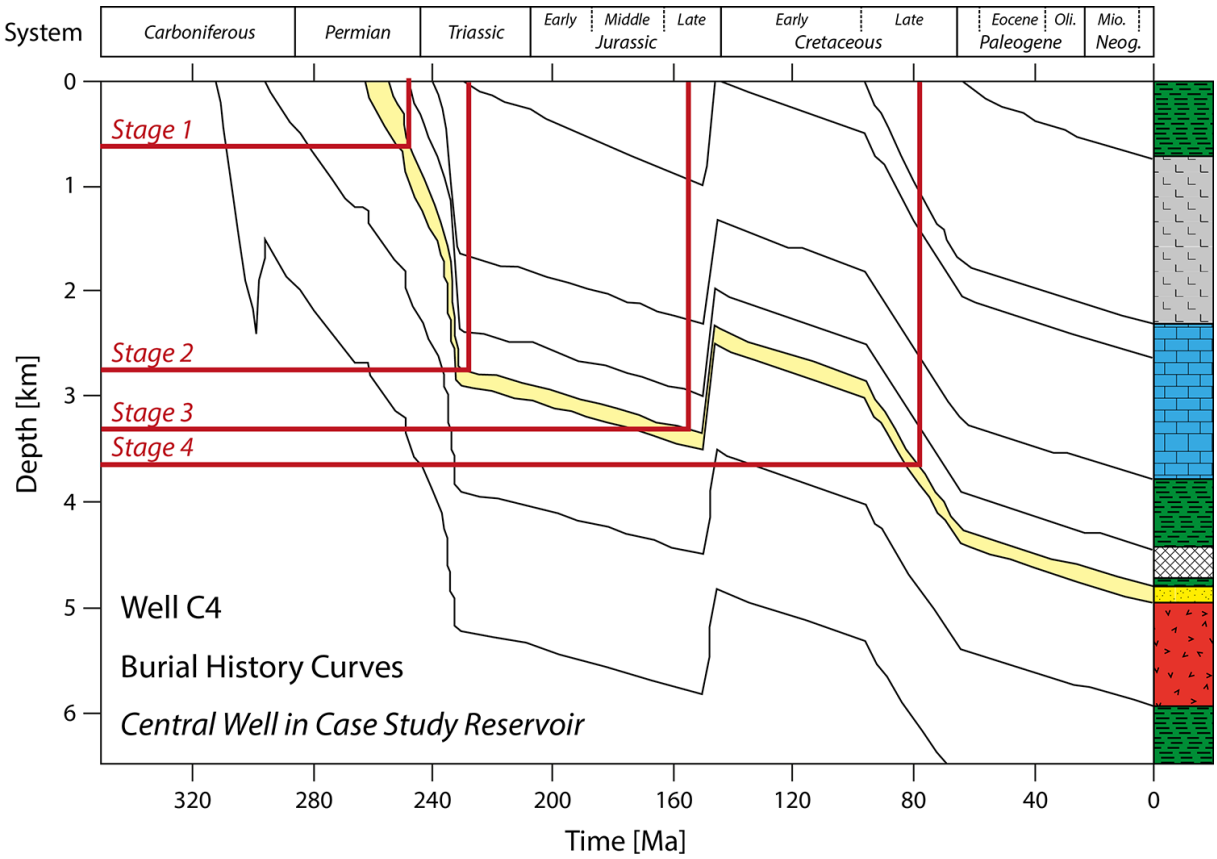

Fig. 8-5. Representative burial history curves of well C4 in the center of the case study reservoir indicating the depth of Rotliegend reservoir sandstone (yellow) since the Permian. Burial history diagrams of 5 wells in the reservoir area are provided by the project partners. The recent stratigraphy and related thicknesses (right) vary to a minor extent between the 5 wells, whereas the trends of the burial curves are the same. The depth of the reservoir in the defined major tectonic stages is indicated by vertical and horizontal lines (red).

Characteristic points in time within the second, third and fourth tectonic stages are marked in the burial curves of the five wells with vertical lines (Fig. 8-5). The depth of the reservoir horizon is then determined at these locations and is indicated by horizontal lines. Averages of these graphically determined values are taken as representative burial depths of the reservoir for the dynamic modeling of these stages (Tab. 8-1). This is justifiable due to the same trend of the burial curves of the several wells and the very minor differences in depth at the defined points in time.

The average depth of top reservoir provides a total overburden thickness for all stages. This overburden is divided into an internal part of the overburden directly incorporated in the model as individual layer and an external part that yields an applied pressure load on top of the model. The internal overburden is 750m on average, but varies due to the horizon topology.

Stage	Average Depth of Top Reservoir	Thickness of Internal Overburden	Thickness of External Overburden
1	750m	~750m	-
2	2780m	~750m	2030m
3	3300m	~750m	2550m
4	3640m	~750m	2890m

Tab. 8-1. Summary of the average depths of top reservoir at the characteristic points in the major tectonic stages. The average depths equal the total thickness of overburden, which is divided into an internal and external part. The internal part is represented by the overburden layer inside the model that comprises approximately 750m, but varies due to horizon topology.

8.2.3 Material Parameter Adjustments

Based on the provided burial history of the reservoir horizon provided, changes in material parameters have to be addressed. These changes concern especially the density, which is increasing due to compaction of the sandstone over time. Variation in thickness indicated by the decreasing distance of burial curves implies that compaction effects were regarded in the reconstruction of the burial history. Due to the lack of specific parameters of the burial reconstruction, the density changes have to be derived indirectly from the thickness changes of units described by the burial curves.

The thickness of the sandstone unit is measured at the respective burial curves for the final, present-day situation and for the defined points in the second, third and fourth tectonic stage (Fig. 8-5). Factors are calculated, which describe the ratio of the stage-specific to the present-day value. These factors represent the decrease in thickness and thus approximately the relative increase in density. The steep trace of the burial curves at the first stage precludes any reasonable thickness measurement. This value has to be extrapolated subsequently from the factors of the other stages.

The factors are calculated individually for all five wells and are averaged due to the minor differences. Based on these factors and the known present-day density, the respectively lower paleo-densities are determined (Tab. 8-2). The corrected densities include those of the internal overburden layer in the model, the reservoir and underburden. Based on the trends in the density logs, the reservoir and underburden layer comprise the same density in the assumptions of the static model. The correction using calculated factors is also applied to the integrated density of the overburden from which the vertical stress gradient is derived (Tab. 8-2). Especially this latter assumption should be regarded as rough approximation only.

	Stage 1*	Stage 2	Stage 3	Stage 4	Recent State
Integrated Overburden	2083 kg/m³	2179 kg/m³	2268 kg/m³	2328 kg/m³	2391 kg/m³
Overburden	2354 kg/m³	2461 kg/m³	2562 kg/m³	2629 kg/m³	2700 kg/m³
Reservoir/Underburden	2267 kg/m³	2369 kg/m³	2467 kg/m³	2532 kg/m³	2600 kg/m³

Tab. 8-2. Summary of the approximated paleo-densities at the major tectonic stages derived indirectly from measurements at the burial curves provided. Values for stage 1 are extrapolated from polynomial correlation functions (*) (Fig. 8-6).

In order to reveal approximate density values for the first stage, the derived densities are plotted and examined for a correlation function. As expected, the resulting diagram illustrates a non-linear increase of density over time and burial depth. Optimal correlation is obtained by polynomial functions, which are then used to estimate the density values for the earliest tectonic stage (Fig. 8-6). The resulting values, and in particular those regarding the integrated density of the overburden,

comprise a considerable uncertainty (Tab. 8-2), but provide a first-order approximation of the temporal changes in density and vertical stress.

The entire approach using graphical measurements at burial curves does not represent the optimal way of deriving the required paleo-densities, but corrections are mandatory for the dynamic modeling approach and no superior data or parameters are available. Therefore this approach is justifiable for the demonstration in this case study, but the related uncertainty has to be kept in mind and future dynamic modeling should be improved in this area.

Besides the correction of applied density, the mechanical parameters, i.e. the elastic moduli of Young's modulus and Poisson ratio, undergo no such correction. The temporal evolution of these mechanical parameters is assumed to be strongly affected by numerous aspects, whose relative impact is presently not known. Therefore no foundation is provided for any reasonable estimation. The same problem applies to the friction coefficient of the faults. This coefficient is taken from the calibrated static geomechanical model and maintained in all stages of the dynamic modeling. Due to the evolution of the mechanical parameters, the friction of faults will not remain constant over various tectonic stages either. However, the specific development of fault friction is assumed to depend on many factors, whose relationships and impact is also presently unknown. Both aspects represent major fields for future research.

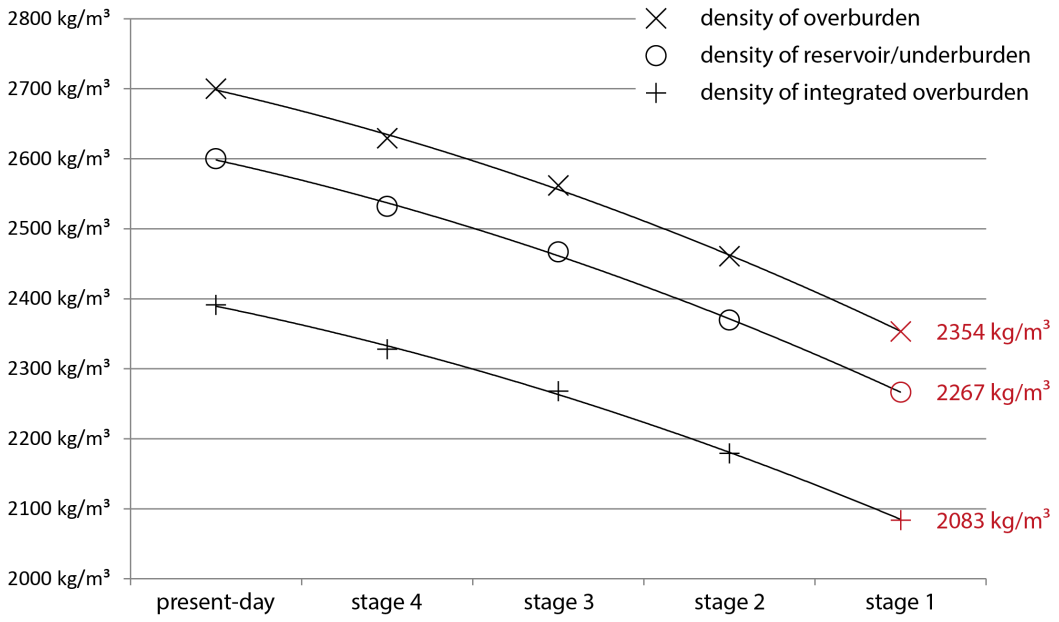

Fig. 8-6. Diagram showing the correlation functions used for extrapolating the densities of the first tectonic stage. The functions elucidate the non-linear increase in density over time due to compaction.

8.2.4 Paleo-Stress Magnitudes

The orientation of horizontal stresses is deduced from the general description of the major tectonic stages and the separate load frame models are rotated accordingly (8.2.1). The burial history provides the reservoir depth at these stages (8.2.2) and information on compaction-related density changes (8.2.3). In the following final preparatory step for the dynamic modeling, the paleo-stress magnitudes are estimated. This determination of vertical and horizontal stress magnitudes completes the input data constraining the dynamic model.

Vertical paleo-stress gradients at the major tectonic stages are derived from the corrected integrated overburden densities (Tab. 8-2) and gravitational acceleration. Depending on these gradients and the thickness of the external overburden (Tab. 8-1), the lithostatic pressure load on top of the model is determined for the specific stages (Tab. 8-3). Compaction-corrected density values assigned to the internal layers yield the vertical stress inside the model. The assumed limitation of overburden thickness in the first stage to ~750m, which is represented by the internal overburden layer, excludes any additional pressure load on top of the model.

Besides the vertical stress, the horizontal stress magnitudes must be defined to complete the boundary conditions, which is significantly more complicated. Due to the lack of direct measurements and possibilities for indirect determination, such as the correlation between vertical stress and density, the horizontal stress magnitudes have to be estimated. Limited constraint is offered by so-called R-values representing the ratio of principal stress differences in paleo-stress fields (Eq. 8-1) (Angelier, 1979). These values are determined in fault-slip analysis and allow the definition of the proportions of horizontal stress magnitudes with respect to the vertical stress. R-values for the defined major tectonic phases in the North German Basin are taken from Kley et al. (2008) and Sippel et al. (2009) (Tab. 8-3).

The overall order of vertical stress, maximum and minimum horizontal stress representing the three principal stresses depends on the prevailing tectonic regime. The first, second and third tectonic stage are assumed to be normal faulting regimes, in which the first principal stress is vertical (Tab. 8-3). Despite the strike-slip component in the transtension of the first stage, it is assumed that the overall tectonic regime is of normal faulting type.

	Stage 1	**Stage 2**	**Stage 3**	**Stage 4**
SHmax Orientation	NNW-SSE	N-S	NW-SE	NE-SW
Stress Order	SV > SH > Sh	SV > SH > Sh	SV > SH > Sh	SH > Sh > SV
Pressure Load	-	43.39 MPa	56.74 MPa	66.00 MPa
SV at reservoir level	18.43 MPa	62.66 MPa	76.80 MPa	86.59 MPa
SHmax at reservoir level	15.67 MPa (0.85 · SV)	51.38 MPa (0.82 · SV)	69.88 MPa (0.91 · SV)	121.22 MPa (1.4 · SV)
Shmin at reservoir level	13.82 MPa (0.75 · SV)	48.88 MPa (0.78 · SV)	68.35 MPa (0.89 · SV)	95.24 MPa (1.1 · SV)
Applied R-value	0.4	0.18	0.18	0.25
Measured R-value (according to references)	0.4	0.1 – 0.2	~0.2	0.1 – 0.3

Tab. 8-3. Summary of the description of the four major tectonic stages as assumed in the dynamic modeling of the case study. The pressure load on top of the model is calculated from the corrected integrated density and the respective depth (Tab. 8-1, Tab. 8-2). The vertical stress on reservoir level emerges from this pressure load, the corrected density inside the model and gravity. A load frame model for each stage is calibrated to the stated magnitudes, which are specified in relation to the vertical stress and with respect to the measured R-values taken from Kley et al. (2008) and Sippel et al. (2009).

The fourth stage comprises a compressive, reverse faulting regime with the least principal stress being vertical. Both horizontal stresses are expressed in relation to the vertical stress. The relating factors control the stress magnitudes and are varied to match the respective R-value (Tab. 8-3). In addition, the magnitudes can be shifted to small amounts in absolute values under consideration of the general knowledge on the tectonic stage. This is done for the second stage that represents the most significant extensional phase in the tectonic history and thus comprises horizontal stress magnitudes more distant to the vertical stress than in the first and third stage (Tab. 8-3).

Within the dynamic modeling approach, the same lateral displacement boundary conditions are used as in the static geomechanical model (4.5). The application of the cut-boundary displacement method yields four separate load frame models – one for each major tectonic stage. These load frame models are rotated to the determined orientations (8.2.1) and are calibrated to generate the defined paleo-stress magnitudes on reservoir level (Tab. 8-3). Node-specific displacements are then interpolated from these calibrated load frame models and are applied sequentially to the reservoir model as lateral boundary condition of the respective tectonic stage.

8.3 Dynamic Model Setup

The dynamic model of the case study reservoir is geometrically based on the static geomechanical model described above (7). The entire reservoir is included and the model comprises the same fault network and layering (7.3). This approach is justifiable due to the fact that the majority of faults in the reservoir are approximately NW-SE to NNW-SSE directed. These fault patterns in the North German Basin are assumed to originate from the late stage of Variscan orogeny (Glennie, 1998). The fact that according to the project partners, most faults are traceable from base Zechstein down to the Upper Carboniferous underlines this assumption. Therefore it is suggested that most faults are generated before or within the first simulated tectonic stage of the dynamic modeling. Those faults could have been reactivated in the following tectonic stages and thus must be continuously implemented in the model to reveal their geomechanical exposure over time.

Omitting geometrical balancing and restoration of fault movements is also justified by the relatively minor offsets in the central reservoir area. In principle, it is possible to change reservoir geometry separately for all tectonic stages and also to successively add newly generated faults, for instance. However, this would necessitate an individual geometrical buildup and discretization of the geomechanical model for each stage. Besides the significant effort, such an approach also requires detailed information on the timing of fault generation, which is not available for the case study. Hence it is more reasonable to maintain fault geometry and keep in mind during interpretation that individual faults may have been emplaced at later stages.

Adapting the dynamic from the static model and maintaining reservoir geometry and discretization (Fig. 8-7) represents a significant practical advantage of the load frame and cut-boundary displacement approach. In this way, the dynamic model provides the exact same spatial resolution as the static model and is directly available – and results are directly comparable. Changes with respect to the implemented tectonic stages do exclusively affect the applied material parameters and boundary conditions. These aspects are addressed in the preparation of the dynamic modeling (8.2).

The mechanical parameters and the friction coefficient of faults had to be taken from the calibrated static geomechanical model as no specific information on the parameter evolution was available. Paleo-densities are elaborated based on the burial history of the reservoir horizon (8.2.2). This correction addressed the density of the internal layers of the model and the integrated density of the overlying stratigraphy (8.2.3). The latter is used in combination with the determined reservoir depth at the tectonic stages to calculate the respective lithostatic pressure load on top of the model. This load and the stage-specific internal density yield the vertical stress inside the model (Tab. 8-3). The orientation of horizontal stresses is deduced from the description of the tectonic stages (8.2.1). Corresponding horizontal stress magnitudes acting at those times in the reservoir area are constrained by using R-values derived from fault-slip analysis (8.2.4) (Kley et al., 2008; Sippel et al., 2009). In addition to the reservoir geometry and discretization, the adjusted material parameters and constrained vertical and horizontal stresses (Tab. 8-3) fully describe the dynamic model at all defined major tectonic stages.

The dynamic model is set-up as a single numerical analysis, which considers the four major tectonic stages as individual load steps to be solved (Fig. 8-7). Following the initial geometrical buildup and discretization – equal to the static model – the material parameters and boundary conditions describing the first tectonic stage are applied (Tab. 8-2, Tab. 8-3). After this first stage is solved as first load step, the material parameters are switched to those corresponding to the second tectonic stage. The boundary conditions are also deleted and re-assigned accordingly and the model is solved for the second stage (Fig. 8-7).

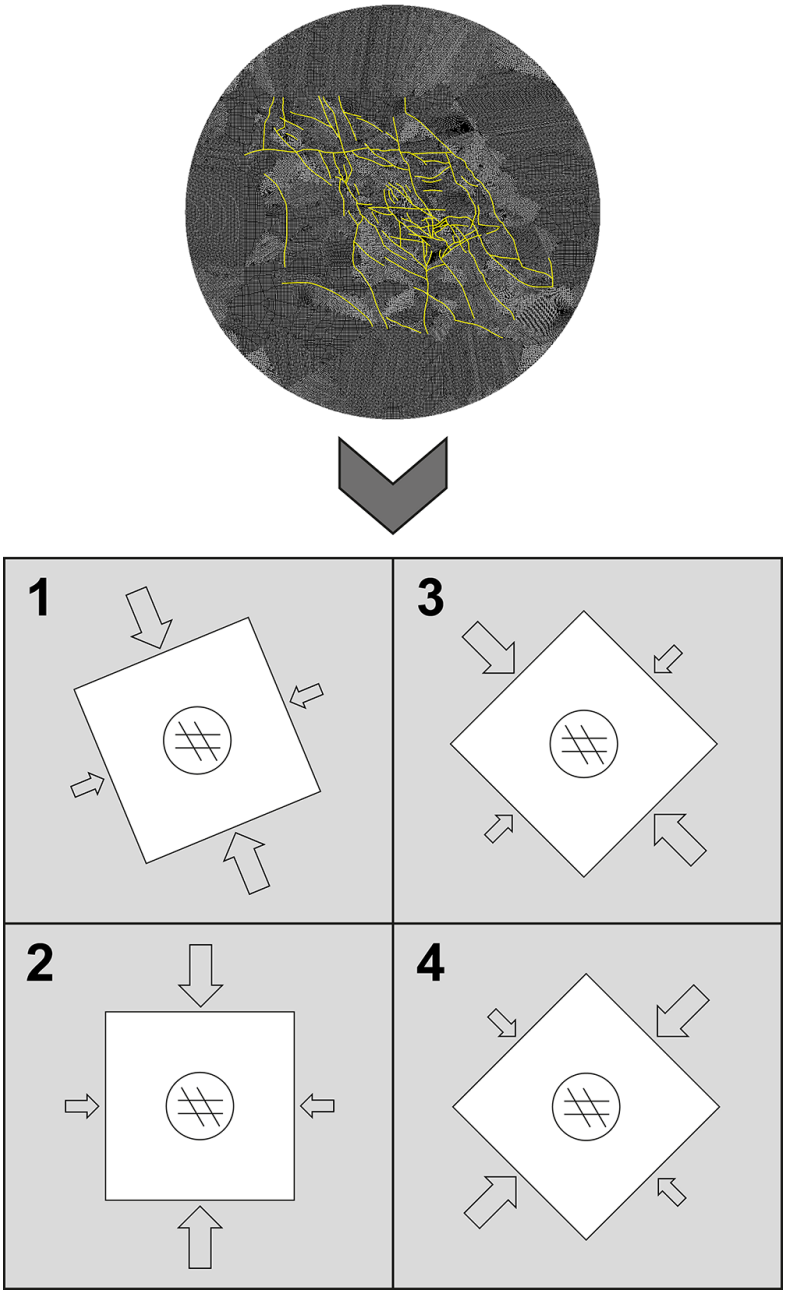

Fig. 8-7. Overview on the setup of the dynamic model. The reservoir geometry and corresponding discretization is taken from the static model of the case study (top). The four major tectonic stages are regarded as separate load steps within a single, continuous modeling approach (bottom). Material parameters and boundary conditions are changed after each load step according to the description of the tectonic stages (8.2).

In this way, the four load steps are solved sequentially and the results of all four tectonic stages are stored in a single results file (Fig. 8-7). Although the pure solution time of entirely separate models for each stage would be the same, such an approach is inefficient concerning the individual geometrical build-up and discretization, and also offers significantly less post-processing capabilities.

The applied sequential solution approach within a single analysis offers the possibility to post-process all results individually for each load step and in context with each other. The latter option allows array operations accessing and using the results of all four tectonic stages simultaneously and calculating stress and strain distributions integrated over these time slices. In this way, cumulative strain information is provided as dynamic modeling result. This possibility of revealing cumulative effects is particularly important for testing the hypothesis, which focuses on the impact of permanent geomechanical exposure of faults over the tectonic history on their present-day hydraulic behavior.

8.4 Results of Dynamic Model

The results of the dynamic modeling are derived and visualized in the same way as for the static model, including contour and vector representations of various quantities. In addition, the dynamic model provides individual results for each tectonic stage as well as results considering the outcome of all stages in summary. This allows the stepwise description of the tectonic evolution of the case study reservoir and the evaluation of cumulative effects.

The first part of modeling results focuses on the individual tectonic stages (8.4.1). These results comprise insights into the in situ stress distribution prevailing in the reservoir at each stage. This includes the stress distribution throughout the reservoir horizon as well as fault-specific stresses. In combination, the stage-specific results thus elucidate the tectonic evolution of the case study reservoir.

Fracture information is compared to the revealed paleo-stress distributions during the simulated tectonic stages in the second part of modeling results (8.4.2). Fracture sets that are observed and described based on image logs are matched with the orientation of modeled in situ stresses in order to determine the specific phase of fracture generation. In addition, the fracture density is calculated at several wellbores and compared to cumulative strain throughout all tectonic stages.

The third part focuses on the faults and their behavior and geomechanical exposure under each individual paleo-stress field and over all tectonic stages in summary (8.4.3). Slip and dilation tendencies indicating movement behavior of faults are calculated for each stage and the entire history. These results are compared to information on baffle faults provided by the project partners. This comparison helps to evaluate the proposed hypothesis of historically increased geomechanical exposure of faults correlating with their present-day hydraulic behavior.

8.4.1 Paleo-Stress Distributions

The first and fundamental part of dynamic modeling results are stress distributions revealed for each tectonic stage. These in situ stress distributions emerge in the reservoir under the regional paleo-stress fields of the specific time interval (8.2). Faults and contrasts in mechanical properties, especially at juxtaposition along vertical fault offsets, locally change the magnitude and orientation of the ambient stresses. The resulting stress perturbations also mutually interact. Intensity and type of modification varies, amongst other, significantly with changing orientation of the stress field with respect to the faults. Different regional paleo-stress fields therefore strongly impact the generation and characteristics of stress perturbations and thus the respective distribution.

The dynamic forward-modeling approach offers snapshot-like insights into the major stages of the reservoir's tectonic history and the prevailing in situ stresses. In order to elucidate the tectonic evolution, the distribution of maximum and minimum horizontal stress magnitude is displayed at these time slices as representative stress quantity (Fig. 8-8, Fig. 8-9, Fig. 8-10, Fig. 8-11).

The first tectonic stage regarded in the dynamic model covers the time at the very beginning of basin initiation in the Permian (8.2.1). The reservoir horizon is deposited within this time interval and the elaborated burial history indicates strong subsidence rates (Fig. 8-5). Hence, the reservoir depth is rapidly changing and a time slice is assumed, at which the reservoir horizon is buried at about 750m (8.2.2) – equal to the thickness of the internal overburden in the model. This relative low reservoir depth yields respectively low vertical stress magnitudes of less than 20MPa at reservoir level (Tab. 8-3). Horizontal stress magnitudes are related by the proposed R-value and are below the vertical stress due to the assumed normal faulting regime (Fig. 8-8).

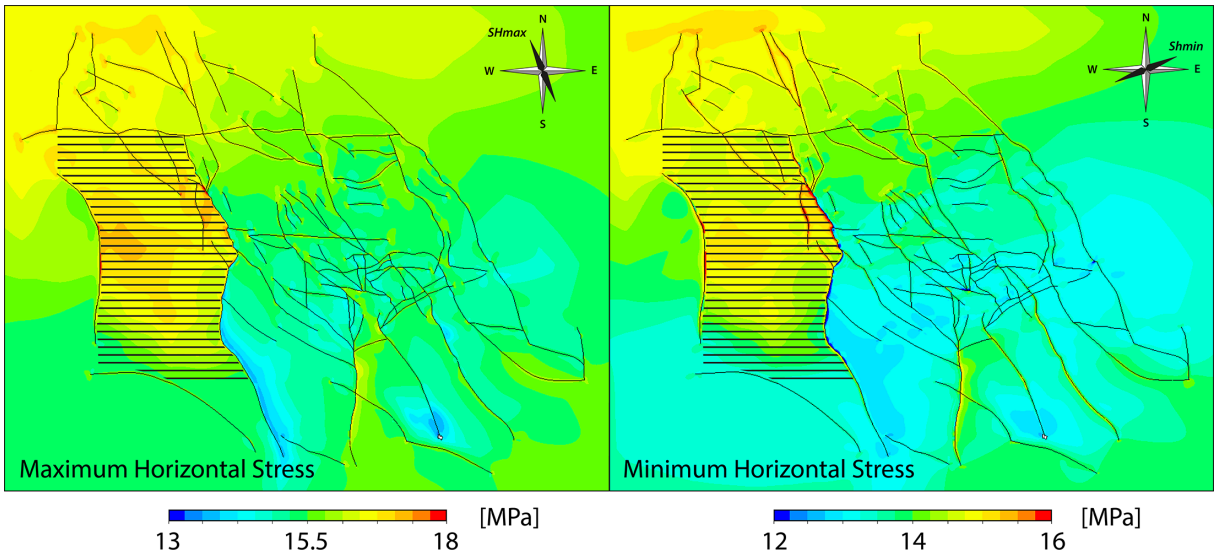

Fig. 8-8. Distribution of maximum (left) and minimum horizontal stress magnitude (right) in [MPa] in the first major tectonic stage of the reservoir. In these times, the maximum horizontal stress (S2) is assumed to be NNW-SSE directed. Increased magnitudes in the western graben structure are regarded as artifacts (hachures).

The distribution of maximum and minimum horizontal stress magnitude in this first stage reflects the relatively low magnitudes and shows no significant local perturbations (Fig. 8-8). Faults only yield very minor changes in the stress distribution. The lack of significant perturbations probably results from the relative orientation of regional stress to the fault network. While the percentage of perturbation intensity relative to absolute magnitudes might remain, the total stress magnitudes would be too low for appropriate visualization.

Area-wide variations in magnitude are driven by the sensitivity to the vertical stress and the specific reservoir depth (Fig. 8-8). However, the maintained topology of the reservoir and its relative internal depth probably do not apply to this first stage. Especially the increased magnitudes in the western graben structure and variations along the corresponding bounding faults thus have to be regarded as artifacts (Fig. 8-8-hachures).

The second tectonic stage covers the E-W extension phase in Triassic to Jurassic times (8.2.1). In contrast to the first stage, the reservoir is assumed to be situated considerably deeper in this interval (Tab. 8-3). Therefore the vertical and horizontal stress magnitudes increased, which is reflected in the distribution of horizontal stress magnitudes (Fig. 8-9). The higher magnitudes are likely to be responsible for the more pronounced stress perturbations occurring along the faults.

Stress perturbations at fault tips show different behavior between the horizontal stresses (Fig. 8-9). Perturbations of maximum horizontal stress magnitude occur predominantly at tips of E-W trending faults and at intersections along these faults. Contrasting, the minimum horizontal stress magnitude shows perturbations especially at tips of N-S trending faults. Magnitude variations do not deviate more than 2-3MPa from the ambient stress level.

Both horizontal stress distributions exhibit higher magnitudes in the deeper region of the western graben structure (Fig. 8-9). Due to its orientation, this structure is assumed to be of Triassic age and thus evolved in this tectonic stage. Consequently, the corresponding magnitudes in this area are not considered to be artifacts from this stage on. The evolution of this structure also yields the vertical offsets along the bounding faults, which cause minima and maxima in both horizontal stress distributions.

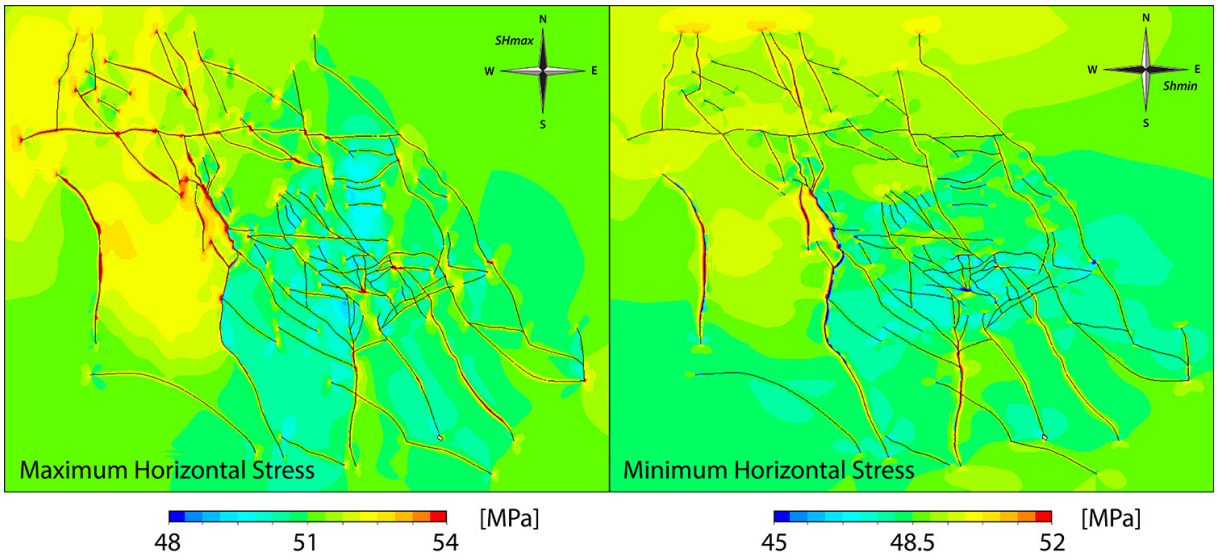

Fig. 8-9. Distribution of maximum (left) and minimum horizontal stress magnitude (right) in [MPa] in the second major tectonic stage of the reservoir. In these times, the minimum horizontal stress (S3) is assumed to be E-W directed.

The third tectonic stage directly follows the previous phase and represents extension in Jurassic to Cretaceous times with a NE-SW directed extension axis (8.2.1). Reservoir depth increased further due to ongoing subsidence, which leads to respectively increased magnitudes of vertical and horizontal stresses (Tab. 8-3). This general increase in magnitudes and the changed orientation of the stress field probably results in the significantly more pronounced stress perturbations in this third stage compared to the previous stages (Fig. 8-10). The central to southeastern part of the reservoir, which comprises the densest fault network, is affected by magnitude minima, whereas the northeastern part is dominated by maxima. Variations in magnitude are highly abundant in this stage and deviate up to 3-4MPa from the ambient stress level.

Regarding the equal range of contour scaling for both distributions, the minimum horizontal stress shows relatively stronger perturbations throughout the reservoir (Fig. 8-10). Especially the juxtaposition of mechanically different lithological layers along the bounding faults of the western graben structure leads to significant stress minima and maxima.

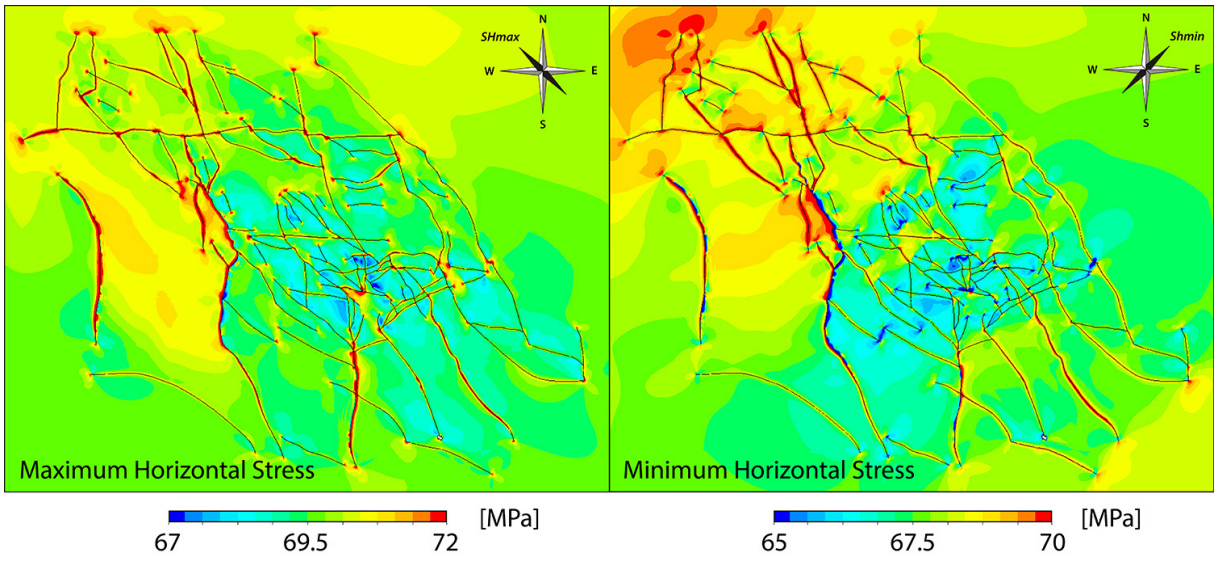

Fig. 8-10. Distribution of maximum (left) and minimum horizontal stress magnitude (right) in [MPa] in the third major tectonic stage of the reservoir. In these times, the minimum horizontal stress (S3) is assumed to be NE-SW directed.

Similar to the results of the static model of the case study (7.6), the stress distributions in this third stage elucidate that despite the generally high abundance of stress perturbations at fault tips, this feature is not occurring regularly, but depends on the local situation (Fig. 8-10).

The fourth tectonic stage represents a phase of compression in the time from Late Cretaceous to Late Oligocene (8.2.1). In the reverse faulting regime of this interval, the maximum and minimum horizontal stress exceed the vertical stress and become the first and second principal stress, respectively. This causes both horizontal stresses to reach higher magnitudes than prevailing in the present-day stress field, despite the deeper recent reservoir location (Tab. 8-3).

The distribution of maximum and minimum horizontal stress magnitude shows significant perturbations throughout the reservoir deviating up to 5-6MPa from the ambient stress level (Fig. 8-11). In contrast to the third stage, the maximum horizontal stress exhibits stronger perturbations than the minimum horizontal stress. Perturbations of both horizontal stresses are generated at vertical offsets along faults, as well as at fault tips and strong curvatures (Fig. 8-11). The perturbations comprise the characteristic elongation and specific shape as proposed by the preliminary parameter studies (6.1.3).

In addition to the overall increase in magnitudes and perturbations, the difference between maximum and minimum horizontal stress magnitude is significantly more pronounced than in the previous tectonic stages (Fig. 8-11). More than about 10MPa divide the highest minimum horizontal stress magnitudes from the lowest maximum horizontal stresses.

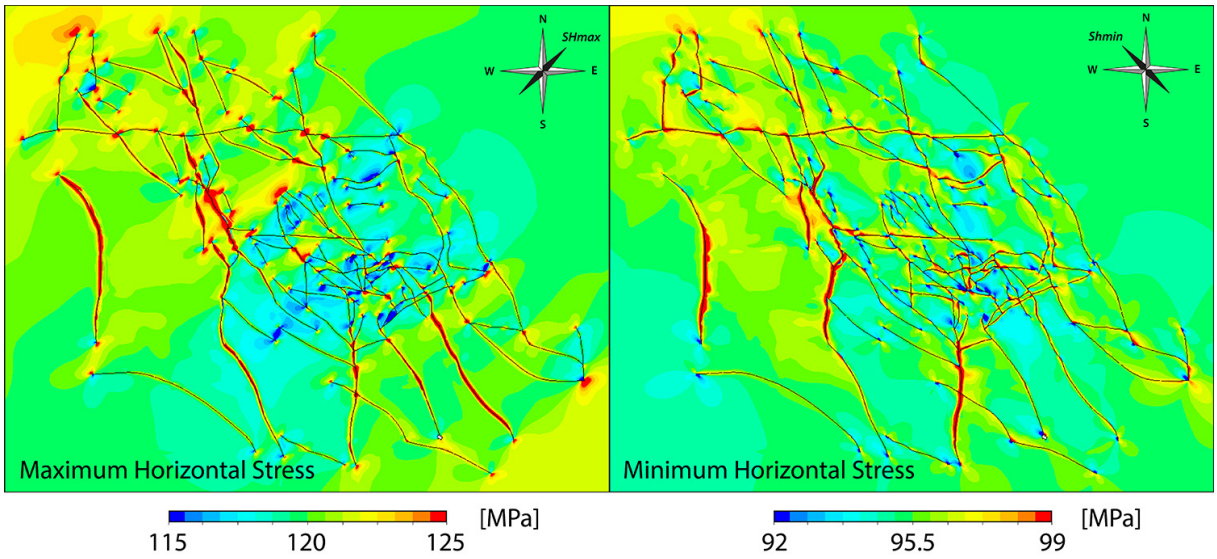

Fig. 8-11. Distribution of maximum (left) and minimum horizontal stress magnitude (right) in [MPa] in the fourth major tectonic stage of the reservoir. In these times, the maximum horizontal stress (S1) is assumed to be NE-SW directed.

In summary, the first tectonic stage shows no significant local variations in stress distribution. The horizontal stress magnitudes are dominated by the specific depth of the reservoir horizon, which comprises high uncertainties in this early phase – especially in the western part of the study area. Stress perturbations first affect the in situ stress distribution in the second tectonic stage representing extension in the Triassic. The graben structure regarded in the variable reservoir depth is assumed to originate in this stage and thus the negative impact of maintaining the present-day horizon topology on the results diminishes.

The horizontal stress distributions of the third and fourth tectonic stage comprise the most significant stress perturbations. This results most likely from the relative orientation of the paleo-stress fields to

the faults and the high horizontal stress magnitudes. Moreover, the horizontal stress difference is very small in the third tectonic stage. The central to southeastern area in the reservoir, which exhibits the densest part of the fault network, is dominated in both stages by minima contrasting to the northwestern part. This change in perturbation intensity implies that the impact of perturbations on the variability of fractures, for instance, is highest for those generated in this third or fourth tectonic stage.

8.4.2 Fracture Correlations

Most characteristic fractures properties, such as type and orientation, are directly controlled by the stress field responsible for fracture generation. Development of shear and tensile fractures is constrained by the respective tectonic regime and the orientation of principal stresses (4.8.2). Stress perturbations resulting in re-orientation thus directly affect fracture generation. The dependency of fractures on the specific prevailing stress field implies that their existence and properties preserve this stress information and reflect paleo-stress states including all perturbations.

Fracture surfaces crossing wellbores appear in image logs as sinuous curves (4.8.2). The position of the sinusoid minimum yields the dip direction and thus the strike of the fracture plane. The arc tangent of twice the amplitude (or height) of the sinusoid divided by the borehole diameter describes the dip angle (Gaillot et al., 2007). Information on strike, dip direction and dip angle of fractures is commonly summarized in stereoplots.

In order to evaluate the capability of the dynamic model to predict fracture networks in the reservoir, the model is validated by comparing the modeling outcome to reservoir-specific fracture data. This fracture data is derived from image logs (FMS®) at 10 wells in the reservoir and compared to the specific in situ stress distribution during the four tectonic stages as revealed by the dynamic model. Stress orientation in the reservoir is visualized by vectors of the maximum horizontal stress. The observed fracture sets can be assigned to those modeled paleo-stress distributions and tectonic stages that most likely have generated these fractures. This assignment eventually allows a description of the timing of fracture network emplacement.

A study was carried out on behalf of the project partners, which analyzed the image logs for bedding surfaces and fractures, and interpreted the logs in terms of depositional facies. The results of this tectono-sedimentary evolution study of the reservoir horizon are summarized in a provided internal report that distinguishes two fracture sets (Fig. 8-12).

Fractures of set ‘A’ are most abundant and generally NE-SW directed. These fractures show a relatively constant orientation and usually do not parallel nearby faults. The study assumes the fracture set ‘A’ to have originated in Late Jurassic to Early Cretaceous times during a North Sea rifting phase, which also comprises a strike of NE-SW. The missing related NE-SW trending faults are explained by the remoteness of the rifting axis and very low resulting offsets.

In addition, a second fracture set ‘B’ is identified (Fig. 8-12). Fractures of this second set are less abundant and generally NW-SE directed. This fracture set comprises a great spread and the fracture commonly parallel the nearby or nearest fault. The related faults belong to the NW-SE aligned fault pattern, which most probably originated in the late stage of Variscan orogeny (Glennie, 1998). These faults are proposed to have been re-activated either in the Late Cretaceous inversion phase or during the Late Jurassic to Early Cretaceous rifting of the North Sea.

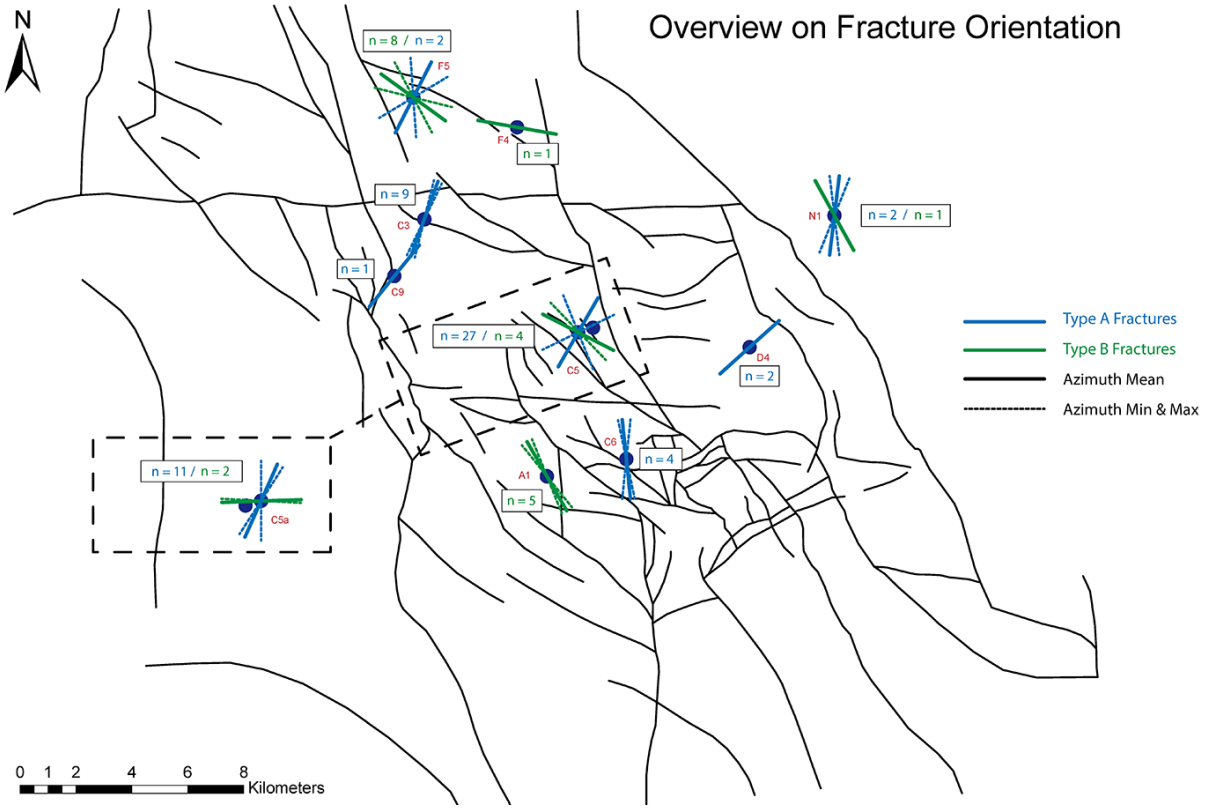

Fig. 8-12. Overview on the fault network of the case study reservoir with those wellbores indicated, at which fractures are observed in image logs (FMS). Two fracture sets are identified and described by the carried out study. A fracture set 'A' showing a general direction of NE-SW and a fairly constant orientation (blue), and a fracture set 'B' comprising a NW-SE orientation with a great spread (green). Mean, minimum and maximum azimuths are indicated as stated in the provided study.

All fractures are detected in the borehole images as white, resistive sinuous curves. Corresponding analysis on drill cores of multiple wells revealed fractures comprising thin cataclastic seams. The fractures are characterized by thin seams of ground grains on the millimeter-scale and below. This grain grinding results in a macroporosity loss and therefore these fractures are assumed to act as permeability barriers or baffles. The low porosity of the seams yields the detection of the fractures as resistive features. This correlation was checked on cores, which correspond to borehole images of good quality.

Prior to the comparison of fracture data to the modeled stress distributions, it is important to reconsider briefly the constraints on fracture generation of the tectonic regimes regarded in the dynamic model. Conjugate shear fractures commonly comprise an angle of 60° around the direction of first principal stress. Therefore those fracture show steeply dipping angles of about 60° in normal faulting regimes (S1 = SV) and strike in direction of the maximum horizontal stress (Fig. 4-16). Corresponding tensile fractures are aligned approximately vertical and show the same strike.

However, shear fractures in reverse faulting regimes commonly appear with dip angles of 30° due to the first principal stress being horizontal (S1 = SHmax) (Fig. 4-16). Contrasting to the normal faulting regime, the shallow dipping shear fractures thus strike in direction of the minimum horizontal stress representing the intermediate principal stress (S2). Corresponding tensile fractures are aligned approximately horizontal due to the least principal stress being vertical and thus these fractures ideally show no strike. Besides the control of fracture generation by the specific prevailing stresses, rock fabric and heterogeneity also affect the final orientation of the fractures and may result in some variability.

Fracture information is compared to the results of the dynamic model by using the provided stereoplots, which summarize the fractures at each wellbore, and vectors describing the in situ stress orientation in the various tectonic stages. The comparison reveals a best fit of fracture set ‘A’ to the second tectonic stage and a significant fit of fracture set ‘B’ to the third stage. All fractures are assumed to be shear fractures or hybrid fractures between shear and tensile type. Pure tensile fractures are unlikely to occur due to the high pore pressures required. In addition, those fracture types are hardly detectable in image logs. The matches of fracture set ‘A’ and ‘B’ with the stresses of second and third tectonic stage, respectively, are subsequently described and illustrated on representative plots of the wells C6, F4 and F5.

Well F5 is located in the north of the reservoir directly south of a step-over between two WNW-ESE trending faults (Fig. 8-13). Ten fractures are determined in the analyzed image log. Two fractures strike N-S and NE-SW and thus are assigned to fracture set ‘A’, whereas eight fractures range in strike between WNW-ESE and NW-SE and are assigned to set ‘B’. The results of the dynamic model reveal almost constant regional orientations of the maximum horizontal stress in the first and fourth tectonic stage (Fig. 8-13). These stress directions are not capable to explain the observed fractures.

However, the maximum horizontal stress in the second tectonic stage is N-S directed and shows some stress rotation towards the faults yielding a NNE-SSW direction (Fig. 8-13). While the N-S orientation of maximum horizontal stress in the prescribed normal fault regime directly matches the N-S strike of the first fracture, the perturbed orientation approximates the NE-SW strike of the second fracture.

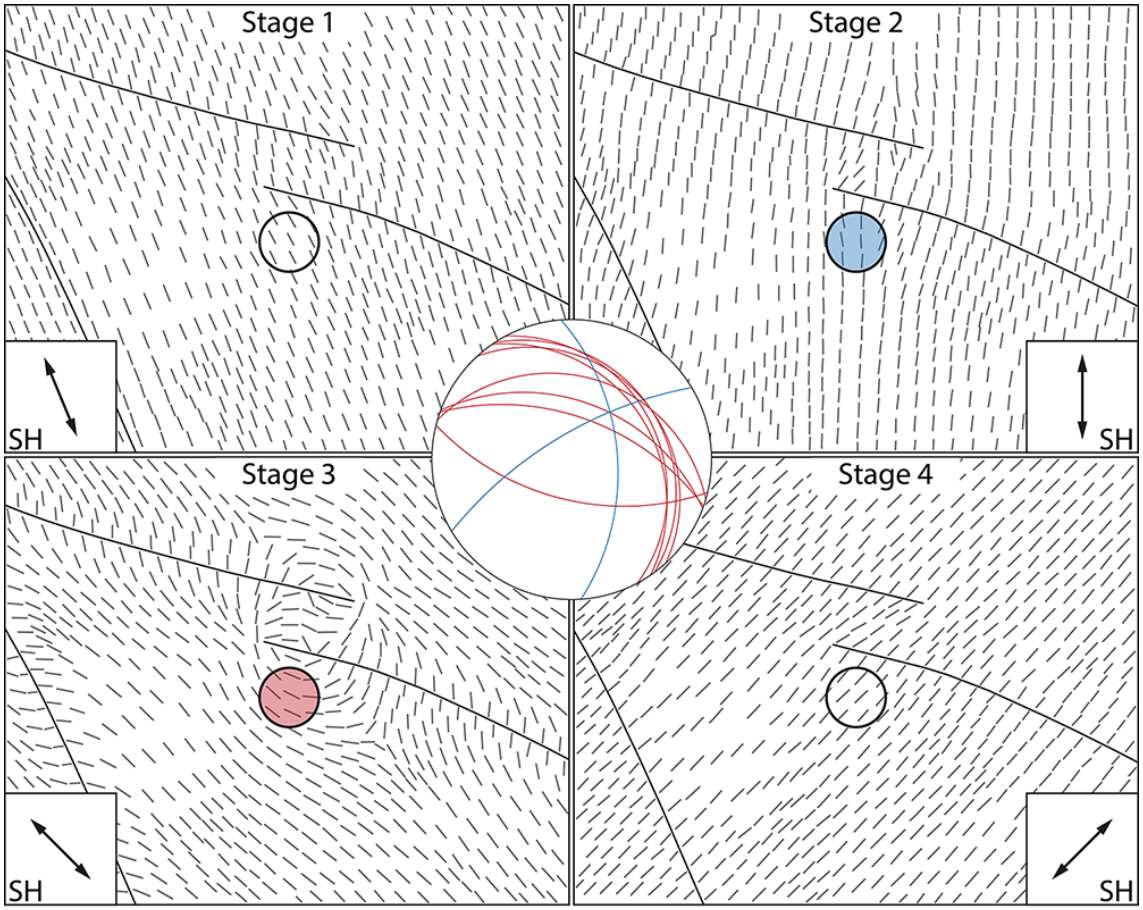

Fig. 8-13. Overview on stress vectors indicating the orientation of maximum horizontal stress on reservoir level at the area of well F5 (circle) during all four tectonic stages simulated by the dynamic model. Regional stress orientation is indicated in the additional boxes. The central stereoplot summarizes the determined fractures and shows that fractures of set ‘A’ fit best to stress orientation at stage 2 (blue), whereas fractures of set ‘B’ significantly match the perturbed stresses in stage 3 (red).

Keeping in mind the role of rock fabric and heterogeneity in fracture generation, as well as the importance of precise fault geometry on the development of stress perturbations, the match is reasonable and no superior match is provided by other stages.

Stress perturbations are most pronounced at this well location in the third tectonic stage leading to significant rotations of the maximum horizontal stress (Fig. 8-13). These re-oriented stress directions ideally match the variable fracture strikes observed ranging from WNW-ESE to NW-SE. The great spread of this fracture set 'B' correlates with the most significant occurrence of stress perturbations in this area of all tectonic stages. Moreover, the relative orientation between the regional paleo-stress field in this third stage and the adjacent faults suggests re-activations to be likely. Such fault activity would directly facilitate and provide the modeled perturbations leading to the great variability in fractures of this set.

The calibration results of the static model suggest that well F5 may be located in fact inside a stepover of faults due to the fact that the nearby faults are only partly traceable in seismics. In this case, the perturbed stress direction would also directly fit to fracture orientations of both sets (Fig. 8-13).

Well F4 is located southeast of well F5 at step-over of two NW-SE trending faults (Fig. 8-14). A single fracture is observed in this well striking almost E-W. Although this strike differs from the average NW-SE strike, this fracture is assigned to set 'B'. Dynamic modeling results show that similar to well F5, the nearby faults do not provoke any significant stress rotations in the first and fourth tectonic stage (Fig. 8-14).

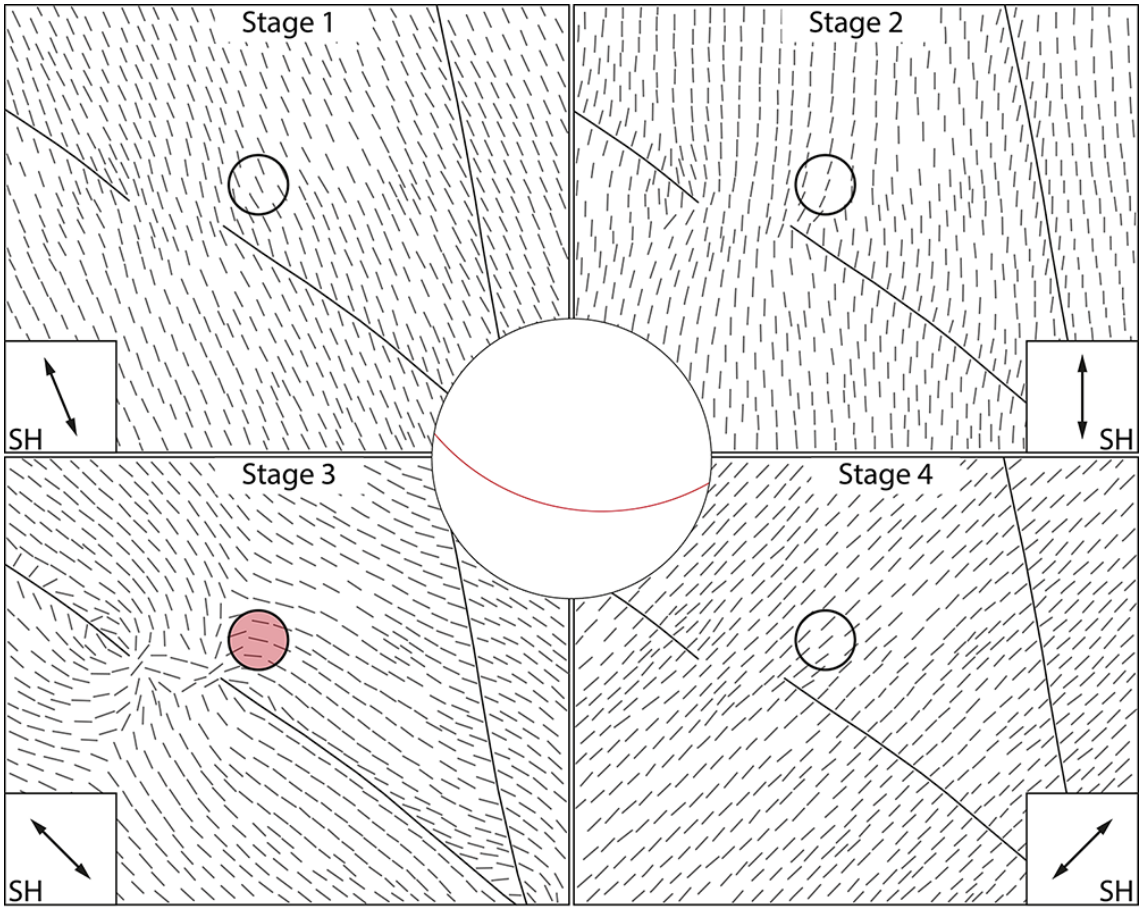

Fig. 8-14. Overview on stress vectors indicating the orientation of maximum horizontal stress on reservoir level at the area of well F4 (circle) during all four tectonic stages simulated by the dynamic model. Regional stress orientation is indicated in the additional boxes. The central stereoplot describes the fracture assigned to set 'B', which significantly matches in orientation with the perturbed stresses in stage 3 (red).

The remaining regional stress orientations in these stages cannot be responsible for generation of this fracture (Fig. 8-14). The second stage comprises minor perturbations, but the stress orientation does not fit to the strike of the fracture as well.

The third stage exhibits severe rotations of the maximum horizontal stress in the area of well F4 (Fig. 8-14). This results in stress orientations directly matching the strike of the observed fracture. As for well F5, it can be assumed that the adjacent faults experience re-activation in this third stage due to the orientation of the stress field. This facilitates the occurrence of the modeled stress perturbations, which impact the orientation of the generated fracture. In accordance with the observation at the previous well, fracture set 'B' is related to the third tectonic stage and the occurring stress perturbations therein.

Well C6 is located in the southern center of the reservoir and close to a WNW-ESE trending fault – similar to the wells F5 and F4 (Fig. 8-15). However, the local fault pattern is denser and comprises additionally E-W and N-S trending faults south and east of the well. Four fractures are observed in image logs that strike N-S and are assigned to fracture set 'A'. The modeled paleo-stress distributions show a significant fit of the fracture strike to the stress orientation of the second tectonic stage (Fig. 8-15).

In this stage, the regional N-S orientation of the maximum horizontal stress is maintained in the well area despite the proximity to the nearby faults (Fig. 8-15). Probably due to the relative orientation between the regional stress field and the faults, no perturbations occur that disturb the local stress and thus the match.

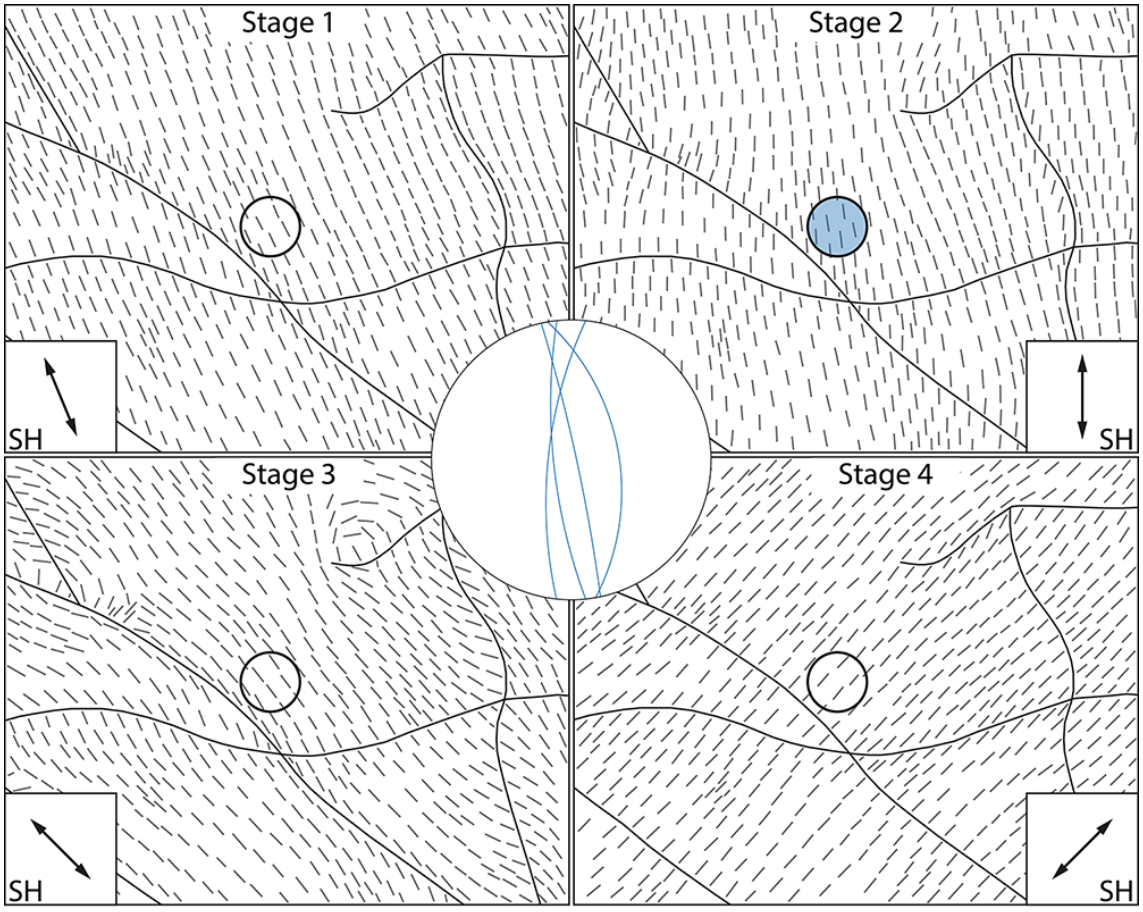

Fig. 8-15. Overview on stress vectors indicating the orientation of maximum horizontal stress on reservoir level at the area of well C6 (circle) during all four tectonic stages simulated by the dynamic model. Regional stress orientation is indicated in the additional boxes. The central stereoplot describes the determined fractures assigned to set 'A', which significantly match with the stress orientation at stage 2 (blue).

The stress orientation of the first, third and fourth tectonic stages do not provide similarly matching stress orientations (Fig. 8-15). Fracture set ‘A’ is thus correlated to the second tectonic stage in agreement with the interpretation at well F5.

The comparison of dynamic modeling results with field observations at these three wells demonstrate the match between the fractures sets ‘A’ and ‘B’ and the in situ paleo-stress distributions during the simulated second and third tectonic stage, respectively. However, these wells were also chosen for detailed results presentation, because they elucidate the impact and appearance of perturbations. The intense perturbations at well F4 and F5 in the third tectonic stage directly explain the great spread in fracture orientation in set ‘B’ and their generation by a single regional stress field (Fig. 8-13, Fig. 8-14).

Furthermore the dynamic modeling results of the three wells C6, F4, and F5 demonstrate that perturbations are not ubiquitous or directly predictable along faults. Only in one of four regional paleo-stress fields, the maximum horizontal stress at well F4 and F5 is severely rotated by the faults. The match of fracture observation and local paleo-stress at well C6 for the second tectonic stage directly relies on the absence of perturbations due to the proximity to a fault. In addition to the three wells described in detail, this analysis is also done for the rest of the wells and yields the same results (see appendix).

Summary of Fracture Correlation

In summary, fractures of set ‘A’ comprise orientations from N-S to NE-SW and match best with the modeled stress distribution of the second tectonic stage. The undisturbed regional N-S orientation of maximum horizontal stress in this second stage directly correlates to the N-S strike of shear fractures. Stress perturbations partly provide rotation of the maximum horizontal stress to NNE-SSW to NE-SW orientations. The extensive amount of NE-SW striking fractures in wells C5 and C5a is not directly matched with respective perturbations.

However, those wells are close to faults and the modeling results demonstrate the possible impact of perturbations and their sensitivity to the specific fault geometry. Keeping in mind the possibility of slight changes in fault trace or regional stress orientation, the observed minor perturbation could rapidly increase in intensity. The relatively dense fault pattern in the area of well C5 and C5a also suggests the presence of subseismic faults or fault-related damage zones that could interfere. This possibility is supported by the extraordinarily high amount of fractures observed in these wells. In addition, the fracture orientation of set ‘A’ cannot be explained by the modeled stress distribution of any other tectonic stage.

Steeply dipping fractures of set ‘A’ are observed in well C6, for instance (Fig. 8-15). They comprise larger dip angles than the typical 60° of shear fractures in a normal faulting regime. The steep dip angles imply that these fractures represent hybrid types between shear and tensile fractures (Fig. 8-16). Such hybrid fractures show intermediate dip angles between the shear and tensile end members. Since tensile fractures develop vertically in a normal faulting regime, hybrid shear-tensile fractures consequently comprise dip angles between 60°-90°.

Such fracture types relate to a shift of the Mohr circle to the left (Fig. 8-16). This shift can result from increased pore pressures. Paleo-pore pressures in the past tectonic stages are thus assumed to play a decisive role in the fracture generation.

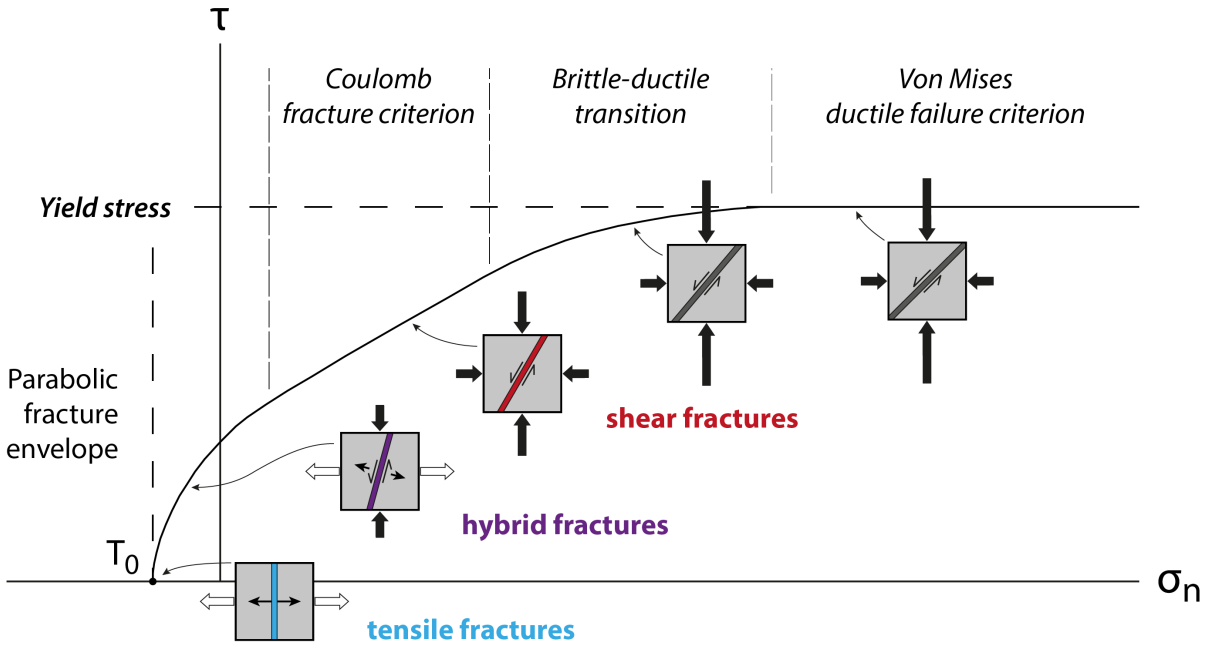

Fig. 8-16. Diagram plotting shear stress (τ) against normal stress (σ_n) and showing a theoretical Mohr envelope. Final yield stresses are indicated, as well as the areas described by the Coulomb and von Mises criterion, and the respective transition zone. The small boxes describe the type and orientation of fractures that will develop under the various stress conditions (modified after Ramsay and Huber (1997)).

Fractures of set 'B' show a significant match with the modeled in situ stresses at the third tectonic stage. Besides the general accordance in NW-SE direction of maximum horizontal stress and fracture striking, the perturbations along faults frequently yield stress rotations that follow and describe precisely the variability of fracture strikes. Therefore stress perturbations are a decisive element for the significant match of set 'B' fractures to the third tectonic stage. These perturbations may result from increases fault activity and are supported by the close magnitudes of maximum and minimum horizontal stress proposed by the applied R-value (8.2.4).

This match of fracture set 'B' elucidates that a single regional stress field is able to yield considerable variability in fracture patterns due to local changes in the specific stress distribution. As demonstrated, those changes can be revealed by geomechanical models and no complex kinematic history of several phases is required to explain variability in observations.

Comparison to the internal report

The described findings and interpretations in terms of fracture origin and timing are also compared to those of the provided internal report. According to the interpretation of the report, fractures of set 'A' coincide in their NE-SW orientation with the strike of the North Sea rifting and thus originate in Late Jurassic to Early Cretaceous times. This interpretation neglects the N-S striking of many fractures in this set, but more important a NE-SW directed rifting axis is assumed. The latter implies a NW-SE oriented least principal stress. However, more recent and comprehensive studies focusing on this area propose NE-SW extension in these times and thus a 90° rotated stress field to the one assumed in the report (Kley et al., 2008). This more recent description of Late Jurassic to Early Cretaceous extension is based on several aspects and is accordance with the tectonic evolution of the Central European Basin System.

The interpretation of the report regarding the generation of fracture set 'A' in this stage, does not match with this novel description. Instead the dynamic modeling shows that these fractures most likely originated in Triassic to Jurassic times. This second tectonic stage comprises pronounced E-W

extension, which directly matches the N-S strike of fractures in this set ‘A’. More abundant NE-SW strike of fractures can be attributed to perturbations indicated in the modeling results. Some graben structures of this Triassic stage, for instance the Glückstadt graben and Horn graben, also exhibit slightly rotated bounding faults (Doornenbal and Stevenson, 2010). This fact may indicate a NNE-SSW direction of the maximum horizontal stress, which would result in more pronounced perturbations and an improved fit. Besides this hypothesis, it is highly unlikely that the fractures of set ‘A’ are generated during the first, third or fourth tectonic stage due to the missing correlation in orientation.

Regarding the second fracture set ‘B’, the report suggests a correlation of these fractures to the NW-SE trending fault pattern and its re-activation in Late Jurassic to Early Cretaceous rifting or under Late Cretaceous compression. An origin of these fractures during re-activation of the faults under the reverse faulting regime in the fourth tectonic stage is highly unlikely due to the dip and strike of the fractures with respect to inversion direction. Neither is it likely that the assumed NW-SE extension during a North Sea rifting phase is responsible for generating these fractures.

However, the paleo-stress field of the third tectonic stage proposed by Kley et al. (2008) provides an ideal orientation for generating this fracture set ‘B’ and supports the hypothesis that the NW-SE fault pattern is re-activated in Late Jurassic to Early Cretaceous time. The results of the dynamic model also support this assumption due to the good match of fracture strike and stress orientation in the respective well areas in this third tectonic stage. Stress perturbations frequently occur along the nearby faults and directly explain the great spread of this fracture set. The occurrence of these stress perturbations suggests activity along the respective faults, which ideally fits to the assumptions of fault re-activation. Similar horizontal magnitudes proposed by the R-value additionally support the generation of perturbations.

While the more recent information on the paleo-stress stages, the specific fracture orientation, and the dynamic modeling results do not support the interpretation of the report regarding fracture set ‘A’, they partly support and specify the interpretation for fracture set ‘B’. In summary, fractures of set ‘A’ are most likely generated within the second tectonic stage in Triassic times due to the overall best fit. Fractures of set ‘B’ are proposed to have originated during re-activation of NW-SE trending faults in the third tectonic stage in Late Jurassic to Early Cretaceous times. This interpretation implies that fractures of set ‘A’ are emplaced prior to those of set ‘B’.

The report further states than the cataclastic seams of the fractures observed in cores require sufficiently deep burial of more than 1km. This requirement is fulfilled for the reservoir at both proposed fracture generating stages.

Fracture Density vs. Cumulative Strain

The interval length of the image logs and the amount of fractures detected therein yield the fracture density for the respective well area. This fracture density is calculated for all ten wells providing image logs. Only three wells comprise more than 10 fractures, whereas half of the wells show less than 5 fractures over the entire logging interval. Due to this overall low amount of fractures, the density values are expressed in fractures per 10m. However, ten data points are insufficient for generating a reasonable contour map of the fracture density distribution. Therefore, the punctual information on fracture density is compared to dynamic modeling results.

The general hypothesis proposes a proportional correlation between strain accumulated during the entire tectonic history and the fracture density observed. According to this hypothesis, those areas

experiencing most strain in total under all tectonic stages yield highest fracture densities. Maintaining reservoir geometry and discretization in the four load steps of the dynamic modeling approach allows the calculation of results across all four tectonic stages. In this way, strain values are calculated and integrated over the tectonic history. This is done for all principal strains and the calculated equivalent strain and horizontal shear strain in the x-y plane. Due to regarding exclusively the elastic domain in the geomechanical model, no plastic strains are provided as results. Elastic strain is considered as a proxy for plastic strain, since areas experiencing the largest elastic strains are most likely those at which rock strength is exceeded first and plastic deformation occurs.

The equivalent elastic strain, or von Mises strain, represents a comprehensive strain quantity incorporating all principal strain components (4.7). The accumulated equivalent strain of the dynamic model is compared to an overview on the calculated fracture densities (Fig. 8-17). Ideally, the fracture densities correspond to distinct strain values throughout the reservoir. However, such an ideal match cannot be observed. The distribution of accumulated equivalent strain is considerably dominated by the distribution of reservoir depth (Fig. 8-17). Large strain values generally correspond to deeper reservoir levels and vice versa. In addition, highest strains accumulate along the large vertical offsets and mechanical juxtapositions at the faults of the western graben structure. Further strain localizations related to stress perturbations are observed especially in the northern part of the reservoir, but are less abundant and of minor intensity (Fig. 8-17).

The specific reservoir depth is maintained in the dynamic model together with the horizon topology and the fault geometry of the reservoir. The strong impact of relative reservoir depth on the accumulated strain distribution most probably results from the dominant normal faulting regimes in the tectonic history (8.2). In three of four tectonic stages, the first principal stress and strain is thus vertical and the internal relative depth of the reservoir horizon becomes decisive and significantly controls the distribution of strain.

The lack of clearly resolved lateral strain localizations in the distribution of accumulated equivalent strain impedes a direct match of strain maxima and minima with fracture densities (Fig. 8-17). However, the strain distribution does show some similarity with the distribution of fracture density. Except for the extraordinarily high fracture density at well C5 and C5a in the center of the reservoir, the northern to northwestern parts show on average higher fracture density values than the southern to southeastern parts. This general trend matches the equivalent strain distribution showing lower accumulated in strains in the southeastern and higher strains in the northwestern part (Fig. 8-17).

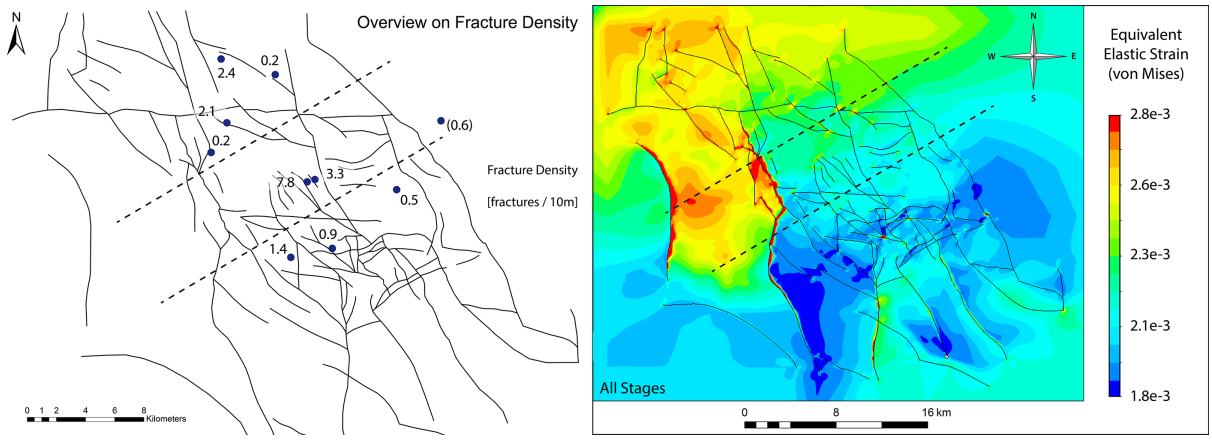

Fig. 8-17. Overview on the distribution of fracture density in [fractures/10m] at ten wells derived from image logs (left) and the contoured distribution of equivalent strain in the reservoir accumulated over all tectonic stages considered in the dynamic model (right). The on average higher fracture densities in the northwestern part of the reservoir in contrast to the southeastern part match with the general distribution of accumulated equivalent strains being respectively higher and lower (dashed lines).

In order to reveal lateral strain localization patterns in the fault network in more detail, the horizontal shear strain in the x-y plane is calculated and integrated over all tectonic stages (Fig. 8-18). This accumulated shear strain does not consider the vertical strain component and thus is not affected by the internal depth distribution of the reservoir.

The contoured distribution of horizontal shear strain shows strain localizations occurring similar to stress perturbations at tips, curvatures and crossings of faults, and also due to interaction and along the juxtaposition of layers at large vertical fault offsets (Fig. 8-18). High shear strain increases the likelihood of fracturing to occur and thus this strain quantity can be seen as a proxy for fracture density as well. However, no distinct maxima or minima in horizontal shear strain are located at the well locations, at which fracture density is described. Despite the resolved lateral strain localizations, a direct match to the observed fracture density is not possible. The potential reasons for this mismatch in detail and are discussed below (8.5).

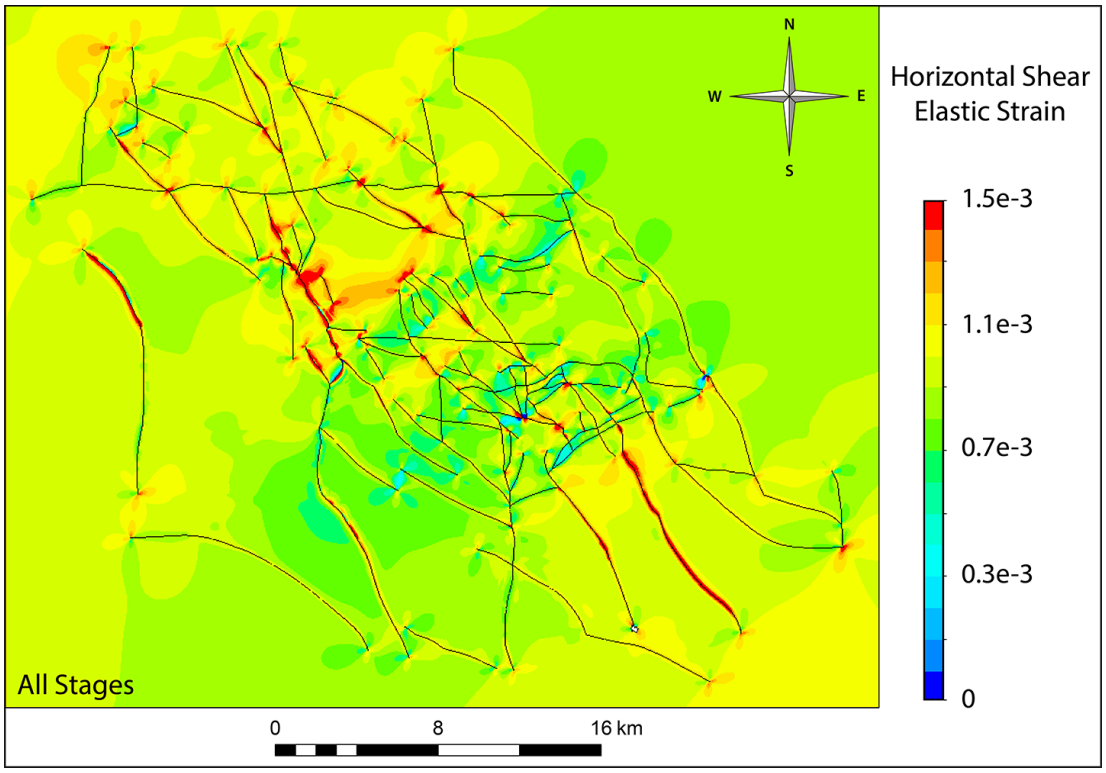

Fig. 8-18. Distribution of horizontal shear strain in the x-y plane accumulated over all tectonic stages regarded in the dynamic model of the case study reservoir.

8.4.3 Fault Behavior

A major objective of the dynamic modeling approach focuses on the analysis of fault behavior during and throughout all tectonic stages. These results are compared to the determined present-day hydraulic behavior in order to reveal correlations. According to information from the project partners, a significant amount of faults is assumed to represent baffles to fluid flow. Some faults even show sealing behavior and establish a compartmentalization of the reservoir into distinct blocks. These insights are based on the production behavior of neighboring wells and their hydraulic communication.

A reservoir simulation was applied by the project partners and used for a history match with production data. The successful match between modeling results and well-specific pressure data indicates multiple faults to represent baffles to fluid flow. The lack of hydraulic communication between neighboring wells suggests that some faults act as seals between adjacent reservoir compartments. The complete closure of such a compartment allows a relatively precise description of the un- or less permeable faults.

However, if several faults are located in the impeding area between hydraulically separated compartments, the individual permeability of these faults can only be estimated from the reservoir simulation. Pressure data also indicates impeded fluid flow between wells that are not hydraulically separated. In those cases, the precise location and the specific permeability of the responsible faults is even more complicated to determine. Especially in reservoirs comprising numerous stepped faults, such as the case study reservoir, it is hardly possible to state whether the faults impeding fluid flow are impermeable and reservoir fluids flow around them, or if the respective faults comprise a reduced permeability only. The resulting uncertainty in the description of faults as baffles and seals has to be kept in mind during the interpretation.

The project partners provided information on those faults in the case study reservoir, which are assumed to allow no or very minor flow according to the history match in the reservoir simulation. Based on the grid of the respective reservoir simulation, this information is summarized in an overview on the fault network (Fig. 8-19). However, the finite difference grid of the reservoir simulation does not precisely reflect the structural model and thus the transfer of fault information is difficult at some locations.

The most assured information, the overview on low permeability faults in the case study reservoir provides, is the description of connected and separated blocks of the gas field (Fig. 8-19). The following relationships are implied by the reservoir simulation and this overview. Block D is separated from block C, C-South, and the area of G, whereas wells in area E are not hydraulically separated from wells in block D (Fig. 8-19). In addition to the separation from block D, wells in block C cannot communicate to those in block C-South, block K and to the well in the small compartment of X2. However, well communication across block A, C, and F is possible.

Moreover, block K is separated from block F and the areas of X1 and X2 (Fig. 8-19). The only compartments, whose boundaries are completely described as baffles, are those of X2 and C-South. All other compartments are either not fully closed or the respective boundaries are not determined. Reservoir quality in area G is significantly decreased and therefore it is increasingly complicated to estimate the low permeable features responsible for the hydraulic separation (pers. comm. T. Mozer).

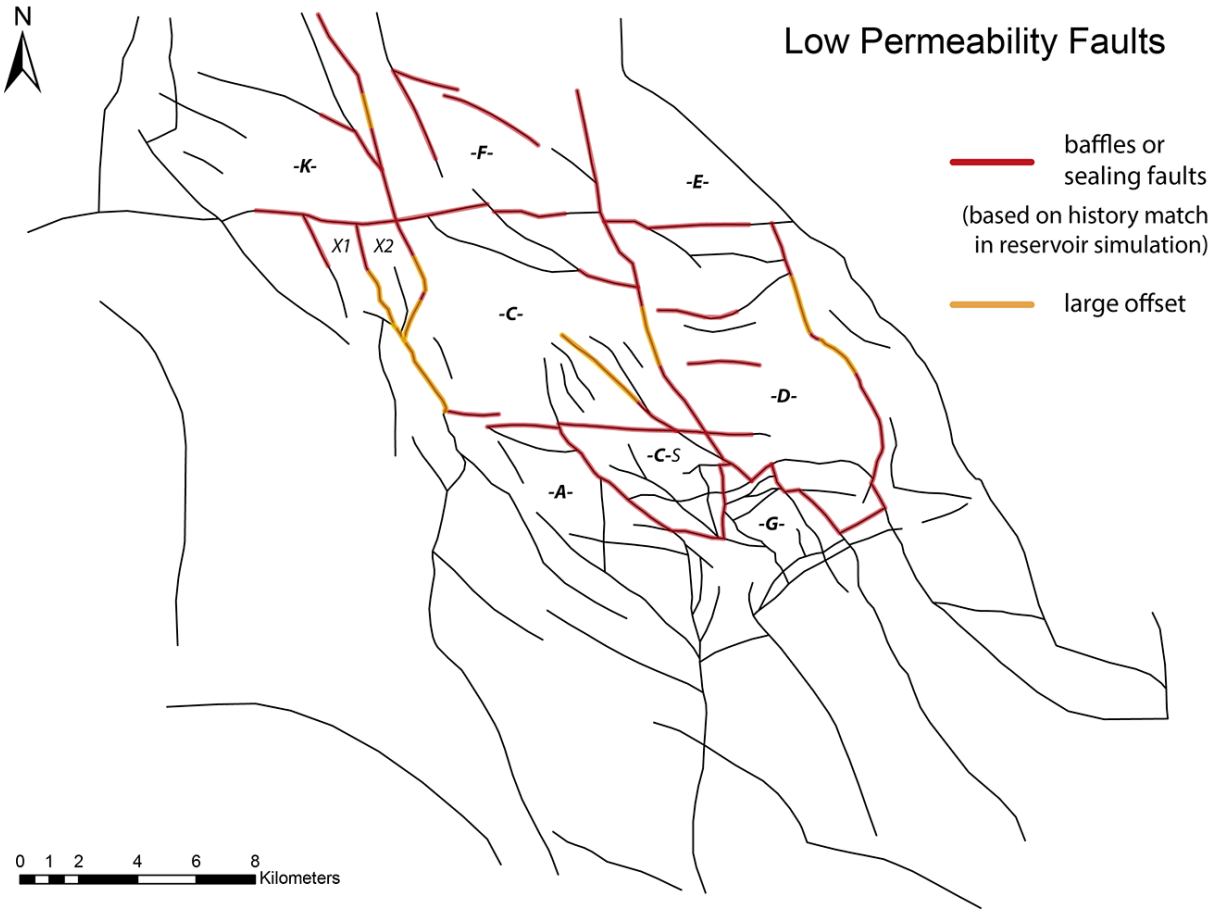

Fig. 8-19. Overview on those faults (red), which are proposed to allow no or very minor flow in the history match of the reservoir simulation. Some of them establish the enclosed compartments of the blocks C-South and X2. While wells located in some large blocks like D, C, and K, cannot communicate with each other, fluid flow is only impeded between block like F and C, and E and D, for instance. Large offsets along faults do only explain the hydraulic behavior at some fault segments (yellow).

In addition to these summarized hydraulic relationships, the overview indicates segments of the low permeable faults that comprise large vertical offsets (Fig. 8-19). Such considerable fault throws are the most direct explanation for sealing behavior (3.3). It may result from juxtaposition of different lithological units like sandstone and shale, or from the displacement process leading to smearing of clay minerals, for instance. All fault throws determined in the case study reservoir are additionally provided by the project partners and summarized in a separate overview (Fig. 8-20).

The overview on fault throws in the case study reservoir shows large offsets along the NNW-SSE and approximately N-S directed bounding faults in the eastern and western part of the production area, respectively (Fig. 8-20). Inside the production area, large offsets are sparse and those present are discontinuous and only found at individual fault segments. The vast majority of offsets inside the production area are of small to medium size (Fig. 8-20). Moreover, some faults indicated as baffles do not comprise any vertical displacement, such as E-W trending fault segments, for instance (Fig. 8-19).

Due to the thickness of the overall sandstone units of up to about 100m, only large offsets of at least more than 50m can be assumed to be responsible for hydraulically sealing behavior. Fault throws can thus explain the hydraulic behavior of the eastern and western bounding faults of the production area (Fig. 8-20).

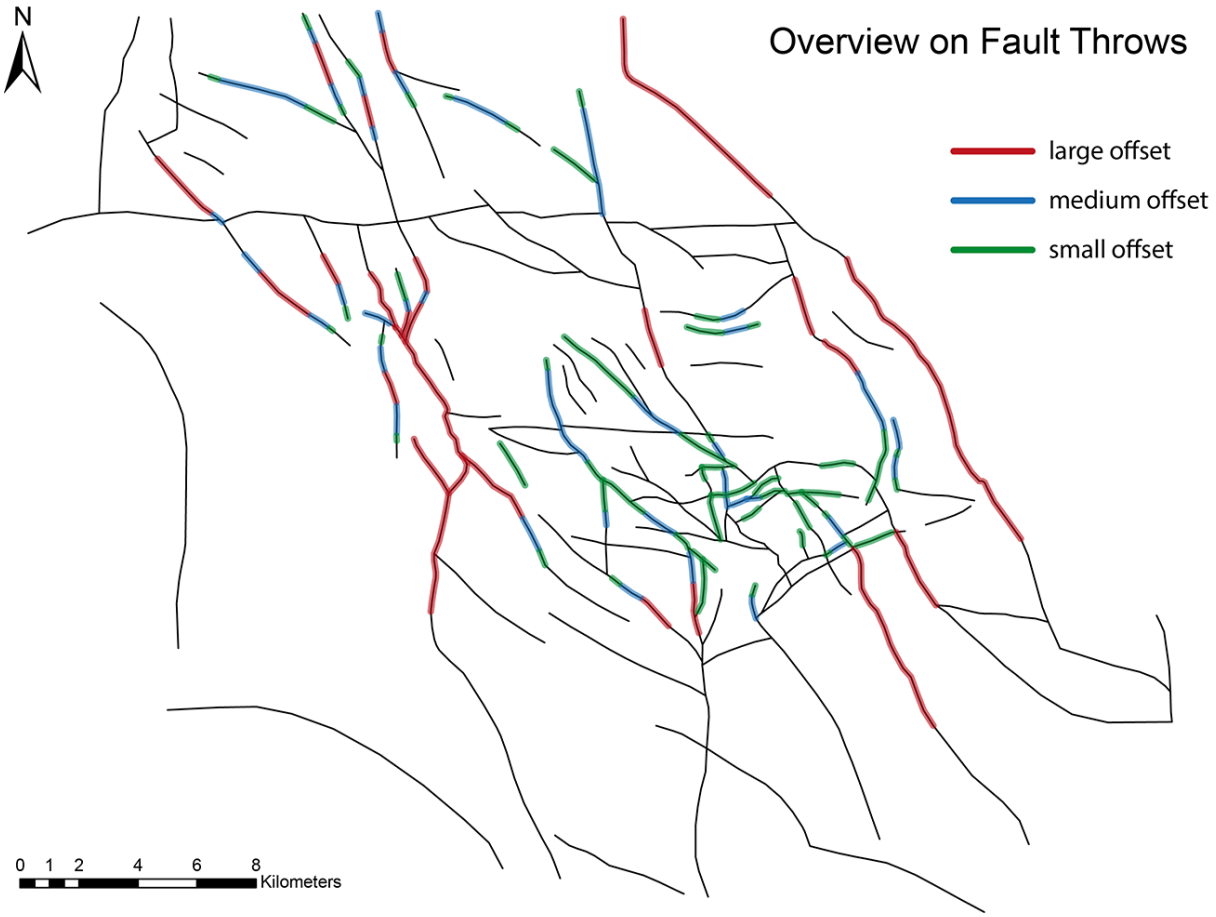

Fig. 8-20. Overview on the fault throws in the case study reservoir according to data provided by the project partners. The NNW-SSE directed fault in the eastern part and the approximately N-S directed fault in the west laterally bound the production area and show large offsets (red). The large offsets in the southwestern part of the reservoir area are south and outside the production area. Inside the production area, the fault throws show offsets of medium (blue) to small size (green).

However, the respective offsets inside the reservoir are either non-existent, too small, or too discontinuous to explain the observed hydraulic behavior. Other aspects thus have to play a role – at least additionally. In general, two phenomena are plausible to result in the observed behavior. The permeability can be significantly reduced by cataclasis due to fault movement or by mineralization from circulating fluids.

Correlation to Dynamic Modeling Results

The dynamic model reveals the geomechanical exposure of incorporated faults in each tectonic stage and cumulative over the entire history. This exposure is best expressed by the slip tendency describing the proximity of a fault to move (4.7). The slip tendency is calculated for all stages and cumulative for the entire history. Faults and fault segments comprising a relatively high slip tendency are most likely to be critically stressed or activated. This description allows two assumptions. The critical state of stress yields actual fault movement and cataclasis (1), or it temporarily increases permeability (2) (Barton et al., 1995). Increased permeability can result in diagenetic changes due to fluids invading the fault compartments from the fault zones and precipitating minerals (Gaupp et al., 1993). Both phenomena can thus lead to the permeability reduction of the fault and/or the closer vicinity that is observed today.

Increased permeability of faults in the past can also be indicated by the dilation tendency (4.7). This fault-specific quantity indicates the likelihood of a fault to open. Relatively high dilation tendencies

thus suggest permeability reduction due to fluid flow and mineralization as well. The analysis of both, slip and dilation tendency, is focused on qualitative description and comparison of their relative increases and decreases. Absolute values of these quantities can be misleading due to their dependency on the specific paleo-stress magnitudes and material parameters, which comprise significant uncertainty.

The slip tendency covering all tectonic stages shows distinct trends in its distribution (Fig. 8-21). Highest values are constantly reached within the reservoir. This observation matches with the present-day results and is most probably related to the maintained Young's modulus being lower for the reservoir layer. In addition to this vertical distribution, there are also trends with respect to fault orientation. In general, highest slip tendency values are found on faults trending E-W to ENE-WSW and N-S to NNE-SSW (Fig. 8-21). In contrast, faults trending NW-SE to NNW-SSE show lower slip tendency on average. Individual local deviations from these general trends may result from intense stress perturbations.

The comparison of the cumulative slip tendency distribution to the overview on low permeable faults reveals some similarities (Fig. 8-22). In particular, E-W trending faults show a significant match. They represent the southern boundaries of blocks K, F, E, C, and C-South. These faults exhibit generally high cumulative slip tendency values and are also proposed to be baffles or seals (Fig. 8-22). This is also valid for some E-W directed fault segments inside block D. Except for one of those fault segments in block D, none of the E-W trending faults show any offset, which could be responsible for the hydraulic behavior (Fig. 8-20). They are assumed to be strike-slip faults lacking any seismically detectable displacement.

The dynamic modeling supports the hypothesis of these faults being present and geomechanically exposed in the past to a considerable amount, which could have led to intense cataclasis and permeability reduction.

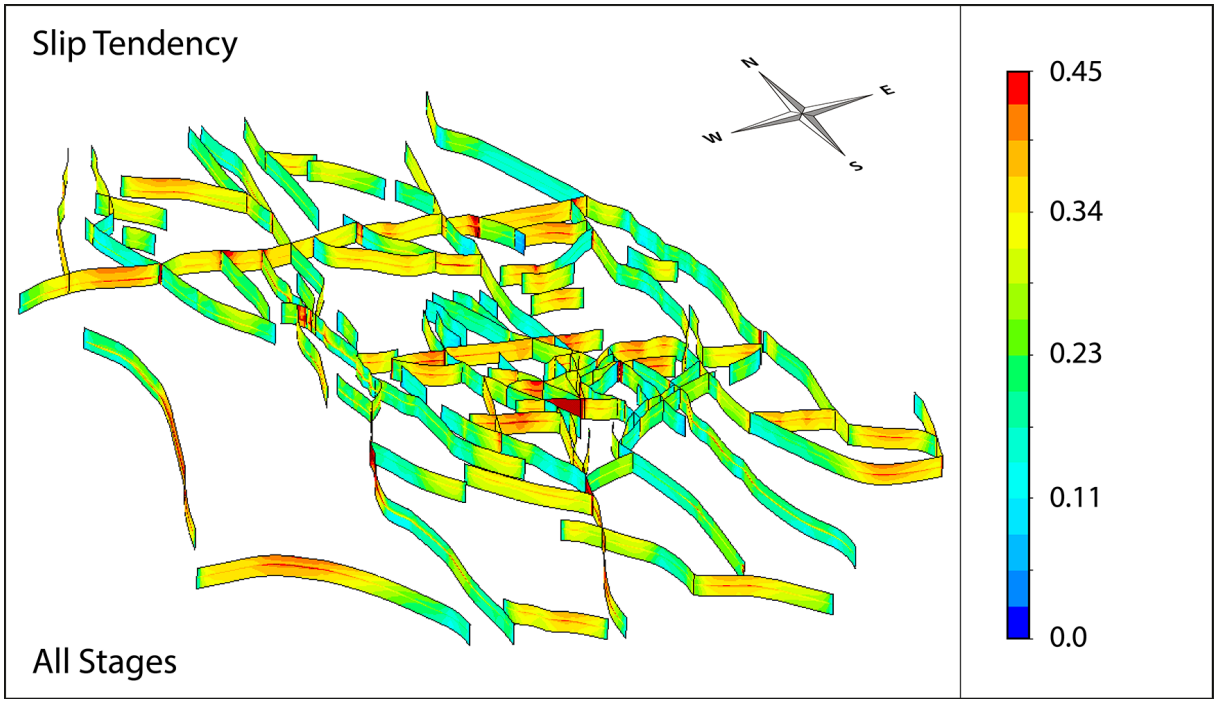

Fig. 8-21. Distribution of the cumulative slip tendency of faults for all tectonic stages. The default color scaling from 0 to 1 is reduced for better representation.

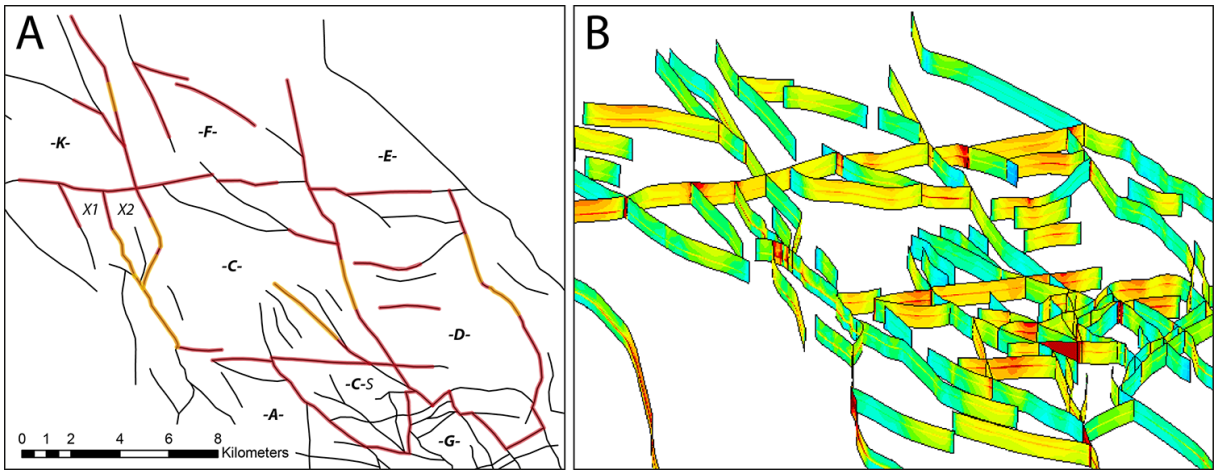

Fig. 8-22. Direct comparison of the compiled overview on low permeable faults (A) to the distribution of cumulative slip tendency regarding all tectonic stages (B). The shown parts are cutouts from Fig. 8-19 (A) and Fig. 8-21 (B).

Some of these E-W trending faults contribute to the complete separation of block C-South and X2, but the majority does not represent absolute barriers to fluid flow (Fig. 8-22). This is attributed to the commonly stepped nature of these faults and the lack of continuity. Therefore, the E-W trending faults between block F and C, and E and D, for instance, do not yield a strict hydraulic separation of these compartments, but only impede fluid flow (Fig. 8-22).

In addition to E-W trending faults, also N-S to NNE-SSW directed faults show a match between high cumulative slip tendency and observed reduced permeability (Fig. 8-22). Due to the lower abundance of these faults and the viewing angle of the result plots, the respective correlation appears less striking. Nevertheless, this match is observed along the southeastern boundaries of blocks C-South, D, and X2, and supports the hypothesis of geomechanical exposure leading to permeability reduction (Fig. 8-22). The bounding faults of the western graben structure also show high cumulative slip tendency values along N-S to NNE-SSW oriented segments, but the respective hydraulic separation is attributed to the considerable vertical offset at these locations (Fig. 8-20).

Faults of both matching orientation sets, i.e. E-W and NNE-SSW, are also present as small segments inside and outside the production area, which are not indicated as baffles (Fig. 8-19). This is attributed to the lack of data outside the production area and the uncertainty in determining baffles inside as mentioned above.

Beside those faults showing a significant fit as clarified above, further differently oriented faults are described as baffles (Fig. 8-19). Although the relatively lower cumulative slip tendency along NW-SE to NNW-SSE trending faults does not necessarily preclude sufficient geomechanical exposure to yield cataclasis, for instance, another more likely scenario is analyzed using the dilation tendency. This quantity describes the likelihood of a fault to open and thus high values indicate segments that may have allowed the circulation of fluids in the past leading to mineralization-related permeability reduction. In order to reveal complementary effects, the cumulative slip and dilation tendency is compared at two locations in the production area (Fig. 8-23). The areas analyzed in detail are located at block C / C-South and block D, and focus is set on the faults at reservoir level.

The comparison confirms the distribution of high cumulative slip tendency along N-S to NNE-SSW and E-W trending faults, and the relatively lower values along NW-SE to NNW-SSE directed faults (Fig. 8-23). Varying orientation of the eastern and western bounding faults of block D reveals the transition from low to high slip tendency and vice versa (Fig. 8-23-A).

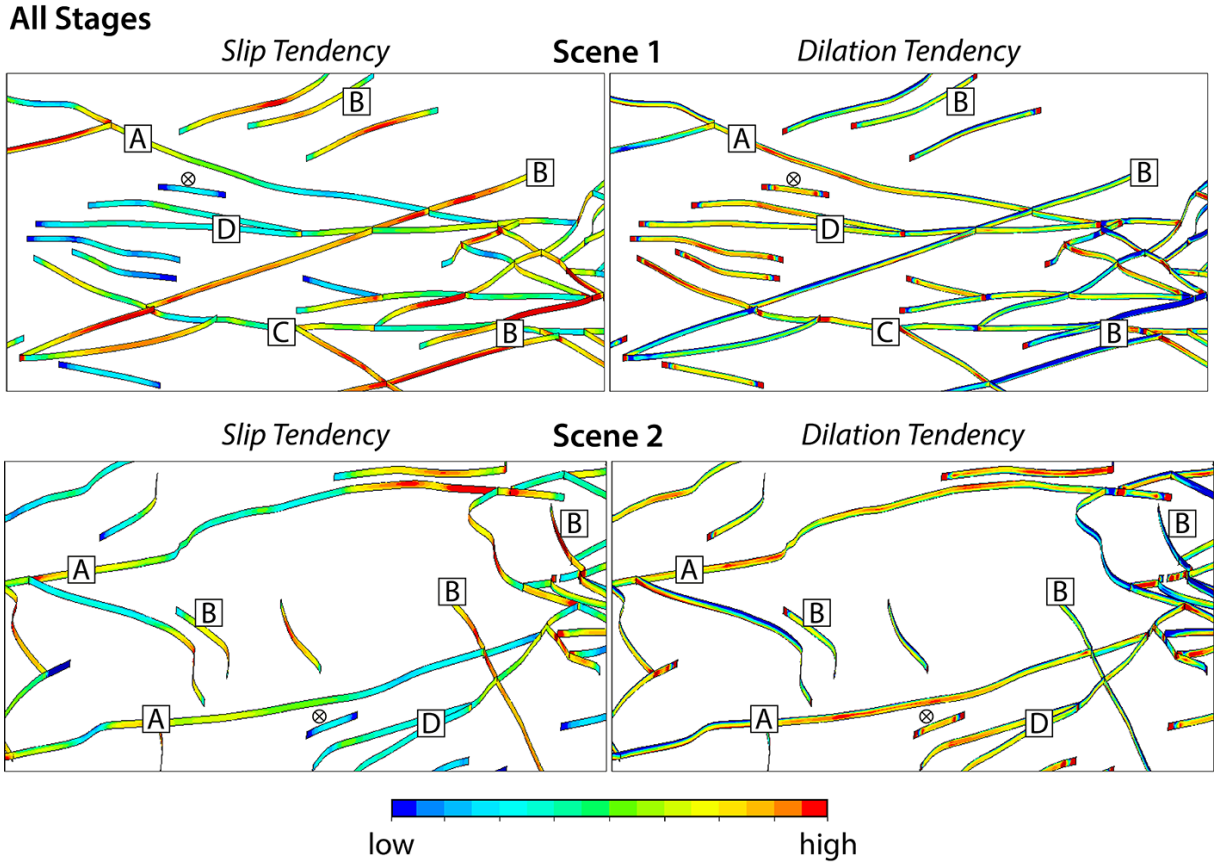

Fig. 8-23. Inclined view on two scenes showing the faults at reservoir level that are contoured by cumulative slip and dilation tendency values. The contour scale varies and is individually adjusted for best visualization, which is why a relative scale is indicated. Faults marked by characters (A-D) are referred to in the text. The crossed circle indicates the location of well C5a.

Moreover, these faults show relatively high dilation tendency values at those segments comprising a low slip tendency. Highest slip tendency values are found along the E-W trending faults as determined before (Fig. 8-23-B). The approximately NW-SE directed bounding fault of block C-South comprises varying slip and dilation tendency values and no clear correlation in distribution (Fig. 8-23-C). However, the fault pattern inside block C confirms the observation at the bounding faults of block D and also shows a complementary distribution of low cumulative slip and high dilation tendency (Fig. 8-23-D). This observation underlines this type of distribution for NW-SE directed faults.

The distribution of low slip tendency values being complemented by high dilation tendencies at the same fault segments suggests an impact of mineralization due to fluid circulation to be likely. Such permeability reducing mineralization can be represented by authigenic illite, for instance. Especially flakey and fibrous authigenic illite reduces permeability significantly, while porosity is only weakly influenced (Kayser, 2006). Illitization is reported for Rotliegend units in the North German Basin and Gaupp et al. (1993) proposes Carboniferous fluids to be responsible for this mineralization. According to Gaupp et al. (2005), the flow of these fluids into the reservoir sandstone is assumed to be enabled during reactivation of faults in the Late Triassic to Early Jurassic.

However, the tectono-sedimentary study provided by the project partners and the correlation of fractures to dynamic modeling results strongly suggest the reactivation of NW-SE to NNW-SSE trending faults in Late Jurassic to Early Cretaceous times representing the third tectonic stage (8.4.2). These faults thus could have provided the flow of Carboniferous fluid during this phase of reactivation. In order to test this hypothesis, the dilation tendency is calculated for the faults on reservoir level during the third tectonic stage (Fig. 8-24).

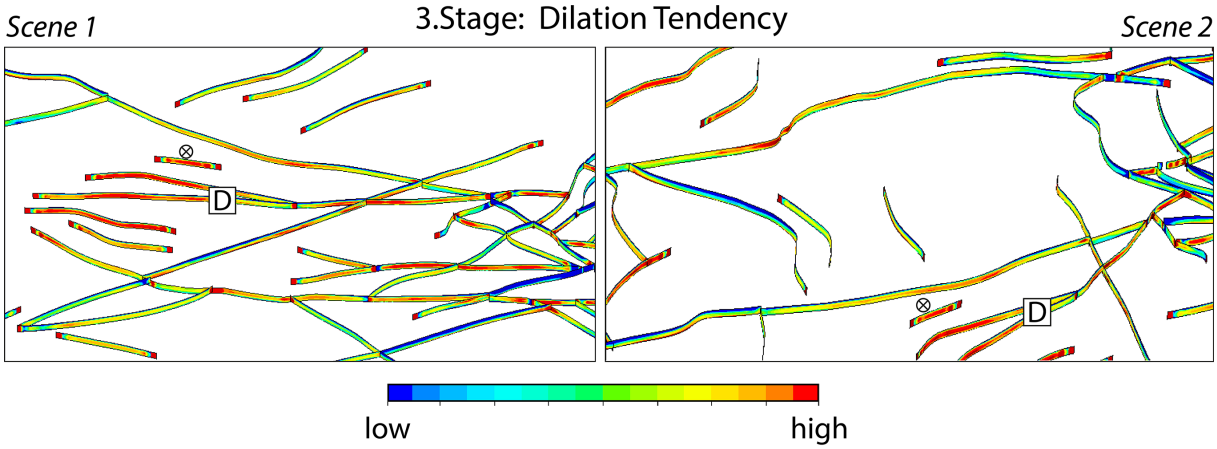

Fig. 8-24. Distribution of dilation tendency on fault at reservoir level in the third tectonic stage considered in the dynamic model. The crossed circle in both scenes marks the location of well C5a. The nearby fault set "D" comprises high dilation tendencies suggesting the access of fluids leading to the illitization detected in well C5a.

The distribution of dilation tendency on the reservoir faults in the third tectonic stage shows even higher relative values for about NW-SE trending faults than the cumulative results (Fig. 8-24). This strong tendency of these faults to open supports the hypothesis that they obtain their reduced permeability by illitization in these times instead of cataclasis. Critical stress states generally indicate increased hydraulic activity and allow fluid flow, which fits to the fact of fault reactivation in this tectonic stage. This phenomenon is therefore not excluded to be participating and partly responsible as well. However, the dilation tendency acts as best proxy for fluid flow in the outcome of the dynamic modeling, since the slip tendency results are not capable of resolving vertical displacement. The latter would require fault inclination to be implemented, which was not possible due to the verticalized faults provided.

In particular, the fault pattern of NW-SE directed faults in the southeast of block C comprises very high dilation tendencies (Fig. 8-24). These results ideally match the observation of pervasive illite cementation in well C5a in the close vicinity of these faults, which is mentioned by the tectono-sedimentary study. This illitization is assumed to be responsible for the unexpectedly poor well performance. Moreover, a preceding DGMK research project (593-8) focused on the reservoir quality of Rotliegend oil and gas fields in the North German Basin. The diagenesis model elaborated therein stated a risk of cataclasis and illitization in the proximity to faults and potential illite-reaction fronts along faults (Gaupp et al., 2005). These propositions are strongly supported by the presented results of the dynamic geomechanical modeling approach.

In summary, the outcome of the dynamic model shows high cumulative slip tendency values for E-W and N-S to NNE-SSW trending faults in the reservoir regarding the entire tectonic history. These results match with the provided information on low permeable faults of this direction. This match suggests that cataclasis plays a major role in the permeability reduction of these faults. Faults oriented NW-SE to NNW-SSE commonly comprise low cumulative slip tendency values, but show high dilation tendencies over time. This suggests mineralization due to fluid flow, such as illitization, to affect the respective permeability. Dilation tendency values of NW-SE to NNW-SSE trending faults are especially high in the third tectonic stage, in which fault reactivation and the income of Carboniferous fluids into the reservoir horizon most likely occurred. This fact supports the assumption of illitization being partly responsible for the low permeability of these faults. Confirmation of illitization at well C5a further underlines this hypothesis of cataclasis and mineralization being complementing factors in yielding the observed low permeable faults and compartmentalization. Further validation requires additional information of the specific fault composition.

Stage-Specific Fault Behavior

In addition to the cumulative slip tendency values covering all tectonic stages, the respective results of the individual stages are analyzed. These results elucidate the activity of different fault sets in the various time intervals (Fig. 8-25). This analysis is qualitative and based on relative increases and decreases only due to the uncertainty of absolute values.

The summarized slip tendency results for each tectonic stage show that the NW-SE to NNW-SSE oriented fault set is most active in the first stage, i.e. in Permian times (Fig. 8-25). This result is concordant with the described origin and activity of these faults in the late stage of the Variscan orogeny and shortly after (Glennie, 1998). Following the first stage, less intense values are prevailing in the second tectonic stage. The slip tendency of this fault set becomes relatively low in the third and fourth tectonic stage (Fig. 8-25). Nevertheless, these faults are assumed to be reactivated in the third tectonic stage according to the results in fracture correlation (8.4.2).

This assumption does not disagree with the low slip tendency values in these times, since the slip tendency in this model reflects the probability of horizontal displacement. Reactivation of these faults in the third tectonic stage most likely occurred in vertical direction due to the orientation of the regional stress field (8.2). In order to assess the likelihood of vertical movement by the slip tendency, the faults must be implemented with their specific inclination. However, this was precluded by the preceding fault verticalization.

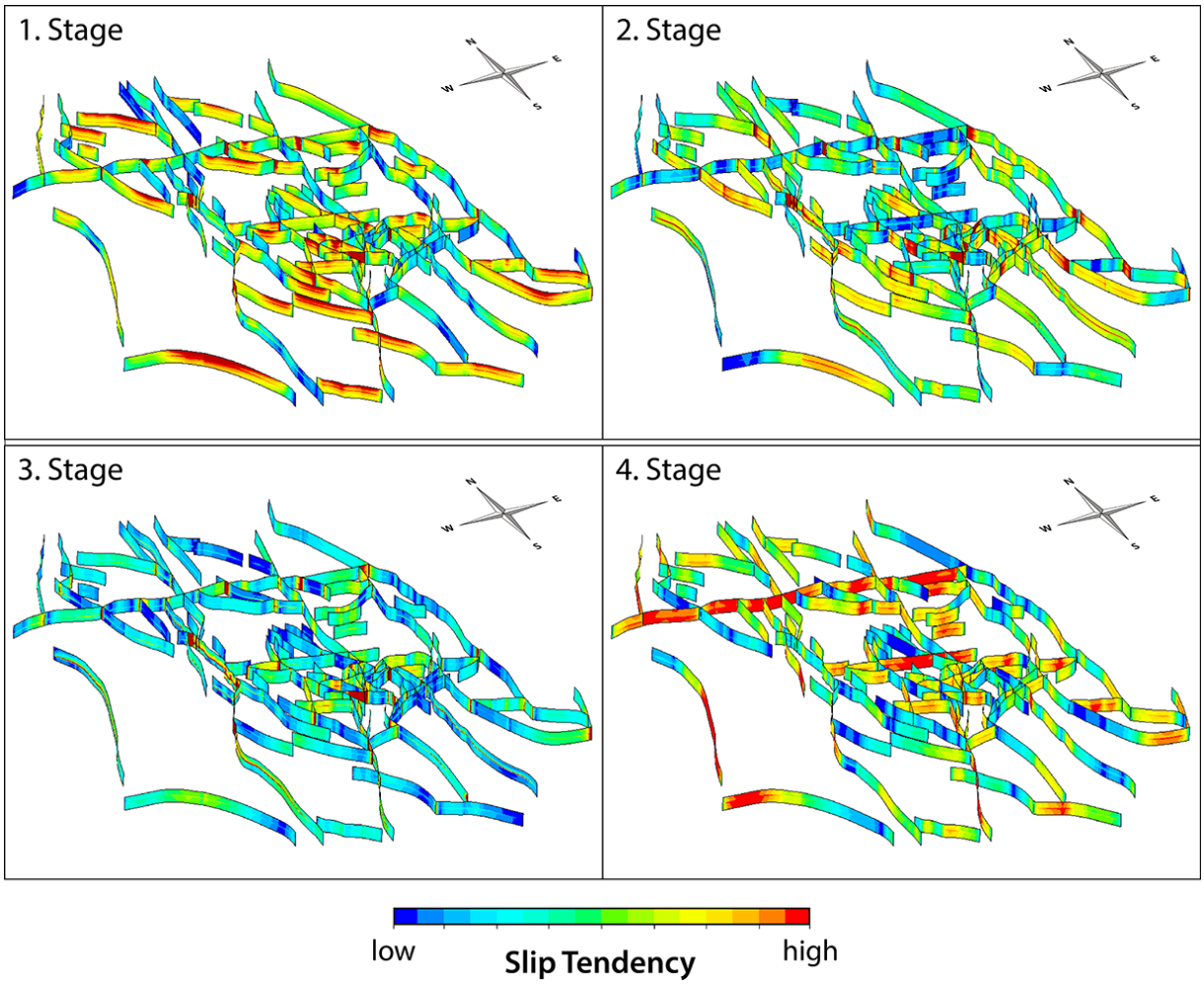

Fig. 8-25. Overview on the slip tendency of the fault network during all four tectonic stages considered in the dynamic modeling. The contour scaling is individually adjusted for best visualization and thus a relative scale is provided only.

The E-W trending set of fault shows intermediate to high slip tendency values in the first tectonic stage (Fig. 8-25). In the following two stages, relatively low values prevail and are replaced by most intense slip tendencies in the fourth tectonic stage. This development may describe an early origin in Permian times without intense activity. Subsequently, these faults are not reactivated in the second and third stage of extension, but are significantly stressed and most probably active in the fourth compressional stage. Consequently, this interpretation suggests a Late Cretaceous age for the cataclastic effects yielding the low permeability of these E-W trending faults.

The N-S to NNE-SSW trending faults experience relatively low slip tendencies in the first three tectonic stages and also most significant values in the fourth stage of compression. This indicates that the cataclastic effects of this faults set and the E-W trending faults most probably have their origin in the same time interval. The lack of intense slip tendencies of the NNW-SSE oriented fault set in this fourth stage underlines the hypothesis of two main factors being responsible for the reduced fault permeability observed.

Summary

In summary, cataclastic effects are proposed to reduce the permeability of E-W and N-S to NNE-SSW trending faults, while the reduction along NW-SE to NNW-SSE oriented faults is attributed to illitization resulting from entering of fluids from the Carboniferous units. This division of responsibility for decreased fault permeability is supported by several observations.

First, the stage-specific analysis of slip tendency supports an origin of the cataclastic features of the E-W and N-S to NNE-SSW trending fault set in the fourth tectonic stage of compression in Late Cretaceous times. However, low slip tendency values exclude this relationship for the NW-SE to NNW-SSE trending fault set. These faults instead show increased values in dilation tendency – in particular during the third tectonic stage. Increased dilation tendencies indicate facilitated fluid flow due to fault opening in these Late Jurassic to Early Cretaceous times.

This timing also matches the interval, at which most likely fault reactivation of this fault set occurred. This supports the assumption that the prevailing stress field actually provokes fault dilation. Fault reactivation in this third stage is suggested by the tectono-sedimentary study provided and also by the significant match of the fracture set ‚B' to the revealed stress orientations. This match applies intense stress perturbations to explain the great variability in fracture orientation in this set. In turn, stress perturbations are more intense with increasing fault activity, which underlines the assumption of reactivation.

Furthermore, an increased intensity of stress perturbations is suggested for the third and fourth stage by the in situ stress distributions revealed for all tectonic stages. These interrelationships underline the likelihood of the stated assumptions and provide a possible and consistent description of fault and fracture evolution based on the dynamic model.

8.5 Discussion of Dynamic Model

The results of the dynamic model demonstrate the capability of the applied modeling approach (8.4). Snapshot-like insights into the in situ stress distribution in the reservoir during the major past tectonic stages are obtained, as well as a description of fracture network development and the behavior of faults in the past. Furthermore, the results indicate cataclasis being partly responsible for reduced fault permeability supporting the respective hypothesis. The interlinked argumentation regarding fault reactivation in Late Jurassic, for instance, underlines the probability of the stated interpretations. The dynamic model thus provides a mechanically consistent simulation of the tectonic evolution of the case study reservoir.

Preparation and Model Setup

Especially the input data and setup of the dynamic modeling approach comprise uncertainties that must be regarded (8.2, 8.3). The definition of major tectonic stages and the calculation of respective steady state models imply that fundamental changes in stress distribution occur only between and not within the selected tectonic stages. Beside the numerical and computational problems accompanying a potential fully transient modeling approach, numerous assumptions concerning the time-dependent behavior of input parameters would be required. These assumptions most likely comprise higher uncertainties than the relatively well-constrained description of major tectonic stages utilized for setting up the steady state modeling.

The comprehensive description of the tectonic history of the case study reservoir area provides reliable information for defining the most important stages (8.2.1) (Kley et al., 2008). This working step of stage definition may be significantly more complicated in less well studied areas of the world. The subsequently required detailed description of the individual stages in terms of reservoir depth, material parameters and boundary conditions is more challenging and demands many assumptions.

Determination of the burial history of the reservoir horizon is common practice in hydrocarbon industry and well-established. The provided burial history is used to define the specific reservoir depth of the horizon within the time intervals of the individual tectonic stages (8.2.2). This selection is decisive and made consistent for all stages at representative points in time. The depths at the selected times have direct impact on the resulting stress magnitudes, for instance. The burial history also provides information on paleo-density changing under compaction. Specific density information for the modeled stages is ideally obtained from the elaboration of burial history. Graphical determination of density changes from burial curves and further extrapolation represents a less ideal approach (8.2.3). This was only justifiable for the case study due to the lack of access to the underlying parameters of burial history.

Especially concerning the extrapolation of overburden paleo-density, the applied approach in dynamic modeling comprises some uncertainty. This uncertainty affects the oldest first stage the most, as well as the fourth stage following an erosional period. In these stages, the extrapolated overburden density is probably higher than it was in reality. Those density values are used in combination with the respective depths to calculate the lithostatic pressure load of the overburden on the model. Hence, the inherent uncertainty directly affects the resulting stress magnitudes.

While the applied density in the dynamic model is changed according to the burial history information, the mechanical parameters remain those of the present-day static geomechanical model. In absence of any clear and reservoir-specific knowledge on how mechanical parameters possibly vary with increasing subsidence, no reasonable estimations for modifying these parameters can be made. Any

estimation would be highly hypothetical and is assumed to yield more uncertainty than the assumption of constant parameters. Determining the specific temporal evolution of mechanical parameters represents a field of future research.

The orientation of the regional stress fields in the modeled tectonic stages is directly provided by the description of these stages and is relatively well-constrained. Identifying the paleo-stress magnitudes is significantly more complicated (8.2.4). Relating the horizontal stress magnitudes to the vertical stress is reasonable due to the dependency of the vertical stress on the relatively reliable burial depth. While the prevailing tectonic regimes define the overall relations of vertical and horizontal stress magnitudes, the R-values provide further constraint. However, the R-values derived from fault-slip analysis for specific stages only describe magnitude proportions and not absolute values. R-values applied in this study are not specific for the reservoir area, but are determined in outcrops along the southern rim of the North German Basin (Sippel et al., 2009). The usage of these values might not have been ideal, but no reservoir-specific values are available.

Further uncertainty that must be kept in mind concerns the constant reservoir geometry and discretization applied in the dynamic modeling (8.3). This probably represents the most controversial assumption of the described approach. Ideally, the reservoir geometry should be specified and adjusted for each tectonic stage with respect to the fault network and the distribution of relative reservoir depth. Such an approach requires detailed information on the paleo-depth distribution of the reservoir and on the timing of fault formation, which are both not available. Moreover, changing reservoir geometries require individual geomechanical models for each stage.

Beside the considerably increased effort of such an approach, the result quality will not naturally improve. The inevitable incomplete data basis would require numerous assumptions, whose impact and uncertainty are extensive. Regarding the data basis for the case study, a reasonable balance between available information and complementing assumptions could not be established to justify a fully transient model. This fact and the fact that most faults in the reservoir are described to be traceable from Zechstein to Carboniferous support the applied approach of constant reservoir geometry (7.2.1). Furthermore, the western graben structure showing significant vertical displacement is located outside the production area. The relative depth variation of the reservoir horizon inside the production area is of minor intensity. Maintaining reservoir geometry and corresponding discretization of blocks and faults also directly allows cross-calculation of results from different load steps, which is not readily possible between separate models. The uncertainties of the applied approach are thus more reasonable than those of a more sophisticated approach including geometry changes and additional advantages are enabled for cumulative post-processing of results.

Additional, improved and more detailed information regarding the description of paleo-stress fields, the development of material parameters, or geometrical changes over time, can significantly reduce assumptions and increase the quality of modeling outcome.

Results

The results of the dynamic model reveal the in situ stress distribution in the case study reservoir at all simulated tectonic stages (8.4.1). This distribution includes stress perturbations along faults and vertical displacements. In addition to this direct impact of maintained fault geometry on the stress perturbations, the topology and relative internal reservoir depth significantly affect the distribution of stress magnitudes. Although most faults are assumed to rely on reactivated basement faults and are thus present in all tectonic stages, this might not be the case for some faults. The corresponding perturbations are thus misleading. This uncertainty is inherently decreasing towards recent times.

Major vertical displacements are assumed to be of Triassic age and thus the results of the first tectonic stage are most affected by the resulting inaccuracy.

The dominance of normal faulting regimes in the major tectonic stages leads to a dominance of vertical stress representing the first principal stress. The vertical stress directly varies with changing reservoir depth. This fact increases the impact of the maintained reservoir geometry on those result quantities including the first principal stress, such as the equivalent, mean and differential stress. This impact of geometry and specific reservoir depth on dynamic modeling results can only be avoided by implementing stage-specific adjustments in reservoir geometry.

The correlation of observed fracture sets with the in situ stress orientations during the individual tectonic stages is affected by the spatial resolution of the geomechanical model (8.4.2). Although the specific depths are known, at which fractures are found in the image logs, the spatial resolution of the field-scale model does not resolve these differences. The comparison is thus performed qualitatively. It regards the proximate well area on reservoir level instead of only those elements cut by the well path. It is assumed that varying vector orientations in the close area of the well also indicate respectively varying stress orientations within the wellbore due to heterogeneity and specific rock properties. Consequently, the varying stress orientations in the closer well area are related to the varying fracture orientations observed.

Any more precise, quantitative and statistical analyses of fracture correlation with modeled stresses require higher spatial resolution and a finer mechanical stratigraphy of the geomechanical model. Higher spatial resolutions conflict with the field-scale approach and thus submodels or fault block refinements are the only option to improve this aspect. In order to reduce uncertainty of the dynamic model, correlation of observed fracture sets could also be used for calibration. Optimization of correlation can be managed by adjusting the applied material parameters. Their impact is significant and demonstrated in the calibration discussion of the static model (7.5.5).

The fracture correlation performed with the results of the dynamic model further assumes all fractures to be of shear type or hybrid type between shear and tensile. Purely tensile fractures are neglected and not considered in interpretation because of two facts. First, purely tensile fractures would require very high pore pressures to develop. Such elevated pore pressures are not reported for the past tectonic stages of the case study area. Second, purely tensile fractures would be aligned parallel to the first principal stress and normal to the least. Tensile fractures are thus oriented either vertical or horizontal depending on the tectonic regime (4.8.2).The vertical fracture orientation would be difficult to detect in image logs. Furthermore the cataclastic seams of the fractures, which are detected in corresponding core analyses, underline the shear type of the described fracture sets.

The comparison of accumulated strain with the fracture densities calculated from the image logs only yields a relatively rough match. Individual strain values cannot be related to distinct fracture density values. This problem can be partly referred to the maintained geometry and internal depth distribution, which leads to the dominant vertical first principal stress and strain. This dominance precludes visualization and analysis of lateral localization patterns of equivalent strain and its comparison to fracture density. Hence, stage-specific correction of reservoir depth can facilitate and improve this correlation significantly. Besides geometrical adjustments of the dynamic model, an increased and more diverse data basis of fracture density is desirable. This may include longer intervals of image logs interpreted for fractures or additional and more sophisticated techniques such as VSP measurements (Vertical Seismic Profile) for seismic fracture characterization. An increased and broader database describing fracture density can be used to create continuous distribution maps, which can be better compared to modeled strain.

However, the basic assumption underlying the comparison of fracture density to the strain results of the dynamic model states that elastic strain can be used as a proxy for plastic strain. The dynamic model only regards the domain of elastic deformation and thus plastic strain is not directly provided as result quantity. Plastic deformation and fracture generation is assumed to be most likely in areas of localized high elastic strain. This assumed correlation is generally justifiable, but may in practice be most appearing at the distribution of large quantities of fractures. However, fractures are detected in image logs of ten wells only and the amount is very limited in most of them.

The missing match of fracture density with strain distribution is thus proposed to result from the typically low amount of fractures and the impact of local effects like microfractures and heterogeneity in material properties on their generation. These aspects are supposed to provide local weaknesses that influence fracture generation significantly and may have more control on the amount of generated fractures than the overall strain distribution. As soon as fractures are generated – independent of the decisive cause – they reflect the specific and locally prevailing stress orientation. This is why the correlation of fracture orientation and in situ stress direction yields a satisfying match, which is not discredited by the mismatch of strain and fracture density.

Cumulative and stage-specific slip and dilation tendency is compared to the present-day hydraulic description of the fault network in order to reveal the origin of recent fault behavior (8.4.3). The elaborated interpretation of cataclasis and mineralization being responsible for reduced fault permeability is consistent with the modeling results and supported by field observations. However, not all faults, whose orientation suggests the appearance of cataclasis or mineralization, are detected as low permeable or establish close compartments. For instance, the E-W trending fault in the northern part of the reservoir does not yield a complete separation of the central and eastern blocks.

This phenomenon can be explained by the lack of continuity of evolved fault properties. Hydraulic separation of a reservoir compartment requires full closure, which is often disturbed by many aspects. Curvature of fault faces and the corresponding change in orientation affects potential displacement and thus the development of cataclastics. Mineralization like illitization results from fluids that will also not flow equally distributed along the respective fault faces. The discontinuity in these processes directly impacts the distribution of permeability reduction along the faults. Furthermore, many faults in the case study reservoir are stepped, which also precludes continuous barriers to fluid flow. The larger a potential reservoir compartment is, the longer are the encompassing faults and the more likely are permeable fault segments to occur. This proposition is underlined by the relatively small compartments in the case study reservoir.

The determination of low permeable faults, to which the results are compared, is also accompanied by considerable uncertainty. Separated compartments and the responsible faults are relatively well detected due to the disabled communication. If fluid flow is only impeded between wells and multiple faults are present in the affected area, it is hardly possible to determine exactly the responsible faults and their permeability. The reservoir simulation can test various scenarios and provide a best match representing the most likely situation of low permeable faults. These provided results match very well with the outcome of the dynamic model, but the underlying uncertainty has to be kept in mind.

Specific data from drill cores describing the fault rock and revealing the cause for permeability reduction are rare and not provided in this study. Such data could be used to further test the elaborated interpretations.

9 Combination of Modeling Results

Two geomechanical modeling approaches are described and applied in this study. The static model considers the present-day situation. It reveals the specific in situ stress prevailing in the reservoir horizon today, which is also acting on all faults and fractures. The dynamic modeling concerns the major stages in the tectonic history of the reservoir area. This model provides insights into the respective paleo-stress distributions during the times of fracture formation allowing determined fracture sets to be assigned to distinct time intervals. The combination of both modeling approaches yields additional information on the present-day hydraulic behavior of the reservoir by indicating critically stressed fracture orientations.

In order to reveal those orientations, the observed fracture sets are compared in well-specific stereoplots to the locally modeled present-day stress direction visualized by vectors (Fig. 9-1, Fig. 9-2). However, these sets only resemble the fractures detected at drilled wells. The assignment of fracture sets to the generating time intervals also allows a comparison of the respective paleo-stress orientations to the recent situation. This comparison is best realized by vector distributions stacking up against each other (Fig. 9-3). Due to the high spatial resolution, the comparing figures focus on the vicinity of well F5 and C5(a).

The result analysis of the dynamic model proposes a most likely origin of fractures of set A and B in the second and third tectonic stage, respectively (8.4.2). The normal faulting regimes and the corresponding vertical first principal stress in both stages resulted in shear fractures comprising characteristic dipping angles of about 60°. Some steeper dipping fractures are assumed to represent hybrid shear-tensile fractures. The recently prevailing normal faulting regime thus yields a generally favorable situation for most fractures to be critically stressed. Additional favorable orientation of the maximum horizontal stress is assumed to be decisive for distinct fracture trends to show enhanced hydraulic properties. Such an orientation comprises an angle of about 30° and less than 45° between fracture strike and maximum horizontal stress.

In general, the results of the static geomechanical model show local rotations of the maximum horizontal stress direction from the regional NNW-SSE trend to about N-S and NW-SE (7.6). More intense re-orientations are not revealed for the recent state. The direction of maximum horizontal stress in the vicinity of well C5 and C5a follows approximately the regional NNW-SSE trend with some minor rotations along faults (Fig. 9-1). Well C5 and C5a comprise significantly more fractures than all other wells analyzed by image logs. The majority of these fractures are oriented NE-SW and yield this trend to be dominant for fracture set A. The unperturbed recent orientation of horizontal stress of NNW-SSE is thus not likely to promote a critically state of stress at these fractures. A small amount of fractures in set A are striking about N-S and are significantly more likely to be critically stressed due to the small angle to the maximum horizontal stress direction (Fig. 9-1).

Fractures of set B show the characteristically large spread in strike ranging from E-W to NNW-SSE (Fig. 9-1). Fractures striking in these end member orientations are less likely to be critically stressed, since a parallel direction to the maximum horizontal stress is as unfavorable as a relative angle exceeding 45°. However, fractures striking in intermediate directions are likely to be critically stressed. The specific likelihood depends strongly on the individual fracture orientation due to the large variation (Fig. 9-1). The stereoplots of well C5 and C5a demonstrate the lower abundance of fractures assigned to set B compared to set A.

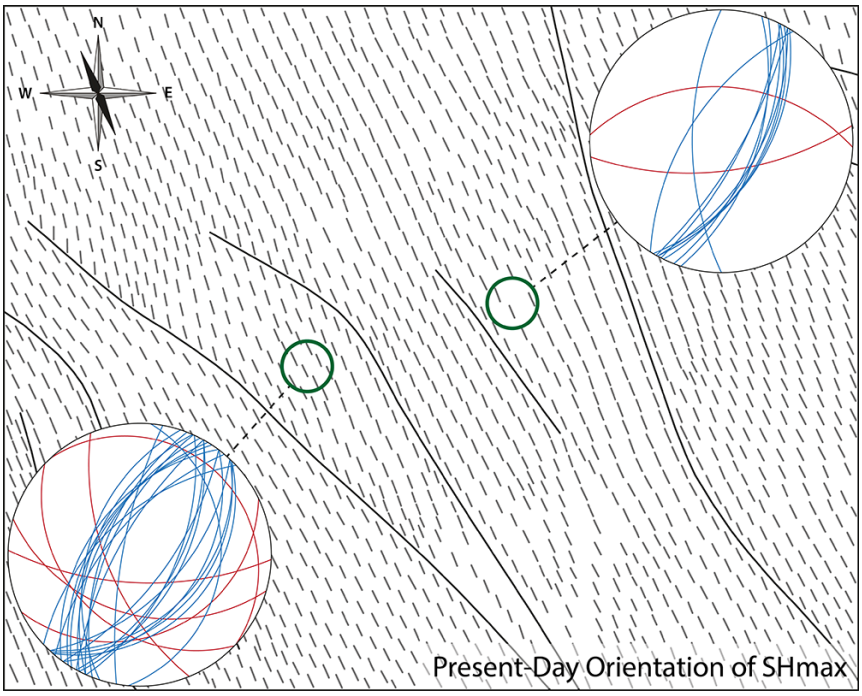

Fig. 9-1. Overview on the vectors describing the orientation of the present-day maximum horizontal stress in the vicinity of well C5 (left) and C5a (right). Stereoplots summarize the information on fractures of set A (blue) and B(red).

Horizontal stress and fracture orientation described for well F5 show similar characteristics (Fig. 9-2). The maximum horizontal stress in the vicinity of well F5 follows the regional NNW-SSE trend and is rotated only in the nearby fault stepover to N-S. Fractures of set A are less abundant in this well and are N-S and NE-SW striking. Hence, the unperturbed horizontal stress yields a higher probability for a critical stress state at the N-S striking fracture than for the NE-SW trend. This equals the observation at well C5 and C5a. Fractures of set B are more abundant in well F5 and also show typical striking of approximately E-W to NNW-SSE (Fig. 9-2). The lack of intense stress re-orientations yields the same individual dependency on strike direction for the occurrence of critically stressed states.

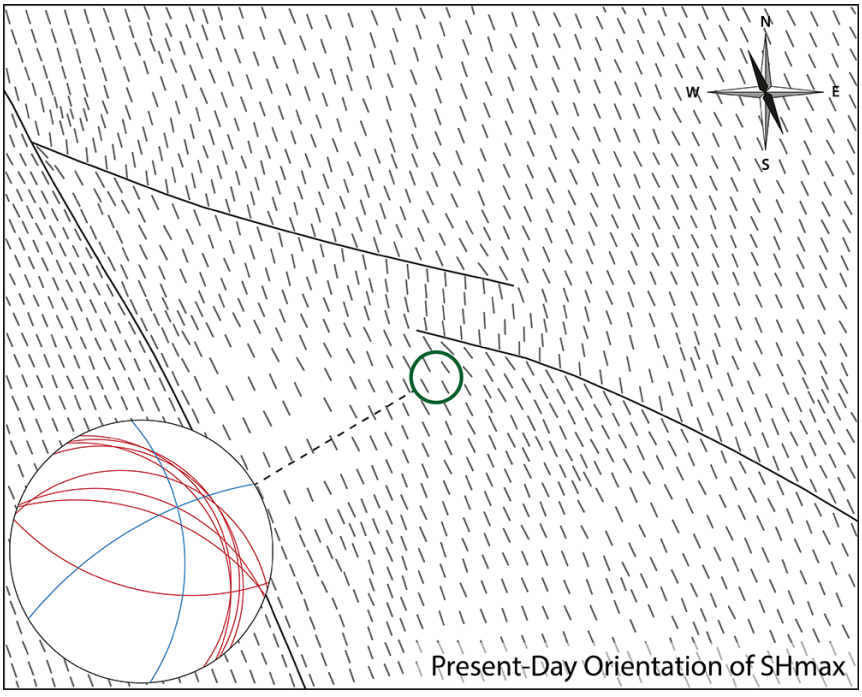

Fig. 9-2. Overview on the vectors describing the orientation of the present-day maximum horizontal stress in the vicinity of well F5. The stereoplot summarizes the information on fractures of set A (blue) and B(red).

The demonstrated situation at these three wells is representative for the entire reservoir. Only those fractures of set A, which are striking approximately N-S, are likely to be critically stressed in the present-day stress field (Fig. 9-1). The more abundant NE-SW striking fractures of this set are most probably not critically stressed. However, the overall high abundance of these fractures in set A is mostly based on well C5 and C5a, and may be misleading for the field-wide distribution. Fractures of set B show the characteristic high variability in striking probably due to intense perturbations of the generating stress field in the third tectonic stage (8.4.2). This spread in orientation yields a strong dependency on the individual striking of fractures for the occurrence of critically stressed states (Fig. 9-2). Especially NW-SE to WNW-ESE striking fractures are likely to be positively affected.

The direct comparison of the fracture generating in situ stress of the second and third tectonic stage to the present-day stress field underlines these observations (Fig. 9-3). Due to the relatively less intense perturbations of stress orientation in the recent stress field, the likelihood of critically stressed fractures strongly depends on the orientation and perturbation of paleo-stress fields and the resulting strike direction of the fractures.

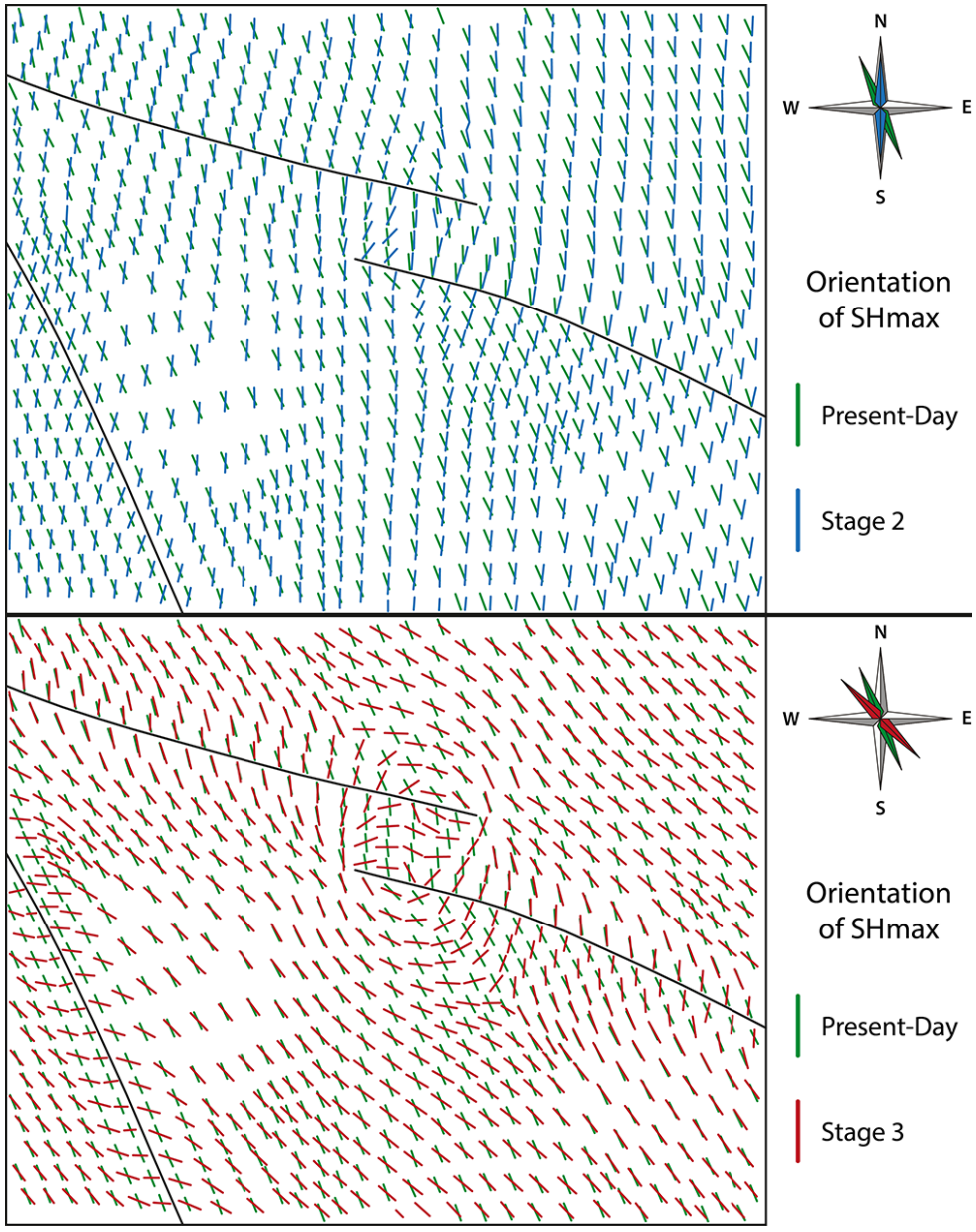

Fig. 9-3. Trajectories illustrating the maximum horizontal stress orientation of the second (top) and third tectonic stage (bottom) compared to the present-day orientation at the fault stepover in the vicinity of well F5.

In summary, only subsets and individual fractures are likely to be critically stressed instead of entire sets of fractures. Critical stress states increase the likelihood of enhance hydraulic behavior. The impact of these potentially enhanced natural fractures on the hydraulic behavior of the entire reservoir is assumed to be rather low due to the overall low amount of natural fractures, of which in turn only subsets may play a role. More pronounced trends in natural fracture networks, which are entirely more optimal oriented, would have much greater impact on the hydraulic behavior of a reservoir.

10 Conclusions

In conclusion, the objectives of this study were achieved and its findings provide advancement and new possibilities in geomechanical modeling for revealing the specific in situ stress distribution in faulted reservoirs. Subsequently, the study outcome is summarized in the context of the stated objectives (1.1).

- ***Development of a generally applicable workflow to generate 3D geomechanical FE models***

A workflow for building and calibrating geomechanical FE models of faulted reservoirs was successfully developed in this study and can be applied to arbitrarily complex geometries. This approved workflow represents a major outcome of the research project and focuses on the spatial variation of in situ stress due to faults and mechanical contrasts. Three options with different levels of sophistication are elaborated for transferring the specific reservoir geometry from geological subsurface models to the numerical code. These transfer options allow the application of the workflow to build field-scale to fault block-scale models of arbitrarily complex reservoirs or reservoir parts.

Geomechanical models built by this workflow consider reservoir-specific material parameters of different sources to establish and incorporate a mechanical stratigraphy. Faults are implemented as distinct planes of weakness simulated by 2D interface elements. This characteristic feature separates this study's approach from many others and allows unique post-processing capabilities for revealing the mechanical exposure and behavior of individual faults and fault segments. In order to fully regard the regional stress field as boundary condition, the specific horizontal tectonic stresses are generated by calibrated displacements. A newly developed technique for load frame handling using the cut-boundary displacement method ensures the most effective element usage and variability in the application of regional stress fields. Moreover, model calibration to field data is successfully conducted in this study and increases the reliability of all results.

- ***Application of the developed workflow to the case study reservoir***

In order to test the validity of the newly developed geomechanical modeling approach, it was applied to a case study reservoir located in the North German Basin. Preliminary studies were carried out comprising generic parameter studies on characteristic fault block geometry, as well as the generation of a base model incorporating simplified reservoir geometry of the case study. Both studies already relied on the principles of the developed workflow, but with limited complexity. These models helped to optimize and finalize the workflow and provided first insights into the behavior of stress perturbations and the in situ stress distribution of the reservoir. The results suggest a relatively stable stress state of the case study reservoir and show stress perturbations of minor intensity. Perturbation sources are found to be fault tips and pronounced fault curvatures, as well as contrasts in mechanical properties. Perturbations can also mutually interact and yield an impact over a larger area. The friction of faults, the specific material parameters and the relative orientation of horizontal stress with respect to the fault network are identified as most controlling factors for stress perturbations.

  - *Buildup of a field-scale geomechanical FE model of the case study reservoir*

Following the preliminary studies, the elaborated workflow was successfully applied to its full extent in two complementing approaches yielding a static and (geo-)dynamic geomechanical model of the case study reservoir. While the static modeling focuses on the present-day stress field and its local variations, the dynamic approach considers paleo-stress distributions in the tectonic history. A detailed model as a basis for both approaches was built truly at field-scale and includes the entire

reservoir area covering more than 400km². It comprises a mechanical stratigraphy of three layers, the accurate topology of the centrally located reservoir horizon, and 86 faults with individual vertical offsets. The high spatial resolution of 100m x 100m x 25m (length x width x depth) in the reservoir layer yields 3.8 million elements in total.

- *Information on specific present-day in situ stress*

The present-day regional stress field in the case study area represents the boundary condition of the static model in order to reveal the specific stress distribution and spatial variations prevailing today. The accomplished model buildup and initial calculation were followed by the successful calibration of the model to local stress measurements in the field. A best fit was obtained by lowering the poorly constrained friction coefficient of the faults. This fit is satisfactory especially with respect to the uncertainty of involved datasets.

The results of the static geomechanical model reveal the present-day in situ stress distribution in the case study reservoir. Local perturbations of maximum and minimum horizontal stress magnitude lead to deviations of up to 10MPa from the regional level and range up to 1-2km from their inducing source. Further stress quantities like mean and differential stress show less intense perturbations. The orientation of maximum horizontal stress deviates from the regional NNW-SSE trend to NW-SE and N-S directions. The lack of more intense stress rotations is attributed to the large horizontal stress difference. Static modeling results show the same sources for perturbations as the preliminary studies, but reveal more intense deviations in magnitude.

- *Disclosure of recent stress distribution on the fault network and corresponding behavior*

In addition to the revealed stress distribution in the reservoir, fault-specific shear and normal stresses were obtained and calculated to slip and dilation tendencies describing the recent fault behavior. Movement or critical stress states are most likely to occur along NW-SE directed fault trends and vertically inside the reservoir layer. Faults oriented NNW-SSE and thus parallel to the maximum horizontal stress are most likely to open, while this behavior is unlikely for WSW-ENE trending faults. Dilation tendencies of fault parts inside the reservoir layer do not follow extreme trends of values in over- and underburden. These insights suggest a controlling impact on fault behavior by the mechanical stratigraphy and the relative orientation between maximum horizontal stress and the fault network. Corresponding local changes of fault-specific stresses directly result in changes of slip and dilation tendency along the affected fault segments. While increased values in both tendencies principally indicate a potential increase in permeability, a high slip tendency also implies an increased likelihood of fault movement.

The slip tendency distribution along the fault network thus can be related to the occurrence of seismicity. However, the modeling results only allow a description of the spatial likelihood of seismic events increasing with slip tendency. Due to the fact that the geomechanical model represents a steady state and not a time-dependent analysis, no information on the timing of events can be inferred. A future comparison is planned between the modeled slip tendency and measurements of a high-resolution monitoring system for microseismic activity carried out in the same area within a DGMK project[3] started in 2013.

[3] DGMK Research Project 761: High-resolution monitoring and analysis of seismicity near Rotenburg with a comparison of monitoring concepts.

- *High spatial resolution of modeling results*

All modeling results are provided in the high spatial resolution of the field-scale model. In addition, the study shows that further increase in spatial resolution can be achieved by fault block refinements inside the field-scale model and by the generation of individual submodels. A significantly higher resolved submodel of the northwestern part of the case study reservoir was built and evaluated. Besides the higher resolution, the results show that the behavior and the related perturbations of the faults in the submodel that are directly connected to the encompassing fault network, are most significantly affected by the absence of surrounding faults due to the isolation of the submodeled area. The feasibility of submodels is shown, as well as the fact that the uncertainty of submodels depends on the specific connectivity of the fault network in the area of interest.

- *Information on fracture networks based on paleo-stress distributions in the tectonic history*

Complementing the present-day stress description by the static model, the dynamic model focuses on the in situ stress during major tectonic stages in the history of the reservoir. Four tectonic stages were defined and input data was adjusted for the respective intervals. This concerns especially the reservoir depth, rock density, and the magnitude and orientation of regional paleo-stress fields. Geometrically the dynamic model is based on the same field-scale model as the static approach. The developed technique of more effectively applying different boundary conditions to the geomechanical model allows the implementation of various paleo-stress fields as individual load steps in the dynamic modeling. Due to the less constrained input data, this model inherently comprises larger uncertainties than the static model. Dynamic modeling results reveal the specific stress distributions at times of fracture formation and the fault behavior in the reservoir's past. Snapshot-like insights are provided at the defined time slices within the past tectonic stages.

The results of the dynamic model show significant magnitude perturbations in the third and the fourth tectonic stage only, i.e. in Late Jurassic to Early Cretaceous and in Late Cretaceous to Late Oligocene, respectively. This is attributed to the deeper burial and the more favorable relative orientation of horizontal stress to the fault network contrasting to the first and second stage. Modeled paleo-stress orientations are compared to fracture data. Two fracture sets are described in the reservoir and are assigned to two stages of the tectonic history. The tectonic regime and horizontal stress orientation suggests a first set (A) of N-S to NE-SW striking fractures to be most likely generated in the second tectonic stage during E-W directed extension in Triassic times. A second fracture set (B) showing E-W to NNW-SSE striking is assigned to the third tectonic stage of NE-SW extension in Late Jurassic to Early Cretaceous times. In particular this second fracture set shows a significant match of its large spread of fracture orientation to the modeled stress perturbations. A tectono-sedimentary study provided by the project partners assumes the reactivation of NW-SE trending faults during this third stage. Such fault activity explains the intensified perturbations and underlines this correlation. These results thus suggest a sequential generation of the fracture network in Triassic and Jurassic times and demonstrate the ability of a single ambient stress field to form different fracture orientations.

The spatial distribution of the fracture network is more complicated to reveal. The comparison of fracture density to strain accumulated over the tectonic history yields only a rough match. This lack of direct correlation may result from inaccurate input data or the usage of elastic strain as a proxy for plastic strain and fracture generation, which may be only valid for large amounts of fractures. Therefore the generation of the relatively small amount of fractures in the reservoir could be influenced rather by distinct local weaknesses than overall strain.

- *Disclosure of paleo-stress distribution on faults and corresponding behavior in the tectonic history & testing the hypothesis relating potential cataclasis to reduced fault permeability*

The comparison of mechanical fault exposure and their behavior in the tectonic past to the present-day hydraulic properties shows distinct correlations. Cumulative slip tendency indicates E-W and N-S to NNE-SSW trending faults to have been most critically stressed throughout the tectonic history and in particular during the compressive fourth tectonic stage in Late Cretaceous times. If reduced fault permeability in the case study reservoir is based on cataclastic effects, these faults are most likely affected. Permeability reduction reported for NW-SE to NNW-SSE trending faults is more likely to be generated by fluid flow and mineralization. This is suggested by high dilation tendency values of these faults over the tectonic history and especially in the third stage in Late Jurassic to Early Cretaceous times. These results support the assumption of fault reactivation in these times, as indicated by fracture correlation. Provided pathways could have been used by Carboniferous fluids to enter the reservoir, which are most likely to be responsible for illitization in the Rotliegend reservoir sandstone (Gaupp et al., 2005; Gaupp et al., 1993). This hypothesis is underlined by illitization detected at well C5a, which is located close to such a NNW-SSE striking fault set.

The initial hypothesis of pronounced cataclasis due to fault slip in the tectonic past leading to the reduction in present-day fault permeability is partly confirmed. It is found that cataclastic effects can be responsible for recent hydraulic behavior along E-W and N-S to NNE-SSW trending faults, but are not able to explain all baffles in the case study. Modeling results instead suggest that mineralization plays an important role for permeability reduction of NNW-SSE directed fault sets complementing potential cataclastic effects.

The correlation of dynamic modeling results to fracture information and recent hydraulic fault behavior yields a mechanically consistent tectonic evolution of the reservoir. This is completed by the combination of the static and dynamic model, which reveals the impact of critically stressed natural fractures on the recent hydraulic behavior of the case study. This impact is assumed to be relatively low due to the unfavorable orientation of most fractures with respect to the present-day stress distribution. Only subsets of the overall low amount of fractures are optimally oriented and thus a significant impact on the reservoir scale is unlikely.

Finally, it is to conclude that the elaborated workflow and the corresponding geomechanical models have the potential to predict the specific tectonic in situ stress in faulted reservoirs including all spatial variations. Inferring fracture information from paleo-stress distributions is also shown to be possible, but is more complicated than modeling the present-day stresses. Results of dynamic modeling comprise higher uncertainty due to the commonly scarce and incomplete datasets available for constraining paleo-stress states. However, the data base describing the recent state of the reservoir can also suffer from irregularly performed measurements and a heterogeneous distribution of provided information. Besides a large amount of high quality input and calibration data, this study elucidates the necessity of consistent and homogeneous datasets for reliable geomechanical modeling results.

11 Perspectives

This study demonstrates and confirms the potential of the elaborated workflow and the resulting geomechanical models. The flexibility of the workflow allows its application to various types of reservoirs for future geomechanical modeling. In addition to the buildup and calibration of new models, both the modeling workflow and the existing field-scale models of the case study can be improved and used further.

The modeling workflow can be significantly improved by accelerating the geometry transfer and model buildup. At the moment, this transfer of reservoir geometry from the geological subsurface model to the numerical code represents a relatively time-consuming process – independent of the specific approach. Accelerating the transfer process by increasingly automated routines would provide a more flexible handling and allow the straightforward incorporation of geometrical changes into the geomechanical model. These changes may result from newly acquired data or revised seismic interpretation. Moreover, the buildup of multiple geometrically evolving models in the dynamic modeling approach is facilitated.

In addition, the direct incorporation of pore pressure into the generated geomechanical models comprises high potential as starting point for hydromechanically-coupled reservoir simulations. Such an approach would allow the impact of pore pressure on the revealed perturbations in stress magnitudes to be studied. The application of the finite element method in the modeling workflow also allows the implementation of plastic deformation or thermal properties, for instance. Possibilities are only limited by the measured parameters in the data base and the capability of the applied numerical code, which has to provide the respective coupling.

Besides the workflow, the existing field-scale model of the case study and its results can be further improved and applied. Pursuing the calibration of the static model represents a promising approach to increase the quality of modeling outcome and its consistency with field observations. Individual friction coefficients of distinct fault trends are assumed to yield such improvement, since it is unlikely that all faults comprise the same frictional behavior. Aside from randomly testing various combinations for a best fit, analyses on drilled fault core are probably able to reveal information that helps to estimate the specific coefficient. Estimates could be based on the thickness of the fault zone and on the fault rock composition focusing on the occurrence of minerals such as clays, for instance. In addition to more specific friction coefficients, laterally varying material parameters have a significant impact and thus potential for improving the static model. This impact is outlined in the discussion of calibration (7.5.5).

Improvement of the static model can also be realized by increasing the spatial resolution in horizontal and vertical direction. Higher resolution of the field-scale model would result in an excessive number of elements, but the introduced fault block refinements and submodels are ideal perspectives to focus on interesting parts of the case study reservoir. In such high resolution models, the mechanical stratigraphy could be refined significantly – in case the appropriate material data is available. These models are able to provide sufficiently detailed results to assist actual decisions in reservoir operation. Geomechanical models of small areas with high spatial resolution and based on extensive datasets can also be used to elaborate a relation between the amount of input and calibration data applied and the resulting quality of the modeling outcome. The gradually diminishing increase in result quality could be used to estimate the mandatory amount of data generally required for reliable geomechanical models.

Complementing the static modeling, the dynamic approach represents a promising tool for prediction of fracture information based on local paleo-stress distributions. Dynamic modeling could also be improved by higher resolution, but probably more significantly by more reliable information describing the evolution of material parameters and reservoir geometry in the past. Especially information on the development of mechanical properties during the burial history of a reservoir would be very valuable. Continuously regarding changes in geometry according to specific tectonic stages is also desirable. If knowledge on the timing of fault network emplacement is available, incorporation of these geometrical changes could be realized with an accelerated geometry transfer in the geomechanical modeling workflow.

Detailed stress results of the existing geomechanical models can also directly be used for further analysis. Stress results can be imported into the standard reservoir simulation of the case study. This would allow the reservoir simulation to regard stress patterns revealed in the geomechanical model for the calculation of fluid flow. A comparison of mean stress results to production data may also show some correlation between relative minima of mean stress and increased production rates, whereas paleo- mean stress distributions could provide additional insights into fluid migration patterns. A comparison between slip tendency results and measurements of microseismic activity for spatial correlation are also possible and in planning.

12 References

Alejano, L.R., Alonso, E., 2005. Considerations of the dilatancy angle in rocks and rock masses. International Journal of Rock Mechanics and Mining Sciences 42, 481-507.

Ali, A.H.A., Brown, T., Delgado, R., Lee, D., Plumb, D., Smirnov, N., Marsden, R., Prado-Velarde, E., Ramsey, L., Spooner, D., Stone, T., Stouffer, T., 2003. Watching rocks change; mechanical earth modeling. Oilfield Review 15, 22-39.

Allan, U.S., 1989. Model for hydrocarbon migration and entrapment within faulted structures. AAPG Bulletin 73, 803-811.

Ameen, M.S., 2003. Fracture and in-situ stress characterization of hydrocarbon reservoirs: definitions and introduction, in: Ameen, M.S. (Ed.), Fracture and In-Situ Stress Characterization of Hydrocarbon Reservoirs. The Geological Society of London, pp. 1-6.

Anderson, E.M., 1951. The dynamics of faulting and dyke formation, with applications to Britain, 2 ed. Oliver and Boyd, Edinburgh, p. 206.

Angelier, J., 1979. Determination of the mean principal directions of stresses for a given fault population. Tectonophysics 56, 17-26.

Angus, D.A., Kendall, J.M., Fisher, Q.J., Segura, J.M., Skachkov, S., Crook, A.J.L., Dutko, M., 2010. Modelling microseismicity of a producing reservoir from coupled fluid-flow and geomechanical simulation. Geophysical Prospecting 58, 901-914.

Ansys Inc., 2012. Ansys 14.0 Release - Help Files, p. 10396.

Arroyo Franco, J.L., Mercado Ortiz, M.A., de, G.S., Renlie, L., Williams, S., 2006. Sonic investigations in and around the borehole. Oilfield Review 18, 14-33.

Arthaud, F., Matte, P., 1977. Late Paleozoic strike-slip faulting in southern Europe and northern Africa: Result of a right-lateral shear zone between the Appalachians and the Urals. Geological Society of America Bulletin 88, 1305-1320.

Aydin, A., 2000. Fractures, faults, and hydrocarbon entrapment, migration and flow. Marine and Petroleum Geology 17, 797-814.

Bachmann, G.H., Grosse, S., 1989. Struktur und Entstehung des Norddeutschen Beckens – geologische und geophysikalische Interpretation einer verbesserten Bouguer-Schwerekarte. Niedersächsische Akademie der Geowissenschaften Veröffentlichungen 2, 23-47.

Bachmann, G.H., Voigt, T., Bayer, U., von Eynatten, H., Legler, B., Littke, R., 2008. Depositional history and sedimentary cycles in the Central European Basin System, in: Littke, R., Bayer, U., Gajewski, D., Nelskamp, S. (Eds.), Dynamics of Complex Intrakontinental Basins - The Central European Basin System. Springer, pp. 157-172.

Baldschuhn, R., Best, G., Kockel, F., 1991. Inversion tectonics in the North-west German basin. Special Publication of the European Association of Petroleum Geoscientists 1, 149-159.

Bamford, W.E., 1976. Evolution of stresses in rock masses, as related to compressive strengths and plate tectonics, Investigation of stress in rock; advances in stress measurement. Australien Geomechanics Society, pp. 63-70.

Bär, K., 2012. Untersuchung der tiefengeothermischen Potenziale von Hessen, Material- und Geowissenschaften. Dissertation.Technische Universität Darmstadt, p. 297.

Barnhill, R.E., 1982. Coon's patches. Computers in Industry 3, 37-43.

Barton, C.A., Zoback, M.D., 1994. Stress Perturbations associated with active Faults penetrated by boreholes - possible evidence for near-complete stress drop and a new technique for stress magnitude measurement. Journal of Geophysical Research - Solid Earth 99, 9373-9390.

Barton, C.A., Zoback, M.D., Burns, K.L., 1988. In-situ stress orientation and magnitude at the Fenton geothermal site, New Mexico, determined from wellbore breakouts. Geophysical Research Letters 15, 467-470.

Barton, C.A., Zoback, M.D., Moos, D., 1995. Fluid flow along potentially active faults in crystalline rock. Geology 23, 683.

Bathe, K.J., 1995. Finite Element Procedures, 2 ed. Prentice-Hall, p. 1037.

Bayer, U., Scheck, M., Rabbel, W., Krawczyk, C.M., Götze, H.-J., Stiller, M., Beilecke, T., Marotta, A.-M., Barrio-Alvers, L., Kuder, J., 1999. An integrated study of the NE German Basin. Tectonophysics 314, 285-307.

Berest, P., Blum, P.A., Charpentier, J.P., Gharbi, H., Vales, F., 2005. Very slow creep tests on rock samples. International Journal of Rock Mechanics and Mining Sciences 42, 569-576.

Biot, M.A., 1941. General Theory of Three-Dimensional Consolidation. Journal of Applied Physics 12, 155-164.

Biot, M.A., 1955. General Solutions of the Equations of Elasticity and Consolidation for a Porous Material. Journal of Applied Mechanics 55, 91-96.

Bourne, S.J., Rijkels, L., Stephenson, B.J., Weber, A., Willemse, E.J.M., 2000. Predictive modelling of naturally fractured reservoirs using geomechanics and flow simulation. GeoArabia 6, 87-102.

Bouzouf, B., Ouazar, D., Himi, M., Casas, A., Elmahi, I., Benkhaldoun, F., 2001. Integrating hydrogeochemical and geophysical data for testing a finite volume based numerical model for saltwater intrusion. Transport in Porous Media 43, 179-194.

Braun, R., Jahns, E., Stromeyer, D., 1999. Rock anisotropy characterization on samples (RACOS); Determination of rock mass structures and stress fields; Part 1, In situ stresses and rock anisotropy. Erdoel Erdgas Kohle 115, 191-197.

Brink, H.-J., 2005a. The evolution of the North German Basin and the metamorphism of the lower crust. International Journal of Earth Sciences 94, 1103-1116.

Brink, H.-J., 2005b. Liegt ein wesentlicher Ursprung vieler großer Sedimentbecken in der thermischen Metamorphose ihrer Unterkruste? Das Norddeutsche Permbecken in einer globalen Betrachtung. Zeitschrift der deutschen Gesellschaft für Geowissenschaften 156, 275-290.

Brink, H.J., Duerschner, H., Trappe, H., 1992. Some aspects of the late and post-Variscan development of the northwestern German Basin. Tectonophysics 207, 65-95.

Brink, H.J., Franke, D., Hoffmann, N., Horst, W., Oncken, O., 1990. Structure and evolution of the North German Basin, in: Freeman, R., Giese, P., Mueller, S. (Eds.), European Geotraverse; integrative studies; results from the Fifth earth science study centre. European Science Foundation, Strasbourg, France, pp. 195-212.

Brudy, M., Zoback, M.D., 1999. Drilling-induced tensile wall-fractures: Implications for determination of in-situ stress orientation and magnitude. International Journal of Rock Mechanics and Mining Sciences 36, 191-215.

Bücker, C., Strobel, J., 2003. Das Voelkersen Gas Feld in Norddeutschland: Anzeichen für zwei Spannungsrichtungen im Rotliegenden?, DGMK/ÖGEW-Frühjahrstagung, Celle, Germany.

Byerlee, J., 1978. Friction of rocks. Pure and Applied Geophysics 116, 615-626.

CADFEM GmbH, 2010. Seminarunterlagen zu "Kontaktmodellierung in der Statik". CADFEM GmbH, Leinfelden-Echterdingen, p. 583.

Camac, B.A., Hunt, S.P., 2009. Predicting the regional distribution of fracture networks using the distinct element numerical method. AAPG Bulletin 93, 1571-1583.

Carpenter, B.M., Marone, C., Saffer, D.M., 2009. Frictional behavior of materials in the 3D SAFOD volume. Geophysical Research Letters 36, L05302.

Carpenter, B.M., Marone, C., Saffer, D.M., 2011. Weakness of the San Andreas Fault revealed by samples from the active fault zone. Nature Geoscience 4, 251-254.

Chanchani, S.K., Zoback, M.D., Barton, C., 2003. A case study of Hydrocarbon transport along active faults and production-related stress changes in the Monterey Formation, California. Geological Society Special Publications 209, 17-26.

Cotrell, M., Dershowitz, B., Enachescu, C., 2012. Analysis of Unconventional Shale Gas Reservoirs using a combined Discrete Fracture Network Model and a Geomechanical Numerical Approach, DGMK/ÖGEW-Frühjahrstagung, Celle, Germany.

Crawford, B.R., Gaillot, P.J., Alramahi, B., 2010. Petrophysical Methodology for Predicting Compressive Strength in Siliciclastic "sandstone-to-shale" Rocks, 44th US Rock Mechanics Symposium and 5th U.S.-Canada Rock Mechanics Symposium, Salt Lake City, USA.

Crouch, S.L., Starfield, A.M., 1983. Boundary Element Method in Solid Mechanics: With Applications in Rock Mechanics and Geological Engineering. HarperCollins Publishers, p. 334.

Cui, A., Brezovski, R., Glover, K., 2013. Controls of Anisotropic In-situ Stress and Permeability in Optimization of Wells and Hydraulic Fractures for Unconventional Reservoirs: Examples from the Western Canada Sedimentary Basin, 47th US Rock Mechanics / Geomechanics Symposium, San Francisco, USA.

Cundall, P.A., Strack, O.D.L., 1979. A discrete numerical model for granular assemblies. Geotechnique 29, 47-65.

Czauner, B., Madl-Szonyi, J., 2011. The function of faults in hydraulic hydrocarbon entrapment; theoretical considerations and a field study from the Trans-Tisza region, Hungary. AAPG Bulletin 95, 795-811.

de Borst, R., Crisfield, M.A., Remmers, J.J., Verhoosel, C.V., 2012. Non-linear Finite Element Analysis of Solids and Structures, 2 ed. John Wiley and Sons, p. 544.

Dee, S.J., Yielding, G., Freeman, B., Healy, D., Kusznir, N.J., Grant, N., Ellis, P., 2007. Elastic dislocation modelling for prediction of small-scale fault and fracture network characteristics, in: Lonergan, L., Jolly, R.J.H., Rawnsley, K., Sanderson, D.J. (Eds.), Fractured Reservoirs. Geological Society, London, pp. 139-155.

DEKORP-BASIN Research Group, 1999. Deep crustal structure of the Northeast German basin: New DEKORP-BASIN '96 deep-profiling results. Geology 27, 55-58.

Dèzes, P., Schmid, S.M., Ziegler, P.A., 2004. Evolution of the European Cenozoic Rift System: interaction of the Alpine and Pyrenean orogens with their foreland lithosphere. Tectonophysics 389, 1-33.

Dongarra, J.J., Grandinetti, L., Kowalik, J., Joubert, G.R., 1995. High Performance Computing: Technology, Methods and Applications. Elsevier, p. 436.

Doornenbal, H., Stevenson, A., 2010. Petroleum Geological Atlas of the Southern Permian Basin Area. EAGE Publications b.v., Houten, p. 354.

Dow, J.O., 1998. A Unified Approach to the Finite Element Method and Error Analysis Procedures. Academic Press p. 533.

Drozdzewski, G., Henscheid, S., Hoth, P., Juch, D., Littke, R., Vieth, A., Wrede, V., 2009. The pre-Permian of NW-Germany - structure and coalification map. Zeitschrift der deutschen Gesellschaft für Geowissenschaften 160, 159-172.

Drucker, D.C., Prager, W., 1952. Soil Mechanics and Plastic Analysis or Limit Design. Quarterly of Applied Mathematics 10, 157-165.

Eissa, E.A., Kazi, A., 1989. Relation between static and dynamic Young's moduli of rocks. International Journal of Rock Mechanics and Mining Sciences & Geomechanics Abstracts 25, 479-482.

Evans, J.P., Forster, C.B., Goddard, J.V., 1997. Permeability of fault-related rocks, and implications for hydraulic structure of fault zones. Journal of Structural Geology 19, 1393-1404.

Farmer, I.W., 1983. Engineering Behavior of Rocks. Springer, p. 224.

Fischer, K., 2010. Stress perturbations in fault-controlled reservoirs - a numerical parameter study from the North German Basin. M.Sc. Thesis. Albert-Ludwigs-Universität Freiburg, p. 159.

Fisher, Q.J., Knipe, R.J., 2001. The permeability of faults within siliciclastic petroleum reservoirs of the North Sea and Norwegian continental shelf. Marine and Petroleum Geology 18, 1063-1081.

Fjaer, E., Holt, R.M., Horsrud, P., Raaen, A.M., Risnes, R., 2008. Petroleum Related Rock Mechanics, 2 ed. Elsevier, p. 515.

Fjaer, E., Stroisz, A.M., Holt, R.M., 2013. Elastic dispersion derived from a combination of static and dynamic measurements, Special Issue: New and Exciting Advances, 3 ed. Springer, Vienna, Austria, pp. 611-618.

Fleckenstein, P., Reuschke, G., Müller, B., Connolly, P., 2004. Predicting stress re-orientations associated with major geological structures in sedimentary sequences. Deutsche Wissenschaftliche Gesellschaft für Erdöl, Erdgas und Kohle e.V. (DGMK), p. 95.

Fordjor, C.K., Bell, J.S., Gough, D.I., 1983. Breakouts in Alberta and stress in the North American Plate. Canadian Journal of Earth Sciences 20, 1445-1455.

Fox, R.J., Bowman, M.B.J., 2010. The challenges and impact of compartmentalization in reservoir appraisal and development. Geological Society Special Publications 347, 9-23.

Franke, D., 1995. The North Variscan Foreland, in: Dallmeyer, R.D., Franke, W., Weber, K. (Eds.), Pre-Permian geology of Central and Eastern Europe. Springer, pp. 554-566.

Fredrich, J.T., Arguello, J.G., Deitrick, G.L., de Rouffignac, E.P., 2000. Geomechanical modeling of reservoir compaction, surface subsidence, and casing damage at the Belridge diatomite field. SPE Reservoir Evaluation & Engineering 3, 348-359.

Fredrich, J.T., Coblentz, D., Fossum, A.F., Thorne, B.J., 2003. Stress Perturbations Adjacent to Salt Bodies in the Deepwater Gulf of Mexico, SPE Annual Technical Conference and Exhibition. Society of Petroleum Engineers, Denver, USA, pp. 5121-5134.

Fredrich, J.T., Engler, B.P., Smith, J.A., Onyia, E.C., Tolman, D.N., 2007. Predrill estimation of subsalt fracture gradient: Analysis of the Spa prospect to validate nonlinear finite element stress analyses, SPE/IADC Drilling Conference and Exhibition. Society of Petroleum Engineers, Amsterdam, Netherlands, pp. 835-842.

Fredrich, J.T., Fossum, A.F., 2002. Large-scale three-dimensional geomechanical modeling of reservoirs; examples from California and the deepwater Gulf of Mexico. Oil & Gas Science and Technology 57, 423-441.

Gaarenstroom, L., Tromp, R.A.J., de Jong, M.C., Brandenburg, A.M., 1993. Overpressures in the central North Sea; implications for trap integrity and drilling safety. Petroleum Geology of Northwest Europe 4, 1305-1313.

Gaillot, P., Brewer, T., Pezard, P., E., Y., 2007. Borehole Imaging Tools - Principles and Applications. Scientific Drilling 5, 1-4.

Gast, R., Pasternak, M., Piske, J., Rasch, H.-J., 1998. Das Rotliegend im nordostdeutschen Raum: Regionale Übersicht, Stratigraphie, Fazies und Diagenese. Geologisches Jahrbuch 149, 59-79.

Gast, R.E., 1988. Rifting in the Rotliegendes of Lower Saxony - Rifting im Rotliegenden Niedersachsens. Die Geowissenschaften (Weinheim, Zeitschrift) 6, 115-122.

Gast, R.E., 1991. The Perennial Rotliegend Saline Lake in NW Germany. Geologisches Jahrbuch 119, 25-59.

Gast, R.E., 1995. Norddeutsches Rotliegendbecken: Rotliegend Monographie Teil II, in: Plein, E. (Ed.), Stratigraphie von Deutschland I. Senckenbergischen Naturforschenden Gesellschaft Frankfurt a.M.

Gast, R.E., Gesner, E., Gundlach, T., 1999. Optimisation of Facies Prediction based on Grainsize Analysis with High Resolution Scanner (Rotliegend, NW-Germany), in: Lippard, S.J., Naess, A., Sinding-Larsen, R. (Eds.), IAMG 1999, Trondheim, pp. 343-348.

Gast, R.G., Thomas 2006. Permian strike slip and extensional tectonics in Lower Saxony, Germany. Zeitschrift der deutschen Gesellschaft für Geowissenschaften 157, 41-56.

Gaupp, R., Baunack, C., Pudlo, D., Solms, M., Trappe, H., Schubarth-Engelschall, J., Samiee, R., Littke, R., Schwarzer, D., Oncken, O., Krawczyk, C., Tanner, D., 2005. Paläo-Öl- und Gasfelder im Rotliegenden des Norddeutschen Beckens: Wirkung der KW-Migration auf die Speicherqualitäts-Entwicklung. Deutsche Wissenschaftliche Gesellschaft für Erdöl, Erdgas und Kohle e.V. (DGMK), p. 242.

Gaupp, R., Matter, A., Platt, J., Ramseyer, K., Walzebuck, J., 1993. Diagenesis and Fluid Evolution of Deeply Buried Permian (Rotliegende) Gas-Reservoirs, Northwest Germany. AAPG Bulletin 77, 1111-1128.

Gebhardt, U., Schneider, J., Hoffmann, N., 1991. Stratigraphic and basin-development models for the Rotliegendes of the North German Basin - Modelle zur Stratigraphie und Beckenentwicklung im Rotliegenden der Norddeutschen Senke. Geologisches Jahrbuch. Reihe A: Allgemeine und Regionale Geologie BR Deutschland und Nachbargebiete, Tektonik, Stratigraphie, Palaeontologie 127, 405-427.

Geertsma, J., 1973. Land subsidence above compacting oil and gas reservoirs. Journal of Petroleum Technology 25, 734-744.

Gercek, H., 2007. Poisson's ratio values for rocks. International Journal of Rock Mechanics and Mining Sciences 44, 1-13.

Gerling, P., Geluk, M.C., Kockel, F., Lokhorst, A., Nicholson, R.A., 1999. NW European gas atlas - new implications for the Carboniferous gas plays in the western part of the southern Permian Basin. Petroleum Geology of Northwest Europe 5, 799-808.

Glennie, K.W., 1972. Permian Rotliegendes of Northwest Europe Interpreted in Light of Modern Desert Sedimentation Studies. AAPG Bulletin 56, 1048-1071.

Glennie, K.W., 1983. Early Permian (Rotliegendes) palaeowinds of the North Sea. Sedimentary Geology 34, 245-265.

Glennie, K.W., 1990. Outline of North Sea History & Structural Framework, in: Glennie, K.W. (Ed.), Introduction to the Petroleum Geology of the North Sea. Blackwell Scientific Publications, pp. 34-77.

Glennie, K.W., 1998. Petroleum geology of the North Sea; basic concepts and recent advances. Blackwell Science, p. 636.

Glennie, K.W., 2007. The Permo-Carboniferous Rotliegend of NW Europe, in: Wong, T.E. (Ed.), Proceedings of the XVth International Congress on Carboniferous and Permian Stratigraphy. Netherlands Academy of Arts and Science, pp. 10-16.

Glennie, K.W., Provan, D.M.J., 1990. Lower Permian Rotliegend reservoir of the southern North Sea gas province. Geological Society Special Publications 50, 399-416.

Gluyas, J., Swarbrick, R., 2004. Petroleum Geoscience. Blackwell Science, p. 359.

Godse, A.P., Godse, D.A., 2009. Fundamentals of Computing and Programming. Technical Publications Pune, p. 580.

Goodman, J.E., O'Rourke, J., 2004. Handbook of Discrete and Computational Geometry, 2 ed. Chapman & Hall / CRC, p. 1560.

Gray, D., Anderson, P., Logel, J., F., D., Schmidt, D., Schmid, R., 2012. Estimation of stress and geomechanical properties using 3D seismic data. First Break 30, 59-68.

Grote, R., 1998. Die rezente horizontale Hauptspannung im Rotliegenden und Oberkarbon in Norddeutschland. Erdöl Erdgas Kohle 114, 478-483.

Guo, L., Latham, J.-P., Xiang, J., Lei, Q., 2013. A Numerical Investigation of Fracture Pattern and Fracture Aperture Development in Multi-layered Rock using a Combined Finite-Discrete Element Method, 47th US Rock Mechanics / Geomechanics Symposium, San Francisco, USA.

Hamdi, P., Stead, D., Elmo, D., 2013. Numerical simulation of damage during laboratory testing on rock using a 3D-FEM/DEM approach, 47th US Rock Mechanics / Geomechanics Symposium, San Francisco, USA.

Harris, G.W., 1974. Sandbox model used to examine the stress distribution around a simulated longwall coal-face. International Journal of Rock Mechanics and Mining Sciences 11, 325-335.

Heffer, K., 2002. Geomechanical influences in water injection projects; an overview. Oil & Gas Science and Technology 57, 415-422.

Heffer, K., Lean, J.C., 1993. Earth stress orientation - a control on, and guide to, flooding directionality in a majority of reservoirs, in: Linville, W. (Ed.), Reservoir Characterization III. PennWell Books, p. 1056.

Heffer, K.J., Koutsabeloulis, N.C., 1995. Stress effects on reservoir flow; numerical modelling used to reproduce field data. Geological Society Special Publications 84, 81-88.

Henk, A., 2005. Pre-drilling prediction of the tectonic stress field with geomechanical models. First Break 23, 53-57.

Henk, A., 2006. Stress and strain during fault-controlled lithospheric extension; insights from numerical experiments. Tectonophysics 415, 39-55.

Henk, A., 2009. Perspectives of geomechanical reservoir models – why stress is important. Oil Gas European Magazine 35, 20-24.

Henk, A., 2010. Geomechanical reservoir models – a case study from the Sirte Basin, Libya. Oil Gas European Magazine 1, 18-22.

Henk, A., Nemcok, M., 2008. Stress and fracture prediction in inverted half-graben structures. Journal of Structural Geology 30, 81-97.

Hennings, P., Allwardt, P., Paul, P., Zahm, C., Reid, R., Alley, H., Kirschner, R., Lee, B., Hough, E., 2012. Relationship between fractures, fault zones, stress, and reservoir productivity in the Suban gas field, Sumatra, Indonesia. AAPG Bulletin 96, 753-772.

Herwanger, J., Koutsabeloulis, N.C., 2011. Seismic Geomechanics - How to build and calibrate geomechanical models using 3D and 4D seismic data, 1 ed. EAGE Publications b.v., Houten, p. 181.

Hirsch, C., 2007. Numerical Computation of Internal and External Flows: Introduction to the Fundamentals of CFD, 2 ed. Butterworth-Heinemann, p. 680.

Hoffmann, N., 1990. Zur paläodynamischen Entwicklung des Präzechsteins in der Nordostdeutschen Senke. Geowissenschaftliche Veröffentlichung der Niedersächsischen Akademie der Wissenschaften 4, 5-18.

Hoffmann, N., Joedicke, H., Gerling, P., 2001. The distribution of pre-Westphalian source rocks in the North German Basin; evidence from magnetotelluric and geochemical data. Geologie en Mijnbouw. Netherlands Journal of Geosciences 80, 71-84.

Holt, R.M., Fjær, E., Bauer, A., 2013. Static and Dynamic Moduli – so equal, and yet so different, 47th US Rock Mechanics / Geomechanics Symposium, San Francisco, USA.

Homberg, C., Hu, J.C., Angelier, J., Bergerat, F., Lacombe, O., 1997. Characterization of stress perturbations near major fault zones: insights from 2-D distinct-element numerical modelling and field studies (Jura mountains). Journal of Structural Geology 19, 703-718.

Huebner, K.H., Dewhirst, D.L., Smith, D.E., Byrom, T.G., 2001. The Finite Element Method for Engineers, 4 ed. Wiley, p. 744.

Huenges, E., Erzinger, J., Kueck, J., Engeser, B., Kessels, W., 1997. The permeable crust; geohydraulic properties down to 9101 m depth. Journal of Geophysical Research 102, 18255-18265.

Jaeger, J.C., Cook, N.G.W., Zimmerman, R.W., 2007. Fundamentals of Rock Mechanics, 4 ed. Blackwell Publishing, p. 475.

Jing, L., Stephansson, O., 2007. Fundamentals of Discrete Element Methods for Rock Engineering: Theory and Applications. Elsevier, p. 545.

Johnston, P.F., Wachi, N., 1994. Estimation of natural fracture orientation using borehole imaging logs and vertical seismic profiles at Orcutt oil field, California, USA. Proceedings - World Petroleum Congress 14, 147-148.

Jones, R.M., Hillis, R.R., 2003. An integrated, quantitative approach to assessing fault-seal risk. AAPG Bulletin 87, 507-524.

Judd, W.R., 1964. Rock stress, rock mechanics and research, in: Judd, W.R. (Ed.), State of stress in the earth's crust. Elsevier, pp. 5-51.

Katsikiadelis, J.T., 2002. Boundary Elements: Theory and Applications. Elsevier p. 330.

Kayser, A., 2006. Herkunft, Auftreten und Visualisierung von Permeabilitätsbarrieren in einer Gaslagerstätte in Sandsteinen des Rotliegenden (Südliches Permbecken, Deutschland) - Bedeutung für Diagenese, Fluidfluß und Produktion. Dissertation. Philipps-Universität Marburg, p. 206.

Kiersnowski, H., Paul, J., Peryt, T.M., Smith, D.B., 1995. Facies, paleogeography, and sedimentary history of the southern Permian basin in Europe, in: Scholle, P.A., Peryt, T.M., Ulmer-Scholle, D.S. (Eds.), The Permian of northern Pangea - Sedimentary basins and economic resources. Springer, pp. 119-136.

Kinzelbach, W., 1992. Numerische Methoden zur Modellierung des Transports von Schadstoffen im Grundwasser, 2 ed. R. Oldenbourg Verlag GmbH, p. 343.

Kley, J., Franzke, H.J., Jähne, F., Krawczyk, C., Lohr, T., Reicherter, K., Scheck-Wenderoth, M., Sippel, J., Tanner, D., van Gent, H., 2008. Strain and Stress, in: Littke, R., Bayer, U., Gajewski, D., Nelskamp, S. (Eds.), Dynamics of Complex Intrakontinental Basins - The Central European Basin System. Springer, pp. 97-124.

Knipe, R.J., Fisher, Q.J., Jones, G., Clennell, M.B., Farmer, B., Kidd, B., McAllister, E., Porter, J.R., White, E.A., 1997. Fault seal prediction methodologies, applications and successes, in: Mùller-Pedersen, P., Koestler, A.G. (Eds.), Hydrocarbon seals - importance for exploration and production. Elsevier, Amsterdam, pp. 15-38.

Koupriantchik, D., Hunt, S.P., Boult, P.J., Meyers, A.G., 2007. Geomechanical modelling of salt diapirs; 3D salt structure from the Officer Basin, South Australia. Special Publication - Northern Territory Geological Survey, 388-396.

Krawczyk, C.M., Eilts, F., Lassen, A., Thybo, H., 2002. Seismic evidence of Caledonian deformed crust and uppermost mantle structures in the northern part of the Trans-European Suture Zone, SW Baltic Sea. Tectonophysics 360, 215-244.

Krawczyk, C.M., Rabbel, W., Willert, S., Hese, F., Götze, H.-J., Gajewski, D., Group, S.-G., 2008. Crustal structures and properties in the Central European Basin System from geophysical evidence, in: Littke, R., Bayer, U., Gajewski, D., Nelskamp, S. (Eds.), Dynamics of Complex Intrakontinental Basins - The Central European Basin System. Springer, pp. 67-95.

Lampe, C., Song, G., Cong, L., Mu, X., 2012. Fault control on hydrocarbon migration and accumulation in the Tertiary Dongying Depression, Bohai Basin, China. AAPG Bulletin 96, 983-1000.

Lee, S., 1994. Fracture Identification and Evaluation Using Borehole Imaging and Full Wave Form Logs in the Permian Basin. AAPG Bulletin 78, 497.

LeVeque, R., 2007. Finite Difference Methods for Ordinary and Partial Differential Equations: Steady-State and Time-Dependent Problems. Society for Industrial and Applied Mathematics, p. 184.

Lin, W., Yamamoto, K., Ito, H., Masago, H., Kawamura, Y., 2008. Estimation of Minimum Principal Stress from an Extended Leak-off Test Onboard the Chikyu Drilling Vessel and Suggestions for Future Test Procedures. Scientific Drilling 6, 43-47.

Littke, R., Bayer, U., Gajewski, D., 2005. Dynamics of sedimentary basins - the example of the Central European Basin system. International Journal of Earth Sciences 94, 779-1116.

Littke, R., Bayer, U., Gajewski, D., Nelskamp, S., 2008. Dynamics of complex intracontinental basins; the Central European Basin system. Springer, p. 519.

Ljunggren, C., Chang, Y., Janson, T., Christiansson, R., 2003. An overview of rock stress measurement methods. International Journal of Rock Mechanics and Mining Sciences 40, 975-989.

Lockner, D.A., Byerlee, J.D., Kuksenko, V.S., Ponomarev, A.V., Sidorin, A., 1991. Quasi-static fault growth and shear fracture energy in granite. Nature 350, 39-42.

Longuemare, P., Mainguy, M., Lemonnier, P., Oniasi, A., Gerard, C., Koutsabeloulis, N., 2002. Geomechanics in reservoir simulation; overview of coupling methods and field case study. Oil & Gas Science and Technology 57, 471-483.

Luo, G., Nikolinakou, M.A., Flemings, P.B., Hudec, M.R., 2012. Geomechanical modeling of stresses adjacent to salt bodies: Part 1 - Uncoupled models. AAPG Bulletin 96, 43-64.

Mackay, F., Inoue, N., Fontoura, S.A.B., Botelho, F., 2008. Geomechanical effects of a 3D vertical salt well drilling by FEA, 42nd U.S. Rock Mechanics - 2nd U.S.-Canada Rock Mechanics Symposium, San Francisco, USA.

Maerten, L., Gillespie, P., Daniel, J.-M., 2006. Three-dimensional geomechanical modeling for constraint of subseismic fault simulation. AAPG Bulletin 90, 1337-1358.

Maerten, L., Gillespie, P., Pollard, D.D., 2002. Effects of local stress perturbation on secondary fault development. Journal of Structural Geology 24, 145-153.

Mastin, L., 1984. The development of borehole breakouts in sandstone. M.Sc. Thesis. Stanford University, p. 100.

Matsuki, K., 2008. Anelastic strain recovery compliance of rocks and its application to in situ stress measurement. International Journal of Rock Mechanics and Mining Sciences 45, 952-965.

Maugeri, L., 2012. Oil: The Next Revolution - The unprecedented upsurge of oil production capacity and what it means for the world. Discussion Paper #2012-10. John F. Kennedy School of Government, Harvard University, p. 86.

Maystrenko, Y., Bayer, U., Brink, H.-J., Littke, R., 2008. The Central European Basin System - an Overview, in: Littke, R., Bayer, U., Gajewski, D., Nelskamp, S. (Eds.), Dynamics of Complex Intrakontinental Basins - The Central European Basin System. Springer, pp. 17-34.

McCann, T., 1998. The Rotliegend of the NE German Basin: background and prospectivity. Petroleum Geoscience 4, 17-27.

Menning, M., Hendrich, A., (Eds.), 2012. Stratigraphic Table of Germany. Deutsche Stratigraphische Kommission, STDKe 2012.

Middleton, G.V., Wilcock, P.R., 1994. Mechanics in the Earth and Environmental Sciences. Cambridge University Press, p. 476.

Minkoff, S.E., Stone, C.M., Bryant, S., Peszynska, M., Wheeler, M.F., 2003. Coupled fluid flow and geomechanical deformation modeling. Journal of Petroleum Science and Engineering 38, 37-56.

Moeck, I., Backers, T., 2006. New ways in understanding borehole breakouts and wellbore stability by fracture mechanics based numerical modeling, EAGE 68th Conference and Exhibition, Vienna, Austria.

Moeck, I., Schandelmeier, H., Holl, H.-G., 2009. The stress regime in a Rotliegend reservoir of the Northeast German Basin. International Journal of Earth Sciences 98, 1643-1654.

Mohamed, F.R., Rasmussen, A., Wendt, A.S., Murineddu, A., 2008. High resolution 3D Mechanical Earth Model using seismic neural netmodeling - Integrating geological, petrophysical and geophysical data, 70th EAGE Conference and Exhibition, Rome, Italy.

Morales, R.H., Marcinew, R.P., 1993. Fracturing of high-permeability formations: Mechanical properties correlations, Proceedings of the SPE Annual Technical Conference and Exhibition. Society of Petroleum Engineers, Houston, USA, pp. 467-475.

Morris, A., Ferrill, D.A., Henderson, D.B., 1996. Slip-tendency analysis and fault reactivation. Geology 24, 275-278.

Morris, A.P., Smart, K.J., Ferrill, D.A., Reish, N.E., Cowell, P.F., 2012. Production-induced fault compartmentalization at Elk Hills Field, California. AAPG Bulletin 96, 1001-1015.

Müller, G., Groth, C., 2000. FEM für Praktiker, 4 ed. Expert Verlag, p. 807.

Munjiza, A., Owen, D.R.J., Bicanic, N., 1995. A combined finite-discrete element method in transient dynamics of fracturing solids. Engineering Computations 12, 145-174.

Nagy, Z.R., Lee, D.W., Sayers, C.M., Zapata, T.R., Silvestro, J.L., 2013. Iterative 3D geomechanical modeling to determine distribution and impact of stresses in deepwater Gulf of Mexico subsalt and near-salt environments, 47th US Rock Mechanics / Geomechanics Symposium, San Francisco, USA.

Newman, W.I., 2012. Continuum Mechanics in the Earth Sciences. Cambridge University Press, p. 182.

Nikolinakou, M.A., Luo, G., Hudec, M.R., Flemings, P.B., 2012. Geomechanical modeling of stresses adjacent to salt bodies: Part 2 - Poroelastoplasticity and coupled overpressures. AAPG Bulletin 96, 65-85.

Nikolinakou, M.A., Merrell, M.P., Luo, G., B., F.P., Hudec, M.R., 2013. Geomechanical modeling of the Mad Dog salt, Gulf of Mexico, 47th US Rock Mechanics / Geomechanics Symposium. American Rock Mechanics Association, San Francisco, USA.

Nur, A., Byerlee, J.D., 1971. An exact effective stress law for elastic deformation of rock with fluids. Journal of Geophysical Research 76, 6414-6419.

Ohlmacher, G.C., Aydin, A., 1997. Mechanics of vein, fault and solution surface formation in the Appalachian Valley and Ridge, northeastern Tennessee, USA: implications for fault friction, state of stress and fluid pressure. Journal of Structural Geology 19, 927-944.

Oñate, E., Rojek, J., 2004. Combination of discrete element and finite element methods for dynamic analysis of geomechanics problems. Computer Methods in Applied Mechanics and Engineering 193, 3087-3128.

Oreskes, N., Shrader-Frechette, K., Belitz, K., 1994. Verification, Validation, and Confirmation of Numerical Models in the Earth Sciences. Science 263, 641-646.

Orlic, B., 2013. Site-specific geomechanical modeling for predicting stress changes around depleted gas reservoirs considered for CO2 storage in the Netherlands, 47th US Rock Mechanics / Geomechanics Symposium, San Francisco, USA.

Orlic, B., Wassing, B.B.T., 2013. A study of stress change and fault slip in producing gas reservoirs overlain by elastic and viscoelastic caprocks, Special Issue: New and Exciting Advances, 3 ed. Springer, Vienna, Austria, pp. 421-435.

Orlic, B., Wassing, B.B.T., Geel, C.R., 2013. Field scale geomechanical modeling for prediction of fault stability during underground gas storage operations in a depleted gas field in the Netherlands, 47th US Rock Mechanics / Geomechanics Symposium, San Francisco, USA.

Ostadhassan, M., Benson, S., Zamiran, S., Bubach, B., 2013. Stress Analysis and Wellbore Stability in Unconventional Reservoirs, 47th US Rock Mechanics / Geomechanics Symposium, San Francisco, USA.

Paillet, F.L., Kim, K., 1987. Character and distribution of borehole breakouts and their relationship to in situ stresses in deep Columbia River Basalts. Journal of Geophysical Research 92, 6223-6234.

Patankar, S.V., 1980. Numerical Heat Transfer & Fluid Flow. Taylor & Francis Inc, p. 197.

Peska, P., Zoback, M.D., 1995. Compressive and tensile failure of inclined well bores and determination of in situ stress and rock strength. Journal of Geophysical Research 100, 12,791-712,811.

Piegl, L., Tiller, W., 2010. The NURBS Book, 2 ed. Springer, p. 664.

Plein, E., 1995. Norddeutsches Rotliegendbecken: Rotliegend Teil II. Deutsche Stratigraphische Kommission, p. 193.

Plumb, R.A., Hickman, S.H., 1985. Stress-induced borehole elongation; a comparison between the four-arm dipmeter and the borehole televiewer in the Auburn geothermal well. Journal of Geophysical Research 90, 5513-5521.

Pollard, D.D., Fletcher, R.C., 2005. Fundamentals of Structural Geology. Cambridge University Press, p. 512.

Popov, Y., 2008. Recent evolution in experimental thermal petrophysics. Geophysical Research Abstracts 10, EGU2008-A-11943.

Popov, Y., Parshin, A., Miklashevskiy, D., Abashkin, V., 2012. Instrument for measurements of linear thermal expansion coefficient of rocks, 46th US Rock Mechanics / Geomechanics Symposium, Chicago, USA, pp. 402-409.

Popov, Y., Tertychnyi, V., Romushkevich, R., Korobkov, D., Pohl, J., 2003. Interrelations between thermal conductivity and other physical properties of rocks; experimental data. Pure and Applied Geophysics 160, 1137-1161.

Poppelreiter, M., Balzarini, M.A., De Sousa, P., Engel, S., Galarraga, M., Hansen, B., Marquez, X., Morell, J., Nelson, R., Rodriquez, F., 2005. Structural control on sweet-spot distribution in a carbonate reservoir: Concepts and 3-D models (Cogollo Group, Lower Cretaceous, Venezuela). AAPG Bulletin 89, 1651-1676.

Potyondy, D.O., Cundall, P.A., 2004. A bonded-particle model for rock. International Journal of Rock Mechanics and Mining Sciences 41, 1329-1364.

Pouya, A., Chalhoub, M., 2008. Numerical homogenization of elastic behavior of fractured rock masses and micro-cracked materials by FEM, 12th International Conference on Computer Methods and Advances in Geomechanics, Goa, India, pp. 403-410.

Qiao, L.P., Wong, R.C.K., Aguilera, R., Kantzas, A., 2012. Determination of biot's effective-stress coefficient for permeability of nikanassin sandstone. Journal of Canadian Petroleum Technology 51, 193-197.

Ramsay, J.G., Huber, M.I., 1997. The Techniques of Modern Structural Geology: Folds and Fractures. Academic Press, p. 406.

Ramsay, J.G., Lisle, R., 2000. The Techniques of Modern Structural Geology: Applications of Continuum Mechanics in Structural Geology, 3 ed. Academic Press, p. 1061.

Ren, N.K., Hudson, P.J., 1985. Predicting the in-situ state of stress using differential wave velocity analysis. Proceedings of the Symposium on Rock Mechanics 26, 1235-1244.

Reynolds, S.D., Mildren, S.D., Hillis, R.R., Meyer, J.J., 2006. Constraining stress magnitudes using petroleum exploration data in the Cooper–Eromanga Basins, Australia. Tectonophysics 415, 123-140.

Richardson, R.M., Solomon, S.C., Sleep, N.H., 1976. Intraplate stress as an indicator of plate tectonic driving forces. Journal of Geophysical Research 81, 1847-1856.

Rieke, H., Kossow, D., McCann, T., Krawczyk, C., 2001. Tectono-sedimentary evolution of the northernmost margin of the NE German Basin between uppermost Carboniferous and Late Permian (Rotliegend). Geological Journal 36, 19-38.

Robinson, E., Clark, D., 1988. Elasticity: Hooke's law. The Leading Edge 7, 58-60.

Röckel, T., Lempp, C., 2003. The State of Stress in the North German Basin. Erdöl Erdgas Kohle 119, 73-80.

Rodriguez-Herrera, A.E., S.-R., R., Handwerger, D., Herring, S., Stevens, K., Marino, S., Paddock, D., L., S., M., H., 2013. Field-scale geomechanical characterization of the Haynesville Shale, 47th US Rock Mechanics / Geomechanics Symposium, San Francisco, USA.

Rogers, S.F., 2003. Critical stress-related permeability in fractured rocks. Geological Society Special Publications 209, 7-16.

Roth, F., Bäsler, H., Weigold, G., Fuchs, K., Palmer, J., Fleckenstein, P., 1998. Spannungsmessungen in Osteuropa – Orientierungsdaten aus Nordost-Deutschland, Weißrussland und der Ukraine, ICDP/KTB-Kolloquium, Wissenschaftliches Programm und Abstracts, Bochum, Germany.

Roth, F., Fleckenstein, P., 2001. Stress orientations found in NE Germany differ from the West European trend. Terra Nova 13, 289-296.

Rutqvist, J., 2012a. Geomechanical aspects of CO2 sequestration and modeling, 12th International Congress on Rock Mechanics of the International Society for Rock Mechanics. Taylor and Francis Inc., Beijing, China, pp. 1803-1808.

Rutqvist, J., 2012b. The Geomechanics of CO2 Storage in Deep Sedimentary Formations. Geotechnical and Geological Engineering 30, 525-551.

Rutqvist, J., Rinaldi, A.P., Cappa, F., Moridis, G.J., 2013. Modeling of fault reactivation and induced seismicity during hydraulic fracturing of shale-gas reservoirs. Journal of Petroleum Science and Engineering 107, 31-44.

Rutter, E.H., Hackston, A.J., Yeatman, E., Brodie, K.H., Mecklenburgh, J., May, S.E., 2013. Reduction of friction on geological faults by weak-phase smearing. Journal of Structural Geology 51, 52-60.

Samier, P., Onaisi, A., de Gennaro, S., 2008. A practical iterative scheme for coupling geomechanics with reservoir simulation. SPE Reservoir Evaluation and Engineering 11, 892-901.

Sassi, W., Faure, J.-L., 1997. Role of faults and layer interfaces on the spatial variation of stress regimes in basins: inferences from numerical modelling. Tectonophysics 266, 101-119.

Scheck-Wenderoth, M., Lamarche, J., 2005. Crustal memory and basin evolution in the Central European Basin System - new insights from a 3D structural model. Tectonophysics 397, 143-165.

Scheck, M., Bayer, U., 1997. The North German Basin; subsidence history and basin configuration. Schriftenreihe der Deutschen Geologischen Gesellschaft 2, 100.

Scheck, M., Bayer, U., 1999. Evolution of the Northeast German Basin - inferences from a 3D structural model and subsidence analysis. Tectonophysics 313, 145-169.

Scheibe, R., Seidel, K., Vormbaum, M., Hoffmann, N., 2005. Magnetic and gravity modelling of the crystalline basement in the North German Basin. Zeitschrift der deutschen Gesellschaft für Geowissenschaften 156, 291-298.

Schiott, C.R., Bertrand-Biran, V., Hansen, H.J., Koutsabeloulis, N., Westeng, K., 2008. Time-lapse inversion and geomechanical modelling of the South Arne Field. First Break 26, 85-91.

Schöner, R., Lüders, V., Ondrak, R., Gaupp, R., Möller, P., 2008. Fluid-rock interactions, in: Littke, R., Bayer, U., Gajewski, D., Nelskamp, S. (Eds.), Dynamics of Complex Intrakontinental Basins - The Central European Basin System. Springer, pp. 389-410.

Schroeder, L., Loesch, J., Schoneich, H., Stancu-Kristoff, G., Tafel, W.D., 1991. Oil and gas in the Northwest German Basin. Special Publication of the European Association of Petroleum Geoscientists 1, 139-148.

Schroeder, L., Plein, E., Bachmann, G.H., Gast, R.E., Gebhardt, U., Graf, R., Helmuth, H.-J., Pasternak, M., Porth, H., Suessmuth, S., 1995. Stratigraphic reclassification of the Rotliegendes in the North German Basin. Geologisches Jahrbuch. Reihe A: Allgemeine und Regionale Geologie BR Deutschland und Nachbargebiete, Tektonik, Stratigraphie, Palaeontologie 148, 1-21.

Schwarz, H.R., 1991. Methode der finiten Elemente. Teubner Verlag, Stuttgart, p. 436.

Schwarz, M., 2005. Evolution und Struktur des Oberrheingrabens - quantitative Einblicke mit Hilfe dreidimensionaler thermomechanischer Modellrechnungen. Dissertation. Albert-Ludwigs-Universität Freiburg, p. 342.

Schwarzer, D., Littke, R., 2007. Petroleum generation and migration in the 'Tight Gas' area of the German Rotliegend natural gas play: a basin modelling study. Petroleum Geoscience 13, 37-62.

Seyferth, M., 2001. Numerische Modellierungen kontinentaler Kollisionszonen: Quantifizierung orogener Prozesse als Beitrag zu Verständnis fossiler und rezenter Orogene. Dissertation. Bayerische Julius-Maximilian-Universität Würzburg, p. 237.

Seyferth, M., Henk, A., 2002. Coupling of PFC2D and ANSYS® – concepts to combine the best of two worlds for improved geodynamic models, in: Konietzky, H. (Ed.), Numerical Modeling in Micromechanics via Particle Methods. Balkema Publishers, pp. 283-290.

Seyferth, M., Henk, A., 2005. A numerical sandbox: high-resolution distinct element models of halfgraben formation. International Journal of Earth Sciences 95, 189-203.

Sibson, R.H., 1974. Frictional constraints on thrust, wrench and normal faults. Nature 249, 542-544.

Sibson, R.H., 1996. Structural permeability of fluid-driven fault-fracture meshes. Journal of Structural Geology 18, 1031-1042.

Simo, J.C., Laursen, T.A., 1992. An Augmented Lagrangian Treatment of Contact Problems Involving Friction. Computers & Structures 42, 97-116.

Sippel, J., Scheck-Wenderoth, M., Reicherter, K., Mazur, S., 2009. Paleostress states at the south-western margin of the Central European Basin System — Application of fault-slip analysis to unravel a polyphase deformation pattern. Tectonophysics 470, 129-146.

Sone, H., Zoback, M.D., 2013. Analysis of intra-reservoir stress variations in shale gas reservoirs based on the variation of viscoelastic properties, 47th US Rock Mechanics / Geomechanics Symposium, San Francisco, USA.

Spencer, A.J.M., 2004. Continuum Mechanics. Dover Publications p. 183.

Sperner, B., Mueller, B., Heidbach, O., Delvaux, D., Reinecker, J., Fuchs, K., 2003. Tectonic stress in the Earth's crust; advances in the World Stress Map project. Geological Society Special Publications 212, 101-116.

Stankowich, R.J., Ewy, R., 2003. Mechanical behavior of some clays and shales from 200 m to 3800 m depth, 39th U.S. Rock Mechanics Symposium/12th Panamerican Conference on Soil Mechanics and Geotechnical Engineering, Cambridge, USA.

Steinbuch, R., 1998. Finite Elemente - Ein Einstieg. Springer, p. 284.

Steinhauser, M.O., 2007. Computational Multiscale Modeling of Fluids and Solids: Theory and Applications. Springer, p. 428.

Stollhofen, H., Bachmann, G.H., Barnasch, J., Bayer, U., Beutler, G., Franz, M., Kästner, M., Legler, B., Mutterlose, J., Radies, D., 2008. Upper Rotliegend to Early Cretaceous basin development, in: Littke, R., Bayer, U., Gajewski, D., Nelskamp, S. (Eds.), Dynamics of Complex Intrakontinental Basins - The Central European Basin System. Springer, pp. 181-210.

Stüwe, K., 2007. Geodynamics of the Lithosphere. Springer, p. 504.

Suarez-Rivera, R., Handwerger, D., Rodriguez Herrera, A., Herring, S., Stevens, K., Vaaland, G.D., Borgos, H., Marino, S., Paddock, D., 2013. Development of a Heterogeneous Earth Model in Unconventional Reservoirs, for Early Assessment of Reservoir Potential, 47th US Rock Mechanics / Geomechanics Symposium, San Francisco, USA.

Tamagawa, T., Pollard, D.D., 2008. Fracture permeability created by perturbed stress fields around active faults in a fractured basement reservoir. AAPG Bulletin 92, 743-764.

Terheege, J.H., Wassing, B.B.T., Orlic, B., Giger, S.B., Clennell, M.B., 2013. Constraints on the sealing capacity of faults with clay smears from discrete element models validated by laboratory experiments, Special Issue: New and Exciting Advances, 3 ed. Springer Vienna, Austria, pp. 465-478.

Terzaghi, K.v., 1923. Theoretical Soil Mechanics. John Wiley, New York, p. 510.

Townend, J., 2003. Mechanical constraints on the strength of the lithosphere and plate-bounding faults. Dissertation. Stanford University, p. 135.

Townend, J., Zoback, M.D., 2000. How faulting keeps the crust strong. Geology 28, 399-402.

Trautwein, U., 2005. Poroelastische Verformung und petrophysikalische Eigenschaften von Rotliegend Sandsteinen. Dissertation. Technische Universität Berlin, p. 141.

Turcotte, D.L., Oxburgh, E.R., 1974. The Driving Mechanism for Plate Tectonics and the State of Stress in the Lithosphere. Eos, Transactions, American Geophysical Union 55, 438.

Turner, P., Jones, M., Prosser, D.J., Williams, G.D., Searl, A., 1993. Structural and sedimentological controls on diagenesis in the Ravenspurn North gas reservoir, UK southern North Sea. Petroleum Geology of Northwest Europe 4, 771-785.

Twiss, R.J., Moores, E.M., 2007. Structural Geology, 2 ed. W.H. Freeman and Company, p. 532.

Vackiner, A.A., 2013. Sedimentary Facies Reconstruction and Kinematic Restoration of Tight Gas Fields: Studies from the Upper Permian in Northwestern Germany. Springer, p. 160.

van der Neut, J., Sen, M.K., Wapenaar, K., 2008. Seismic reflection coefficients of faults at low frequencies: A model study, What Can E and P Learn from Seismology and Vice Versa, 3 ed. Blackwell Publishing Ltd, Oxford, United Kingdom, pp. 287-292.

van der Pluijm, B.A., Marshak, S., 2003. Earth Structure: An Introduction to Structural Geology and Tectonics, 2 ed. W. W. Norton & Company, p. 672.

van Hulten, F.F.N., 2010. Geological factors effecting compartmentalization of Rotliegend gas fields in the Netherlands. Geological Society Special Publications 347, 301-315.

van Wees, J.-D., Stephenson, R.A., Ziegler, P.A., Bayer, U., McCann, T., Dadlez, R., Gaupp, R., Narkiewicz, M., Bitzer, F., Scheck, M., 2000. On the origin of the Southern Permian Basin, Central Europe. Marine and Petroleum Geology 17, 43-59.

van Wees, J.D., Orlic, B., van Eijs, R., Zijl, W., Jongerius, P., Schreppers, G.J., Hendriks, M., Cornu, T., 2003. Integrated 3D geomechanical modelling for deep subsurface deformation: a case study of tectonic and human-induced deformation in the eastern Netherlands, in: Nieuwland, D.A. (Ed.), New Insights into Structural Interpretation and Modelling. Geological Society, London, pp. 313-328.

Vernik, L., Zoback, M.D., Brudy, M., 1992. Methodology and application of the wellbore breakout analysis in estimating the maximum horizontal stress magnitude in the KTB pilot hole. Scientific Drilling 3, 161-169.

Vidal-Gilbert, S., Nauroy, J.-F., Brosse, E., 2009. 3D geomechanical modelling for CO2 geologic storage in the Dogger carbonates of the Paris Basin. International Journal of Greenhouse Gas Control 3, 288-299.

Vidal-Gilbert, S., Tenthorey, E., Dewhurst, D., Ennis-King, J., Van Ruth, P., Hillis, R., 2010. Geomechanical analysis of the Naylor Field, Otway Basin, Australia: Implications for CO2 injection and storage. International Journal of Greenhouse Gas Control 4, 827-839.

Wang, H.F., 2000. Theory of linear poroelasticity with applications to geomechanics and hydrogeology. Princeton University Press, Princeton, USA, p. 276.

Wang, H.F., Anderson, M.P., 1982. Introduction to Groundwater Modeling: Finite Difference and Finite Element Methods. Academic Press, p. 237.

Yale, D.P., 2003. Fault and stress magnitude controls on variations in the orientation of in situ stress, in: Ameen, M. (Ed.), Fracture and In-Situ Stress Characterization of Hydrocarbon Reservoirs. Geological Society, London, pp. 55-64.

Yegorova, T., Maystrenko, Y., Bayer, U., Scheck-Wenderoth, M., 2008. The Glueckstadt Graben of the North-German Basin: new insights into the structure from 3D and 2D gravity analyses. International Journal of Earth Sciences 97, 915-930.

Yielding, G., Bretan, P., Freeman, B., 2010. Fault seal calibration; a brief review. Geological Society Special Publications 347, 243-255.

Yielding, G., Freeman, B., Needham, D.T., 1997. Quantitative fault seal prediction. AAPG Bulletin 81, 897-917.

Zang, A., Stephansson, O., Heidbach, O., Janouschkowetz, S., 2012. World Stress Map Database as a Resource for Rock Mechanics and Rock Engineering. Geotechnical and Geological Engineering 30, 625-646.

Zhang, X., Koutsabeloulis, N., Heffer, K., 2007. Hydromechanical modeling of critically stressed and faulted reservoirs. AAPG Bulletin 91, 31-50.

Ziegler, P.A., 1990. Geological Atlas of Western and Central Europe, 2 ed. Shell Internationale Petroleum Mij. B.V., The Hague, Netherlands, p. 256.

Ziegler, P.A., Dezes, P., 2006. Crustal evolution of Western and Central Europe. Memoirs of the Geological Society of London 32, 43-56.

Zienkiewicz, O.C., Taylor, R.L., 2005. The Finite Element Method for Solid and Structural Mechanics, 6 ed. Elsevier Butterworth-Heinemann, p. 736.

Zienkiewicz, O.C., Taylor, R.L., Zhu, J.Z., 2005. The Finite Element Method: Its Basis and Fundamentals, 6 ed. Elsevier Butterworth-Heinemann, p. 752.

Zoback, M.D., 2007. Reservoir Geomechanics. Cambridge University Press, p. 461.

Zoback, M.D., Barton, C.A., Brudy, M., Castillo, D.A., Finkbeiner, T., Grollimund, B.R., Moos, D.B., Peska, P., Ward, C.D., Wiprut, D.J., 2003. Determination of stress orientation and magnitude in deep wells. International Journal of Rock Mechanics and Mining Sciences 40, 1049-1076.

Zoback, M.D., Healy, J.H., 1984. Friction, faulting and "in situ" stress. Annales Geophysicae 2, 689-698.

Zoback, M.D., Healy, J.H., 1992. In situ stress measurements to 3.5 km depth in the Cajon Pass scientific research borehole; implications for the mechanics of crustal faulting. Journal of Geophysical Research 97, 5039-5057.

Zoback, M.D., Moos, D., Mastin, L., Anderson, R.N., 1985. Well bore breakouts and in situ stress. Journal of Geophysical Research 90, 5523-5530.

Zoback, M.D., Townend, J., 2001. Implications of hydrostatic pore pressures and high crustal strength for the deformation of intraplate lithosphere. Tectonophysics 336, 19-30.

Zoback, M.D., Townend, J., Grollimund, B., 2002. Steady-state failure equilibrium and deformation of intraplate lithosphere. International Geology Review 44, 383-401.

Zoback, M.D., Zoback, M.L., Mount, V.S., Suppe, J., Eaton, J.P., Healy, J.H., Oppenheimer, D.H., Reasenberg, P.A., Jones, L.M., Raleigh, C.B., Wong, I.G., Scotti, O., Wentworth, C.M., 1987. New evidence on the state of stress of the San Andreas fault system. Science 238, 1105-1111.

Zoback, M.L., 1992. First- and second-order patterns of stress in the lithosphere; the World Stress Map Project. Journal of Geophysical Research 97, 11,703-728.

Zoback, M.L., Zoback, M.D., Adams, J., Assumpcao, M., Bell, S., Bergman, E.A., Bluemling, P., Brereton, N.R., Denham, D., Ding, J., Fuchs, K., Gay, N., Gregersen, S., Gupta, H.K., Gvishiani, A., Jacob, K., Klein, R., Knoll, P., Magee, M., Mercier, J.L., Mueller, B.C., Paquin, C., Rajendran, K., Stephansson, O., Suarez, G., Suter, M., Udias, A., Xu, Z.H., Zhizin, M., 1989. Global patterns of tectonic stress. Nature 341, 291-298.

13 Appendix

The appendix of this thesis is provided on the attached DVD. It contains the following files:

1) The dissertation in PDF format.

2) Original plots of the geomechanical models:

   I. Static Model – Results of the calibrated model

   II. Static Model – Results of the uncalibrated model

   III. Static Model – Slip Tendency distribution with decreasing fault friction

   IV. Static Model – Results of the submodel

   V. Dynamic Model – Results integrated over all tectonic stages

   VI. Dynamic Model – Stage-specific results

   VII. Dynamic Model – Stage-specific vector plots & stereoplots at well locations

Statement of Authorship / Erklärung

I hereby certify that this thesis has been composed by myself and describes my own work unless otherwise acknowledged in the text. All references and verbatim extracts have been quoted and all sources of information have been specifically acknowledged. This thesis has not been accepted in any previous application for a degree.

Hiermit versichere ich, dass ich die vorliegende Arbeit selbstständig und ohne Benutzung anderer als der angegebenen Hilfsmittel angefertigt habe. Stellen, die wörtlich oder sinngemäß aus anderen Schriften entnommen sind, sind als solche kenntlich gemacht. Die Arbeit ist in gleicher oder ähnlicher Form noch nicht als Prüfungsarbeit eingereicht worden.

Darmstadt, den 11.09.2013 Unterschrift 

CURRICULUM VITAE

FISCHER, KARSTEN

WORK EXPERIENCE

MAR 2012 – PRESENT
Institute of Applied Geosciences, Technische Universität Darmstadt
Scientific Staff and PhD Student in the Group of Engineering Geology

AUG 2008 – DEZ 2012
HTCO GmbH – Engineering Consultants (www.htco.de), Freiburg
Member of Scientific Staff

OCT 2010 – MAR 2012
Institute of Geosciences, Albert-Ludwigs-Universität Freiburg
Scientific Staff and PhD Student in the Group of Applied Geology

APR 2010 – SEP 2010
Institute of Geosciences, Albert-Ludwigs-Universität Freiburg
Research Assistant in the Group of Applied Geology

EDUCATION

OCT 2008 – OCT 2010
Institute of Geosciences, Albert-Ludwigs-Universität Freiburg
Studies in 'Geology'
Master of Science (M.Sc.), Final Grade: 1.1

OCT 2005 – SEP 2008
Institute of Geosciences, Albert-Ludwigs-Universität Freiburg
Studies in 'Geosciences'
Bachelor of Science (B.Sc.), Final Grade: 1.5

JUL 2004
Theodor-Heuss-Gymnasium Freiburg
General Qualification for University Entrance, Final Grade: 1.9

SOFTWARE SKILLS

MS Office (Word, Excel, Powerpoint, Outlook, Access), Adobe Illustrator, Adobe Photoshop, Prezi

Petrel, Ansys Classic (Mechanical APDL), Autodesk Inventor, Star-CCM+, Spaceclaim, Gambit, Ansys Workbench & Fluent, Geomagic Studio, Surfer

MEMBERSHIPS

AAPG, DGG, EAGE